

**UNIVERSITAT POLITÈCNICA DE VALÈNCIA**

DOCTORADO EN INGENIERÍA Y PRODUCCIÓN INDUSTRIAL



**UNIVERSITAT  
POLITÈCNICA  
DE VALÈNCIA**



Instituto de Tecnología de los Materiales

## **DOCTORAL THESIS**

**Procesado y caracterización de formulaciones industriales de poliésteres alifáticos mediante tecnologías de inyección y fabricación aditiva**

**Processing and characterization of industrial formulations of aliphatic polyesters by injection moulding and additive manufacturing technologies**

**Author:**

Juan Ivorra Martínez

**Supervised by:**

Dr. Rafael Antonio Balart Gimeno

Dr. Teodomiro Boronat Vitoria

February 2023



A todos los que han aportado su granito de arena para que esto sea posible.





“Sube despacio, firme y con constancia, y al acabar de escalar la montaña solo disfruta el momento y agradece a aquellos que lo hicieron posible.”

**V.M.G.**



## ACKNOWLEDGEMENTS

First of all, I would like to thank the unconditional support of my thesis directors Rafa and Teo. Thank you Rafa for spreading your love for work and your never-ending knowledge ambition. Secondly, I really appreciate Teo because all I know about processing techniques is his doing.

I also thank the ministry of universities for their financial support through the FPU grant FPU19/01759 regarding my PhD studies.

I am very grateful to Universitat Politècnica de València for their financial support through the FPI PhD grant PAID-2019- SP20190011.

I thank the ministry of science and innovation for their financial support to the research group in the projects RTI2018-097249-B-C21, MAT2017-84909-C2-2-R and PID2020-116496RB-C22.

I acknowledge Generalitat Valenciana for their grants AICO/2021/025 and CIGE/2021/094 as a support to the research group.

I am also grateful to the Sociedad de Ingeniería de Fabricación – SIF for their financial support in the two stays I have made abroad.

I thank the technological institute of materials – ITM and the Universitat Politècnica de València's campus of Alcoy, in which the present work was carried out.

Many thanks to the professors David García, Juan López and Lourdes Sánchez, who, along with the rest of the members of the research group helped to acquire the equipment needed in the laboratories.

I also thank Octavio Fenollar, Néstor Montañés, Dani García and Mado, who shared with me all the knowledge they possess in an altruistic way in order to grow up altogether.

I really appreciate the work of the laboratory technicians Matías, Javi, Rafa and Pedro, for their excellent maintenance of the laboratories all these years and for their help in the different daily problems that appeared.

I also thank my laboratory colleagues: Diego, Sandra, Antonio, Pelayo, Harrison and Cris for having taken part in this stage of my life.

I thank Ines Ferrer and Universitat of Girona for having taken me in their facilities for carrying out my research. Also, to María Luisa and Marc Delgado for helping me in doing my experimental work.

I can't thank enough Professor Luigi Torre and Universidad of Perugia in Italia for welcoming me in their university. To Debora and Franco for their guidance during my stay in Terni. I would like to especially thank Franco for letting me be his "extrusorista" and for transmitting me all his vast knowledge in such a short time.

I want to dedicate a special acknowledgement to Luis and Jaume for those great moments we spent together in Italy and for those equally special moment inside and outside of the laboratory. I also want to especially thank Ramón, for being a true companion who I could always trust. And finally, I am very grateful to Virginia, who, in spite of having been a very short time in our group, she always transmits positivism and intensity to our daily routine.

## **Procesado y caracterización de formulaciones industriales de poliésteres alifáticos mediante tecnologías de inyección y fabricación aditiva.**

El principal objetivo de la presente tesis doctoral se centra en la obtención de poliésteres alifáticos con propiedades mejoradas para su empleo en procesos industriales aplicando técnicas de fabricación específicas de polímeros como son el proceso de inyección o la fabricación aditiva. Para alcanzar dicho objetivo se proponen diferentes estrategias como la incorporación de aditivos plastificantes de origen natural, la incorporación de cargas naturales, la obtención de mezclas con otros polímeros, así como la incorporación de aditivos orientados al sector médico.

En una primera fase, se han estudiado los poliésteres alifáticos de la familia de los polihidroxicanoatos - PHA. Las modificaciones realizadas a los polihidroxicanoatos van desde la incorporación de residuos de cáscara de almendra para la obtención de composites, el desarrollo de mezclas binarias con poli( $\epsilon$ -caprolactona) para la mejora de las propiedades dúctiles y el análisis del efecto de diferentes plastificantes derivados de terpenoides, concretamente ésteres de geraniol. En esta primera fase se propone el uso del moldeo mediante inyección para la determinación precisa de las propiedades que alcanzan las formulaciones tras las modificaciones realizadas.

Posteriormente se propone el uso de los polihidroxicanoatos para su empleo en el sector médico debido a sus propiedades biocompatibles y bioabsorbibles. En un primer momento se opta por analizar el efecto de los parámetros a emplear en fabricación aditiva empleando PHA, siendo polímeros con una ventana de procesado bastante estrecha, y con una alta sensibilidad al grado de cristalinidad que alcanzan en función de las condiciones de enfriamiento. La incorporación de aditivos osteoconductores como la hidroxiapatita tiene un especial interés para la mejora del proceso de regeneración ósea; es por ello que se considera como aditivo para PHA en el sector médico. En un primer trabajo, se propone el uso del proceso de moldeo por inyección para determinar las propiedades que se obtienen con la incorporación de las nanopartículas de hidroxiapatita. Posteriormente, esas mismas formulaciones se emplean en impresión 3D para ofrecer una aplicación más directa al sector médico mediante la obtención de *scaffolds* que pueden ser empleados en procesos de regeneración ósea.

Finalmente, esta tesis aborda el empleo de ácido poliláctico - PLA, empleando las técnicas de conformado mediante inyección y fabricación aditiva. El PLA es un

## RESUMEN

---

poliéster alifático con propiedades y coste interesante, pero presenta una elevada fragilidad; es por ello que el uso de plastificantes naturales derivados de ésteres del ácido itacónico ofrece una especial relevancia para el desarrollo de formulaciones con alta ductilidad. Adicionalmente, el PLA es un material con alto interés en fabricación aditiva. El empleo de diferentes patrones y la cantidad de relleno tiene un efecto marcado sobre el comportamiento mecánico de los componentes fabricados mediante impresión 3D, que también está vinculado con el tiempo necesario para completar la impresión. Una de las aplicaciones interesantes de la fabricación aditiva con PLA, es la fabricación de dispositivos médicos con la capacidad de ser reabsorbidos por el cuerpo humano de forma progresiva. En este sentido se propone el diseño y validación de una prótesis de fijación ósea para fémur.

---

**Processament i caracterització de formulacions industrials de polièsters alifàtics mitjançant tecnologies d'injecció i fabricació additiva.**

El principal objectiu de la present tesi doctoral se centra en l'obtenció de polièsters alifàtics amb propietats millorades per al seu ús en processos industrials aplicant tècniques de fabricació específiques de polímers com són el procés d'injecció o la fabricació additiva. Per a aconseguir aquest objectiu es proposen diferents estratègies com la incorporació d'additius plastificants d'origen natural, la incorporació de càrregues naturals, l'obtenció de mescles amb altres polímers, així com la incorporació d'additius orientats al sector mèdic.

En una primera fase, s'han estudiat els polièsters alifàtics de la família dels polihidroxicanoats - PHA. Les modificacions realitzades als polihidroxicanoats van des de la incorporació de residus de corfa d'ametla per a l'obtenció de compòsits, el desenvolupament de mescles binàries amb poli( $\epsilon$ -caprolactona) per a la millora de les propietats dúctils i l'anàlisi de l'efecte de diferents plastificants derivats de terpenoids, concretament èsters de geraniol. En aquesta primera fase es proposa l'ús del moldeig mitjançant injecció per a la determinació precisa de les propietats que aconseguen les formulacions després de les modificacions realitzades.

Posteriorment es proposa l'ús d'aquests polihidroxicanoats per al seu ús en el sector mèdic donat que tenen propietats biocompatibles i bioabsorbibles. En un primer moment s'opta per analitzar l'efecte dels paràmetres a emprar en fabricació additiva en els utilitzant PHA, donat que es tracta de polímers amb una finestra de processament bastant estreta, i amb una alta sensibilitat pel grau de cristal·linitat que aconseguen en funció de les condicions de refredament. La incorporació d'additius osteoconductors com la hidroxiapatita té un especial interès per a la millora del procés de regeneració òssia; és per això que es considera com a additiu per a PHA per al sector mèdic. En un primer treball, es proposa l'ús del procés de moldeig per injecció per a determinar les propietats que s'aconsegueixen amb la incorporació de les nanopartícules d'hidroxiapatita. Posteriorment, aqueixes mateixes formulacions s'utilitzen en impressió 3D per oferir una aplicació més directa al sector mèdic mitjançant l'obtenció d'*scaffolds* que poden ser emprats en processos de regeneració òssia.

Finalment, aquesta tesi aborda l'ús de l'àcid polilàctic - PLA emprant les tècniques de conformat mitjançant injecció i fabricació additiva. El PLA és un polièster alifàtic amb propietats i cost interessants, però presenta una elevada fragilitat; és per això que l'ús de plastificants naturals derivats d'èsters de l'àcid itacònic té una especial

## RESUM

---

rellevància per al desenvolupament de formulacions amb alta ductilitat. Addicionalment, el PLA és un material amb alt interès en fabricació additiva. L'ús de diferents patrons i la quantitat de farciment té un efecte marcat sobre el comportament mecànic dels components fabricats mitjançant impressió 3D, que també està vinculat amb el temps necessari per a completar la impressió. Una de les aplicacions interessants de la fabricació additiva amb PLA, és la fabricació de dispositius mèdics amb la capacitat de ser reabsorbits pel cos humà de manera progressiva. En aquest sentit es proposa el disseny i validació d'una pròtesi de fixació òssia per a fèmur.



**Processing and characterization of industrial formulations of aliphatic polyesters by injection moulding and additive manufacturing technologies.**

The main objective of this thesis is to obtain aliphatic polyesters with improved properties for their application in industrial processes by applying conventional polymer processing techniques such as injection moulding and additive manufacturing. In order to reach the aforementioned objective several strategies are proposed such as the incorporation of natural origin plasticizing additives, the incorporation of natural fillers, the development of polymer blends and the incorporation of additives for the medical sector.

The first stage of this research consists in the study of aliphatic polyesters from polyhydroxyalkanoates - PHA. The modifications made to those polymers have been the introduction of almond shell wastes to produce composites, the development of binary blends with poly( $\epsilon$ -caprolactone) to improve ductile properties and the addition of different plasticizers derived from terpenoids, more specifically geraniol esters. In this first stage, injection-moulding is proposed to obtain all the properties and features of the formulations after the aforementioned modifications.

Afterwards, the use of these polyhydroxyalkanoates in the medical sector due to they are biocompatible and resorbable, is proposed. First, the effect of the parameters to be used in additive manufacturing of PHA is analysed. These polymers possess a very narrow processing window and a great sensitiveness to the degree of crystallinity depending on the cooling conditions. The incorporation of osteoconductive additives such as hydroxyapatite is of great interest for the improvement of the bone regeneration process, so it is considered as an additive of PHA for medical applications. It is for this reason that in the first work, injection moulding is used for determining the effect of nanohydroxyapatite have on the polymer matrix. Then, the developed formulations are used in 3D printing to assess the feasibility of this technology for the medical sector by obtaining scaffolds structures that can be used in bone regeneration processes.

Finally, poly(lactic acid) - PLA is processed by injection-moulding and additive manufacturing to assess the feasibility of these techniques. PLA is a cost-effective aliphatic polyester with balanced properties; nevertheless, it shows high intrinsic brittleness. Therefore, the use of natural plasticizers derived from esters of itaconic acid are of especial interest for the development of formulations with improved toughness. Additionally, PLA is a material with a great interest in additive manufacturing. The use of different patterns and infills used in 3D printing play a key role on mechanical

## ABSTRACT

---

behavior of the 3D-printed components, which is also related to the overall 3D-printing time. One of the interesting applications of additive manufacturing with PLA, is the production of medical devices with the ability to be progressively reabsorbed by the human body. In this sense, the design and validation of a femur fixing prosthesis is proposed.

# TABLE OF CONTENT.

LIST OF ARTICLES. ....	17
EQUATIONS. ....	19
ABBREVIATIONS. ....	23
I. INTRODUCTION. ....	29
<b>I.1. Polymers in engineering.</b> .....	<b>31</b>
I.1.1. Polymers and the environment. ....	31
I.1.2. Classification of polymers attending to environmental issues. ....	32
I.1.3. Recent trends in biopolymer uses and applications. ....	35
<b>I.2. Biobased and biodegradable aliphatic polyesters.</b> ....	<b>46</b>
I.2.1. Poly(lactic acid) – PLA. ....	46
I.2.2. Poly(hydroxyalkanoates) – PHA. ....	50
I.2.3. Modification of polyesters. ....	54
<b>I.3. Additive Manufacturing – AM.</b> .....	<b>62</b>
I.3.1. Additive manufacturing processes. ....	63
I.3.2. Medical Additive Manufacturing applications. ....	64
I.3.3. Additive manufacturing processes. ....	69
I.3.4. Materials used in Additive Manufacturing for medical applications. ....	70
II. OBJECTIVES. ....	77
<b>II.1. General objectives.</b> ....	<b>79</b>
<b>II.2. Partial objectives.</b> .....	<b>79</b>
III. RESULTS & DISCUSSION. ....	83
<b>Section I: Development of environmentally friendly formulations and composites with polyhydroxyalkanoates.</b> .....	<b>89</b>
III.1.1 Manufacturing and properties of binary blend from bacterial polyester poly(3-hydroxybutyrate-co-3-hydroxyhexanoate) and poly( $\epsilon$ -caprolactone) with improved toughness. ....	91
III.1.2 Development and characterization of sustainable composites from bacterial polyester poly(3-hydroxybutyrate-co-3-hydroxyhexanoate) and almond shell flour by reactive extrusion with oligomers of lactic acid. ....	127
III.1.3 Plasticization of poly(3-hydroxybutyrate) with biobased terpenoid esters of geraniol. ....	171
<b>Section II: Manufacturing of polyhydroxyalkanoates by 3D printing and injection moulding for medical applications.</b> ....	<b>203</b>

III.2.1 The effects of processing parameters on mechanical properties of 3D-printed polyhydroxyalkanoates parts. ....	205
III.2.2 Assessment of the mechanical and thermal properties of injection-moulded poly(3-hydroxybutyrate-co-3-hydroxyhexanoate)/hydroxyapatite nanoparticles parts for use in bone tissue engineering. ....	243
III.2.3 P(3HB-co-3HHx)/nanohydroxyapatite (nHA) composites for the manufacturing of scaffolds by means of fused deposition modelling. ....	283
<b>Section III: Development of environmentally friendly formulations of polylactide for injection moulding and 3D printing. ....</b>	<b>317</b>
III.3.1 The potential of an itaconic acid diester as environmentally friendly plasticizer for injection-moulded polylactide parts. ....	319
III.3.2 Effect of infill parameters on mechanical properties in additive manufacturing. ....	367
III.3.3 Design and simulation of a resorbable bone fixation plate made by Additive Manufacturing for femoral MID-shaft fractures. ....	389
<b>IV. CONCLUSIONS. ....</b>	<b>409</b>
<b>IV.1. Partial conclusions. ....</b>	<b>411</b>
IV.1.1. With regard to the development of environmentally friendly formulations and composites with polyhydroxyalkanoates. ....	411
IV.1.2. With regard to the manufacturing of polyhydroxyalkanoates by 3D printing and injection moulding for medical applications. ....	412
IV.1.3. With regard to the development of environmentally friendly formulations of polylactide for injection moulding and 3D printing. ....	413
<b>IV.2 General conclusions. ....</b>	<b>414</b>
<b>VI. REFERENCES. ....</b>	<b>415</b>
<b>VII. APPENDIX. ....</b>	<b>437</b>
<b>VII.1. Table index. ....</b>	<b>439</b>
<b>VII.2. Figure index. ....</b>	<b>442</b>

# LIST OF ARTICLES.

The present doctoral thesis has been structured and carried out on the basis of the compendium of the following articles:

- I. Manufacturing and properties of binary blend from bacterial polyester poly(3-hydroxybutyrate-*co*-3-hydroxyhexanoate) and poly( $\epsilon$ -caprolactone) with improved toughness.
- II. Development and characterization of sustainable composites from bacterial polyester poly(3-hydroxybutyrate-*co*-3-hydroxyhexanoate) and almond shell flour by reactive extrusion with oligomers of lactic acid.
- III. Plasticization of poly(3-hydroxybutyrate) with biobased terpenoid esters of geraniol.
- IV. The effects of processing parameters on mechanical properties of 3D-printed polyhydroxyalkanoates parts.
- V. Assessment of the mechanical and thermal properties of injection-moulded poly(3-hydroxybutyrate-*co*-3-hydroxyhexanoate)/nanohydroxyapatite parts for use in bone tissue engineering.
- VI. P(3HB-*co*-3HHx)/nanohydroxyapatite (nHA) composites for the manufacturing of scaffolds by means of fused deposition modelling.
- VII. The potential of an itaconic acid diester as environmentally friendly plasticizer for injection-moulded polylactide parts.
- VIII. Effect of infill parameters on mechanical properties in additive manufacturing.
- IX. Design and simulation of a resorbable bone fixation plate made by additive manufacturing for femoral MID-shaft fractures.



# EQUATIONS.

---

$$W_l (\%) = \frac{W_d - W_0}{W_0} 100$$

$W_l$  = Weight loss.

$W_d$  = Weight of dry sample after a period of testing.

$W_0$  = Initial weight of the sample.

---

$$W_g (\%) = \frac{W_t - W_0}{W_0} 100$$

$W_g$  = Weight gain.

$W_t$  = Weight of the sample after a period of testing.

$W_0$  = Initial weight of the sample.

---

$$\frac{W_t}{W_s} = \frac{4}{d} \left( \frac{D t}{\pi} \right)^{1/2}$$

$\frac{W_t}{W_s}$  = Linear representation for calculating the diffusion coefficient.

$d$  = Initial sample thickness.

$D$  = Diffusion coefficient.

---

$$D_c = D \left( 1 + \frac{d}{h} + \frac{d}{w} \right)^{-2}$$

$D_c$  = Diffusion coefficient correction coefficient.

$h$  = Sample length.

$w$  = Sample width.

$d$  = Sample thickness.

---

$$\text{Total porosity} = 1 - \frac{\rho_{\text{scaffold}}}{\rho_{\text{material}}}$$

Total porosity = Porosity value of a scaffold.

$\rho_{\text{scaffold}}$  = Density of the scaffold calculate with the apparent volume and its weight.

$\rho_{\text{material}}$  = Measured density of the material.

---

---


$$\chi_c(\%) = \frac{\Delta H_m - \Delta H_{cc}}{\Delta H_m^0 (1 - w)} 100$$

$\chi_c$  = Degree of crystallinity.

$\Delta H_m$  = Melting enthalpy.

$\Delta H_{cc}$  = Cold crystallization enthalpy.

$\Delta H_m^0$  = Melting enthalpy of the theoretical 100 % crystalline polymer.

w = Weight fraction of the polymer.

---

$$\delta = \sqrt{\delta_d^2 + \delta_p^2 + \delta_h^2}$$

$\delta$  = Solubility parameter.

$\delta_d$  = Dispersive forces contribution to the solubility parameter.

$\delta_p$  = Polar forces contribution to the solubility parameter.

$\delta_h$  = Hydrogen bond contribution to the solubility parameter.

---

$$\delta_d = \frac{\sum F_{di}}{V_m}$$

$\delta_d$  = Dispersive forces contribution to the solubility parameter.

$F_{di}$  = Dispersive forces.

$V_m$  = Molar volume.

---

$$\delta_p = \frac{\sqrt{\sum F_{pi}^2}}{V_m}$$

$\delta_p$  = Polar forces contribution to the solubility parameter.

$F_{pi}$  = Polar forces.

$V_m$  = Molar volume.

---

$$\delta_h = \frac{\sqrt{\sum E_{hi}}}{V_m}$$

$\delta_h$  = Hydrogen bond contribution to the solubility parameter.

$E_{hi}$  = Hydrogen bonding energy.

$V_m$  = Molar volume.

---



---

$$R_a = \sqrt{4(\delta_{d2} - \delta_{d1})^2 + (\delta_{p2} - \delta_{p1})^2 + (\delta_{h2} - \delta_{h1})^2}$$

$R_a$  = Geometrical distance between the solubility parameters.

$\delta_{d2} - \delta_{d1}$  = Difference between the dispersive forces contribution of two materials.

$\delta_{p2} - \delta_{p1}$  = Difference between the polar forces contribution of two materials.

$\delta_{h2} - \delta_{h1}$  = Difference between the hydrogen bond forces contribution of two materials.

---

$$RED = \frac{R_a}{R_0}$$

RED = Relative Energy Difference.

$R_a$  = Geometrical distance between the solubility parameters.

$R_0$  = Radius of the solubility sphere.

---



# ABBREVIATIONS.

<b>3HB</b>	3-hydroxybutyrate.
<b>3HHx</b>	3-hydroxyhexanoic.
<b>3HV</b>	3-hydroxyvaleric.
<b>ABS</b>	Poly(acrylonitrile–butadiene–styrene).
<b>AM</b>	Additive Manufacturing.
<b>ASF</b>	Almond Shell Flour.
<b>ATBC</b>	Acetyl tributyl citrate.
<b>ATEC</b>	Acetyl triethyl citrate.
<b>BJ</b>	Binder Jetting.
<b>BN</b>	Boron Nitride.
<b>CAD</b>	Computer Aided Design.
<b>CLTE</b>	Coefficient of Linear Thermal Expansion.
<b>CNC</b>	Computer Numerical Control.
<b>CT</b>	Computed Tomography.
<b>DBI</b>	Dibutyl itaconate.
<b>DEA</b>	Diethyl adipate.
<b>DED</b>	Directed Energy Deposition.
<b>DLMS</b>	Direct Metal Laser Sintering.
<b>DMTA</b>	Dynamic–Mechanic Thermal Analysis.
<b>DOA</b>	Diisooctyl adipate.
<b>DSC</b>	Differential Scanning Calorimetry.
<b>DTG</b>	Differential Thermogravimetry Curve.
<b>E'</b>	Storage modulus.

<b>E''</b>	Loss modulus.
<b>EG</b>	Ethylene Glycol.
<b>E<sub>hi</sub></b>	Cohesive energy group contribution.
<b>ELO</b>	Epoxidized Linseed Oil.
<b>EO</b>	Ethylene Oxide.
<b>EVOs</b>	Epoxidized Vegetable Oils.
<b>F<sub>di</sub></b>	Molar attraction constant related with the dispersive forces.
<b>FDM</b>	Fused Deposition Modelling.
<b>FEM</b>	Finite Element Modelling.
<b>FESEM</b>	Field Emission Scanning Electron Microscopy.
<b>FFF</b>	Fused Filament Fabrication.
<b>F<sub>pi</sub></b>	Molar attraction constant related with the polar forces.
<b>FTIR</b>	Fourier-Transform Infrared Spectroscopy.
<b>GA</b>	Glycolide Acid.
<b>HA</b>	Hydroxyapatite.
<b>IA</b>	Itaconic Acid.
<b>LENS</b>	Laser-Engineered Net Shaping.
<b>ME</b>	Material Extrusion.
<b>MFI</b>	Melt Flow Index.
<b>MJ</b>	Material Jetting.
<b>MRI</b>	Magnetic Resonance Imaging.
<b>M<sub>w</sub></b>	Molecular Weight.
<b>nHA</b>	Nano hydroxyapatite.
<b>OES</b>	2-ethylhexyl epoxystearate.
<b>OLA</b>	Oligomer of Lactic Acid.

<b>P(3HB-<i>co</i>-3HHx)</b>	Poly(3-hydroxybutyrate- <i>co</i> -3-hydroxyhexanoate).
<b>P(3HB-<i>co</i>-3HV)</b>	Poly(3-hydroxybutyrate- <i>co</i> -3-hydroxyvalerate).
<b>P3HB</b>	Poly(3-hydroxybutyrate).
<b>P3HO</b>	Poly(3-hydroxyoctanoate).
<b>PA</b>	Poly(amide).
<b>PA1010</b>	Polyamide 1010.
<b>PA1012</b>	Polyamide 1012.
<b>PA11</b>	Polyamide 11.
<b>PA410</b>	Polyamide 410.
<b>PAI</b>	Poly(amide imide).
<b>PBAT</b>	Poly(butylene adipate- <i>co</i> -terephthalate).
<b>PBF</b>	Powder Bed Fusion.
<b>PBS</b>	Phosphate Saline Buffer.
<b>PBS</b>	Poly(butylene succinate).
<b>PBSA</b>	Poly(butylene succinate- <i>co</i> -adipate).
<b>PBT</b>	Poly(butylene terephthalate).
<b>PC</b>	Poly(carbonate).
<b>PC</b>	Polycondensation.
<b>PCL</b>	Poly( $\epsilon$ -caprolactone).
<b>PDLA</b>	Poly(D-lactic acid).
<b>PDO</b>	Poly(dioxanone).
<b>PE</b>	Poly(ethylene).
<b>PEG</b>	Poly(ethylene glycol).
<b>PEGA</b>	Polyethylene glycol acrylate.
<b>PEI</b>	Poly(ether imide).

<b>PEK</b>	Poly(ether ketone).
<b>PES</b>	Poly(ether sulfone).
<b>PET</b>	Poly(ethylene terephthalate).
<b>PGA</b>	Poly(glycolide).
<b>PHAs</b>	Polyhydroxyalkanoates.
<b>PHHx</b>	Poly(3-hydroxyhexanoate).
<b>phr</b>	Per Hundred Resin.
<b>PLA</b>	Poly(lactic acid).
<b>PLA-co-PCL</b>	Poly(lactide-co-caprolactone).
<b>PLGA</b>	Poly(lactide-co-glycolide).
<b>PLLA</b>	Poly(L-lactic acid).
<b>PMMA</b>	Poly(methyl methacrylate).
<b>PMO</b>	Poly(methylene oxide).
<b>POE</b>	Poly(oxyethylene).
<b>PP</b>	Poly(propylene).
<b>PPG</b>	Poly(propylene glycol).
<b>PS</b>	Poly(styrene).
<b>PUT</b>	Polyurethanes.
<b>PVA</b>	Poly(vinyl alcohol).
<b>PVC</b>	Poly(vinyl chloride).
<b>R<sub>0</sub></b>	Radius of the solubility sphere.
<b>R<sub>a</sub></b>	Geometrical distance of the solubility parameter of two materials.
<b>RED</b>	Relative Energy Difference.
<b>REX</b>	Reactive extrusion.
<b>ROP</b>	Ring-opening.

<b>SAN</b>	Poly(styrene- <i>co</i> -acrylonitrile).
<b>SFF</b>	Solid Free Form.
<b>SL</b>	Sheet Lamination.
<b>SLM</b>	Selective Laser Melting.
<b>SLS</b>	Selective Laser Sintering.
<b>TA</b>	Terephthalic Acid.
<b>tan <math>\delta</math></b>	Dynamic damping factor.
<b>TBC</b>	Tributyl citrate.
<b>T<sub>cc</sub></b>	Cold crystallization temperature.
<b>TCP</b>	Tricalcium phosphate.
<b>TEC</b>	Triethyl citrate.
<b>T<sub>g</sub></b>	Glass transition temperature.
<b>TGA</b>	Thermogravimetry analysis.
<b>T<sub>m</sub></b>	Melting temperature.
<b>TMA</b>	Thermo-Mechanical Analysis.
<b>TPA</b>	Terephthalic acid.
<b>TPS</b>	Thermoplastic starch.
<b>V<sub>m</sub></b>	Molar volume.
<b>WPC</b>	Wood Plastic Composite.
<b><math>\chi_c</math></b>	Degree of crystallinity.
<b><math>\delta</math></b>	Global solubility parameter.
<b><math>\delta_d</math></b>	Dispersive forces contribution to the solubility parameter.
<b><math>\delta_h</math></b>	Hydrogen bonding forces contribution to the solubility parameter.
<b><math>\delta_p</math></b>	Polar forces contribution to the solubility parameter.
<b><math>\Delta H_{cc}</math></b>	Cold crystallization enthalpy.

$\Delta H_m$	Melt enthalpy.
$\epsilon_b$	Elongation at break.
$\sigma_b$	Tensile strength at break.
$\sigma_f$	Flexural strength.



## **I. INTRODUCTION.**



## I.1. Polymers in engineering.

Polymeric materials have gained great relevance in different areas both industrial and high technological applications. Polymers cover a wide range of properties (mechanical, thermal, physical, biological, electrical, among others), which have favoured their wide use in commodities but, increasingly, they find new applications in engineering and high performance uses. Although the packaging sector is the largest consumer of plastic products, currently it is possible to find polymeric materials in a wide variety of sectors such as medicine and medical devices [1-3], electrical-electronics [4,5] construction and building [6-8], 3D printing [9-11], automotive [12-14], aeronautics/aerospace [15,16], among others.

However, the massive use of plastic materials unfortunately causes environmental problems since the most actual industrial polymers are obtained as petroleum derivatives, thus contributing to an increased carbon footprint, and also because they take a long time to undergo degradation [17-19].

### I.1.1. Polymers and the environment.

Concern about synthetic (petroleum-based) plastic wastes has been growing in recent decades and our society is becoming more and more environmentally aware. As a result, concepts such as recycling, upgrading, biodegradation, etc. are becoming more and more widespread in our society. Product development is increasingly integrating Life Cycle Assessment - LCA with the aim of developing changing from traditional linear economies to more sustainable circular economies [18,20,21]. In this sense, polymeric materials or plastics offer a series of problems related to environmental issues [22].

a) They cannot be easily compressed (*e.g.* plastics from the packaging sector). This is why they are large volume wastes mostly deposited in controlled landfills and, proportionally, they require a lot of space in relation to their weight.

b) Energy recover by incineration is another alternative. However, the combustion of plastics releases a large amount of toxic gases, thus contributing to global warming [23].

c) Recycling is certainly a viable option from a technical, economic and environmental point of view, plastics cannot always be recycled, as they are often contaminated, and in many cases, recycling requires costly separation processes [24].

d) In general, petroleum-based polymers do not undergo degradation over time or take extremely long periods of time. Therefore, they cannot be incorporated into the biological cycles of micro-organisms.

Polymers have, in general, the advantage of allowing very versatile manufacturing processes. Most polymers can be processed by injection moulding, extrusion, thermoforming, rotational moulding, blow moulding, and so on. In addition, the employed working temperatures are in a moderate temperature ranges compared to other materials such as metals and ceramics. Polymerization processes allow the final properties of the polymers to be tailored. In general, the high molecular weight of polymers is responsible for the polymer's resistance to biodegradation. Polymeric chains or macromolecules are extremely long to be metabolized by various microorganisms and bacteria. In fact, biodegradation stands for the ability of some microorganisms to transform or mineralize organic compounds into others, through incorporation into their metabolism. To undergo biodegradation, a series of conditions are necessary. Among these factors, it is important to highlight the moisture levels, the type and quantity of nutrients, the amount of oxygen, the pH, the temperature, and so on [25-27].

In fact, instead of biodegradation it is more correct to say that biopolymers can undergo disintegration in controlled compost soil. These conditions allow chain scission (*e.g.* by hydrolysis), so that the low molecular weight moieties can be incorporated into certain microorganisms metabolism.

### **I.1.2. Classification of polymers attending to environmental issues.**

Traditionally, polymers or plastics have been classified according to their structure (thermoplastics, thermosets or elastomers), or according to their performance: commodities, technical plastics and high performance polymers.

However, given the strong social awareness about the environment, these issues are increasingly being taken into account. These environmental issues can be related to the beginning of the life cycle of the material (petrochemical origin or renewable origin), or to the end of the life cycle (possibility of biodegradation or not). **Figure I.1.2.1.** shows schematically the classification of polymers according to these environmental criteria.

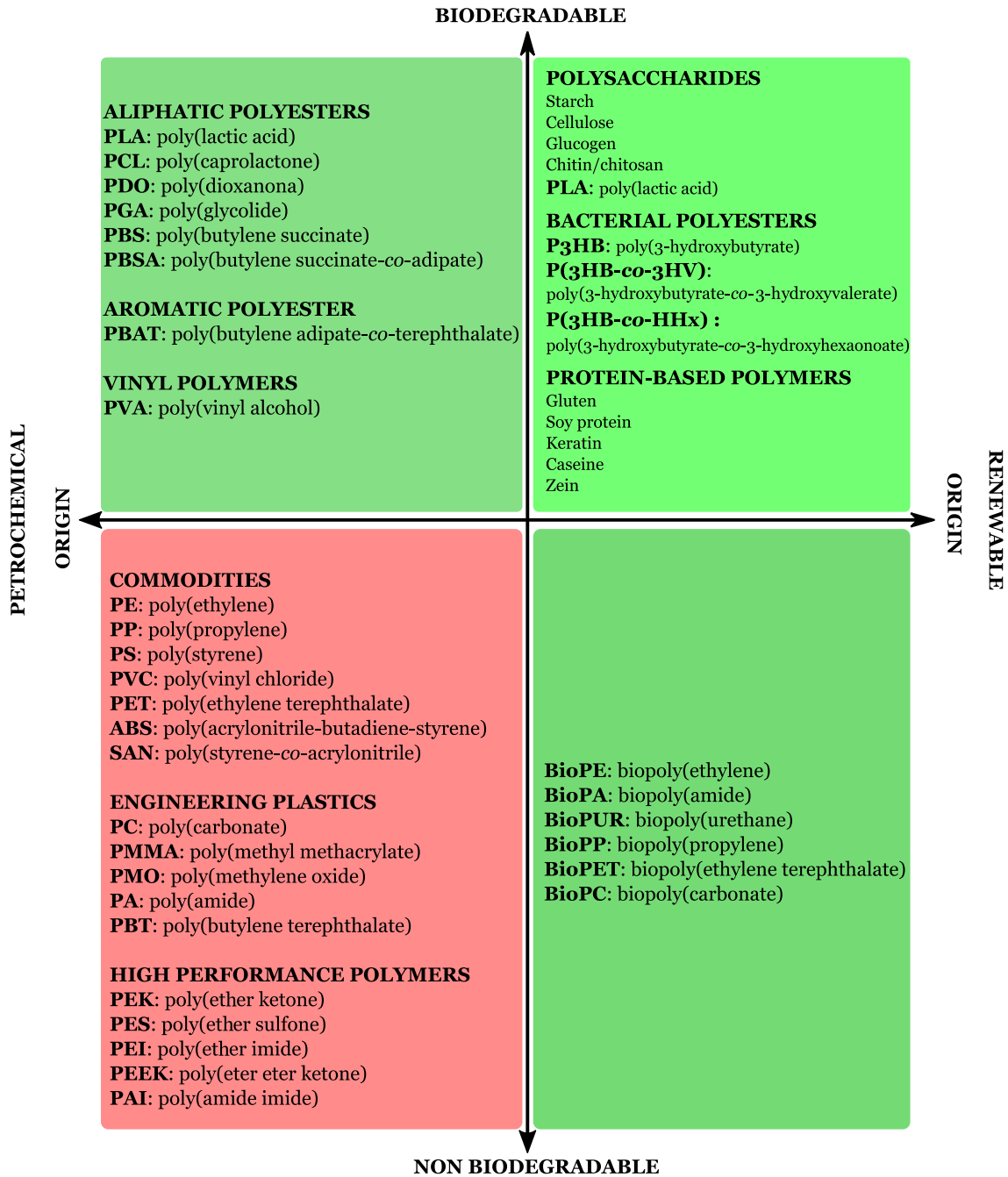


**Figure I.1.2.1.** Classification of thermoplastic polymers according to their origin (petrochemical or renewable resources) and their potential biodegradation at the end of the life cycle.

Based on environmental criteria, polymers can be classified according to their biodegradability (ability to disintegrate under controlled composting conditions) into biodegradable and non-biodegradable. As described above, biodegradability or disintegrability is the process by which bacteria, fungi, yeasts and their enzymes consume a polymeric substance as a food source such that its original form disappears. The disintegration process is a relatively quick process under appropriate conditions of moisture, pH, temperature and available oxygen [28,29].

The main requirement for a polymer to be considered as biodegradable is that it should contain labile (easily attacked or reactive) groups in its polymeric chains that can be easily broken by an external physical or chemical agent. In this sense, most biodegradable polymers contain hydrolytically unstable functional groups such as ester [30], anhydride [31], amide [32], among others. The biodegradable nature is not exclusive to polymers from renewable resources. It is possible to find a large group of petroleum-based polyesters, which can undergo biodegradation. Among these polymers, it is worth highlighting poly(glycolide) - PGA, poly( $\epsilon$ -caprolactone) - PCL, poly(butylene succinate) - PBS and its copolymer with adipic acid, poly(butylene succinate-*co*-adipate) - PBSA, poly(vinyl alcohol) - PVA, among others [33-36].

In recent years, concerns about the depletion of fossil resources and environmental pollution have driven research into other fields such as the replacement of conventional petroleum-based plastics by others derived from renewable resources such as biomass. These biopolymers offer a promising future since, on the one hand, their price is increasingly competitive (and invariable depending on the price of crude oil) and, on the other hand, the renewable origin contributes to developing circular economies and avoiding or reducing the rate of depletion of fossil resources. However, it is not all advantages in the field of biopolymers. Biopolymers have a number of limitations and disadvantages compared to petrochemical polymers, particularly in terms of performance and high production costs [37]. Thus, while a commodity plastic has a cost of about 1.0 - 1.5 €/kg (depending on the price of crude oil and availability), in the field of biopolymers it is possible to find a wide range of costs, ranging from 2.0 - 3.0 €/kg for poly(lactic acid) - PLA to almost 20 €/kg for other polyesters like PBS and PBSA or bacterial polyesters like the polyhydroxyalkanoates - PHA.

Work has also been done on the development of conventional polymers such as poly(ethylene) - PE [38,39], poly(propylene) [40], poly(amide) - PA [41,42], poly(carbonate) - PC [43,44], or even poly(ethylene terephthalate) - PET [45], from totally or partially renewable resources. These developments are interesting in that they avoid the depletion of fossil resources, but, like their analogous petroleum-derived ones, they are not biodegradable, giving rise to the same environmental problem at the end of the life cycle.

### I.1.3. Recent trends in biopolymer uses and applications.

#### I.1.3.1. Biobased but non-biodegradable polymers.

In recent years, research has focused on the development of polymers with chemical structures analogous to those obtained from petroleum, from renewable resources such as biomass. These polymers have virtually identical properties to their corresponding petrochemical counterparts, but with the advantages of being obtained from renewable feedstock. This situation has two advantages from an environmental standpoint. On the one hand, as these polymers are synthesized from renewable feedstock, they have a positive balance in relation to the carbon footprint. On the other hand, they positively contribute to reduce the depletion rate of fossil resources. Thus, for example, the biobased poly(ethylene) or bioPE, developed by the Brazilian company BrasChem is obtained from sugar cane. More specifically, bioPE is obtained from bioethanol derived from biomass fermentation, followed by a dehydration process to convert bioethanol into bioethylene, which is the building block or base-monomer for bioPE (see **Figure I.1.3.1.**) [46,47]. From bioethylene, the corresponding biopoly(ethylene) is obtained by conventional polymerization processes.

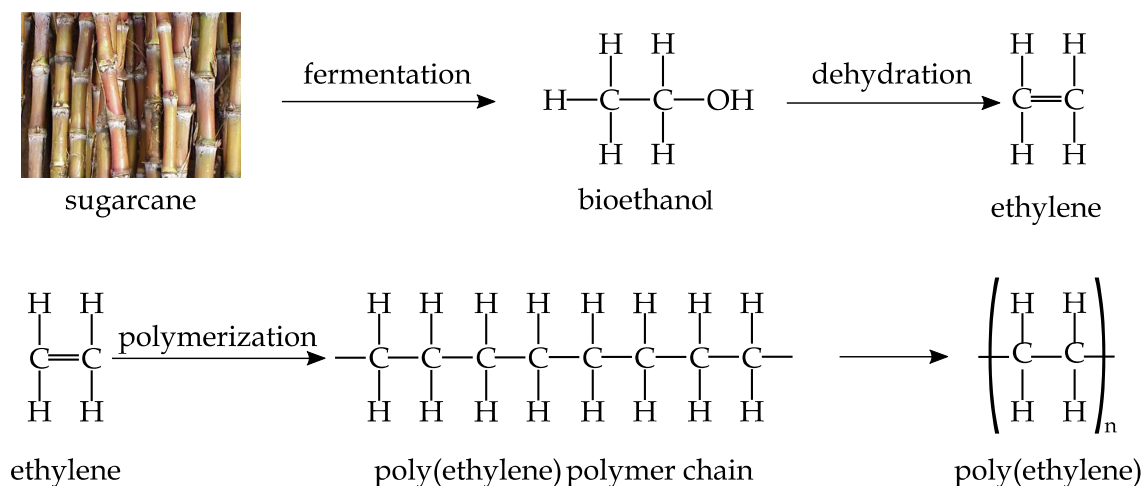


**Figure I.1.3.1.** Scheme of biobased poly(ethylene) synthesis from sugarcane.

The process of obtaining biopoly(ethylene) allows to fix up to 2.5 tons of  $\text{CO}_2$  per ton of bioPE produced, while the carbon footprint of poly(ethylene) derived from petroleum is the emission of approximately 2.0 - 2.5 tons of  $\text{CO}_2$  per ton of PE.

Biopolypropylene - bioPP can be obtained from natural resources by fermenting glucose to give isobutanol. By means of a dehydration process, butylene is obtained which, after several intermediate processes, is converted into biobased propylene which, appropriately subjected to a polymerization process, allows bioPP to be obtained.

However, the technology related to these processes is not yet mature and their use is not extensive at an industrial level. Several routes have been proposed for the synthesis of bioPP by obtaining 1,2-propanediol or acetone through fermentation processes to subsequently convert it to 2-propanol and, finally, to obtain the propylene monomer through a dehydration process [48]. Other researches include the development of partially biobased polymers such as bio poly(ethylene terephthalate) – bioPET in which, biobased ethylene glycol contributes to increase the renewable content. Some research has been conducted to fully replace terephthalic acid – TPA acid from a biobased TPA from furfural [49,50].

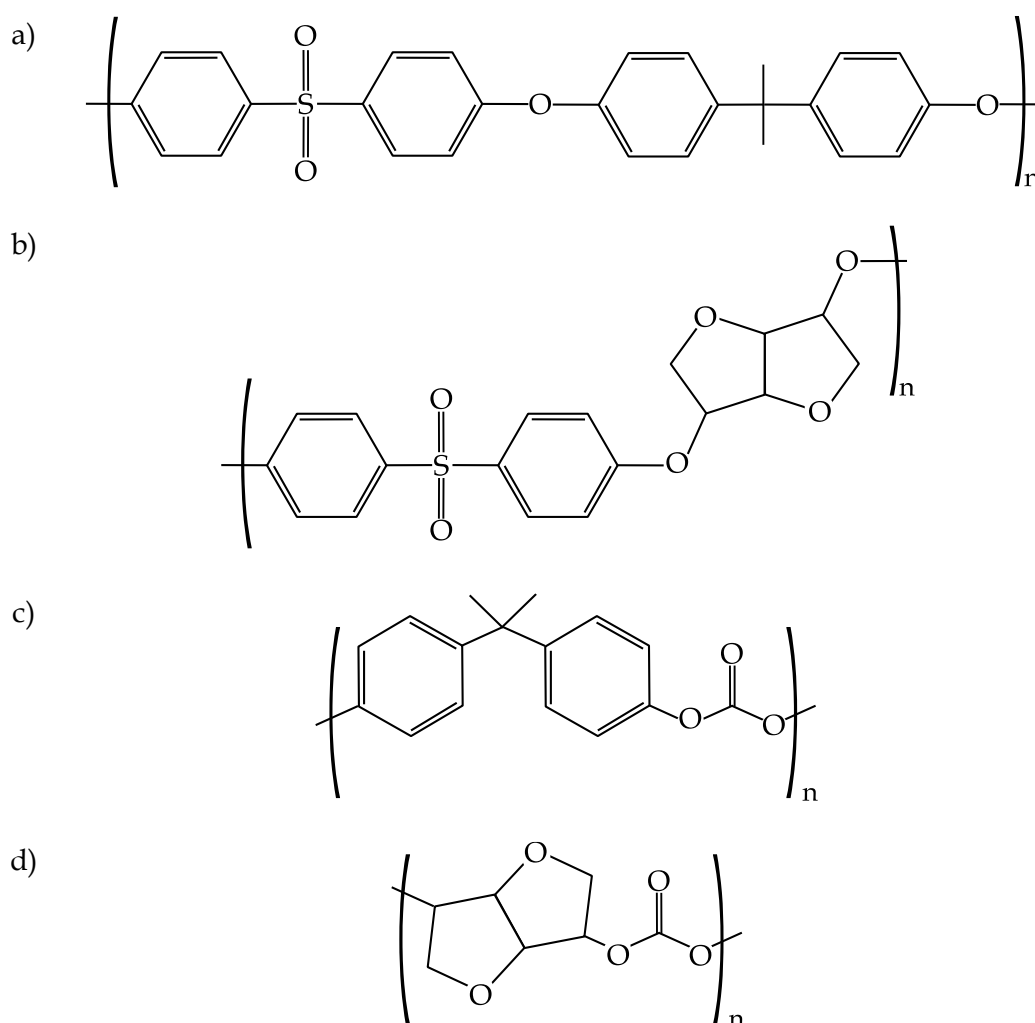


**Figure I.1.3.2.** Chemical structure of a) petroleum-based poly(sulfone), b) isosorbide-based poly(sulfone), c) petroleum-based poly(carbonate), and d) isosorbide-based poly(carbonate).

Another interesting strategy to give fully or partially biobased polymers is the replacement of some building blocks by similar biobased ones. This is the case of Bisphenol A which has been related to some toxicity problems [51]. Bisphenol A can be replaced by biobased isosorbide, which a similar chemical structure, thus giving rise to



low toxicity polymers with a high percentage of renewable content such as isosorbide-derived poly(carbonate) [52], or even high performance polymers such as isosorbide-based poly(sulfone) [53], as shown in **Figure I.1.3.2**.

As previously seen, isosorbide represents a feasible alternative to bisphenol A. Other developments include replacement of Terephthalic Acid – TA by a dicarboxylic acid from natural resources, namely 2,5-furandicarboxylic acid – FDCA, with a similar chemical structure to that of TA. Polycondensation of FDCA with biobased Ethylene Glycol – EG leads to a fully biobased and very promising polyester, *i.e.* poly(ethylene furanoate) – PEF with interesting applications in manufacturing plastic bottles, films and fibers (see **Figure I.1.3.3**) [54–56].



**Figure I.1.3.3.** Chemical structure of a) petroleum-based poly(ethylene terephthalate) and b) biobased poly(ethylene furanoate) from 2,5-furandicarboxylic acid.

Polyurethanes – PUR are a family of polymers with a wide range of applications. They are obtained by polymerization processes of polyols and diisocyanates. Depending on the monomers used, polymers with very different properties can be obtained in the adhesives, coatings, rigid and flexible foams, sealants, composites industry, and so on. Much of the progress in the field of renewable polyurethanes focuses on polyols, as a wide range of polyols of renewable origin can be obtained, including: polyols derived from vegetable oils [57], polyether-type polyols based on sugars (sorbitol and sucrose) [58] and polyester-type polyols derived from succinic and adipic acid, among others [59].

Within technical or engineering plastics, polyamides deserve special attention as important research has also been carried out to obtain fully or partially biobased polyamides. Polyamides are obtained by polycondensation processes of dicarboxylic acids with diamines, or by Ring Opening Polymerization– ROP of lactams.

By heating castor oil, it is possible to obtain sebacic acid, a dicarboxylic fatty acid with 10 carbon atoms (C10) which plays a key role in biobased polyamides [60]. **Figure I.1.3.4** shows the schematic plot of castor oil with a typical triglyceride structure.

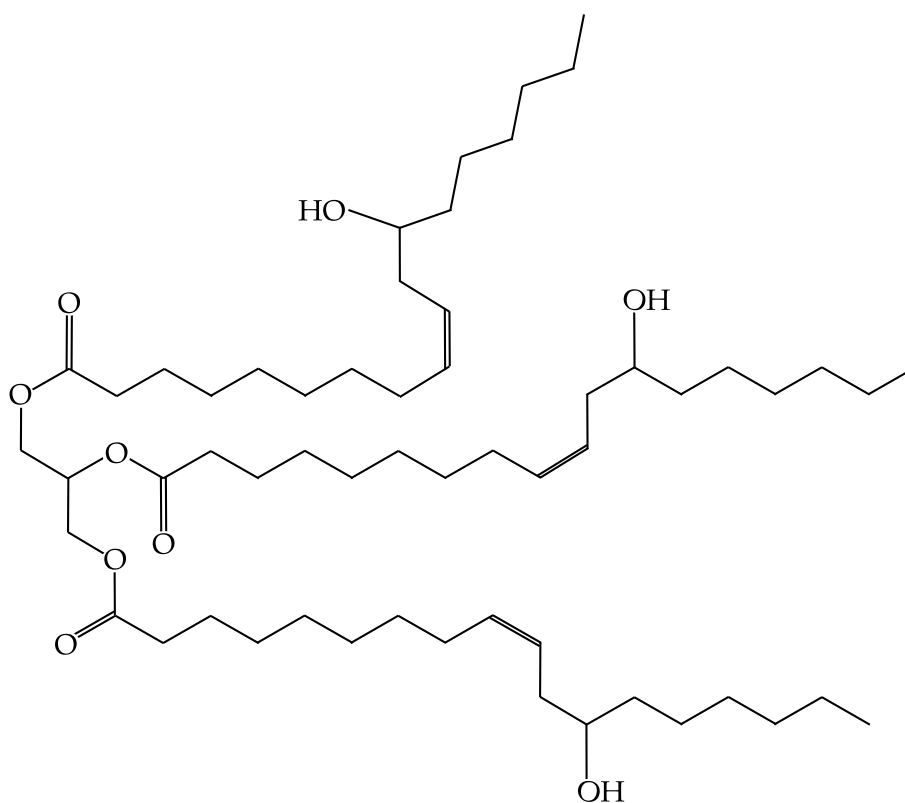


**Figure I.1.3.4.** Schematic representation of the molecular structure of castor oil, basic triglyceride for obtaining sebacic acid for the synthesis of bio poly(amides) and base polyol for the synthesis of bio poly(urethanes).

Currently, biopolyamides - bioPA include several 100 % renewable polymers, such as polyamide 11 - PA11 [61], and polyamide 1010 - PA1010 [62] as well as polyamides with different percentages of renewable contents, such as polyamide 610 - PA610, polyamide 1012 - PA1012, polyamide 410 - PA410. Most of these are derived from monomers of renewable origin such as sebacic acid, 1,10-decandiamine and  $\omega$ -amino-undecanoic acid, which are obtained from castor oil as mentioned above, and other biobased polyamines [63,64]. **Figure I.1.3.5.** shows the structure of a partially biobased polyamide (PA610) and two fully biobased polyamides (PA1010 and PA1012).

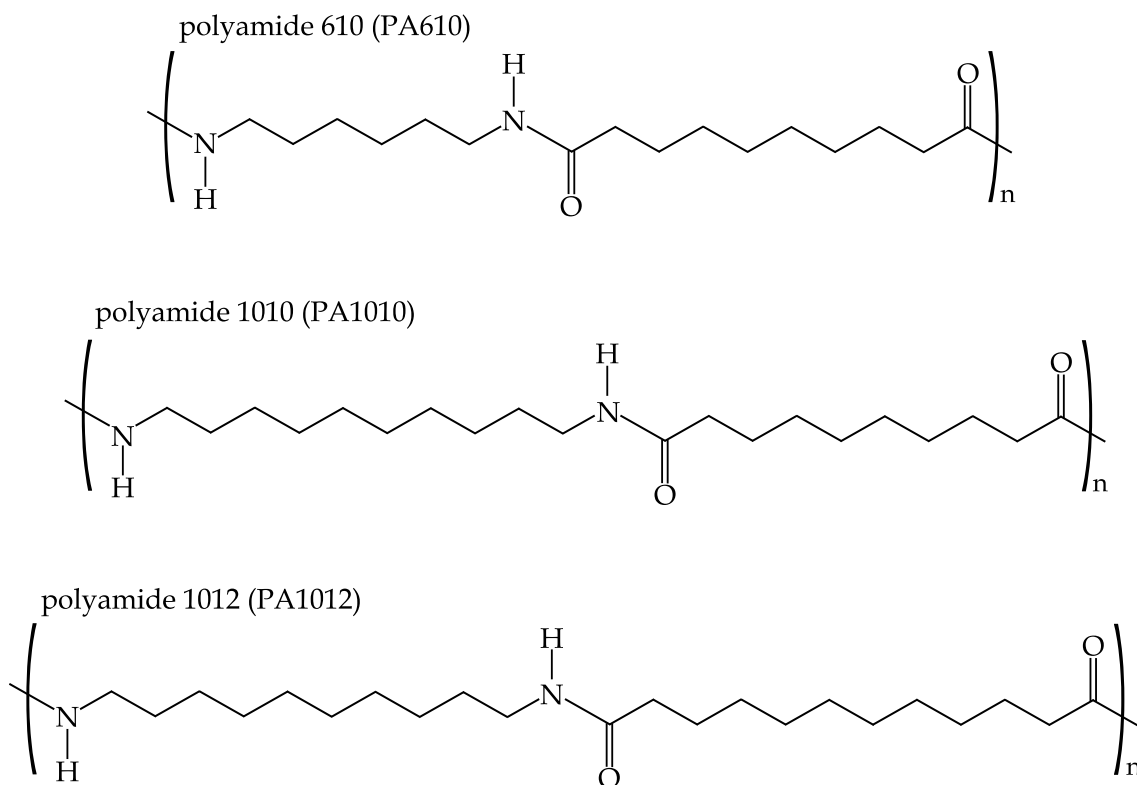


**Figure I.1.3.5.** Schematic representation of the chemical structure of different types of polyamides with different renewable content.

### I.1.3.2. Petroleum-derived and biodegradable polymers.

In the last decade, the development of polymers which are susceptible for biodegradation (or disintegration under controlled composting conditions) has increased in a remarkable way. Although many labile chemical groups are capable of undergoing hydrolysis processes such as amide [65,66], anhydride [67], the ester group is one of the most susceptible for hydrolytic cleavage and, subsequently, polyesters (mainly aliphatic) have been developed with the addition feature of disintegration in controlled compost soil. The ester group is easily hydrolysable under suitable conditions of moisture, temperature, pH, among others. In this way, it is possible to promote chain scission by hydrolytic cleavage until they reach sufficiently small sizes to be incorporated into the metabolic processes of various microorganisms [68,69].

Among these aliphatic polyesters, PCL, PGA and PLA as well as their blends and copolymers are increasingly used [70-72]. It is important to note that PLA had a petrochemical origin in the past, but nowadays the commercial grades that can be found on the market are obtained from renewable resources.

All these polyesters are being used in several industrial applications with approved food contact grades, which promotes to their massive use in the packaging

sector. Moreover, all these polyesters are resorbable or bioabsorbable by the human body, which means that the polymer chains can be hydrolysed into basic compounds such as lactic acid, glycolic acid, succinic acid, and so on that can be managed by our metabolic system and expelled [73]. This is why many of these poly(esters) have commercial grades for use in medicine at extremely high costs due to the high purity standards demanded by the medical sector. They have been used in sutures, fixation plates, catheters, scaffolds, among others [74-76].

Alongside these medical grades (with extremely high cost), manufacturers offer industrial grades of these poly(esters) at reasonable costs for engineering use ranging from 2.0 - 2.5 €/kg to 20 - 25 €/kg. These polyesters (PLA, PBS, PCL, PGA, among others) can be used in the form of rods, films, fibres, fabrics, small parts, and so on. It is worthy to note the increasing use of these poly(esters) in 3D printing by Fused Deposition Modelling - FDM which has widened the potential use of these polymers in medical applications [77-79]. **Figure I.1.3.6.** shows schematically the structure of these poly(esters).

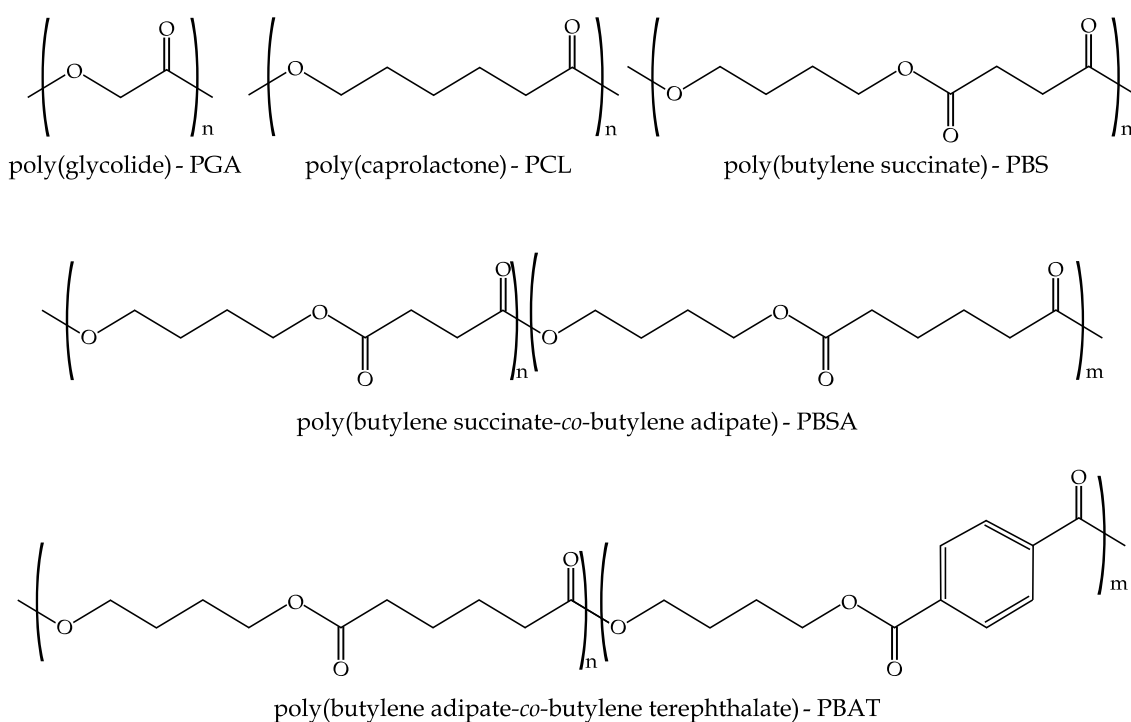


**Figure I.1.3.6.** Schematic representation of the monomer unit of various petroleum-derived poly(esters) with the additional feature of biodegradability.

### I.1.3.3. Biobased and biodegradable polymers.

The abovementioned developments in polymers considering their environmental impact are indeed interesting. However, the most interesting group is that of polymers obtained from renewable resources and with the additional property of biodegradation. These polymers are very interesting from an environmental point of view due to their origin (renewable feedstock) and their disintegration ability. This promising group includes polysaccharides such as starch, cellulose, chitosan, and so on, as well as other polymers obtained by bacterial fermentation such as poly(3-hydroxybutyrate) - P3HB. Finally, a third group corresponding to protein structures is included in this type of polymers. Despite their environmental efficiency is higher to the previous groups in this section, from a technical point of view, the properties they offer are relatively inferior to most commodities and technical plastics. However, due to their structure, many of them are biocompatible and/or resorbable, hence their use in the medical sector is growing steadily [80-83].

#### a) Polysaccharide-derived polymers.

Polysaccharides are natural polymers with carbohydrate structure whose basic units or monomers (monosaccharides) are linked by glycosidic bonds (see **Figure I.1.3.7.**). Their function is to act either as a structural material or as an energy storage material.

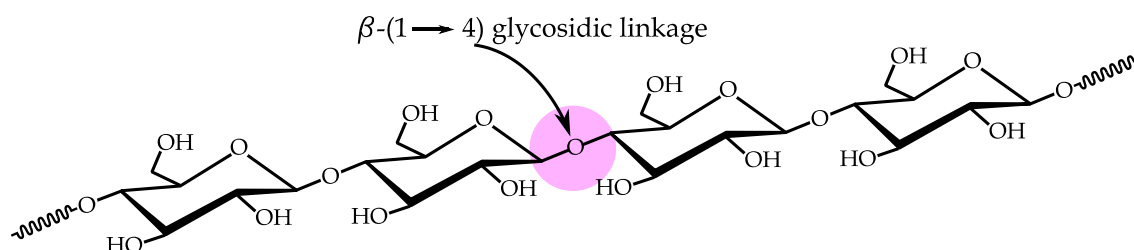


**Figure I.1.3.7.** Schematic representation of the chemical structure of cellulose with  $\beta$ -(1 $\rightarrow$ 4) glycosidic linkages.

Among the structural polysaccharides, cellulose and chitin are the most abundant. Chemically, cellulose and chitin are very similar (**Figure I.1.3.8.**). The structure of chitin is similar to cellulose, but one of its hydroxyl groups is acetylated.

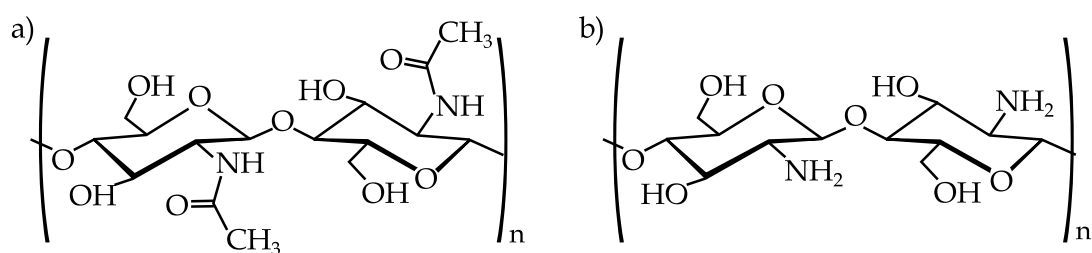
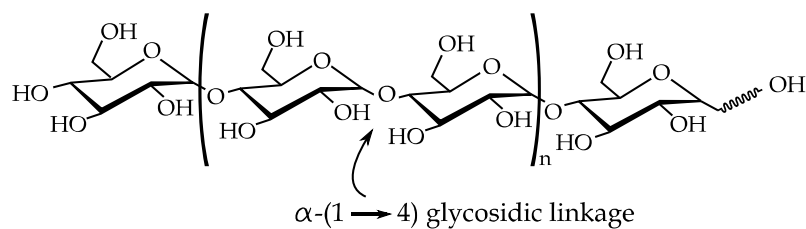


**Figure I.1.3.8.** Representation of the chemical structure of: a) cellulose and b) chitin.

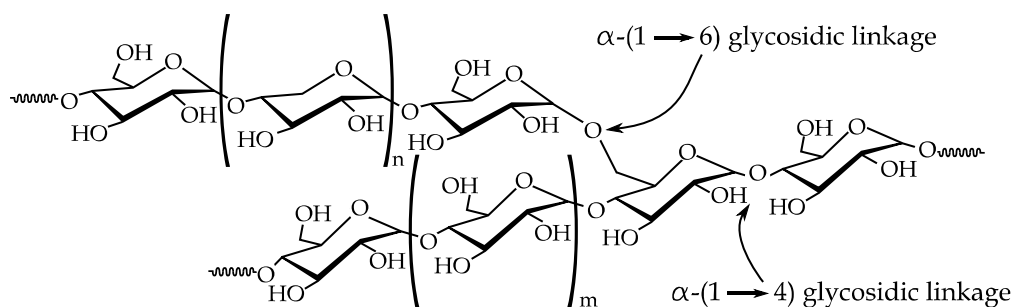
Cellulose is the most abundant natural polymer in nature. Its main source comes from plant fibres, although some bacteria also produce this polymer, so it can be mass-produced by culturing such bacteria [84]. In plants, cellulose is present in plant cell walls. Cellulose macromolecules in plants are in the form of fibrils consisting of 18–36 individual cellulose chains. These fibrils have a width of 10 to 30 nm, and an indefinite length, and very long fibres can be obtained [85,86]. Chitin is the most abundant polysaccharide after cellulose. It occurs naturally in animals and fungi. In animals, it is found forming the exoskeleton of arthropods. In fungi, it provides the skeleton that gives them structural rigidity. It is an insoluble polymer in water, dilute acids and both dilute and concentrated bases and in all organic solvents. Its biodegradability and biocompatibility are advantageous for its use in biomedical applications, either directly or in one of its derivatives, chitosan [87].

In addition to the above mentioned polysaccharides, other polysaccharides have different functions in living organisms. These are the energy storage polysaccharides. They represent the polymeric form of glucose. In plants, starch, with  $\alpha$ -(1→4)-glycosidic linkages, is the most important, while in animals, glycogen, with branching due to  $\alpha$ -(1→6)-glycosidic linkages, is the most important energy storage polysaccharide. **Figure I.1.3.9.** shows schematically the structure of starch and glycogen, widely used in drug delivery systems in medicine [88].

a) amylose



amylopectin



b)

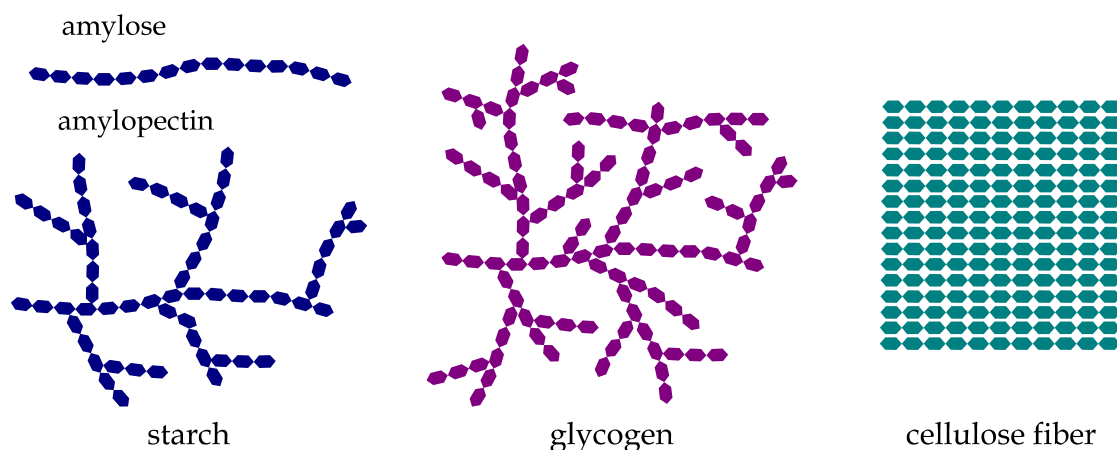


**Figure I.1.3.9.** Schematic representation of the constituent chains of starch: linear amylose and branched amylopectin molecules, b) comparison of the structure of polysaccharides based on glycosidic bonds: starch, glycogen and cellulose.

This group also includes PLA, as the bio route to obtain this polymer derives from the fermentation of starches which are converted into lactates, then to lactide, and finally, polymerized to polylactide by Ring Opening Polymerization - ROP. PLA has an aliphatic polyester structure and hence, it is susceptible for biodegradation. It is also resorbable and therefore, its use in medical applications is widely extended [77,89].

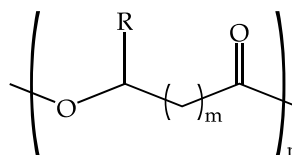
### b) Bacterial polyesters or polyhydroxyalkanoates – PHA.

PHAs comprise a very broad group of polymers that are obtained by bacterial fermentation processes. Just as plants store energy in the form of starch (polymer structure of glucose), certain bacteria can store energy in the form of polymers derived from hydroxyalkanoic acids such as 3-hydroxybutyric acid – 3HB, 3-hydroxyvaleric acid – 3HV, 3-hydroxyhexanoic acid – 3-HHx, among others. These bacteria, instead of storing hydroxyalkanoic acids, polymerize them to provide energy reserves, giving rise to the corresponding polyhydroxyalkanoates. There are currently more than 150 bacterial strains that can synthesize these polymers when subjected to limiting conditions of certain nutrients such as nitrogen, phosphorus, sulphur, magnesium, in the presence of high amounts of biomass-derived carbon [90,91].

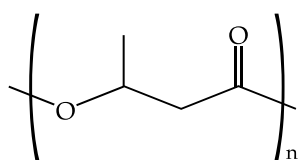
Among the PHA, the most common is poly(3-hydroxybutyrate) – P3HB [92], which is also commercially available as a copolymer with 3-hydroxyvaleric acid. The latter is the so called poly(3-hydroxybutyrate-*co*-3-hydroxyvalerate – P(3HH-*co*-3HV), which provides improved flexibility and ductility (**Figure I.1.3.10.**) [93]. In general, PHAs are biocompatible and easily biodegradable and resorbable, hence their use in the medical sector is widely extended [91,94,95]. Furthermore, due to their excellent biodegradability, they are widely used in the packaging sector [96]. Depending on the acids involved in energy storage in bacteria, a wide variety of PHA can be obtained as homopolymers or copolymers (**Figure I.1.3.10.**).



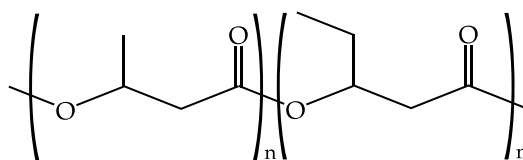
generic structure of  
a bacterial polyester,  
polyhydroxyalkanoate - PHA



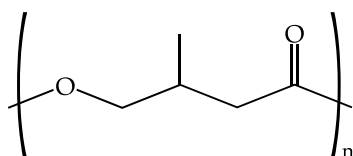
m	R	monomer	abbreviation
1	-H	3-hydroxypropionic acid	3HP
1	-CH <sub>3</sub>	3-hydroxybutyric acid	3HB
1	-CH <sub>2</sub> CH <sub>3</sub>	3-hydroxyvaleric acid	3HV
1	-CH <sub>2</sub> CH <sub>2</sub> CH <sub>3</sub>	3-hydroxyhexanoic acid	3HHx
1	-CH <sub>2</sub> CH <sub>2</sub> CH <sub>2</sub> CH <sub>2</sub> CH <sub>3</sub>	3-hydroxyoctanoic acid	3HO
2	-H	4-hydroxybutyric acid	4HB
2	-CH <sub>3</sub>	4-hydroxyvaleric acid	4HV



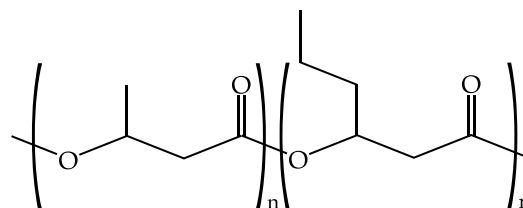
poly(3-hydroxybutyrate)-P3HB



poly(3-hydroxybutyrate-co-3-hydroxyvalerate)-P(3HB-co-3HV)



poly(4-hydroxybutyrate)-P4HB



poly(3-hydroxybutyrate-co-3-hydroxyhexanoate)-P(3HB-co-3HHx)

**Figure I.1.3.10.** Schematic representation of the general basic unit of PHA and the different possibilities depending on the repeating unit "m" and the radical or side group "R" (up) and schematic representation of the monomer unit of the most commercially used PHA (down).

Many PHAs have a glass transition temperature -  $T_g$  below room temperature and this leads to a physical ageing process by secondary crystallization. This results in increased stiffening and embrittlement of the materials over time [97,98]. On the other hand, although it is technically possible to synthesize a wide range of PHA, at a commercial level there are several that offer a reasonable price, although much higher than that of commodities or even PLA [99,100].

### c) Protein-based polymers.

The use of proteins in the food sector and in the medical field is obvious due to proteins possess high biological activity [101]. However, their industrial use has become more widespread in recent years as society has become more aware of environmental issues. Traditionally, one of the most relevant applications of proteins has been in the adhesives sector. Thus, curiously, the term gluten comes from Latin and means "glue". In relation to collagen, the term comes from the Greek "κόλλα" which also means "glue". In this sense, the use of proteins in the formulation of adhesives has been and is extensive, with gluten [102], soy protein, whey protein [103], casein [104], zein [105] and so on.

## **I.2. Biobased and biodegradable aliphatic polyesters.**

### **I.2.1. Poly(lactic acid) - PLA.**

PLA, is one of the most widely used biopolymers. It is obtained after Ring Opening Polymerization of lactide derived from sugar-rich biomass fermentation or by direct condensation as seen in **Figure I.2.1.1**. PLA started to gain importance in recent decades, but its beginnings date back to the 18<sup>th</sup> century. In 1780, the Swedish chemist Carl Wilhelm Scheele purified lactic acid by crystallizing calcium salt, and thought it was a natural component of milk. However, it was Charles Avery who managed to obtain a larger quantity of lactic acid in 1880. In 1932, Wallace Carothers obtained a low molecular weight product by heating lactic acid and subjecting it to a vacuum [106]. However, it was not until the middle of the 20<sup>th</sup> century that Dupont company finally patented PLA as a 100 % natural material. The high cost of producing polylactic acid has been one of the main drawbacks in the development of this polymer over time. However, thanks to innovation and advances in glucose fermentation, manufacturing costs are increasingly coming down, driving industrial and scientific interest in this biopolymer.

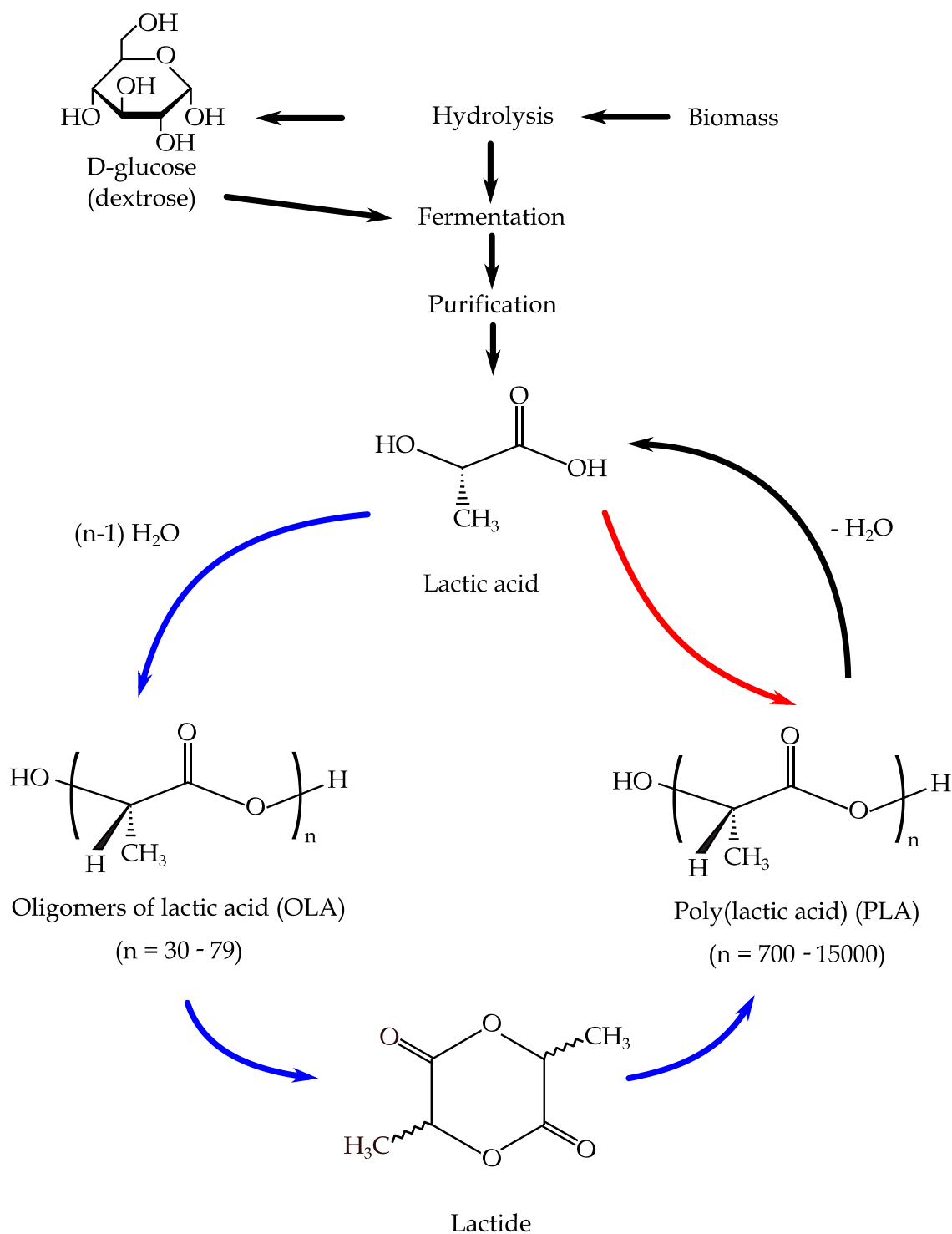


**Figure I.2.1.1.** a) Schematic representation of PLA synthesis routes from biomass fermentation.

The properties of PLA can be tailored by combining the D(-) and L(+) isomers during polymerization (**Figure I.2.1.2.**). Thus, it is possible to obtain a fully amorphous PLA or a semicrystalline grade. Commercially, the most used PLA is a mixture of poly(L-lactic acid) - PLLA and poly(D-lactic acid) - PDLA but it is worthy to note that the L(+) isomer is the most abundant in nature [107].

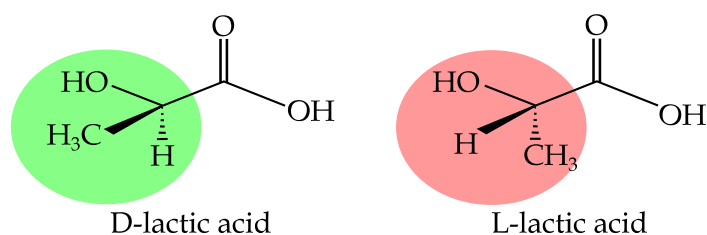


**Figure I.2.1.2.** Chemical structure of lactic acid isomers

PLA has mechanical properties very similar to those of some petroleum-based polymers. Its tensile strength and tensile modulus are comparable to those of PET [108]. With average values of 60 MPa and 3500 MPa, respectively. In contrast, PLA is an excessively brittle material. It has low toughness values and an elongation at break of less than 10 %.

The thermal properties of PLA are determined by the weight ratio of the two lactic acid molecules (L and D). Therefore, PLA can vary from an amorphous polymer to a semi- or highly crystalline material [109]. For this reason, the crystallization rate, degree of crystallinity and thermal properties of PLA are highly dependent on the molecular weight and the synthesis process of PLA.

Poly(lactic acid) is a thermoplastic polymer with a glass transition temperature between 55 – 70 °C and a melting peak temperature between 165 – 190 °C. Actually, the  $T_g$  depends directly on the L- and D- monomer ratio. It has interesting barrier properties due to its crystallinity [110]. Crystallization reduces the overall amount of amorphous regions thus reducing its permeability to gases since small gas and vapor molecules move, preferentially, along the amorphous regions. In general terms, the barrier properties of PLA are comparable to those of poly(styrene) – PS [111]. Additivation is a feasible strategy to tailor the barrier properties of PLA since it is widely used in packaging applications [112,113].

As indicated previously, PLA undergo biodegradation or disintegration in controlled compost soil due to hydrolytic degradation, although it also depends on other factors such as molecular weight, degree of crystallinity, purity, temperature, pH, presence of carboxyl or hydroxyl end-groups, water permeability and additives [114]. This causes the structural integrity of the material to change, thus reducing the molecular weight [115], and allowing the lactic acid and low molecular weight oligomers to be metabolized by microorganisms with the subsequent generation of  $\text{CO}_2$  and  $\text{H}_2\text{O}$  [116]. This hydrolytic cleavage can be seen in **Figure I.2.1.3**. PLA is also sensitive to thermal degradation during processing, resulting in a decrease in molecular weight. This phenomenon is more pronounced in presence of moisture due to the ester group is labile

to hydrolytic scission. Therefore, it is important to dry in an appropriate way PLA before processing. In fact, it is quite common the use of chain extenders to recover the molecular weight after the thermal degradation [117].

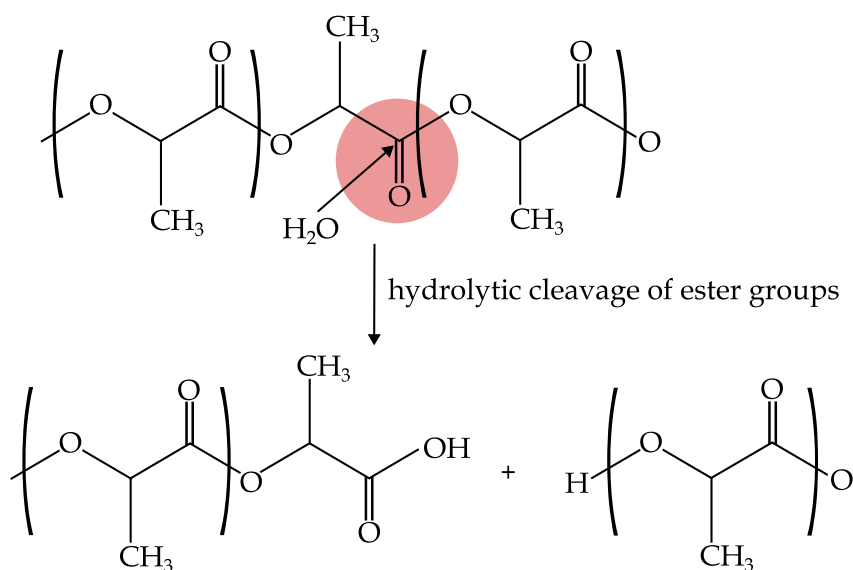


**Figure I.2.1.3.** Schematic plot of the hydrolytic degradation or cleavage of polylactide.

With regard to its applications, PLA finds uses in the packaging industry [118], automotive [119], wood plastic composites for structural applications [120], and, recently, PLA is the choice for the emerging 3D-printing and 4D-printing technologies since PLA offers additional shape memory behaviour, tuneable by heating-cooling cycles [121,122].

Thanks to its structure and high biocompatibility with the human body, PLA has been widely used in the medical sector. Some of the uses of PLA in surgical applications include resorbable sutures [123], fixation plates [124], screws and pins [125], porous scaffolds for tissue engineering [126], and so on. In the pharmaceutical field, the biocompatibility of PLA allows it to be used for controlled drug release due to the progressive degradation of this biopolymer, the release of drugs such as insulin, anti-inflammatory drugs, inhibitors, among others, can be controlled [127].

### I.2.2. Poly(hydroxyalkanoates) - PHA.

Unlike some biodegradable polymers are obtained from renewable sources like PLA, PHA are fully biosynthesized and biopolymerized by microorganisms. In addition, they can exhibit mechanical and thermal properties similar to those of commodities from fossil resources, making them, very sound candidates as future substitutes for petroleum-based polymers.

PHAs are thermoplastic polyesters of R-hydroxyalkanoic acid ((R)-HA) monomers that are synthesized by a wide variety of Gram-positive and Gram-negative bacteria (more than 300 types), although there are studies in which PHAs have been synthesized from plants [128]. PHA-producing bacteria accumulate the polymer in their cytoplasm as carbon and energy reserve granules, using it as a reservoir of nutrients that may be required in the absence of these in order to maintain their metabolism [129]. PHA accumulation occurs when bacteria experience a nutrient imbalance, such as a lack of nitrogen, phosphorus, magnesium, sulphur or oxygen and an excess of carbon sources. However, there are also bacteria that do not require nutrient limitation for PHA synthesis, such as recombinant *Escherichia coli* [130]. The accumulated amount of this biopolymer can represent more than 90 % of the dry weight of the cell, although this amount depends on the type of bacteria and the conditions in which it is cultured [131]. As shown in **Figure I.2.2.1.**, the PHAs inclusions inside the bacteria take the form of spherical granules of different sizes.

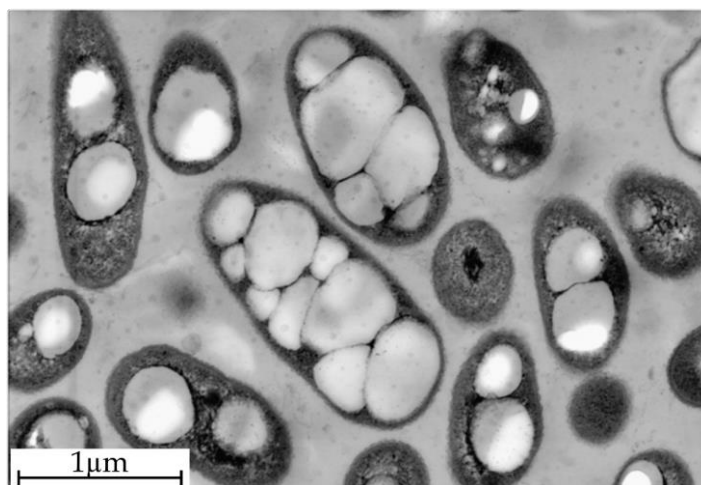


**Figure I.2.2.1.** Electron microscopy image of *C. necator* DSM 545 cells with P3HB inclusions. Image reproduced from [132].

PHA can be homopolymers, if they consist of a single type of hydroxyalkanoic acid as a monomer unit or heteropolymers (copolymers), if they consist of more than one hydroxyalkanoic acid as a monomer unit. PHAs can be broadly classified into two groups depending on the number of carbon atoms in their monomer unit. According to this, there are PHAs with short chain length (scl-PHA), with 3 and 5 carbon atoms in their monomer unit, and medium chain length PHA (mcl-PHA), which contain between 6 and 14 carbon atoms in their monomer unit. There is a third group called hybrid or mixed PHA which are composed of a mixture of short-chain and medium-chain monomers [133]. **Figure I.2.2.2.** shows some of the PHA included in each group.

POLYHYDROXYALKANOATES - PHA		
short chain (scl-PHA) 3-5 carbon atoms	medium chain (mcl-PHA) 6-14 carbon atoms	hybrid PHA scl-PHA/mcl-PHA
P3HP P3HB P3HV P4HB P(3HB-co-3HV) P(3HB-co-4HB)	P3HHx P3HO P4HHx P(3HHx-co-3HO)	P(3HB-co-3HHx)

**Figure I.2.2.2.** Classification of PHA depending on the carbon atoms in the monomer unit.

Scl-PHA exhibit a wide range of properties depending on their monomer composition. However, in general, scl-PHA are characterized by a high degree of crystallinity, reaching up to 80 %. This makes them highly rigid and brittle materials. Thermal properties also vary considerably between the different scl-PHAs, but they are generally characterized by melting temperatures ranging from 175 °C to 180 °C and glass transition temperatures in the 5 - 10 °C range. Among the best known scl-PHA, it is worthy to highlight poly(3-hydroxybutyrate) - P3HB, poly(4-hydroxybutyrate) - P4HB or poly(3-hydroxyvalerate) - P3HV, and the copolymer poly(3-hydroxybutyrate-co-3-hydroxyvalerate) -P(3HB-co-3HV) [98,134].

Moreover, mcl-PHAs are elastomers with a low crystallinity of around 25 %, low tensile strength, low elastic modulus and high elongation at break. In terms of thermal properties, these type of PHA are characterized by glass transition temperatures in the - 50 °C to - 25 °C range, melting temperatures between 40 °C and 60 °C. Among the best known medium-chain-length PHAs are the homopolymers poly(3-hydroxyhexanoate) - P3HHx and poly(3-hydroxyoctanoate) - P3HO, and the copolymer poly(3-hydroxyhexanoate-co-3-hydroxyoctanoate) - P(3HHx-co-3HO) [135,136].

As mentioned above, there is a third group called hybrid PHAs or PHAs which are comprised of short-chain and medium-chain monomeric units. These copolymers exhibit a wide range of properties, which will depend on the mole fraction of each of the monomers in the copolymer. One of the most studied hybrid PHAs is poly(3-hydroxybutyrate-*co*-3-hydroxyhexanoate) - P(3HB-*co*-3HHx) [137].

PHAs are efficiently degraded by a large number of micro-organisms and fungi present in nature, which is why this type of polymers can be degraded in different environments such as in soil, in compost, in marine sediment, in salt water (sea), in fresh water (lake) or in sewage sludge, although the time get the polymer degraded will depend on several environmental factors such as microbial activity, humidity, moisture, temperature, pH and nutrients in the medium, as well as specific factors of PHA, such as molecular weight, PHA composition, crystallinity and exposed surface area [25,138].

Among all PHA, P3HB owns a privileged position. P3HB is a highly crystalline thermoplastic material with a melting temperature of 170 - 180 °C and a glass transition temperature of 0 - 5 °C [139]. However, P3HB is characterized by low thermal stability during processing, as its thermal degradation starts at temperatures close to its melting temperature, between 170 °C and 200 °C; this causes the processing window of P3HB to be very narrow [96]. The narrow processing window of P3HB is another major drawback. Thermal degradation of P3HB occurs almost exclusively by a non-radical random chain scission reaction (cis-elimination) [140]. Random chain scission takes place at the ester groups, resulting in a transition state of a six-membered ester ring, which decomposes leading to the formation of crotonic acid and P3HB oligomers [141]. The mechanism of thermal degradation is shown in **Figure I.2.2.3**. Thermal degradation of P3HB leads to a reduction in the molecular weight of the biopolymer, which significantly affects its mechanical properties as well as its viscosity in the molten state [142].



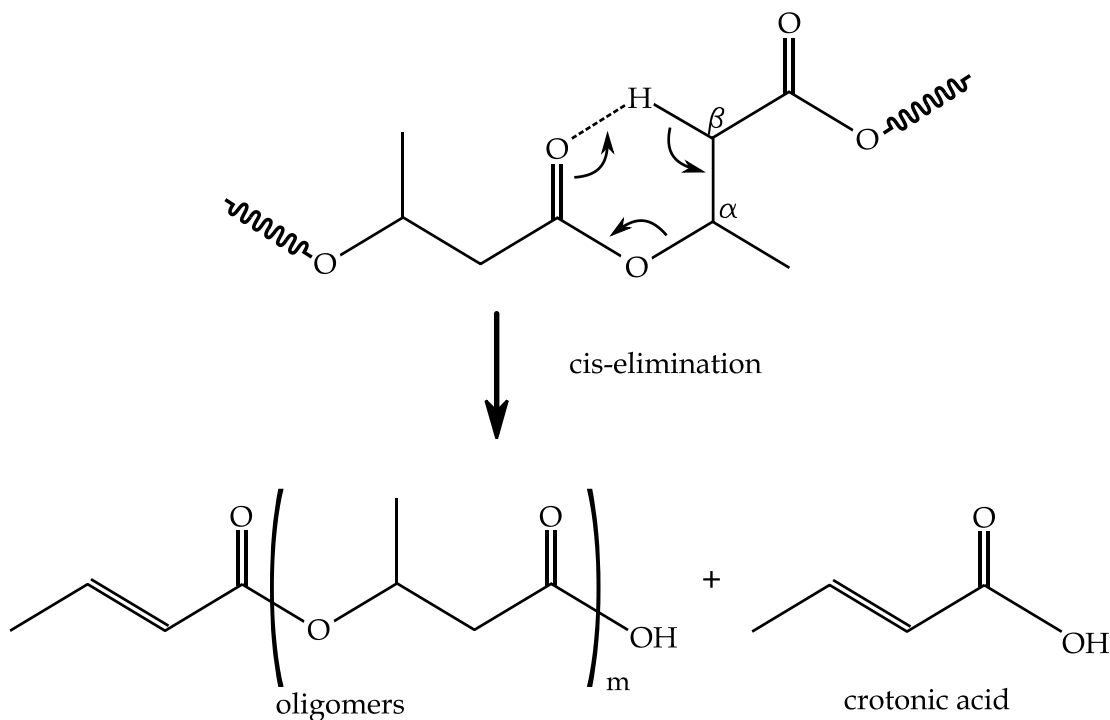


**Figure I.2.2.3.** Schematic representation of the mechanism of thermal degradation of poly(3-hydroxybutyrate) by cis-elimination.

Due to the properties of PHA such as biodegradability, biocompatibility, non-toxicity, piezoelectricity, water insolubility, UV resistance, good barrier properties, variety of mechanical properties, good enough processability in conventional processing equipment, among others, PHA are set to become substitutes for commodities. These properties mean that PHA are used in a wide variety of sectors such as the packaging sector [143], for the manufacture of beverage bottles, in films for food packaging or as a coating for paper sheets to protect food products, as well as in the agricultural sector for the manufacture of mulch films [133], or as a controlled release system for insecticides or herbicides [144]. But it is in the medical and pharmaceutical sector where PHAs have experienced the greatest development, being used in a multitude of applications such as in the manufacture of cardiovascular products (heart valves, coronary stents, vascular grafts, blood vessels) [145], in controlled drug release systems [146], for wound healing (sutures, sleeves, swabs, dressings) [147], tissue engineering [148], or in orthopaedics (screws, tissue engineering matrices, bone graft substitutes) [149].

### I.2.3. Modification of polyesters.

As seen in the previous section, PHAs have a series of limitations, such as high brittleness and low thermal stability, which, together with their high cost, impede biopolymer from being widely used at an industrial level. Despite PLA has a more competitive cost, it is also a brittle polymer which is important drawback for a massive use of this biopolymer.

In order to overcome (or minimize) these limitations and increase the competitiveness of these polymers, it is necessary to modify their properties. The following is a general description of the most commonly used methodologies to improve the properties of the polymers, such as copolymerization, plasticization, and physical blending with the main aim of improving toughness.

#### I.2.3.1. Copolymerization.

The intrinsic fragility of most aliphatic polyesters such as PLA and P3HB, can be improved by using copolymerization. Copolymerization is a chemical polymerization reaction in which two or more different monomers are used at the same time, resulting in polymer chains in which the two monomers are arranged differently. Such polymers are known as copolymers (or terpolymers by using three different monomers). Depending on the arrangement of the monomers in the polymer chain, four types of copolymers (*-co-*) can be distinguished, including random (*-ran-*) copolymers (the most common), alternating (*-alt-*) copolymers, block (*-b-*) copolymers, and graft (*-g-*) copolymers. Copolymerization makes it possible to combine the characteristics of the different monomers used, resulting in polymers with excellent performance properties. These properties will largely depend on the composition of the copolymer, *i.e.* the relative proportion of each monomer in the copolymer.

With regard to PLA copolymers, it is worthy to note the combination of lactide and glycolide to tailor de bioabsorption rate, resulting in PLA-*co*-PGA copolymers or just PLGA. With the aim of overcoming the intrinsic brittleness of PLA, some copolymers are obtained by polymerization of different amounts of Lactic Acid - LA, caprolactone - CL, Glycolide Acid - GA, butadiene, thus leading to the corresponding copolymers with improved toughness [150,151], as shown in **Figure I.2.3.1**.

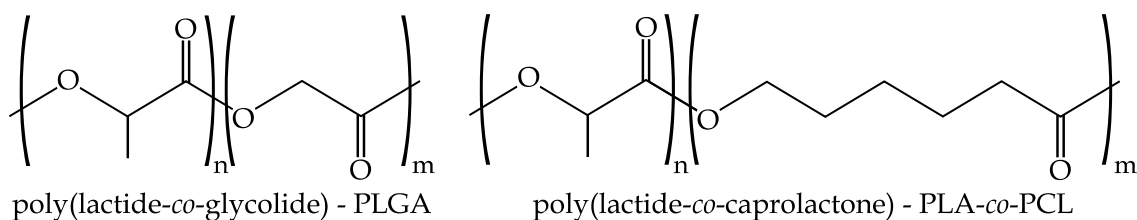


**Figure I.2.3.1.** Schematic representation of the chemical structure of different PLA-based copolymers with improved toughness.

There are several methods to copolymerize PLA with different monomers depending on the chemical structure of the monomers. The two main routes of copolymerization with lactide are polycondensation - PC and ring opening copolymerization - ROCOP. A wide variety of PLA copolymers with different monomers such as caprolactone - CL, Ethylene Oxide - EO, Ethylene Glycol - EG, Glycolide Acid - GA, valerolactone, trimethylene carbonate - TMC, among others, have been proposed to overcome the intrinsic brittleness of PLA thus widening its applications in medical field. Specific catalysts are required to obtain a particular copolymer structure, including stannous octoate, aluminium isopropoxide, organic amino calcium, among others for ROP reactions while dimethyl amino pyridine is widely used for polycondensation reactions [150].

In the case of P3HB, copolymers are also biosynthesized by certain microorganisms and by using different culture conditions, *e.g.* by using mixed substrates. Generally, when a mixture of substrates is used, the resulting copolymers are random copolymers; however, it is possible to obtain block copolymers synthesized by bacteria by alternating substrates over time [152]. Some of the most studied P3HB copolymers at present are P(3HB-*co*-3HV), P(3HB-*co*-4HB) or P(3HB-*co*-3HHx), whose chemical structures can be seen in **Figure I.2.3.2**.

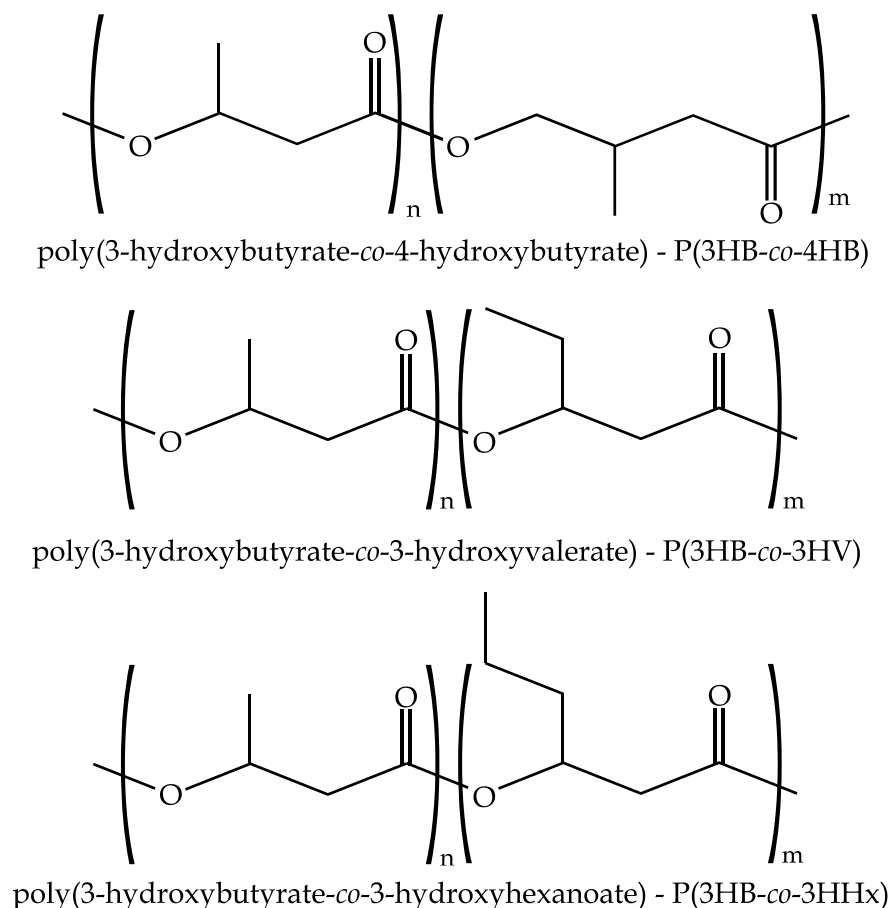


**Figure I.2.3.2.** Schematic representation of the chemical structure of different P3HB-based copolymers with improved toughness.

### I.2.3.2. Plasticization.

The International Union of Pure and Applied Chemistry – IUPAC defines a plasticizer as “as a substance or material incorporated in a material (usually a plastic or an elastomer) to increase its flexibility, workability, or distensibility” [153]. The main functions of plasticizers in the polymer field are to provide an increase in ductility, a reduction in the  $T_g$ , as well as to improve processability. Typically, these changes are achieved by modifying the molecular weight, end-groups and polarity of the plasticizer. In general, the main characteristics that plasticizers should possess are:

- Low molecular weight.
- High boiling point.
- Low volatility.
- No toxicity.

The incorporation of plasticizers in polymers leads to a decrease in resistant mechanical properties such as hardness, tensile strength or elastic modulus, and an increase in ductile mechanical properties such as elongation at break or impact energy

absorption. On the other hand, plasticizer addition leads to an increase in the flexibility of the polymer chains causing a decrease in the viscosity of the melt and an increase in the Melt Flow Index – MFI, which enhances its processability. The thermal properties of the polymers are also affected by the incorporation of plasticizers, generally resulting in lower melting and glass transition temperatures, which means lower energy consumption during processing. Other properties of polymers that are affected by the incorporation of plasticizers are the degree of crystallization, wettability, transparency, gas permeability, electrical conductivity, or degradation rate [154].

There are different classical theories to explain the effect of plasticization in polymers. Despite this, it is worthy to highlight three of them: the lubrication theory, the gel theory and the free volume theory. In general, these theories argue that the low molecular weight of plasticizers allows them to place between the polymer chains. As a result a reduction of the secondary attractive forces between the polymer chains and modification of the three-dimensional organization of the polymers, resulting in a decrease of the energy required for molecular motion [155].

a) The lubrication theory.

The lubrication theory considers that the plasticizer acts as a lubricant for the polymer chains, *i.e.* it inserts itself between the polymer chains reducing intermolecular friction and facilitating the movement of the molecules when the plasticized polymer is subjected to stress. This model assumes that the macromolecules slide over each other when the plasticized material is stressed. Therefore, according to this theory, the stiffness of the polymer is given by the internal friction of the molecules due to surface irregularities and the plasticizer acts as a lubricant.

b) The gel theory.

The gel theory considers that the plasticized polymer consists of a three-dimensional network with plasticizer molecules linked to the polymer chains by weak secondary forces. In this case, the plasticizer acts by breaking the bonds and interactions between the polymer, disabling them as a potential cross-linking point with other neighbouring chains. With fewer bonds, the chains are more mobile, making the material more ductile. According to this theory, the stiffness of the polymer is given by the bonds between the polymer chains and the plasticizer acts by reducing the number of active sites capable of forming bonds.

## c) The free volume theory.

The free volume theory is the most accepted theory today and assumes that there is free space between the polymer molecules that allows their movement, therefore, rigid polymers have little free volume. After the incorporation of the plasticizer into the polymer, the free volume is increased, obtaining a larger space that allows greater movement of the polymer chains, thus improving their ductility and lowering their glass transition temperature.

**Figure I.2.3.4.** shows a representation of the plasticization effect in polymers according to the different classical theories.

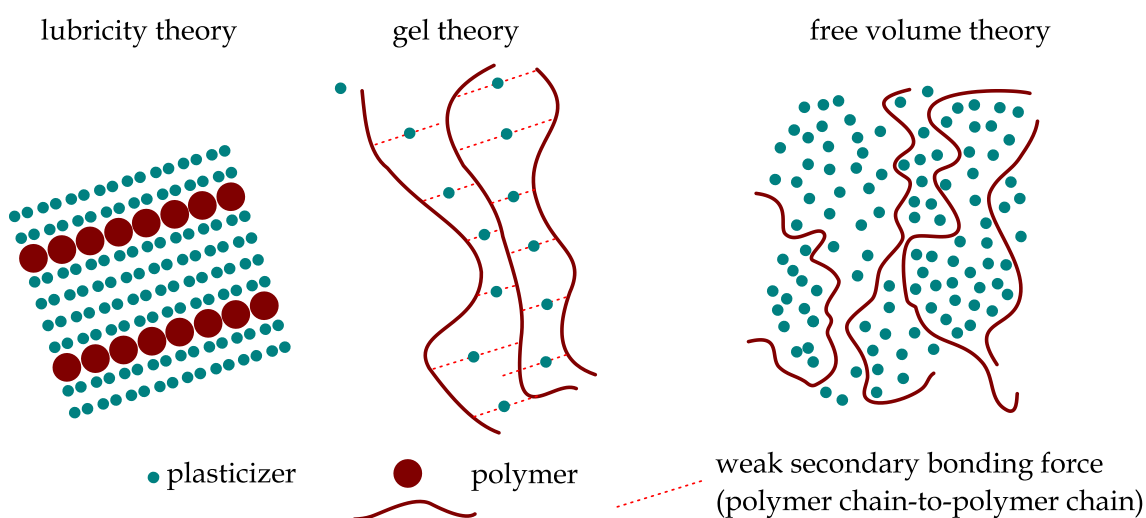


**Figure I.2.3.4.** Schematic representation of the different classical plasticization theories. Adapted from [154].

Compatibility between the plasticizer and the polymer is a key factor for effective plasticizing. Numerous parameters can influence the compatibility of the system, such as polarity, hydrogen bonds, chemical groups, molecular weight, chain length, crystallinity, dielectric constant or solubility parameters, among others.

There are different ways to estimate the compatibility between plasticizer and polymer. One of the most commonly used is by comparing the solubility parameters ( $\delta$ ) of the two components. It has been observed that the closer the values of the solubility parameter of the plasticizer and the polymer are, a higher miscibility between them is expected and therefore a higher compatibility is supposed to appear [156]. Although the solubility parameter can be of great help in choosing the appropriate plasticizer. A solubility value from the polymer close to the solubility parameter from the plasticizer is not always indicative of effective plasticization, since it can happen that both components are incompatible, resulting in poor or plasticization. So the solubility

study, can be as a preselection tool.

Plasticizers can be classified according to several criteria. Depending on their compatibility with the base polymer, plasticizers can be primary or secondary. Primary plasticizers are fully miscible with the base polymer, even at high concentrations. On the other hand, secondary plasticizers offer limited miscibility with the polymer and tend to promote plasticizer migration and/or exudation. Secondary plasticizers, are used in low concentrations to tailor the main properties of a primary plasticizer.

Plasticizers can also be classified according to their structure and molecular weight. By using this criteria, plasticizers can be monomeric or polymeric. Monomeric plasticizers have a simple and unique chemical structure, together with a low molecular weight comprised between 300 - 600 g/mol. In general, monomeric plasticizers are rather volatile and tend to migrate. On the other hand, polymeric plasticizers have molecular weights comprised between 1000 - 10000 g/mol, with a characteristic molecular weight distribution. Despite they offer lower volatility and migration, its compatibility with polymers is, sometimes, limited.

PLA and PHA are often plasticized since plasticization leads to improved ductile properties. A wide variety of monomeric and polymeric plasticizers have been proposed (see **Figure I.2.3.5.**) for these polyesters. Among the monomeric plasticizers, it is worthy to note the effectiveness of citrates (triethyl citrate - TEC, tributyl citrate - TBC, acetyl triethyl citrate - ATEC and acetyl tributyl citrate - ATBC), glycerol, isosorbide, epoxidized vegetable oils, triacetin, tributyrin, among others. With regard to polymeric plasticizers, polyethers and polyesters offer interesting plasticization properties. Polymeric plasticizers such as poly(ethylene glycol) - PEG, poly(propylene glycol) - PPG, poly( $\epsilon$ -caprolactone) - PCL, poly(oxyethylene) - POE, polyadipates, polysebacates, among others have provided improved toughness to PLA and P3HB.

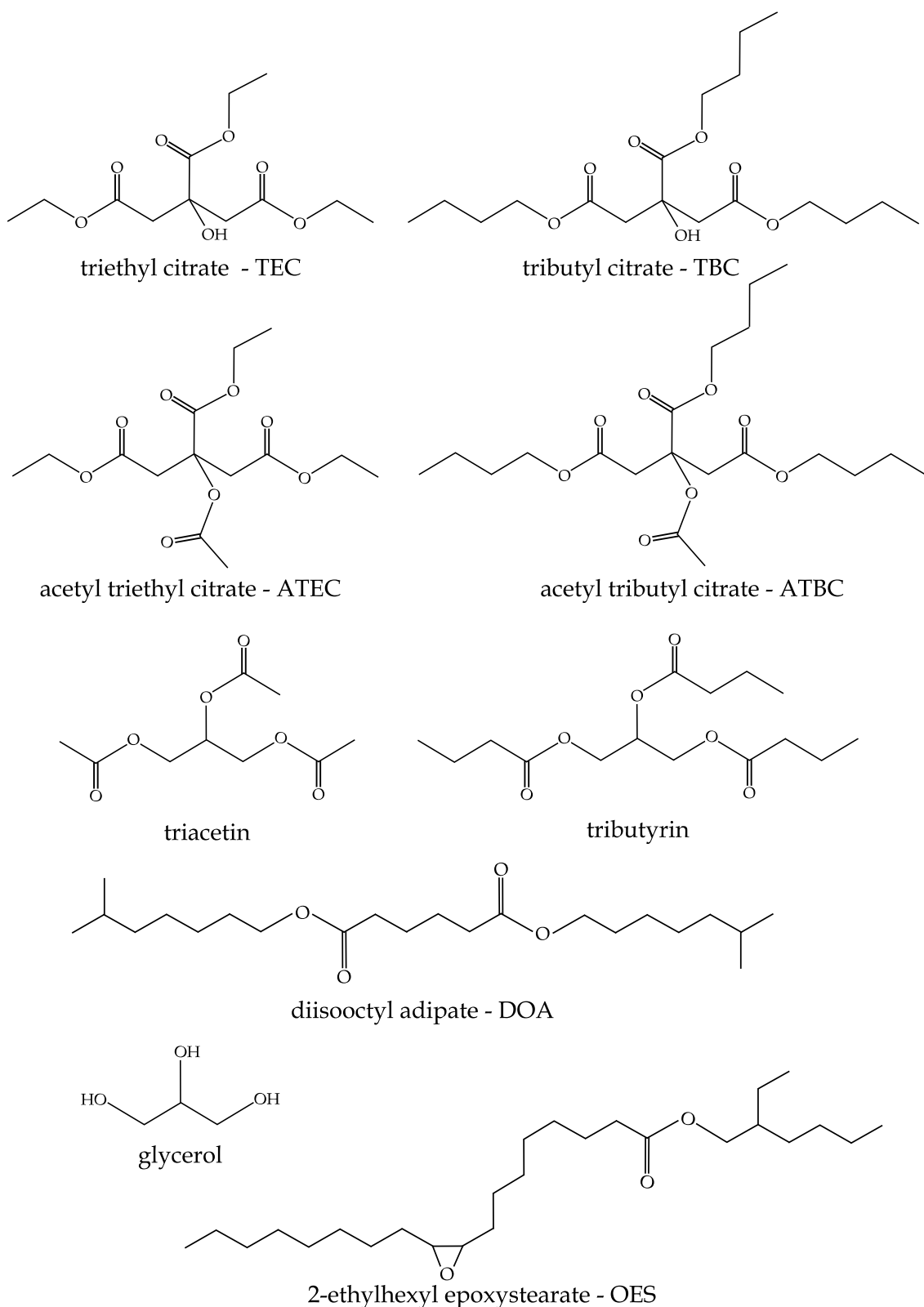


**Figure I.2.3.5.** Schematic representation of the chemical structure of some common plasticizers for PLA and PHA.



**Table I.2.3.1.** shows the main thermal and mechanical properties of some commonly plasticizers for PLA while **Table I.2.3.2.** gathers some relevant information about the plasticization efficiency of different compounds on P3HB.

**Table I.2.3.1.** Effectiveness of some plasticizers in terms of mechanical and thermal properties of PLA. Adapted from [157].

Modifier	M <sub>w</sub> (g/mol)	Concentration (wt.%)	T <sub>g</sub> (°C)	Tensile modulus, E (MPa)	Elongation at break, ε <sub>b</sub> (%)	Tensile strength, σ <sub>y</sub> (MPa)
PLA	137000	100	59	1720	7	51.7
TEC	276	20	32.6	-	382	12.6
TBC	360	20	17.6	-	350	7.1
ATEC	318	20	30	-	320	9.6
ATBC	402	20	17	-	420	9.2
POE	10000	21	31	320	7	49
PCL	10000	20	35	961	25	19
Glycerol	92.09	20	53	-	-	-
PEG monolaurate	400	20	21	-	142	-
Plasticized TPS	-	25	-	-	2.9	30.2
PEG	1500	10	34.3	1750	150	15.1
PEG	1500	20	23.2	1460	150	14.6

**Table I.2.3.2.** Effectiveness of some plasticizers in terms of mechanical and thermal properties of P(3HH-co-3BV). Adapted from [157].

Modifier	M <sub>w</sub> (g/mol)	Concentration (wt.%)	T <sub>g</sub> (°C)	Elongation at break, ε <sub>b</sub> (%)	Tensile strength, σ <sub>y</sub> (MPa)
P(3HH-co-3BV)	680000	100	- 6.6	6	43.1
Soybean oil	814.3	20	- 3.4	3	33.7
Soybean oil	814.3	10	-	5.09	18.7
Epoxidized soy oil	874.2	20	- 19.0	7.2	22.1
Dibutyl phthalate	278.2	20	- 28.5	10	11.7
TEC	276.1	20	- 30.0	10	10.9
Epoxy soyate	-	20	-	7.51	13.8
Epoxidized linseed oil	1037	10	-	7.46	19.6

### I.2.3.3. Physical blending.

Physical blending is the process by which two or more polymers are mixed together in a melt state, without chemical reaction. During this process, the polymers are melted together and mechanically mixed to form a new material, which, after cooling, has different properties from those of the base polymers. This process can be carried out using conventional polymer processing techniques, the most widespread industrially being extrusion, so that this modification approach does not require large investments.

In short, physical blending is a process that allows new materials to be obtained with a desired combination of properties to meet the requirements of specific applications. Moreover, these can be obtained in a relatively short time and at low cost compared to the development of new monomers and polymerization techniques.

Physical melt blending of polymers is, therefore, one of the simplest and most cost-effective methods for improving polymer properties and is one of the most widely used modification systems at industrial level.

Depending on the structure and nature of the polymers to be blended, different compatibility phenomena can be obtained, which decisively affect the final properties of the resulting material. The compatibility between the different phases in polymeric systems depends mainly on the intrinsic polarity of the individual polymers, the interactions between them, the properties of the interface/interphase formed during mixing, as well as the structure of the blend. Taking into account the compatibility between the polymers, there are three types of blends: miscible blends, partially miscible blends and immiscible blends. Despite there are many technical approaches to improve compatibility/miscibility between immiscible or partially miscible polymers, the use of copolymers is generalized. Copolymers provide dual functionality to give interaction with both polymers and, hence, improve the overall properties of the blend [158–160].

In the case of PLA, in addition to improving its high brittleness, physical blends with other polymers are also used to modify its permeability, thermal properties or mechanical properties, in order to fit the requirements of a particular application [161–163]. In this regard, special interest has been shown in the last decade in PLA blends with other biodegradable polymers for application in the field of biodegradable food packaging [164], and also in the field of medical applications that require resorbable, biodegradable and antibacterial materials [165–167]. Therefore, a wide variety of PLA-based binary blends have been proposed in recent years, blending it with different types of polymers such as PHA [168–171], PBAT [172,173], thermoplastic starch – TPS [174,175] and so on. Also some petroleum-derived polymers are currently used in such binary blends due to their ability to disintegrate in a controlled compost soil, such as PCL [72,162,163], PBS [176], or PBSA [177].

### **I.3. Additive Manufacturing – AM.**

AM, or as it is commonly known, 3D printing, is a new manufacturing process in which physical parts are developed using a procedure known as a tool-less process. This procedure is divided into two stages: in the first stage, the computer-aided design is developed and in the second stage, the parts are manufactured layer by layer. There are other processes that also rely on layer-by-layer manufacturing, but do so by providing the shape, not the material, such as laser forming and incremental sheet forming [178]. Additive manufacturing is finding applications in numerous sectors such as aerospace

and marine, automotive, industrial spare parts and medicine [179–183]. Compared to conventional manufacturing processes, AM is a technique that allows product customization and is not affected by the complexity of the geometries to be obtained [184]. This does not mean that AM is cheap, it can be more expensive than conventional manufacturing if an object is designed for mass production and only is considered the manufacturing cost [185]. Given the great future of AM, it is evolving rapidly and new companies are emerging in an increasingly competitive market. Large companies such as HP and GE are making new in-house developments and other new companies are investing heavily such as Desktop Metal, Formlabs and Carbon. Although the basic principles of AM technology remain constant, new developments allow the technology to advance, opening up new possibilities in medical applications [186–188].

### I.3.1. Additive manufacturing processes.

AM processes can be classified into seven different categories: Directed Energy Deposition – DED, Binder Jetting – BJ, Material Extrusion – ME, Powder Bed Fusion – PBF, Sheet Lamination – SL, Powder Bed Fusion – PBF and Material Jetting – MJ [202]. Each category includes many different suppliers, solutions and material options.

The names of the different AM process variants, a brief description, trade names and how the process is used to manufacture, the type of starting material whether polymeric, metallic or ceramic are listed in **Figure I.3.1.1**. On the other hand, there are some processes that are in the research and development phase and therefore are not listed in the standard [202], such as lamination of ceramic films, directed energy deposition of plastics and ceramics and material jetting for metals. There may be scientific studies and trials on these, but there are no commercial suppliers. In general, new process and material combinations are developed on a demand-driven basis, which highlights the existence of large industries and a significant need. This usually leads to the selection of a commonly used material, as it can be used in many areas.

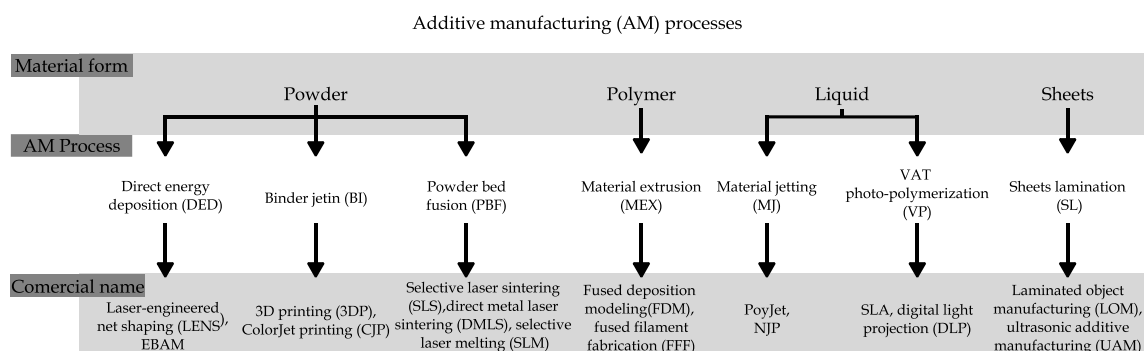


**Figure I.3.1.1.** Properties of the different AM processes.

In stereolithography, the standard tessellation language, Standard Triangle Language – STL, is used to generate a 3D model of the object to be manufactured. This model must be sliced to be processed to obtain the specific G-code of the AM equipment to be used.

The different AM technologies available need the raw material in a different format, it can be either filament, powder, pellets, liquid or paste sheet. And also depending on the technology used the raw material can be dispensed, melted, fused or cured to generate the object layer by layer. Manufacturing processes do not have a standardized name and the same process can be found under different names, which can lead to confusion.

### **I.3.2. Medical Additive Manufacturing applications.**

In the medical field, each patient is unique and therefore AM has great potential to be used in personalized medical applications. The most common medical clinical uses are in customized implants, prostheses and medical models [189]. In the field of dentistry, AM is used in splints, orthodontic appliances, dental models and drill guides. However, the possibility of obtaining artificial organs and tissues using AM has also been explored [190]. To reconstruct three-dimensional models of patient's anatomy, it is necessary to digitize medical images. The standard workflow for obtaining customized medical devices starts with 3D scanning methods such as computed tomography of the patient's geometry. This data is then manipulated to obtain a 3D model of the patient's anatomy, and this can be an example of AM as a medical model. The medical model can then be used to design specific implants for each particular patient and can be obtained by AM. This process is not final and usually requires post-processing such as polishing, afterwards it can be applied clinically and subsequent followed up [190].

Different studies have listed the benefits of the application of AM in the medical field. Ballard *et al.* [191] described both the economic and time efficiency of AM implantation for orthopedic and maxillofacial surgery. Tack *et al.* [192] managed to reduce radiation exposure times by achieving time savings in the performance of surgeries. On the other hand Yang *et al.* [193] emphasized that the application of AM allows a better understanding of the patient's anatomy to be achieved, which translates into greater precision in surgery. The area of dentistry is one of the areas of medicine that has benefited most from the application of AM techniques, Salmi *et al.* [194] pointed out that the manual work required is reduced, which translates into cost and time savings [195,196]. The fabrication of dental implants has taken a great step forward with

AM, since it is easier to obtain templates to form implants [197], they can be fabricated with complex geometries [198] and a rough texture can be applied to them to improve stabilization and facilitate osseointegration [199]. AM offers the opportunity to receive more customized and patient-specific parts [200], with faster turnaround, lower inventory level and reduced delivery costs [201]. The main benefits of applying AM in the medical field have been summarized in **Figure I.3.1**. These benefits can be carried over to other subject areas, such as the industry.

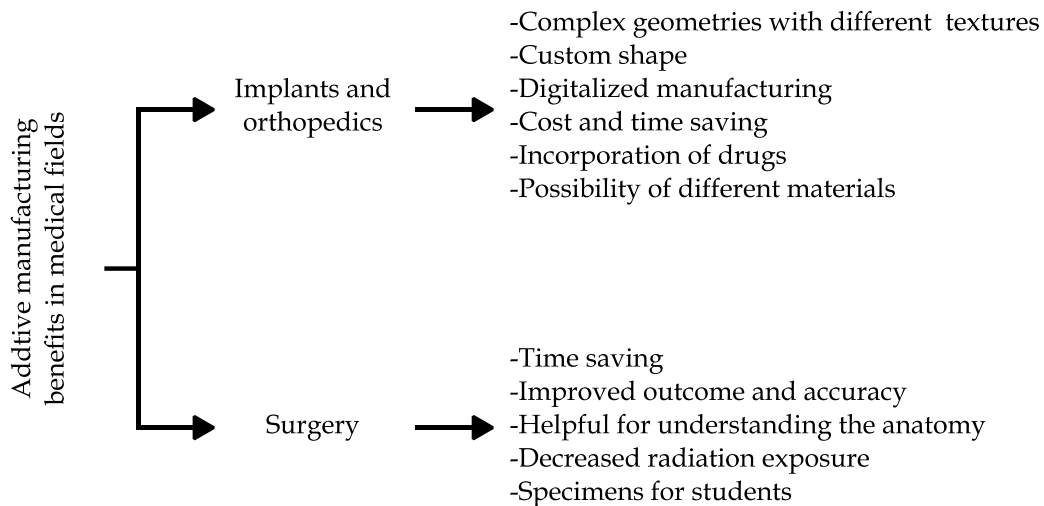


**Figure I.3.2.1.** Main benefits of AM in medical field.

The different categories into which the medical applications of AM can be classified are: implants, medical models, biomanufacturing, splints and prostheses, support guides and medical aids and parts, instruments and tools for medical devices [203]. An example of each of the categories is shown in the **Figure I.3.2.2**.

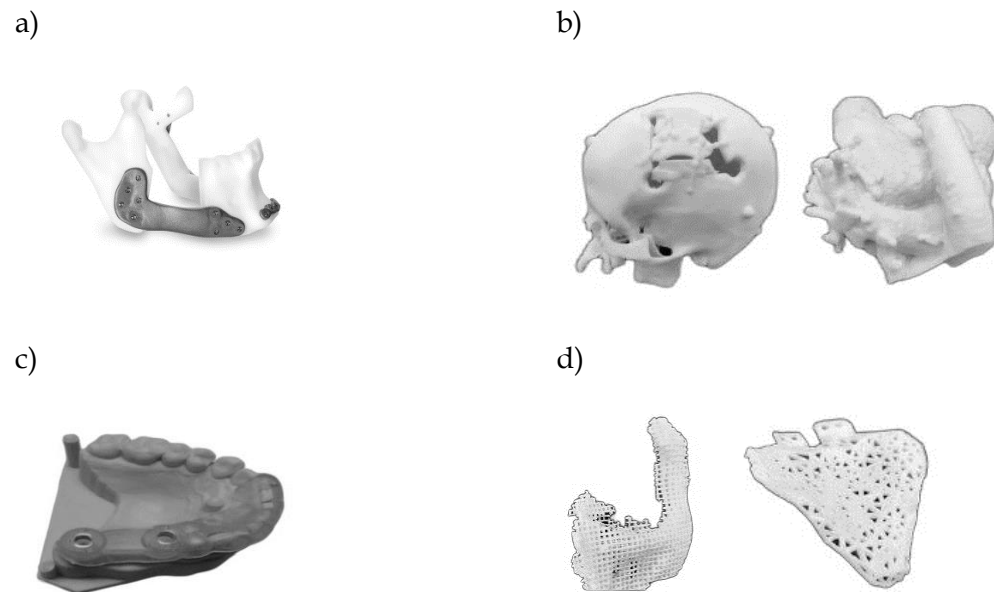


**Figure I.3.2.2.** a) implants, b) medical models, c) tools, instruments and parts for medical devices and d) scaffolds for biomanufacturing.

### I.3.2.1. Medical models.

Medical models are objects based on the patient's anatomy that are used for the training of medical students, to provide information to relatives and patients and for pre- and post-operative planning [192,204]. When generating the model, it can be made to scale by both redrawing and enlarging and only the interesting section can be taken. In cases of traumatological training it is interesting that the feel of the model resembles the bone. In the area of traumatology models are widely used for bony structures such as pelvis and spine and mainly in craniomaxillofacial [192,205]. Since the models are only used for observation, they have no material requirements, so there is freedom. If it is desired to introduce them in the operating room, it is necessary to sterilize them previously. The usual workflow for the development of a model is shown in **Figure I.3.2.3**. The starting point is a medical image that provides the patient's anatomy, which can be an ultrasound, Magnetic Resonance Imaging - MRI or Computed Tomography - CT. The 3D model is then constructed using the information obtained from the medical image. This 3D model is used for AM fabrication prior to segmentation and obtaining the G-code [206,207]. Once the model is available, depending on the geometry, it may be necessary to remove the supporting structures.

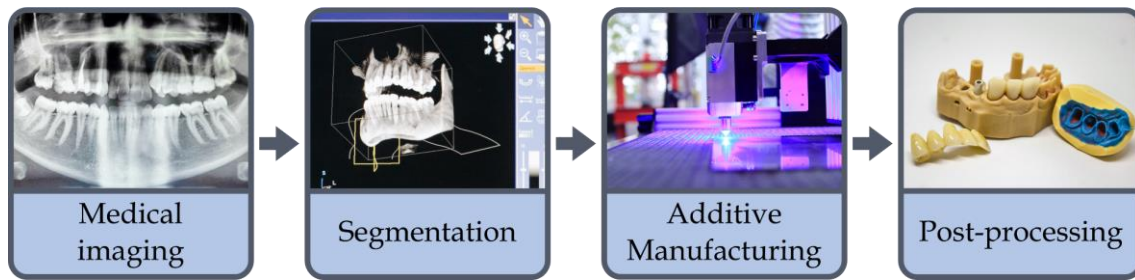


**Figure I.3.2.3.** Workflow employed for the obtention of medical models.

### **I.3.2.2. Implants.**

Missing or diseased tissues can be replaced by implants that can be manufactured by AM [208,209]. The requirements for the materials are very strict and they must also be compatible with the tissues, which means that the materials must be approved by the regulatory agencies, which takes a long time. To improve cell adhesion, it is necessary to modify surface properties. New developments take advantage of the inclusion of drug delivery systems inside implants [210,211]. Additive manufacturing makes it possible to obtain implants customized to the patient, which improves results, but it is necessary to capture the patient's anatomy beforehand in a manner similar to medical models. The digital model is used as a reference to adjust the design specifically to the patient's anatomy [212,213]. Implants are usually metallic and the most common process for their fabrication is powder bed fusion. Post-processing is required to remove the supports, by machining and polishing and possible heat treatments. As in the previous ones, it starts from medical images that are used for the formation of 3D models of the patient, then the implant geometry must be designed to fit the model of the patient's anatomy so it can be manufactured by AM and finally sterilized.

### **I.3.2.3. Instruments, tools and parts for medical devices.**

Instruments, tools and parts for medical devices are used to improve clinical interventions. These devices when manufactured by AM can be made to patient specific geometries and dimensions such as drill guides [214]. These devices being in contact with tissues, membranes, body fluids need to be sterilized. To customize an instrument to a patient, a procedure similar to that described for implants and models is followed, starting from 3D scanning or medical imaging. To obtain the three-dimensional modelling necessary to manufacture the objects, it is possible to start from the 3D model or from scratch if it is not patient-specific. Post-processing is necessary, which varies according to the needs of each instrument, such as heat treatments, removal of supports, machining and sterilization, since it is in contact with parts of the body.

### **I.3.2.4. Support guides, medical aids, prostheses and splints.**

In this category, medical devices obtained by AM are disposed externally to the body so that sterilization processes are not necessary. They also have the ability to be attached to standard devices, which allows them to be customized. Examples of this type of devices are customized splints, prosthesis sockets, fixators, external prostheses, orthopedic applications and postoperative supports [215–217]. As with all other medical devices it is necessary to start the process from the patient's anatomy data obtained by 3D measurements to perform segmentation and subsequent modelling. After manufacturing the device by AM it may be necessary to perform some type of post-processing such as heat treatment, removal of some support or perform some coating or painting. These devices can also be fabricated using Computer Numerical Control - CNC machining techniques [218].

### **I.3.2.5. Biomanufacturing.**

Biomanufacturing with AM processes enters the field of regenerative medicine as it allows new cellular tissues to be created on structures fabricated with AM [219]. To achieve this goal the materials used must be biocompatible and allow cell regeneration such as polymers, hydrogels, ceramics and composites to meet the specific needs of different body tissues [220]. The architecture of the scaffold created during the AM process allows precise control of cell encapsulation, viability, activity, proliferation and attachment. Biomanufacturing is a solution for many diseases due to its ability to inject non-toxic material including healthy and regenerative cells. In addition, the architecture of the scaffolds can be modified as desired to match the tissue structure *in vivo*. This technology has a great impact in traumatology where structures are fabricated using osteoconductive, osteoinductive or resorbable materials [221]. The geometry of the scaffolds is fabricated at will to adapt to the tissue structure *in vivo* and conduct cell regeneration at will [222]. To customize the shape of the structure to suit the lesion, it is necessary to obtain three-dimensional medical images beforehand to design porous scaffolds that allow cell growth. The manufacturing processes applied must be sterile or the objects produced must be sterilized once manufactured since they are going to be introduced inside the body. **Figure I.3.2.4.** shows the procedure to be followed for biomanufacturing.



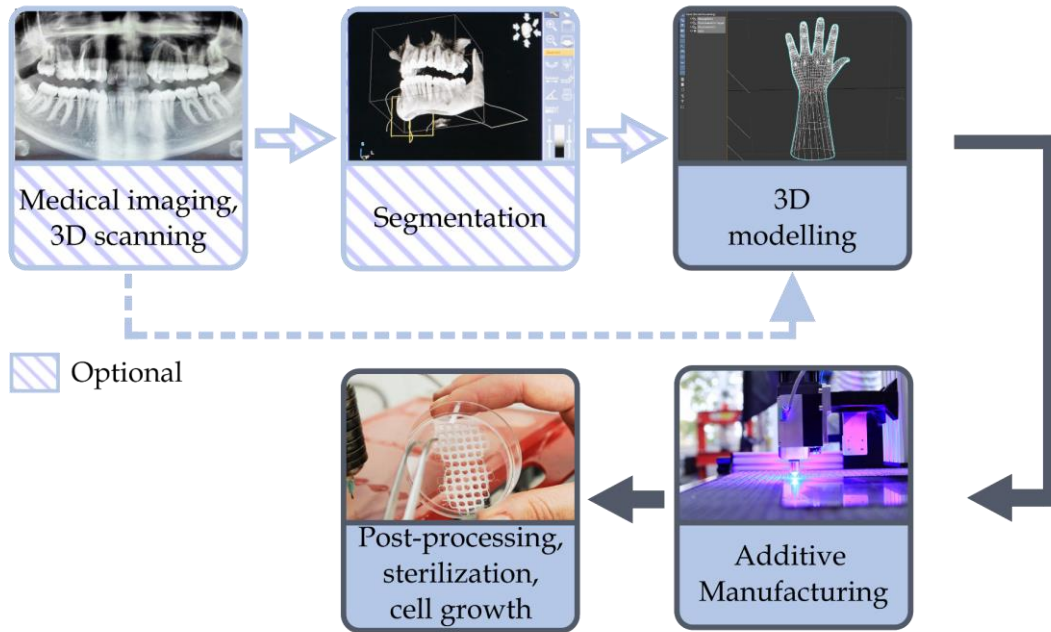


Figure I.3.2.4. Workflow employed for biomanufacturing.

### I.3.3. Additive manufacturing processes.

Different AM techniques can be used for the applications described in the previous section. To identify them, a literature search was carried out using the standardized terminology [202] combined with the trade names and the name of the manufacturing company. Previous studies have been found of some AM processes used in medical applications such as biomaterials in AM of medical instruments [223,224], metal powder bed fusion to obtain implants [222] and tissue regeneration applying structures obtained with AM [225]. These previous studies only examine a single process and do not classify it according to the standards. According to the results obtained in the literature search, **Figure I.3.3.1.** summarizes the processes and materials used in several categories.

<b>Medical models</b>					
<b>PBF</b>	<b>MEX</b>	<b>VP</b>	<b>MJ</b>	<b>BJ</b>	<b>SL</b>
PA, PP	ABS, PLA	Photocurable resin	VeroWhite, VeroClear, TangoPlus, Multi-material	ZP150, ZP151, PMMA	Paper
<b>Implants</b>					
<b>PBF</b>	<b>MEX</b>	<b>VP</b>	<b>BJ</b>	<b>DED</b>	
Ti6Al4VTi64, Co-Cr-Mo, Al2O3-ZnO2	PEEK	Clear resin V4, ATZ, NextDent C&B	ZP150, TCP, nickel-based alloy 625, Titanium	Ti6Al4V	
<b>Tools and instruments</b>					
<b>PBF</b>	<b>MEX</b>	<b>VP</b>	<b>MJ</b>	<b>SL</b>	
PA, Co-Cr, Ti	ABS, PLA	ProtoGen O-XT18420, Dental SG, Dental LT, Clear resin V2, Photocurable resin WaterShed XC 111133	TangoPlus, HeartPrint Flex, MED610	Paper	
<b>Medical guides and aids</b>					
<b>PBF</b>	<b>MEX</b>	<b>VP</b>	<b>MJ</b>	<b>BJ</b>	
PA	ABS, PLA, Nylon	Clear resin, Ciba-Geigy 5170, Somos 6110, Epoxy	Multi-material, Full Core 720, ABS like, VeroWhite	ZP151, Stainless steel	
<b>Biomanufacturing</b>					
<b>PBF</b>	<b>MEX</b>	<b>VP</b>	<b>BJ</b>		
PLA, PLGA	PCL, PLA, PLGA, TCP	PDLLA, HA	Visijet PXL, Calcium phosphate, barium titanate		

**Figure I.3.3.1.** Additive manufacturing processes applied in medical applications.

### I.3.4. Materials used in Additive Manufacturing for medical applications.

The materials used in the manufacture of medical devices have varied throughout history, ranging from materials such as gold or silver to coconut. During the 16<sup>th</sup> century, xenografts were used, attempting to reconstruct the human bones like the skull by using bones from different animals [226].

An alloplastic is a material that is introduced inside the human organism with the aim of remodelling or replacing an area of the body [227]. The ideal material to be used in bone surgery should be able to adapt to the lesion, be permeable to radiation, biocompatible, resistant to biomechanical stresses and as far as possible have a low cost [228].

The biocompatibility of a material is the differentiating advantage of some materials that allows their implantation inside the human body without receiving an immune response [229]. The biomaterials that are commonly being used belong to the families of metals, ceramics and polymers. Each of the families of materials present different differentiating properties that make them suitable for a type of application [230].

#### **I.3.4.1. Metals.**

The most commonly used metal for in bone surgeries is titanium, specifically Ti-6Al-4V alloy (C < 0.08 %, Fe < 0.25 %, N<sub>2</sub> < 0.05 %, O<sub>2</sub> < 0.2 %, Al 5.5 - 6.76 %, V 3.5 - 4.5 %, Ti) is present in most devices. Its high mechanical properties, high biocompatibility in the human body and corrosion resistance have led to its use in a large number of medical devices and implants [231].

There are cheaper alternatives such as 316L stainless steel (C < 0.08 %, Mn < 2 %, S < 0.03 %, P < 0.045 %, Si < 0.75 %, Cr 16 - 18, Ni 10 - 14, Mb 2 - 3, N < 0.1). Even biodegradable options based on magnesium alloys that allow the device to be reabsorbed after having fulfilled its function within the organism. Some of the elements introduced in the alloy with magnesium are yttrium, neodymium or zirconium [230].

On the other hand, during long periods of implantation metallic devices can give rise to problems. Infections, metal accumulations in the tissues, as well as the presence of localized pain may develop. Such problems may require a second surgical intervention for removal. This kind of problems are promoting the development of polymer based implants that can be reabsorbed by the human body [232].

#### **I.3.4.2. Ceramics.**

Ceramic materials have high hardness, high compressive strength and a low friction coefficient. The main problem associated with them is the low toughness that can produce breakage due to the action of an impact, which means that they are mainly used as additives within a polymeric matrix or as a coating [230].

An example of ceramics applied in cranial operations are calcium orthophosphates - Ca<sub>3</sub>(PO<sub>4</sub>)<sub>2</sub> that present high osteoconductivity. Osteoconductivity promotes the generation of bone cells and thus improves bone regeneration capacity. This property is due to the fact that the chemical structure of these substances is very similar to that of human bone [233].

### **I.3.4.3. Polymers and biopolymers.**

The first polymer used for bone repair uses at the end of the 19<sup>th</sup> century was celluloid, the main problem was its low biocompatibility. In the 60's, polymethylmethacrylate - PMMA appeared for its use in cranial surgeries. A polymerization process from methyl methacrylate monomers by means of free radical vinyl polymerization. This resulted in an exothermic reaction that could lead to tissue necrosis in the area near the treated site [228]. Porous polyethylene was also used in the 20<sup>th</sup> century. The presence of pores allows the vascularization of the medical device favouring its integration into the body [228].

Currently, the use of biopolymers with bioabsorption capacity offers a wide range of properties that allow them to be applied in various areas of medicine. This positions biocompatible biopolymers as the family of materials with the greatest future prospects in the field of biomedicine [234].

Biopolymers are organic molecules formed by monomers produced by living organisms [235]. There are different types of organisms that produce this type of polymers such as plants that produce starch and cellulose. Other ways to obtain this type of materials are animals that produce substances such as chitosan, keratin or silk. Finally, the last way to obtain these polymers is by fermentation with bacteria, which can be used to obtain the PHA [236].

These types of polymers are positioned as materials that offer high biocompatibility [237]. Biocompatibility is the property that allows certain materials to perform a function in a medical therapy without producing any risk of suffering rejection by the body in which it is implanted [229].

In certain cases, biopolymers have the ability to biodegrade. This process can occur in different environments and one of them is inside the human body. The process consists of two fundamental phases. In the first phase, the polymer chains are broken as a result of a hydrolysis process or by the action of an enzyme from the body itself. After breaking the polymer chains, the human body has to assimilate the fragments, and for this purpose a process of phagocytosis or a metabolic process takes place [238].

The biodegradation process is largely dependent on the temperature and pH of the medium in which the process takes place. Other influencing factors are the type of polymer bond, molecular weight and crystallinity [238]. The advantage offered by this type of resorbable device is that it rules out the need for a second intervention for its removal. During the time it is inside the body, the device slowly degrades until it

disappears completely after having fulfilled its function [239].

A clear example of a polymer that combines biocompatibility and the ability to biodegrade is the family of polyhydroxyalkanoates or PHA. They are currently positioned as a future alternative for the manufacture of different medical devices [240].

#### **I.3.4.4. Additives and fillers in biopolymers.**

The incorporation of additives in biopolymers seeks to modify some of their properties. The modifications that can be achieved are mainly on the mechanical, thermal, aging, degradation and other properties. In short, the aim is to make the polymer more attractive and optimized for use in an industrial process [241].

With the same objective of obtaining a polymer with more attractive properties, different types of chains can also be mixed. With this practice, the aim is to correct the problems that some polymers propose. The mixture of different types of polymers sometimes presents a lack of miscibility. To correct this, compatibilizing additives can be used to improve the adhesion between different chains [242].

The addition of fillers and additives to a polymer alters its processability since its characteristics are modified. The properties to be controlled are thermal and rheological. Adding a filler alters the glass transition temperature, as well as the melting temperature and the degradation temperature. These temperatures, determine the working range of the material. On the other hand, viscosity is also altered, as the addition of a filler usually increases the viscosity, thus compromising the process parameters used with the neat material.

The addition of nanotubes allows to have an empty tubular structure that can be loaded with different substances inside. This allows its controlled release over time. This type of technology can be applied in the human body, for the application of long-lasting treatments, as well as in food preservation through the release of substances by the packaging [243].

To enhance bone repair, an osteoconductive filler can be introduced. An osteoconductive material allows the growth of bone cells inside the pores [244]. An example of this are calcium orthophosphates, they are characterized by having a structure very similar to that of bone which makes it a highly biocompatible material, thus allowing the creation of medical devices for bone reconstruction [245]. In addition, calcium orthophosphates have bioactive properties that increase bone cell proliferation (osteinduction) [246].

### - Calcium orthophosphates.

This is a group of materials that belong to the bioceramics and are therefore characterized by high brittleness. To solve this problem, they are usually used in nanometre size within a polymeric matrix or in the form of a surface coating. In the family of calcium orthophosphates there are different formulations as shown in **Table I.3.4.1.**

**Table I.3.4.1.** Calcium orthophosphate formulations [245].

Compound	Formula
Monocalcium phosphate monohydrate (MCPM)	$\text{Ca}(\text{H}_2\text{PO}_4)_2 \cdot \text{H}_2\text{O}$
Monocalcium phosphate anhydrous (MCPA or MCP)	$\text{Ca}(\text{H}_2\text{PO}_4)_2$
Dicalcium phosphate dihydrate (DCPD), mineral brushite	$\text{CaHPO}_4 \cdot 2\text{H}_2\text{O}$
Dicalcium phosphate anhydrous (DCPA or DCP), mineral monetite	$\text{CaHPO}_4$
Octacalcium phosphate (OCP)	$\text{Ca}_8(\text{HPO}_4)_2(\text{PO}_4)_4 \cdot 5\text{H}_2\text{O}$
$\alpha$ -Tricalcium phosphate ( $\alpha$ -TCP)	$\alpha\text{-Ca}_3(\text{PO}_4)_2$
$\beta$ -Tricalcium phosphate ( $\beta$ -TCP)	$\beta\text{-Ca}_3(\text{PO}_4)_2$
Amorphous calcium phosphates (ACP)	$\text{Ca}_x\text{H}_y(\text{PO}_4)_z \cdot n\text{H}_2\text{O}$ , $n = 3 - 4.5$ ; 15 - 20% $\text{H}_2\text{O}$
Calcium-deficient hydroxyapatite (CDHA or Ca-def HA)	$\text{Ca}_{10-x}(\text{HPO}_4)_x(\text{PO}_4)_{6-x}(\text{OH})_{2-x}$ ( $0 < x < 1$ )
Hydroxyapatite (HA, HAp or OHAp)	$\text{Ca}_{10}(\text{PO}_4)_6(\text{OH})_2$
Fluoroapatite (FA or FAp)	$\text{Ca}_{10}(\text{PO}_4)_6\text{F}_2$
Oxyapatite (OA, OAp or OXA) mineral voelckerite	$\text{Ca}_{10}(\text{PO}_4)_6\text{O}$
Tetracalcium phosphate (TTCP or TetCP), mineral hilgenstockite	$\text{Ca}_4(\text{PO}_4)_2\text{O}$

Orthophosphates are characterized by high bioactivity because they are able to interact with the surrounding bone tissue. The osteoblasts responsible for bone formation are able to adhere to this type of substance, thus allowing their proliferation [247].

This type of substance also has the capacity to biodegrade inside the human body by two possible routes. The first option is through a process of reabsorption in the human body. The second mechanism consists of the dissolution of phosphates by the action of hydrolysis [247].

Of the different orthophosphates available there are two fundamental families, the different forms of apatites as well as the groups with acid phases. Within the biomedical field, hydroxyapatite is the most widely used in the manufacture of different medical devices. An example of this is the fabrication of hydroxyapatite-reinforced PMMA cranial reconstruction prostheses [248].

### - Hydroxyapatite.

Hydroxyapatite – HA is part of the aforementioned bioceramics. In this case, this material is found naturally in the interior of human bone in the form of nanometre-scale threads. This means that among the different bioceramics, this one has the highest

biocompatibility and is therefore the most widely used. Its use is mainly intended for the realization of surface coatings [249].

The particle size has an effect on the adhesion and proliferation capacity of bone cells, with sizes around 20 nm being of interest to achieve the greatest effect. With this particle size, structures with nanopores can be achieved, the presence of pores allows to increase the hydroxyapatite/cell contact area and thus maximize the osteoinductive effect of hydroxyapatite [249].

In order to obtain nanoparticles with the desired size and shape, the different processes with which the synthesis can be performed. As well as the parameters applied in each technique, have a great influence. There are different processes such as hydrolysis, chemical precipitation or a mechanical-chemical process, among others, with which hydroxyapatite is obtained [249].

In **Table I.3.4.2.**, several examples of the use of hydroxyapatite acting as a filler within different polymers can be seen. The tests performed on the different combinations of materials seek to quantify the improvement in terms of bone regeneration. For this purpose, *in vivo/in vitro* tests are carried out in which the polymer with hydroxyapatite is introduced into the body of animals and its evolution over time is analysed. In addition, some test are done in the laboratory by adding cells to determine their behavior in contact with the hydroxyapatite biocomposites.

As a result of these studies, in **Table I.3.4.2**, several examples can be seen in which the addition of hydroxyapatite has led to an improvement in osteoconductivity, which translates into an improvement in the bone regeneration process.

## I. INTRODUCTION

---

**Table I.3.4.2.** Hydroxyapatite with biopolymers. Reproduced from [250].

Biocomposite	Study	Materials/Models	Results
PCL/CS/nao-ZnHA	In vivo	haD-MSCs	Increased biocompatibility, cell adhesion enhanced proliferation and protein adsorption
PCL/HA	In vivo	Mouse calvaria defects	New bone formation after 6 weeks with perceivable woven bone structure, osteocytes and lacunae
P3HB/HA	In vivo	Female Wistar rats and male chinchilla rabbits	Biocompatible, enhanced osteoplastic properties, and slow degradation rate consistent with the repair of bone defects
PLA/HA	In vivo	Critical sized rat calvaria defects	Superior osteoconductivity. Bone formation with little inflammation and higher resorption rate than $\beta$ -TCP and DBM scaffolds
PLGA/HA	In vitro	MG63 cells	Biocompatibility, increased osteoconductivity, and osteoblast adhesion
PLGA/ $\beta$ -TCP/HA	In vivo	Rabbits femoral defects	Scaffold were biocompatible, osteoconductive, osteoinductive and biodegradable in 12 weeks

To achieve the best possible performance in stimulating bone regeneration, it is necessary to control roughness, pore size and interconnection. A rough surface can promote cell adhesion and proliferation. A large pore size causes the adhesion surface to decrease while too small pores hinder cell migration on the implant [250].

This leads to a reduction in the mechanical properties of the structure. The immersion process resulted in a slight change in the pH of the medium, as well as a deposition of Ca-P on the surface of the structure that may favour the biocompatibility of the composite.



## **II. OBJECTIVES.**



## II.1. General objectives.

The context of this work describes an increasing interest in environmentally friendly based biopolymers, such as aliphatic polyesters poly(lactic acid) - PLA and polyhydroxyalkanoates - PHA. From this context, a hypothesis is proposed where several environmentally friendly additives will be used for the improvement of the final properties of different aliphatic polyesters. At the same time, the processing techniques utilized to obtain samples of those materials will also be studied. To meet this end two techniques are proposed, polymer injection and AM through fused deposition modelling. On the one hand, polymer injection is a fabrication technique that is nowadays widely employed. On the other hand, AM is a technique that is under current development in several industrial sectors. It is for this reason that the study of both processing methodologies is of high interest. The final objective of this thesis is that of developing aliphatic esters with improved properties by incorporating several additives and utilizing both aforementioned processing techniques. It is of great interest that the proposed formulations could be used in different industrial sectors with an advanced technological component, in which the medical sector is included.

## II.2. Partial objectives.

In order to achieve the general objective, different partial objectives have been presented, which are divided in the three main blocks that compose the doctoral thesis.

Development of environmentally friendly formulations and composites with polyhydroxyalkanoates:

- Analysis of the incorporation of poly( $\epsilon$ -caprolactone) - PCL in different proportions in weight for the improvement of the ductile properties of a polyhydroxyalkanoate as it is poly(3-hydroxybutyrate-*co*-3-hydroxyhexanoate) - P(3HB-*co*-3HHx).
- Analysis of the incorporation of almond shell wastes for the obtention of a wood plastic composite from P(3HB-*co*-3HHx)..
- Evaluation of the plasticizing effect and the coupling effect through the incorporation of a lactic acid oligomer in a P(3HB-*co*-3HHx) composite with almond shell.
- Determination of the plasticizing effect after the incorporation of different geranile derived esters in a poly(3-hydroxybutyrate) - P3HB matrix for the improvement of their ductile properties.

## II. OBJECTIVES

---

Manufacturing of polyhydroxyalkanoates by 3D printing and injection moulding for medical applications:

- Statistical analysis of the effect of the additive manufacturing processing parameters over the final properties of P(3HB-*co*-3HHx).
- Measurement of the effect of the introduction of nanohydroxyapatite as an additive utilized in the medical sector over the final properties of samples obtained through injection and additive manufacturing.
- Evaluation of the effect of the processing cycles of the hydroxyapatite and poly(3-hydroxybutyrate-*co*-3-hydroxyhexanoate) nanocomposites.
- Obtention of scaffolds of poly(3-hydroxybutyrate-*co*-3-hydroxyhexanoate) and nanohydroxyapatite for bone regeneration obtained by means of AM techniques.
- Study of the *in vitro* degradation of the scaffolds by immersing them in Phosphate Saline Buffer - PBS.

Development of environmentally friendly formulations of polylactide for injection moulding and 3D printing:

- Evaluation of the introduction of dibutyl itaconate - DBI as a plasticizer of PLA formulations.
- Analysis of the pattern effect employed in the infill of polylactide - PLA samples obtained through AM.
- Design and validation of a prototype of a fixation plate for a femur bone using PLA.

The proposed objectives are graphically shown in **Figure II.1**.

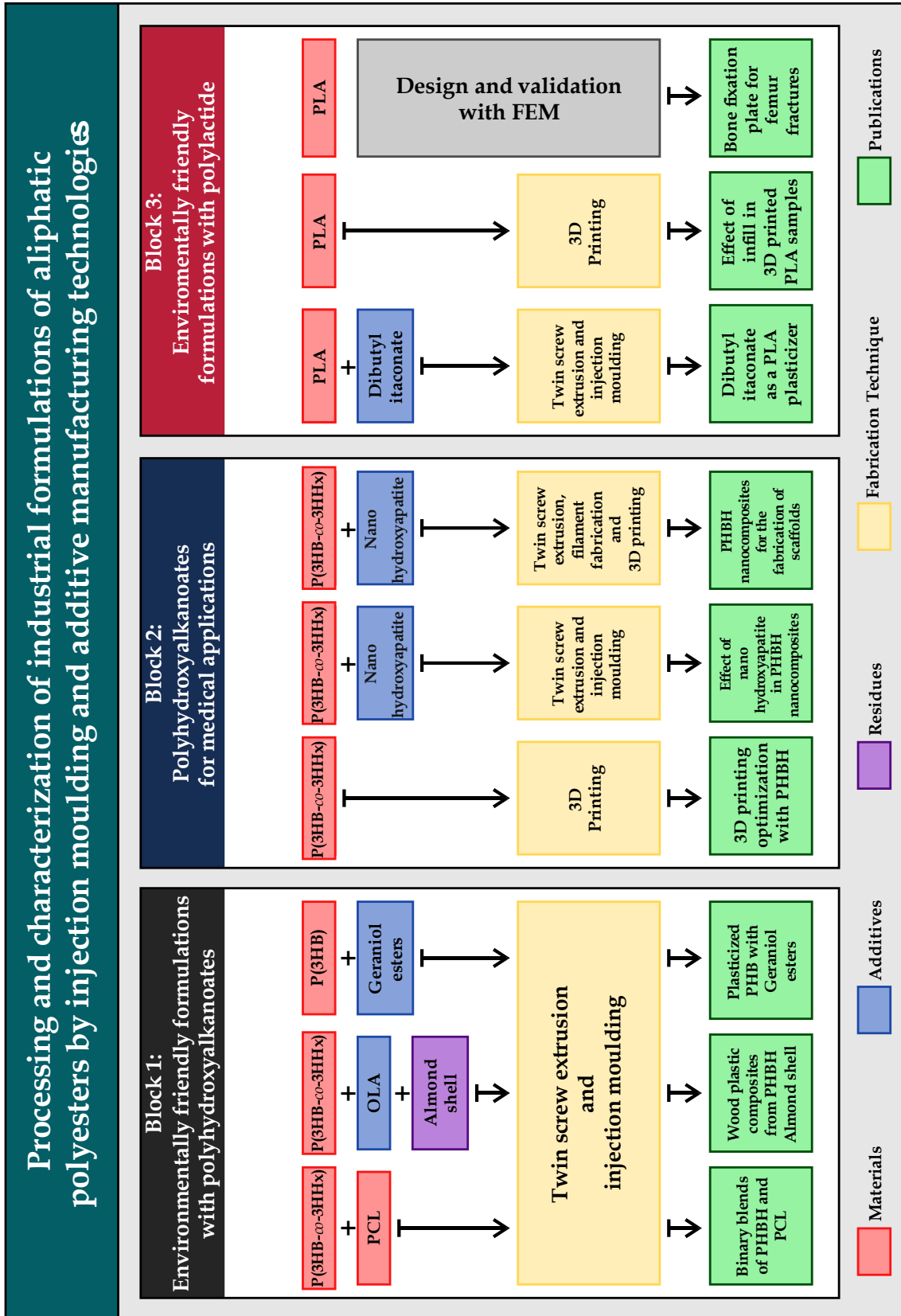


Figure II.1. Summary diagram of the work carried out.



### **III. RESULTS & DISCUSSION.**





The obtained results have been divided in 3 clearly different sections and 9 chapters, each one corresponding to one journal article. The different works have been grouped according to the materials employed and the manufacture techniques used.

**Section I: Development of environmentally friendly formulations and composites with polyhydroxyalkanoates.**

This section explores the development of high environmentally friendly formulations with polyhydroxyalkanoates - PHA. Due to the high brittleness of PHA after a relative short aging time of 15 to 20 days, several approaches have been addressed. On the one hand, the effect of new promising biobased plasticizers from terpenoids is evaluated as a technical solution to overcome the intrinsic low toughness of PHA, particularly on poly(3-hydroxybutyrate) - P3HB. The effects of the carboxylic acid length used to esterify geraniol to give the corresponding geranyl ester is evaluated in terms of mechanical, thermal, thermo-mechanical properties, as well as their effect on biodegradation or disintegration in compost soil. Another interesting approach in this section is the development of binary blends of poly(3-hydroxybutyrate-co-3-hydroxyhexanoate) - P(3HB-co-3HHx) and poly( $\epsilon$ -caprolactone) - PCL to improve toughness. The effect of the PCL content on mechanical, thermal, thermo-mechanical properties and morphology is addressed. Finally, this section includes the development of Wood Plastic Composites - WPC by using P(3HB-co-3HHx) and a widely available biomass filler, namely Almond Shell Flour - ASF. The effect of the amount of filler and the polymer-fillers interactions is studied to assess the feasibility of these composites to contribute to the transition of linear to circular economies. This section includes the following chapters, which are the adapted versions from the corresponding journal articles.

**Chapter III.1.1.:** Manufacturing and properties of binary blend from bacterial polyester poly(3-hydroxybutyrate-co-3-hydroxyhexanoate) and poly( $\epsilon$ -caprolactone) with improved toughness.

**Chapter III.1.2.:** Development and characterization of sustainable composites from bacterial polyester poly(3-hydroxybutyrate-co-3-hydroxyhexanoate) and almond shell flour by reactive extrusion with oligomers of lactic acid.

**Chapter III.1.3.:** Plasticization of poly(3-hydroxybutyrate) with biobased terpenoid esters of geraniol.

#### **Section II: Manufacturing of polyhydroxyalkanoates by 3D printing and injection moulding for medical applications.**

This second section focuses on the potential of polyhydroxyalkanoates on medical applications. First, an in-depth study of the 3D-printing process is carried out, by identifying the main parameters to be considered for optimum 3D-printing with PHA. This first chapter addresses the effect of the processing parameters (pattern, bed temperature, the activation of the cooling layer fan, among others) on the 3D-printability and their effects on mechanical properties. A second chapter in this section focuses on the development and characterization of specific formulations based on P(3HB-co-3HHx) and hydroxyapatite, for uses in medical applications such as bone tissue engineering. The work explores the optimum processing conditions of these materials by injection moulding and the effect of the varying amount of hydroxyapatite on mechanical, thermomechanical, morphological properties and so on. After optimization of the processing conditions and formulations of P(3HB-co-3HHx) and hydroxyapatite, a third chapter addresses the optimization of the processing conditions by 3D-printing as a way to design customized solutions in the medical sector and shows the feasibility of this technique to obtain accurate parts for scaffolds. The chapters include the adapted versions of the corresponding journal articles.

**Chapter III.2.1.:** The effects of processing parameters on mechanical properties of 3D-printed polyhydroxyalkanoates parts.

**Chapter III.2.2.:** Assessment of the mechanical and thermal properties of injection-moulded poly(3-hydroxybutyrate-co-3-hydroxyhexanoate)/nanohydroxyapatite parts for use in bone tissue engineering.

**Chapter III.2.3.:** P(3HB-co-3HHx)/nanohydroxyapatite - nHA composites for the manufacturing of scaffolds by means of fused deposition modelling.

**Section III: Development of environmentally friendly formulations of polylactide for injection moulding and 3D printing.**

Despite PHA represent a feasible solution for medical applications, poly(lactic acid) or polylactide - PLA, is currently, one of the most used polymers for medical applications, together with poly(glycolide) - PGA, poly( $\epsilon$ -caprolactone) - PCL, poly(dioxanone) - PDO, and their copolymers. Therefore, this section includes some works focused on improving the intrinsic brittleness of PLA and assessing the potential of 3D-printing technologies to customize printed parts for medical uses. This section includes a first work in which, the potential of a biobased plasticizer, namely dibutyl itaconate - DBI, is studied. This work contains an in-depth study of the theoretical solubility between PLA and DBI through calculating their solubility parameters -  $\delta$ , and the corresponding contributions due to dispersive forces -  $\delta_d$ , polar forces -  $\delta_p$ , and hydrogen bonding -  $\delta_h$ . The obtained results are very promising and indicate DBI could be a feasible solution to develop high environmentally friendly formulations based on PLA with improved ductile properties. The second chapter in this section explores the effect of some 3D-printing parameters in final properties of 3D-printed PLA parts. This allows defining the possibility of 3D-printing to obtain accurate parts for medical applications. Subsequently, a case report on the development of a bone fixation plate for femoral MID-shaft fractures is described in the third chapter. An in-depth analysis of the material properties obtained by 3D-printing process is used in combination with simulation techniques as the Finite Element Modelling - FEM to assess the feasibility of AM with PLA-based formulations for medical applications. The section includes the adapted versions of the corresponding journal articles.

**Chapter III.3.1.:** The potential of an itaconic acid diester as environmentally friendly plasticizer for injection-moulded polylactide parts.

**Chapter III.3.2.:** Effect of infill parameters on mechanical properties in additive manufacturing.

**Chapter III.3.3.:** Design and simulation of a resorbable bone fixation plate made by additive manufacturing for femoral MID-shaft fractures.



**Section I:  
Development of environmentally friendly  
formulations and composites with  
polyhydroxyalkanoates.**

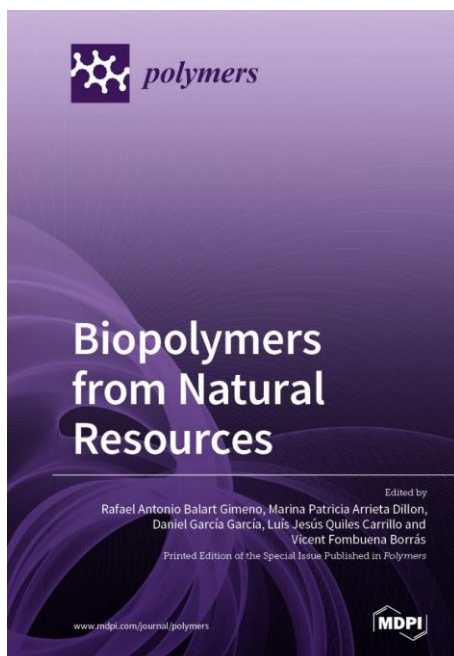


Adapted from the original manuscript.

### III.1.1 Manufacturing and properties of binary blend from bacterial polyester poly( $\beta$ -hydroxybutyrate-*co*- $\beta$ -hydroxyhexanoate) and poly( $\epsilon$ -caprolactone) with improved toughness.

Juan Ivorra-Martinez<sup>1</sup>, Isabel Verdu<sup>1</sup>, Octavio Fenollar<sup>1</sup>, Lourdes Sanchez-Nacher<sup>1</sup>, Rafael Balart<sup>1</sup> and Luis Quiles-Carrillo<sup>1</sup>.

<sup>1</sup>Technological Institute of Materials - ITM, Universitat Politècnica de València - UPV, Plaza Ferrándiz y Carbonell 1, 03801 Alcoy (Spain).



**Polymers.**

**2020, 12(5): 1118.**





Article

# Manufacturing and Properties of Binary Blend from Bacterial Polyester Poly(3-hydroxybutyrate-co-3-hydroxyhexanoate) and Poly(caprolactone) with Improved Toughness

Juan Ivorra-Martinez <sup>\*</sup>, Isabel Verdu, Octavio Fenollar, Lourdes Sanchez-Nacher, Rafael Balart  and Luis Quiles-Carrillo 

Technological Institute of Materials (ITM), Universitat Politècnica de València (UPV), Plaza Ferrándiz y Carbonell 1, 03801 Alcoy, Spain; isvergar@epsa.upv.es (I.V.); ocfegi@epsa.upv.es (O.F.); lsanchez@mcm.upv.es (L.S.-N.); rbalart@mcm.upv.es (R.B.); luiquic1@epsa.upv.es (L.Q.-C.)

\* Correspondence: juaivmar@doctor.upv.es; Tel.: +34-966-528-421

Received: 29 April 2020; Accepted: 12 May 2020; Published: 14 May 2020



**Abstract:** Polyhydroxyalkanoates (PHAs) represent a promising group of bacterial polyesters for new applications. Poly(3-hydroxybutyrate-co-3-hydroxyhexanoate) (PHBH) is a very promising bacterial polyester with potential uses in the packaging industry; nevertheless, as with many (almost all) bacterial polyesters, PHBH undergoes secondary crystallization (aging) which leads to an embrittlement. To overcome or minimize this, in the present work a flexible petroleum-derived polyester, namely poly( $\epsilon$ -caprolactone), was used to obtain PHBH/PCL blends with different compositions (from 0 to 40 PCL wt %) using extrusion followed by injection moulding. The thermal analysis of the binary blends was studied by means of differential scanning calorimetry (DSC) and thermogravimetry (TGA). Both TGA and DSC revealed immiscibility between PHBH and PCL. Mechanical dynamic thermal analysis (DMTA) allowed a precise determination of the glass transition temperatures ( $T_g$ ) as a function of the blend composition. By means of field emission scanning electron microscopy (FESEM), an internal structure formed by two phases was observed, with a PHBH-rich matrix phase and a finely dispersed PCL-rich phase. These results confirmed the immiscibility between these two biopolymers. However, the mechanical properties obtained through tensile and Charpy tests, indicated that the addition of PCL to PHBH considerably improved toughness. PHBH/PCL blends containing 40 PCL wt % offered an impact resistance double that of neat PHBH. PCL addition also contributed to a decrease in brittleness and an improvement in toughness and some other ductile properties. As expected, an increase in ductile properties resulted in a decrease in some mechanical resistant properties, e.g., the modulus and the strength (in tensile and flexural conditions) decreased with increasing wt % PCL in PHBH/PCL blends.

**Keywords:** bacterial polyesters; poly(3-hydroxybutyrate-co-3-hydroxyhexanoate)—PHBH; poly( $\epsilon$ -caprolactone)—PCL; binary blends; improved toughness; mechanical and thermal characterization

## 1. Introduction

Nowadays, awareness of environmental protection, sustainable development, and the use of renewable energies has become a priority for our society. The high volume of wastes generated that are harmful for the environment, oceans, ecosystems, and so on, has become a major problem to be solved. Furthermore, the waste generated in a consumer society, such as the present one, comes mainly from the packaging sector. This need has favoured the development of new environmentally friendly



**Abstract.**

Polyhydroxyalkanoates, PHAs represent a promising group of bacterial polyesters for new applications. Poly(3-hydroxybutyrate-*co*-3-hydroxyhexanoate) - P(3HB-*co*-3HHx) is a very promising bacterial polyester with potential uses in the packaging industry; nevertheless, as many (almost all) bacterial polyesters, P(3HB-*co*-3HHx) undergoes secondary crystallization (aging) which leads to an embrittlement. To overcome or minimize this, in the present work a flexible petroleum-derived polyester, namely poly( $\epsilon$ -caprolactone) - PCL was used to obtain P(3HB-*co*-3HHx)/PCL blends with different compositions (from 0 to 40 PCL wt.%) by extrusion followed by injection moulding. The thermal analysis of the binary blends was studied by means of Differential Scanning Calorimetry - DSC and thermogravimetry analysis - TGA. Both TGA and DSC revealed immiscibility between P(3HB-*co*-3HHx) and PCL. Dynamic-Mechanical Thermal Analysis - DMTA allowed a precise determination of the glass transition temperatures -  $T_g$  as a function of the blend composition. By means of Field Emission Scanning Electron Microscopy - FESEM, an internal structure formed by two phases was observed, with a P(3HB-*co*-3HHx) rich matrix phase, and a finely dispersed PCL rich phase. These results confirmed the immiscibility between these two biopolymers. However, the mechanical properties obtained through tensile and Charpy tests, indicated that the addition of PCL to P(3HB-*co*-3HHx), considerably improved toughness. P(3HB-*co*-3HHx)/PCL blends containing 40 PCL wt.% offered an impact resistance double than that of neat P(3HB-*co*-3HHx). PCL addition also contributed to decrease brittleness, improve toughness and some other ductile properties. As expected, an increase in ductile properties, provided the decrease in some mechanical resistant properties, *e.g.* the modulus and the strength (in tensile and flexural conditions) decreased with increasing wt.% PCL in P(3HB-*co*-3HHx)/PCL blends.

**Keywords:** bacterial polyesters; poly(3-hydroxybutyrate-*co*-3-hydroxyhexanoate) - P(3HB-*co*-3HHx); poly( $\epsilon$ -caprolactone) - PCL; binary blends; improved toughness; mechanical characterization and thermal characterization.

---



## INTRODUCTION.

Nowadays, awareness on environmental protection, sustainable development, and the use of renewable energies has become a priority for our society. The high volume of wastes generated that are harmful for the environment, oceans, ecosystems, and so on, has become a major problem to be solved. Furthermore, the waste generated in a consumer society such as the present one, comes mainly from the packaging sector. This need has favoured the development of new environmentally friendly materials [1]. For this reason, the use of the called biopolymers is increasing in the packaging sector. Most of these materials are obtained from renewable resources and they are, in many cases, biodegradable (or compostable in controlled compost soil). Therefore, they positively contribute to minimize plastic wastes, thus reducing the carbon footprint, and also contributing to circular economies by upgrading industrial wastes [2] and/or by-products [3].

In this area, researchers have successfully developed new polymeric materials from renewable and/or biodegradable sources. These important research works have allowed the optimization of interesting biopolymers to be scaled in the industry such as poly(lactic acid) - PLA [4], poly(hydroxyalkanoates) - PHA [5], thermoplastic starch - TPS [6], poly( $\epsilon$ -caprolactone) - PCL [7], poly(butylene succinate) - PBS [8], among others. Biopolymers can perfectly replace some petroleum-derived polymers [9], since they offer similar performance to most commodities and some engineering plastic. Biopolyesters is an interesting group which includes petroleum-based polymers such as poly(glycolic acid) - PGA, PBS, poly(butylene adipate-*co*-terephthalate) - PBAT, PCL, among others. But biopolyesters also include bacterial polyesters as the polyhydroxyalkanoates - PHAs, and some starch-derived polymers such as PLA. The main advantage of polyesters (from both natural or fossil resources) is that they can undergo biodegradation (disintegration in controlled conditions with special compost soil), through the action of microorganisms. This makes composting an important and simple sustainable option for the management of these wastes [10].

Nowadays, biopolymers produced by bacterial fermentation such as PHAs, are becoming very promising as there are more than 300 potential PHAs and copolymers. Despite this wide variety, the most commonly used, and commercially available PHAs are poly(3-hydroxybutyrate) - P3HB and poly(3-hydroxybutyrate-*co*-3-hydroxyvalerate) - P(3HH-*co*-3HV) [11,12]. PHAs are biologically synthesized polyesters by controlled fermentation with bacteria, such as Gram-negative bacteria

(Azobacter, Bacillus and Pseudomonas) and Gram-positive bacteria (Rhodococcus, Nocardia and Streptomyces). These bacteria, under food stress, can produce energy reserves as intracellular food in the form of granules called PHAs [13].

Arrieta *et al.* [10], reported that these bacteria, under feeding conditions of limited macro-elements (such as phosphorus, nitrogen, trace elements or oxygen), and in the presence of an abundant source of carbon (*e.g.* glucose or sucrose) and/or lipids (*e.g.* vegetable oils or glycerine), are capable of accumulating up to 60 – 80 wt.% in the form of PHAs. In this way, they can subsist under conditions of food restriction [14,15]. Similar to plants that store energy in the form starch polymer, some bacteria are able to accumulate energy reserves in the form of PHAs [16].

It should be noted that these bacterial polyesters are high-molecular-weight, semi-crystalline, biocompatible thermoplastic polymers. They have very good biodegradability even under environmental conditions. They tend to exhibit rigid behaviour, due to high crystallinity, low thermal stability, and small temperature windows for conventional processing [14,17].

These limitations have been improved by the bacterial synthesis of different copolymers. In this way, a wide range of physical and thermal properties can be tailored, depending on the chemical structure of the used comonomers. More than 150 types of monomers have been successfully synthesized by selecting different raw or modified bacteria and/or the fermentation conditions [13]. The work of Alata *et al.* [18], reported the effect of medium-length side groups of 3-hydroxyhexanoate (3-HHx) units from 5 to 18 mol % on properties of poly(3-hydroxybutyrate-*co*-3-hydroxyhexanoate) – P(3HB-*co*-3HHx). They observed a remarkable decrease in crystallinity ( $\chi_c$ ) from 41.6 % to 25.1 % for copolymers containing 5 mol% and 18 mol% 3-HHx, respectively. In addition, due to the reduced crystallinity, secondary crystallization is very low for high 3-HHx (above 10 mol %) content in P(3HB-*co*-3HHx). Other studies have also reported similar results, together with an interesting decrease in the melting temperature of P(3HB-*co*-3HHx) [15].

P(3HB-*co*-3HHx) consists on a random copolymer of 3-HB and 3-HHx (see **Figure III.1.1.1.**). 3-HHx medium-length chains act as short branches of the main 3-HB chains; therefore, stereoregularity is lost and as a result, crystallinity is remarkably reduced. Besides this, presence of randomly 3-HHx chains, broadens the melt peak, but the storage modulus and the overall strength is reduced [17,19]. Nevertheless, P(3HB-*co*-3HHx) copolymers with low 3-HHx content, undergo physical aging with

time (increase in modulus, strength and reduction of ductile properties such as elongation at break, toughness, and, impact strength) [20], which is ascribed to secondary crystallization above the glass transition temperature,  $T_g$  [21]. It is worthy to note that typical values of  $T_g$  for P3HB are  $-5\text{ }^\circ\text{C}$  to  $5\text{ }^\circ\text{C}$  and this interval is remarkably reduced to values as lower as  $-38\text{ }^\circ\text{C}$  for medium-to-long alkananoate chains, *e.g.* the  $T_g$  of poly(3-hydroxyhexanoate) is close to  $-28\text{ }^\circ\text{C}$  [22].

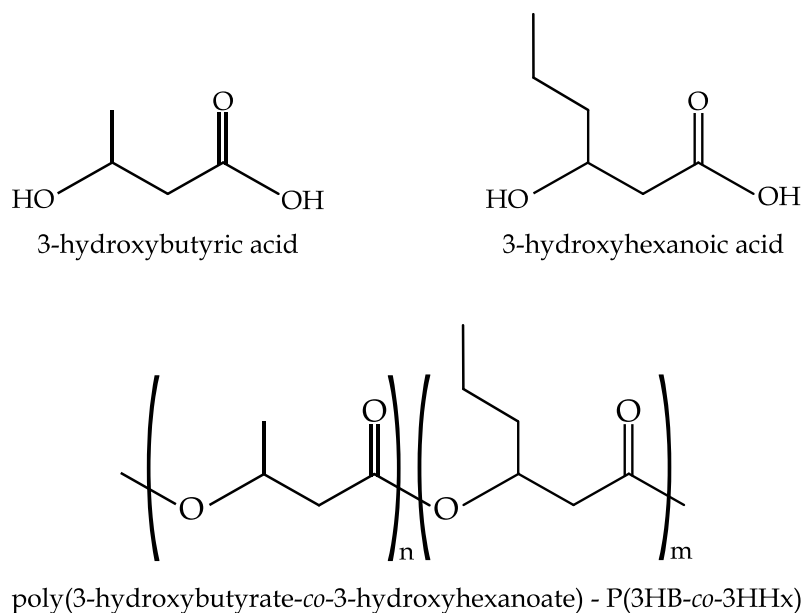


**Figure III.1.1.1.** Chemical structure of 3-hydroxyalkanoic acids used to synthesize P(3HB-co-3HHx).

Another key issue in the massive use of PHAs at industrial scale, is their “relatively” low cost due to the use of renewable resources such as coconut oil, sugarcane, beet, molasses, some other vegetable oils and, what is more important, carbon-rich industrial wastes as those obtained from agro-food industry or even, sludges coming from sewage treatment plants, by selecting the appropriate bacteria or using bacterial engineering to tailor the desired behaviour of a particular bacteria strain [23,24]. These properties make P(3HB-co-3HHx) an environmentally efficient biopolymer suitable for applications in different packaging applications such as disposable plastic bags, food packaging, catering, agricultural mulch films, and so on [25]. However, as above mentioned, most PHAs undergo secondary crystallization or aging that makes them fragile, thus limiting their possible applications [26]. Xu *et al.* suggested that one disadvantage of P(3HB-co-3HHx) is that the secondary crystallization process is very slow (for low mol % 3-HHx), due to the irregularity of its polymer chain [27]. Large spherulites and secondary crystallization give them poor mechanical properties.

Plasticization of PHAs has been studied with an improvement on ductile properties [28]. Since plasticizers are based on a low-molecular-weight-compounds usually they show potential migration problems [29]. An interesting approach to overcome this drawback is blending P(3HB-*co*-3HHx) with another ductile polymer. But it is important to bear in mind, that the selected polymer for the blend must not compromise biodegradation or disintegration in controlled compost soil. Some researchers have already used PCL in blends with PHAs. PCL is a semi-crystalline biodegradable polyester, with a very low  $T_g$  of about  $-60\text{ }^\circ\text{C}$ , which gives an overall ductile behaviour with high elongation at break [26,30]. The addition of PCL decreases the fragility of the PHAs, reducing the elastic modulus and improving the blend processability. However, its low melting temperature (around  $50 - 60\text{ }^\circ\text{C}$ ) means the obtained blends should not be used at temperatures above  $50 - 60\text{ }^\circ\text{C}$  since dimensional stability could be compromised. Garcia-Garcia *et al.* reported a noteworthy improvement in the impact behaviour of P3HB by blending it with PCL [31]. In addition, P3HB/PCL blends improved the flexibility and ductility.

The aim of this work is to overcome the intrinsic fragility of a bacterial copolyester like P(3HB-*co*-3HHx) by blending with a flexible polyester as PCL. The effect of the incorporation of different amounts of PCL is evaluated by means of mechanical, thermal, thermo-mechanical and morphological characterization. The evaluation of the results allows establishing the optimum P(3HB-*co*-3HHx)/PCL blends for applications in the packaging sector, that do not compromise the environment at the end of life cycle. In this way, it contributes to the reduction of the current serious problem of eliminating the large volume of plastic waste generated by the packaging sector. In addition, these developed formulations could be used in medical applications as improved toughness is expected with PCL addition and both are resorbable biopolyesters.

## MATERIALS AND METHODS.

### Materials.

P(3HB-*co*-3HHx) commercial grade ErcrosBio® PH 110, was supplied in pellet form by Ercros S.A. (Barcelona, Spain). This has a density of  $1.2\text{ g/cm}^3$  and a melt flow index of  $1.0\text{ g/10 min}$ , measured at  $160\text{ }^\circ\text{C}$ . As indicated by the supplier, it is suitable for injection moulded parts and it can be melt-blended with other polyesters to obtain tailored properties. Regarding PCL, a commercial grade Capa™ 6800, in pellet form, with a mean molecular weight of  $80000\text{ Da}$ , was supplied by Perstorp (Cheshire, UK).



**Manufacturing of P(3HB-*co*-3HHx)/PCL binary blends.**

P(3HB-*co*-3HHx) pellets were dried for 8 h at 80 °C, while PCL pellets were dried at 45 °C for 24 h, in an air-circulating oven CARBOLITE Eurotherm 2416 CG (Hope Valley, UK). As it has been reported in other works, the typical weight content (wt.%) of flexible polymer blended with brittle polymers to improve toughness is comprised between the 20 – 40 wt.% range. In this work, a maximum PCL content of 40 wt.% was selected since at this composition, PCL is still the minor component in the blend [32–34]. Garcia *et al.* studied the whole P3HB/PCL system and they revealed, as expected, that above 50 wt.% PCL, it is PCL which defines the properties of the blend [31]. Ferry *et al.* also confirmed a maximum loading of 30 wt.% PCL to improve the high brittleness of neat PLA [35]. Then, different wt.% of P(3HB-*co*-3HHx) and PCL (see **Table III.1.1.1.**) were mechanically mixed in a zipper bag to provide initial homogenization. After that, all compositions were extruded using a twin-screw co-rotating extruder manufactured by DUPRA S.L. (Alicante, Spain) with a temperature profile (four barrels, from the hopper to the extrusion die) of 110 – 120 – 130 – 140 °C respectively and a screw speed of 20 rpm. The extruded material was cooled in air and, subsequently pelletized for further processing. After pelletizing, the different blends were subjected to an injection moulding process in a Meteor 270/75 from Mateu & Solé (Barcelona, Spain). The temperature profile in the injection moulding process was 150 – 140 – 130 – 120 °C (nozzle) in a heated mold at 60 °C as recommended by the supplier. The filling time was set to 1 s while the cooling time was 30 s. Standard samples (rectangular and dog-bone shape) were obtained for further characterization. After processing, the specimens were stored at room temperature in a vacuum desiccator for 15 days before characterization, due to the secondary crystallization process or aging that P(3HB-*co*-3HHx) undergoes with time at 25 °C [21,26,27].

**Table III.1.1.1.** Code and composition in weight % - (wt.%) of binary blends of P(3HB-*co*-3HHx)/PCL.

Code	P(3HB- <i>co</i> -3HHx) (wt.%)	PCL (wt.%)
P(3HB- <i>co</i> -3HHx)-0PCL	100	0
P(3HB- <i>co</i> -3HHx)-10PCL	90	10
P(3HB- <i>co</i> -3HHx)-20PCL	80	20
P(3HB- <i>co</i> -3HHx)-30PCL	70	30
P(3HB- <i>co</i> -3HHx)-40PCL	60	40
100PCL	0	100

**Thermal and thermo-mechanical characterization.**

The thermal transitions of P(3HB-co-3HHx)/PCL binary blends were analysed by Differential Scanning Calorimetry - DSC in a Q2000 DSC from TA Instruments (Delaware, USA). The temperature program was scheduled in three different stages: first heating, first cooling and second heating. The first heating was scheduled from - 50 °C to 200 °C. The second stage consisted on a cooling program from 200 °C down to - 50 °C (this stage is interesting to remove the thermal history and allow crystallization); finally, a second heating cycle identical to the first one (- 50 °C to 200 °C) was launched. The heating/cooling rates were all set to 10 °C/min. All the DSC runs were performed in an inert nitrogen atmosphere with a flow rate of 66 mL/min. In addition to parameters such as the melting temperature -  $T_m$ , the cold crystallization temperature -  $T_{cc}$ , melting enthalpies -  $\Delta H_m$  and cold crystallization enthalpies -  $\Delta H_{cc}$ . The degree of crystallinity-  $\chi_c$  was calculated for each polymer in the blend as:

$$\chi_c(\%) = \frac{\Delta H_m - \Delta H_{cc}}{\Delta H_m^0 \cdot (1 - w)} \cdot 100 \quad \text{Equation III.1.1.1.}$$

The normalized enthalpy values ( $\Delta H_m^0$ ) for a theoretical 100 % crystalline ( $\Delta H_m^0$ ) of P(3HB-co-3HHx) and PCL were taken as 146 J/g and 156 J/g, respectively as reported in the literature [19,36,37]. Finally, the term (1 - w) stands for the actual weight of the polymer whose crystallinity is being evaluated.

To study the thermal degradation, thermogravimetry analysis - TGA was carried out in a Mettler-Toledo Inc. TGA 851-E thermobalance (Schwerzenbach, Switzerland). The thermal program used in this case was a unique dynamic ramp from 30 °C up to 700 °C at 20 °C/min, in N<sub>2</sub> inert atmosphere with a flow rate of 66 mL/min. In this analysis, the onset degradation temperature was taken as the temperature related to a mass loss of 2 wt.% and was denoted as  $T_{2\%}$  and the maximum degradation rate -  $T_{max}$  obtained from the first derivative curve - DTG.

Dynamic-Mechanical Thermal Analysis - DMTA, was carried out in a Mettler-Toledo dynamic analyser DMA1 (Columbus, USA), in single cantilever mode on rectangular samples sizing 40 × 10 × 4 mm<sup>3</sup>. The maximum dynamic deflection was 10 μm and the frequency for the sinusoidal stress wave was set to 1 Hz. Samples were subjected to slightly different temperature ramps since PCL melts at 58 - 60 °C. Thus, for neat PCL the heating range was from - 70 °C to 50 °C to avoid melting. In the case of neat P(3HB-co-3HHx) the heating ramp was set from - 70 °C to 100 °C and, finally, P(3HB-co-3HHx)/PCL blends were subjected to a heating program from - 70 °C to

70 °C. The heating rate was the same, 2 °C/min, for all the different scheduled temperature programs. During the test, parameters such as storage modulus -  $E'$  and the dynamic damping factor -  $\tan \delta$  were collected for the analysis.

To evaluate the dimensional stability, neat P(3HB-*co*-3HHx) and PCL, as well as P(3HB-*co*-3HHx)/PCL blends a Thermo-Mechanical Analysis - TMA was performed in a Q400 from TA Instruments (Delaware, USA) on rectangular samples sizing  $10 \times 10 \times 4 \text{ mm}^3$ . The temperature sweep was from - 70 °C to 70 °C, with a constant heating rate of 2 °C/min and a constant load of 20 mN. The Coefficient of Linear Thermal Expansion - CLTE of all specimens was determined as the slope for the linear correlation between the expansion and temperature, both below and above  $T_g$ .

### **Mechanical properties.**

The mechanical characterization of the P(3HB-*co*-3HHx)/PCL blends was studied by means of tensile, flexural, impact and hardness tests on five standardized specimens for each test. The tensile and flexure tests were carried out according to ISO 527 and ISO 178 respectively, in a universal machine ELIB 30 from S.A.E. Ibertest (Madrid, Spain). The load cell was 5 kN for both tests and the crosshead rate was 5 mm/min for flexural tests and 20 mm/min for the tensile tests. Parameters like the maximum tensile strength -  $\sigma_t$ , elongation at break -  $\epsilon_b$  and tensile modulus -  $E_t$  were obtained during the tensile test. In the flexural test, flexural strength -  $\sigma_f$  and flexural modulus -  $E_f$  were measured.

The impact resistance (absorbed energy during impact conditions, per unit area) was determined according to ISO 179, using a Charpy pendulum from Metrotec S.A. (San Sebastian, Spain) with an energy of 1-J. A standardized "V-type" notch was produced on standard rectangular samples.

The hardness properties were measured according to ISO 868. The equipment used was a Shore D hardness tester model 673-D from J. Bot, S.A. (Barcelona, Spain).

### **Morphology characterization.**

The surface analysis of the fractured specimens from impact tests was performed with a Field Emission Scanning Electron Microscope - FESEM, model ZEISS ULTRA55 (Oxford Instruments). The working accelerating voltage was 2 kV. Prior to this analysis, the samples were metallized with a gold-palladium alloy in a sputter coater EMITECH mod. SC7620 from Quorum Technologies Ltd. (East Sussex, UK). In a second analysis,

the samples were subjected to a selective PCL extraction in acetone at room temperature for 24 h. In this way, PCL can be extracted and, therefore, it is possible to observe more accurately the phase distribution in the developed binary blends [38].

## RESULTS AND DISCUSSION.

### Thermal properties of P(3HB-co-3HHx)/PCL blends.

Thermal analysis by DSC of P(3HB-co-3HHx)/PCL binary blends with different amounts of PCL (wt.%), and neat P(3HB-co-3HHx) and PCL, was done from the first heating cycle (**Figure III.1.1.2a.**) to obtain the thermal parameters of the starting material, just after 15 days from its processing, thus allowing secondary crystallization. Besides, the second heating cycle after a slow cooling (**Figure III.1.1.2b.**), allowed to remove the thermal history of the material and to obtain the main thermal characterization parameters. **Table III.1.1.2.** summarizes the main thermal parameters corresponding to the DSC thermograms of the first heating cycle after an aging time of 15 days (**Figure III.1.1.2a.**). The thermogram of neat PCL, showed a single endothermic peak around 62 °C ( $T_m$  of PCL), which was attributed to the melting of packed crystallites of PCL embedded in an amorphous PCL fraction. Since DSC tests were run from - 50 °C, the  $T_g$  of PCL, could not be clearly observed. This was because the  $T_g$  of PCL is very low, with values below - 50 °C, so that, with this thermal program it could not be accurately determined. On the other hand, the DSC thermogram of neat P(3HB-co-3HHx), did not allow to identify its  $T_g$  either. This is because the crystalline fraction of P(3HB-co-3HHx) remarkably increased after the aging for 15 days; therefore, the remaining amorphous fraction was noticeable reduced and then, the step in the baseline (around 0 °C), attributed to the  $T_g$ , could not be clearly seen. As one can see in **Figure III.1.1.2a.**, only the melt process of the crystalline fraction in P(3HB-co-3HHx) could be observed with a peak located at 138 °C ( $T_{m,2}$ ). Regarding binary P(3HB-co-3HHx)/PCL blends, the two endothermal peaks above mentioned could be seen in all the developed compositions. A first peak around 60 °C, corresponding to melting of PCL, and a second peak around 135 °C, related to the melting of P(3HB-co-3HHx). One can see that as the PCL wt.% increased in P(3HB-co-3HHx)/PCL blends, the melt peak of PCL became larger while, inversely, the melt peak of P(3HB-co-3HHx) was slightly diluted. These two independent peaks suggested some lack of miscibility between the two biopolyesters, as each polymer melted at its corresponding temperature [26,31].

The results in **Table III.1.1.2.** indicate that neat P(3HB-co-3HHx) is characterized by a small degree of crystallinity,  $\chi_{c,2}$  around 13 %, even after the 15-day aging process at room temperature. According to the results of Xu *et al.*, this low  $\chi_c$  was due to the irregularities in the structure of the polymer chain of the copolymer, which hinders the formation of crystallites, with increasing mol % 3-HHx [27]. The addition of PCL wt.% slightly increases the crystallinity values, from 15 % for the sample with 10 PCL wt.% to 18 % for 40 PCL wt.%. Garcia-Garcia *et al.* found similar results in the P3HB/PCL system with an increase in the degree of crystallization  $\chi_c$  from 55.1 % to 58.2 % with 25 wt.% PCL [31]. They attributed this to the fact that PCL can affect the crystallization kinetics of neat P3HB. As expected, P(3HB-co-3HHx) showed lower  $\chi_c$  due to the hindering effects of 3-HHx as above mentioned. Contrary to this, Antunes *et al.* reported a decrease in the degree of crystallinity of P3HB by increasing PCL wt.% up to 20 wt.%, while an increase was observed for 30 wt.% PCL [39]. The thermograms in **Figure III.1.1.2a.**, are interesting as they clearly indicate the aging process after 15 days, has been able to complete the secondary crystallization. Moreover, the results gathered in **Table III.1.1.2.** corroborated the absence of a cold crystallization peak after 15 aging days.

**Table III.1.1.2.** Thermal properties of P(3HB-co-3HHx)/PCL binary blends during the first heating cycle 15 day after processing to complete secondary crystallization.

Code	$T_{m,1}$ (°C)	$\Delta H_{m,1}$ (J/g)	$\Delta H_{m,1}^*$ (J/g)	$\chi_{c,1}$ (%)	$T_{m,2}$ (°C)	$\Delta H_{m,2}$ (J/g)	$\Delta H_{m,2}^*$ (J/g)	$\chi_{c,2}$ (%)
P(3HB-co-3HHx)-0PCL	-	-	-	-	138.3	18.92	18.92	13.0
P(3HB-co-3HHx)-10PCL	58.0	6.05	60.52	38.6	134.0	19.72	21.91	15.0
P(3HB-co-3HHx)-20PCL	59.5	13.41	67.00	42.7	134.0	19.70	24.62	16.8
P(3HB-co-3HHx)-30PCL	60.8	17.34	57.70	36.8	135.0	18.69	26.68	18.2
P(3HB-co-3HHx)-40PCL	60.1	25.27	63.21	40.3	135.0	15.91	26.51	18.1
100PCL	62.0	72.23	72.23	46.0	-	-	-	-

\*Standardized enthalpies based on the actual weight of the polymer present in the samples.

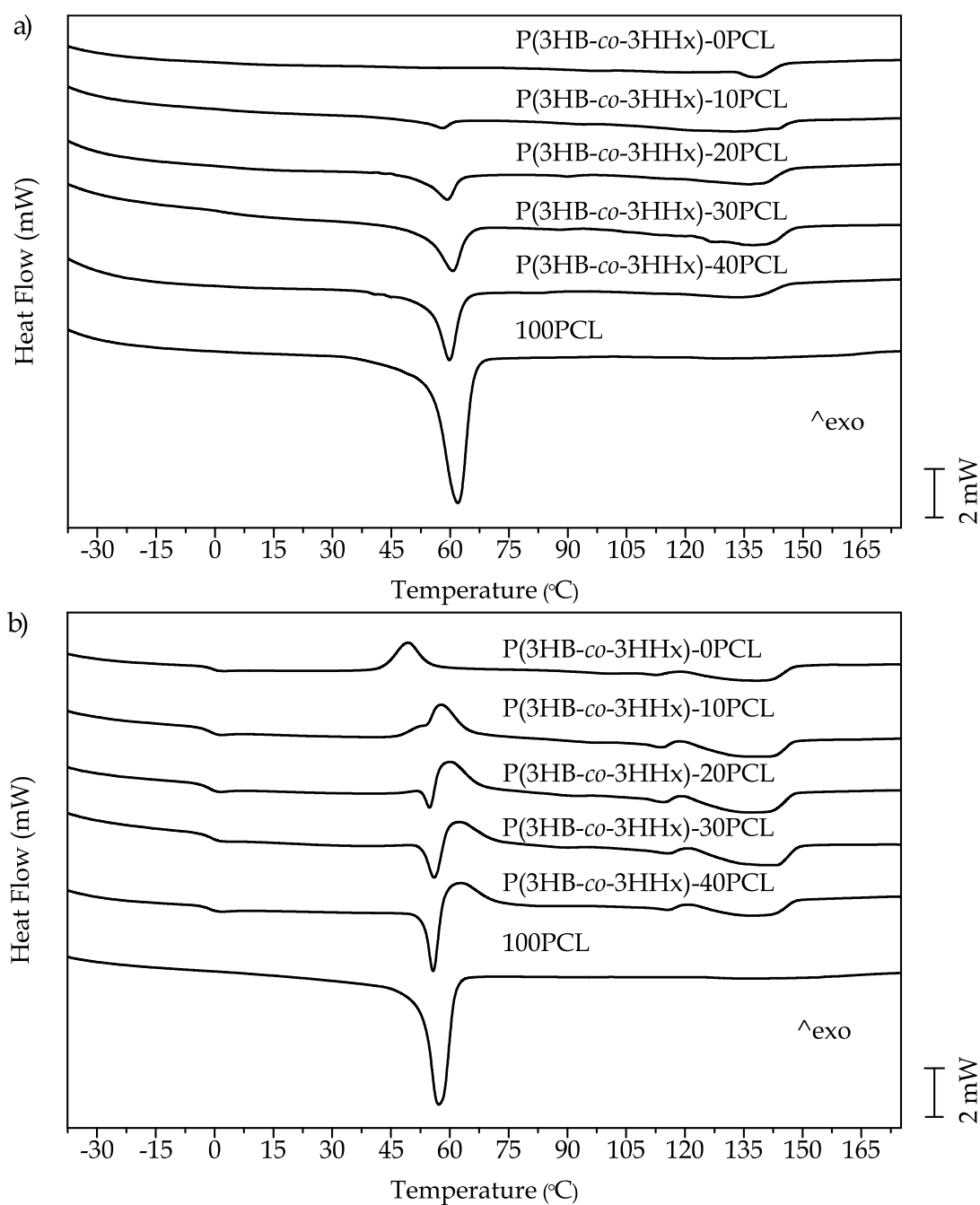


**Figure III.1.1.2.** Comparative plot of the differential scanning calorimetry, DSC thermograms of P(3HB-co-3HHx)/PCL blends: a) first heating cycle after processing and aging for 15 days, b) second heating after cooling in a controlled rate.

With respect to the DSC thermograms obtained in a second heating cycle, **Figure III.1.1.2b.** and **Table III.1.1.3.** it is worthy to note that these showed a clear change. In these DSC thermograms a step in the base line at about 0 °C could be clearly observed, which was attributable to the T<sub>g</sub> of P(3HB-co-3HHx) [38]. In this case, as the thermal history is completely different, the results regarding crystallinity were somewhat variable. Przybysz *et al.* [40] reported a remarkable decrease in P3HB/PCL

blends due to the addition of different peroxide-based compatibilizers, while Oyama *et al.* showed completely different results on P(3HB-*co*-3HHx)/PCL system with peroxide-based compatibilizers, which showed an increase in  $\chi_c$  of P(3HB-*co*-3HHx) [26]. Nevertheless Antunes *et al.* reported a decrease in  $\chi_c$  of P(3HB-*co*-3HHx) without any compatibilizer, which was attributed to changes in crystallization kinetics [39]. In this work, we obtained somewhat varying effects of PCL wt.% on the degree of crystallinity of P(3HB-*co*-3HHx) as its complex structure (hindering crystallization due 3-HHx units) and the additional effects of PCL on crystallization kinetics, could overlap some simultaneous processes and lead to these changes. Obviously, PCL did not show its corresponding step change in the baseline as its  $T_g$  of PCL is lower than  $-50\text{ }^\circ\text{C}$ . The compatibility of a polymer blend can be assessed by changes in  $T_g$  as Garcia *et al.* reported [41]. In this case, the addition of different PCL wt.% to P(3HB-*co*-3HHx)/PCL blends did not affect the  $T_g$  of P(3HB-*co*-3HHx) values obtained, as shown in **Table III.1.1.3**.

The thermogram corresponding to 100 % P(3HB-*co*-3HHx) showed an exothermic peak around  $49\text{ }^\circ\text{C}$  which stood for the cold crystallization peak of P(3HB-*co*-3HHx), with a crystallization enthalpy of  $21.14\text{ J/g}$  [19]. At temperatures close to  $113\text{ }^\circ\text{C}$ , P(3HB-*co*-3HHx) showed a first and small endothermic peak that corresponded to the melting of P(3HB-*co*-3HHx) crystalline fraction ( $T_{m,2}$ ), and a second melt peak located at  $120\text{ }^\circ\text{C}$  ( $T_{m,3}$ ). These two endothermic peaks could be due to two effects. The first is based on the polymorphism presented by some copolymers such as P(3HB-*co*-3HHx), as observed in other aliphatic polyesters. Due to the heterogeneous composition of the copolymer itself, different crystalline morphologies can be formed, with different thermal behaviour. The second effect is that crystallization produces primary crystals with low degree of perfection; these may melt and recrystallize to produce crystals of greater perfection or greater thickness, and this could be the explanation of the presence of two overlapped melting peaks [21,23,25,42].

On the other hand, 100 PCL wt.% sample only showed a very marked endothermic peak at  $55\text{ }^\circ\text{C}$  which corresponded to its melting temperature,  $T_m$  of PCL, as above mentioned. Due to the similarity between the cold crystallization process of P(3HB-*co*-3HHx) and the melting of the crystalline fraction of PCL, the binary P(3HB-*co*-3HHx)/PCL blends showed two overlapped endothermal phenomena like the PCL melting-exothermal peak and the P(3HB-*co*-3HHx) cold crystallization in the DSC thermograms (**Figure III.1.1.2b**). This overlapping did not allow to quantify accurately neither the melting enthalpy of the PCL and the cold crystallization enthalpy

of the P(3HB-*co*-3HHx). This effect did not allow the correct calculation of  $\chi_c$  in the P(3HB-*co*-3HHx)/PCL system blends in this second heating cycle as they were overlapped. Nevertheless, this second heating DSC runs were interesting as samples had undergone a thermal heating-cooling cycle to remove the thermal history and, subsequently, all the thermal transitions could be detected in a clearer way. In particular, the secondary crystallization peak of P(3HB-*co*-3HHx), which disappeared after the aging process (**Figure III.1.1.2a.**) and could not be detected, was clearly seen in the second heating cycle.

**Table III.1.1.3.** Thermal properties of P(3HB-*co*-3HHx)/PCL binary blends obtained during the second heating cycle after a heating-cooling process to remove thermal history.

Code	$T_g$ (°C)	$T_{m,1}$ (°C)	$\Delta H_{m,1}$ (°C)	$\Delta H_{m,1}^*$ (°C)	$T_{m,2}$ (°C)	$T_{m,3}$ (°C)	$\Delta H_{m,2}$ (°C)	$\Delta H_{m,2}^*$ (°C)
P(3HB- <i>co</i> -3HHx)-0PCL	0.46	-	-	-	112.8	137.8	24.9	24.9
P(3HB- <i>co</i> -3HHx)-10PCL	0.12	54.6	**	**	114.5	138.0	28.4	31.5
P(3HB- <i>co</i> -3HHx)-20PCL	- 0.17	55.0	**	**	113.5	139.0	26.2	32.7
P(3HB- <i>co</i> -3HHx)-30PCL	0.59	56.0	**	**	112.4	141.3	20.3	28.9
P(3HB- <i>co</i> -3HHx)-40PCL	- 0.46	55.6	**	**	114.8	139.4	15.4	25.7
100PCL	-	57.0	45.7	45.7	-	-	-	-

\*Standardised enthalpies based on the actual weight of the polymer present in the samples.

\*\*Melting enthalpies of PCL on P(3HB-*co*-3HHx)/PCL blends could not be obtained by the overlapping with cold crystallization process in P(3HB-*co*-3HHx).

On the other hand, the thermograms of the binary P(3HB-*co*-3HHx)/PCL blends showed the characteristic melting peak corresponding to PCL, and the two melting peaks of P(3HB-*co*-3HHx). It should be noted that as the PCL wt.% in P(3HB-*co*-3HHx)/PCL blends increased, it had virtually no influence on the melting peak temperatures of P(3HB-*co*-3HHx) ( $T_{m,2}$  and  $T_{m,3}$ ), which was the major component in the developed P(3HB-*co*-3HHx)/PCL blends. The immiscibility between P(3HB-*co*-3HHx) and PCL suggested that they form two separate phases with almost independent thermal parameters [30].

Regarding the enthalpies of the thermal transitions related to melting, the results obtained are shown in **Table III.1.1.3**. The addition of small amounts of PCL (10 and 20 wt.%), slightly increased the values of  $\Delta H_{m,2}^*$ , which indicated the need of more energy to melt the crystalline fraction or, what is the same, there was a slight increase in crystallinity. Higher amounts of PCL (30 and 40 wt.%), offers the opposite effect by a decrease in crystallinity, probably due to changes in the crystallization kinetics due to the intrinsic structural complexity of P(3HB-*co*-3HHx) (with 3-HHx units which hinder crystallization), and PCL which could affect crystallization as it has been described previously. When comparing these results with those obtained from samples aged for



15 days, the values of the melting enthalpies were slightly higher. Slow cooling favoured the phenomenon of cold crystallization of P(3HB-co-3HHx), so that the final melting enthalpy of the crystalline fraction was higher in samples with no previous thermal history.

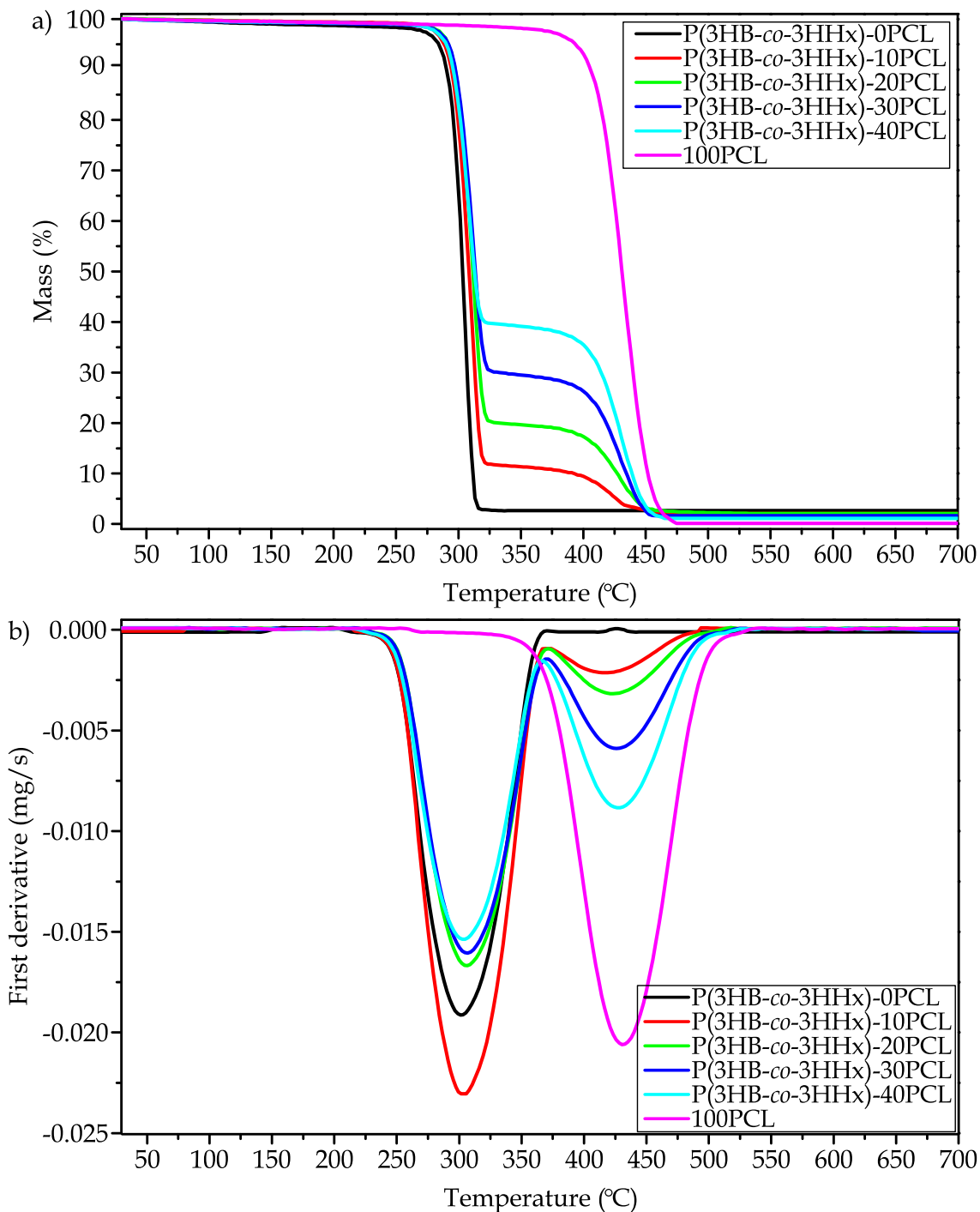


**Figure III.1.1.3.** Thermal degradation of P(3HB-co-3HHx)/PCL: a) TGA degradation curves in terms of mass loss *vs* temperature and b) first derivative of TGA thermograms *vs* temperature.

The thermal stability of binary P(3HB-*co*-3HHx)/PCL blends was analysed by TGA. **Figure III.1.1.3.** gathers a comparative plot of the TGA curves for neat P(3HB-*co*-3HHx) and PCL, and P(3HB-*co*-3HHx)/PCL blends with different PCL wt.%. The TGA curve of neat P(3HB-*co*-3HHx) showed a single-step thermal degradation process. The  $T_{2\%}$  for neat P3HB was 264.6 °C. Once the thermal degradation/decomposition had started, it proceeded very fast with a  $T_{\max}$  of 301.3 °C. These results for individual P(3HB-*co*-3HHx) were in accordance with those reported by Hosoda *et al.* [43] and Mahmood *et al.* [19]. Almost all the mass was thermally decomposed very quickly with an end set degradation temperature of 321 °C. A small residual char of 2.72 wt.% was obtained for neat P(3HB-*co*-3HHx). It is worthy to remark that the thermal degradation of P(3HB-*co*-3HHx) occurred in a very narrow temperature range of 57 °C. On the other hand, despite its crystalline fraction melted at relatively low temperature (58 - 60 °C), it is important to note that PCL was much more thermally stable since its  $T_{2\%}$  was 358 °C. Once the onset degradation temperature was reached, the thermal degradation proceeded in a single step degradation process, with a maximum degradation rate at 430.9 °C and also occurred in a very narrow range up to 474.8 °C, with a residual mass of 0.12 wt.%.

The immiscibility between P(3HB-*co*-3HHx) and PCL was also reflected in the TGA curves of the blends. In all of them, two separated degradation steps could be observed: a first step at around 300 - 310 °C, which corresponded to the degradation of the P(3HB-*co*-3HHx) phase; and a second step, at a higher temperature comprised in the 390 - 440 °C range, which corresponded to the degradation of PCL in the blend, as reported by Garcia-Garcia *et al.* in P3HB-PCL binary blends. The immiscibility was clearly detected by observing the TGA curves for example by observing the TGA curve of the P(3HB-*co*-3HHx)-40PCL sample, the mass loss after the first degradation step was almost 40 wt.%, which corresponded exactly to the PCL wt.% in the blend [31]. The same effect was observed in all other binary blends, which corroborated the lack of miscibility between P(3HB-*co*-3HHx) and PCL. On the other hand, the blends also presented low residual char formation, between 2 wt.% and 1.13 wt.%. Comparatively, there was a very slight shift of TGA thermograms to the right with increasing PCL wt.% content.

The DTG curve (**Figure III.1.1.3b.**), showed two clearly differentiated thermal degradation processes without almost any overlapping, which corroborated the above mentioned immiscibility, of the P(3HB-*co*-3HHx)/PCL binary blends. The first peak observed at temperatures between 301 - 307 °C corresponded to  $T_{\max}$  of P(3HB-*co*-3HHx) in all blends. On the other hand, the second peak, located between

420 – 430 °C, was attributed to the maximum degradation rate temperature of PCL in all the blends. There were very slight changes in the peak maximum values for each process, thus corroborating this immiscibility.

#### Thermo-mechanical properties of P(3HB-*co*-3HHx)/PCL blends.

In addition to the thermal stability, it is important to evaluate the effect of temperature on dimensional stability. To this, samples of the different P(3HB-*co*-3HHx)/PCL blends were subjected to a thermo-mechanical characterization that allowed obtaining the CLTE, which are summarized in **Table III.1.1.4.**, both below and above the  $T_g$ .

**Table III.1.1.4.** CLTE of P(3HB-*co*-3HHx)/PCL blends with different PCL wt.%, below and above  $T_g$ , obtained by TMA.

Code	CLTE below $T_g$ ( $\mu\text{m}/\text{m}^\circ\text{C}$ )	CLTE above $T_g$ ( $\mu\text{m}/\text{m}^\circ\text{C}$ )
P(3HB- <i>co</i> -3HHx)-0PCL	68.0 $\pm$ 1.2	172.5 $\pm$ 2.8
P(3HB- <i>co</i> -3HHx)-10PCL	70.7 $\pm$ 1.5	175.6 $\pm$ 2.7
P(3HB- <i>co</i> -3HHx)-20PCL	93.4 $\pm$ 1.1	178.6 $\pm$ 2.2
P(3HB- <i>co</i> -3HHx)-30PCL	104.6 $\pm$ 1.0	196.6 $\pm$ 3.5
P(3HB- <i>co</i> -3HHx)-40PCL	106.9 $\pm$ 0.5	198.9 $\pm$ 3.0

\*Considered  $T_g$  of P(3HB-*co*-3HHx)

At temperatures below  $T_g$ , the CLTE values were much lower than those obtained above  $T_g$ . The dimensional expansion of the material was lower below the characteristic  $T_g$ , since the material offers a rigid, brittle, glassy behaviour. On the other hand, above  $T_g$ , the polymer material changed its behaviour to a plastic, rubbery-like behaviour and, subsequently, the dimensional expansion was enhanced. Neat P(3HB-*co*-3HHx) showed a CLTE of 68  $\mu\text{m}/\text{m}^\circ\text{C}$  below its  $T_g$  as PCL is a much more flexible polymer, its addition to P(3HB-*co*-3HHx)/PCL blends provided increased flexibility and, subsequently, the CLTE increased accordingly to PCL wt.% contained in the blends. This increase in CLTE was proportional and increased up to 106.9  $\mu\text{m}/\text{m}^\circ\text{C}$  for the blend with 40 PCL wt.%. This increase in the CLTE, which was directly proportional to the PCL wt.%, was representative for somewhat loss of fragility and an improvement on ductile behaviour of P(3HB-*co*-3HHx) at low temperatures. The same effect was observed for the CLTE values obtained at temperatures above  $T_g$  in the blends. In this case, neat P(3HB-*co*-3HHx) offered a remarkable increase in its CLTE to 172.5  $\mu\text{m}/\text{m}^\circ\text{C}$ , which was remarkably higher than the CLTE below its  $T_g$  (68  $\mu\text{m}/\text{m}^\circ\text{C}$ ). The increasing tendency for the CLTE was like the above mentioned, and the P(3HB-*co*-3HHx)/PCL blend with 40 PCL wt.%, showed a CLTE of 198.9  $\mu\text{m}/\text{m}^\circ\text{C}$ .

The DMTA of P(3HB-*co*-3HHx)/PCL blends allowed obtaining the variation of the  $E'$ , and  $\tan \delta$ . The damping factor was directly related to the phase angle -  $\delta$ , which is representative for the delay between the applied dynamic stress and the obtained dynamic elongation. The DMTA technique is much more sensitive to the  $T_g$  detection since this technique measures changes in mechanical properties as a function of temperature, which includes the definition of  $T_g$  with a change from a glassy state to a rubber-like behaviour [30,31,34,37,38]. The dependence of  $E'$  on temperature is shown graphically in **Figure III.1.1.4a**.

The values of  $E'$  obtained for neat P(3HB-*co*-3HHx) at very low temperature (*e.g.* - 70 °C) were high, of about 2 GPa, since this temperature zone corresponds to an elastic-glassy behavior of the material, which means it was far (below) from its  $T_g$ . For example, at - 40 °C,  $E'$  of neat P(3HB-*co*-3HHx) was 1903.4 MPa. For this same temperature,  $E'$  for neat PCL was much lower, with a value of 596.3 MPa. In this case, the material showed a visco-elastic behavior as it was supposed this temperature (- 40 °C) was above  $T_g$  of PCL (about - 60 °C). Thus, by adding different PCL wt.% to the P(3HB-*co*-3HHx), led to blends with a clear decreasing tendency on  $E'$  which was proportional to the PCL wt.%.

As the temperature increased, a remarkable decrease in  $E'$  values was observed, which represented the change from a glassy state (rigid with high  $E'$  values), to a viscous, rubber-like behaviour (visco-plastic with low  $E'$  values). Obviously, this was directly related to the glass transition temperature range from - 10 °C to 20 °C. By taking the  $T_g$  criterium corresponding to the peak maximum of the dynamic damping factor,  $T_g$  of P(3HB-*co*-3HHx) was 9 °C. Since the  $T_g$  of both P(3HB-*co*-3HHx) and PCL is relatively low, at room temperature both polymers are in the rubbery-plateau zone, with a relatively flexible viscoelastic behavior, as shown in the respective  $E'$  plots. This is the typical behaviour of polymers above their  $T_g$  as Burgos *et al.* and Avolio *et al.* reported [44,45]. At 25 °C, the value of  $E'$  was 653.2 MPa, almost three times lower than neat P(3HB-*co*-3HHx) below its  $T_g$ . At higher temperatures,  $E'$  tended to very low values (close to 0 MPa) for blends with high PCL wt.%. This effect was because PCL melted at about 60 °C, and once this temperature was overpassed, PCL changed from a rubber-like state to a melt state with extremely low elastic properties. Nevertheless, in blends with 10 and 20 wt.% PCL (it is important to bear in mind that P(3HB-*co*-3HHx) content in these blends was still very high and is not highly affected by PCL addition in terms of dynamic-mechanical behaviour at high temperatures) the effect was less pronounced so that at 60 °C,  $E'$  was 178.5 MPa and 142.0 MPa respectively.

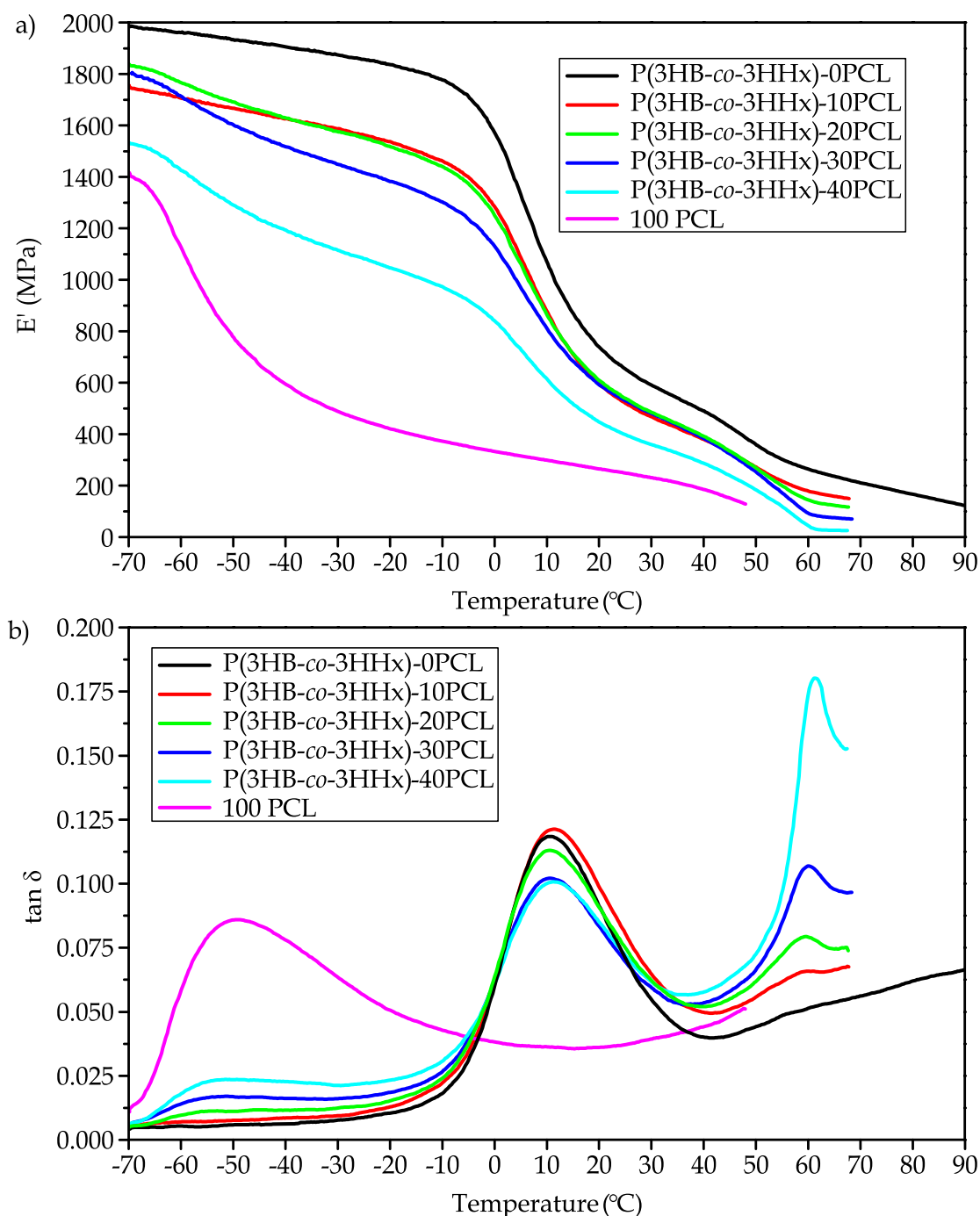


**Figure III.1.1.4.** DMTA of P(3HB-co-3HHx)/PCL blends: a)  $E'$  vs temperature, and b)  $\tan \delta$  vs temperature.

**Figure III.1.1.4b.** shows the variation of the  $\tan \delta$  as a function of temperature, for neat P(3HB-co-3HHx) and PCL, and for their blends with different PCL wt.%. With respect to the neat PCL curve, a marked and broad peak was observed with a peak maximum located at  $-47^\circ\text{C}$ , corresponding to the glass transition temperature  $T_g$  of PCL [30,31]. With regard to neat P(3HB-co-3HHx), a narrow peak (compared to that of PCL) can be seen, with its maximum peak value located at  $9^\circ\text{C}$ . As above mentioned, all the

applied techniques suggested poor (or even lack) of miscibility between these two polymers. Therefore, the changes in the respective  $T_g$  values of neat PCL ( $-47\text{ }^\circ\text{C}$ ) and neat P(3HB-*co*-3HHx) ( $9\text{ }^\circ\text{C}$ ) were not changed in a significant way, therefore, corroborating the lack of miscibility of P(3HB-*co*-3HHx)/PCL blends [38]. In addition, close to  $60\text{ }^\circ\text{C}$ , P(3HB-*co*-3HHx)/PCL blends show a third peak which was related to the partial melting of one of PCL. This third peak was much more pronounced in blends with high PCL wt.% and show proportionality to the PCL wt.%, but this third peak appears always at the same temperature of about  $60\text{ }^\circ\text{C}$ .

#### **Mechanical properties and morphology of P(3HB-*co*-3HHx)/PCL blends.**

**Table III.1.1.5.** gathers a summary of the mechanical properties obtained from tensile, flexural and hardness (Shore D) tests, corresponding to neat P(3HB-*co*-3HHx) and PCL and P(3HB-*co*-3HHx)/PCL binary blends with different PCL wt.%. All the blends of this binary system offered a noticeable decrease in the  $E_t$  with the increase of PCL wt.% content compared to neat P(3HB-*co*-3HHx). P(3HB-*co*-3HHx)/PCL blends with 40 PCL wt.% showed an  $E_t$  value of 722 MPa, which was remarkably lower than that of neat P(3HB-*co*-3HHx) of about 1022 MPa. This represented a % decrease of almost 30 %. The addition of PCL resulted in lowering the overall stiffness of the P(3HB-*co*-3HHx)/PCL blends. Similar results were reported by Hinüber *et al.* in P(3HB-*co*-3HHx)/PCL blends [46]. It should be noted that neat PCL is a biopolymer characterized by very low  $\sigma_t$  of 12.2 MPa (typical of a rubber-like polymer), high  $\epsilon_b$  (no break means more than 600 % as this is the maximum elongation in the used machine) and a low  $E_t$  of 386 MPa. All these properties positively contributed to improve ductility of neat P(3HB-*co*-3HHx) by blending with PCL. The same tendency could be observed for tensile strength of P(3HB-*co*-3HHx)/PCL blends. The addition of different PCL wt.% progressively decreased the values of  $\sigma_t$ , from 16 MPa for neat P(3HB-*co*-3HHx), to 13.4 – 13.9 MPa with 20 PCL wt.% and 40 % PCL wt.%, respectively. This decrease in the resistance parameters was due to the two-phase structure of the blends, resulting from the lack (or very poor) miscibility as above mentioned. The immiscibility between P(3HB-*co*-3HHx) and PCL, forms a dispersed PCL phase that interrupts the continuity of the P(3HB-*co*-3HHx) rich matrix phase, making difficult the stress transfer and, subsequently, decreasing the  $E_t$  and  $\sigma_t$  of the P(3HB-*co*-3HHx)/PCL blends with increasing PCL wt.%.

**Table III.1.1.5.** Summary of the mechanical properties from tensile, flexural and hardness tests, of P(3HB-*co*-3HHx)/PCL.

Code	$\sigma_t$ (MPa)	$E_t$ (MPa)	$\epsilon_b$ (%)	$\sigma_f$ (MPa)	$E_f$ (MPa)	Shore D hardness
P(3HB- <i>co</i> -3HHx)-0PCL	16.0 ± 0.9	1022 ± 412	13.9 ± 1.3	29.5 ± 0.6	1029 ± 31	61.0 ± 0.8
P(3HB- <i>co</i> -3HHx)-10PCL	14.4 ± 0.9	966 ± 22	19.4 ± 0.8	30.2 ± 1.7	966 ± 36	59.0 ± 0.8
P(3HB- <i>co</i> -3HHx)-20PCL	13.4 ± 0.7	837 ± 29	67.9 ± 4.1	29.3 ± 1.5	946 ± 47	58.4 ± 1.1
P(3HB- <i>co</i> -3HHx)-30PCL	13.3 ± 1.2	817 ± 29	308.3 ± 3.6	29.2 ± 1.0	813 ± 20	58.3 ± 0.6
P(3HB- <i>co</i> -3HHx)-40PCL	14.0 ± 0.5	722 ± 52	461.0 ± 4.1	28.3 ± 1.1	802 ± 64	58.0 ± 0.1
100PCL	12.2 ± 0.9	386 ± 22	No break	22.3 ± 0.3	354 ± 26	55.0 ± 2.0

With respect to the elongation at break,  $\epsilon_b$  (%), the effect was opposite and very positive. The increase in  $\epsilon_b$  (%) in P(3HB-*co*-3HHx)/PCL blends also increased ductility with PCL wt.%. P(3HB-*co*-3HHx) is a rather fragile polymer (after aging or secondary crystallization) with only 13.9 % elongation at break. Some researchers attributed this fragility to the secondary crystallization or aging on P(3HB-*co*-3HHx), which reduced the amorphous fraction [18,19]. With the addition of only 20 PCL wt.%, the  $\epsilon_b$  (%) increased up to 67.8 % (which represented a percentage increase of almost 387 %). Even more, the  $\epsilon_b$  (%) for the blend with the highest PCL wt.% considered in this study, *i.e.* 40 wt.%, showed an  $\epsilon_b$  (%) of 461 % (this was 33 times higher than neat P(3HB-*co*-3HHx)).

Same **Table III.1.1.5.** offers the flexural parameters of neat P(3HB-*co*-3HHx), PCL and P(3HB-*co*-3HHx)/PCL blends. As in tensile conditions, P(3HB-*co*-3HHx)/PCL blends became less rigid with PCL addition. This can be confirmed by a clear decrease in  $E_f$ . Neat P(3HB-*co*-3HHx) had an  $E_f$  value of 1029 MPa, and this decreased progressively to 801.7 MPa for the P(3HB-*co*-3HHx)/PCL blend containing 40 PCL wt.%. In this case, the decrease in the  $\sigma_f$  was not so pronounced as that observed in tensile conditions.

In addition, the Shore D hardness, as it is a mechanical resistant property, it followed the same tendency as that observed for both modulus and strength. P(3HB-*co*-3HHx) showed a Shore D of 61, and the addition of the flexible PCL to P(3HB-*co*-3HHx) decreased the Shore D values down to 55 for the blend with 40 PCL wt.%. Despite this, all Shore D values were close to 58 with very slight variations.

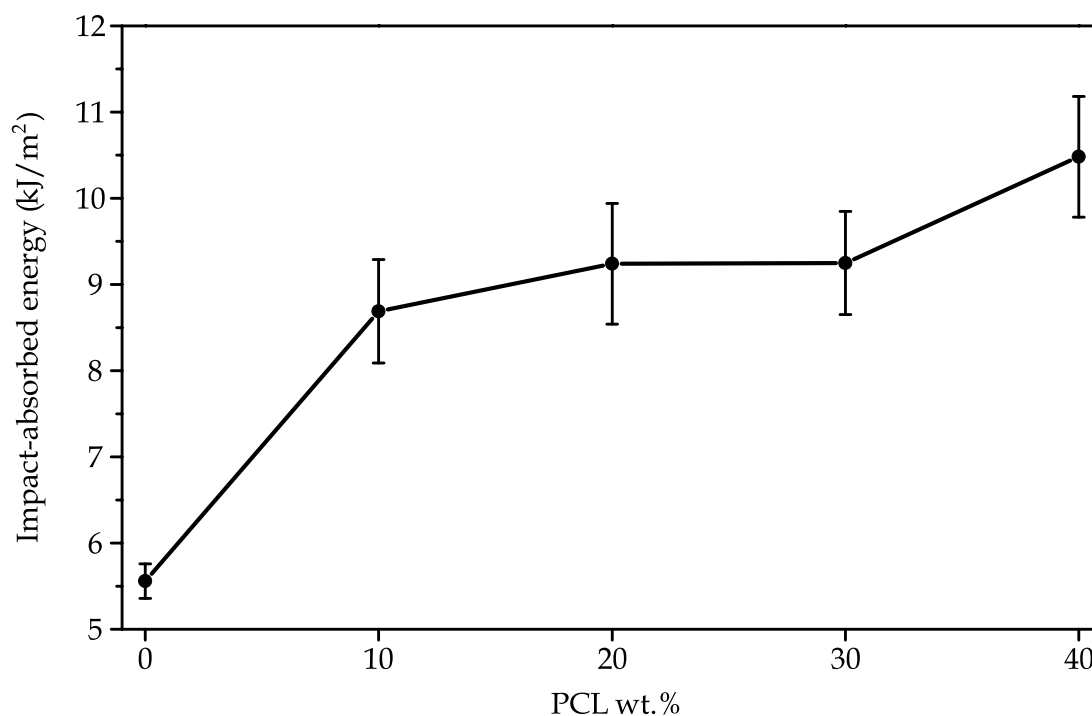


**Figure III.1.1.5.** Plot evolution of the impact absorbed energy of neat P(3HB-*co*-3HHx) and P(3HB-*co*-3HHx)/PCL blends with increasing PCL wt. %.

Another important property of polymers is toughness. **Figure III.1.1.5.** shows the variation of the absorbed energy per unit area (impact resistance) obtained by a Charpy's test. P(3HB-*co*-3HHx) is rather brittle and, consequently, it offers low toughness. Graphically, an interesting increase in the impact resistance of P(3HB-*co*-3HHx)/PCL blends could be observed as the PCL wt. % increased. It is important to bear in mind that the energy absorption capacity under impact conditions is directly related to the plastic deformation capacity of the material before the breakage occurs, and the supported stress, too [47]. The presence of a biphasic structure (as reported in morphology analysis) could contribute to improve the toughness as Ferri *et al.* reported [48]. Thus, the results obtained corroborated those previously analysed for tensile and flexural characterizations. Neat P(3HB-*co*-3HHx) showed a low impact resistance of 5.56 kJ/m<sup>2</sup>; by the addition of only 10 PCL wt. % it was increased to 8.7 kJ/m<sup>2</sup> (which represented a % increase of 56 %). This same trend was proportionally maintained as the PCL wt. % increased. It is worthy to note that the impact energy for the P(3HB-*co*-3HHx)/PCL blend with 40 PCL wt. % was around 10.5 kJ/m<sup>2</sup>, almost twice as much as neat P(3HB-*co*-3HHx). These results were consistent with the above mentioned decrease in the intrinsic brittleness of neat P(3HB-*co*-3HHx) by blending with PCL [37].



**Figure III.1.1.6.** gathers the FESEM images of the impact fracture surfaces of the P(3HB-*co*-3HHx)/PCL binary blends with different PCL wt.%. All the images show a structure with a continuous and homogeneous matrix phase, which corresponded to the P(3HB-*co*-3HHx), and a scattered phase of special morphology, which corresponded to the PCL. This two-phase structure confirmed the lack of miscibility between P(3HB-*co*-3HHx) and PCL as already concluded with previous thermal analyses. Similar findings were proposed by Quiles-Carrillo *et al.* [49]. Nevertheless, the typical drop-like structure could not be observed in this system. In addition, the special morphology of the dispersed phase of the PCL, forming small, thin "sheets or flakes" homogeneously distributed with very regular sizes, must be emphasized. FESEM images also revealed how the higher PCL wt.%, the greater the amount of dispersed phase could be observed.

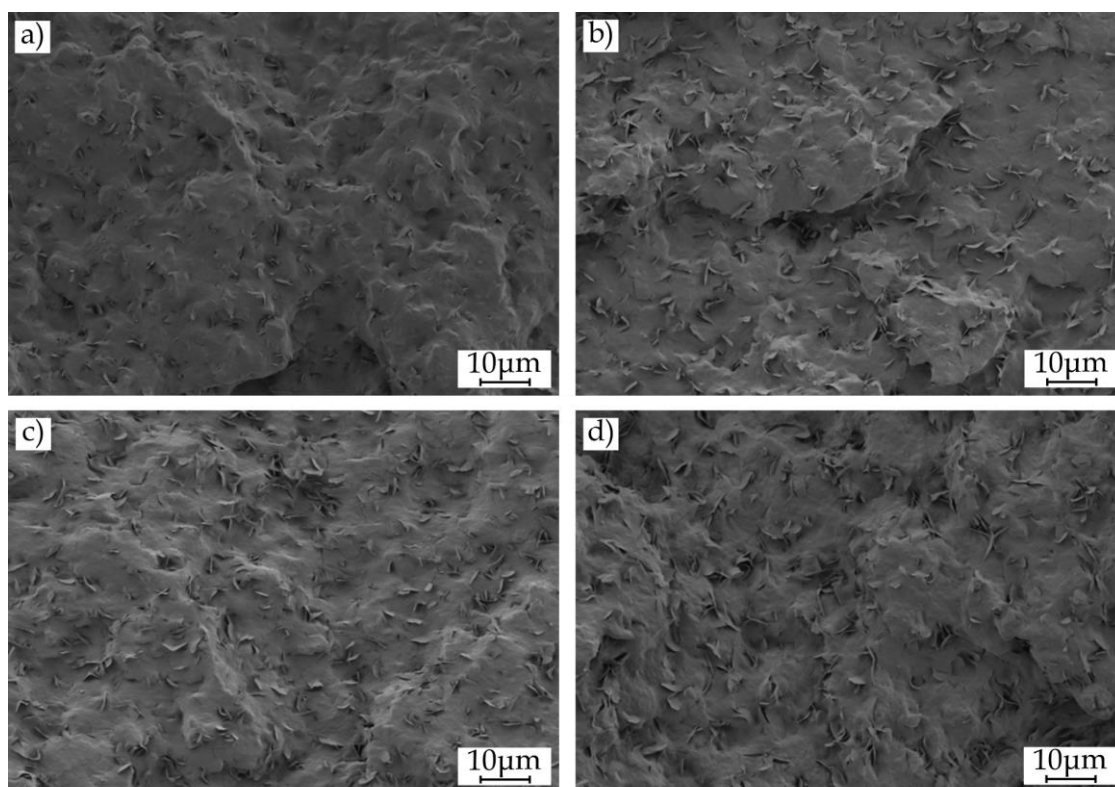


**Figure III.1.1.6.** FESEM images at 1000 × of the impact fracture surface morphologies of P(3HB-*co*-3HHx)/PCL binary blends with different PCL wt.%. a) 10, b) 20, c) 30 and d) 40.

To check that this dispersed phase corresponded to PCL present in the binary blends, a selective PCL extraction with acetone was performed for 24 h [38] **Figure III.1.1.7.** shows the FESEM images obtained after this selective extraction. In all of them, the dispersed phase with small flake-like shapes was no longer observed. Instead, small, and thin empty voids appeared, which corresponded exactly to the

geometric shape of the PCL phase before the selective attack, (see **Figure III.1.1.7.**). This observation allowed us to conclude that the dispersed phase corresponded, indeed, to the PCL present in the binary blend. The lack of miscibility between the biopolymers of the P(3HB-*co*-3HHx)/PCL system was responsible for the internal biphasic structure formed in the blends. In addition, FESEM images showed how the dispersed PCL rich phase, interrupted the continuity of the P(3HB-*co*-3HHx) matrix, so that the stress transmission inside the material when subjected to external stresses was not adequate [38]. This reduced the mechanical resistant parameters, which corroborated the results obtained in the mechanical characterization of the PBHB/PCL binary blends.

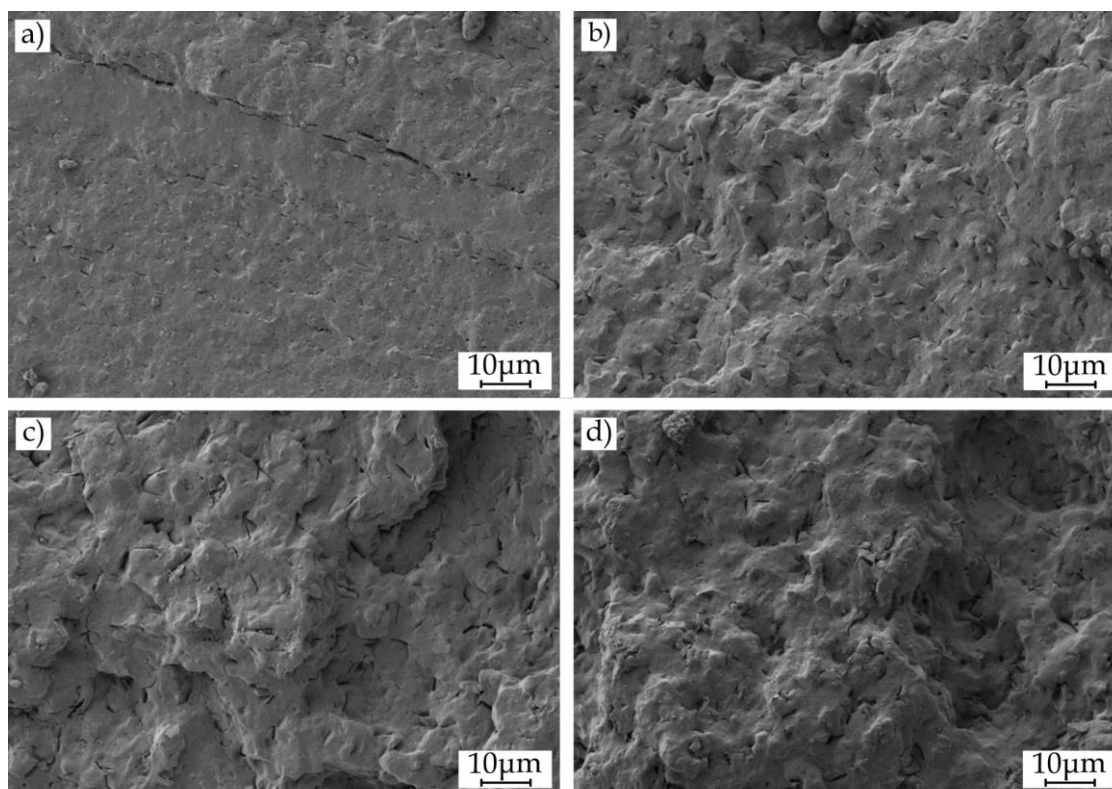


**Figure III.1.1.7.** FESEM images at 1000 × of the impact fracture surface morphologies of P(3HB-*co*-3HHx)/PCL binary blends, subjected to PCL selective extraction, with different PCL wt. %: a) 10, b) 20, c) 30 and d) 40.

### CONCLUSIONS.

The processing and obtaining of P(3HB-*co*-3HHx)/PCL binary blends, allowed obtaining a new environmentally friendly material with improved toughness and ductile properties, suitable for industrial use in the packaging sector and for medical applications too. Considering the intrinsic fragility of P(3HB-*co*-3HHx), the addition of different PCL wt. %, allowed improving its toughness, ductility, and above all, the impact resistance. Blends with a 10 PCL wt. %, offered a percentage increase in the impact

resistance of about 56 %. The impact resistance was even improved up to double the initial value of neat P(3HB-*co*-3HHx) by adding 40 PCL wt.%. This effect of increasing ductility of P(3HB-*co*-3HHx) by increasing PCL content in P(3HB-*co*-3HHx)/PCL blends, had an opposite effect on mechanical resistant properties such as modulus and strength (tensile and flexural). On the contrast, the elongation at break was remarkably improved from 13.9 % for neat P(3HB-*co*-3HHx) up to 461 % for the P(3HB-*co*-3HHx)/PCL blend with 40 PCL wt.%.

On the other hand, thermal analysis as suggested high immiscibility between P(3HB-*co*-3HHx) and PCL, since the main thermal parameters of neat P(3HB-*co*-3HHx) and PCL, remained unchanged in blends, which is characteristic of very poor or lack of miscibility. Only a slight increase in the thermal stability of neat P(3HB-*co*-3HHx) was obtained by adding different PCL wt.%, since PCL is much more thermally stable than most biopolyesters. The DMTA allowed obtaining accurate values of  $T_g$ , with two clear and unchanged values located at - 47 °C ( $T_g$  of PCL) and at 9 °C ( $T_g$  of P(3HB-*co*-3HHx)). These characteristic  $T_g$  values remained unchanged in P(3HB-*co*-3HHx)/PCL blends, thus suggesting lack of miscibility. Regarding morphology of P(3HB-*co*-3HHx)/PCL blends they did not show the typical drop-like PCL phase embedded in a P(3HB-*co*-3HHx) matrix. PCL appeared in the form of small size flakes which could exert a positive effect on ductile properties.

#### **FUNDING.**

This research work was funded by the Spanish Ministry of Science, Innovation, and Universities (MICIU) project numbers MAT2017-84909-C2-2-R. This work was supported by the POLISABIO program grant number (2019-A02).

#### **ACKNOWLEDGMENTS.**

Juan Ivorra-Martinez is the recipient of an FPI grant from Universitat Politècnica de València (PAID-2019-SP20190011). Luis Quiles-Carrillo wants to thank GVA for his FPI grant (ACIF/2016/182) and MECD for his FPU grant (FPU15/03812). Microscopy services at UPV are acknowledged for their help in collecting and analysing FESEM images.

#### REFERENCES.

1. Fombuena, V.; MD, S. Study of the properties of thermoset materials derived from epoxidized soybean oil and protein fillers. *Journal of the American Oil Chemists' Society* **2013**, *90*, 449–457 doi: 10.1007/s11746-012-2171-2.
2. Carbonell-Verdu, A.; Bernardi, L.; Garcia-Garcia, D.; Sanchez-Nacher, L.; Balart, R. Development of environmentally friendly composite matrices from epoxidized cottonseed oil. *European Polymer Journal* **2015**, *63*, 1–10 doi: 10.1016/j.eurpolymj.2014.11.043.
3. Ferrero, B.; Boronat, T.; Moriana, R.; Fenollar, O.; Balart, R. Green composites based on wheat gluten matrix and *Posidonia oceanica* waste fibers as reinforcements. *Polymer Composites* **2013**, *3*, 33–99 doi: 10.1002/pc.22567.
4. Quiles-Carrillo, L.; Montanes, N.; Sammon, C.; Balart, R.; Torres-Giner, S. Compatibilization of highly sustainable polylactide/almond shell flour composites by reactive extrusion with maleinized linseed oil. *Industrial Crops and Products* **2018**, *111*, 878–888 doi: 10.1016/j.indcrop.2017.10.062.
5. Wong, J.X.; Ogura, K.; Chen, S.; Rehm, B.H. Bioengineeringengineered polyhydroxyalkanoates as immobilized enzyme scaffolds for industrial applications. *Frontiers in Bioengineeringengineering and Biotechnology* **2020**, *8*, 1–22 doi: 10.3389/fbioe.2020.00156.
6. Dang, K.M.; Yoksan, R. Development of thermoplastic starch blown film by incorporating plasticized chitosan. *Carbohydrate Polymers* **2015**, *115*, 575–581 doi: 10.1016/j.carbpol.2014.09.005.
7. Carter, P.; Rahman, S.M.; Bhattarai, N. Facile fabrication of aloe vera containing PCL nanofibers for barrier membrane application. *Journal of Biomaterials Science, Polymer Edition* **2016**, *27*, 692–708 doi: 10.1080/09205063.2016.1152857.
8. Zhang, W.; Xiang, Y.; Fan, H.; Wang, L.; Xie, Y.; Zhao, G.; Liu, Y. Biodegradable urea-formaldehyde/PBS and its ternary nanocomposite prepared by a novel and scalable reactive extrusion process for slow-release applications in agriculture. *Journal of Agricultural and Food Chemistry* **2020**, *68*, 4595–4606 doi: 10.1021/acs.jafc.0c00638.

9. Boronat, T.; Fombuena, V.; Garcia-Sanoguera, D.; Sanchez-Nacher, L.; Balart, R. Development of a biocomposite based on green polyethylene biopolymer and eggshell. *Materials & Design* **2015**, *68*, 177–185 doi: 10.1016/j.matdes.2014.12.027.
10. Arrieta, M.P.; Samper, M.D.; Aldas, M.; López, J. On the use of PLA-PHB blends for sustainable food packaging applications. *Materials* **2017**, *10*, 1–26 doi: 10.3390/ma10091008.
11. Mukherjee, T.; Kao, N. PLA based biopolymer reinforced with natural fibre: a review. *Journal of Polymers and the Environment* **2011**, *19*, 714–725 doi: 10.1007/s10924-011-0320-6.
12. Averous, L. Biodegradable multiphase systems based on plasticized starch: a review. *Journal of Macromolecular Science, Part C: Polymer Reviews* **2004**, *44*, 231–274 doi: 10.1081/MC-200029326.
13. Pilia, G.; Iverson, C.N.; Lookman, T.; Marrone, B.L. Machine-Learning-Based Predictive modeling of glass transition temperatures: a case of polyhydroxyalkanoate homopolymers and copolymers. *Journal of chemical information and modeling* **2019**, *59*, 5013–5025 doi: 10.1021/acs.jcim.9b00807.
14. Asrar, J.; Valentin, H.E.; Berger, P.A.; Tran, M.; Padgett, S.R.; Garbow, J.R. Biosynthesis and properties of poly(3-hydroxybutyrate-co-3-hydroxyhexanoate) polymers. *Biomacromolecules* **2002**, *3*, 1006–1012 doi: 10.1021/bm025543a.
15. Misra, S.K.; Valappil, S.P.; Roy, I.; Boccaccini, A.R. Polyhydroxyalkanoate (PHA)/inorganic phase composites for tissue engineering applications. *Biomacromolecules* **2006**, *7*, 2249–2258 doi: 10.1021/bm060317c.
16. Torres-Giner, S.; Montanes, N.; Boronat, T.; Quiles-Carrillo, L.; Balart, R. Melt grafting of sepiolite nanoclay onto poly(3-hydroxybutyrate-co-4-hydroxybutyrate) by reactive extrusion with multi-functional epoxy-based styrene-acrylic oligomer. *European Polymer Journal* **2016**, *84*, 693–707 doi: 10.1016/j.eurpolymj.2016.09.057.

17. Corre, Y.-M.; Bruzaud, S.; Audic, J.-L.; Grohens, Y. Morphology and functional properties of commercial polyhydroxyalkanoates: A comprehensive and comparative study. *Polymer Testing* **2012**, *31*, 226–235 doi: 10.1016/j.polimerotesting.2011.11.002.
18. Alata, H.; Aoyama, T.; Inoue, Y. Effect of aging on the mechanical properties of poly(3-hydroxybutyrate-co-3-hydroxyhexanoate). *Macromolecules* **2007**, *40*, 4546–4551 doi: 10.1021/ma070418i.
19. Mahmood, H.; Pegoretti, A.; Brusa, R.S.; Ceccato, R.; Penasa, L.; Tarter, S.; Checchetto, R. Molecular transport through 3-hydroxybutyrate-co-3-hydroxyhexanoate biopolymer films with dispersed graphene oxide nanoparticles: gas barrier, structural and mechanical properties. *Polymer Testing* **2020**, *81*, 106181–106190 doi: 10.1016/j.polymertesting.2019.106181.
20. Garcia-Garcia, D.; Fenollar, O.; Fombuena, V.; Lopez-Martinez, J.; Balart, R. Improvement of mechanical ductile properties of poly(3-hydroxybutyrate) by using vegetable oil derivatives. *Macromolecular Materials and Engineering* **2017**, *302*, 1600330–1600342 doi: 10.1002/mame.201600330.
21. Hu, Y.; Zhang, J.; Sato, H.; Noda, I.; Ozaki, Y. Multiple melting behavior of poly(3-hydroxybutyrate-co-3-hydroxyhexanoate) investigated by differential scanning calorimetry and infrared spectroscopy. *Polymer* **2007**, *48*, 4777–4785 doi: 10.1016/j.polymer.2007.06.016.
22. Sharma, P.K.; Munir, R.I.; Blunt, W.; Dartailh, C.; Cheng, J.; Charles, T.C.; Levin, D.B. Synthesis and physical properties of polyhydroxyalkanoate polymers with different monomer compositions by recombinant *pseudomonas putida* LS46 expressing a novel PHA synthase (PhaC116) enzyme. *Applied Sciences* **2017**, *7*, 242–262 doi: 10.3390/app7030242.
23. Watanabe, T.; He, Y.; Fukuchi, T.; Inoue, Y. Comonomer compositional distribution and thermal characteristics of bacterially synthesized poly(3-hydroxybutyrate-co-3-hydroxyhexanoate). *Macromolecular Bioscience* **2001**, *1*, 75–83 doi: 10.1002/1616-5195(20010301)1:23.0.CO;2-Q.

24. Morgan–Sagastume, F.; Valentino, F.; Hjort, M.; Cirne, D.; Karabegovic, L.; Gerardin, F.; Johansson, P.; Karlsson, A.; Magnusson, P.; Alexandersson, T. Polyhydroxyalkanoate (PHA) production from sludge and municipal wastewater treatment. *Water science and technology* **2014**, *69*, 177–184 doi: 10.2166/wst.2013.643.
25. Sato, H.; Nakamura, M.; Padermshoke, A.; Yamaguchi, H.; Terauchi, H.; Ekgasit, S.; Noda, I.; Ozaki, Y. Thermal behavior and molecular interaction of poly(3-hydroxybutyrate-co-3-hydroxyhexanoate) studied by wide-angle X-ray diffraction. *Macromolecules* **2004**, *37*, 3763–3769 doi: 10.1021/ma049863t.
26. Oyama, T.; Kobayashi, S.; Okura, T.; Sato, S.; Tajima, K.; Isono, T.; Satoh, T. Biodegradable compatibilizers for poly(hydroxyalkanoate)/poly( $\epsilon$ -caprolactone) blends through click reactions with end-functionalized microbial poly(hydroxyalkanoate)s. *ACS Sustainable Chemistry & Engineering* **2019**, *7*, 7969–7978 doi: 10.1021/acssuschemeng.9b00897.
27. Xu, P.; Cao, Y.; Lv, P.; Ma, P.; Dong, W.; Bai, H.; Wang, W.; Du, M.; Chen, M. Enhanced crystallization kinetics of bacterially synthesized poly(3-hydroxybutyrate-co-3-hydroxyhexanoate) with structural optimization of oxalamide compounds as nucleators. *Polymer Degradation and Stability* **2018**, *154*, 170–176 doi: 10.1016/j.polymdegradstab.2018.06.001.
28. Gamba, A.; Fonseca, J.S.; Mendez, D.; Vilorio, A.; Fajardo, D.; Moreno, N.; Rojas, I.C. Assessment of different plasticizer-polyhydroxyalkanoate mixtures to obtain biodegradable polymeric films. *Chemical Engineering Transactions* **2017**, *57*, 1363–1368 doi: 10.3303/CET1757228.
29. Fenollar, O.; Sanchez–Nacher, L.; Garcia–Sanoguera, D.; López, J.; Balart, R. The effect of the curing time and temperature on final properties of flexible PVC with an epoxidized fatty acid ester as natural-based plasticizer. *Journal of Materials Science* **2009**, *44*, 3702–3711 doi: 10.1007/s10853-009-3495-7.
30. Gassner, F.; Owen, A. Physical properties of poly( $\beta$ -hydroxybutyrate) – poly( $\epsilon$ -caprolactone) blends. *Polymer* **1994**, *35*, 2233–2236 doi: 10.1016/0032-3861(94)90258-5.

31. Garcia-Garcia, D.; Ferri, J.; Boronat, T.; López-Martínez, J.; Balart, R. Processing and characterization of binary poly(3-hydroxybutyrate) (PHB) and poly( $\epsilon$ -caprolactone) (PCL) blends with improved impact properties. *Polymer Bulletin* **2016**, *73*, 3333–3350 doi: 10.1007/s00289-016-1659-6.
32. Garcia-Garcia, D.; Garcia-Sanoguera, D.; Fombuena, V.; Lopez-Martinez, J.; Balart, R. Improvement of mechanical and thermal properties of poly(3-hydroxybutyrate) (PHB) blends with surface-modified halloysite nanotubes (HNT). *Applied Clay Science* **2018**, *162*, 487–498 doi: 10.1016/j.clay.2018.06.042.
33. Garcia-Garcia, D.; Lopez-Martinez, J.; Balart, R.; Jònec, E.; Moriana, R. Reinforcing capability of cellulose nanocrystals obtained from pine cones in a biodegradable poly(3-hydroxybutyrate)/poly( $\epsilon$ -caprolactone) (PHB/PCL) thermoplastic blend. *European Polymer Journal* **2018**, *104*, 10–18 doi: 10.1016/j.eurpolymj.2018.04.036.
34. Garcia-Campo, M.J.; Quiles-Carrillo, L.; Masia, J.; Reig-Pérez, M.J.; Montanes, N.; Balart, R. Environmentally friendly compatibilizers from soybean oil for ternary blends of poly(lactic acid) - PLA, poly( $\epsilon$ -caprolactone) - PCL and poly(3-hydroxybutyrate) - PHB. *Materials* **2017**, *10*, 1339–1358 doi: 10.3390/ma10111339.
35. Ferri, J.M.; Fenollar, O.; Jorda-Vilaplana, A.; García-Sanoguera, D.; Balart, R. Effect of miscibility on mechanical and thermal properties of poly(lactic acid)/polycaprolactone blends. *Polymer International* **2016**, *65*, 453–463 doi: 10.1002/pi.5079.
36. Arifin, W.; Kuboki, T. Effects of thermoplastic elastomers on mechanical and thermal properties of glass fiber reinforced poly(3-hydroxybutyrate-co-3-hydroxyhexanoate) composites. *Polymer Composites* **2018**, *39*, 1331–1345 doi: 10.1002/pc.24188.
37. Simões, C.; Viana, J.; Cunha, A. Mechanical properties of poly( $\epsilon$ -caprolactone) and poly(lactic acid) blends. *Journal of Applied Polymer Science* **2009**, *112*, 345–352 doi: 10.1002/app.29425.



- 
38. Katsumata, K.; Saito, T.; Yu, F.; Nakamura, N.; Inoue, Y. The toughening effect of a small amount of poly( $\epsilon$ -caprolactone) on the mechanical properties of the poly(3-hydroxybutyrate-*co*-3-hydroxyhexanoate)/PCL blend. *Polymer journal* **2011**, *43*, 484–492 doi: 10.1038/pj.2011.12.
39. Antunes, M.C.M.; Felisberti, M.I. Blends of poly(3-hydroxybutyrate) and poly(epsilon-caprolactone) obtained from melting mixture. *Polímeros* **2005**, *15*, 134–138 doi: 10.1590/S0104-14282005000200014.
40. Przybysz, M.; Marć, M.; Klein, M.; Saeb, M.R.; Formela, K. Structural, mechanical and thermal behavior assessments of PCL/PHB blends reactively compatibilized with organic peroxides. *Polymer Testing* **2018**, *67*, 513–521 doi: 10.1016/j.polymertesting.2018.03.014.
41. Garcia, D.; Balart, R.; Sanchez, L.; Lopez, J. Compatibility of recycled PVC/ABS blends. Effect of previous degradation. *Polymer Engineering & Science* **2007**, *47*, 789–796 doi: 10.1002/pen.20755.
42. Ding, C.; Cheng, B.; Wu, Q. DSC analysis of isothermally melt-crystallized bacterial poly(3-hydroxybutyrate-*co*-3-hydroxyhexanoate) films. *Journal of thermal analysis and calorimetry* **2011**, *103*, 1001–1006 doi: 10.1007/s10973-010-1135-8.
43. Hosoda, N.; Tsujimoto, T.; Uyama, H. Green composite of poly(3-hydroxybutyrate-*co*-3-hydroxyhexanoate) reinforced with porous cellulose. *ACS Sustainable Chemistry & Engineering* **2014**, *2*, 248–253 doi: 10.1021/sc400290y.
44. Burgos, N.; Tolaguera, D.; Fiori, S.; Jiménez, A. Synthesis and characterization of lactic acid oligomers: Evaluation of performance as poly(lactic acid) plasticizers. *Journal of Polymers and the Environment* **2014**, *22*, 227–235 doi: 10.1007/s10924-013-0628-5.
45. Avolio, R.; Castaldo, R.; Gentile, G.; Ambrogi, V.; Fiori, S.; Avella, M.; Cocca, M.; Errico, M.E. Plasticization of poly(lactic acid) through blending with oligomers of lactic acid: effect of the physical aging on properties. *European Polymer Journal* **2015**, *66*, 533–542 doi: 10.1016/j.eurpolymj.2015.02.040.

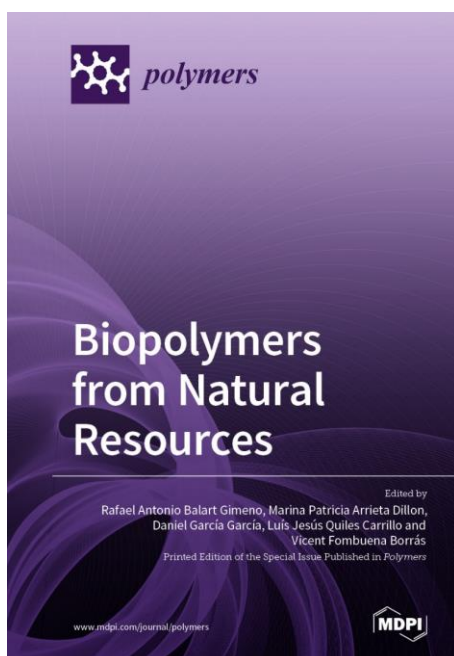
46. Hinüber, C.; Häussler, L.; Vogel, R.; Brünig, H.; Heinrich, G.; Werner, C. Hollow fibers made from a poly(3-hydroxybutyrate)/poly- $\epsilon$ -caprolactone blend. *Express Polymer Letters* **2011**, *5*, 643–652 doi: 10.3144/expresspolymlett.2011.62.
47. Quiles-Carrillo, L.; Duart, S.; Montanes, N.; Torres-Giner, S.; Balart, R. Enhancement of the mechanical and thermal properties of injection-moulded polylactide parts by the addition of acrylated epoxidized soybean oil. *Materials & Design* **2018**, *140*, 54–63 doi: 10.1016/j.matdes.2017.11.031.
48. Ferri, J.; Garcia-Garcia, D.; Carbonell-Verdu, A.; Fenollar, O.; Balart, R. Poly(lactic acid) formulations with improved toughness by physical blending with thermoplastic starch. *Journal of Applied Polymer Science* **2018**, *135*, 45751–45759 doi: 10.1002/app.45751.
49. Quiles-Carrillo, L.; Blanes-Martínez, M.; Montanes, N.; Fenollar, O.; Torres-Giner, S.; Balart, R. Reactive toughening of injection-moulded polylactide pieces using maleinized hemp seed oil. *European Polymer Journal* **2018**, *98*, 402–410 doi: 10.1016/j.eurpolymj.2017.11.039.

Adapted from the original manuscript.

### III.1.2 Development and characterization of sustainable composites from bacterial polyester poly(3-hydroxybutyrate-co-3-hydroxyhexanoate) and almond shell flour by reactive extrusion with oligomers of lactic acid.

Juan Ivorra-Martinez<sup>1</sup>, Jose Manuel-Mañogil<sup>1</sup>, Teodomiro Boronat<sup>1</sup>, Lourdes Sanchez-Nacher<sup>1</sup>, Rafael Balart<sup>1</sup> and Luis Quiles-Carrillo<sup>1</sup>.

<sup>1</sup>Technological Institute of Materials – ITM, Universitat Politècnica de València – UPV, Plaza Ferrándiz y Carbonell 1, 03801 Alcoy (Spain).



**Polymers.**

**2020, 12(5): 1097.**





Article

# Development and Characterization of Sustainable Composites from Bacterial Polyester Poly(3-Hydroxybutyrate-co-3-hydroxyhexanoate) and Almond Shell Flour by Reactive Extrusion with Oligomers of Lactic Acid

Juan Ivorra-Martinez <sup>\*</sup>, Jose Manuel-Mañogil, Teodomiro Boronat , Lourdes Sanchez-Nacher, Rafael Balart and Luis Quiles-Carrillo

Technological Institute of Materials (ITM), Universitat Politècnica de València (UPV), Plaza Ferrándiz y Carbonell 1, 03801 Alcoy, Spain; jomaoam@epsa.upv.es (J.M.-M.); tboronat@dim.upv.es (T.B.); lsanchez@mcm.upv.es (L.S.-N.); rbalart@mcm.upv.es (R.B.); luiquic1@epsa.upv.es (L.Q.-C.)

\* Correspondence: juaivmar@doctor.upv.es; Tel.: +34-966-528-421

Received: 9 April 2020; Accepted: 8 May 2020; Published: 11 May 2020



**Abstract:** Eco-efficient Wood Plastic Composites (WPCs) have been obtained using poly(hydroxybutyrate-co-hexanoate) (PHBH) as the polymer matrix, and almond shell flour (ASF), a by-product from the agro-food industry, as filler/reinforcement. These WPCs were prepared with different amounts of lignocellulosic fillers (wt %), namely 10, 20 and 30. The mechanical characterization of these WPCs showed an important increase in their stiffness with increasing the wt % ASF content. In addition, lower tensile strength and impact strength were obtained. The field emission scanning electron microscopy (FESEM) study revealed the lack of continuity and poor adhesion among the PHBH-ASF interface. Even with the only addition of 10 wt % ASF, these green composites become highly brittle. Nevertheless, for real applications, the WPC with 30 wt % ASF is the most attracting material since it contributes to lowering the overall cost of the WPC and can be manufactured by injection moulding, but its properties are really compromised due to the lack of compatibility between the hydrophobic PHBH matrix and the hydrophilic lignocellulosic filler. To minimize this phenomenon, 10 and 20 phr (weight parts of OLA-Oligomeric Lactic Acid per one hundred weight parts of PHBH) were added to PHBH/ASF (30 wt % ASF) composites. Differential scanning calorimetry (DSC) suggested poor plasticization effect of OLA on PHBH-ASF composites. Nevertheless, the most important property OLA can provide to PHBH/ASF composites is somewhat compatibilization since some mechanical ductile properties are improved with OLA addition. The study by thermomechanical analysis (TMA), confirmed the increase of the coefficient of linear thermal expansion (CLTE) with increasing OLA content. The dynamic mechanical characterization (DTMA), revealed higher storage modulus,  $E'$ , with increasing ASF. Moreover, DTMA results confirmed poor plasticization of OLA on PHBH-ASF (30 wt % ASF) composites, but interesting compatibilization effects.

**Keywords:** PHBH; almond shell flour; mechanical properties; thermal characterization; WPCs

## 1. Introduction

The current problem related to the negative environmental impact of large volumes of wastes [1] in a consumer society has promoted a significant awareness and sensitiveness about this problem. Some governments are facing this through legislation that protects environment and minimizes the



**Abstract.**

Eco-efficient Wood Plastic Composites - WPCs have been obtained using poly(3-hydroxybutyrate-co-3-hexanoate) - P(3HB-co-3HHx) as the polymer matrix, and Almond Shell Flour - ASF, a by-product from the agro-food industry, as filler/reinforcement. These WPCs were prepared with different amounts of lignocellulosic fillers (wt.%) at 10, 20 and 30. The mechanical characterization of these WPCs showed an important increase in their stiffness with increasing the wt.% ASF content. In addition, lower tensile strength and impact strength were obtained. The Field Emission Scanning Electron Microscopy - FESEM study revealed the lack of continuity and poor adhesion among the P(3HB-co-3HHx)-ASF interface. Even with the only addition of 10 wt.% ASF, these green composites become highly brittle. Nevertheless, for real applications, the WPC with 30 wt.% ASF is the most attracting material since it contributes to lowering the overall cost of the WPC and can be manufactured by injection moulding, but its properties are really compromised due to the lack of compatibility between the hydrophobic P(3HB-co-3HHx) matrix and the hydrophilic lignocellulosic filler. To minimize this phenomenon, 10 and 20 phr (weight parts of Oligomer of Lactic Acid - OLA per one hundred weight parts of polymer) were added to P(3HB-co-3HHx)/ASF (30 wt.% ASF) composites. Differential Scanning Calorimetry - DSC suggested poor plasticization effect of OLA on P(3HB-co-3HHx)-ASF composites. Nevertheless, the most important property OLA can provide to P(3HB-co-3HHx)/ASF composites is somewhat compatibilization since some mechanical ductile properties are improved with OLA addition. The study by Thermo Mechanical Analysis - TMA, confirmed the increase of the Coefficient of Linear Thermal Expansion - CLTE with increasing OLA content. The Dynamic Thermal Mechanical Analysis - DTMA, revealed higher storage modulus -  $E'$ , with increasing ASF. Moreover, DTMA results confirmed poor plasticization of OLA on P(3HB-co-3HHx)-ASF (30 wt.% ASF) composites, but interesting compatibilization effects.

**Keywords:** P(3HB-co-3HHx); almond shell flour; mechanical properties; thermal characterization; WPCs.

---





**INTRODUCTION.**

Nowadays, awareness on environmental protection, sustainable development, and the use of renewable energies has become a priority for our society. The high volume of wastes generated that are harmful for the environment, oceans, ecosystems, and so on, has become a major problem to be solved. Furthermore, the waste generated in a consumer society such as the present one, comes mainly from the packaging sector. This need has favoured the development of new environmentally friendly materials [1]. For this reason, the use of the so-called biopolymers is increasing in the packaging sector. Most of these materials are obtained from renewable resources and they are, in many cases, biodegradable (or compostable in controlled compost soil). Therefore, they positively contribute to minimize plastic wastes, thus reducing the carbon footprint, and also contributing to circular economies by upgrading industrial wastes [2] and/or by-products [3].

The current problem related to the negative environmental impact of large volumes of wastes [1] in a consumer society, has promoted a significant awareness and sensitiveness about this problem. Some governments are facing this through legislation that protects environment and minimizes the harmful impact on nature. This, in part, has led to the extensive development of new eco-efficient materials, from the point of view of their renewable origin, low carbon footprint, possibility of composting, biodegradability, and so on [2]. An interesting family of these new eco-efficient materials are the so-called Wood Plastic Composites - WPC. These composites consist on a polymeric matrix in which wood (or whatever lignocellulosic subproduct of the food industry or agroforestry) particles (from 10 wt.% to 60 wt.%, depending on the manufacturing process) are embedded, leading to an appearance and surface finishing similar to natural wood. Lignocellulosic fillers are by-products from different industrial sectors, they are cheap and do not increase the cost of the WPC; in addition they come from natural resources and, subsequently, they represent a sustainable source for use in new and environmentally friendly materials [3-5].

These WPCs are already replacing the use of traditional woods in some applications, which is an important protection of forest resources. WPCs formulations have been optimized in sectors as important as automotive, outdoor furniture, interior design, railings, floors, coatings, decks, fences, pergolas, decking, and so on [3-8]. The fact that they are composed by a polymeric matrix, gives them better behaviour against water or in humid environments. According to Singh *et al.* WPCs have gained a

significant share of the consumer market, becoming the fastest growing segment of the plastics industry [4]. Within the wide range of possibilities that these eco-efficient materials offer as substitutes for wood, those that use thermoplastic polymers as the matrix, are of particular interest, precisely because of the ease and versatility of manufacturing processes. Poly(ethylene) - PE, poly(styrene) - PS, poly(vinyl chloride) - PVC and poly(propylene) - PP are some of the most widely used polymers in WPCs. Nevertheless, these polymer matrices are petroleum-derived polymers.

Due to the need to protect the environment, the possibility of using biopolymers as matrices in WPCs are currently being studied. The use of a biodegradable thermoplastic polymer from natural resources, together with a natural lignocellulosic filler from industrial wastes or by-products, allows the obtaining of totally biodegradable and eco-efficient WPCs [6]. These new green composites represent the new generation of biobased, sustainable, low environmental impact WPCs. Nowadays, there are already a large number of natural biopolymers on a commercial level, among which three main families stand out. The first one, consists on polymers from biomass which include polysaccharides such as starch (and starch-derived polymers such as poly(lactic acid), cellulose, chitosan, chitin, and proteins such as casein, keratin, collagen, and so on. The second group includes conventional polymers such as poly(ethylene), poly(urethanes), poly(amides), that are partially or fully obtained from natural resources but they show identical (or very similar) properties to their petroleum-derived counterparts. Finally, a new family of very promising polymers is that of bacterial polyesters which are generally referred as polyhydroxyalkanoates - PHAs. PHAs include more than 300 different polyesters and copolymers such as poly(3-hydroxybutyrate) - P3HB, poly(3-hydroxybutyrate-co-3-hydroxyvalerate) - P(3HH-co-3HV), among others [5,9].

One of the most interesting biopolymers, obtained by bacterial fermentation, is poly(3-hydroxybutyrate-co-3-hydroxyhexanoate) - P(3HB-co-3HHx). This copolymer is obtained by incorporating into the poly(3-hydroxybutyrate) chain some 3-hydroxyhexanoate units with medium-length side groups to form P(3HB-co-3HHx). Mahmood and Corre *et al.* studies identify a structure formed by branches of short 3HHx units, on the main 3HB chain, thus reducing regularity. Yang and Liao *et al.*, compare the formation of these units by dielectric spectroscopy and melt viscosity [10,11]. Moreover, the addition of the 3HH units extends the temperature range for processing of this copolymer, but the storage modulus and the strength is reduced

[12–15]. Watanabe and Oyama *et al.*, synthesized P(3HB-*co*-3HHx) from cheap natural resources such as coconut oil, biomass, beet, sugar cane, molasses and vegetable oils [16,17]. These characteristics allow it to be used as a substitute for traditional petroleum-derived polymers in some applications, such as disposable plastic bags, food packaging, catering, agricultural mulch film, and so on [18].

The main objective of this work is to obtain fully biobased WPCs. For this purpose, P(3HB-*co*-3HHx) was chosen as the thermoplastic matrix and as reinforcement Almond Shell Flour - ASF was used. The ASF, is a waste of the agro-food industry which is very cheap, fully biobased and biodegradable. By incorporating ASF into the P(3HB-*co*-3HHx) matrix it gives a wood-like appearance. In this work, the effect of the amount of ASF on the mechanical, thermal, thermo-mechanical and water absorption properties of P(3HB-*co*-3HHx)-ASF composites is investigated. In addition, the optimization of the behavior of these composites is used by the addition of an Oligomer of Lactic Acid - OLA, to provide some plasticization and to increase toughness. Due to the lack of compatibility between the different elements, reactive extrusion- REX has been proposed as a strategy to improve the properties of the mixtures by improving the chemical bonding of the biopolymer chains to the surface of the lignocellulosic fillers.

## MATERIALS AND METHODS.

### Materials.

The P(3HB-*co*-3HHx) commercial grade (ErcrosBio® PH 110) used in this study was supplied in pellet by Ercros S.A. (Barcelona, Spain). This polymer has a density of 1.2 g/cm<sup>3</sup> and a Melt Flow Index - MFI of 1 g/10 min measured at 160 °C. Even with this low MFI, this is suitable for injection moulding as it has very low melt strength, so requires an appropriate temperature profile for extrusion and injection moulding. ASF was purchased from Jesol Materias Primas (Valencia, Spain). This powder was sieved in a vibrational sieve RP09 CISA® (Barcelona, Spain) to obtain a maximum particle size of 150 µm. **Figure III.1.2.1.** shows the irregular particle size of ASF with average size below 150 µm (the average size is 75 µm). As plasticizer/impact modifier, an Oligomer of Lactic Acid commercial grade Glyplast OLA 8 was kindly provided by Condensia Química S.A. (Barcelona, Spain). Glyplast OLA 8 is a liquid polyester (with an ester content above 99 %) with a viscosity of 22.5 mPa s measured at 100 °C. Its density is 1.11 g/cm<sup>3</sup>; it has a maximum acid index of 1.5 mg KOH/g and a maximum moisture content of 0.1 %.

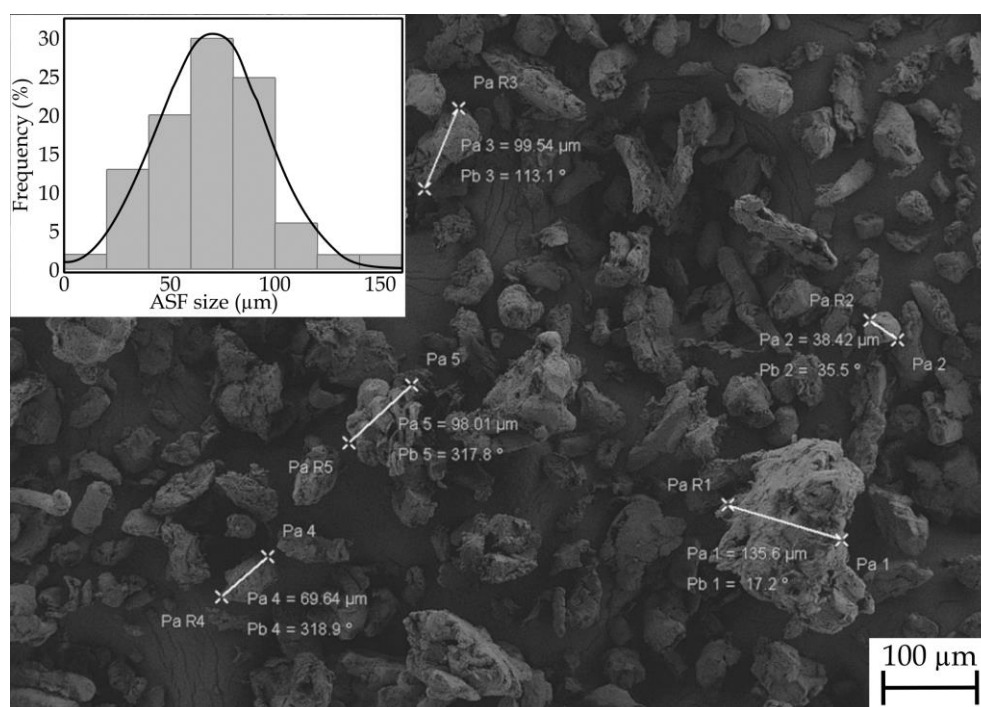


**Figure III.1.2.1.** Visual aspect of almond shell flour particles obtained by FESEM at 100 × and a histogram of their size distribution.

#### Manufacturing of P(3HB-*co*-3HHx)-ASF/OLA composites.

Before further processing of composites, P(3HB-*co*-3HHx) pellets and ASF were dried for 6 h at 80 °C, in a dehumidifier model MDEO, supplied by Industrial Marsé (Barcelona, Spain). Then, different amounts (see **Table III.1.2.1.**) of P(3HB-*co*-3HHx), ASF (in wt.%) and OLA (in phr - weight parts of OLA per one hundred weight parts of polymer) were mechanically pre-mixed in a zipper bag. The proposed compositions were then extruded in a twin-screw co-rotating extruder from DUPRA S.L. (Alicante, Spain). The four temperature barrels were programmed to the following temperature program: 110 - 120 - 130 - 140 °C (extrusion die) and the screw speed was maintained in the 20 - 25 rpm range. The extruded material was cooled down to room temperature and then, pelletized for further processing by injection moulding. The injection moulding process was carried out in a Sprinter 11 injection machine from Erınca S.L. (Barcelona, Spain) to obtain standard samples for further characterization. As P(3HB-*co*-3HHx) has low melt strength, it needs some particular processing conditions. The injection temperature profile was set as 150 - 140 - 130 - 120 °C (nozzle). In addition, it requires a tempered mould at 60 °C. The filling and cooling times were set to 1 s and 20 s, respectively.

It is well known that bacterial polyesters undergo secondary crystallization or recrystallization with time (sometimes designed as physical aging since this leads to an embrittlement), especially at temperatures above  $T_g$ . Recrystallization rate is directly related to temperature; therefore samples have been subjected to a recrystallization process at 25 °C for 15 days since it has been reported that almost all recrystallization takes place after two weeks from the processing [17,19,20].

**Table III.1.2.1.** Summary of sample compositions according to the weight content - wt.% of P(3HB-*co*-3HHx) and ASF and the addition of OLA as parts Per Hundred Resin - phr of P(3HB-*co*-3HHx)-ASF composite.

Code	P(3HB- <i>co</i> -3HHx) (wt.%)	ASF (wt.%)	OLA (phr)
P(3HB- <i>co</i> -3HHx)	100	-	-
P(3HB- <i>co</i> -3HHx)-10ASF	90	10	-
P(3HB- <i>co</i> -3HHx)-20ASF	80	20	-
P(3HB- <i>co</i> -3HHx)-30ASF	70	30	-
P(3HB- <i>co</i> -3HHx)- 30ASF/10OLA	70	30	10
P(3HB- <i>co</i> -3HHx)- 30ASF/20OLA	70	30	20

#### **Mechanical properties of P(3HB-*co*-3HHx)-ASF/OLA composites.**

The mechanical characterization of P(3HB-*co*-3HHx)-ASF/OLA composites was carried out by means of tensile tests according to ISO 527-2:2012 in a universal testing machine, model ELIB-50 from Ibertest (Madrid, Spain). A 5 kN load cell was used and the crosshead rate was set to 10 mm/min. The standardized specimens corresponded to the designation A12 from ISO 20753:2018. Parameters like the maximum tensile strength -  $\sigma_t$ , elongation at break -  $\varepsilon_b$ , tensile modulus -  $E_t$  were obtained during the tensile test.

Impact resistance was quantified by means of a Charpy test, with a 1-J pendulum from Metrotec S.A. (San Sebastian, Spain), on specimens with a standardized "V" notch, according to ISO 179-1:2010. In addition, the hardness of P(3HB-*co*-3HHx)-ASF/OLA composites, was obtained using a Shore D hardness tester model 673-D from J. Bot Instruments, S.A. (Barcelona, Spain) according to ISO 868:2003. All mechanical tests were performed on 5 specimens of each composition.

#### **Morphology of P(3HB-*co*-3HHx)-ASF/OLA composites.**

The morphology study of the impact fractured specimens from impact tests was carried out by Field Emission Scanning Electron Microscopy - FESEM in a ZEISS ULTRA 55 microscope from Oxford Instruments (Abingdon, Oxfordshire, UK). The accelerating

voltage was 2 kV. Prior to this analysis, the samples were metallized with platinum in a sputtering metallizer EMITECH mod. SC7620 from Quorum Technologies Ltd. (East Sussex, UK).

**Thermal characterization of P(3HB-co-3HHx)-ASF/OLA composites.**

The thermal characterization of P(3HB-co-3HHx)-ASF/OLA composites, by means of Differential Scanning Calorimetry - DSC, was performed in a TA Instruments calorimeter mod. Q2000 (Delaware, USA). For the thermal study, a dynamic temperature cycle was scheduled with the following sequence: first cycle: - 50 °C to 200 °C at a constant heating rate of 10 °C/min, second cycle: 200 °C to - 50 °C at a constant cooling rate of 10 °C/min; this step was scheduled to remove the thermal history. Finally, a third cycle from - 50 °C up to 200 °C at 10 °C/min was programmed. The DSC analysis was performed in an inert nitrogen atmosphere with a flow rate of 50 mL/min, with samples between 5 - 10 mg, in standard 40 µL aluminium crucibles. Parameters like glass transition temperature -  $T_g$ , melting temperature -  $T_m$ , cold crystallization temperature -  $T_{cc}$ , melting enthalpy -  $\Delta H_m$ , cold crystallization enthalpy -  $\Delta H_{cc}$  were obtained from DSC runs. The degree of crystallinity -  $\chi_c$  was calculated by using the **Equation III.1.2.1.** where  $\Delta H_m^0$  (J/g) is the theoretical value that corresponds to fully crystalline P(3HB-co-3HHx), this was taken as 146 (J/g) as reported in literature [14]. Finally,  $w$  is the fraction weight of P(3HB-co-3HHx).

$$\chi_c(\%) = \frac{\Delta H_m - \Delta H_{cc}}{\Delta H_m^0 \cdot (1 - w)} \cdot 100 \quad \text{Equation III.1.2.1.}$$

Thermogravimetric analysis - TGA was carried out in a Mettler-Toledo TGA/SDTA 851 thermobalance (Schwerzenbach, Switzerland). Samples consisted of small pieces with a total weight of 5 - 7 mg. These samples were placed in standard alumina pans (70 µL), and then subjected to a heating ramp from 30 °C to 700 °C at a constant heating rate of 20 °C/min in nitrogen atmosphere. All the thermal tests were done in triplicate. The initial degradation of the material was considered at 2 wt.% loss -  $T_{2\%}$  and the maximum degradation rate -  $T_{max}$  was obtained from the first derivative curve - DTG.

**Thermo-mechanical characterization of P(3HB-co-3HHx)-ASF/OLA composites.**

The Dynamic-Mechanical Thermal Analysis - DMTA, was done in a Mettler-Toledo dynamic analyser (Columbus, USA), on rectangular samples of 40 × 10 × 4 mm<sup>3</sup>. Heating was programmed from - 70 °C to 70 °C at a constant rate of

2 °C/min; samples were subjected to a single cantilever test in dynamic conditions with a maximum deflection of 10 µm and a frequency of 1 Hz to measure the storage modulus - E' and the dynamic damping factor - tan δ as a function of the temperature. The Coefficient of Linear Thermal Expansion - CLTE of the P(3HB-co-3HHx)-ASF/OLA composites were determined under Thermo-Mechanical Analysis - TMA using a TA Instruments mod. Q400 (Delaware, USA). The heating program was set from - 70 °C to 70 °C, using a constant heating rate of 2 °C/min. Rectangular samples with dimensions 10 × 10 × 4 mm<sup>3</sup> were subjected to a constant force of 0.02 N.

**Water uptake of P(3HB-co-3HHx)-ASF/OLA composites.**

The water absorption study was carried out according to the method described in ISO 62:2008, with distilled water at 23 ± 1 °C for 9 weeks. The specimens had rectangular dimensions of 80 × 10 × 4 mm<sup>3</sup>. Before starting the immersion, samples were dried at 60 °C for 24 h in an air circulating oven, model 2001245 DIGIHEAT-TFT from J.P. Selecta, S.A. (Barcelona, Spain).

Samples were extracted periodically from the water every planned period. They were dried to remove any remaining surface moisture and weighed on a precision analytical balance model AG245 from Mettler Toledo Inc. (Schwerzenbach, Switzerland). After this measurement, they were re-immersed in the distilled water bath. The amount of absorbed water (W<sub>g</sub>) during the water uptake process can be calculated following **Equation III.1.2.2.**

$$W_g (\%) = \frac{W_t - W_0}{W_0} \cdot 100 \quad \text{Equation III.1.2.2.}$$

Where W<sub>t</sub> stands for the sample weight after an immersion time; W<sub>0</sub> corresponds to the initial weight of the dried sample, before the immersion.

ISO 62:2008 establishes the application of first Fick's law to determine the diffusion coefficient - D, from the collected data regarding the increase of mass by immersion, by means of the expression (**Equation III.1.2.3.**). The calculation of D can be done in the linear zone of the water absorption plot. In this initial stage, W<sub>t</sub>/W<sub>s</sub> is a linear function W<sub>g</sub> =f(√t), that allows to determine D from the slope, θ [21-24].

$$\frac{W_t}{W_s} = \frac{4}{d} \left( \frac{D t}{\pi} \right)^{1/2} \quad \text{Equation III.1.2.3.}$$

Where  $D$  represents the coefficient of diffusion,  $d$  stands for the initial thickness of the specimen and  $W_s$  stands for the saturation mass in the linear zone. If we plot  $W_t/W_s$  against  $\sqrt{t}$ , it is possible to obtain the slope ( $\theta$ ) as this condition is met,  $W_t/W_s (\leq 0.5)$ , then the  $D$  value can be calculated by following the above mentioned expression [25].

A correction of  $D$  parameter -  $D_c$  by the Stefan's approximation is applied to this calculation for the exact calculation of the  $D$  according to the dimensions of the specimens:

$$D_c = D \left( 1 + \frac{d}{h} + \frac{d}{w} \right)^{-2} \quad \text{Equation III.1.2.4.}$$

Where  $D_c$  is the geometrically corrected diffusion coefficient,  $h$  is the length,  $w$  is the width of the sample and  $d$  is the thickness. This equation is based on the assumption that the diffusion velocities are the same in all directions [23-25].

## RESULTS AND DISCUSSION.

### Mechanical properties of P(3HB-co-3HHx)-ASF/OLA composites.

**Table III.1.2.2.** shows the results obtained from mechanical characterization (tensile test, hardness and impact Charpy) of P(3HB-co-3HHx)-ASF/OLA composites. The addition of ASF to the P(3HB-co-3HHx) matrix resulted in composites with greater stiffness with increasing ASF wt.%. With only 10 wt.% ASF, the elastic modulus in tensile test increases to 1310 MPa from 1065 MPa for neat P(3HB-co-3HHx). This means an increase of 23%. This % increase is, obviously, higher for P(3HB-co-3HHx) composites containing 30 wt.% ASF. Regarding the maximum tensile strength, the incorporation of natural fillers to the polymeric P(3HB-co-3HHx) matrix, promotes a noticeable decrease. Neat P(3HB-co-3HHx) offers a tensile strength of 20 MPa, which decreases to 16 MPa with only 10 wt.% ASF and to 12 MPa with 30 wt.% ASF. Singh *et al.* established that the decrease of tensile strength results from stress concentration at the polymer/filler interfaces [4]. There is a lack of interface interactions between the polymeric matrix (highly hydrophobic) and the lignocellulosic particles (highly hydrophilic), which gets more pronounced with increasing particle content [4]. The mechanical behaviour of these composites highly depends on the potential interactions between the polymer matrix and the surrounding lignocellulosic filler/particle. The lack of (or poor) adhesion leads to formation of microscopic gaps that are responsible for a discontinuous material with the subsequent stress concentration phenomenon [26].



**Table III.1.2.2.** Summary of the mechanical properties of the P(3HB-*co*-3HHx)-ASF/OLA composites with different compositions.

Code	$\sigma_t$ (MPa)	$E_t$ (MPa)	$\epsilon_b$ (%)	Hardness Shore D	Impact Strength (kJ/m <sup>2</sup> )
P(3HB- <i>co</i> -3HHx)	20 ± 1	1065 ± 23	8.1 ± 0.7	60.2 ± 0.2	4.3 ± 0.3
P(3HB- <i>co</i> -3HHx)-10ASF	16 ± 1	1310 ± 35	5.2 ± 0.4	63.5 ± 0.4	1.8 ± 0.2
P(3HB- <i>co</i> -3HHx)-20ASF	14 ± 1	1543 ± 23	4.0 ± 0.4	64.7 ± 0.6	1.7 ± 0.2
P(3HB- <i>co</i> -3HHx)-30ASF	12 ± 1	1744 ± 31	3.5 ± 0.3	66.2 ± 0.6	1.6 ± 0.3
P(3HB- <i>co</i> -3HHx)-30ASF/10OLA	10 ± 1	1158 ± 23	6.2 ± 0.2	58.6 ± 0.5	2.4 ± 0.4
P(3HB- <i>co</i> -3HHx)-30ASF/20OLA	8 ± 1	735 ± 28	9.7 ± 0.8	50.0 ± 0.4	2.9 ± 0.3

Furthermore, as usual in composites with lignocellulosic fillers/reinforcements [27-34], the plastic deformation capacity of WPCs decreases in a dramatic way. If we focus on the  $\epsilon_b$ , the intrinsic very low  $\epsilon_b$  values for neat P(3HB-*co*-3HHx) (around 8 % after an aging time of 15 days), are reduced to half with 20 wt.% ASF. Composites with 30 wt.% ASF, has an  $\epsilon_b$  of only 3.5 %. This means a much more fragile and less resistant behaviour of P(3HB-*co*-3HHx)-ASF composites with increasing wt.% ASF without any other component. This mechanical behaviour is like those obtained in other thermoplastic matrix composite systems with natural fillers [3,26,35-37]. Nevertheless, the addition of OLA leads to an improvement of the elongation at break due to a compatibilization between P(3HB-*co*-3HHx)/ASF by the interaction of compatibilizer with terminal groups of P(3HB-*co*-3HHx) and lignocellulosic particles. Also, a plasticization effect on the matrix can be expected by OLA acting as lubricant inside de polymer chain. Both effects were reported by Quiles-Carrillo *et al.* with different biobased and petroleum-derived compatibilizers on PLA/ASF [38].

With respect to the hardness values, the increase in the wt.% ASF content favours a slight increase in Shore D hardness as expected since tensile characterization suggested increased stiffness. In fact, the Shore D hardness increases from 60.2 (neat P(3HB-*co*-3HHx)) to 66.2 (composite containing 30 wt.% ASF) [30]. On the other hand, the impact resistance is one of the properties with the greatest decrease in uncompatibilized P(3HB-*co*-3HHx)-ASF composites. First, it should be noted that P(3HB-*co*-3HHx) is a thermoplastic with an intrinsically low impact resistance. This fragile behaviour of P(3HB-*co*-3HHx) was greatly affected by the addition of ASF (even with low wt.% ASF content. The results show how the addition of 10 wt.% ASF,

decreases the impact strength to values lower to the half ( $1.8 \text{ kJ/m}^2$ ) of neat P(3HB-co-3HHx) ( $4.3 \text{ kJ/m}^2$ ).

It is worthy to note that WPCs are widely used in applications that include fencing, garden objects, furniture, decking, and so on. The technical requirements will depend on the final application. Considering the mechanical results, these WPCs offer relatively low tensile strength and low elongation at break even without ASF filler. The addition of ASF up to 30 wt.% and OLA as compatibilizer, gives interesting materials with a wood-like appearance but they cannot be used for medium technological applications as mechanical properties are low. Moreover, addition of 30 wt.% ASF leads to a cost-effective material as P(3HB-co-3HHx) matrix is still an expensive bacterial polyester.

The impact resistance values dropped down to similar values with increasing wt.% ASF content. For 30 wt.% ASF the absorbed energy per unit area is around  $1.6 \text{ kJ/m}^2$  which represents a loss of almost 63 % of the capacity to absorb energy during impact conditions, which is representative for the overall toughness. These results showed a clear embrittlement and loss of toughness on P(3HB-co-3HHx)-ASF composites as the wt.% ASF content increases. The small lignocellulosic ASF particles form a dispersed phase in the thermoplastic matrix (due to the high hydrophilicity of ASF particles, it is possible to form aggregates which lead to worse properties). This dispersed phase interrupts the continuity of the P(3HB-co-3HHx) matrix; in these conditions, the stress transfer between the particle and the matrix is not allowed. In addition, as observed in **Figure III.1.2.1.**, ASF particles are not spherical; their shape is very irregular (with angular shapes) and could act as micro-notches that promote formation of microcracks and subsequent, their growth. This phenomenon justifies the decrease in toughness in P(3HB-co-3HHx)-ASF composites [3,4,29,37,39]. Furthermore, since the polymeric matrix is non-polar (hydrophobic) and the ASF particles are highly polar (highly hydrophilic due to its lignocellulosic composition), there is no (or very poor) matrix-particle interaction along the interface. This lack of interface causes a fragilizing effect by concentrating the stresses and decreasing the potential plastic deformation capacity in P(3HB-co-3HHx)-ASF composites [26,35,40-43].

**Figure III.1.2.2.** shows in a detailed way the lack of interface between P(3HB-co-3HHx) and ASF particles. **Figure III.1.2.2a.** and **Figure III.1.2.2b.** show a clear micro-gap surrounding the ASF particle. This gap sizes from  $1 \mu\text{m}$  to  $3 - 4 \mu\text{m}$  (see white arrows) is formed by the for lack of interactions in the polymer-particle interface. This gap is responsible for interrupting the continuity in uncompatibilized

P(3HB-co-3HHx)-ASF composites and does not allow stress transfer. This suggests ASF particles do not act as reinforcing material; even more, they promote stress concentration leading to a brittle material. Despite this, addition of an OLA, could potentially provide improved toughness as observed in **Figure III.1.2.2c.** and **Figure III.1.2.2d.**, which correspond to the compatibilized composite with 10 phr OLA. At higher magnifications ASF particles are completely embedded by the P(3HB-co-3HHx) rich matrix (**Figure III.1.2.2d.**, see white arrow with a circle end). This situation is similar to that obtained in composites with 20 phr OLA (**Figure III.1.2.e.** and **Figure III.1.2.f.**) which shows absence of gap between the ASF particles and the surrounding matrix. This oligomer has carboxylic acid and hydroxyl terminal groups that can readily react (interact) with hydroxyl terminal groups in P(3HB-co-3HHx) and, obviously, with the hydroxyl groups in ASF (mainly, cellulose, lignin and hemicelluloses). As it can be seen, the gap is remarkably reduced (white arrow) and this could contribute to improve toughness and stress transfer [44,45]. Despite high polarity ester groups can establish somewhat interactions with polar groups in cellulose, the main compatibilizing effects are obtained with high reactive groups such as maleic anhydride, carboxyl acids, end-chain hydroxyl groups, glycidyl methacrylate as reported by Pracela *et al.* by using functionalized copolymers to provide increased interface interactions between a polymer matrix and cellulose particles [46]. Some interactions between ester groups and cellulose particles have been described by Chabros *et al.* in thermosetting unsaturated polyester resins with cellulose fillers; in particular they describe some interactions between the polar ester groups and hydroxyl groups in cellulose by hydrogen bonding [47]. These small range interactions can also occur in P(3HB-co-3HHx)/ASF composites, but their intensity is lower than that provided by the reaction of carboxylic acid and hydroxyl terminal groups in OLA with both hydroxyl groups in cellulose and P(3HB-co-3HHx) through condensation or esterification reactions. As described by Mokhena *et al.* [48] the ester groups in PLA are not enough to provide intense interactions between the polyester-type matrix and the cellulose filler. They report the need of different treatments on cellulose such as acetylation, glyoxalization, silylation, treatment with glycidyl methacrylate - GMA, among others to improve polymer-matrix interactions. This could be related not only to the polarity but also with the hydrophilic nature of ASF and the hydrophobic nature of P(3HB-co-3HHx).

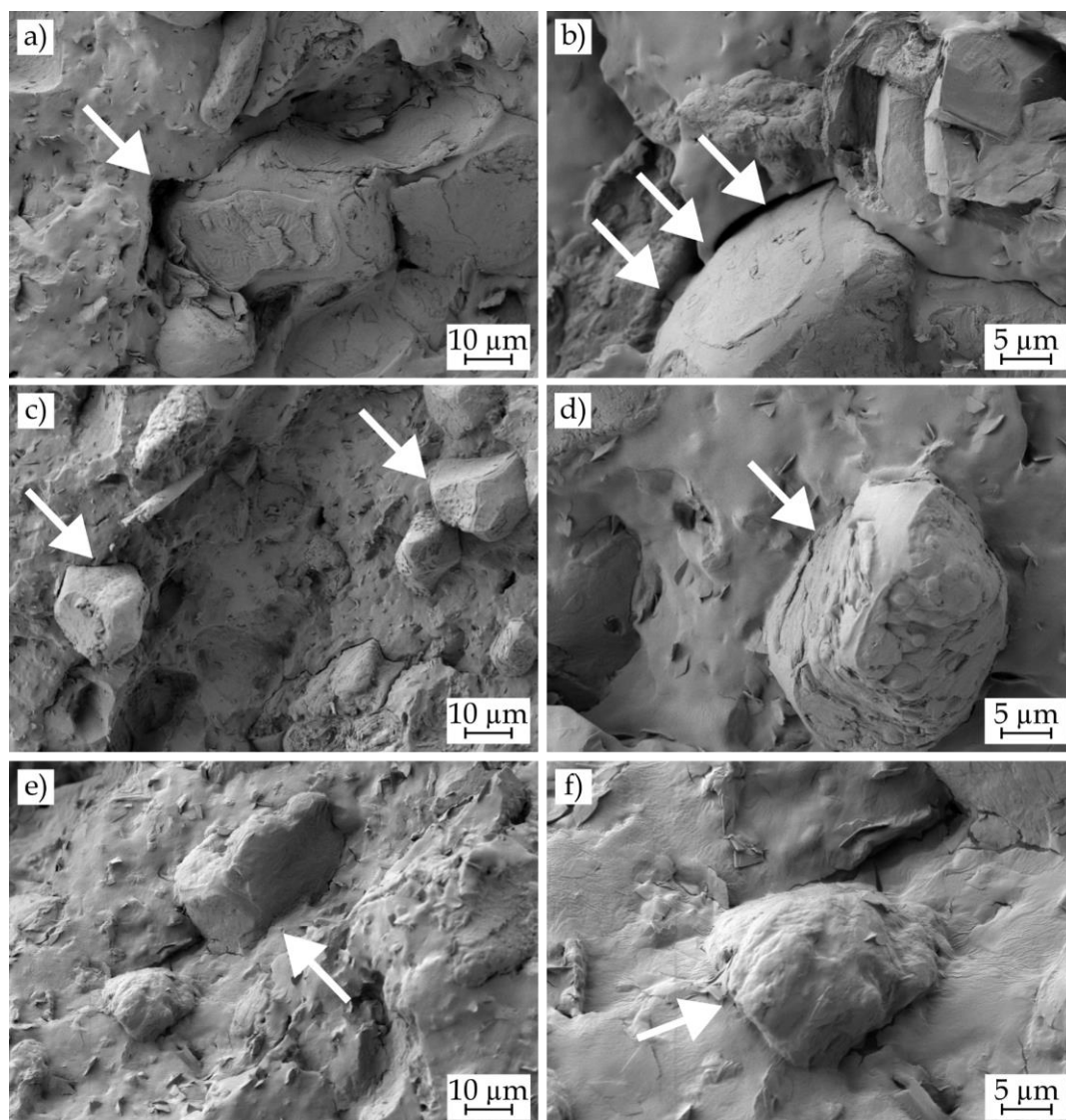


**Figure III.1.2.2.** FESEM images at  $1000\times$  (left side) and  $2500\times$  (right side) corresponding to P(3HB-*co*-3HHx)-ASF composite with 30 wt.% ASF with different OLA content, a) & b) 0 phr OLA, b) & c) 10 phr OLA and e) & f) 20 phr OLA.

The P(3HB-*co*-3HHx)-ASF composite with 30 wt.% ASF, showed the worst mechanical properties in terms of ductility and toughness. This was taken as a reference material to improve its properties by the addition of a compatibilizer/plasticizer. An OLA was added in different proportions (10 and 20 phr) to provide compatibilization and some plasticization [49,50]. In **Table III.1.2.2.**, the increase in impact resistance for the reference uncompatibilized composite is observed with the addition of 10 phr and 20 phr of OLA. The addition of small amounts (10 phr  $\approx$  0.1 wt.%) of this oligomer significantly improves the impact resistance of the composite [51]. It changes from 1.6 kJ/m<sup>2</sup> (uncompatibilized P(3HB-*co*-3HHx)-ASF with 30 wt.% ASF) to 2.4 kJ/m<sup>2</sup> for the same composite with 20 phr OLA, which represents a % increase of

33 %. Considering that this increase in toughness is related to an improvement in ductility, subsequently, Shore D hardness values decreased, changing from 66.2 to 58.6 and 50.0 for 10 phr and 20 phr OLA content, respectively.

This improvement on toughness is corroborated by the capacity of deformation observed in compatibilized composites. By adding only 10 phr OLA to the reference uncompatibilized P(3HB-*co*-3HHx)-ASF composite, its elongation at break is almost doubled. The compatibilization effect reported in FESEM images (gap reduction) provided a more efficient load transfer between P(3HB-*co*-3HHx) and ASF leading to an improvement of elongation at break as Quiles-Carrillo *et al.* reported [38]. With 20 phr OLA, the  $\epsilon_b$  increase up to 9.7 %, which means an increase of 177 % compared to the same composite without OLA. But the most striking thing is that the  $\epsilon_b$  with 20 phr OLA is even higher than that of neat P(3HB-*co*-3HHx) which is a very positive feature, mainly in this highly brittle material. The composite with 30 wt.% ASF and 20 phr OLA shows a  $\epsilon_b$  value of almost 20 % higher than neat P(3HB-*co*-3HHx) without any filler. These results indicate a marked plasticizing effect of this OLA oligomer, which is corroborated by the values of the tensile strength and the elastic modulus. The incorporation of short-chain oligomers OLA increases the free volume of the polymer chains in P(3HB-*co*-3HHx), which leads to a reduction in the stiffness and an increase in the ductility of composites. The improvement in ductility these P(3HB-*co*-3HHx)-ASF composites with the addition of OLA, produces a decrease in  $\sigma_t$  to 8 MPa with 20 phr OLA, which is slightly lower than the  $\sigma_t$  compared to the same composite without OLA (12 MPa). On the other hand, the decrease in the  $E_t$  observed by OLA addition, indicated that the compatibilized composites are not as rigid as uncompatibilized materials. The obtained  $E_t$  values for 10 and 20 phr OLA are 1158 MPa and 735 MPa respectively. This represents a decrease of 33 % and 58 %, with regard to the reference uncompatibilized composite with an  $E_t$  value of 1744 MPa [51].

#### **Thermal properties of P(3HB-*co*-3HHx)-ASF/OLA composites.**

A comparative plot of the DSC thermograms is represented in **Figure III.1.2.3.** and the main thermal parameters are summarized in **Table III.1.2.3.** All thermograms are characterized by a first change in the corresponding baseline at very low temperature (around 0 °C), which is attributable to the corresponding  $T_g$ . Neat P(3HB-*co*-3HHx) is a thermoplastic with low  $T_g$ , close to 0 °C; similar values to this have been reported in several studies with P(3HB-*co*-3HHx) [14]. In a first analysis, it was determined that the addition of lignocellulosic filler, ASF, to

P(3HB-*co*-3HHx), slightly decreases the  $T_g$  to values comprised in the - 0.5 and 1.9 °C range for all uncompatibilized composites. Considering that  $T_g$  are not a unique temperature, but a temperature range in which the material undergoes a change from a glassy state to a rubbery state, it can be assessed that these slight variations in  $T_g$  are not significative. The marked exothermic peak observed in the DSC thermogram of neat P(3HB-*co*-3HHx) corresponds to the cold crystallization phenomenon, and its peak (corresponding to the temperature in which the crystallization rate is maximum) is located at 54.6 °C. The addition of lignocellulosic ASF particles does not influence the  $T_{cc}$  of P(3HB-*co*-3HHx) in the developed composites. It can only be observed a dilution effect (the cold crystallization peak height is smaller in P(3HB-*co*-3HHx)/ASF composites, compared to neat P(3HB-*co*-3HHx); this is because the P(3HB-*co*-3HHx)/ASF composite contains 30 wt.% ASF which has no thermal transition in this temperature range, and consequently, the intensity of the peak is lower). At higher temperatures, the DSC thermograms show three small and broad endothermic peaks corresponding to the melting process of P(3HB-*co*-3HHx) [52]. As already indicated in other studies [16,18,19,53-55], due to the polymorphism of the P(3HB-*co*-3HHx) crystals during the crystallization process, its melting occurs at different temperatures. This situation of P(3HB-*co*-3HHx) is identical to other polyhydroxyalkanoates - PHAs which present three melting peaks at different temperatures  $T_{m1}$ ,  $T_{m2}$  and  $T_{m3}$ , too. Neat P(3HB-*co*-3HHx) used in this work, show three melting peak temperatures located at 111 °C, 130 °C and 162 °C, respectively. The addition of lignocellulosic ASF particles does not produce significant changes in melting temperatures as observed in other studies [36]. The analysis of the enthalpies corresponding to  $\Delta H_{cc}$ , indicated that the highest enthalpy corresponded to neat P(3HB-*co*-3HHx) during the second heating cycle ( $\Delta H_{cc2} = 26.7$  J/g). These values decreased gradually with the addition of ASF particles, down to values of 3.7 J/g for the sample with 30 wt.% ASF. The dilution effect (which means considering the actual P(3HB-*co*-3HHx) content without taking into account the wt.% ASF for the cold crystallization enthalpy calculation), would give a theoretical diluted enthalpy of 18.69 J/g which is remarkably higher than the actual obtained value of 3.7 J/g. These differences are not so pronounced for 10 and 20 wt.% ASF.

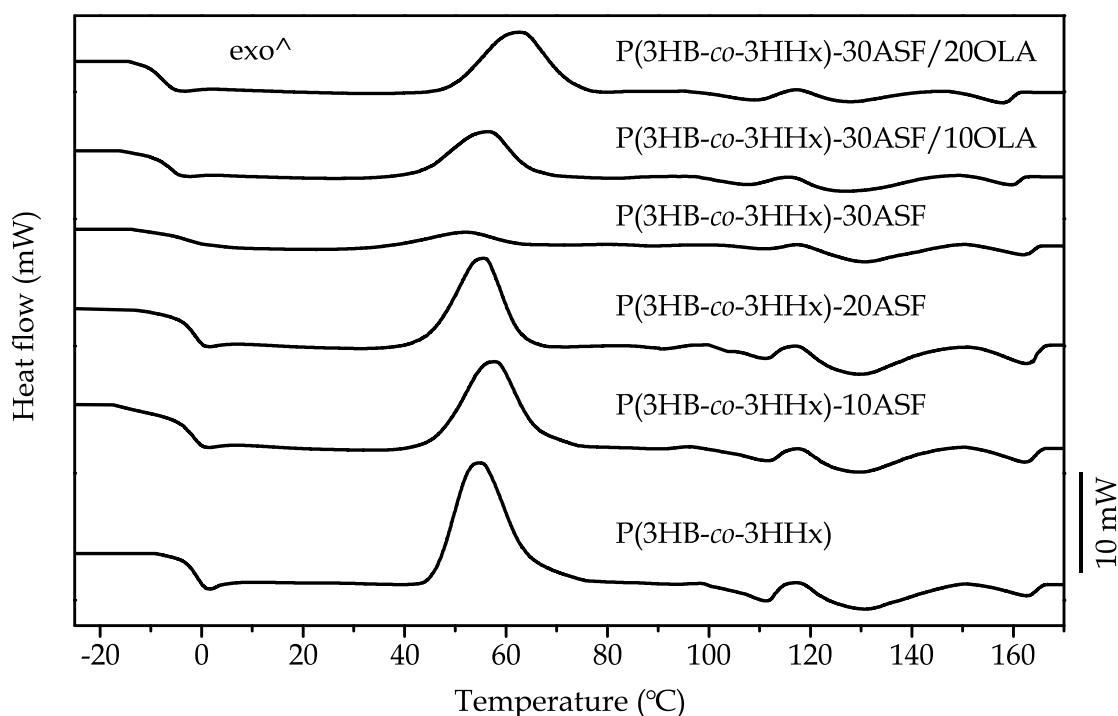


**Figure III.1.2.3.** Comparative plot of the second heating curves obtained by dynamic DSC of the different P(3HB-*co*-3HHx)-ASF/OLA composites with different compositions.

In a second stage, OLA was added to improve toughness of the P(3HB-*co*-3HHx)-ASF composite with worst toughness, *i.e.* composite with 30 wt.% ASF. The DSC thermograms, (**Figure III.1.2.3.**), show a similar thermal behaviour to the OLA-free composites. The addition of 10 phr and 20 phr OLA to this composite, shows a decrease of the P(3HB-*co*-3HHx)  $T_g$  down to values around  $-5\text{ }^\circ\text{C}$ , compared with the composite without OLA. The low molecular weight OLA chains offer slightly increased mobility in comparison with the polymer chains of neat P(3HB-*co*-3HHx), similar results were reported by Quiles-Carrillo *et al.* [56]. This phenomenon increases the free volume in the polymeric structure and leads to a poor plasticizing effect. It is true that addition of oligomers of lactic acid to PLA, usually leads to a remarkable decrease in PLA's  $T_g$  as reported by Burgos *et al.* [57] from  $66\text{ }^\circ\text{C}$  (neat PLA) down to  $-10\text{ }^\circ\text{C}$ . Nevertheless, the decrease in  $T_g$ , is directly related to the PLA and OLA structure. Lascano *et al.* [51] reported a decrease of PLA  $T_g$  from  $63.3\text{ }^\circ\text{C}$  (neat PLA; different grade) down to  $50.8\text{ }^\circ\text{C}$  with 20 % OLA (different commercial grade of OLA). Armentano *et al.* [58] reported a dual plasticization effect of P3HB and OLA on PLA, but the decrease in  $T_g$  was not as important as the above mentioned by Burgos *et al.* Moreover, Amor *et al.* [59], reported a slight plasticization effect on PLA/P(3HB-*co*-3HHx) blends by using OLA in with a dual plasticization effect of P(3HB-*co*-3HHx) (which provided a  $3\text{ }^\circ\text{C}$  decrease in  $T_g$  of PLA with a P(3HB-*co*-3HHx) at 10 wt.%) and OLA (which provided a

decrease of 1 °C with 1 wt.%). All these results show the disparity in plasticization of PLA with OLA even they share the same chemical structure. Therefore, the plasticization effect on PHAs is even more complex and has not been studied previously independently of blends with PLA. In this work, this decrease in  $T_g$  values are very low, but we must bear in mind that P(3HB-co-3HHx) structure contains medium chain hydroxyalkanoates and these, contribute to lowering crystallinity compared to P3HB. Therefore, this slight decrease could be representative of somewhat plasticization effect provided by OLA. Besides this, it corroborates the mechanical results analysed previously [31,40,51].  $T_{cc}$  values increased from 52 °C for the sample without OLA, to 62 °C for the sample with 20 phr OLA. This is not the typical effect of a plasticizer which increases chain mobility and, therefore, the cold crystallization process is shifted to lower temperatures as reported by Lascano *et al.* [51] and Ferri *et al.* [60]. Nevertheless, some additives such as Maleinized Linseed Oil – MLO, maleinized cottonseed oil – MCSO, or even epoxidized vegetable oils, promote an overlapping of several phenomena such as slight plasticization, chain extension, branching and, in some cases, potential crosslinking due to the multifunctionality of these compounds. Some of these vegetable-oil derivatives, produce the same behaviours as observed in this study, *i.e.* a shift of the cold crystallization process to higher temperatures, due to the disrupted overall structure they provide with branches, chain extension, and so on as reported by Garcia-Campo *et al.* [61]. Limiñana *et al.* [62] reported the potential of these modified vegetable oils as compatibilizers for PBS and lignocellulosic fillers, due to reaction of oxirane, maleic anhydride groups with hydroxyl groups in almond shell flour. In this study, it seems OLA has a similar effect to those modified vegetable oils, since changes in  $T_g$  are very low. Also, the cold crystallization is shifted to higher temperatures, thus indicating that other phenomena could be occurring, such as compatibilization and/or chain extension.

The  $\Delta H_{cc2}$  values of P(3HB-co-3HHx) in OLA-compatibilized composites is 11.4 J/g and 15.9 J/g, for 10 phr and 20 phr OLA respectively. It strikes the fact that the same composite without OLA shows a much lower  $\Delta H_{cc2}$ , 3.7 J/g. With respect to  $T_{m1}$ ,  $T_{m2}$  and  $T_{m3}$  it was observed that these thermal transitions were slightly decreased with the addition OLA which could be related to less perfect crystals [51].



**Table III.1.2.3.** Main thermal parameters of the P(3HB-*co*-3HHx)-ASF/OLA composites with different compositions, obtained by DSC.

Code	T <sub>g</sub> (°C)	T <sub>cc</sub> (°C)	T <sub>m1</sub> (°C)	T <sub>m2</sub> (°C)	T <sub>m3</sub> (°C)	ΔH <sub>m1</sub> * (J/g)	ΔH <sub>cc2</sub> (J/g)	ΔH <sub>m2</sub> (J/g)	χ <sub>c1</sub> * (%)	χ <sub>c1</sub> (%)
P(3HB- <i>co</i> -3HHx)	0.3 ± 0.1	54.6 ± 1.1	111.5 ± 1.9	130.8 ± 2.0	162.5 ± 1.2	20.3 ± 0.5	26.7 ± 0.8	33.6 ± 1.3	13.9 ± 1.1	4.7 ± 0.3
P(3HB- <i>co</i> -3HHx)-10ASF	-0.5 ± 0.1	57.5 ± 1.8	112.1 ± 1.8	129.7 ± 1.7	162.3 ± 1.8	19.6 ± 0.4	17.4 ± 0.4	29.0 ± 2.2	14.9 ± 1.1	8.8 ± 0.4
P(3HB- <i>co</i> -3HHx)-20ASF	-1.9 ± 0.2	55.5 ± 1.9	111.5 ± 2.0	129.6 ± 2.1	163.4 ± 1.4	18.1 ± 0.3	15.0 ± 0.1	26.4 ± 2.1	15.5 ± 0.8	9.8 ± 0.7
P(3HB- <i>co</i> -3HHx)-30ASF	-1.1 ± 0.1	51.8 ± 1.2	111.3 ± 1.3	130.6 ± 1.9	164.1 ± 1.2	8.5 ± 0.2	3.7 ± 0.3	21.4 ± 0.9	8.3 ± 0.7	17.3 ± 0.9
P(3HB- <i>co</i> -3HHx)-30ASF/10OLA	-5.2 ± 0.2	56.3 ± 1.4	107.6 ± 2.1	127.0 ± 1.8	159.4 ± 1.6	7.4 ± 0.1	11.4 ± 0.1	26.1 ± 1.3	8.0 ± 0.8	14.7 ± 0.8
P(3HB- <i>co</i> -3HHx)-30ASF/20OLA	-5.6 ± 0.3	62.6 ± 2.0	109.9 ± 2.3	127.5 ± 2.0	157.9 ± 1.5	6.4 ± 0.3	15.9 ± 0.4	22.6 ± 1.5	7.5 ± 1.2	6.7 ± 0.4

\* ΔH<sub>m1</sub> and χ<sub>c1</sub> correspond to the first heating scan.

On the first heating scan the polymer has been recrystallized at 25 °C for 15 days. Consequently, the cold crystallization peak did not appear which means that the polymer structure wasn't able to form crystallites. Under this condition, P(3HB-*co*-3HHx) reaches a χ<sub>c1</sub> value of 13.9 %. This increases with the amount of ASF filler up to 15.5 % with 20 wt.% ASF which suggests that ASF (mainly crystalline cellulose fractions) acts as a nucleant agent [62]. Furthermore, with the addition of 30 wt.% ASF, χ<sub>c1</sub> decreases to 8.3 % due to the decrease of free volume necessary for nucleation of polymer as Thomas *et al.* reported [63]. Mechanical characterization shows no correlation between the degree of crystallinity, while elastic modulus increases up to 30 wt.% ASF, the degree of crystallinity is saturated with only 20 wt.%. The second scan was performed after a controlled cooling process of 10 °C/min, as a result in the second scan the polymer was able to form crystallites due to a cold crystallization process. Under this condition the degree of crystallinity could increase until 30 wt.% ASF. The compatibilizing effect of OLA in both conditions decreased the degree of crystallinity by reducing the gaps between the filler and the matrix as it is reported in FESEM analysis and Gong *et al.* proposed [64].

TGA, allowed to analyse the thermal stability of P(3HB-*co*-3HHx)-ASF composites. The TGA curves of the studied materials are gathered in **Figure III.1.2.4.**, and the main thermal degradation parameters are summarized in **Table III.1.2.4.** The thermal degradation process of neat P(3HB-*co*-3HHx) occurs in a single step. P(3HB-*co*-3HHx) shows good thermal stability up to 266.8 °C (the onset degradation temperature was taken as the temperature for a weight loss of 2 %, and it is denoted as T<sub>2%</sub>) of P(3HB-*co*-3HHx). Above this temperature, thermal degradation starts, with a very fast weight loss and a temperature of maximum degradation rate, T<sub>max</sub>, of 308.9 °C, obtained from peak corresponding to the first derivative of its TGA curve or DTG (**Figure III.1.2.4b.**). The results obtained by Singh for P(3HH-*co*-3BV) indicated that the

degradation process involves the breaking of polymer chains and hydrolysis. Since P(3HB-*co*-3HHx) presents a similar structure, the mechanism of degradation should be similar [4]. Reaching the end set of the degradation process, located at 371 °C, P(3HB-*co*-3HHx) generates a small residue or ash of 2.4 wt.% of its initial weight. These results are in accordance to those obtained in other works [14,65].

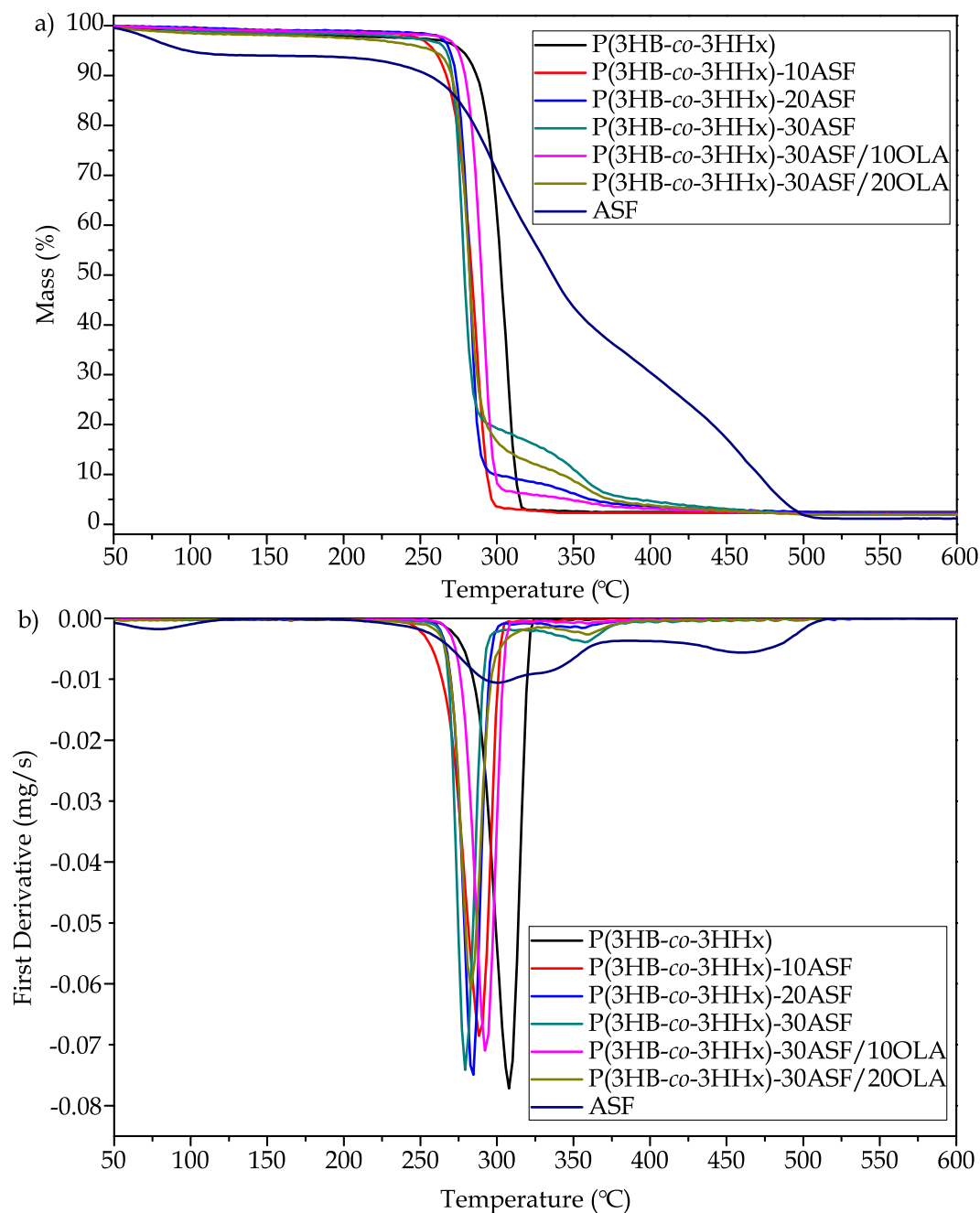


**Figure III.1.2.4.** Comparative plot P(3HB-*co*-3HHx)-ASF/OLA composites with different compositions: a) TGA curves *vs* temperature and b) DTG *vs* temperature.

**Table III.1.2.4.** Summary of the main thermal degradation parameters of P(3HB-co-3HHx)-ASF/OLA composites with different compositions.

Code	T <sub>2%</sub> (°C)	T <sub>max</sub> (°C)	Residual Mass (wt.%)
ASF	101.4*	300.6/460.7	1.5 ± 0.2
P(3HB-co-3HHx)	286.8	308.9	2.4 ± 0.3
P(3HB-co-3HHx)-10ASF	253.2	288.1	2.3 ± 0.2
P(3HB-co-3HHx)-20ASF	250.5	284.3	2.1 ± 0.1
P(3HB-co-3HHx)-30ASF	223.6	279.1	2.0 ± 0.3
P(3HB-co-3HHx)-30ASF/10OLA	258.4	292.0	2.0 ± 0.2
P(3HB-co-3HHx)-30ASF/20OLA	226.3	283.5	2.0 ± 0.2

\*Initial weight loss in ASF due to residual water evaporation.

The thermogram obtained for ASF particles shows different degradation processes corresponding to three different sections [31,35,37]. Since it is an agro-food waste of lignocellulosic nature, it shows a first weight loss around 100 °C, which corresponds to the loss of remaining water in ASF, specifically 6.3 wt.%. During the dynamic degradation process, when temperature reaches 213 °C, a rapid weight loss is observed in two main steps. The first step of weight loss of about 44.2 wt.%, corresponds to the degradation of the cellulose and hemicellulose contained in ASF particles. The first component to start degradation is hemicellulose, followed by cellulose and lignin. Lignin shows a slower (in a wide temperature range) degradation process, so the third section of the TGA curve shows a lower slope, starting at 357.3 °C (temperature change of slope in the thermogram) up to 500 °C, with a loss of 47.6 wt.%. Complete degradation occurs around 500 °C, leaving a final carbonaceous residue or ash of 1.5 wt.%, mainly from lignin. In **Figure III.1.2.4b.**, it can be seen how the temperature corresponding to the maximum degradation rate of hemicellulose-cellulose fraction is located at 300.6 °C, while the lignin fraction maximum degradation rate is close to 460.7 °C. Perinovic *et al.* determined that degradation of polysaccharides, hemicellulose and cellulose starts between 220 °C - 290 °C, while lignin degradation range is comprised between 200 °C and 500 °C [32,33,35,37,41,66].

The TGA curves of P(3HB-co-3HHx)-ASF composites indicated that the thermal degradation process is a linear combination of the two individual degradation phenomena observed in P(3HB-co-3HHx) and ASF, the first part of the curve is identical to neat P(3HB-co-3HHx) and, a small hump at the end of the curve can be detected, which is attributable to residual degradation of ASF which changes with the ASF wt.% [4,31]. For any wt.% content in almond shells, the TGAs are characterized by presenting

degradation start temperatures -  $T_{2\%}$  slightly lower than neat P(3HB-*co*-3HHx) (with a  $T_{2\%}$  of 286.8 °C), in the 220 °C - 250 °C temperature range. The addition of lignocellulosic fillers leads to slightly lower thermal stability, since ASF particles degrade separately from P(3HB-*co*-3HHx), and the overall effect is the P(3HB-*co*-3HHx)-ASF composites has reduced its thermal stability. This is due to the initial degradation of low molecular weight components on almond shell flour such as hemicelluloses. Quiles-Carrillo *et al.* [38] reported similar results with PLA composites with almond shell flour.

TGA curves of composites are very similar to those of the P(3HB-*co*-3HHx) (as it is the main component), with practically only one step degradation stage, but with a small hump at higher temperatures, corresponding to lignin degradation. As the ASF content increases, this hump becomes more pronounced. This process ends at temperatures around 500 °C, generating small amounts of residue close to 2 wt.%. The TGA curves of P(3HB-*co*-3HHx)-ASF composites indicated that from a thermal point of view, the incorporation of lignocellulosic fillers such as ASF, slightly reduces the stability, but even in this case, the processing window is not compromised since all the onset degradation temperatures are above 250 °C, and the recommended processing temperature for this polymer is 140 - 150 °C.

On the other hand, composites with 10 phr and 20 phr OLA, show a very similar thermal degradation behaviour to the reference uncompatibilized composite (P(3HB-*co*-3HHx)-ASF with 30 wt.% ASF) without OLA. The addition of 10 phr OLA seems to slightly improve the thermal stability of the developed composites. The characteristic thermal degradation values are delayed by 34 °C in  $T_{2\%}$  and by 10 °C in  $T_{max}$  compared to the unmodified reference composite without OLA. The biggest improvement in thermal stability is observed for the composite with 10 wt.% OLA by the chemical interaction of the compatibilizer with both components of the composite as above mentioned. The complex structure formed after reaction of OLA with both P(3HB-*co*-3HHx) and ASF, can act as a physical barrier that obstructs the removal of volatile products produced during decomposition [67].

#### **Thermo-mechanical properties of P(3HB-*co*-3HHx)-ASF/OLA composites.**

**Figure III.1.2.5b.** shows the variation of the  $E'$ , with respect to temperature, obtained by DMTA analysis. It can be seen graphically how  $E'$  decreases with increasing temperature in all the developed composites, as expected due to the softening of the polymeric P(3HB-*co*-3HHx) matrix. At low temperatures,  $E'$  values are high in all composites, since this temperature range corresponds to the elastic-glassy behaviour of

the P(3HB-*co*-3HHx) matrix. In this first zone,  $E'$  for neat P(3HB-*co*-3HHx) is 1869 MPa at - 40 °C, which is lower than  $E'$  values of any of the uncompatibilized P(3HB-*co*-3HHx)-ASF composites (*i.e.*  $E'$  is 2019 MPa for the P(3HB-*co*-3HHx)-ASF composite with 30 wt.% ASF at - 40 °C). These results are in accordance with those obtained by mechanical characterization which suggested a stiffening as the wt.% ASF increased [37]. **Table III.1.2.5.** shows the numerical comparison of the variation of  $E'$  as a function of ASF wt.% and OLA phr, at two different temperatures.

**Table III.1.2.5.** Main DMTA parameters of P(3HB-*co*-3HHx)-ASF/OLA composites with different compositions.

Code	$T_g$ (°C)	$E'$ at - 40 °C (MPa)	$E'$ at 25 °C (MPa)
P(3HB- <i>co</i> -3HHx)	10.6 ± 0.9	1869 ± 42	1345 ± 28
P(3HB- <i>co</i> -3HHx)-10ASF	14.3 ± 0.8	1910 ± 49	1431 ± 40
P(3HB- <i>co</i> -3HHx)-20ASF	12.0 ± 0.7	1948 ± 30	1512 ± 20
P(3HB- <i>co</i> -3HHx)-30ASF	11.4 ± 0.9	2019 ± 52	1604 ± 45
P(3HB- <i>co</i> -3HHx)- 30ASF/10OLA	9.7 ± 0.7	1601 ± 36	1352 ± 29
P(3HB- <i>co</i> -3HHx)- 30ASF/10OLA	9.3 ± 0.6	853 ± 25	767 ± 23

As the temperature increases,  $E'$  decreases rapidly as it acquires a rubbery state behaviour. This is related to the  $\alpha$ -relaxation phenomenon due to  $T_g$ . **Table III.1.2.5.** shows how at 25 °C, the  $E'$  value for neat P(3HB-*co*-3HHx) has decreased to 1345 MPa from 1869 MPa at - 40 °C and, subsequently, the stiff-elastic behaviour changes to a rubber-like behaviour. The same trend can be observed for uncompatibilized P(3HB-*co*-3HHx)-ASF composites. However, when compared to the neat P(3HB-*co*-3HHx) matrix, at the same temperature, the higher the wt.% of ASF, the stiffer the composite becomes. With only 10 wt.% ASF,  $E'$  at 25 °C increases 6.4 % with respect to P(3HB-*co*-3HHx) at the same temperature. Accordingly, the composite with 30 wt.% ASF offers higher stiffness (a percentage increase of 19 % regarding neat P(3HB-*co*-3HHx)). The presence of ASF particles finely dispersed in the P(3HB-*co*-3HHx) matrix restricts the mobility of the polymer chains, thus decreasing their viscous behaviour, which causes an increase in the  $E'$  value as the ASF loading increases [4,27-29,39]. In addition, at this temperature range, lignocellulosic components are below its  $T_g$ , which means they show a glassy behaviour that promotes increased stiffness. Nevertheless, it is important to bear in mind that the main component in P(3HB-*co*-3HHx)/ASF composites is P(3HB-*co*-3HHx) and the dynamic behaviour is highly influenced by P(3HB-*co*-3HHx) behaviour. In addition these results corroborate those obtained in the mechanical characterization of P(3HB-*co*-3HHx)-ASF composites.

As in previous analyses, by adding small amounts of OLA to the P(3HB-*co*-3HHx)-ASF composite with the highest ASF loading, which shows the worst ductile/toughness properties, the DMTA graphs in **Figure III.1.2.5a.** show the lowest  $E'$  in the temperature range analysed. At  $-40\text{ }^{\circ}\text{C}$ ,  $E'$  decreases from 2019 MPa without OLA addition, to 1601 MPa and 853 MPa for the addition of 10 phr and 20 phr OLA, respectively. The trend is the same at room temperature ( $25\text{ }^{\circ}\text{C}$ ). With an addition of only 10 phr OLA the  $E'$  is decreased by 16 %, and with 20 phr OLA  $E'$  is reduced even more, thus decreasing the rigidity of P(3HB-*co*-3HHx)-ASF composites and, subsequently their  $E'$  [40]. It is worthy to note the extremely small changes in  $T_g$  obtained by DMTA which suggests, as DSC, very poor plasticization effect, so compatibilization is one of the most representative effects of OLA in this P(3HB-*co*-3HHx)/ASF system.

**Figure III.1.2.5b.** shows the variation of the dynamic damping factor  $-\tan\delta$  as a function of temperature, for neat P(3HB-*co*-3HHx), uncompatibilized P(3HB-*co*-3HHx)-ASF and P(3HB-*co*-3HHx)-ASF/OLA composites. Despite there are several criteria to obtain the  $T_g$  from TMA graphs, the most used is the peak maximum of  $\tan\delta$ . The  $T_g$  values obtained for all developed materials are gathered in **Table III.1.2.5.** It can be observed that  $\tan\delta$  peaks are slightly moved towards higher temperatures in uncompatibilized P(3HB-*co*-3HHx)-ASF composites, compared to neat P(3HB-*co*-3HHx) (a maximum shift of 3 - 4  $^{\circ}\text{C}$ ). This change is not significant as observed in other techniques such as DSC. On the other hand, the addition of OLA leads to slightly lower  $T_g$  values by DMTA, but once again, these changes are not high enough to give clear evidence of the chain mobility restriction by ASF particles or increased chain mobility by OLA.

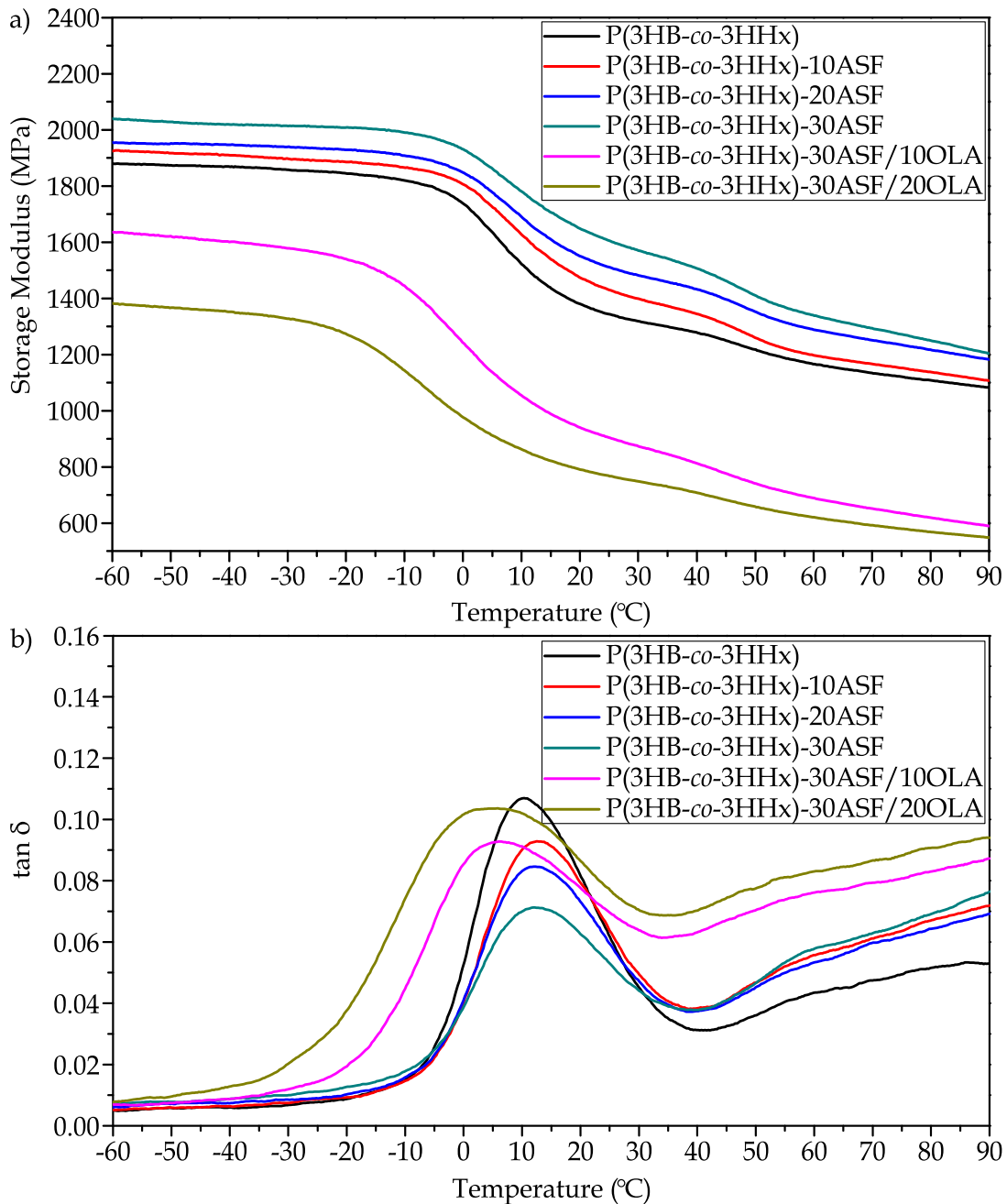


**Figure III.1.2.5.** Comparative plot of DMTA curves of P(3HB-co-3HHx)-ASF/OLA composites with different compositions: a) Storage modulus *vs* temperature and b) tan  $\delta$  *vs* temperature.

For potential structural/engineering/conventional applications of WPCs, it is very important to know their dimensional stability with temperature. This can be assessed by DTMA which allows obtained the CLTE. It must be stated that a good dimensional stability involves low CLTE values. **Table III.1.2.6.** summarizes the CLTE values for the developed composites, at temperatures below and above their corresponding  $T_g$ . In general, at temperatures below  $T_g$  the CLTE values are much lower than above their  $T_g$ . The dimensional expansion of the material is lower at low temperatures because the material is more rigid, which is the typical glassy behaviour

below  $T_g$ . Above  $T_g$ , the behaviour is viscous or rubber-like and so that, the dimensional expansion is favoured, with higher CLTE values.

**Table III.1.2.6.** Summary of the main TMA properties of neat P(3HB-*co*-3HHx) and P(3HB-*co*-3HHx)-ASF/OLA with different compositions.

Code	$T_g$ (°C)	CLTE ( $\mu\text{m}/\text{m}^\circ\text{C}$ )	
		Below $T_g$	Above $T_g$
P(3HB- <i>co</i> -3HHx)	$-0.3 \pm 0.1$	$77.1 \pm 2.2$	$160.7 \pm 2.3$
P(3HB- <i>co</i> -3HHx)-10ASF	$0.2 \pm 0.1$	$76.9 \pm 2.1$	$157.0 \pm 1.3$
P(3HB- <i>co</i> -3HHx)-20ASF	$-0.4 \pm 0.1$	$75.6 \pm 2.1$	$157.4 \pm 2.9$
P(3HB- <i>co</i> -3HHx)-30ASF	$1.4 \pm 0.2$	$66.8 \pm 0.8$	$140.3 \pm 2.6$
P(3HB- <i>co</i> -3HHx)-30ASF/10OLA	$-1.3 \pm 0.1$	$72.0 \pm 0.9$	$169.1 \pm 3.8$
P(3HB- <i>co</i> -3HHx)-30ASF/20OLA	$-1.4 \pm 0.2$	$90.7 \pm 4.1$	$194.3 \pm 2.8$

First, the analysis of the CLTE values at temperatures below  $T_g$  shows that increasing wt.% ASF gives more dimensional stability, which is in accordance with previous mechanical results that suggested a clear stiffening with ASF addition. Pure P(3HB-*co*-3HHx) has an initial value of  $77.1 \mu\text{m}/\text{m}^\circ\text{C}$ , which decreases to  $66.8 \mu\text{m}/\text{m}^\circ\text{C}$  with 30 wt.% ASF particles (which represents a % decrease of 13 %), which involves improved dimensional stability. However, OLA addition significantly increases the CLTE values, as typical plasticizers do, thus leading to slightly lower dimensional stability. With 10 phr and 20 phr OLA, CLTE is  $72.0$  and  $90.7 \mu\text{m}/\text{m}^\circ\text{C}$ , respectively.

Secondly, the results obtained in the study at temperatures above  $T_g$  show the same tendency as the results discussed in the previous paragraph. Neat P(3HB-*co*-3HHx) shows an initial CLTE of  $160.7 \mu\text{m}/\text{m}^\circ\text{C}$  (much higher than below  $T_g$ ), which decreases to  $140.3 \mu\text{m}/\text{m}^\circ\text{C}$  with 30 wt.% ASF particles. Identically as observed previously, CLTE becomes greater again with the addition of OLA, reaching values of  $194.3 \mu\text{m}/\text{m}^\circ\text{C}$  with 20 phr OLA. In general, as the ASF content increases, composites show improved dimensional stability [4,29,68]. However, these dimensional expansions are higher than those of neat P(3HB-*co*-3HHx) in P(3HB-*co*-3HHx)-ASF composites (30 wt.% ASF) with 10 phr and 20 phr OLA, due to the plasticizing effect [51].

#### **Evolution of the water uptake and water diffusion process in P(3HB-*co*-3HHx)-ASF/OLA composites.**

The water absorption capacity of WPCs is an important feature in some applications due to the lignocellulosic component. This creates a 3D-path inside the polymer matrix that allows water entering (for example when the composite is subjected to high relative humidity environments) and this causes an expansion. It is possible that



after this initial stage, this WPC could be subjected to drying at sun with low humidity; then this 3D-path allows water/moisture removal, promoting a contraction. This situation is quite usual in WPCs such as those used in fences, decking, and so on. This repeated expansion-contraction cycles could lead to formation of microcracks. **Figure III.1.2.6.** shows the mass increase (wt.%) with respect to immersion time in water for the P(3HB-co-3HHx)-ASF/OLA composites. It can be seen graphically that during the first week of immersion, the developed composites show a rapid increase in mass by water absorption. As immersion time increases, the mass increase is slower. Some samples even show an asymptotic behaviour, which indicates that saturation has been reached. This type of behaviour corresponds to that indicated by the first Fick's Law.

Obviously, due to the hydrophobicity of neat P(3HB-co-3HHx), it shows the lowest water absorption for 9 weeks. After 35 days of immersion, it reaches a constant saturation mass of 0.53 %, which is maintained practically until 63 days of immersion. The addition of ASF (highly hydrophilic particles due to its composition: cellulose, hemicellulose and lignin as the main components) considerably increases water absorption. The composite with 10 wt.% ASF reaches a water saturation mass of 1.46 wt.% after 42 days. In a similar way, uncompatibilized composites containing 20 wt.% show a relatively low weight gain saturation of 3.1 wt.%. This is almost double the previous value (with 10 wt.% ASF). Nevertheless, the composite containing 30 wt.% ASF, shows a remarkable increase up to values of 7.1 wt.% after 9 weeks, which represents almost 14 times the value for neat P(3HB-co-3HHx), representing a typical result in most WPCs [23,36,43]. The result is higher than the extrapolation from the ASF wt.% (should be of about three times the value of the composite with 10 wt.% ASF, *i.e.* 4.5 wt.%); despite this, we have to bear in mind that the  $\chi_c$  of P(3HB-co-3HHx) in this composite has decreased down to 8.3 % and this has a negative effect on water absorption as amorphous regions allow water entering [69,70]. Therefore, the increase in water absorption is not only related to the amount of lignocellulosic components, it is also linked with the degree of crystallinity of the polymer matrix. It is well known that cellulose, promotes water absorption due to hydroxyl (-OH) groups that interact with water molecules [21-23,25,41,71].

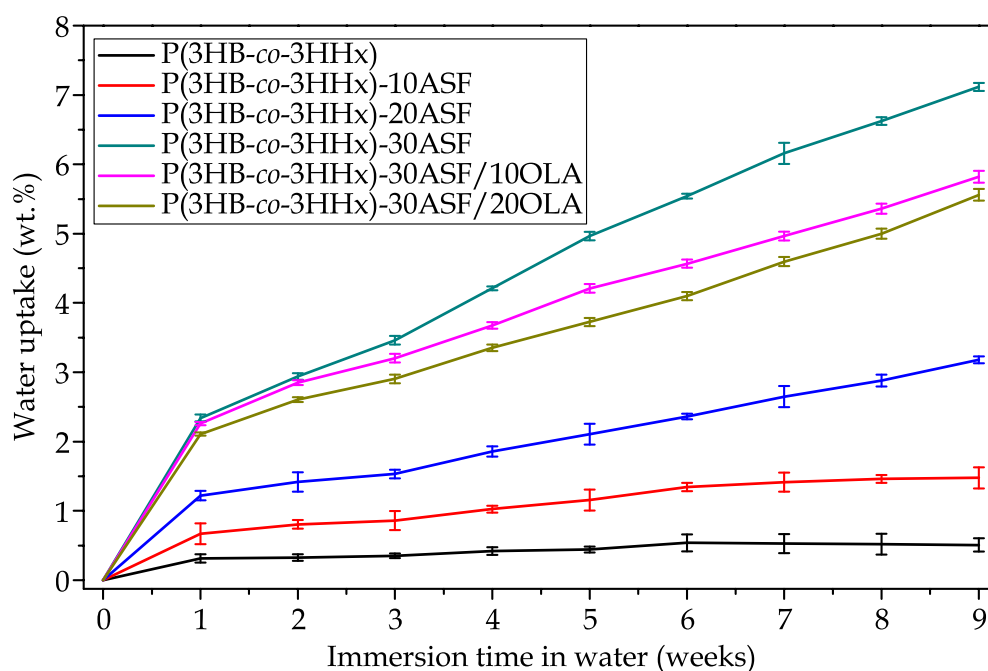


**Figure III.1.2.6.** Water uptake of P(3HB-co-3HHx)-ASF/OLA composites with different compositions. Evolution of the water uptake for a period of 9 weeks.

On the other hand, the addition of OLA to the reference composite (P(3HB-co-3HHx) with 30 wt.% ASF), shows an unexpected behaviour. As one can see in **Figure III.1.2.6.**, the water absorption curve with OLA, moves to lower wt.% absorbed water. The values of the mass increase after 9 weeks of immersion reach values of 5.8 wt.% and 5.5 wt.% for OLA contents of 10 phr and 20 phr, respectively. This means a decrease in water absorption of 18 % and 22.6 % respectively when OLA is added to the P(3HB-co-3HHx)-ASF system. Typical plasticizers, increase the water absorption as they are responsible for an increase in the free volume, thus allowing water molecules to enter. Nevertheless, OLA does not only provides plasticization effects, but also improved polymer-particle interaction among the interface due to the interaction between the hydroxyl groups in OLA and the hydroxyl groups of both P(3HB-co-3HHx) (terminal groups), and cellulose/hemicellulose/lignin in ASF particles. Therefore, in addition to a plasticization phenomenon, the compatibilization effect which was also evidenced in **Figure III.1.2.2.** (FESEM characterization), in which the gap size was higher on OLA-free composites than composites with OLA.

**Table III.1.2.7.** shows the values of the diffusion coefficient -  $D$  or diffusivity of water into the developed composites, by applying the first Fick's Law. The lowest corrected diffusion coefficient,  $D_c$  value is offered by neat P(3HB-co-3HHx), as expected due to its hydrophobicity. The only addition of 10 wt.% ASF, leads to a  $D_c$  value, almost triple compared to neat P(3HB-co-3HHx). Obviously, ASF is responsible for water

entering the composite structure; therefore, uncompatibilized composites with 30 wt.% ASF, shows an increase of two orders of magnitude. Due to the hydrophilic nature of ASF particles, and possibly accentuated by the capillarity of the micro-gaps between P(3HB-*co*-3HHx) and the embedded ASF particles, water molecules can easily enter into the composite structure as in most WPCs [51,71]. Finally, the  $D_c$  values P(3HB-*co*-3HHx)-ASF/OLA composites remain with similar values to those of the same composite without OLA. Thus, it was deduced that the amount of wt.% ASF is the parameter with the greatest influence on the water diffusion process in P(3HB-*co*-3HHx)-ASF/OLA composites, together with the degree of crystallinity as previously discussed with the relationship of the water absorption and the wt.% ASF loading and the degree of crystallinity of the P(3HB-*co*-3HHx) matrix. Since the  $D_c$  values for the composites with 10 and 20 phr OLA are similar to that of the same composite with 30 wt.% ASF, it is possible to conclude the poor plasticization effect of this OLA, suggesting, once again, that compatibilization is the main acting mechanisms of OLA on P(3HB-*co*-3HHx)/ASF composites.

**Table III.1.2.7.** Values of the diffusion coefficient and the corrected diffusion coefficient for P(3HB-*co*-3HHx) and the P(3HB-*co*-3HHx)-ASF composites processed with OLA.

Code	$D \times 10^{-9}$ (cm <sup>2</sup> /s)	$D_c \times 10^{-9}$ (cm <sup>2</sup> /s)
P(3HB- <i>co</i> -3HHx)	0.14 ± 0.03	0.07 ± 0.01
P(3HB- <i>co</i> -3HHx)-10ASF	0.54 ± 0.05	0.25 ± 0.02
P(3HB- <i>co</i> -3HHx)-20ASF	1.56 ± 0.07	0.74 ± 0.04
P(3HB- <i>co</i> -3HHx)-30ASF	6.08 ± 0.08	2.89 ± 0.05
P(3HB- <i>co</i> -3HHx)-30ASF/10OLA	6.66 ± 0.09	3.17 ± 0.07
P(3HB- <i>co</i> -3HHx)-30ASF/20OLA	7.08 ± 0.09	3.37 ± 0.03

## CONCLUSIONS.

The results obtained in this study indicate that the analysed system of P(3HB-*co*-3HHx) and ASF, is suitable for the manufacture of fully bio-based and environmentally friendly WPCs. P(3HB-*co*-3HHx)-ASF composites, present a very interesting set of properties for technical applications, as wood substitute materials. The characterization of P(3HB-*co*-3HHx)-ASF composites, showed that the addition of lignocellulosic particles of ASF leads to an embrittlement and reduced toughness. These effects are much more evident with increasing the wt.% ASF. To overcome or minimize these negative properties, an oligomer of lactic acid, OLA was added to give P(3HB-*co*-3HHx)-ASF/OLA composites with improved ductile properties and, subsequently, improved toughness. It is worthy to note a remarkable increase in impact strength with 20 phr OLA. A higher mobility of the P(3HB-*co*-3HHx) polymer chains by

the addition of OLA is one of reasons for the improvement on toughness even on composites with 30 wt.% ASF. The improved interaction with the REX extrusion also has an important effect on the final properties of the composites.

The study of the PLA-ASF/OLA composites allowed to obtain good balanced properties and, therefore, these materials can be used in the WPC industry as it is suitable for technical applications that require certain stiffness and thermal stability, in an interesting range of properties depending on the wt.% ASF content. Furthermore, the addition of OLA oligomer decreases the water absorption capacity of P(3HB-co-3HHx)-ASF/OLA, thus broadening potential uses in high humidity environments. Finally, its thermoplastic nature allows it to be easily processed by conventional extrusion-injection moulding, and overall, these composites contribute to a sustainable development and a reduction of the carbon footprint as all the used materials are bio-sourced.

#### **FUNDING.**

This research work was funded by the Spanish Ministry of Science, Innovation, and Universities (MICIU) project number MAT2017-84909-C2-2-R. This work was supported by the POLISABIO program grant number (2019-A02).

#### **ACKNOWLEDGMENTS.**

Juan Ivorra-Martinez is the recipient of an FPI grant from Universitat Politècnica de València (PAID-2019). Luis Quiles-Carrillo wants to thank GVA for his FPI grant (ACIF/2016/182) and MECD for his FPU grant (FPU15/03812). Microscopy services at UPV are acknowledged for their help in collecting and analysing FESEM images.

#### **REFERENCES.**

1. Carbonell-Verdu, A.; Bernardi, L.; Garcia-Garcia, D.; Sanchez-Nacher, L.; Balart, R. Development of environmentally friendly composite matrices from epoxidized cottonseed oil. *European Polymer Journal* **2015**, *63*, 1-10 doi: 10.1016/j.eurpolymj.2014.11.043.
2. España, J.; Samper, M.; Fages, E.; Sánchez-Nácher, L.; Balart, R. Investigation of the effect of different silane coupling agents on mechanical performance of basalt fiber composite laminates with biobased epoxy matrices. *Polymer Composites* **2013**, *34*, 376-381 doi: 10.1002/pc.22421.

3. Basalp, D.; Tihminlioglu, F.; Sofuoglu, S.C.; Inal, F.; Sofuoglu, A. Utilization of municipal plastic and wood waste in industrial manufacturing of wood plastic composites. *Waste and Biomass Valorization* **2020**, *3*, 33–99 doi: 10.1007/s12649-020-00986-7.
4. Singh, S.; Mohanty, A.K. Wood fiber reinforced bacterial bioplastic composites: fabrication and performance evaluation. *Composites Science and Technology* **2007**, *67*, 1753–1763 doi: 10.1016/j.compscitech.2006.11.009.
5. Rodriguez-Contreras, A. Recent advances in the use of polyhydroxyalkanoates in biomedicine. *Bioengineering* **2019**, *6*, 82–96 doi: 10.3390/bioengineering6030082.
6. Mohanty, A.K.; Misra, M.; Drzal, L.T. Sustainable bio-composites from renewable resources: Opportunities and challenges in the green materials world. *Journal of Polymers and the Environment* **2002**, *10*, 19–26 doi: 10.1023/A:1021013921916.
7. Petchwattana, N.; Covavisaruch, S. Mechanical and morphological properties of wood plastic biocomposites prepared from toughened poly(lactic acid) and rubber wood sawdust (*hevea brasiliensis*). *Journal of Bionic Engineering* **2014**, *11*, 630–637 doi: 10.1016/s1672-6529(14)60074-3.
8. Summerscales, J.; Dissanayake, N.; Virk, A.; Hall, W. A review of bast fibres and their composites. Part 2-composites. *Composites Part A – Applied Science and Manufacturing* **2010**, *41*, 1336–1344 doi: 10.1016/j.compositesa.2010.05.020.
9. Averous, L. Biodegradable multiphase systems based on plasticized starch: A review. *Journal of Macromolecular Science-Polymer Reviews* **2004**, *44*, 231–274 doi: 10.1081/mc-200029326.
10. Yang, Y.; Ke, S.; Ren, L.; Wang, Y.; Li, Y.; Huang, H. Dielectric spectroscopy of biodegradable poly(3-hydroxybutyrate-co-3-hydroxyhexanoate) films. *European Polymer Journal* **2012**, *48*, 79–85 doi: 10.1016/j.eurpolymj.2011.10.002.
11. Liao, Q.; Noda, I.; Frank, C.W. Melt viscoelasticity of biodegradable poly(3-hydroxybutyrate-co-3-hydroxyhexanoate) copolymers. *Polymer* **2009**, *50*, 6139–6148 doi: 10.1016/j.polymer.2009.10.049.

12. Alata, H.; Aoyama, T.; Inoue, Y. Effect of aging on the mechanical properties of poly(3-hydroxybutyrate-co-3-hydroxyhexanoate). *Macromolecules* **2007**, *40*, 4546–4551 doi: 10.1021/ma070418i.
13. Misra, S.K.; Valappil, S.P.; Roy, I.; Boccaccini, A.R. Polyhydroxyalkanoate (PHA)/inorganic phase composites for tissue engineering applications. *Biomacromolecules* **2006**, *7*, 2249–2258 doi: 10.1021/bm060317c.
14. Mahmood, H.; Pegoretti, A.; Brusa, R.S.; Ceccato, R.; Penasa, L.; Tarter, S.; Checchetto, R. Molecular transport through 3-hydroxybutyrate-co-3-hydroxyhexanoate biopolymer films with dispersed graphene oxide nanoparticles: Gas barrier, structural and mechanical properties. *Polymer Testing* **2019**, *8*, 106181-106190 doi: 10.1016/j.polymertesting.2019.106181.
15. Corre, Y.-M.; Bruzaud, S.; Audic, J.-L.; Grohens, Y. Morphology and functional properties of commercial polyhydroxyalkanoates: a comprehensive and comparative study. *Polymer Testing* **2012**, *31*, 226–235 doi: 10.1016/j.polymertesting.2011.11.002.
16. Watanabe, T.; He, Y.; Fukuchi, T.; Inoue, Y. Comonomer compositional distribution and thermal characteristics of bacterially synthesized poly(3-hydroxybutyrate-co-3-hydroxyhexanoate)s. *Macromolecular Bioscience* **2001**, *1*, 75–83 doi: 10.1002/1616-5195(20010301)1:23.0.CO;2-Q.
17. Oyama, T.; Kobayashi, S.; Okura, T.; Sato, S.; Tajima, K.; Isono, T.; Satoh, T. Biodegradable compatibilizers for poly(hydroxyalkanoate)/poly( $\epsilon$ -caprolactone) blends through click reactions with end-functionalized microbial poly(hydroxyalkanoate)s. *Acs Sustainable Chemistry & Engineering* **2019**, *7*, 7969–7978 doi: 10.1021/acssuschemeng.9b00897.
18. Sato, H.; Nakamura, M.; Padermshoke, A.; Yamaguchi, H.; Terauchi, H.; Ekgasit, S.; Noda, I.; Ozaki, Y. Thermal behavior and molecular interaction of poly(3-hydroxybutyrate-co-3-hydroxyhexanoate) studied by wide-angle X-ray diffraction. *Macromolecules* **2004**, *37*, 3763–3769 doi: 10.1021/ma049863t.
19. Hu, Y.; Zhang, J.; Sato, H.; Noda, I.; Ozaki, Y. Multiple melting behavior of poly(3-hydroxybutyrate-co-3-hydroxyhexanoate) investigated by differential scanning calorimetry and infrared spectroscopy. *Polymer* **2007**, *48*, 4777–4785 doi: 10.1016/j.polymer.2007.06.016.

- 
20. Xu, P.; Cao, Y.; Lv, P.; Ma, P.; Dong, W.; Bai, H.; Wang, W.; Du, M.; Chen, M. Enhanced crystallization kinetics of bacterially synthesized poly(3-hydroxybutyrate-co-3-hydroxyhexanate) with structural optimization of oxalamide compounds as nucleators. *Polymer Degradation and Stability* **2018**, *154*, 170–176 doi: 10.1016/j.polymdegradstab.2018.06.001.
  21. Tham, W.L.; Ishak, Z.A.M.; Chow, W.S. Water absorption and hygrothermal aging behaviors of SEBS-g-MAH toughened poly(lactic acid)/halloysite nanocomposites. *Polymer-Plastics Technology and Engineering* **2014**, *53*, 472–480 doi: 10.1080/03602559.2013.845208.
  22. Tham, W.L.; Poh, B.T.; Ishak, Z.A.M.; Chow, W.S. Water absorption kinetics and hygrothermal aging of poly(lactic acid) containing halloysite nanoclay and maleated rubber. *Journal of Polymers and the Environment* **2015**, *23*, 242–250 doi: 10.1007/s10924-014-0699-y.
  23. Arbelaz, A.; Fernandez, B.; Ramos, J.A.; Retegi, A.; Llano-Ponte, R.; Mondragon, I. Mechanical properties of short flax fibre bundle/polypropylene composites: influence of matrix/fibre modification, fibre content, water uptake and recycling. *Composites Science and Technology* **2005**, *65*, 1582–1592 doi: 10.1016/j.compscitech.2005.01.008.
  24. Deroine, M.; Le Duigou, A.; Corre, Y.-M.; Le Gac, P.-Y.; Davies, P.; Cesar, G.; Bruzaud, S. Accelerated ageing of polylactide in aqueous environments: comparative study between distilled water and seawater. *Polymer Degradation and Stability* **2014**, *108*, 319–329 doi: 10.1016/j.polymdegradstab.2014.01.020.
  25. Gil-Castell, O.; Badia, J.D.; Kittikorn, T.; Stromberg, E.; Martinez-Felipe, A.; Ek, M.; Karlsson, S.; Ribes-Greus, A. Hydrothermal ageing of polylactide/sisal biocomposites. Studies of water absorption behaviour and physico-chemical performance. *Polymer Degradation and Stability* **2014**, *108*, 212–222 doi: 10.1016/j.polymdegradstab.2014.06.010.
  26. Petinakis, E.; Yu, L.; Edward, G.; Dean, K.; Liu, H.; Scully, A.D. Effect of matrix-particle interfacial adhesion on the mechanical properties of poly(lactic acid)/wood-flour micro-composites. *Journal of Polymers and the Environment* **2009**, *17*, 83–94 doi: 10.1007/s10924-009-0124-0.

27. Pilla, S.; Gong, S.; O'Neill, E.; Rowell, R.M.; Krzysik, A.M. Polylactide–pine wood flour composites. *Polymer Engineering and Science* **2008**, *48*, 578–587 doi: 10.1002/pen.20971.
28. Shah, B.L.; Selke, S.E.; Walters, M.B.; Heiden, P.A. Effects of wood flour and chitosan on mechanical, chemical, and thermal properties of polylactide. *Polymer Composites* **2008**, *29*, 655–663 doi: 10.1002/pc.20415.
29. Balart, J.F.; Garcia–Sanoguera, D.; Balart, R.; Boronat, T.; Sanchez–Nacher, L. Manufacturing and properties of biobased thermoplastic composites from poly(lactic acid) and hazelnut shell wastes. *Polymer Composites* **2018**, *39*, 848–857 doi: 10.1002/pc.24007.
30. Kumar, S.; Vedrtnam, A.; Pawar, S.J. Effect of wood dust type on mechanical properties, wear behavior, biodegradability, and resistance to natural weathering of wood–plastic composites. *Frontiers of Structural and Civil Engineering* **2019**, *13*, 1446–1462 doi: 10.1007/s11709-019-0568-9.
31. Ling, S.L.; Koay, S.C.; Chan, M.Y.; Tshai, K.Y.; Chantara, T.R.; Pang, M.M. Wood Plastic composites produced from postconsumer recycled polystyrene and coconut shell: effect of coupling agent and processing aid on tensile, thermal, and morphological properties. *Polymer Engineering and Science* **2020**, *60*, 202–210 doi: 10.1002/pen.25273.
32. Quitadamo, A.; Massardier, V.; Valente, M. Eco–friendly approach and potential biodegradable polymer matrix for WPC composite materials in outdoor application. *International Journal of Polymer Science* **2019**, *19*, 1–9 doi: 10.1155/2019/3894370.
33. Salasinska, K.; Polka, M.; Jònec, M.; Ryszkowska, J. Natural fiber composites: the effect of the kind and content of filler on the dimensional and fire stability of polyolefin–based composites. *Polimery* **2016**, *61*, 255–265 doi: 10.14314/polimery.2016.255.
34. Wang, X.; Yu, Z.; McDonald, A.G. Effect of different reinforcing fillers on properties, interfacial compatibility and weatherability of wood–plastic composites. *Journal of Bionic Engineering* **2019**, *16*, 337–353 doi: 10.1007/s42235-019-0029-0.



35. Yussuf, A.A.; Massoumi, I.; Hassan, A. comparison of polylactic acid/kenaf and polylactic acid/rise husk composites: the influence of the natural fibers on the mechanical, thermal and biodegradability properties. *Journal of Polymers and the Environment* **2010**, *18*, 422–429 doi: 10.1007/s10924-010-0185-0.
36. Kuciel, S.; Jakubowska, P.; Kuzniar, P. A study on the mechanical properties and the influence of water uptake and temperature on biocomposites based on polyethylene from renewable sources. *Composites Part B-Engineering* **2014**, *64*, 72–77 doi: 10.1016/j.compositesb.2014.03.026.
37. Liminana, P.; Quiles-Carrillo, L.; Boronat, T.; Balart, R.; Montanes, N. The effect of varying almond shell flour (ASF) loading in composites with poly(butylene succinate (PBS) matrix compatibilized with maleinized linseed oil (MLO). *Materials* **2018**, *11*, 2179–2196 doi: 10.3390/ma11112179.
38. Quiles-Carrillo, L.; Montanes, N.; Garcia-Garcia, D.; Carbonell-Verdu, A.; Balart, R.; Torres-Giner, S. Effect of different compatibilizers on injection-moulded green composite pieces based on polylactide filled with almond shell flour. *Composites Part B: Engineering* **2018**, *147*, 76–85 doi: 10.1016/j.compositesb.2018.04.017.
39. Mathew, A.P.; Oksman, K.; Sain, M. Mechanical properties of biodegradable composites from poly lactic acid (PLA) and microcrystalline cellulose (MCC). *Journal of Applied Polymer Science* **2005**, *97*, 2014–2025 doi: 10.1002/app.21779.
40. Ghaffar, S.H.; Madyan, O.A.; Fan, M.; Corker, J. The influence of additives on the interfacial bonding mechanisms between natural fibre and biopolymer composites. *Macromolecular Research* **2018**, *26*, 851–863 doi: 10.1007/s13233-018-6119-8.
41. Tserki, V.; Matzinos, P.; Kokkou, S.; Panayiotou, C. Novel biodegradable composites based on treated lignocellulosic waste flour as filler. Part I. Surface chemical modification and characterization of waste flour. *Composites Part A-Applied Science and Manufacturing* **2005**, *36*, 965–974 doi: 10.1016/j.compositesa.2004.11.010.

42. Niaraki, P.R.; Krause, A. Correlation between physical bonding and mechanical properties of wood plastic composites: Part 1: interaction of chemical and mechanical treatments on physical properties. *Journal of Adhesion Science and Technology* **2020**, *34*, 744–755 doi: 10.1080/01694243.2019.1683325.
43. Akesson, D.; Fazelinejad, S.; Skrifvars, V.-V.; Skrifvars, M. Mechanical recycling of polylactic acid composites reinforced with wood fibres by multiple extrusion and hydrothermal ageing. *Journal of Reinforced Plastics and Composites* **2016**, *35*, 1248–1259 doi: 10.1177/0731684416647507.
44. Torres-Giner, S.; Montanes, N.; Fenollar, O.; García-Sanoguera, D.; Balart, R. Development and optimization of renewable vinyl plastisol/wood flour composites exposed to ultraviolet radiation. *Materials & Design* **2016**, *108*, 648–658 doi: 10.1016/j.matdes.2016.07.037.
45. Juárez, D.; Ferrand, S.; Fenollar, O.; Fombuena, V.; Balart, R. Improvement of thermal inertia of styrene-ethylene/butylene-styrene (SEBS) polymers by addition of microencapsulated phase change materials (PCMs). *European Polymer Journal* **2011**, *47*, 153–161 doi: 10.1016/j.eurpolymj.2010.11.004.
46. Pracella, M.; Haque, M.; Alvarez, V. Functionalization, compatibilization and properties of polyolefin composites with natural fibers. *Polymers* **2010**, *2*, 554–574 doi: 10.3390/polym2040554.
47. Chabros, A.; Gawdzik, B.; Podkościelna, B.; Goliszek, M.; Pączkowski, P. Composites of unsaturated polyester resins with microcrystalline cellulose and its derivatives. *Materials* **2020**, *13*, 62–75 doi: 10.3390/ma13010062.
48. Mokhena, T.; Sefadi, J.; Sadiku, E.; John, M.; Mochane, M.; Mtibe, A. Thermoplastic processing of PLA/cellulose nanomaterials composites. *Polymers* **2018**, *10*, 1363–1392 doi: 10.3390/polym10121363.
49. Patwa, R.; Saha, N.; Saha, P.; Katiyar, V. Biocomposites of poly(lactic acid) and lactic acid oligomer-grafted bacterial cellulose: Its preparation and characterization. *Journal of Applied Polymer Science* **2019**, *136*, 47903–47916 doi: 10.1002/app.47903.

- 
50. Tripathi, N.; Katiyar, V. Lactic acid oligomer (OLLA) grafted gum arabic based green adhesive for structural applications. *International Journal of Biological Macromolecules* **2018**, *120*, 711–720 doi: 10.1016/j.ijbiomac.2018.07.199.
51. Lascano, D.; Moraga, G.; Ivorra–Martinez, J.; Rojas–Lema, S.; Torres–Giner, S.; Balart, R.; Boronat, T.; Quiles–Carrillo, L. Development of injection–moulded polylactide pieces with high toughness by the addition of lactic acid oligomer and characterization of their shape memory behavior. *Polymers* **2019**, *11*, 2099–2118 doi: 10.3390/polym11122099.
52. Zhou, Y.–x.; Huang, Z.–g.; Diao, X.–q.; Weng, Y.–x.; Wang, Y.–Z. Characterization of the effect of REC on the compatibility of P(3HB–co–3HHx) and PLA. *Polymer Testing* **2015**, *42*, 17–25 doi: 10.1016/j.polymertesting.2014.12.014.
53. Asrar, J.; Valentin, H.E.; Berger, P.A.; Tran, M.; Padgette, S.R.; Garbow, J.R. Biosynthesis and properties of poly(3–hydroxybutyrate–co–3–hydroxyhexanoate) polymers. *Biomacromolecules* **2002**, *3*, 1006–1012 doi: 10.1021/bm025543a.
54. Ding, C.; Cheng, B.; Wu, Q. DSC analysis of isothermally melt–crystallized bacterial poly(3–hydroxybutyrate–co–3–hydroxyhexanoate) films. *Journal of Thermal Analysis and Calorimetry* **2011**, *103*, 1001–1006 doi: 10.1007/s10973–010–1135–8.
55. Jacquél, N.; Tajima, K.; Nakamura, N.; Miyagawa, T.; Pan, P.; Inoue, Y. Effect of orotic acid as a nucleating agent on the crystallization of bacterial poly(3–hydroxybutyrate–co–3–hydroxyhexanoate) copolymers. *Journal of Applied Polymer Science* **2009**, *114*, 1287–1294 doi: 10.1002/app.30587.
56. Quiles–Carrillo, L.; Duarte, S.; Montanes, N.; Torres–Giner, S.; Balart, R. Enhancement of the mechanical and thermal properties of injection–moulded polylactide parts by the addition of acrylated epoxidized soybean oil. *Materials & Design* **2018**, *140*, 54–63 doi: 10.1016/j.matdes.2017.11.031.
57. Burgos, N.; Martino, V.P.; Jiménez, A. Characterization and ageing study of poly(lactic acid) films plasticized with oligomeric lactic acid. *Polymer Degradation and Stability* **2013**, *98*, 651–658 doi: 10.1016/j.polymdegradstab.2012.11.009.

58. Armentano, I.; Fortunati, E.; Burgos, N.; Dominici, F.; Luzi, F.; Fiori, S.; Jiménez, A.; Yoon, K.; Ahn, J.; Kang, S. Processing and characterization of plasticized PLA/PHB blends for biodegradable multiphase systems. *Express polymer letters* **2015**, *9*, 583–596 doi: 10.3144/expresspolymlett.2015.55.
59. Miquelard, G.; Guinault, A.; Sollogoub, C.; Gervais, M. Combined compatibilization and plasticization effect of low molecular weight poly(lactic acid) in poly(lactic acid)/poly(3-hydroxybutyrate-co-3-hydroxyvalerate) blends. *Express polymer letters* **2018**, *12*, 114–125 doi: 10.3144/expresspolymlett.2018.10.
60. Ferri, J.M.; Garcia-Garcia, D.; Montanes, N.; Fenollar, O.; Balart, R. The effect of maleinized linseed oil as biobased plasticizer in poly(lactic acid) – based formulations. *Polymer International* **2017**, *66*, 882–891 doi: 10.1002/pi.5329.
61. Garcia-Campo, M.J.; Quiles-Carrillo, L.; Masia, J.; Reig-Pérez, M.J.; Montanes, N.; Balart, R. Environmentally friendly compatibilizers from soybean oil for ternary blends of poly(lactic acid) – PLA, poly(ε-caprolactone) – PCL and poly(3-hydroxybutyrate) – PHB. *Materials* **2017**, *10*, 1339–1358 doi: 10.3390/ma10111339.
62. Liminana, P.; Garcia-Sanoguera, D.; Quiles-Carrillo, L.; Balart, R.; Montanes, N. Development and characterization of environmentally friendly composites from poly(butylene succinate) (PBS) and almond shell flour with different compatibilizers. *Composites Part B: Engineering* **2018**, *144*, 153–162 doi: 10.1016/j.compositesb.2018.02.031.
63. Thomas, S.; Shumilova, A.; Kiselev, E.; Baranovsky, S.; Vasiliev, A.; Nemtsev, I.; Kuzmin, A.P.; Sukovatyi, A.; Avinash, R.P.; Volova, T. Thermal, mechanical and biodegradation studies of biofiller based poly-3-hydroxybutyrate biocomposites. *International journal of biological macromolecules* **2019**, *155*, 1373–1384 doi: 10.1016/j.ijbiomac.2019.11.112.
64. Gong, X.; Gao, X.; Tang, C.Y.; Law, W.C.; Chen, L.; Hu, T.; Wu, C.; Tsui, C.P.; Rao, N. Compatibilization of poly(lactic acid)/high impact polystyrene interface using copolymer poly(styrene-ran-methyl acrylate). *Journal of Applied Polymer Science* **2018**, *135*, 45799–45808 doi: 10.1002/app.45799.

- 
65. Hosoda, N.; Tsujimoto, T.; Uyama, H. Green composite of poly(3-hydroxybutyrate-co-3-hydroxyhexanoate) reinforced with porous cellulose. *Acs Sustainable Chemistry & Engineering* **2014**, *2*, 248-253 doi: 10.1021/sc400290y.
  66. Perinovic, S.; Andricic, B.; Erceg, M. Thermal properties of poly(L-lactide)/olive stone flour composites. *Thermochimica Acta* **2010**, *510*, 97-102 doi: 10.1016/j.tca.2010.07.002.
  67. Quiles-Carrillo, L.; Montanes, N.; Sammon, C.; Balart, R.; Torres-Giner, S. Compatibilization of highly sustainable polylactide/almond shell flour composites by reactive extrusion with maleinized linseed oil. *Industrial Crops and Products* **2018**, *111*, 878-888 doi: 10.1016/j.indcrop.2017.10.062.
  68. Liminana, P.; Garcia-Sanoguera, D.; Quiles-Carrillo, L.; Balart, R.; Montanes, N. Optimization of maleinized linseed oil loading as a biobased compatibilizer in poly(butylene succinate) composites with almond shell flour. *Materials* **2019**, *12*, 685-699 doi: 10.3390/ma12050685.
  69. Yin, C.; Wang, Z.; Luo, Y.; Li, J.; Zhou, Y.; Zhang, X.; Zhang, H.; Fang, P.; He, C. Thermal annealing on free volumes, crystallinity and proton conductivity of Nafion membranes. *Journal of Physics and Chemistry of Solids* **2018**, *120*, 71-78, doi: 10.1016/j.jpics.2018.04.028.
  70. Oliver-Ortega, H.; Méndez, J.A.; Espinach, F.X.; Tarrés, Q.; Ardanuy, M.; Mutjé, P. Impact strength and water uptake behaviors of fully bio-based PA11-SGW composites. *Polymers* **2018**, *10*, 717-729 doi: 10.3390/polym10070717.
  71. Pfister, D.P.; Larock, R.C. Thermophysical properties of conjugated soybean oil/corn stover biocomposites. *Bioresource Technology* **2010**, *101*, 6200-6206 doi: 10.1016/j.biortech.2010.02.070.



Sent to the journal.

### **III.1.3 Plasticization of poly(3-hydroxybutyrate) with biobased terpenoid esters of geraniol.**

Juan Ivorra-Martinez<sup>1</sup>, Yago Valencia<sup>1</sup>, Jaume Gomez-Caturla<sup>1</sup>, Ángel Agüero<sup>1,2</sup>, Marina Patricia Arrieta<sup>2,3</sup>, Teodomiro Boronat<sup>1</sup>, Rafael Balart<sup>1</sup>.

<sup>1</sup>Technological Institute of Materials - ITM, Universitat Politècnica de València - UPV, Plaza Ferrándiz y Carbonell 1, 03801, Alcoy, Alicante (Spain).

<sup>2</sup>Departamento de Ingeniería Química Industrial y del Medio Ambiente, Escuela Técnica Superior de Ingenieros Industriales, Universidad Politécnica de Madrid ETSII-UPM, (Spain).

<sup>3</sup>Grupo de Polímeros, Caracterización y Aplicaciones - POLCA Madrid, (Spain).





**Abstract.**

Polyhydroxyalkanoates - PHA include a wide number of biodegradable aliphatic polyesters produced when bacteria are cultured with nutrient-limiting concentrations. Poly(3-hydroxybutyrate) - P3HB is, by far, one of the most promising bacterial polyesters at commercial scale. Despite some of its properties are comparable to that of poly(propylene) - PP, P3HB is a brittle polymer due to a physical aging occurring at room temperature which promotes secondary crystallization leading to its intrinsic low toughness. Plasticization is a cost effective and technical approach to overcome, or minimize, this drawback. In this work, the use of terpenoid-based organic compounds are proposed as plasticizers for P3HB with improved toughness. The efficiency of different plasticizers resulting from the esterification of geraniol with different chain length carboxylic acids, namely acetic (C2), propionic (C3), butyric (C4), and isovaleric (C5) is assessed. The effects of a constant weight percentage of geranyl acetate - GEA, geranyl propionate - GEP, geranyl butyrate - GEB, and geranyl isovalerate - GEI on mechanical and thermal properties, morphology and disintegration is addressed in this work. The obtained results are promising since the glass transition temperature -  $T_g$  is reduced from 4.3 °C (neat P3HB) to - 13.6 °C (P3HB with geranyl isovalerate) which corroborates high plasticization efficiency. The ductile properties also improve with the incorporation of the geranyl-based plasticizers. The tensile strength of the plasticized P3HB formulations remains at moderate values of 13.5 - 14.6 MPa while the elongation at break increases from 7.4 % (neat P3HB) up to 9.7 % for P3HB with geranyl isovalerate. A remarkable increase in toughness is also observed with increasing the impact strength from 2.2 kJ/m<sup>2</sup> (neat P3HB) up to 3.4 kJ/m<sup>2</sup> for the plasticized formulation containing geranyl acetate. Thus, the proposed terpenoid-based compounds widen the potential uses of P3HB since its ductile properties are improved.

**Keywords:** poly(3-hydroxybutyrate); geraniol; terpenoids; plasticizer.

---



## INTRODUCTION.

Currently, petroleum-derived polymers offer a wide application range in both single-use and long-lasting products [1]. This has led to an exponential growth in the worldwide production of plastics, with the subsequent environmental issues. As a matter of fact, it has been estimated that 8300 Mt of plastics have been produced between 1950 and 2015 and the amount of plastic wastes reached 6300 Mt in this period. But the most worrying issue is that around 79 % of these wastes have ended up in controlled landfills or directly in the natural environment [2]. To avoid plastic waste accumulation, biodegradable polymers (or more specifically, disintegrable under controlled compost soil) have gained interest in the last decades [3].

Moreover, there is an increasing interest in the transition from linear to circular economies. For this reason, upgrading wastes as raw materials for new polymers has gained much interest. Polyhydroxyalkanoates - PHAs include a family of linear polyesters with interesting properties from an environmental standpoint. PHAs can be obtained through a fermentation process by using specific bacteria such as *Cupriavidus necator*, *Bacillus*, *Streptomyces*, among others. These bacteria can digest a carbon source in an anaerobic process. In many cases, the carbon source can derive from the food industry wastes [1,4-6]. To achieve PHA synthesis, these microorganisms have to be subjected to some nutrient limitation in combination with an excess of carbon. In these conditions, bacteria can synthesize PHAs in the form of granules that act as energy storage [7].

Among all the existing PHAs, poly(3-hydroxybutyrate) - P3HB is one of the most studied to date. It is a high brittle polymer due to its high degree of crystallinity associated to the formation of large spherulites. After processing it is quite ductile but P3HB, as other PHAs, undergo a physical ageing process related to secondary crystallization that leads to the high brittleness and limited elongation [5]. Due to this phenomenon, some strategies have been carried out to improve its ductility. One interesting approach is blending P3HB with other biobased/biodegradable polymers such as starch and cellulose-based polymers [8]. On the other hand, the use of plasticizers is, traditionally, more interesting from an industrial point of view to achieve the desired ductile properties on P3HB since plasticizers also provide improved processing conditions [9].

Plasticizers can be divided into two main groups depending on their molecular weight, namely polymeric and monomeric plasticizers. Polymeric plasticizers include polyadipates, polyazelates, polysebacates, polyglycols, among others, with typical molecular weights ranging from 1000 to 8000 g/mol and are widely used in the PVC industry to minimize plasticizer migration [10]. Monomeric plasticizers are, usually, low molecular weight organic compounds such as trimellitates, adipates, sebacates, carboxylates, maleates, and so on. Due to their low molecular weight, they mix easily with polymers, thus providing high plasticization efficiency. In contrast, they do show higher migration than polymeric plasticizers [11]. Most of the commonly used plasticizers are derived from petroleum. Traditionally, phthalates have been widely used as plasticizers in a wide variety of polymers and applications. Nevertheless, it has been demonstrated their potential toxicity [12]. Thus, new green alternatives are being searched [13]. In the last decades, research has focused on the plasticization efficiency of bioderived plasticizers such as citrate esters like acetyl tributyl citrate - ATBC, triethyl citrate - TEC, glycerol and its esters (*e.g.* triacetin, tributyrin), fumaric acid esters, isosorbide and its esters, among others. Most of these plasticizer systems are very promising in terms of their plasticization efficiency on PVC and PLA. Moreover, these alternative green plasticizers have been proposed as plasticizers in different polyhydroxyalkanoates [14-17]. Recently, terpenes and terpenoids have been proposed as building blocks for polymer synthesis and modification [18]. Terpenes include a wide range of organic compounds derived from isoprene. Depending on the isoprene units contained, terpenes are classified as hemiterpenes (1), monoterpenes (2), sesquiterpenes (3) and diterpenes (4). On the other hand, terpenoids or isoprenoids, are terpene-based compounds with additional functional groups, usually oxygen-based functionalities. Terpenes and terpenoids include more than 80000 chemical compounds which play a key role in flavour, fragrance, cosmetics and food industry [19,20] and their use is increasing in pharmacology and medicine due to their exceptional bioactive properties [21-23]. Terpenoid esters include a group of organic compounds that result from the esterification of a terpenoid containing a hydroxyl group and a carboxylic acid. For example, geraniol is a monoterpene with a hydroxyl group. If reacted with a carboxylic acid (*e.g.* formic, acetic, propionic, butyric, and so on), leads to formation of the corresponding ester, namely geranyl formate, acetate, propionate, butyrate, respectively. These terpenoid esters also find applications in the fragrance and cosmetics and, together with terpenes, have been proposed as biobased plasticizers as reported by Mangeon *et al.* [24]. They obtained interesting plasticization properties of several terpenoids, namely linalool, geraniol and geranyl acetate on P3HB. Geranyl acetate gave

the best results with an increase in elongation at break on physically aged (10 days) samples from 2 % (neat P3HB) up to 13 %.

The present research aims to assess the potential of a series of terpenoid esters as biobased plasticizers for P3HB to be used in conventional extrusion–injection moulding process. As previous works have demonstrated the higher efficiency of the terpenoid esters compared to their corresponding terpenoid, this research gives an in–depth study of the effect of the chain length of the carboxylic acid attached to the terpenoid by esterification. In particular, different esters of geraniol are proposed as environmentally friendly plasticizers for P3HB formulations, namely geranyl acetate, propionate, butyrate and isovalerate. Their effect on mechanical, thermal and microstructure of P3HB plasticized formulations is addressed. This research broadens the potential applications of terpenoid–based compounds in the polymer industry.

## MATERIALS AND METHODS.

### Materials.

A commercial grade of P3HB P226 ( $M_w = 426000$  Da) was supplied by Biomer (Krailling, Germany) in pellet form. Geranyl acetate (> 97 % purity), geranyl propionate (> 95 %), geranyl butyrate (> 95 %), and geranyl isovalerate (> 95 %) were supplied by Sigma Aldrich (Madrid, Spain). **Table III.1.3.1.** gathers some physical properties of the geranyl esters while **Figure III.1.3.1.** shows the chemical structure of the base polymer, poly(3–hydroxybutyrate) and the different geranyl–based plasticizers.

**Table III.1.3.1.** Physical properties and chemical structure of geranyl esters uses as plasticizers for P3HB.

Terpenoid	Molecular weight (g/mol)	Density (g/cm <sup>3</sup> )	Boiling point (°C) at 760 mmHg	Molar volume (cm <sup>3</sup> /mol)
Geranyl acetate	196.29	0.907	243	216.4
Geranyl propionate	210.32	0.899	253	233.9
Geranyl butyrate	224.34	0.896	257	250.4
Geranyl isovalerate	238.37	0.889	277	268.1

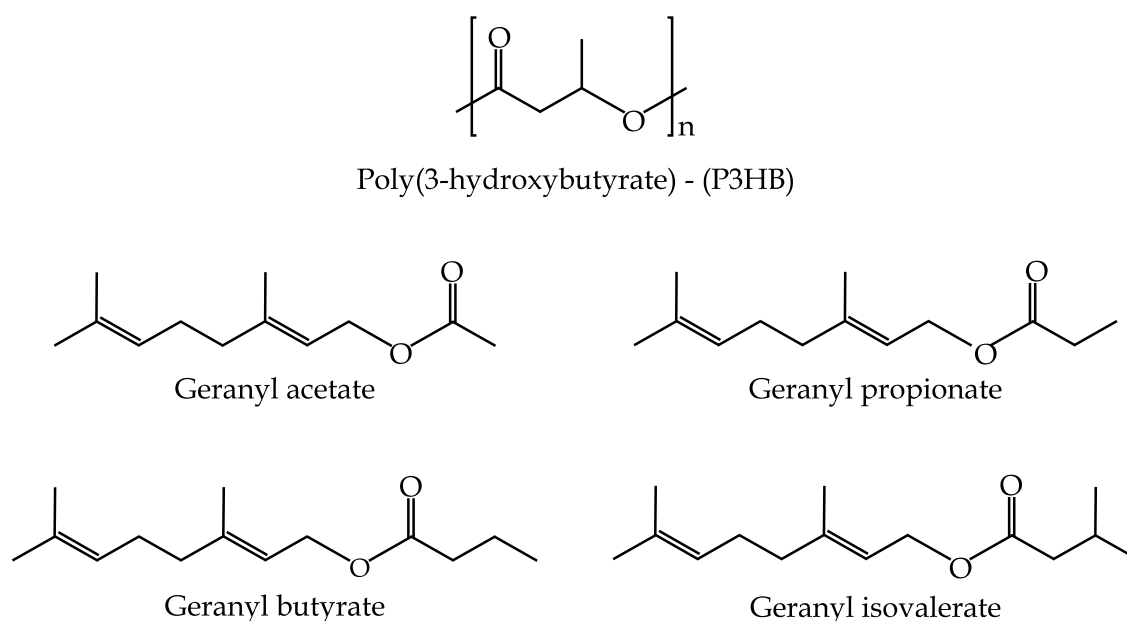


**Figure III.1.3.1.** Chemical structure of poly(3-hydroxybutyrate) and different geranyl-based plasticizers.

#### Calculation of theoretical solubility parameters.

The solubility parameters ( $\delta$ ) of P3HB and all geranyl-based plasticizers were obtained by using the group contribution method proposed by Hoftyzer and Van Krevelen [25]. This method takes into account different contributions to the total solubility parameter -  $\delta$ , namely, the dispersive forces contribution -  $\delta_d$ , the polar forces contribution -  $\delta_p$ , and the hydrogen bonding contribution -  $\delta_h$ . If the solubility parameters of the polymer and the plasticizer are similar, then, good miscibility could be expected. Otherwise, phase separation occurs and miscibility is poor. In fact, as the solubility parameter is obtained from three different coordinates ( $\delta_d$ ,  $\delta_p$  and  $\delta_h$ ), the solubility region is defined by a spherical (or what is more accurate, an ellipsoid) region. If the solubility parameter coordinates of the proposed plasticizer fall into this region, good miscibility could be expected. Otherwise, poor miscibility will be obtained. As managing ellipsoid regions is somewhat more complicated than using spherical regions, a simple 2D model simplification allows determining the solubility region by plotting  $\delta_h$  vs  $\delta_v$ , where  $\delta_v$  includes both dispersive and polar contributions as follows:  $\delta_v = (\delta_d^2 + \delta_p^2)^{1/2}$ . In this plot, the ellipsoid solubility region is represented by a circle with the centre on the corresponding  $\delta_d$  and  $\delta_h$  values of P3HB and a characteristic radius -  $R_0$  depending on the chemical structure. This radius is set on  $8.5 \text{ (MJ/m}^3\text{)}^{1/2}$  for P3HB as reported in literature [26]. If the solubility coordinates of a proposed plasticizer fall into this circle, then, miscibility will be good enough and, subsequently, the

plasticization properties will be good too. All those plasticizers with solubility parameter coordinates out of this circle, will indicate poor miscibility and hence, poor plasticization properties. Additionally, to this graphical method to assess the suitability of a plasticizer for a particular polymer, it is possible to calculate the distance -  $R_a$  between the three solubility parameter coordinates of P3HB and the different geranyl ester (GEX) considered in a 3D space, as shown in **Equation III.1.3.1**. In this equation, the constant 4 applied to the dispersive contributions is usually employed to obtain spherical solubility regions instead of ellipsoids. Once this distance has been calculated, it is possible to give an accurate estimation of the solubility by calculating the relative energy difference - RED, by the ratio between  $R_a$  and  $R_0$  as indicated in **Equation III.1.3.2**.

$$R_a = \sqrt{4(\delta_{d \text{ GEX}} - \delta_{d \text{ P3HB}})^2 + (\delta_{p \text{ GEX}} - \delta_{p \text{ P3HB}})^2 + (\delta_{h \text{ GEX}} - \delta_{h \text{ P3HB}})^2} \quad \text{Equation III.1.3.1.}$$

$$\text{RED} = \frac{R_a}{R_0} \quad \text{Equation III.1.3.2.}$$

**Equation III.1.3.2.** suggests that RED values below 1 are representative for good miscibility while RED values above 1 indicate poor miscibility. A RED value of 1 represents the threshold for solubility [27].

#### **Processing of P3HB formulations plasticized with geranyl esters.**

Prior to sample processing, P3HB pellets were dried in an air circulating oven for 24 h at 60 °C in order to remove moisture as PHA and other aliphatic polyesters are highly sensitive to moisture. The P3HB pellets were then manually mixed with 20 phr (20 parts by weight of plasticizer with respect to one hundred weight parts of P3HB) of each of the different geranyl-ester terpenoids in a zipper bag. Compounding of plasticized P3HB formulations was carried out in a twin-screw co-rotating extruder (L/D = 24, D = 25 mm) from DUPRA S.L. (Castalla, Spain) with a rotating speed of 40 rpm and a temperature profile of the extrusion barrel from the feeder to the nozzle of 170 - 170 - 175 - 180 °C. After cooling down to room temperature, the compounded strands were ground to pellets in a mill. Finally, the P3HB plasticized pellets were processed by injection moulding in a Meteor 270/75 from Mateu & Solé (Barcelona, Spain) in order to obtain standard samples. In this case, the temperature profile used in the injection moulding machine was 170 - 175 - 175 - 180 °C from the hopper to the injection nozzle with a cooling time of the material inside the mold of 10 s. The labels and composition of each formulation processed in the present work can be seen in

**Table III.1.3.2.** As PHA undergo physical aging above their characteristic glass transition temperature -  $T_g$ , after processing, all samples were stored in a vacuum desiccator and aged at room temperature for 21 days before testing [28].

**Table III.1.3.2.** Composition and labelling of different formulations of P3HB plasticized with different geranyl esters in terms of weigh percentage - wt.% and per hundred resin - phr.

Code	P3HB (wt.%)	Geranyl acetate (phr)	Geranyl propionate (phr)	Geranyl butyrate (phr)	Geranyl isovalerate (phr)
P3HB	100	-	-	-	-
P3HB/GEA	100	20	-	-	-
P3HB/GEP	100	-	20	-	-
P3HB/GEB	100	-	-	20	-
P3HB/GEI	100	-	-	-	20

### Mechanical properties.

Tensile properties were measured using a universal test machine Ibertest ELIB 30 from SAE Ibertest (Madrid, Spain) equipped with a 5 kN load cell following ISO 527. Samples were tested at room temperature at a crosshead speed was 5 mm/min. Five different specimens were tested and average values of the main tensile parameters were calculated, namely the maximum tensile strength -  $\sigma_{max}$  and the elongation at break -  $\epsilon_b$ . In addition, the elastic modulus -  $E_t$  was accurately determined using an axial extensometer IB/MFQ-R2 from Ibertest (Madrid, Spain) coupled to the universal test machine.

The impact strength of P3HB plasticized with geranyl esters was obtained using a Charpy impact pendulum (1-J) from Metrotec S.A. (San Sebastian, Spain), following ISO 179. Since the aging process in PHA leads to a dramatic decrease in plastic deformation ability, the impact strength was obtained from the average of 5 different unnotched specimens.

The hardness of the different formulations was determined with a shore D durometer model 673-D from J. Bot S.A. (Barcelona, Spain) following the ISO 868. The hardness of each plasticized P3HB formulation was determined by averaging 10 values taken at different points of 5 specimens.



**Differential scanning calorimetry - DSC.**

The most relevant thermal information of P3HB and plasticized P3HB formulations with different geranyl esters was obtained by DSC. Tests were carried out in triplicate using a DSC Mettler-Toledo 821 calorimeter from Mettler-Toledo Inc. (Schwerzenbach, Switzerland) in nitrogen atmosphere using a flow rate of 66 mL/min. Samples weighing between 7 - 9 mg, were subjected to a dynamic program with three stages: a first heating cycle from - 50 °C to 180 °C was followed by a cooling to - 50 °C, and finally, subjected to a second heating cycle from - 50 °C to 250 °C. The heating/cooling rate for all the stages was 10 °C/min. The melt peak temperatures -  $T_m$ , and their corresponding melting enthalpies -  $\Delta H_m$  were obtained from the second heating cycle. The degree of crystallinity of P3HB -  $\chi_c$  was determined according to the following equation:

$$\chi_c(\%) = \frac{\Delta H_m}{\Delta H_m^0 \cdot (1 - w)} \cdot 100 \quad \text{Equation III.1.3.3.}$$

Where  $\Delta H_m^0$  is the melting enthalpy of a theoretical fully crystalline P3HB and was taken as 146 J/g, and  $(1 - w)$  represents the weight fraction of P3HB in the corresponding plasticized formulation according to **Table III.1.3.2.**

**Dynamic-Mechanical Thermal Analysis - DMTA.**

DMTA of the neat P3HB and plasticized P3HB formulations with different geranyl esters was carried out on a Mettler-Toledo DMA1 (Columbus, OH, USA) using a single cantilever. DMTA runs were conducted at a constant frequency of 1 Hz and a force of 0.02 N and a maximum deflection in single cantilever mode of 10 micrometres. Rectangular samples with a size of  $20 \times 6 \times 3 \text{ mm}^3$  were subjected to a temperature sweep program from - 100 °C to 100 °C at a constant heating rate of 2 °C/min. Plots of the evolution of the storage modulus -  $E'$  and the dynamic damping factor -  $\tan \delta$  were measured to be plotted as function of temperature. The glass transition temperature -  $T_g$  of neat P3HB and plasticized P3HB formulations were obtained from the peak temperature  $\tan \delta$  curves.

**Field Emission Scanning Electron Microscopy - FESEM.**

The effect of geranyl esters on microstructure of plasticized P3HB formulations was analysed in a FESEM ZEISS ULTRA55 from Oxford instruments (Abingdon, UK) operated at a voltage of 2 kV and an average working distance of 4 mm. Fractured samples from impact tests were firstly coated with a platinum alloy in high vacuum

sputter coater EM MED20 from Leica Microsystem (Milton Keynes, United Kingdom).

#### **Disintegration test in compost soil.**

Biodegradation test, or what is more accurate, disintegration test in compost soil of neat P3HB and plasticized P3HB formulations with different geranyl esters was carried out following ISO 20200:2015 at 58 °C and 55 % relative humidity. To this, rectangular samples with dimensions 25 × 25 × 1 mm<sup>3</sup> were previously obtained by a hot press process at 160 °C. The weight loss was monitored from weekly extraction of samples and calculating the weight loss following **Equation III.1.3.4.**, where  $W_d$  is the weight of the dried sample after the disintegration test and  $W_0$  is the initial weight of the sample.

$$W_l (\%) = \frac{W_d - W_0}{W_0} \cdot 100 \quad \text{Equation III.1.3.4.}$$

### **RESULTS AND DISCUSSION.**

#### **Theoretical approach to solubility of P3HB and geranyl esters as potential plasticizers.**

The solubility parameters of P3HB and the different geranyl esters were calculated using the group contribution method proposed by Hoftyzer and Van Krevelen. **Table III.1.3.3.** gathers the solubility parameter coordinates corresponding to dispersive forces ( $\delta_d$ ), polar forces ( $\delta_p$ ), and hydrogen bonding ( $\delta_h$ ) of P3HB and the proposed terpenoid-based plasticizers. The volar volume of the geranyl esters is shown in **Table III.1.3.1.**, while the molar volume of P3HB was taken as 73.2 cm<sup>3</sup>/mol as indicated in literature [26]. As can be seen in **Table III.1.3.3.**, P3HB has a solubility parameter of 19.79 (MJ/m<sup>3</sup>)<sup>1/2</sup> calculated using the Hoftyzer and Van Krevelen method. This is close with the  $\delta$  parameter of P3HB calculated by the Hoy's group contribution method, with a value of 19.2 (MJ/m<sup>3</sup>)<sup>1/2</sup>. It has been reported that P3HB is soluble in a wide range of organic solvents with  $\delta$  parameters ranging from 15.2 (MJ/m<sup>3</sup>)<sup>1/2</sup> for camphor, to 27.2 (MJ/m<sup>3</sup>)<sup>1/2</sup> for propylene carbonate. In contrast, P3HB is insoluble in n-hexane with a  $\delta$  parameter of 14.9 (MJ/m<sup>3</sup>)<sup>1/2</sup> or methanol, with a  $\delta$  value of 29.7 (MJ/m<sup>3</sup>)<sup>1/2</sup> [29]. Therefore, it is expectable good miscibility between P3HB and all four geranyl esters used, due to their  $\delta$  parameters range from 16.55 to 16.94 (MJ/m<sup>3</sup>)<sup>1/2</sup> [30]. There is a clear decreasing tendency on  $\delta$  parameter of geranyl esters as the number of carbon atoms of the carboxylic acid used to esterify geraniol increase. This is also evidenced by the distance  $R_a$  values between the  $\delta$  parameters of geranyl esters and P3HB, with values ranging from 6.03 (geranyl acetate) to 6.75 (geranyl

isovalerate). Since the solubility sphere of P3HB has a radius of  $8.5 \text{ (MJ/m}^3\text{)}^{1/2}$ , the RED values are lower than 1 for all geranyl esters considered in this work, with the lowest value for geranyl acetate (0.71) and the highest value for geranyl isovalerate (0.79). As indicated previously, as the RED value becomes lower, the better solubility will be expected. Brüster *et al.* have reported RED values of 0.29 for PEG which is a well-known plasticizer for polylactide while very good plasticization properties have been obtained with myrcene and limonene as plasticizers for PLA with RED values of 0.99 and 0.93, respectively [27]. Hence, the low RED values of geranyl esters suggest good plasticization on P3HB.

**Table III.1.3.3.** Solubility parameters of P3HB and the different geraniol esters employed as plasticizers.

	$\delta_d$ (MJ/m <sup>3</sup> ) <sup>1/2</sup>	$\delta_p$ (MJ/m <sup>3</sup> ) <sup>1/2</sup>	$\delta_h$ (MJ/m <sup>3</sup> ) <sup>1/2</sup>	$\delta$ (MJ/m <sup>3</sup> ) <sup>1/2</sup>	R <sub>a</sub>	RED
P3HB	15.85	6.69	9.78	19.79	-	-
Geranyl acetate	15.80	2.26	5.69	16.94	6.03	0.71
Geranyl propionate	15.78	2.09	5.47	16.83	6.31	0.74
Geranyl butyrate	15.81	1.96	5.29	16.79	6.52	0.77
Geranyl isovalerate	15.63	1.83	5.11	16.55	6.75	0.79

**Mechanical properties of plasticized P3HB.**

**Table III.1.3.4.** gathers the main tensile properties of neat P3HB and plasticized P3HB formulations with geranyl esters after the physical aging at room temperature. Neat P3HB has a tensile strength of 26.5 MPa and a tensile modulus of 1640 MPa with a very low elongation at break of 7.4 % which are typical of this PHA, which is, by far, one of the main drawbacks of PHA in general [29,31]. This low elongation ability is due to its high degree of crystallinity after physical aging at room temperature. Smith *et al.* have reported an even lower elongation at break 1.5 % on P3HB obtained from sugar beet molasses [32]. This P3HB polymer was characterized by a high degree of crystallinity of 60 %. In fact, most commercial grades of P3HB include some additives to avoid excessive crystallization as it is the commercial P3HB Biomer P226 used in this study that contains low-molecular-weight softeners and nucleating agents to minimize the effects of secondary crystallization or physical aging. Plasticization of P3HB leads to lower tensile strength and tensile modulus since plasticizers contribute to weaken polymer-to-polymer interactions which in turn, have a positive effect on elongation

[33,34]. The tensile modulus of P3HB-plasticized materials with geranyl esters is remarkably reduced to values in the 600 – 700 MPa range, which represents a percentage decrease of about 60 % with regard to neat P3HB. Similar tendency can be observed for tensile strength that is reduced to values ranging from 13.5 MPa to 14.6 MPa which is a typical effect of plasticization. Panaitescu *et al.* have reported similar results in plasticized P3HB formulations with ESO, PEG and ATBC [35]. They observed a decreasing tendency on both tensile modulus and tensile strength as the plasticizer amount increased. With regard to the elongation at break, interesting results are obtained with the different geranyl esters. Neat P3HB shows an elongation at break value of 7.4 %, while the plasticized P3HB formulation containing 20 phr geranyl isovalerate noticeably improved elongation at break up to 9.7 %, which represents a percentage increase of about 31 %. Similar results were reported by Panaitescu *et al.* regarding elongation at break [35]. They concluded that plasticized P3HB formulations containing 5 wt.% ESO or ATBC, led to a percentage increase in elongation at break of 45 % and 37 % respectively, with regard to neat P3HB. Despite the plasticization effects of all four geranyl esters is corroborated by a clear decrease in both tensile strength and modulus, the effect on elongation at break is not as noticeable as in other aliphatic polyesters such as polylactide – PLA. Plasticization of PLA with 5 – 30 wt.% plasticizers such as TEC, ATBC, PEG, epoxidized vegetable oils – EVOs, leads to a clear decrease on tensile strength and modulus, but the elongation at break is remarkably improved from 5 – 10 % (neat PLA) up to 15 – 300 % with these plasticizers [36–38]. As the crystallization rate of P3HB is low and the nucleation density is low, large spherulites are formed during cooling. Subsequent physical aging promotes secondary crystallization which, in turn, will promote some internal shrinkage which leads to microcrack formation. That is why the elongation at break is so low and, even by the addition of miscible plasticizers, the elongation at break is not improved in a remarkable way [39]. As observed by Bibers *et al.* in general, plasticization of P3HB gives exceptional results for a plasticizer content above 30 wt.%, while moderate increases in elongation at break are obtained with lower plasticizer contents [40]. They also concluded this threshold for high plasticization effects highly depends on the chemical structure of a proposed plasticizer. On the other hand, Mangeon *et al.* reported high deformative characteristics on P3HB with more complex plasticizers derived from interpenetrating networks based on Sunflower Oil – SO and trimethylolpropane tris(3-mercaptopropionate) – TriSH [41].

With regard to the impact strength, all geranyl-based esters provide an improvement. Neat P3HB has an impact strength of 2.2 kJ/m<sup>2</sup> while the plasticized

P3HB formulation with geranyl acetate, gives an impact strength of 3.4 kJ/m<sup>2</sup> which represents a percentage increase of about 54.5 %. These results agree with those reported by Nosal *et al.* in plasticized P(3HB-co-3HV) with fatty acid esters with different hydrocarbon chain length [42]. They concluded that fatty acid-based plasticizers with shorter chain length, provide the best impact strength properties on notched samples, by increasing from 1.4 kJ/m<sup>2</sup> P(3HB-co-3HV) to 4.0 - 4.1 kJ/m<sup>2</sup> for plasticized formulations with oleic acid methyl ester, palmitic acid methyl ester or lauric acid ethylene glycol monoester. By using geranyl esters as plasticizers for P3HB, the obtained results suggest that the shorter the chain length of the esterifying acid of geraniol, the higher the impact resistance. Umemura *et al.* have also reported improved impact resistance in plasticized P3HB with TEC at weight fractions ranging from 0 to 0.3 [43]. They observed an increase in the impact resistance (Izod impact test) on 28 days aged samples from 49 J/m (neat P3HB) up to 253, 301 and 371 J/m for TEC weight fractions of 0.1, 0.2, and 0.3, respectively. Despite they concluded a linear relationship between mechanical properties and the logarithm of time, these changes are more pronounced at the initial stages and are almost stabilized at aging times of 14 - 21 days.

Regarding Shore D hardness, as expected, all four geranyl esters show a similar decrease. The Shore D hardness of neat P3HB is 48.7 while all plasticized P3HB formulations with geranyl esters show a Shore D hardness in the 34.7 - 36.2 range. This softening effect is directly linked with the increased free volume after plasticization and the subsequent weakening of the polymer-to-polymer chain interactions. This phenomenon has also been reported by Bouit *et al.* in plasticized PLA with different amounts of epoxidized sunflower oil [44]. Garcia-Garcia *et al.* reported a similar decrease in Shore D hardness in P3HB plasticized with several epoxidized vegetable oils [45]. In particular, they obtained the optimum plasticization properties with 10 wt.% Epoxidized Linseed Oil -ELO, with a decrease in Shore D hardness from 57.3 (neat P3HB) to 53.5.

**Table III.1.3.4.** Main mechanical properties of the P3HB and plasticized P3HB formulations with different geranyl esters.

Sample	E (MPa)	$\sigma_{\max}$ (MPa)	$\epsilon_b$ (%)	Impact strength (kJ/m <sup>2</sup> )	Hardness Shore D
P3HB	1640 ± 86	26.3 ± 1.2	7.4 ± 1.0	2.2 ± 0.3	48.7 ± 3.5
P3HB/GEA	668 ± 16	14.6 ± 0.4	8.5 ± 0.6	3.4 ± 0.2	36.2 ± 3.3
P3HB/GEP	606 ± 21	13.9 ± 0.3	8.4 ± 0.6	3.1 ± 0.1	35.9 ± 2.4
P3HB/GEB	651 ± 46	13.5 ± 0.4	7.4 ± 0.6	2.8 ± 0.2	34.7 ± 3.1
P3HB/GEI	706 ± 19	13.5 ± 0.3	9.7 ± 0.5	2.5 ± 0.2	36.2 ± 3.4

**Thermal properties of plasticized P3HB.**

The main thermal parameters of P3HB and its plasticized formulations with geranyl esters obtained by DSC, are gathered in **Table III.1.3.5.** and **Figure III.1.3.2.** The stage (first heating cycle) in **Figure III.1.3.2a.** shows the thermal behaviour after an aging of 21 days. The second stage corresponds to a cooling process in which the crystallization can be observed (**Figure III.1.3.2b.**) and finally, the third stage (second heating) contains thermal information after the controlled cooling stage without additional aging (**Figure III.1.3.2c.**). First, it is worthy to note the presence of two peaks, a small peak at about 50 °C and a second peak at 170 °C. The first peak, at about 50 °C, corresponds to the additives used in commercial P3HB grades, usually stabilizers, lubricants, and low molecular weight flexible poly(hydroxyalkanoates) or other polyesters which exhibit low melting temperatures, as reported by Panaitescu *et al.* and Garcia-Garcia *et al.* [35,46]. The second peak, located at 170 °C corresponds to the melting of the crystalline fraction of P3HB. In the first heating cycle it is possible to see that addition of geranyl-based plasticizers leads to a decrease in the characteristic melting peak temperature of P3HB by 10 °C. This phenomenon has been attributed to the weakening effect of the polymer-to-polymer chain interactions due to the plasticizers as observed by Kurusu *et al.* [11]. A slight decrease of 7 - 10 °C can also be observed with regard to the small peak related to low molecular weight polyesters. Another interesting phenomenon provided by plasticizers is an increase in  $\chi_c$ . The higher mobility of the polymer chains allows them to pack into a crystalline structure and therefore the degree of crystallinity of the plasticized P3HB formulations is higher. This phenomenon has been reported by Chaos *et al.* in plasticized PLA and P3HB with tributyl citrate - TbC [47]. Despite having a higher degree of crystallinity, the plasticized P3HB offered increased ductile properties as mentioned in the previous section, this being a key issue after aging at room temperature. Additionally, it is also worth noting that the shape of the melting peak of the geranyl-plasticized P3HB samples (especially with geranyl isovalerate and geranyl propionate), shows two melting peaks which can be attributed to formation of different crystals [35]. It is important to bear in mind that PH3B can crystallize into two different crystal structures, the thermally stable  $\alpha$ -form, which is obtained during the crystallization from the melt. The metastable  $\beta$ -form that can appear as a consequence of the orientation of the free chains in the amorphous regions. While the amount of  $\beta$ -form crystals remains almost constant during storage or aging, the amount of  $\alpha$ -form crystals increases during the aging at

room temperature [48].

The crystallization can be observed in the cooling stage (see **Figure III.1.3.2b.**). One interesting phenomenon that stands out is that the crystallization peak temperature is moved to lower temperatures in the geranyl-plasticized P3HB formulations. Kurusu *et al.* [11], proposed this phenomenon is due to the presence of a plasticizer that allows polymer chains to rearrange in a packed way since the plasticizers contributes to increased polymer chain mobility.

With regard to the enthalpies, once they are normalized by taking into account the actual P3HB content, allowed to calculate the degree of crystallinity by using **Equation III.1.3.3.** **Table III.1.3.5.** includes the  $\chi_c$  for all three stages scheduled in the DSC. The effect of the plasticizers can be clearly observed in the first heating cycle applied on samples subjected to a 21-day aging. The  $\chi_c$  of neat P3HB is 36.5 % while this is increased to values ranging from 45.9 % for geranyl acetate-plasticized P3HB to 42.5 % for geranyl isovalerate-plasticized P3HB, thus suggesting, the shorter the chain length of the carboxylic acid esterified with geraniol, the higher the crystallinity since polymer chain mobility is less restricted with lower molecular weight compounds. With regard to the second heating cycle, a slight decrease in the characteristic melting temperatures can be observed. This is due to a controlled cooling cycle which is by far, slower than the fast cooling down after injection moulding. This difference in the cooling rate is responsible for the slightly higher degree of crystallinity values of all P3HB-based formulations in the second heating cycle. This effect has been reported by Chen *et al.* [49]. They revealed the effect of the cooling rate on the degree of crystallinity in a P(3HB-co-3HHx) copolymer.

**Table III.1.3.5.** Main thermal properties of neat P3HB and plasticized P3HB formulations with different geranyl esters.

Sample	First heating			Cooling			Second heating		
	$T_m$ (°C)	$\Delta H_m$ (J/g)	$\chi_c$ (%)	$T_c$ (°C)	$\Delta H_c$ (J/g)	$\chi_c$ (%)	$T_m$ (°C)	$\Delta H_m$ (J/g)	$\chi_c$ (%)
P3HB	174.9 ± 0.3	53.3 ± 0.4	36.5 ± 0.7	117.7 ± 0.2	59.3 ± 0.5	40.6 ± 0.8	171.0 ± 0.3	69.2 ± 0.4	47.4 ± 0.7
P3HB/GEA	165.5 ± 0.2	67.0 ± 0.6	45.9 ± 0.5	110.0 ± 0.3	63.1 ± 0.4	43.2 ± 0.8	164.6 ± 0.3	68.6 ± 0.5	47.0 ± 0.6
P3HB/GEP	166.0 ± 0.2	61.7 ± 0.5	42.3 ± 0.7	114.9 ± 0.2	58.8 ± 0.6	40.3 ± 0.9	163.9 ± 0.3	64.4 ± 0.4	44.1 ± 0.5
P3HB/GEB	166.7 ± 0.3	65.3 ± 0.7	44.7 ± 0.6	108.3 ± 0.4	66.5 ± 0.3	45.5 ± 1.2	164.4 ± 0.2	69.0 ± 0.3	47.3 ± 0.5
P3HB/GEI	166.2 ± 0.3	62.0 ± 0.4	42.5 ± 0.6	114.4 ± 0.2	56.3 ± 0.5	38.6 ± 1.4	162.6 ± 0.2	66.0 ± 0.5	45.2 ± 0.6

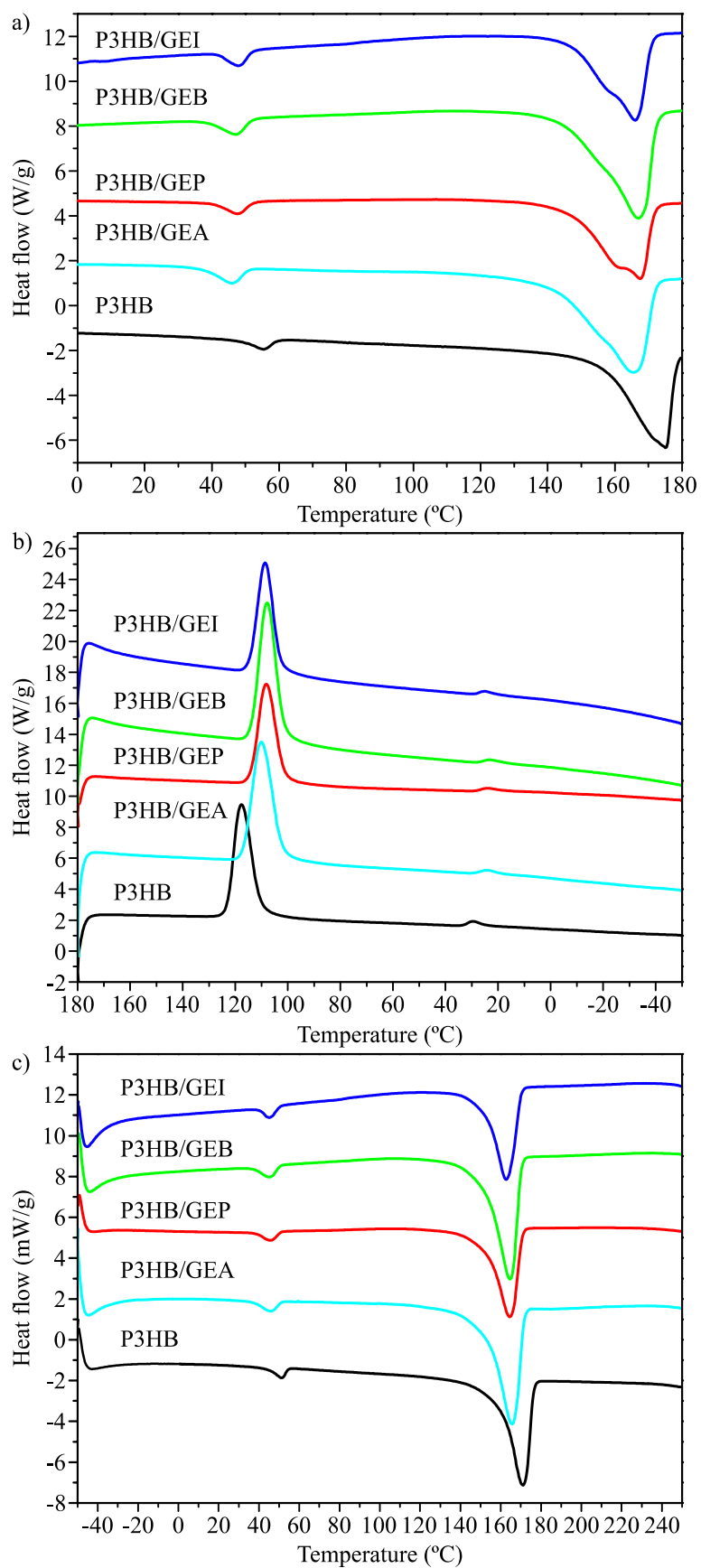


**Figure III.1.3.2.** DSC analysis of neat P3HB and plasticized P3HB formulations with different geranyl esters: a) first heating scan, b) cooling and c) second heating scan.



**Dynamic-Mechanical Thermal Analysis of plasticized P3HB.**

The effects of plasticizer addition on dynamic mechanical thermal properties of neat P3HB and its plasticized formulations with geranyl esters is summarized in **Figure III.1.3.3.** and **Table III.1.3.6.** In general, the storage modulus,  $E'$  decreases with increasing temperature. The first phenomenon to be highlighted is the lower  $E'$  values obtained in all plasticized P3HB formulations with geranyl acetate, compared to neat P3HB above  $-100$  °C. As previously indicated, plasticizer addition leads to increased free volume, so that, the polymer chain mobility is improved and, subsequently, the rigidity decreases. The storage modulus of neat P3HB at  $-20$  °C is 1756 MPa and this is reduced to values in the 893 – 1013 MPa range for all four geranyl esters used in this work. This behaviour was observed by Barbosa *et al.* [50], in plasticized P(3HB-co-3HV) with oligomeric polyester.

With regard to the  $\tan \delta$ , which represents the dissipated-to-stored energy ratio ( $E''/E'$ ), the peak maximum around  $0$  °C could be taken as  $T_g$ . For neat P3HB, the  $T_g$  is close to  $4.3$  °C; this thermal transition is related to an  $\alpha$ -relaxation process in which the polymer changes from a glassy to a rubbery state. The effect of plasticizer addition on  $T_g$  can be clearly detected by a decrease in the peak maximum temperature of  $\tan \delta$  plots [51,52]. It is worthy to note that the  $T_g$  for the plasticized P3HB formulation with geranyl isovalerate is the lowest of all four geranyl esters used in this study, with a value of  $-13.6$  °C which is responsible for the highest elongation at break (9.7 %) observed in tensile test. As indicated by Greco *et al.* [53], an indicator of the plasticization efficiency is the decrease in  $T_g$  a plasticizer can provide to a polymer. In this case, all four geranyl esters provide a decrease in  $T_g$ , which suggests geranyl esters are suitable as environmentally friendly plasticizers for P3HB.

**Table III.1.3.6.** Main thermal properties of P3HB and plasticized P3HB formulations with different geranyl esters, obtained by DMTA.

Sample	$E'$ (MPa) at $-120$ °C	$E'$ (MPa) at $-20$ °C	$E'$ (MPa) at $90$ °C	$T_g$ (°C)
P3HB	$2773 \pm 84$	$1756 \pm 56$	$290 \pm 21$	$4.3 \pm 0.3$
P3HB/GEA	$3017 \pm 92$	$983 \pm 44$	$209 \pm 20$	$-10.5 \pm 0.5$
P3HB/GEP	$3049 \pm 75$	$987 \pm 44$	$199 \pm 16$	$-0.9 \pm 0.4$
P3HB/GEB	$2975 \pm 86$	$1017 \pm 51$	$188 \pm 18$	$-8.6 \pm 0.4$
P3HB/GEI	$2749 \pm 69$	$1013 \pm 37$	$196 \pm 18$	$-13.6 \pm 0.5$

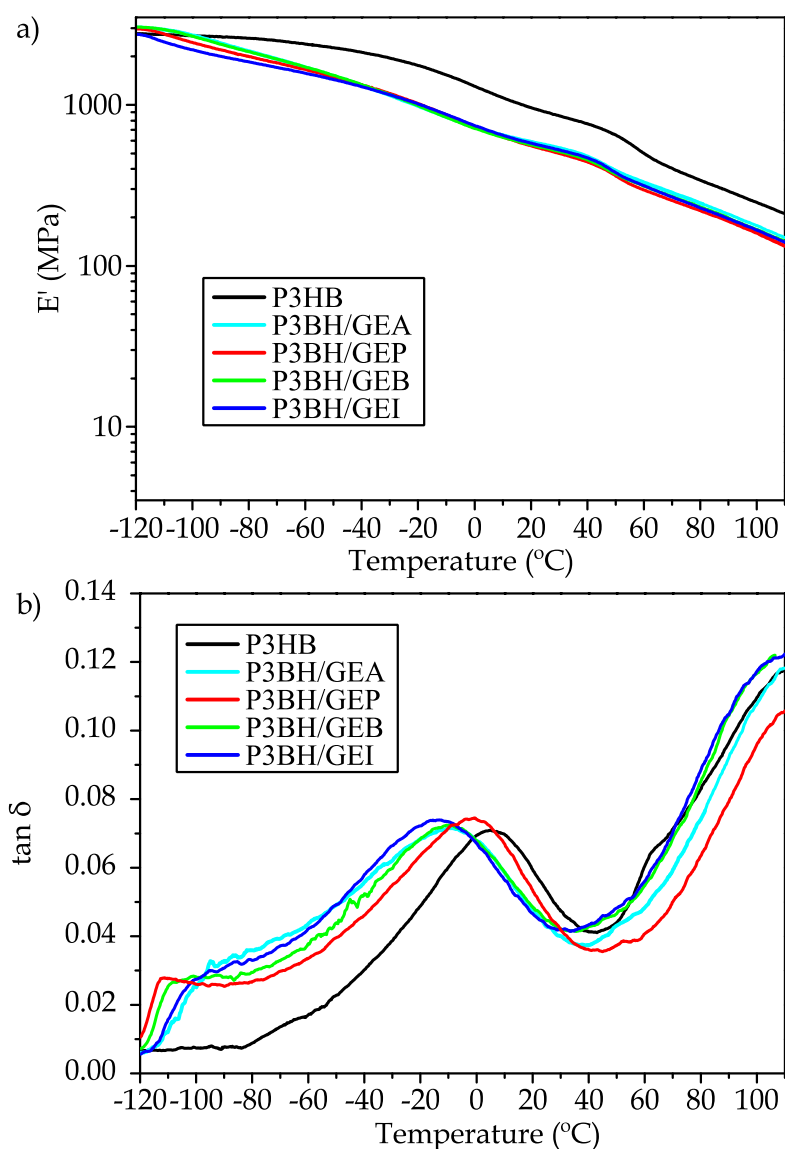


**Figure III.1.3.3.** DMTA curves of neat P3HB and plasticized P3HB formulations with different geranyl esters in terms of: a)  $E'$  vs temperature and b)  $\tan \delta$  vs temperature.

### Morphology study of plasticized P3HB.

The analysis of the fracture morphology after Charpy impact test was carried out using FESEM (see **Figure III.1.3.4.**). Neat P3HB shows the typical brittle fracture characterized by a flat fracture surface (see the inset image at 2500  $\times$ ), indicating the low plastic deformation capacity that took place during fracture. Melendes-Rodríguez *et al.* [54], also obtained similar fracture morphologies for different PHA Blends. With the introduction of geranyl esters, there is an increase in the energy absorption capacity as mentioned above, which results in a change in the fracture surface which is less flat as a consequence of the plastic deformation and, subsequently the surface roughness is increased. Moreover, a phenomenon that arises in plasticized P3HB formulations is the

presence of spherical shapes associated with phase separation since plasticizer preferentially locate into the amorphous regions and, in less extent into the crystalline lamellae. This phenomenon can be easily observed in detail images taken at  $2500\times$ . Jeong *et al.* [55], attributed this phenomenon to a partial miscibility of the plasticizer that leads to the phase separation that results in the formation of this morphology.

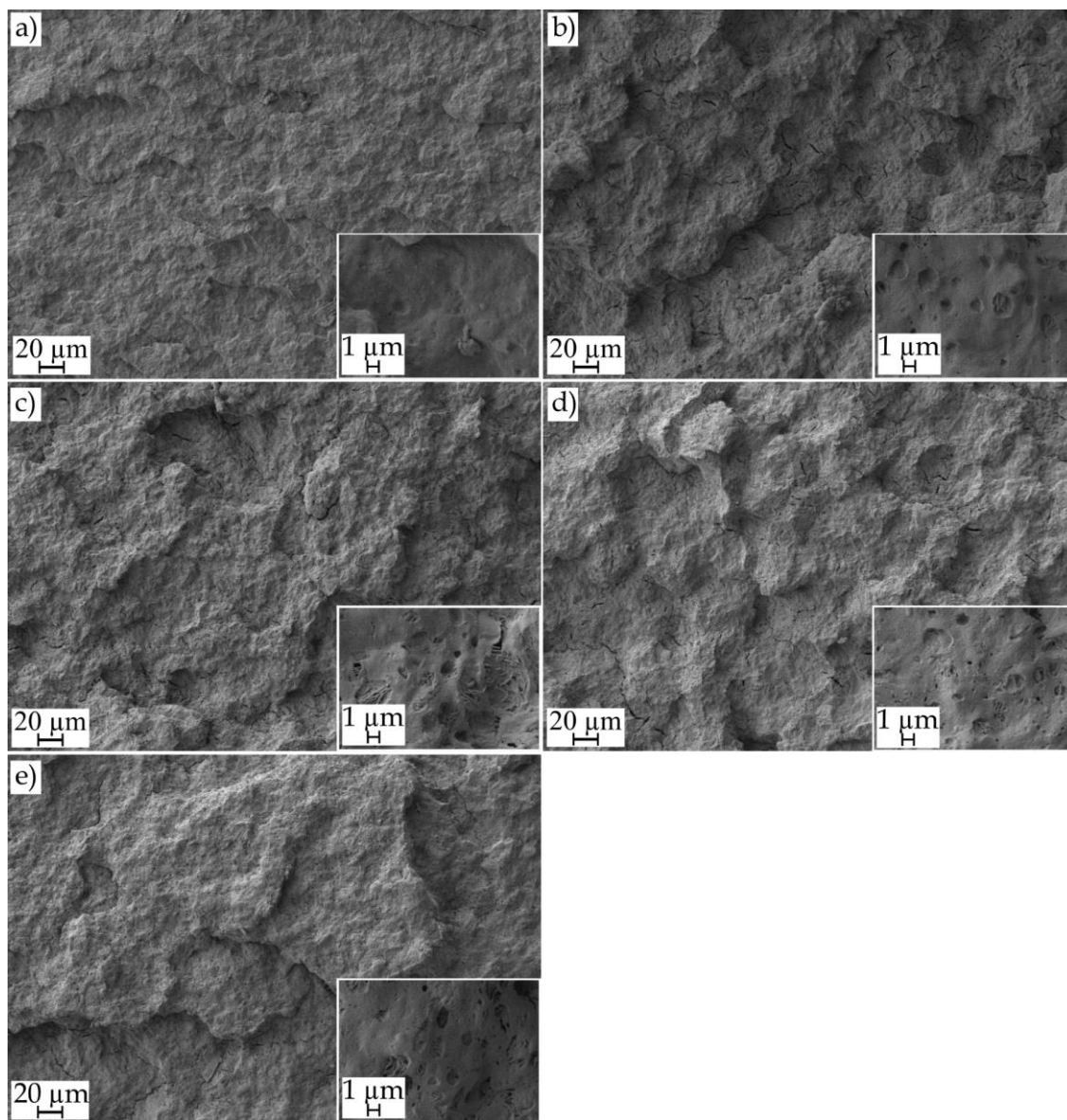


**Figure III.1.3.4.** FESEM images of impact fractured samples ( $250\times$  and insets at  $2500\times$ ) of neat P3HB and plasticized P3HB formulations with different geranyl esters: a) P3HB, b) P3HB/GEA, c) P3HB/GEP, d) P3HB/GEB and e) P3HB/GEI.

Another interesting phenomenon observable in plasticized P3HB formulations is the presence of microcracks which are more evident in plasticized P3HB with geranyl acetate. Kurusu *et al.* [11] observed this phenomenon and attributed it the plasticizer migration. Even with the presence of these microcracks, almost all plasticized P3HB

formulations with geranyl esters show improved impact strength. As it can be seen in **Figure III.1.3.4d.** (inset image at 2500 ×), there is clear evidence of plastic deformation by appearance of filament like structures resulting from plastic deformation before fracture. These morphologies can be observed in all four plasticized P3HB formulations with geranyl esters.

#### **Effect of geranyl esters on disintegration of plasticized P3HB formulations.**

One of the great advantages of PHA such as P3HB is their ability to biodegrade in different environments such as composting under controlled conditions. During the disintegration process, chains scission occurs and, subsequently, low molecular weight chains are obtained, allowing some microorganisms such as fungi and bacteria to metabolize them, releasing CO<sub>2</sub>, H<sub>2</sub>O, and humus [56]. Weng *et al.* studied the disintegration process of PHA from the surface to the bulk material [57]. They observed a noticeable degradation on low thickness samples after 10 days in compost. As reported by Arrieta *et al.* it is possible to obtain a full disintegration in a polyester such as polylactide, PLA, in controlled compost soil on samples with thickness comprised between 200 – 500 μm in just 4 weeks, while the disintegration time takes 6 – 8 weeks for samples with a thickness of 4 mm [58]. In this work, the disintegration test has been carried out on sample sheets with a thickness of 1 mm. Thus, higher degradation times could be expected with regard to films with lower thickness. **Figure III.1.3.5.** shows the visual appearance of the specimens during the disintegration process in compost soil. As one can see, some slight evidence of degradation is obtained after 35 days incubation period while important signs of disintegration are seen after 49 days. It is important to note the effect of plasticizers on the disintegration rate. The incorporation of geranyl-based plasticizers into P3HB matrix leads to an increased disintegration rate in compost soil. The disintegration time (for a 90 % mass loss as described in the standard) is close to 60 days for neat P3HB while this time is reduced to 50 days in all four plasticized P3HB formulations with geranyl esters (see **Figure III.1.3.6.**). Arrieta *et al.* concluded that the incorporation of plasticizers accelerates the disintegration process even considering that plasticizers also promote increased crystallinity [58]. This is due the increase in the free volume that the plasticizers provide, thus exposing hydroxyl groups with high affinity to water, which plays a key role in the first disintegration stages. In general, the increase in crystallinity has a negative effect on the disintegration since the highly packed crystalline phase is much more resistant to chain scission [59]. Nevertheless, the plasticizer counteracts this effect and the disintegration is improved with plasticizers.

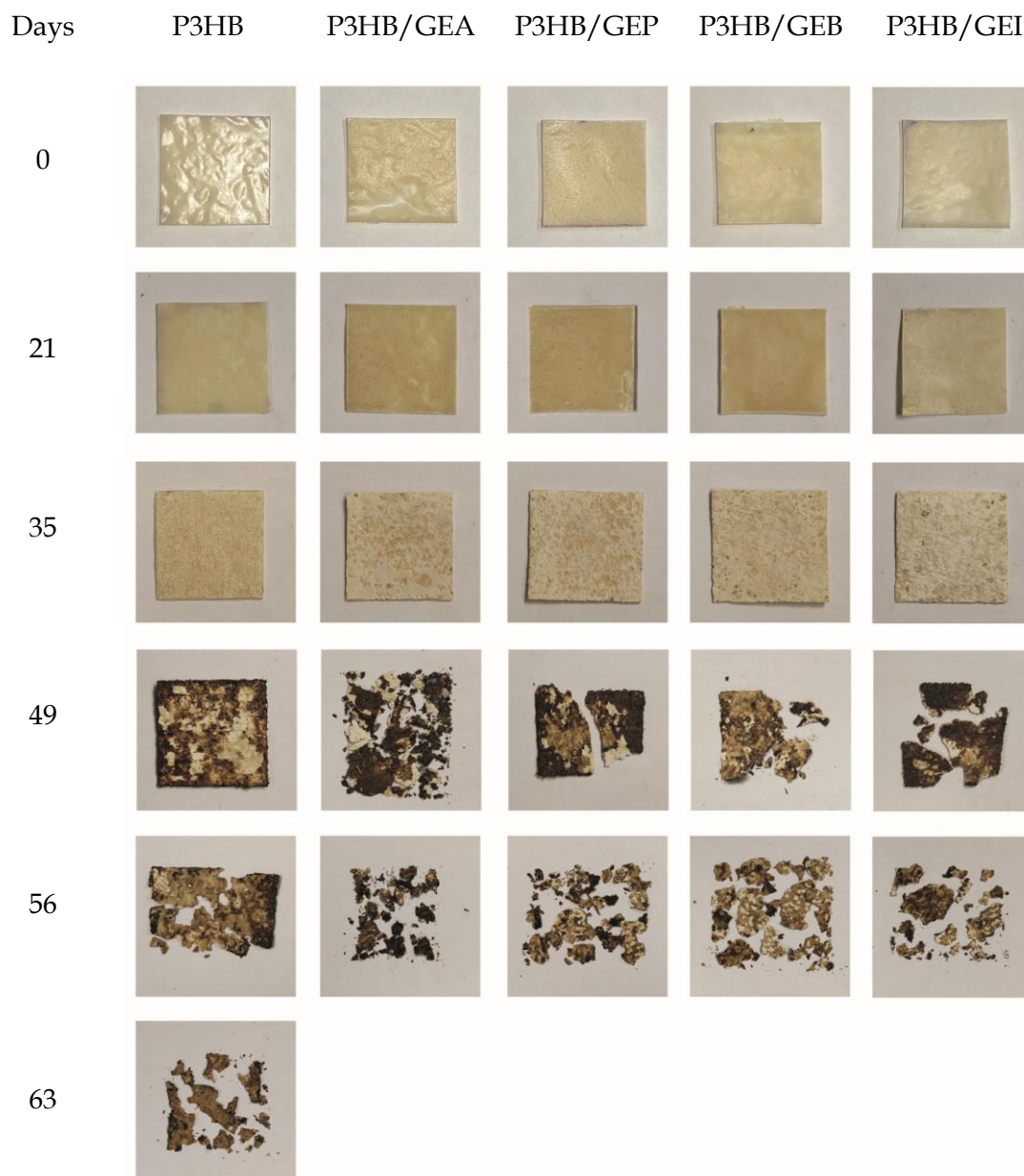


**Figure III.1.3.5.** Visual aspect of neat P3HB and plasticized P3HB formulations with different geranyl esters at different incubation times during the disintegration test in controlled compost soil.

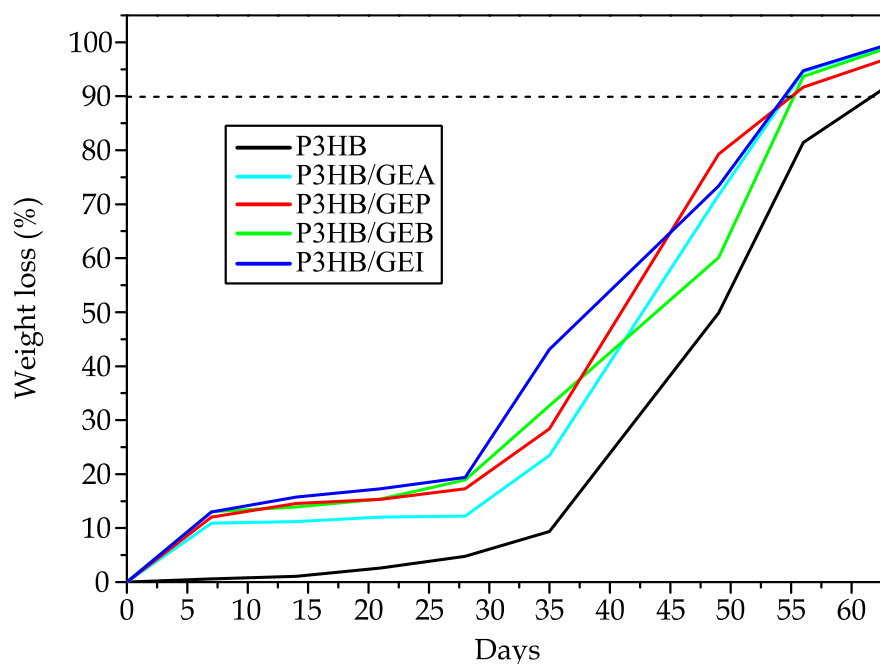


**Figure III.1.3.6.** Weight loss evolution over time at the disintegration test in controlled compost soil of neat P3HB and plasticized P3HB formulations with different geranyl esters.

## CONCLUSIONS.

Geranyl esters have been proposed as green plasticizers for P3HB. Geranyl esters were incorporated into P3HB by melt compounding and subsequent injection moulding, thus showing the feasibility of these plasticized formulations for industrial processing since the boiling point of these terpenoids is above the typical processing window of P3HB. A constant plasticizer content of 20 phr was used with four different geranyl esters with varying the chain length of the esterifying carboxylic acid, namely geranyl acetate, geranyl propionate, geranyl butyrate, and geranyl isovalerate. The obtained results suggest these geranyl-based plasticizers provide an increase in ductile properties such as elongation at break and impact strength and overcome or at least, minimize, the intrinsic brittleness of P3HB. The elongation at break of the plasticized P3HB with geranyl isovalerate increases by 31 % while the best impact strength properties are obtained in formulations with geranyl acetate, with a percentage increase in impact strength of 54.5 % on unnotched samples. In general, the shorter the chain length of the esterifying acid (acetic - C2, propionic - C3, butyric - C4, or isovaleric - C5), the better ductile properties are obtained. The plasticization efficiency has been assessed by a decrease in  $T_g$ , changing from 4.3 °C for neat P3HB down to values of - 13.6 °C for the plasticized formulation with geranyl isovalerate. These plasticizers do not compromise the

biodegradation/disintegration in compost soil; in fact, these green plasticizers increase the disintegration rate by reducing the disintegration time (90 % mass loss) from 60 days for neat P3HB to 50 days for all geranyl-plasticized formulations. These plasticizers represent an environmentally friendly alternative to petroleum-based plasticizers and additives for P3HB with improved ductile behaviour.

#### ACKNOWLEDGEMENTS.

This research is a part of the grant PID2020-116496RB-C22, funded by MCIN/AEI/10.13039/501100011033 and the grant TED2021-131762A-I00, funded by MCIN/AEI/10.13039/501100011033 and by the European Union “NextGenerationEU”/PRTR. Authors also thank Generalitat Valenciana-GVA for funding this research through the grant numbers AICO/2021/025 and CIGE/2021/094. Jaume Gomez-Caturla wants to thank Generalitat Valenciana-GVA, for his FPI grant (ACIF/2021/185) and grant FPU20/01732 funded by MCIN/AEI/10.13039/501100011033 and by ESF Investing in your future. Juan Ivorra-Martinez wants to thank FPU19/01759 grant funded by MCIN/AEI/10.13039/501100011033 and by ESF Investing in your future. Likewise, Ángel Agüero thanks his Margarita Salas postdoctoral contract with the Universitat Politècnica de València, financed through the Ministry of Universities, by the European Union-Next generation EU. Microscopy Services at UPV are also acknowledged by their help in collecting and analysing images.

#### REFERENCES.

1. Pandey, A.; Adama, N.; Adjallé, K.; Blais, J.F. Sustainable applications of polyhydroxyalkanoates in various fields: a critical review. *International Journal of Biological Macromolecules* **2022**, *221*, 1184–1201, doi: 10.1016/j.ijbiomac.2022.09.098.
2. Polman, E.M.N.; Gruter, G.J.M.; Parsons, J.R.; Tietema, A. Comparison of the aerobic biodegradation of biopolymers and the corresponding bioplastics: a review. *Science of The Total Environment* **2021**, *753*, 141953–149166 doi: 10.1016/j.scitotenv.2020.141953.
3. Sanchez-Salvador, J.L.; Balea, A.; Monte, M.C.; Negro, C.; Blanco, A. Chitosan grafted/cross-linked with biodegradable polymers: A review. *International Journal of Biological Macromolecules* **2021**, *3*, 33–99, doi: 10.1016/j.ijbiomac.2021.02.200.

4. Gahlawat, G.; Kumari, P.; Bhagat, N.R. Technological advances in the production of polyhydroxyalkanoate biopolymers. *Current Sustainable/Renewable Energy Reports* **2020**, *7*, 73–83 doi: 10.1007/s40518-020-00154-4.
5. Ten, E.; Jiang, L.; Zhang, J.; Wolcott, M.P. Mechanical performance of polyhydroxyalkanoate (PHA)-based biocomposites. In *Biocomposites: Design and Mechanical Performance*, 1 ed.; Elsevier Inc.: **2015**; Vol. 1, pp. 39-52.
6. Valappil, S.P.; Boccaccini, A.R.; Bucke, C.; Roy, I. Polyhydroxyalkanoates in Gram-positive bacteria: Insights from the genera Bacillus and Streptomyces. *Antonie van Leeuwenhoek, International Journal of General and Molecular Microbiology* **2007**, *91*, 1–17 doi: 10.1007/s10482-006-9095-5.
7. Alves, M.I.; Macagnan, K.L.; Piecha, C.R.; Torres, M.M.; Perez, I.A.; Kesslerlingh, S.M.; Da Silva Rodrigues, R.; De Oliveira, P.D.; Da Silveira Moreira, A. Optimization of *Ralstonia solanacearum* cell growth using a central composite rotational design for the P(3HB) production: effect of agitation and aeration. *PLoS ONE* **2019**, *14*, 211211–211224 doi: 10.1371/journal.pone.0211211.
8. Kumar, V.; Sehgal, R.; Gupta, R. Blends and composites of polyhydroxyalkanoates (PHAs) and their applications. *European Polymer Journal* **2021**, *161*, 110824–110837 doi: 10.1016/j.eurpolymj.2021.110824.
9. Kfoury, G.; Raquez, J.M.; Hassouna, F.; Odent, J.; Toniazzo, V.; Ruch, D.; Dubois, P. Recent advances in high performance polylactide: from "green" plasticization to super-tough materials via (reactive) compounding. *Frontiers in Chemistry* **2013**, *1*, 1–46 doi: 10.3389/fchem.2013.00032.
10. Sunny, M.C.; Ramesh, P.; George, K.E. Use of polymeric plasticizers in polyvinyl chloride to reduce conventional plasticizer migration for critical applications. *Journal of Elastomers & Plastics* **2004**, *36*, 19–31 doi: 10.1177/0095244304038016.
11. Kurusu, R.S.; Siliki, C.A.; David, T.; Demarquette, N.R.; Gauthier, C.; Chenal, J.M. Incorporation of plasticizers in sugarcane-based poly(3-hydroxybutyrate) (PHB): changes in microstructure and properties through ageing and annealing. *Industrial Crops and Products* **2015**, *72*, 166–174 doi: 10.1016/j.indcrop.2014.12.040.



12. Wang, Y.; Zhang, G.; Wang, L. Potential toxicity of phthalic acid esters plasticizer: Interaction of dimethyl phthalate with trypsin in vitro. *Journal of Agricultural and Food Chemistry* **2015**, *63*, 75–84 doi: 10.1021/jf5046359.
13. Bocqué, M.; Voirin, C.; Lapinte, V.; Caillol, S.; Robin, J.-J. Petro-based and bio-based plasticizers: chemical structures to plasticizing properties. *Journal of Polymer Science Part A: Polymer Chemistry* **2016**, *54*, 11–33 doi: 10.1002/pola.27917.
14. Erceg, M.; Kovačić, T.; Klarić, I. Thermal degradation of poly(3-hydroxybutyrate) plasticized with acetyl tributyl citrate. *Polymer Degradation and Stability* **2005**, *90*, 313–318 doi: 10.1016/j.polymdegradstab.2005.04.048.
15. Quispe, M.M.; Lopez, O.V.; Boina, D.A.; Stumbé, J.F.; Villar, M.A. Glycerol-based additives of poly(3-hydroxybutyrate) films. *Polymer Testing* **2021**, *93*, 107005–107020 doi: 10.1016/j.polymertesting.2020.107005.
16. Alhanish, A.; Abu Ghalia, M. Developments of biobased plasticizers for compostable polymers in the green packaging applications: a review. *Biotechnology Progress* **2021**, *37*, 3210–3227 doi: 10.1002/btpr.3210.
17. Farrag, Y.; Barral, L.; Gualillo, O.; Moncada, D.; Montero, B.; Rico, M.; Bouza, R. Effect of different plasticizers on thermal, crystalline, and permeability properties of poly(3-hydroxybutyrate-co-3-hydroxyhexanoate) films. *Polymers* **2022**, *14*, 3503–3520 doi: 10.3390/polym14173503.
18. Della Monica, F.; Kleij, A.W. From terpenes to sustainable and functional polymers. *Polymer Chemistry* **2020**, *11*, 5109–5127 doi: 10.1039/d0py00817f.
19. Caputi, L.; Aprea, E. Use of terpenoids as natural flavouring compounds in food industry. *Recent Patents on Food, Nutrition & Agriculture* **2011**, *3*, 9–16 doi: 10.2174/2212798411103010009.
20. Masyita, A.; Mustika Sari, R.; Dwi Astuti, A.; Yasir, B.; Rahma Rumata, N.; Emran, T.B.; Nainu, F.; Simal-Gandara, J. Terpenes and terpenoids as main bioactive compounds of essential oils, their roles in human health and potential application as natural food preservatives. *Food Chemistry: X* **2022**, *13*, 100217–100231 doi: 10.1016/j.fochx.2022.100217.

21. Yang, W.; Chen, X.; Li, Y.; Guo, S.; Wang, Z.; Yu, X. Advances in Pharmacological Activities of Terpenoids. *Natural Product Communications* **2020**, *15*, 1–13 doi: 10.1177/1934578X20903555.
22. Bergman, M.E.; Davis, B.; Phillips, M.A. Medically useful plant terpenoids: biosynthesis, occurrence, and mechanism of action. *Molecules* **2019**, *24*, 3961–3984 doi: 10.3390/molecules24213961.
23. Jaeger, R.; Cuny, E. Terpenoids with special pharmacological significance: a review. *Natural Product Communications* **2016**, *11*, 1373–1390 doi: 10.1177/1934578x1601100946.
24. Mangeon, C.; Michely, L.; Rios De Anda, A.; Thevenieau, F.; Renard, E.; Langlois, V. Natural terpenes used as plasticizers for poly(3-hydroxybutyrate). *ACS Sustainable Chemistry & Engineering* **2018**, *6*, 16160–16168 doi: 10.1021/acssuschemeng.8b02896.
25. Van Krevelen, D.W. *Properties of Polymers: Their Correlation with Chemical Structure; their Numerical Estimation and Prediction from Additive Group Contributions*, 4 ed.; Elsevier: **2009**; Vol. 1.
26. Terada, M.; Marchessault, R.H. Determination of solubility parameters for poly(3-hydroxyalkanoates). *International Journal of Biological Macromolecules* **1999**, *25*, 207–215 doi: 10.1016/S0141-8130(99)00036-7.
27. Brüster, B.; Adjoua, Y.O.; Dieden, R.; Grysan, P.; Federico, C.E.; Berthé, V.; Addiego, F. Plasticization of polylactide with myrcene and limonene as bio-based plasticizers: Conventional *vs.* reactive extrusion. *Polymers* **2019**, *11*, 1363–1384 doi: 10.3390/polym11081363.
28. Kurusu, R.S.; Demarquette, N.R.; Gauthier, C.; Chenal, J.M. Effect of ageing and annealing on the mechanical behaviour and biodegradability of a poly(3-hydroxybutyrate) and poly(ethylene-co-methyl-acrylate-co-glycidyl-methacrylate) blend. *Polymer International* **2014**, *63*, 1085–1093 doi: 10.1002/pi.4616.
29. Brandrup, J.; Immergut, E.H.; Grulke, E.A.; Abe, A.; Bloch, D.R. *Polymer handbook*, 1 ed.; Wiley New York: **1999**; Vol. 89.

30. Hattori, K. Recycling of expanded polystyrene using natural solvents. In *Recycling materials based on environmentally friendly techniques*, 1 ed.; IntechOpen: **2015**; Vol. 1, pp.100-126.
31. Koller, M.; Mukherjee, A. A new wave of industrialization of PHA biopolyesters. *Bioengineering* **2022**, *9*, 74–103 doi: 10.3390/bioengineering9020074.
32. Schmid, M.T.; Sykacek, E.; O'Connor, K.; Omann, M.; Mundigler, N.; Neureiter, M. Pilot scale production and evaluation of mechanical and thermal properties of P(3HB) from *Bacillus megaterium* cultivated on desugarized sugar beet molasses. *Journal of Applied Polymer Science* **2022**, *139*, 51503–51514 doi: 10.1002/app.51503.
33. Vieira, M.G.A.; Da Silva, M.A.; Dos Santos, L.O.; Jõnec, M.M. Natural-based plasticizers and biopolymer films: a review. *European Polymer Journal* **2011**, *47*, 254–263 doi: 10.1016/j.eurpolymj.2010.12.011.
34. Jost, V.; Langowski, H.C. Effect of different plasticisers on the mechanical and barrier properties of extruded cast PHBV films. *European Polymer Journal* **2015**, *68*, 302–312 doi: 10.1016/j.eurpolymj.2015.04.012.
35. Panaitescu, D.M.; Nicolae, C.A.; Frone, A.N.; Chiulan, I.; Stanescu, P.O.; Draghici, C.; Iorga, M.; Mihailescu, M. Plasticized poly(3-hydroxybutyrate) with improved melt processing and balanced properties. *Journal of Applied Polymer Science* **2017**, *134*, 44810–44824 doi: 10.1002/app.44810.
36. Maiza, M.; Benaniba, M.T.; Massardier-Nageotte, V. Plasticizing effects of citrate esters on properties of poly(lactic acid). *Journal of Polymer Engineering* **2016**, *36*, 371–380 doi: 10.1515/polyeng-2015-0140.
37. Chieng, B.W.; Ibrahim, N.A.; Then, Y.Y.; Loo, Y.Y. Epoxidized vegetable oils plasticized poly(lactic acid) biocomposites: mechanical, thermal and morphology properties. *Molecules* **2014**, *19*, 16024–16038 doi: 10.3390/molecules191016024.
38. Li, D.; Jiang, Y.; Lv, S.; Liu, X.; Gu, J.; Chen, Q.; Zhang, Y. Preparation of plasticized poly(lactic acid) and its influence on the properties of composite materials. *PLoS ONE* **2018**, *13*, 193520–193535 doi: 10.1371/journal.pone.0193520.

39. Garcia-Garcia, D.; Quiles-Carrillo, L.; Balart, R.; Torres-Giner, S.; Arrieta, M.P. Innovative solutions and challenges to increase the use of poly(3-hydroxybutyrate) in food packaging and disposables. *European Polymer Journal* **2022**, *178*, 111505–111525 doi: 10.1016/j.eurpolymj.2022.111505.
40. Bibers, I.; Tupureina, V.; Dzene, A.; Kalnins, M. Improvement of the deformative characteristics of poly- $\beta$ -hydroxybutyrate by plasticization. *Mechanics of Composite Materials*. **1999**, *35*, 357–364 doi: 10.1007/BF02259726.
41. Mangeon, C.; Modjinou, T.; Rios De Anda, A.; Thevenieau, F.; Renard, E.; Langlois, V. Renewable semi-interpenetrating polymer networks based on vegetable oils used as plasticized systems of poly(3-hydroxyalkanoate)s. *ACS Sustainable Chemistry & Engineering* **2018**, *6*, 5034–5042 doi: 10.1021/acssuschemeng.7b04692.
42. Nosal, H.; Moser, K.; Warzała, M.; Holzer, A.; Stańczyk, D.; Sabura, E. Selected fatty acids esters as potential PHB-V bioplasticizers: effect on mechanical properties of the polymer. *Journal of Polymers and the Environment* **2021**, *29*, 38–53 doi: 10.1007/s10924-020-01841-5.
43. Umemura, R.T.; Felisberti, M.I. Modeling of the properties of plasticized poly(3-hydroxybutyrate) as a function of aging time and plasticizer content. *Materials Today Communications* **2020**, *25*, 101439–101448 doi: 10.1016/j.mtcomm.2020.101439.
44. Bouti, M.; Irinislmane, R.; Belhaneche-Bensemra, N. Properties investigation of epoxidized sunflower oil as bioplasticizer for poly(lactic acid). *Journal of Polymers and the Environment* **2022**, *30*, 232–245 doi: 10.1007/s10924-021-02194-3.
45. Garcia-Garcia, D.; Ferri, J.M.; Montanes, N.; Lopez-Martinez, J.; Balart, R. Plasticization effects of epoxidized vegetable oils on mechanical properties of poly(3-hydroxybutyrate). *Polymer International* **2016**, *65*, 1157–1164 doi: 10.1002/pi.5164.
46. Garcia-Garcia, D.; Fenollar, O.; Fombuena, V.; Lopez-Martinez, J.; Balart, R. Improvement of mechanical ductile properties of poly(3-hydroxybutyrate) by using vegetable oil derivatives. *Macromolecular Materials and Engineering* **2017**, *302*, 1600330–160342 doi: 10.1002/mame.201600330.

- 
47. Chaos, A.; Sangroniz, A.; Gonzalez, A.; Iriarte, M.; Sarasua, J.R.; del Río, J.; Etxeberria, A. Tributyl citrate as an effective plasticizer for biodegradable polymers: effect of plasticizer on free volume and transport and mechanical properties. *Polymer International* **2019**, *68*, 125–133 doi: 10.1002/pi.5705.
48. Eesaee, M.; Ghassemi, P.; Nguyen, D.D.; Thomas, S.; Elkoun, S.; Nguyen-Tri, P. Morphology and crystallization behaviour of polyhydroxyalkanoates-based blends and composites: a review. *Biochemical Engineering Journal* **2022**, *187*, 108588–108615 doi: 10.1016/j.bej.2022.108588.
49. Chen, C.; Cheung, M.K.; Yu, P.H. Crystallization kinetics and melting behaviour of microbial poly(3-hydroxybutyrate-co-3-hydroxyhexanoate). *Polymer International* **2005**, *54*, 1055–1064 doi: 10.1002/pi.1809.
50. Barbosa, J.L.; Perin, G.B.; Felisberti, M.I. Plasticization of poly(3-hydroxybutyrate-co-3-hydroxyvalerate) with an oligomeric polyester: miscibility and effect of the microstructure and plasticizer distribution on thermal and mechanical properties. *ACS Omega* **2021**, *6*, 3278–3290 doi: 10.1021/acsomega.0c05765.
51. Martelli, S.M.; Sabirova, J.; Fakhoury, F.M.; Dyzma, A.; de Meyer, B.; Soetaert, W. Obtention and characterization of poly(3-hydroxybutyric acid-co-hydroxyvaleric acid)/mcl-PHA based blends. *LWT* **2012**, *47*, 386–392 doi: 10.1016/j.lwt.2012.01.036.
52. Audic, J.L.; Lemiègre, L.; Corre, Y.M. Thermal and mechanical properties of a polyhydroxyalkanoate plasticized with biobased epoxidized broccoli oil. *Journal of Applied Polymer Science* **2014**, *131*, 39983–39990 doi: 10.1002/app.39983.
53. Greco, A.; Ferrari, F.; Maffezzoli, A. Thermal analysis of poly(lactic acid) plasticized by cardanol derivatives. *Journal of Thermal Analysis and Calorimetry* **2018**, *134*, 559–565 doi: 10.1007/s10973-018-7059-4.
54. Meléndez-Rodríguez, B.; Torres-Giner, S.; Reis, M.A.M.; Silva, F.; Matos, M.; Cabedo, L.; Lagarón, J.M. Blends of poly(3-hydroxybutyrate-co-3-hydroxyvalerate) with fruit pulp biowaste derived poly(3-hydroxybutyrate-co-3-hydroxyvalerate-co-3-hydroxyhexanoate) for organic recycling food packaging. *Polymers* **2021**, *13*, 1155–1174 doi: 10.3390/polym13071155.

55. Jeong, H.; Yuk, J.S.; Lee, H.; Kang, S.; Park, H.; Park, S.H.; Shin, J. Lactide-derived ester oligomers for highly compatible polylactide plasticizer produced through an eco-friendly process: renewable resources, biodegradation, enhanced flexibility, and elastomeric performance. *Green Chemistry Journal* **2021**, *23*, 7549–7565 doi: 10.1039/d1gc02049h.
56. Fortunati, E.; Luzi, F.; Puglia, D.; Dominici, F.; Santulli, C.; Kenny, J.M.; Torre, L. Investigation of thermo-mechanical, chemical and degradative properties of PLA-limonene films reinforced with cellulose nanocrystals extracted from Phormium tenax leaves. *European Polymer Journal* **2014**, *56*, 77–91 doi: 10.1016/j.eurpolymj.2014.03.030.
57. Weng, Y.X.; Wang, X.L.; Wang, Y.Z. Biodegradation behavior of PHAs with different chemical structures under controlled composting conditions. *Polymer Testing* **2011**, *30*, 372–380 doi: 10.1016/j.polymertesting.2011.02.001.
58. Arrieta, M.P. Influence of plasticizers on the compostability of polylactic acid. *Journal of Applied Research in Technology & Engineering* **2021**, *2*, 1–9 doi: 10.4995/jarte.2021.14772.
59. Sedničková, M.; Pekařová, S.; Kucharczyk, P.; Bočkaj, J.; Janigová, I.; Kleinová, A.; Johec-Mošková, D.; Omaníková, L.; Perďochová, D.; Koutný, M., *et al.* Changes of physical properties of PLA-based blends during early stage of biodegradation in compost. *International Journal of Biological Macromolecules* **2018**, *113*, 434–442 doi: 10.1016/j.ijbiomac.2018.02.078.

**Section II:  
Manufacturing of polyhydroxyalkanoates by  
3D printing and injection moulding for  
medical applications.**



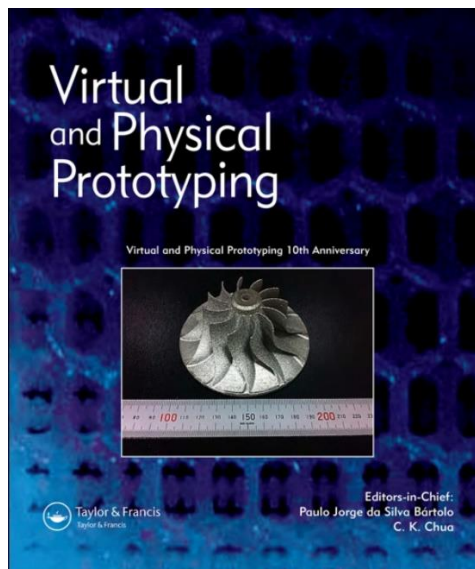


Adapted from the original manuscript.

### III.2.1 The effects of processing parameters on mechanical properties of 3D-printed polyhydroxyalkanoates parts.

Juan Ivorra-Martinez<sup>1</sup>, Miguel Angel Peydro<sup>1</sup>, Jaume Gomez-Caturla<sup>1</sup>, Lourdes Sanchez-Nacher<sup>1</sup>, Teodomiro Boronat<sup>1</sup>, Rafael Balart<sup>1</sup>.

<sup>1</sup>Technological Institute of Materials - ITM, Universitat Politècnica de València - UPV, Plaza Ferrándiz y Carbonell 1, 03801 Alcoy (Spain).



**Virtual and Physical Prototyping.**

**2023, 18(1): 2164734.**



## The effects of processing parameters on mechanical properties of 3D-printed polyhydroxyalkanoates parts

Juan Ivorra-Martinez , Miguel Ángel Peydro , Jaime Gomez-Caturla , Lourdes Sanchez-Nacher, Teodomiro Boronat  and Rafael Balart 

Institute of Materials Technology (ITM), Universitat Politècnica de València (UPV), Alcoy, Spain

### ABSTRACT

The crystallisation process of polyhydroxyalkanoates (PHA) polymers plays a key role on final properties of manufactured parts due to most PHA are highly sensitive to physical aging which leads to embrittlement. The secondary crystallisation associated with the aging process can be partially controlled by the cooling process during manufacturing or, even, by heat treatments such as annealing. A critical parameter in additive manufacturing is the difficulty to achieve good adhesion of the material to the printing bed. The bed temperature plays a key role on PHBH crystallisation, which leads to shrinkage having a negative effect on polymer-to-bed adhesion. In this work, a study of the effect of different processing parameters such as the printing temperature, the bed temperature, the cooling conditions, as well as raster direction on the final properties of PHBH 3D-printed parts is carried out.

### ARTICLE HISTORY

Received 9 October 2022  
 Accepted 29 December 2022

### KEYWORDS

Mechanical properties; optimisation; PHA; PHBH

### 1. Introduction

The idea of 3D printing was developed by Charles Hull in the 1980s through the development of the first stereo lithography apparatus (SLA) printer (Hull 1998). It was not until 1989 when Scott Crump developed the fused deposition modelling (FDM) technology (Crump 1989; Gardan 2019). Since then, the use of additive manufacturing techniques has become particularly important, and their use is set to lead to the next industrial revolution (Singh and Jonnalagadda 2020). The principle of operation of FDM technology is focused mainly on thermoplastic polymers. Among the different FDM techniques, the Fused Filament Fabrication (FFF) is the most common. In this case, a prefabricated filament is extruded through the nozzle by a roller-based extruder that pushes the filament into the heating zone (Singh et al. 2020). As an alternative to filament printers, some FDM machines replace the roller-based extruder by a single-screw extruder that feeds the nozzle thus allowing direct 3D printing with pellets. By applying heat and shear, pellets are melted progressively along the screw to achieve a homogeneous melt that can feed the nozzle to give 3D-printed parts (Gonzalez-Gutierrez et al. 2018; Liu et al. 2019; Singamneni et al. 2018).

Heating polymers above their characteristic melting temperatures ( $T_m$ , for semicrystalline polymers), or

above their glass transition temperature ( $T_g$ , for amorphous polymers) allows the polymer to flow through a nozzle. In this way, the fused material is deposited in a controlled way following a selected pattern. The process allows the stacking of layers to finally achieve the desired geometry. By using this technique, it is possible to generate complex shapes without using complex and high-cost equipment (Gonzalez-Gutierrez et al. 2018). Some of the most commonly used materials in FDM are poly(lactic acid) (PLA) and poly (acrylonitrile-butadiene-styrene) (ABS) (Solomon, Sevel, and Gunasekaran 2020). While ABS is an amorphous petroleum-derived copolymer with good impact resistance, PLA can be obtained from renewable resources and it is easier to print (Rodríguez-Panes, Claver, and Camacho 2018; Bermudez et al. 2021). Among the different thermoplastics currently available on the market, it is worthy to note the increasing use of polyhydroxyalkanoates (PHA) which have been proposed as the bioplastics of the future. PHA include a wide family of polymers that are accumulated in the cells of some microorganisms in a controlled environment of a carbon source such as food industry wastes (Anjum et al. 2016; Kovalcik 2021). As PLA, PHA are biopolymers that can be disintegrated in compost soil which made them an interesting solution for the manufacturing of single use products like

**CONTACT** Juan Ivorra-Martinez  [juaivmar@doctor.upv.es](mailto:juaivmar@doctor.upv.es)  Institute of Materials Technology (ITM), Universitat Politècnica de València (UPV), Plaza Ferrandiz y Carbonell 1, 03801, Alcoy, Spain

© 2023 The Author(s). Published by Informa UK Limited, trading as Taylor & Francis Group

This is an Open Access article distributed under the terms of the Creative Commons Attribution-NonCommercial License (<http://creativecommons.org/licenses/by-nc/4.0/>), which permits unrestricted non-commercial use, distribution, and reproduction in any medium, provided the original work is properly cited.



**Abstract.**

The crystallization process of polyhydroxyalkanoates - PHA polymers plays a key role on final properties of manufactured parts due to most PHA are highly sensitive to physical aging which leads to embrittlement. The secondary crystallization associated to the aging process can be partially controlled by the cooling process during manufacturing or, even, by heat treatments such as annealing. A critical parameter in Additive Manufacturing - AM is the difficulty to achieve good adhesion of the material to the printing bed. Increasing the bed temperature usually improves the sample adhesion, but in this case plays a key role on P(3HB-*co*-3HHx) crystallization, which leads to shrinkage having a negative effect on polymer-to-bed adhesion. In this work, a study of the effect of different processing parameters such as the printing temperature, the bed temperature, the cooling conditions, as well as raster direction on the final properties of P(3HB-*co*-3HHx) 3D-printed parts is carried out.

**Keywords:** PHA; P(3HB-*co*-3HHx); optimization; mechanical properties.

---



**INTRODUCTION.**

The idea of 3D printing was developed by Charles Hull in the 1980s through the development of the first Stereo Lithography Apparatus - SLA printer [1]. It was not until 1989 when Scott Crump developed the Fused Deposition Modelling - FDM technology [2,3]. Since then, the use of Additive Manufacturing - AM techniques has become particularly important, and their use is set to lead to the next industrial revolution [4]. The principle of operation of FDM technology is focused mainly on thermoplastic polymers. Among the different FDM techniques, the Fused Filament Fabrication - FFF is the most common. In this case, a prefabricated filament is extruded through the nozzle by a roller-based extruder that pushes the filament into the heating zone [5]. As an alternative to filament printers, some FDM machines replace the roller-based extruder by a single-screw extruder that feeds the nozzle thus allowing direct 3D printing with pellets. By applying heat and shear, pellets are melted progressively along the screw to achieve a homogeneous melt that can feed the nozzle to give 3D-printed parts [6-8].

Heating polymers above their characteristic melting temperatures -  $T_m$  (for semicrystalline polymers), or above their glass transition temperature -  $T_g$  (for amorphous polymers) allows the polymer to flow through a nozzle. In this way, the fused material is deposited in a controlled way following a selected pattern. The process allows the stacking of layers to finally achieve the desired geometry. By using this technique, it is possible to generate complex shapes without using complex and high-cost equipment [6]. Some of the most commonly used materials in FDM are poly(lactic acid) - PLA and poly(acrylonitrile-butadiene-styrene) - ABS [9]. While ABS is an amorphous petroleum-derived copolymer with good impact resistance, PLA can be obtained from renewable resources and it is easier to print [10,11]. Among the different thermoplastics currently available on the market, it is worthy to note the increasing use of polyhydroxyalkanoates - PHA which have been proposed as the bioplastics of the future. PHA include a wide family of polymers that are accumulated in the cells of some microorganisms in a controlled environment of a carbon source such as food industry wastes [12,13]. As PLA, PHA are biopolymers that can be disintegrated in compost soil which made them an interesting solution for the manufacturing of single use products like packaging. Also they are biocompatible and resorbable which give a great potential for the manufacture of medical devices so they can be introduced inside the human body and eliminated due to they are bioabsorbable or resorbable [13,14]. Additionally, the introduction of AM techniques in medicine is gaining special interest

due to the possibility of manufacturing medical customized devices [15].

Currently, it is possible to find a wide number of materials based on PLA. Even more, some recent developments offer a full PHA filament for 3D-printing (allPHA by colorFabb). Nevertheless, PHA usually are blended (up to 20 - 25 %) with PLA to enhance good processability to tailor the desired properties [13,16,17]. Kovakcik *et al.* showed that poly(3-hydroxybutyrate) - P3HB or poly(3-hydroxybutyrate-co-3-hydroxyvalerate) - P(3HH-co-3HV) can undergo degradation during hot-melt processing, since their working temperature is very close to the degradation temperature making it difficult to obtain the corresponding filament. However, they concluded that poly(3-hydroxybutyrate-co-3-hydroxyhexanoate) - P(3HB-co-3HHx) has less degradation during processing and, therefore, P(3HB-co-3HHx) is a good candidate to obtain filaments for 3D-printing [18]. In spite of the fact that P(3HB-co-3HHx) is less sensitive to thermal degradation during processing compared to other PHA, it still suffers more degradation than PLA. Consequently, the use of a pellet printer avoids one thermal cycle required to obtain filaments from pellets. Another way that has been investigated, is the employment of selective laser sintering techniques to manufacture PHA parts [19].

One of the main problems in 3D-printing is the possibility of warping due to the shrinkage suffered by the material during cooling. To avoid this, a heated bed can help to avoid undesired deformations due to detachment of the first layer. Additionally, an enclosed 3D-printer allows a more homogeneous cooling, which is key for some materials such as ABS. Other parameters like the surface on which the material is deposited, the use of adhesives, or adhesion enhancement methods such as raft, skirt or brim can help to improve adhesion [17,20,21]. In addition to the cooling conditions, shrinkage also occurs in semicrystalline polymers during crystallization, with the subsequent negative effect on debonding or warping defects [22].

Depending on the conditions under the crystallization of PHA, differences in the degree of crystallinity of the material can be obtained. Therefore, the properties of PHA are highly influenced by the cooling conditions [23,24]. Furthermore, P(3HB-co-3HHx) is a medium-chain length PHA (mcl-PHA), which results in a more flexible behaviour compared to P3HB. On the other hand, PHA suffers physical aging at room temperature due to secondary crystallization which leads to embrittlement [25,26]. Considering this, the thermal treatments after the processing play an important role. Annealing is a very usual applied thermal treatment on semicrystalline polymers subjected to rapid cooling. Annealing is a very useful tool to tailor the final properties of the material due to the



different degree of crystallinity obtained, depending on time and temperature [27,28].

This research aims to assess the effects of the main processing parameters of a 3D-printing process using P(3HB-co-3HHx) pellets instead of filament to prevent polymer from degradation. More specifically, the effect of the nozzle temperature in the 175 - 185 °C range, the bed temperature in the 60 - 80 °C range and the layer fan cooling activation, on mechanical properties and 3D-printability of P(3HB-co-3HHx) is studied. In addition, the raster angle (transversal and longitudinal to the applied load) was also evaluated. The study of a PHA in AM is interesting for the development of medical devices. Nowadays the development of medical devices that can be resorbable and adapted to the special needs of the patient is gaining special attention. Until now, the number of studies in which a PHA is employed without blending with other polymers is very limited and the effect of the working parameters in AM has not been assessed.

## **MATERIALS AND METHODS.**

### **Materials.**

P(3HB-co-3HHx) grade PH110 from Ercros S.A. (Barcelona, Spain) with a Melt Flow Index - MFI of 1 g/10 min (ISO 1133-2 at 160°C and 2.16 kg) and a melting temperature of 124 °C was used in pellet form. To avoid hydrolysis, P(3HB-co-3HHx) pellets were dried 6 h at 80°C to remove residual moisture.

### **3D-printing with P(3HB-co-3HHx) pellets.**

The tensile test samples were manufactured in a 3D printer Tumaker equipped with a single-screw extruder to work directly with pellets. This is a side-wall enclosed unit with external dimensions of 450 × 410 × 410 mm<sup>3</sup> and a printing volume of 270 × 190 × 200 mm<sup>3</sup>. The printing process was carried out at a controlled room temperature range between 23 - 25 °C. 3DLAC adhesive spray (San Cristóbal de Entreviñas, Spain) was used as an adhesive to ensure correct adhesion of the polymer to the glass bed. The G-code generation was made using Simplify3D 4.1 (Cincinnati, United States) following the conditions provided in **Table III.2.1.1.**

**Table III.2.1.1.** Printing parameters used for G-code generation of P(3HB-co-3HHx) 3D-printed materials.

	Value	Unit
Layer height	0.4	mm
Initial layer speed	8	mm/s
Nominal speed	12	mm/s
Layer fan	100 (from layer 2) or 0	%
Brim	4 (only layer 1)	mm
Nozzle	0.8	mm
Line width	0.8	mm
Wall line count	0	-
Infill	100	%
Raster direction	0 or 90	°

The temperatures employed for the manufacture of the samples were chosen according to the observed working range established by an iterative process in which, different temperatures were tested until a good first layer adhesion was obtained in a range from 60 °C to 80 °C. The proper rotation of the screw was obtained in the 170 °C - 185 °C range. A deeper explanation of the process followed to obtain the working parameters has been done in the results section. Regarding the cooling process of the 3D-printed samples, a 5015-fan working at 3500 rpm was assembled next to the hot end that produced an air flow directly to 3D-printed sample to increase the cooling rate of the melted deposited polymer.

The polymer flow calibration was performed iteratively. To obtain the extruder steps per millimetre, different tests were carried out initially by using different values. A single wall cube was 3D-printed, and the wall thickness was measured with a micrometre. The steps were calibrated, when a line width of 0.8 mm was reached. A Tesa Technology (Renens, Switzerland) micrometre with a measuring range of 0 - 25 mm and a precision of 0.01 mm was used for the measurement.

The designation of the samples was made according to the following criteria: Heat zone 1/Bed temperature. The samples with a longitudinal pattern (raster direction aligned with the applied axial loading direction in tensile test) were designated with L, and those with a transverse pattern (raster direction perpendicular to the applied axial loading direction in tensile test) were designated with T. Additionally, different combinations were analysed with regard to the layer fan: one consisting on switching the fan on for 100 % from the second printed layer (F), and another one consisting on switched off fan (NF). **Table III.2.1.2.** summarizes the main varying parameters for 3D-printing with P(3HB-co-3HHx).

**Table III.2.1.2.** Printing conditions used for 3D-printing P(3HB-co-3HHx)-based materials.

Nozzle temperature or hotend (°C)	Bed temperature or heat bed (°C)	Stepper motor (steps/mm)
175, 180 or 185	60,70 or 80	300

Due to the influence of temperature on the recrystallization process, in order to consider the same conditions in all cases, the specimens were processed individually. After ending the 3D-printing process, specimens were left inside the printer until the bed temperature reached room temperature.

### **Mechanical properties.**

Tensile tests samples were 3D-printed and tested according to ISO 527 after a 14-day aging period at room temperature, since these properties are more representative for the long-term behaviour of PHA as reported in literature [29]. For this purpose, an ELIB 30 universal testing machine from Ibertest (Madrid, Spain) equipped with a 5 kN load cell was used. Each measurement was performed 5 times to obtain an average of the main tensile parameters and the corresponding standard deviation. ANOVA statistical analysis was carried out using Statgraphics 18 (The Plains, USA). During the test, the main results annotated were tensile strength -  $\sigma_t$ , elongation at break -  $\varepsilon_b$  and tensile modulus -  $E_t$ .

### **Infrared spectroscopy properties.**

Chemical structure analysis was performed by Attenuated Total Reflection-Fourier Transform Infrared Spectroscopy - ATR-FTIR. The analyses were carried out with a Vector 22 from Bruker S.A. (Madrid, Spain) to which the ATR accessory was supplied by PIKE Technologies (Madison, USA). Ten measurements with a precision of  $4 \text{ cm}^{-1}$  and a range of  $4000 \text{ to } 700 \text{ cm}^{-1}$  were performed.

### **Fracture morphology.**

Images of the tensile test specimens fractured surface morphology were taken by means of ZEISS ULTRA 55 microscope from Oxford Instruments (Abingdon, UK) with an acceleration voltage of 2 kV. Prior to collecting the images, a sputtering process was performed with gold-palladium alloy in a SC7620 sputter coater from Quorum Technologies Ltd. (East Sussex, UK).

**Differential scanning calorimetry properties.**

Differential Scanning Calorimetry – DSC was used to assess the effect of working parameters in the thermal properties of P(3HB-co-3HHx). The main thermal parameters, namely the melting temperature –  $T_m$ , the melting enthalpy –  $\Delta H_m$ , and the degree of crystallinity –  $\chi_c$  were obtained from the corresponding DSC runs. The degree of crystallinity was calculated with **Equation III.2.1.1.** where  $\Delta H_m^0$  is the melt enthalpy of a theoretically fully crystalline sample of P(3HB-co-3HHx), which was considered as 146 J/g as reported in literature [30], and  $\Delta H_m$  is the obtained melt enthalpy for P(3HB-co-3HHx) measured during the test.

$$\chi_c(\%) = \frac{\Delta H_m}{\Delta H_m^0} \cdot 100 \quad \text{Equation III.2.1.1.}$$

DSC runs were performed in a DSC Mettler-Toledo Inc. (Schwerzenbach, Switzerland) under a nitrogen atmosphere (66 mL/min) using a sample weight between 5 and 7.5 mg. The dynamic DSC run was performed from – 50 °C to 200 °C at 10 °C/min to measure the thermal properties of the samples after the aging.

**RESULTS AND DISCUSSIONS.****Mechanical properties of the P(3HB-co-3HHx) 3D-printed parts.**

The mechanical properties of the 3D-printed tensile tests specimens with the different processing parameters cooled with the layer fan are gathered in **Table III.2.1.3.** (transversal raster) and **Table III.2.1.4.** (longitudinal raster), while the tensile properties of 3D-printed specimens cooled down without the fan are described in **Table III.2.1.5.** and **Table III.2.1.6.** Due to the large amount of data obtained, an ANOVA statistical study was used to determine the differences that arise depending on the selected parameters presented in **Figure III.2.1.1.** and **Figure III.2.1.2.**, respectively.

**Table III.2.1.3.** Summary of the mechanical properties of the samples printed with transversal (T) raster angle and with the layer fan working.

<b>T-F</b>	<b><math>\sigma_t</math> (MPa)</b>	<b><math>\epsilon_b</math> (%)</b>	<b><math>E_t</math> (MPa)</b>
175-60	14.5 ± 0.6	13.6 ± 0.5	760 ± 38
180-60	15.1 ± 0.5	14.4 ± 0.4	817 ± 16
185-60	12.6 ± 0.5	13.3 ± 0.4	765 ± 15
175-70	14.0 ± 0.6	14.0 ± 0.4	699 ± 28
180-70	14.8 ± 0.6	14.5 ± 0.6	770 ± 39
185-70	13.0 ± 0.5	13.3 ± 0.5	682 ± 27
175-80	14.2 ± 0.4	14.4 ± 0.6	649 ± 26
180-80	14.4 ± 0.4	14.5 ± 0.4	707 ± 28
185-80	13.6 ± 0.4	13.6 ± 0.4	645 ± 19

**Table III.2.1.4.** Summary of the mechanical properties of the samples printed with longitudinal (L) raster angle and with the layer fan working.

<b>L-F</b>	<b><math>\sigma_t</math> (MPa)</b>	<b><math>\epsilon_b</math> (%)</b>	<b><math>E_t</math> (MPa)</b>
175-60	17.8 ± 0.5	17.0 ± 0.7	846 ± 17
180-60	18.0 ± 0.5	17.3 ± 0.5	847 ± 25
185-60	16.5 ± 0.7	16.1 ± 0.6	795 ± 16
175-70	18.2 ± 0.5	17.1 ± 0.5	801 ± 24
180-70	18.6 ± 0.7	17.2 ± 0.7	804 ± 16
185-70	17.3 ± 0.5	16.1 ± 0.6	757 ± 38
175-80	15.8 ± 0.6	16.5 ± 0.7	746 ± 33
180-80	16.2 ± 0.5	16.4 ± 0.5	758 ± 35
185-80	15.1 ± 0.6	14.9 ± 0.6	737 ± 37

The ANOVA analysis of the obtained results shows that some parameters have a marked influence (bars above the red line) on the different tensile properties of the 3D-printed samples. Regarding the tensile strength, the raster has a highly remarkable influence. In this case the best results were obtained in those parameters in which the raster was aligned (L) with the axial load applied during the tensile test. The tensile strength showed lower values for specimens obtained using a transverse pattern (T), since the strength was transferred between adjacent beads. These results agree with those reported by Rajpurohit *et al.* [31]. They concluded that the fracture in a 3D-printed specimen is related to the separation of the interface of the beams when the other patterns is perpendicular to that of the applied load. This phenomenon is common when characterizing samples obtained by 3D-printing, resulting in anisotropy and therefore, the mechanical properties are highly dependent on the selected orientation [32-35].

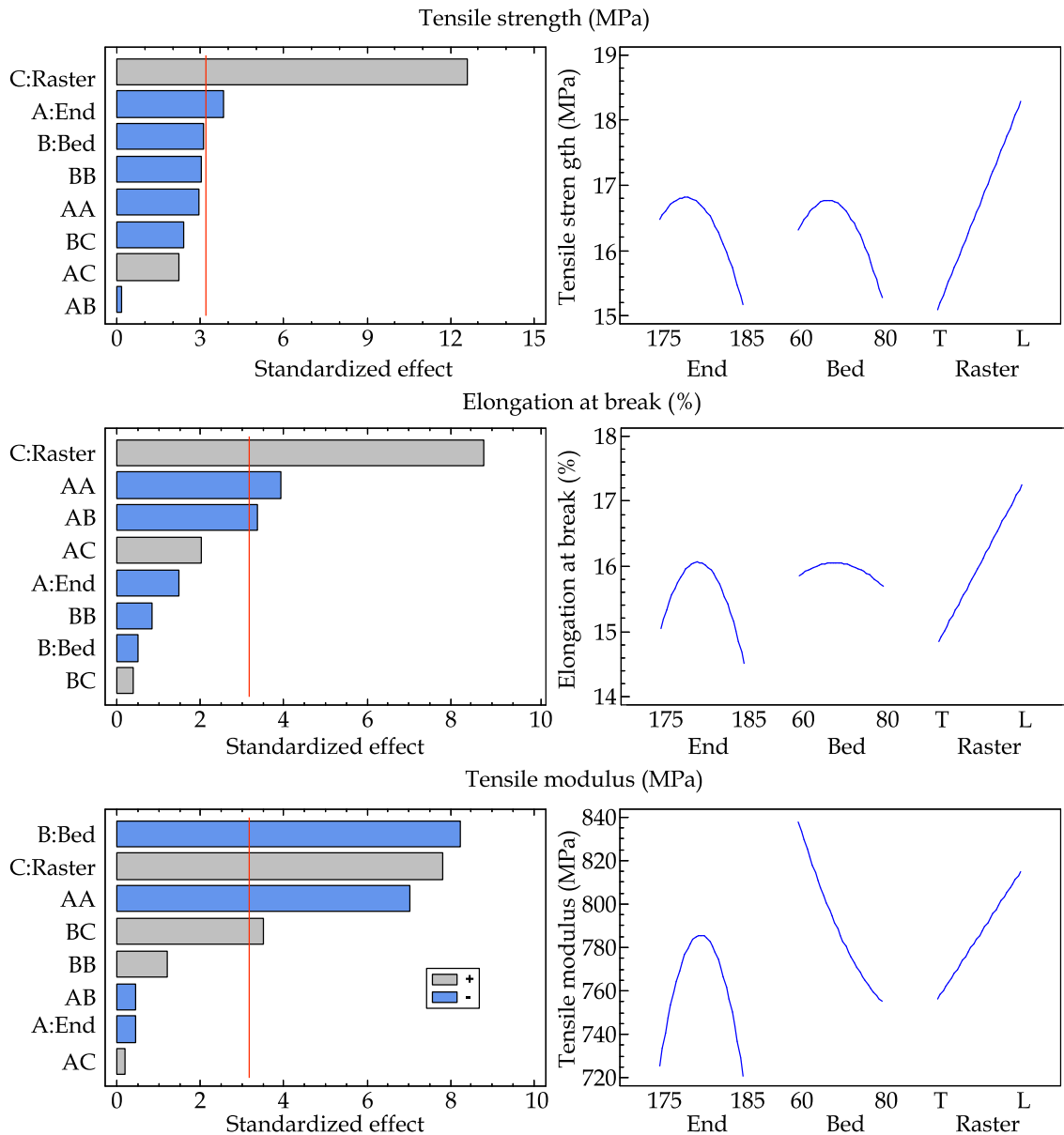


**Figure III.2.1.1.** Summary of the ANOVA analysis for PHPH 3D-printed samples by using the layer fan during the cooling process. This shows the Pareto diagram standardized effect (left row) and the main effects diagram (right row) for tensile strength, elongation at break and tensile modulus.

Another parameter that had a significant influence on the tensile strength according to the results shown by the ANOVA analysis was the hot-end temperature. This parameter did not show a linear trend; the best results were obtained for the intermediate temperature value considered (180 °C). Between 175 °C and 180 °C an increase in strength was observed, which is probably related to the improved adhesion between the beads and the 3D-printed samples. As proposed in the work of Alafaghani *et al.* with PLA, an improvement of tensile strength was observed between 175 °C and 190 °C. A further temperature increases up to 205 °C, did not lead to a significant increase

in tensile strength [36]. However, PHA polymers are particularly sensitive to thermal degradation even at temperatures slightly above the melting temperature (very narrow processing window) [37]. For this reason, a decreasing trend for tensile strength can be observed for P(3HB-co-3HHx) 3D-printed samples above 180 °C, with 15.1 MPa for 180-60 T samples and 12.6 MPa for the 185-60 T samples, which means a reduction of 16.5 %. The thermogravimetric properties of the commercial grade employed in this work were analysed in a previous study in which the initial mass loss started at 286.6 °C, and the maximum degradation rate occurred at 308.9 °C. Therefore, no severe degradation associated with a mass loss is expected by using the temperatures employed in the extruder [38]. Shojaeiarani *et al.* studied the effect of five extrusion cycles for two biopolymers, namely PLA and P(3HH-co-3BV) working with a maximum temperature of 166 °C for PLA and 177 °C for poly(3-hydroxybutyrate-co-3-hydroxyvalerate) - P(3HH-co-3BV). Under these conditions, the polymers employed were working at temperatures below their corresponding onset degradation observed by TGA, with a mass loss starting at 287 °C for PLA and 251 °C for P(3HH-co-3BV). As a result of the extrusion cycles performed, the molecular weight of PLA changed from 203500 g/mol to 44149 g/mol and for P(3HH-co-3BV) from 298500 g/mol to 52262 g/mol confirming that even below the mass loss temperature polymers suffer from thermal degradation, mainly due to chain scission [39].

As for the elongation at break, the main parameter with a clear effect on it is the raster angle used. When the raster angle is aligned with the applied load, the best results are obtained and as expected, the use of a perpendicular raster direction during the 3D-printing, clearly leads the decreased elongation at break values. While the maximum elongation at break for 3D-printed samples with a longitudinal pattern was 17.3 %, by using a transversal pattern the maximum elongation at break was reduced to 14.4 %. Such results are in agreement with those reported by Algarni *et al.* [40], and Zhang *et al.* [41]. As proposed above, the samples with a perpendicular pattern are limited by the deposition lines adhesion, as a result the ability for plastic deformation is somewhat restricted. With regard to the hot end temperature, the best results were obtained at 180 °C; above this temperature, the effects of thermal degradation of P(3HB-co-3HHx) are reflected in a decrease in elongation at break due to the narrow processing window of PHA. Samples printed with a longitudinal pattern and same heated bed temperature achieved differences up to 9 % by changing the hot end temperature from 180 °C to 185 °C. The heated bed had a negligible effect, as the line obtained was practically flat showing no differences between de temperatures considered in this study.

Regarding the tensile modulus of P(3HB-co-3HHx) 3D-printed specimens with different processing parameters, the highest modulus was achieved for a heated bed temperature of 60 °C (lowest temperature considered in this study), so the fastest cooling of the sample was achieved. Despite the 3D-printer used in this work has enclosed side walls, there is not any enclosure for the top. In any case, by using a heated bed, the environment surrounding the sample was at a higher temperature than the room temperature and depends on the temperature of the heated bed. This warm environment was equivalent to a post-annealing treatment since specimens were subjected to moderate-to-high temperatures during the printing time, thus enhancing crystallization. As it has been reported in literature, the mechanical properties of many PHA are highly dependent on the post-processing heat treatments, usually annealing [42-44]. Kurusu *et al.* used a post-processing annealing for P3HB, and as result stiffness was increased [43]. Additives can also exert an important effect on the annealing process by acceleration it or slowing down it, depending on the additive, amount, and chemical structure.

For the raster angle, as mentioned above, when the applied load direction is aligned with the pattern, then the highest values were obtained in all the measured parameters (for samples manufactured at the same temperatures). This trend is in accordance with that obtained by Zhang *et al.* [41]. In this work, different printing parameters were analysed to assess their effect on the final properties of PLA. Among the parameters analysed, the different raster angles were considered. A linear trend could be observed for the tensile modulus against the raster angle with the highest values close to the applied load direction (L), and a decreasing trend when the beams were oriented in perpendicular direction (T). While the highest tensile modulus for samples with a longitudinal pattern was 847 MPa, 3D-printed samples with a transversal pattern reached a slightly lower tensile modulus of 817 MPa, so differences around 3.5 % were obtained for the highest values.

After collecting the mechanical properties of 3D-printed specimens obtained with the layer fan switched off, an ANOVA test was carried out to identify the most relevant parameters having a direct influence on final performance. The main mechanical properties are included in **Table III.2.1.5.** and **Table III.2.1.6.**, while the ANOVA analysis results can be found in **Figure III.2.1.2.** A priori, some differences can clearly be detected. In this case, the heated bed temperatures considered were only 60 °C and 70 °C. When the layer fan was switched off, the 3D-printing process with P(3HB-co-3HHx) using a heated bed at a temperature of 80 °C, a clear evidence of



warping was observed resulting in defective specimens, and therefore, they could not be tested. This phenomenon is related with the P(3HB-co-3HHx) crystallization; the slowest cooling conditions allowed the polymer chains to rearrange more easily leading to an increase in crystallinity which, in turn, resulted in higher shrinkage. This shrinkage was responsible for warping and promoted specimen detachment from the heated bed [22].

**Table III.2.1.5.** Summary of the mechanical properties of the samples printed with transversal (T) raster angle and without the layer fan.

T-NF	$\sigma_t$ (MPa)	$\epsilon_b$ (%)	$E_t$ (MPa)
175-60	15.1 ± 0.3	14.6 ± 0.4	645 ± 19
180-60	15.1 ± 0.6	15.2 ± 0.6	640 ± 13
185-60	14.3 ± 0.3	14.9 ± 0.3	614 ± 12
175-70	14.7 ± 0.7	14.5 ± 0.4	618 ± 25
180-70	14.8 ± 0.4	14.8 ± 0.3	605 ± 12
185-70	14.0 ± 0.3	14.1 ± 0.4	577 ± 29
175-80	*	*	*
180-80	*	*	*
185-80	*	*	*

\* Could not be 3D-printed due to excessive warping and detachment.

**Table III.2.1.6.** Summary of the mechanical properties of the samples printed with longitudinal (L) raster and without the layer fan.

L-NF	$\sigma_t$ (MPa)	$\epsilon_b$ (%)	$E_t$ (MPa)
175-60	16.2 ± 0.5	15.8 ± 0.5	666 ± 33
180-60	16.3 ± 0.3	16.1 ± 0.5	669 ± 13
185-60	16.0 ± 0.3	15.3 ± 0.8	649 ± 19
175-70	15.4 ± 0.5	15.1 ± 0.8	622 ± 12
180-70	15.3 ± 0.6	15.5 ± 0.5	627 ± 31
185-70	14.5 ± 0.6	14.6 ± 0.7	611 ± 12
175-80	*	*	*
180-80	*	*	*
185-80	*	*	*

\* Could not be 3D-printed due to excessive warping and detachment.

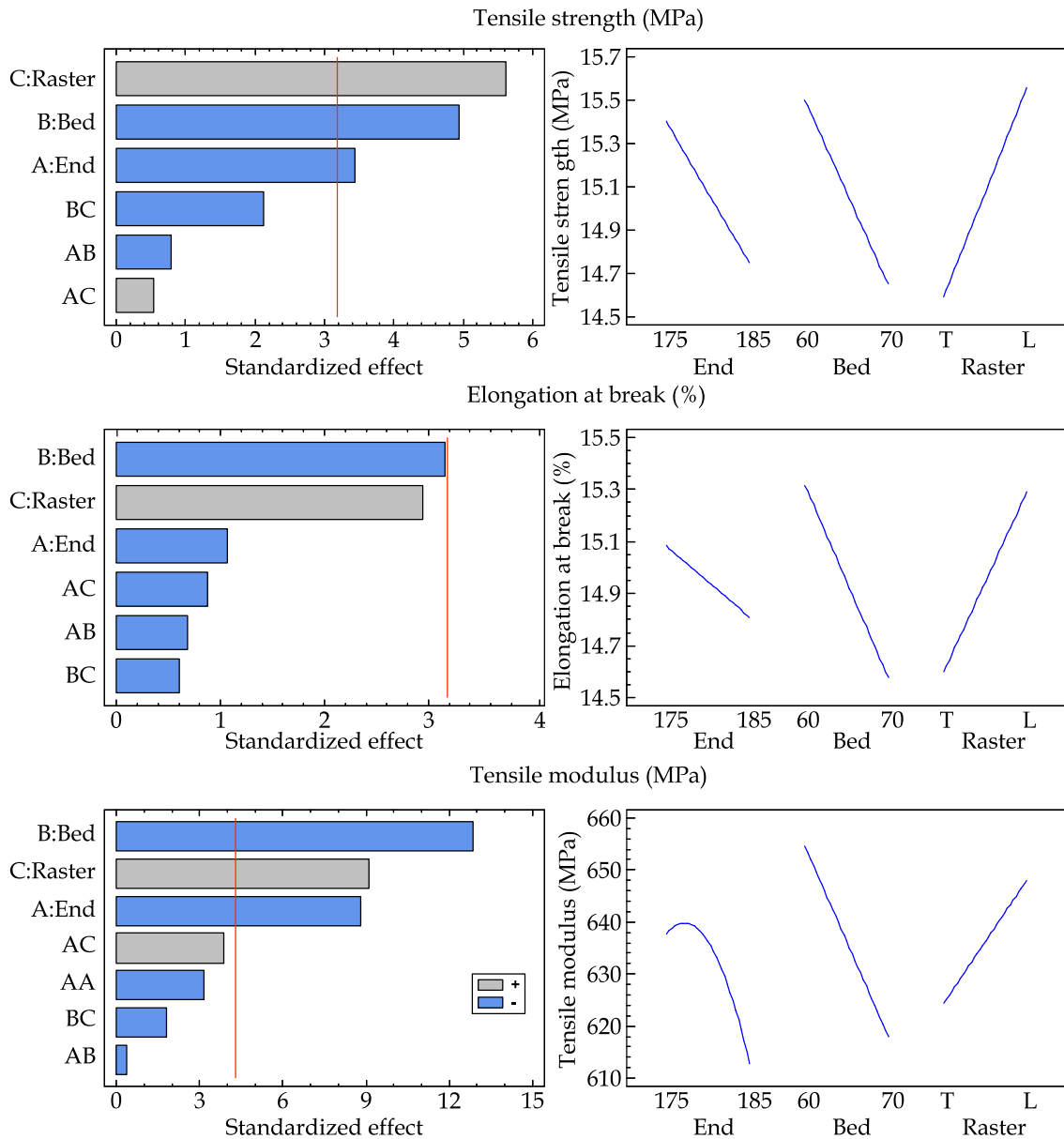


**Figure III.2.1.2.** Summary of the ANOVA analysis for PHPH 3D-printed samples by switching off the layer fan during the cooling process. This shows the Pareto diagram standardized effect (left row) and the main effects diagram (right row) for tensile strength, elongation at break and tensile modulus.

As for the tensile stress measured for the 3D-printed specimens with the layer fan activated, the most important parameter with the layer fan switched off was the raster angle. This result corroborates the high importance of the direction considered when analysing the results of the mechanical properties of 3D-printed parts due to the anisotropy showed. While tensile strength in 175–60 T samples was 15.1 MPa, the corresponding 3D-printed samples with a longitudinal pattern offered a slightly higher tensile strength of 16.2 MPa (which represents a percentage variation of 6.7 %). Under these conditions, with no layer fan, the effect of the heated bed temperature had a

significant influence. The tensile stress was reduced when the heated bed temperature increased, for example, 3D-printed samples with coded as 185-60 L achieved a maximum tensile strength of 16.0 MPa, whilst the 3D-printed samples with the heated bed at 70 °C reached a tensile strength of 14.5 MPa which represents a percentage difference of 9 %. This is related to the internal structure of P(3HB-co-3HHx) since most PHA, under slow cooling conditions, promote the formation of big spherulites that enhance microcrack formation and growing, as proposed by El-Hadi *et al.* [45]. The presence of these microcracks in the internal structure are responsible for a decrease in material's cohesion, with the subsequent decrease in tensile strength. Safari *et al.* analysed the effect of cooling temperature on the internal structure of P3HB films and the effect on final properties [46]. They observed a clear decrease in tensile strength as the cooling rate increased.

Additionally, the temperature used in the hot end also had a negative effect on the tensile strength. In the previous case, the intermediate temperature value (180 °C) showed a slight improvement in tensile strength, but regarding specimens with no layer fan, a decreasing tendency of tensile strength was observed with increased hot end temperature. In this case the reduction achieved was around 5.4 % for 3D-printed samples a heated bed at 70 °C and a using longitudinal (L) pattern. This is due to the fact that the improvement in the adhesion between the beads could improve with the increase in hotend temperature (as shown before). But this effect was not such an important to counteract the thermal degradation.

With regard to elongation at break, the statistical analysis showed that there was no parameter having a clear and relevant influence on it. However, as for samples obtained with layer fan, the heated bed temperature and the raster angle have certain effect over elongation at break. Again, the presence of microcracks in the internal structure results in premature failure and, therefore, in a lower elongation at break. As expected, the use of a longitudinal raster pattern (L) provides higher elongation at break values up to 16.1 %, while specimens obtained with transversal pattern (T) led to slightly lower elongation at break values of 15.2 %, thus indicating a percentage change of 5.5 %. The longitudinal raster pattern provides higher material's cohesion than the transversal raster pattern.

The elastic modulus was significantly affected by the heated bed temperature, the raster angle and hotend temperature. In the previous case in which the layer fan was used, a negative effect was also observed with increasing the hotbed temperature. During the 3D-printing process, these specimens were thermally affected by the bed temperature giving to somewhat annealing which resulted in lowering the stiffness. The use of a raster pattern aligned with the applied load direction, again had a positive effect on the tensile modulus. Finally, the effect of the nozzle temperature had a negative effect due to the thermal degradation as mentioned above. While 3D-printed samples with a transversal pattern and a heated bed at 60 °C and the hot end at 185 °C led to a tensile modulus of 614 MPa, slightly higher tensile modulus was obtained for same conditions but using a hot end temperature of 175 °C (tensile modulus of about 645 MPa, thus showing a percentage increase of 4.8 %).

**Figure III.2.1.3.** shows the ANOVA analysis regarding the effects of using the layer fan or not, on tensile properties of the 3D-printed specimens. As observed, the effect of using the layer fan had a positive influence on all three tensile parameters (tensile strength, tensile modulus, elongation at break). With regard to both tensile strength and elongation at break, despite having a positive influence as the ANOVA analysis revealed, there was no significant difference between using the layer fan or not. As mentioned above, when a slow cooling process is applied to a PHA polymer, the crystallization is enhanced and internal stresses are generated due to the shrinkage associated to crystallization. These internal stresses result in micro (or macro) crack formation with a negative effect on cohesion and toughness. The use of the layer fan leads to a faster cooling process which prevents from excessive crystallization and therefore, less micro (or macro) cracks are generated. The ANOVA statistical analysis showed that the use of the layer fan had a significant effect on the tensile modulus. The tensile modulus values obtained for 3D-printed samples coded as 175-60 L with the layer fan on was 846 MPa. In contrast, 3D-printed samples with the same conditions but without the layer fan showed a lower tensile modulus of 666 MPa (which stands for a percentage decrease of 21.2 %), thus confirming the importance of the layer fan on final mechanical properties. When the layer fan was used, the 3D-printed layers are cooled down faster, resulting in a structure with a lower degree of crystallinity [45]. A lower proportion of crystalline phase implies a higher presence of amorphous phase. PHA are characterized by having a Rigid Amorphous Fraction – RAF which has a higher stiffness, and therefore modifies the final tensile modulus of the material [47].

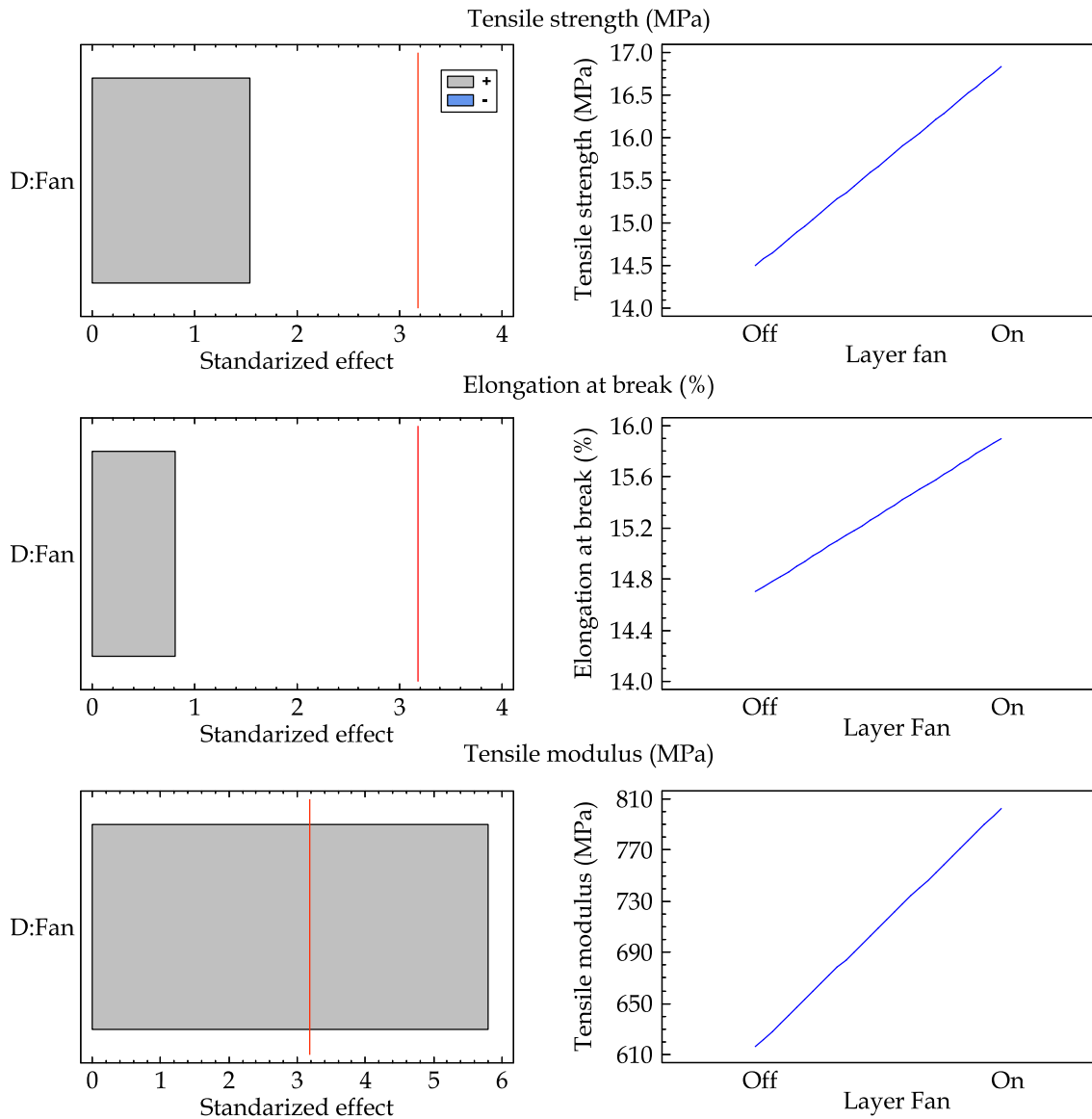


**Figure III.2.1.3.** Summary of the ANOVA analysis for 3D-printed P(3HB-co-3HHx) specimens with and without the layer fan, Pareto diagram standardized effect (left row) and the main effects diagram (right row) for tensile strength, elongation at break and tensile modulus.

Regarding other works with PHA in which a FDM was employed to obtain tensile test samples, four works can be highlighted. One parameter to consider is that different types of PHA polymer can be found in the market with different mechanical properties, so it is difficult to compare the here in results with those reported by other authors. Another parameter to consider is the effect of the aging in the samples. As mentioned above, the mechanical properties of the manufactured samples highly depend on the time elapsed from manufacture until characterization, since PHA undergo physical aging. Tian *et al.* employed a PHA polymer blended with wood flour and employed a micro-screw extrusion. They reported a maximum tensile strength of 40 MPa and an elongation at break of around 2.5 % for the composite containing 10 wt. %

wood flour load and a printing pattern of  $0^\circ$  [48]. Wu *et al.* used palm fiber to manufacture filaments of PHA for 3D-printing. The tensile strength of the neat PHA 3D-printed specimens was 16.5 MPa while in other work, they reported a tensile strength of 17.4 MPa for the neat PHA 3D-printed part, and a surprisingly high elongation at break of 600 % [49,50]. Finally, Valentini *et al.* manufactured filament for 3D-printing with P(3HB-co-3HHx) and subsequently, they obtained tensile test specimens for further characterization. They reported a tensile strength of 21.6 MPa and an elongation at break of 10.4 % for samples obtained using a raster angle of  $\pm 45^\circ$  [51].

#### **Fracture morphology of the P(3HB-co-3HHx) obtained by Additive Manufacturing.**

**Figure III.2.1.4.** gathers some FESEM images of the 3D-printed P(3HB-co-3HHx) specimens obtained by using a hot end at 185 °C, a heated bed at 70 °C and the fan layer switched on. The different conditions proposed in this work did not provide different surface morphologies due to the mechanical properties measured did not change in a wide range. **Figure III.2.1.4a.** shows the fracture surface of a 3D-printed specimen using a transversal raster (T), *i.e.* perpendicular to the applied load in the tensile test. In the fracture section, each of the raster had a direction parallel to the direction of breakage. Thus, the gap that can be seen was caused by the printing process. In contrast, **Figure III.2.1.4b.** shows the fracture surface of a 3D-printed specimen using a longitudinal pattern (L), resulting in the hole that can be observed having a triangular geometry (0.1 mm length) due to the shape adopted by the melt polymer during the 3D-printing process. In this sense, Torrado *et al.* [52] concluded that the presence of voids in the 3D-printing process was due to the deposition process of the different raster lines. In addition to the different shapes of the holes or voids formed depending on the 3D-printing direction, a clear difference also emerges in the morphology of the fracture surface. The 3D-printed specimen with a transverse raster (T) has a flat and smooth surface with no signs of plastic deformation. This type of microstructure is characterized by a separation of the raster prints giving rise to a flat surface as proposed by Torrado *et al.* [53]. On the other hand, if a longitudinal raster pattern (L) is used, the fracture morphology is remarkably different. In particular, it is possible to observe a rough surface as a result of the plastic deformation occurring before fracture. Quiles-Carrillo *et al.* and Petchwattana *et al.* propose that there is a relationship between the plastic deformation and the morphology of the fracture surface [54,55]. A brittle fracture is characterized by a flat and smooth surface, whereas higher plastic deformation provokes higher roughness to appear. The morphologies observed on fractured surfaces, are in agreement with the mechanical properties mentioned above. As it has been said

previously, the specimens printed with a longitudinal pattern (L) showed higher elongation at break. On the other hand, specimens with a transverse pattern (T), the elongation at break values were lower because the fracture was governed by the adhesion between the different raster lines.

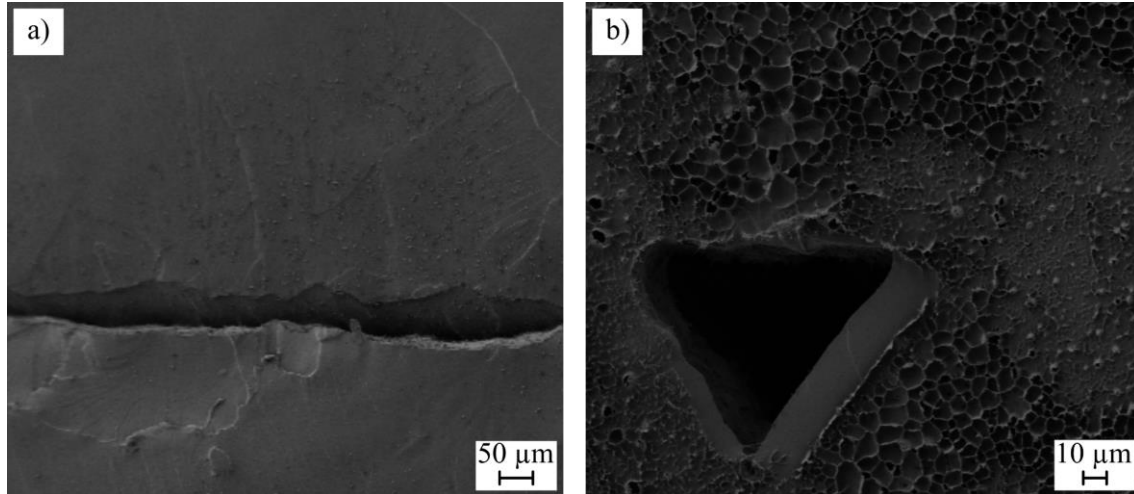


**Figure III.2.1.4.** Fracture morphology of 3D-printed P(3HB-co-3HHx) tensile specimens obtained by Field Emission Scanning Electron Microscopy FESEM: a) Image taken at 100 × magnifications of a specimen 3D-printed with transversal raster (T) and b) Image taken at 200 × magnifications of a specimen 3D-printed with longitudinal raster (L).

#### Thermal characterization of P(3HB-co-3HHx).

The main thermal properties obtained by DSC are gathered in **Table III.2.1.7.** with the aim of assessing the effect of the annealing conditions and the cooling of P(3HB-co-3HHx) on mechanical properties. To analyse the final state of the material after aging under the different processing conditions proposed, a single heating cycle from - 50 °C to 200 °C was scheduled. The P(3HB-co-3HHx) used in this research is characterized by a  $T_g$  close to 0 °C. This parameter must be considered to select the temperature of the heated bed so that it is above to ensure the best adhesion of the samples. This is a critical issue on P(3HB-co-3HHx) since its  $T_g$  is below room temperature and, therefore, only by using a heated bed above 60 °C good adhesion and absence of warping was observed on 3D-printed specimens. This effect was measured by Spoerk *et al.* that demonstrated that the adhesion forces to the heated bed increased above the  $T_g$  [56]. A noticeable effect after the aging process of the samples was the absence of a cold crystallization peak, which showed that the polymer reached a stable packed structure that could no longer be modified by heat treatment. On the other hand, different melting peaks appeared due to the fact that the material used is a semi-crystalline copolymer in which different types of crystals are formed and melt at

different temperatures in the temperature range between 110 °C and 161 °C. This parameter is of special interest because it allows the selection of the working temperature range. For this work, a temperature of 175 °C was selected as the minimum temperature needed in the 3D-printing process, which is high enough to ensure full melting of crystallites. It is worthy to highlight the increase of the temperature at which these characteristic melting peaks were observed as a function of the processing conditions used. This shift is related to the change in the degree of crystallinity of the samples. A higher degree of crystallinity results in an increase in the perfection of the crystals so that a higher temperature is required to melt them. This effect is described by Srubar *et al.* work in P3HB and P(3HH-co-3BV) subjected to different aging times. They observed a small increase in the melting temperatures in the characteristic DSC thermograms as the aging time increased [57].

**Table III.2.1.7.** Summary of the DSC test of the samples under different AM conditions.

Code	T <sub>g</sub> (°C)	T <sub>m1</sub> (°C)	T <sub>m2</sub> (°C)	T <sub>m3</sub> (°C)	ΔH <sub>m</sub> (J/g)	χ <sub>c</sub> (%)
175-60 F	0.8 ± 0.2	110.5 ± 0.1	123.2 ± 0.1	158.3 ± 0.2	38.0 ± 0.2	26.0 ± 0.1
175-70 F	1.0 ± 0.1	111.3 ± 0.3	124.7 ± 0.2	159.0 ± 0.2	39.2 ± 0.3	26.9 ± 0.2
175-80 F	0.8 ± 0.1	111.7 ± 0.2	125.2 ± 0.2	161.1 ± 0.1	40.5 ± 0.1	27.7 ± 0.1
175-60 NF	1.1 ± 0.2	111.6 ± 0.1	125.3 ± 0.1	160.6 ± 0.2	40.3 ± 0.1	27.6 ± 0.1

As proposed, an annealing process associated with the heated bed conditions used during printing had a clear effect on the degree of crystallinity of the sample which changes from 26.0 % for the sample manufactured with the lowest heated bed temperature up to 27.7 % for 3D-printed samples with a heated bed of 80 °C. Additionally, the removal of the layer fan gave rise to a similar effect to that produced by increasing the temperature of the heated bed. In this case the cooling rate of the polymer deposited in the melt state is slower, thus allowing to reach a higher degree of crystallinity. Vitorino *et al.* studied the effect of the cooling rate in a P3HB/babassu composites under non-isothermal conditions showing that the composite with 10 wt.% filler achieved a degree of crystallinity of 57.8 % at 2 °C/min and this value decreased up to 39.6 % with a cooling rate of 32 °C/min [58].



**Printability of P(3HB-co-3HHx).**

One of the main drawbacks when using P(3HB-co-3HHx) by AM is the difficulty in achieving good adhesion of the 3D-printed part to the heated bed due to the shrinkage related to fast crystallization as it has been aforementioned. At first, an attempt was made with the bed at room, to check 3D-printability in these conditions since the heated bed includes a new variable to the process. In this case, the first layer did not obtain a good adhesion. Due to this poor adhesion, a search for the minimum heated bed temperature to achieve good adhesion on the first layer was carried out. This minimum temperature was 60 °C; below this threshold, the adhesion of the first layer was poor. Subsequently, the 3D-printing process was not possible. Above this temperature threshold, adhesion is good enough to guarantee the 3D-printing process.

After overcoming the previously mentioned drawback, a second problem arose. This was related to the physical aging of PHA which leads to secondary crystallization which, in turn, leads to an additional shrinkage that could potentially compromise the 3D-printing process, mainly due to undesired warping. This phenomenon affecting PHA was analysed by Chan *et al.* for P(3HH-co-3BV) [59]. In order to ensure the adhesion of 3D-printed parts to the heated bed, a 4 mm brim around the shape was included in the G-code. This allowed good adhesion during all the 3D-printing process, thus preventing it from detachment. Despite considering all these issues, some of the combinations scheduled in the design of experiments resulted in some undesired warping, and the corresponding 3D-printing process was stopped. Additionally, when the heated bed temperature was set above 80 °C, some additional warping appeared, thus establishing 80 °C as the upper temperature threshold for P(3HB-co-3HHx) processing by 3D-printing. Usually, the polymer-bed adhesion improves by increasing the heated bed temperature, as in the case of ABS. This phenomenon is even much pronounced above the glass transition temperature of the polymer. Above  $T_g$ , the polymer achieves a higher chain mobility, thus improving the adhesion to the bed [56]. Under high heated bed temperatures, P(3HB-co-3HHx) crystallization was enhanced, and hence a higher shrinkage was obtained, so that the warping phenomena was more noticeable.

For P(3HB-co-3HHx), the adhesion strength to the bed is also linked to the degree of crystallinity that the samples acquire. This parameter can be estimated by using infrared spectroscopy as proposed by Kansiz *et al.* in PHA [60]. The 1739  $\text{cm}^{-1}$  band is usually assigned to the amorphous domain while the 1722  $\text{cm}^{-1}$  band corresponds to the crystalline phase. Depending on the prominence of each one of these characteristic

bands, the degree of crystallinity of a sample can be compared qualitatively. In this case, changes in these bands when the temperature of the heated bed was modified, was collected by FTIR and the results are shown in **Figure III.2.1.5.**, which also includes the deconvoluted peaks.

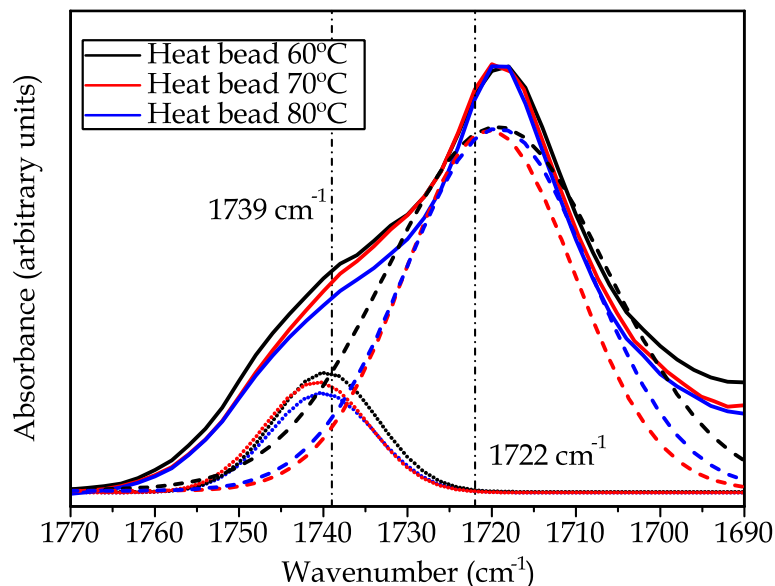


**Figure III.2.1.5.** Comparison of the normalized FTIR spectra in the 1770 - 1690  $\text{cm}^{-1}$  range, for 3D-printed specimens with different heated bead temperatures, a constant hotend of 175  $^{\circ}\text{C}$ , and the layer fan switched on. Deconvoluted peaks are indicated in dashed lines.

For the different temperatures considered, it can be seen that the higher the heated bed temperature, the absorption of the band associated with the amorphous part decreases, the deconvoluted peak obtained at 1722  $\text{cm}^{-1}$  was also reduced. This indicates that P(3HB-co-3HHx) has reached a higher degree of crystallinity. As a result, samples have higher shrinkage, giving rise to warping problems above 80  $^{\circ}\text{C}$ . These results agree with those reported by Gopi *et al.* [61]. They concluded that the degree of crystallinity acquired by the sample is clearly influenced by the cooling conditions which is a key parameter in 3D-printing. They also reported an increase in crystallinity on PHA after isothermal crystallization (or annealing). The degree of crystallization was higher as the annealing temperature increased. This effect could also be observed in the DSC characterization analysis mentioned above.

In addition to the heated bed temperature, there is also a parameter that plays a key role in the cooling process. When layer fan is switched on during the 3D-printing process, the melt polymer through the nozzle cools down quickly. In Xie *et al.* work the effect of cooling rates on different PHA was analysed. In all cases, a higher degree of crystallinity was achieved at slow cooling rates [62].

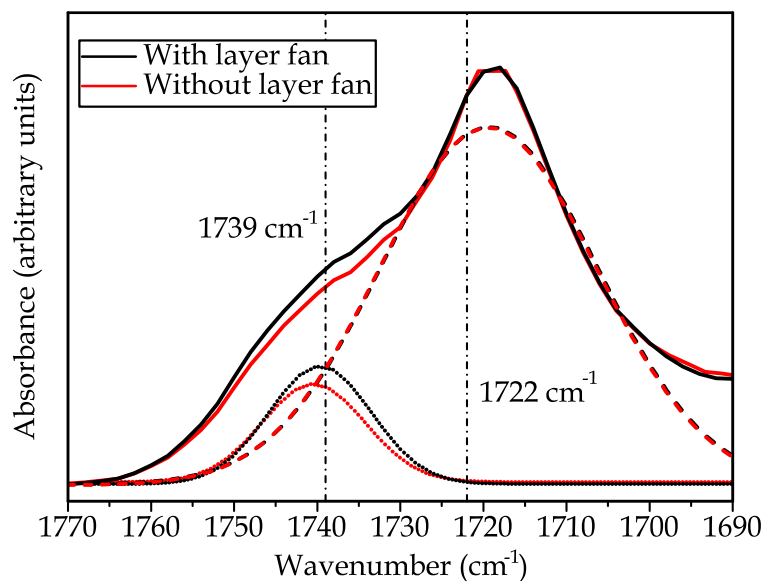


**Figure III.2.1.6.** Comparison of the normalized FTIR spectra in the 1770 – 1690  $\text{cm}^{-1}$  range, for different samples 3D-printed at 175 °C hotend and 60 °C heated bed with and without layer fan. Deconvoluted peaks are indicated in dashed lines.

As mentioned above, when a higher degree of crystallinity was reached, the dimensional shrinkage was more pronounced leading to warping at heated bed temperatures above 70 °C (without layer fan) thus limiting the processing range. This phenomenon can be seen in **Figure III.2.1.6**. In this case FTIR spectra with a constant nozzle temperature of 175 °C and a heated bed of 60 °C were compared depending on the use or not of the layer fan. When the layer fan is switched off, a higher degree of crystallinity was acquired by P(3HB-co-3HHx) as one can see since the deconvoluted peak of the amorphous region had lower intensity.

Finally, the temperatures at which P(3HB-co-3HHx) could be processed ranged from 175 °C to 185 °C in the heat zone 1. At lower temperatures, the stepper motor was not able to achieve continuous screw rotation and, therefore, the extrusion of the material was not uniform. The maximum temperature at which it was possible to process P(3HB-co-3HHx) was limited by the jam formation. Above 185 °C, the heat zone 2 exceeded 104 °C due to heat transmission along the screw and the printing process was not possible. The used P(3HB-co-3HHx) had a broad melting range with the onset located at around 100 °C, while the end set is close to 165 °C as it is a copolymer of P3HB and P3HH [38]. To prevent jam formation, a single-screw equipment requires the material to be in a solid state in the initial zone and then melt progressively along the screw [7].

**Visual appearance of the P(3HB-co-3HHx) 3D-printed parts.**

In **Figure III.2.1.7.**, an example of some of the P(3HB-co-3HHx) 3D-printed parts can be seen. It includes examples of the specimens used for mechanical characterization, with both types of patterns used in the longitudinal (L) and transverse (T) directions. In addition, these incorporate the necessary brim to achieve the correct manufacturing process and avoid detachment.

Moreover, other more complex shapes were 3D-printed to assess the printability of P(3HB-co-3HHx). In general, the visual appearance of the 3D-printed parts was satisfactory. It should be noted that no retraction movements have been used because the 3D-printer equipped with the single-screw, does not deal with this type of movement properly. Despite this, there has been no significant stringing as it can be seen in the benchy.

Regarding the level of detail, in any case is not very high, because the configuration used is the same as that of the test specimens, in which a layer height of 0.4 mm and a line width of 0.8 mm was used.

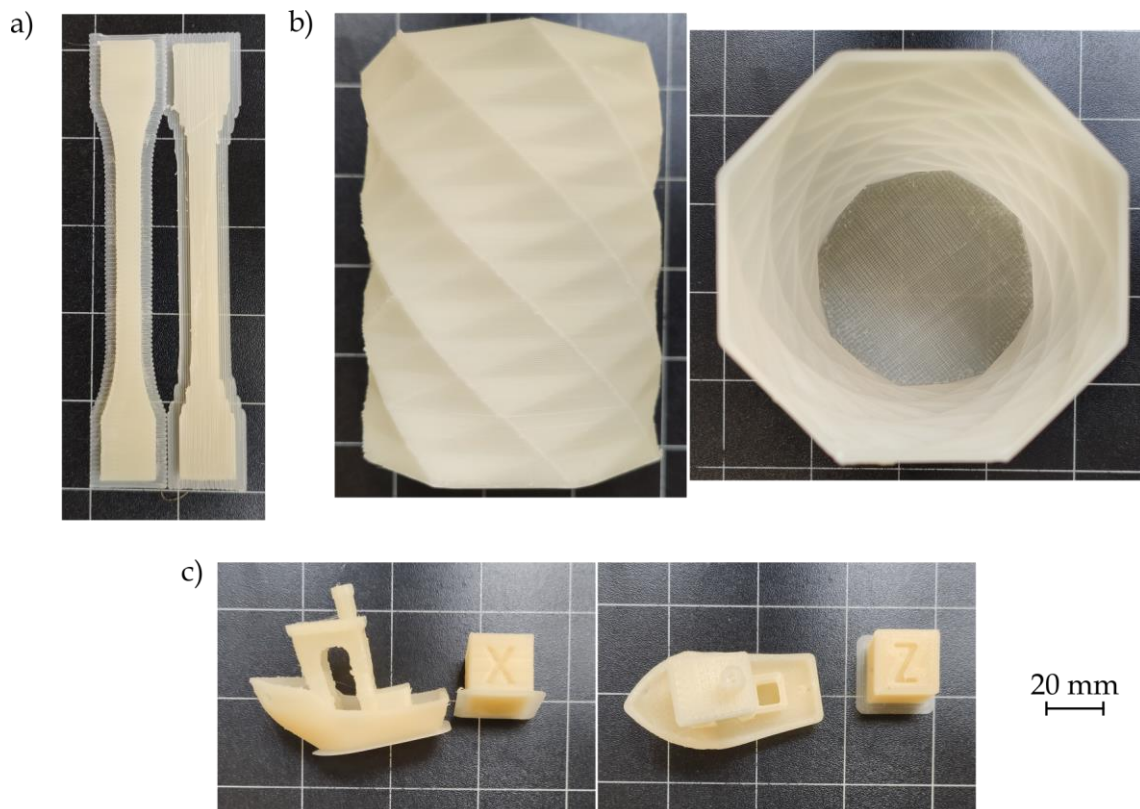


**Figure III.2.1.7.** Examples of the P(3HB-co-3HHx) 3D-printed parts: a) dog bone samples with both infills; b) pencil pot and c) benchy and a calibration cube.

**CONCLUSIONS.**

The effect of different 3D-printing parameters for AM with P(3HB-co-3HHx) were analysed. Due to the high sensitiveness of P(3HB-co-3HHx) to thermal degradation during processing as a result of the very narrow processing window, this work has concluded it is possible to 3D-print high quality parts without filament, by using a 3D-printer with a coupled single screw extruder fed with P(3HB-co-3HHx) pellets. The most relevant parameter having a remarkable effect on mechanical properties is the raster angle. As expected, the best results were obtained for those samples manufactured with a longitudinal raster pattern (L) aligned with the applied loading direction in the tensile test. Regarding the temperature ranges, the hot end allowed to improve the beads adhesion that improved the mechanical performance, but above 180 °C this effect disappeared due to the thermal degradation of the polymer. The effect of the heated bed temperature was linked with the layer fan used for the cooling. Under slow cooling conditions, the mechanical properties were rather poor due to a higher degree of crystallinity achieved that typically promotes crack formation in the internal structure. Changes in the internal structure of the samples were observed by FTIR and DSC showing that the modification of the printing parameters had an effect in the polymer internal structure that promoted the differences in the mechanical properties. As it has been shown in this work, the effect of the working temperatures and cooling conditions play a key role during the manufacturing process. In future works in which a PHA is manufactured by 3D-printing, these parameters must be considered as relevant to assess the desired final properties

**ACKNOWLEDGEMENTS.**

This research is a part of the grant PID2020-116496RB-C22 funded by MCIN/AEI/10.13039/501100011033. Authors also thank Generalitat Valenciana-GVA for funding this research through the grant numbers AICO/2021/025 and CIGE/2021/094. Juan Ivorra-Martinez wants to thank the Spanish Ministry of Science, Innovation and Universities for his FPU grant (FPU19/01759). Jaume Gomez-Caturla wants to thank Generalitat Valenciana-GVA, for his FPI grant (ACIF/2021/185) and grant FPU20/01732 funded by MCIN/AEI/10.13039/ 501100011033 and by ESF Investing in your future. Microscopy services of the Universitat Politècnica de València - UPV are acknowledged for their help in collecting and analysing the FESEM images.

#### REFERENCES.

1. Hull, C.W. Method for production of three-dimensional objects by stereolithography. US4575330A. 1998.
2. Crump, S.S. Apparatus and method for creating three-dimensional objects. US4801477A. 1989.
3. Gardan, J. Smart materials in additive manufacturing: state of the art and trends. *Virtual and Physical Prototyping* **2019**, *3*, 33–99 doi: 10.1080/17452759.2018.1518016.
4. Singh, M.; Jonnalagadda, S. Advances in bioprinting using additive manufacturing. *European Journal of Pharmaceutical Sciences* **2020**, *143*, 105167–105180 doi: 10.1016/j.ejps.2019.105167.
5. Singh, S.; Singh, G.; Prakash, C.; Ramakrishna, S. Current status and future directions of fused filament fabrication. *Journal of Manufacturing Processes* **2020**, *55*, 288–306 doi: 10.1016/j.jmapro.2020.04.049.
6. Gonzalez-Gutierrez, J.; Cano, S.; Schuschnigg, S.; Kukla, C.; Sapkota, J.; Holzer, C. Additive manufacturing of metallic and ceramic components by the material extrusion of highly-filled polymers: A review and future perspectives. *Materials* **2018**, *11*, 840–876 doi: 10.3390/ma11050840.
7. Liu, S.; Zhao, P.; Wu, S.; Zhang, C.; Fu, J.; Chen, Z. A pellet 3D printer: device design and process parameters optimization. *Advances in Polymer Technology* **2019**, *2019*, 1–8 doi: 10.1155/2019/5075327.
8. Singamneni, S.; Smith, D.; LeGuen, M.J.; Truong, D. Extrusion 3D printing of polybutyrate-adipate-terephthalate-polymer composites in the pellet form. *Polymers*. **2018**, *10*, 922–935 doi: 10.3390/polym10080922.
9. Solomon, I.J.; Sevel, P.; Gunasekaran, J. A review on the various processing parameters in FDM. *Materials today: Proceedings*, **2021**, *37*, 509–514 doi: 10.1016/j.matpr.2020.05.484.

10. Rodríguez-Panes, A.; Claver, J.; Camacho, A.M. The influence of manufacturing parameters on the mechanical behaviour of PLA and ABS pieces manufactured by FDM: a comparative analysis. *Materials*. **2018**, *11*, 1333–1354 doi: 10.3390/ma11081333.
11. Bermudez, D.; Quiñonez, P.A.; Vasquez, E.J.; Carrete, I.A.; Word, T.J.; Roberson, D.A. A comparison of the physical properties of two commercial 3D printing PLA grades. *Virtual and Physical Prototyping* **2021**, *16*, 178–195 doi: 10.1080/17452759.2021.1910047.
12. Anjum, A.; Zuber, M.; Zia, K.M.; Noreen, A.; Anjum, M.N.; Tabasum, S. Microbial production of polyhydroxyalkanoates (PHAs) and its copolymers: a review of recent advancements. *International Journal of Biological Macromolecules* **2016**, *89*, 161–174 doi: 10.1016/j.ijbiomac.2016.04.069.
13. Kovalcik, A. Recent advances in 3D printing of polyhydroxyalkanoates: a review. *The EuroBiotech Journal* **2021**, *5*, 48–55 doi: 10.2478/ebtj-2021-0008.
14. Diederichs, E.V.; Picard, M.C.; Chang, B.P.; Misra, M.; Mielewski, D.F.; Mohanty, A.K. Strategy to improve printability of renewable resource-based engineering plastic tailored for fdm applications. *ACS Omega* **2019**, *4*, 20297–20307 doi: 10.1021/acsomega.9b02795.
15. Kumar, R.; Kumar, M.; Chohan, J.S. The role of additive manufacturing for biomedical applications: A critical review. *Journal of Manufacturing Processes* **2021**, *64*, 828–850 doi: 10.1016/j.jmapro.2021.02.022.
16. Relinque, J.J.; de León, A.S.; Hernández-Saz, J.; García-Romero, M.G.; Navas-Martos, F.J.; Morales-Cid, G.; Molina, S.I. Development of surface-coated poly(lactic acid)/polyhydroxyalkanoate (PLA/PHA) nanocomposites. *Polymers* **2019**, *11*, 400–412 doi: 10.3390/polym11030400.
17. Menčík, P.; Přikryl, R.; Stehnová, I.; Melčová, V.; Kontárová, S.; Figalla, S.; Alexy, P.; Bočkaj, J. Effect of selected commercial plasticizers on mechanical, thermal, and morphological properties of poly(3-hydroxybutyrate)/poly(lactic acid)/plasticizer biodegradable blends for three-dimensional (3D) print. *Materials*. **2018**, *11*, 1893–1913 doi: 10.3390/ma11101893.

18. Kovalcik, A.; Sangroniz, L.; Kalina, M.; Skopalova, K.; Humpolíček, P.; Omastova, M.; Mundigler, N.; Müller, A.J. Properties of scaffolds prepared by fused deposition modeling of poly(hydroxyalkanoates). *International Journal of Biological Macromolecules* **2020**, *161*, 364–376 doi: 10.1016/j.ijbiomac.2020.06.022.
19. Pereira, T.; Silva, M.; Oliveira, M.; Maia, I.; Silva, J.; Costa, M.; Thiré, R. Effect of process parameters on the properties of selective laser sintered poly(3-hydroxybutyrate) scaffolds for bone tissue engineering. *Virtual and Physical Prototyping* **2012**, *7*, 275–285 doi: 10.1080/17452759.2012.738551.
20. Singh, K. Experimental study to prevent the warping of 3D models in fused deposition modeling. *International Journal of Plastics Technology* **2018**, *22*, 177–184 doi: 10.1007/s12588-018-9206-y.
21. Morales, M.A.; Atencio Martinez, C.L.; Maranon, A.; Hernandez, C.; Michaud, V.; Porras, A. Development and characterization of rice husk and recycled polypropylene composite filaments for 3d printing. *Polymers* **2021**, *13*, 1067–1084 doi: 10.3390/polym13071067.
22. Spoerk, M.; Holzer, C.; Gonzalez-Gutierrez, J. Material extrusion-based additive manufacturing of polypropylene: a review on how to improve dimensional inaccuracy and warpage. *Journal of Applied. Polymer Science* **2020**, *137*, 48545–48561 doi: 10.1002/app.48545.
23. Kabe, T.; Hongo, C.; Tanaka, T.; Hikima, T.; Takata, M.; Iwata, T. High tensile strength fiber of poly[(R)-3-hydroxybutyrate-co-(R)-3-hydroxyhexanoate] processed by two-step drawing with intermediate annealing. *Journal of Applied Polymer Science* **2015**, *132*, 41258–41266 doi: 10.1002/app.41258.
24. Kabe, T.; Tsuge, T.; Kasuya, K.I.; Takemura, A.; Hikima, T.; Takata, M.; Iwata, T. Physical and structural effects of adding ultrahigh-molecular-weight poly[(R)-3-hydroxybutyrate] to wild-type poly[(R)-3-hydroxybutyrate]. *Macromolecules* **2012**, *45*, 1858–1865 doi: 10.1021/ma202285c.
25. Laycock, B.; Halley, P.; Pratt, S.; Werker, A.; Lant, P. The chemomechanical properties of microbial polyhydroxyalkanoates. *Progress in Polymer Science* **2014**, *39*, 397–442 doi: 10.1016/j.progpolymsci.2013.06.008.



26. Ivorra-Martinez, J.; Verdu, I.; Fenollar, O.; Sanchez-Nacher, L.; Balart, R.; Quiles-Carrillo, L. Manufacturing and properties of binary blend from bacterial polyester poly(3-hydroxybutyrate-co-3-hydroxyhexanoate) and poly( $\epsilon$ -caprolactone) with improved toughness. *Polymers* **2020**, *12*, 1118–1138 doi: 10.3390/POLYM12051118.
27. Cherpinski, A.; Torres-Giner, S.; Cabedo, L.; Lagaron, J.M. Post-processing optimization of electrospun submicron poly(3-hydroxybutyrate) fibers to obtain continuous films of interest in food packaging applications. *Food Additives & Contaminants: Part A* **2017**, *34*, 1817–1830 doi: 10.1080/19440049.2017.1355115.
28. Yeo, J.C.C.; Muiruri, J.K.; Thitsartarn, W.; Li, Z.; He, C. Recent advances in the development of biodegradable PHB-based toughening materials: approaches, advantages and applications. *Materials Science and Engineering: C* **2018**, *92*, 1092–1116 doi: 10.1016/j.msec.2017.11.006.
29. Xu, P.; Cao, Y.; Lv, P.; Ma, P.; Dong, W.; Bai, H.; Wang, W.; Du, M.; Chen, M. Enhanced crystallization kinetics of bacterially synthesized poly(3-hydroxybutyrate-co-3-hydroxyhexanoate) with structural optimization of oxalamide compounds as nucleators. *Polymer Degradation and Stability* **2018**, *154*, 170–176 doi: 10.1016/j.polymdegradstab.2018.06.001.
30. Mahmood, H.; Pegoretti, A.; Brusa, R.S.; Ceccato, R.; Penasa, L.; Tarter, S.; Checchetto, R. Molecular transport through 3-hydroxybutyrate-co-3-hydroxyhexanoate biopolymer films with dispersed graphene oxide nanoparticles: gas barrier, structural and mechanical properties. *Polymer Testing* **2020**, *81*, 106181–106190 doi: 10.1016/j.polymertesting.2019.106181.
31. Rajpurohit, S.R.; Dave, H.K. Effect of process parameters on tensile strength of FDM printed PLA part. *Rapid Prototyping Journal* **2018**, *24*, 1317–1324 doi: 10.1108/RPJ-06-2017-0134.
32. Dizon, J.R.C.; Espera, A.H.; Chen, Q.; Advincula, R.C. Mechanical characterization of 3D-printed polymers. *Additive Manufacturing* **2018**, *20*, 44–67 doi: 10.1016/j.addma.2017.12.002.
33. Jònec, C.; Racz, L. Effects of Raster Orientation, Infill rate and infill pattern on the mechanical properties of 3d printed materials. *Acta Universitatis Cibiniensis. Technical Series* **2017**, *69*, 23–30 doi: 10.1515/aucts-2017-0004.

34. Dave, H.K.; Patadiya, N.H.; Prajapati, A.R.; Rajpurohit, S.R. Effect of infill pattern and infill density at varying part orientation on tensile properties of fused deposition modeling–printed poly–lactic acid part. *Proceedings of the Institution of Mechanical Engineers, Part C: Journal of Mechanical Engineering Science* **2021**, *235*, 1811–1827 doi: 10.1177/0954406219856383.
35. Ayatollahi, M.R.; Nabavi–Kivi, A.; Bahrami, B.; Yazid Yahya, M.; Khosravani, M.R. The influence of in–plane raster angle on tensile and fracture strengths of 3D–printed PLA specimens. *Engineering Fracture Mechanics* **2020**, *237*, 107225–1072238 doi: 10.1016/j.engfracmech.2020.107225.
36. Alafaghani, A.; Qattawi, A.; Alrawi, B.; Guzman, A. Experimental optimization of fused deposition modelling processing parameters: a design for manufacturing approach. *Procedia Manufacturing* **2017**, *10*, 791–803 doi: 10.1016/j.promfg.2017.07.079.
37. Bordes, P.; Pollet, E.; Bourbigot, S.; Avérous, L. Structure and properties of PHA/clay nano–biocomposites prepared by melt intercalation. *Macromolecular Chemistry and Physics*. **2008**, *209*, 1473–1484 doi: 10.1002/macp.200800022.
38. Ivorra–Martinez, J.; Manuel–Mañogil, J.; Boronat, T.; Sanchez–Nacher, L.; Balart, R.; Quiles–Carrillo, L. Development and characterization of sustainable composites from bacterial polyester poly(3–hydroxybutyrate–co–3–hydroxyhexanoate) and almond shell flour by reactive extrusion with oligomers of lactic acid. *Polymers* **2020**, *12*, 1097–1120 doi: 10.3390/polym12051097.
39. Shojaeiarani, J.; Bajwa, D.S.; Rehovsky, C.; Bajwa, S.G.; Vahidi, G. Deterioration in the physico–mechanical and thermal properties of biopolymers due to reprocessing. *Polymers* **2019**, *11*, 58–75 doi: 10.3390/polym11010058.
40. Algarni, M. The influence of raster angle and moisture content on the mechanical properties of PLA parts produced by fused deposition modeling. *Polymers* **2021**, *13*, 237–249 doi: 10.3390/polym13020237.
41. Zhang, X.; Chen, L.; Mulholland, T.; Osswald, T.A. Effects of raster angle on the mechanical properties of PLA and Al/PLA composite part produced by fused deposition modeling. *Polymers for Advanced Technologies* **2019**, *30*, 2122–2135 doi: 10.1002/pat.4645.

42. Kurusu, R.S.; Demarquette, N.R.; Gauthier, C.; Chenal, J.-M. Effect of ageing and annealing on the mechanical behaviour and biodegradability of a poly(3-hydroxybutyrate) and poly(ethylene-co-methyl-acrylate-co-glycidyl-methacrylate) blend. *Polymer International* **2014**, *63*, 1085–1093 doi: 10.1002/pi.4616.
43. Kurusu, R.S.; Siliki, C.A.; David, T.; Demarquette, N.R.; Gauthier, C.; Chenal, J.M. Incorporation of plasticizers in sugarcane-based poly(3-hydroxybutyrate) (PHB): Changes in microstructure and properties through ageing and annealing. *Industria Crops and Prodproducts* **2015**, *72*, 166–174 doi: 10.1016/j.indcrop.2014.12.040.
44. Chen, L.; Mao, R.; Zhang, L.; Xu, J.; Li, D.; Bao, J.; Wang, Z. Dramatic toughness improvement of poly(3-hydroxybutyrate-co-3-hydroxyvalerate) by supercritical carbon dioxide-assisted annealing. *Polymers for Advanced Technologies* **2021**, *32*, 3646–3654 doi: 10.1002/pat.5373.
45. El-Hadi, A.; Schnabel, R.; Straube, E.; Müller, G.; Henning, S. Correlation between degree of crystallinity, morphology, glass temperature, mechanical properties and biodegradation of poly(3-hydroxyalkanoate) PHAs and their blends. *Polymer Testing* **2002**, *21*, 665–674 doi: 10.1016/S0142-9418(01)00142-8.
46. Safari, S.; van de Ven, T.G.M. Effect of crystallization conditions on the physical properties of a two-layer glassine paper/polyhydroxybutyrate structure. *Journal of Material Science* **2015**, *50*, 3686–3696 doi: 10.1007/s10853-015-8929-9.
47. Wang, S.; Chen, W.; Xiang, H.; Yang, J.; Zhou, Z.; Zhu, M. Modification and potential application of short-chain-length polyhydroxyalkanoate (scl-PHA). *Polymers* **2016**, *8*, 273–301 doi: 10.3390/polym8080273.
48. Tian, J.; Zhang, R.; Wu, Y.; Xue, P. Additive manufacturing of wood flour/polyhydroxyalkanoates (PHA) fully bio-based composites based on micro-screw extrusion system. *Materials & Design* **2021**, *199*, 109418–109432 doi: 10.1016/j.matdes.2020.109418.
49. Wu, C.-S.; Liao, H.-T.; Cai, Y.-X. Characterisation, biodegradability and application of palm fibre-reinforced polyhydroxyalkanoate composites. *Polymer Degradation and Stability* **2017**, *140*, 55–63 doi: 10.1016/j.polymdegradstab.2017.04.016.

50. Wu, C.-S. Characterization, functionality and application of siliceous sponge spicules additive-based manufacturing biopolymer composites. *Additive Manufacturing* **2018**, *22*, 13–20 doi: 10.1016/j.addma.2018.04.034.
51. Valentini, F.; Dorigato, A.; Rigotti, D.; Pegoretti, A. Polyhydroxyalkanoates/fibrillated nanocellulose composites for additive manufacturing. *Journal of Polymers and the Environment* **2019**, *27*, 1333–1341 doi: 10.1007/s10924-019-01429-8.
52. Torrado Perez, A.R.; Roberson, D.A.; Wicker, R.B. Fracture surface analysis of 3D-printed tensile specimens of novel ABS-based materials. *Journal of Failure Analysis and Prevention* **2014**, *14*, 343–353 doi: 10.1007/s11668-014-9803-9.
53. Torrado, A.R.; Roberson, D.A. Failure analysis and anisotropy evaluation of 3D-printed tensile test specimens of different geometries and print raster patterns. *Journal of Failure Analysis and Prevention* **2016**, *16*, 154–164 doi: 10.1007/s11668-016-0067-4.
54. Quiles-Carrillo, L.; Duarte, S.; Montanes, N.; Torres-Giner, S.; Balart, R. Enhancement of the mechanical and thermal properties of injection-moulded polylactide parts by the addition of acrylated epoxidized soybean oil. *Materials & Design* **2018**, *140*, 54–63 doi: 10.1016/j.matdes.2017.11.031.
55. Petchwattana, N.; Covavisaruch, S. Mechanical and morphological properties of wood plastic biocomposites prepared from toughened poly(lactic acid) and rubber wood sawdust (*hevea brasiliensis*). *Journal of Bionic Engineering* **2014**, *11*, 630–637 doi: 10.1016/S1672-6529(14)60074-3.
56. Spoerk, M.; Gonzalez-Gutierrez, J.; Sapkota, J.; Schuschnigg, S.; Holzer, C. Effect of the printing bed temperature on the adhesion of parts produced by fused filament fabrication. *Plastics Rubber and Composites*. **2018**, *47*, 17–24 doi: 10.1080/14658011.2017.1399531.
57. Srubar Iii, W.; Wright, Z.; Tsui, A.; Michel, A.; Billington, S.; Frank, C. Characterizing the effects of ambient aging on the mechanical and physical properties of two commercially available bacterial thermoplastics. *Polymer Degradation and Stability* **2012**, *97*, 1922–1929 doi: 10.1016/j.polymdegradstab.2012.04.011.

- 
58. Vitorino, M.B.C.; Cipriano, P.B.; Wellen, R.M.R.; Canedo, E.L.; Carvalho, L.H. Nonisothermal melt crystallization of PHB/babassu compounds. *Journal of Thermal Analysis and Calorimetry* **2016**, *126*, 755-769 doi: 10.1007/s10973-016-5514-7.
59. Chan, C.M.; Vandi, L.-J.; Pratt, S.; Halley, P.; Richardson, D.; Werker, A.; Laycock, B. Mechanical performance and long-term indoor stability of polyhydroxyalkanoate (PHA)-based wood plastic composites (WPCs) modified by non-reactive additives. *European Polymer Journal* **2018**, *98*, 337-346 doi: 10.1016/j.eurpolymj.2017.11.041.
60. Kansiz, M.; Domínguez-Vidal, A.; McNaughton, D.; Lendl, B. Fourier-transform infrared (FTIR) spectroscopy for monitoring and determining the degree of crystallisation of polyhydroxyalkanoates (PHAs). *Analytical and Bioanalytical Chemistry*. **2007**, *388*, 1207-1213 doi: 10.1007/s00216-007-1337-5.
61. Gopi, S.; Kontopoulou, M.; Ramsay, B.A.; Ramsay, J.A. Manipulating the structure of medium-chain-length polyhydroxyalkanoate (mcl-PHA) to enhance thermal properties and crystallization kinetics. *International Journal Biological Macromolecules* **2018**, *119*, 1248-1255 doi: 10.1016/j.ijbiomac.2018.08.016.
62. Xie, Y.; Noda, I.; Akpalu, Y.A. Influence of cooling rate on the thermal behavior and solid-state morphologies of polyhydroxyalkanoates. *Journal of Applied Polymer Science* **2008**, *109*, 2259-2268 doi: 10.1002/app.28278.



Adapted from the original manuscript.

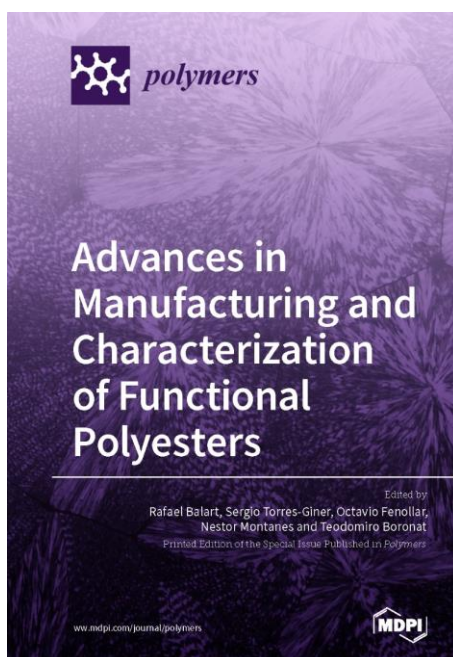
### III.2.2 Assessment of the mechanical and thermal properties of injection-moulded poly(3-hydroxybutyrate-co-3-hydroxyhexanoate)/hydroxyapatite nanoparticles parts for use in bone tissue engineering.

Juan Ivorra-Martinez<sup>1</sup>, Luis Quiles-Carrillo<sup>1</sup>, Teodomiro Boronat<sup>1</sup>, Sergio Torres-Giner<sup>2</sup> and José A. Covas<sup>3</sup>.

<sup>1</sup>Technological Institute of Materials - ITM, Universitat Politècnica de València - UPV, Plaza Ferrándiz y Carbonell 1, 03801 Alcoy (Spain).

<sup>2</sup>Novel Materials and Nanotechnology Group, Institute of Agrochemistry and Food Technology - IATA, Spanish National Research Council - CSIC, Calle Catedrático Agustín Escardino Benlloch 7, 46980 Paterna (Spain).

<sup>3</sup>Institute for Polymers and Composites, University of Minho, 4804-533 Guimarães (Portugal).



**Polymers.**

**2020, 12(6): 1389.**







Article

# Assessment of the Mechanical and Thermal Properties of Injection-Molded Poly(3-hydroxybutyrate-co-3-hydroxyhexanoate)/Hydroxyapatite Nanoparticles Parts for Use in Bone Tissue Engineering

Juan Ivorra-Martinez <sup>1</sup>, Luis Quiles-Carrillo <sup>1</sup>, Teodomiro Boronat <sup>1</sup>, Sergio Torres-Giner <sup>2,\*</sup> and José A. Covas <sup>3,\*</sup>

<sup>1</sup> Technological Institute of Materials (ITM), Universitat Politècnica de València (UPV), Plaza Ferrándiz y Carbonell 1, 03801 Alcoy, Spain; juaivmar@doctor.upv.es (J.I.-M.); luiquic1@epsa.upv.es (L.Q.-C.); tboronat@dim.upv.es (T.B.)

<sup>2</sup> Novel Materials and Nanotechnology Group, Institute of Agrochemistry and Food Technology (IATA), Spanish National Research Council (CSIC), Calle Catedrático Agustín Escardino Benlloch 7, 46980 Paterna, Spain

<sup>3</sup> Institute for Polymers and Composites, University of Minho, 4804-533 Guimarães, Portugal

\* Correspondence: storresginer@iata.csic.es (S.T.-G.); jcovas@dep.uminho.pt (J.A.C.); Tel.: +34-963-900-022 (S.T.-G.); +35-1253-510-320 (J.A.C.)

Received: 18 May 2020; Accepted: 17 June 2020; Published: 21 June 2020



**Abstract:** In the present study, poly(3-hydroxybutyrate-co-3-hydroxyhexanoate) [P(3HB-co-3HHx)] was reinforced with hydroxyapatite nanoparticles (nHA) to produce novel nanocomposites for potential uses in bone reconstruction. Contents of nHA in the 2.5–20 wt % range were incorporated into P(3HB-co-3HHx) by melt compounding and the resulting pellets were shaped into parts by injection molding. The addition of nHA improved the mechanical strength and the thermomechanical resistance of the microbial copolyester parts. In particular, the addition of 20 wt % of nHA increased the tensile ( $E_t$ ) and flexural ( $E_f$ ) moduli by approximately 64% and 61%, respectively. At the highest contents, however, the nanoparticles tended to agglomerate, and the ductility, toughness, and thermal stability of the parts also declined. The P(3HB-co-3HHx) parts filled with nHA contents of up to 10 wt % matched more closely the mechanical properties of the native bone in terms of strength and ductility when compared with metal alloys and other biopolymers used in bone tissue engineering. This fact, in combination with their biocompatibility, enables the development of nanocomposite parts to be applied as low-stress implantable devices that can promote bone reconstruction and be reabsorbed into the human body.

**Keywords:** P(3HB-co-3HHx); nHA; nanocomposites; mechanical properties; bone reconstruction

## 1. Introduction

Bone fracture is one of the most common injuries. Bone regeneration encompasses three stages, namely inflammation, bone production, and bone remodeling [1]. During the latter, it is extremely important to expose the bone to the natural load-bearing conditions associated to its function [2]. Currently, titanium alloys such as Ti-6Al-4V are the most used for the manufacture of orthopedic fixing devices and bone implants due to their excellent biocompatibility and high mechanical resistance [3]. However, they prevent the bone from being subjected to the required mechanical loadings [4]. Indeed, while natural bone has a modulus ranging between 8 to 25 GPa, metals have a modulus of 110–210 GPa, which results in the load being imparted onto the device rather than the bone which then causes a



**Abstract.**

In the present study, poly(3-hydroxybutyrate-*co*-3-hydroxyhexanoate) - P(3HB-*co*-3HHx) was reinforced with nanohydroxyapatite - nHA to produce novel nanocomposites for potential uses in bone reconstruction. Contents of nHA in the 2.5 - 20 wt.% range were incorporated into P(3HB-*co*-3HHx) by melt compounding and the resulting pellets were shaped into parts by injection moulding. The addition of nHA improved the mechanical strength and the thermo-mechanical resistance of the microbial copolyester parts. In particular, the addition of 20 wt.% of nHA increased the tensile modulus -  $E_t$  and flexural modulus -  $E_f$  by approximately 64 % and 61 %, respectively. At the highest contents, however, the nanoparticles tended to agglomerate, and the ductility, toughness, and thermal stability of the parts also declined. The P(3HB-*co*-3HHx) parts filled with nHA contents of up to 10 wt.% matched more closely the mechanical properties of the native bone in terms of strength and ductility when compared with metal alloys and other biopolymers used in bone tissue engineering. This fact, in combination with their biocompatibility, enables the development of nanocomposite parts to be applied as low-stress implantable devices that can promote bone reconstruction and be reabsorbed into the human body.

**Keywords:** P(3HB-*co*-3HHx); nHA; nanocomposites; mechanical properties; bone reconstruction.

---



**INTRODUCTION.**

Bone fracture is one of the most common injuries. Bone regeneration encompasses three stages, namely inflammation, bone production, and bone remodelling [1]. During the latter, it is extremely important to expose the bone to the natural load-bearing conditions associated to its function [2]. Currently, titanium alloys such as Ti-6Al-4V are the most used for the manufacture of orthopedic fixing devices and bone implants due to their excellent biocompatibility and high mechanical resistance [3]. However, they prevent the bone from being subjected to the required mechanical loadings [4]. Indeed, while natural bone has a modulus ranging between 8 to 25 GPa, metals have a modulus of 110 - 210 GPa, which results in the load being imparted onto the device rather than the bone which then causes a localized decrease in bone mineral density [5]. Meanwhile, metal ion leaching increases inflammation and irritation around the implant [6]. As a result, there is often a need for a second surgery to remove the fixation device, leading to higher medical costs and greatly increased patient discomfort. A current alternative is the use of fixation devices that metabolize in the human body after fulfilling their function [7]. In particular, the use of biopolymers with biocompatibility and reabsorption capacities is very promising [8]. Biocompatibility involves the capability of a given substance to perform with a suitable host response in a particular use. Furthermore, no substance or material can be biocompatible if it releases cytotoxic substances. The degradation process of a given biopolymer within the human body consists of two phases. First, the biopolymer chains break, either as a consequence of hydrolysis or due to the action of a body enzyme. Thereafter, the human body assimilates the fragments. For this purpose, either a phagocytotic or metabolic process develops [9]. Surface porosity, shape, and tissue environment, including chemical build-up of the materials, play a significant role in biocompatibility [10,11].

For the past few decades, polymers of the polyhydroxyalkanoates - PHAs family have been paving the way for the development of new biomedical products. These microbial biopolyesters degrade when exposed to marine sediment, soil or compost. Hydrolysing enzymes, so-called PHA depolymerases, to degrade PHA into their oligomers and monomers, which subsequently act as nutrients inside the cells [12]. Their potential as alternatives for the manufacture of a wide range of medical devices, such as absorbable sutures, surgical pins or staples, is well recognized on account of their biodegradable nature as well as disintegration by surface erosion [13]. Broadly, the

biocompatibility of PHA materials can be differentiated into two categories, immunocompatibility and nonallergic response. The former involves the extent of antigenic resemblance between the tissues of various individuals that determines the acceptance or rejection of allografts. PHAs are essentially immunocompatibility for use in medical applications, that is, their materials should not elicit harsh immune responses upon introduction into the soft tissues or blood of a host organism [14]. Indeed, 3-hydroxybutyrate (3HB), the main monomeric constituent of most PHAs, is a result of cellular metabolism that is formed by oxidation of fatty acid within the liver cells and it is a usual component of human blood [15]. Other previous studies have also revealed that PHA did not elicit an allergic response or any hypersensitive immune reaction [10,16].

Depending on the number of carbon atoms in the monomers, PHAs can be classified as short-chain-length PHAs (scl-PHAs; 3 – 5 C-atoms) and medium-chain-length PHAs (mcl-PHAs; 6 – 14 C-atoms). Generally, scl-PHAs are rigid and brittle, while mcl-PHAs have higher flexibility and toughness [17]. Poly(3-hydroxybutyrate) – P3HB is the simplest and most common member of the PHA family. However, the high brittleness of P3HB and other scl-PHAs, such as poly(3-hydroxybutyrate-co-3-hydroxyvalerate) – P(3HH-co-3HV) with less than 15 mol % fraction of 3-hydroxyvalerate (3HV), restricts their application in bone fixing devices [18]. In this regard, poly(3-hydroxybutyrate-co-3-hydroxyhexanoate) – P(3HB-co-3HHx), represents a recent addition to the group of PHAs for biomedical applications. The introduction of the mcl 3-hydroxyhexanoate – 3HHx co-monomer into the polymer backbone of P3HB significantly increases the flexibility and reduces stiffness [19]. Therefore, the macroscopic properties of P(3HB-co-3HHx) vary with the proportion of each monomer in the copolyester [20], in which the higher the 3HHx content, the higher the ductility [21]. Apart from the changes in the mechanical properties, the most remarkable transformation that P(3HB-co-3HHx) brings along is its ability to undergo enzymatic degradation by lipase [22], which is not seen in either P3HB or P(3HH-co-3BV). Prior experiments have shown that materials based on P(3HB-co-3HHx) and other mcl-PHAs have good biocompatibility for chondrocytes [23], nerve cells [24] as well as osteoblast and fibroblast cells [25,26]. This property should make P(3HB-co-3HHx) a suitable choice for several tissue engineering applications since it adds a further variable that can be used to tailor its degradation [27].

While PHAs are biocompatible substrates for cell propagation and are potentially an effective template for the repair of osseous and chondral defects, there is still a need

to improve the mechanical strength, thermal resistance, and biological response of these biomaterials in order to make them more suitable for bone tissue engineering. Osteoconductive fillers can be introduced into polymer matrices with the aim of improving the mechanical properties and also accelerating the bone repair process by favouring the growth of bone cells inside the pores [28,29]. For example, calcium orthophosphates –  $\text{CaPO}_4$  have bioactive properties that increase bone cell proliferation, the so-called osteoinduction [30]. As a rule, both the mechanical resistance and bioactivity of composites prepared with collagen, chitin and/or gelatine, increase with increasing  $\text{CaPO}_4$  content [31]. Hydroxyapatite,  $\text{Ca}_5(\text{PO}_4)_3\text{OH}$ , which is the principal crystalline constituent of bone, shows a high degree of biocompatibility and good osteoconductive and osteoinductive properties. Therefore, nanohydroxyapatite – nHA is the most widely used bioceramic for the manufacture of medical devices and dental implants [32]. This fact is exemplified by the production of prostheses for cranial reconstruction using poly(methyl methacrylate) –PMMA nHA composites [33]. Indeed, nHA exists in the human bone in the form of nanometre-sized threads, thus ensuring biocompatibility. At present, it is mostly used to produce surface coatings, as its biomimetic mineralization enables the production of biomaterials with biomimetic compositions and hierarchical micro/nanostructures that closely mimic the extracellular matrix of native bone tissue [34,35].

Due to the well-known high bioactive properties in terms of bone regeneration of PHA/nHA composites, this study aims to determine the physical properties of injection-moulded parts made of P(3HB-co-3HHx)/nHA composites, for potential use as bone resorbable devices. To this end, different contents of nHA were incorporated into P(3HB-co-3HHx) and the mechanical, thermal, and thermo-mechanical properties were analysed and compared to some metal alloy-based solutions currently available in the biomedical field. As a first, the parts showed sufficient dimensional and thermal stability for bone tissue engineering and their elasticity was nearer to that of the natural bone when compared to the metal alloys used for bone implants.

## **MATERIALS AND METHODS.**

### **Materials.**

P(3HB-co-3HHx) copolymer was supplied by Ercros S.A. (Barcelona, Spain) as ErcrosBio PH110. The ratio of 3HHx in the copolyester is ~ 10 mol % and its number average molecular weight –  $M_w$  is  $1.22 \times 10^5$  g/mol. It shows a Melt Flow Index – MFI of 1 g/10 min (2.16 kg/160 °C) according to the ISO 1133-2 standard and a true density of

1.20 g/cm<sup>3</sup> following the UNE EN ISO 1183-1 standard. Hydroxyapatite synthetic nano-powder was procured from Sigma-Aldrich S.A. (Madrid, Spain) with commercial reference 677418. According to the manufacturer, it presents the following properties: particle size < 200 nm, surface area > 9.4 m<sup>2</sup>/g by Brunauer-Emmett-Teller - BET analysis, purity ≥ 97 %, and M<sub>w</sub> of 502.31 g/mol.

**Preparation and Processing of P(3HB-co-3HHx)/nHA parts.**

Both P(3HB-co-3HHx) pellets and nHA powder were dried separately for at least 6 h at 80 °C in a dehumidifying oven from Industrial Marsé S.A. (Barcelona, Spain). The materials were then pre-mixed manually in closed zip-bags at the ratios presented in **Table III.2.2.1.**

**Table III.2.2.1.** Code and composition of the samples prepared according to the % weight content - wt.% of P(3HB-co-3HHx) and nHA.

Sample	P(3HB-co-3HHx) (wt.%)	nHA (wt.%)
P(3HB-co-3HHx)	100	0
P(3HB-co-3HHx)/2.5nHA	97.5	2.5
P(3HB-co-3HHx)/5nHA	95	5
P(3HB-co-3HHx)/10nHA	90	10
P(3HB-co-3HHx)/20nHA	80	20

The different P(3HB-co-3HHx) and nHA mixtures weighing 800 g were melt-compounded using a co-rotating twin-screw extruder from Dupra S.L. (Castalla, Spain). It features two screws with a diameter - D of 25 mm and a length-to-diameter ratio (L/D) of 24, while the modular barrel is equipped with 4 individual heating zones coupled to a strand die. Further details of the extruder can be found elsewhere [36]. Extrusion was performed with a screw speed of 20 - 25 rpm to prevent material degradation due to shear-induced viscous dissipation, a feed of 1.2 kg/h, and a barrel set temperature profile of 110 - 120 - 130 - 140 °C from hopper to die. The extruded filaments were cooled down in an air stream and pelletized using an air-knife unit.

Test parts for characterization were obtained by injection moulding. The equipment (Meteor 270/75, Mateu & Solé, Barcelona, Spain) was operated with a barrel set temperature profile of 115 - 120 - 125 - 130 °C from hopper to nozzle, with the mold kept at 60 °C. An injection time of 1 s was used to avoid material degradation by shear-induced viscous dissipation. The clamping force was 75 tons and the cooling time was set at 60 s. Parts with a thickness of approximately 4 mm were obtained for characterization. Since P(3HB-co-3HHx) develops secondary crystallization with time,



the parts were allowed to age for 14 days at room temperature prior to characterization.

### Mechanical Tests.

Uniaxial tensile tests were performed according to the ISO 527-2: 2012 standard using a universal testing machine ELIB-50 (Ibertest S.A., Madrid, Spain) fitted with a load cell of 5 kN and using a 3542-050M-050-ST extensometer from Epsilon Technology Corporation (Jackson, WY, USA). Flexural properties were determined following the ISO 178: 2011 standard using the same equipment. Both tests were carried out at 5 mm/min using  $150 \times 10 \times 4$  mm<sup>3</sup> parts. The main parameters obtained were tensile strength -  $\sigma_t$ , elongation at break -  $\varepsilon_b$ , tensile modulus -  $E_t$ , flexural strength -  $\sigma_f$  and flexural modulus -  $E_f$ .

Charpy impact tests were performed following the ISO 179-1: 2010 standard. Samples with a V-shaped notch with a radius of 0.25 mm and dimensions  $80 \times 10 \times 4$  mm<sup>3</sup> were subjected to the impact of a 1-J pendulum impact tester from Metrotec S.A. (San Sebastián, Spain). Shore hardness was measured with a 673-D durometer (J. Bot Instruments, Barcelona, Spain), following the ISO 868: 2003 standard. At least six parts were tested for each mechanical test.

### Thermal Tests.

Samples weighing 5 - 10 mg were analysed by Differential Scanning Calorimetry - DSC in a Q200 from TA Instruments (New Castle, DE, USA) to study the thermal transitions. The samples were subjected to a three-stage thermal cycle in which the samples were first heated from - 50 to 200 °C and cooled down to - 50 °C in order to eliminate the thermal history and then reheated to 200 °C. All the heating and cooling scans were performed at 10 °C/min. Testing was performed under inert atmosphere using a nitrogen flow of 50 mL/min. Parameters like glass transition temperature -  $T_g$ , melting temperature -  $T_m$ , cold crystallization temperature -  $T_{cc}$ , melting enthalpy -  $\Delta H_m$ , cold crystallization enthalpy -  $\Delta H_{cc}$  were obtained from DSC runs. The degree of crystallinity -  $\chi_c$  was calculated using **Equation III.2.2.1.** [37]:

$$\chi_c(\%) = \frac{\Delta H_m}{\Delta H_m^0 \cdot (1 - w)} \cdot 100 \quad \text{Equation III.2.2.1.}$$

Where  $\Delta H_m^0$  (J/g) is the theoretical value of a fully crystalline of P(3HB-co-3HHx), taken as 146 J/g [38], an 1 - w indicates the weight fraction of P(3HB-co-3HHx) in the sample.

Thermogravimetric analysis - TGA was performed to determine the thermal stability of the injection-moulded parts. Samples weighing 10 - 20 mg were heated from 30 to 700 °C at a heating rate of 20 °C/min in a TGA 100 from Linseis Messgeräte GmbH (Selb, Germany) under nitrogen atmosphere with a flow rate of 25 mL/min. All thermal tests were carried out in triplicate. The initial degradation temperature of the sample was considered at 5 wt.% loss -  $T_{5\%}$  and the maximum degradation rate was taken as the peak in the first derivative curve -  $T_{max}$ .

#### **Thermo-mechanical Tests.**

Injection-moulded parts sizing  $10 \times 5 \times 4 \text{ mm}^3$  were subjected to a Dynamic-Mechanical Thermal Analysis - DMTA with temperature sweep from - 70 to 100 °C at a heating rate of 2 °C/min using a DMA-1 from Mettler-Toledo S.A. (Barcelona, Spain). Dynamic Thermo-Mechanical Analysis - DMTA was carried out in bending mode with a maximum bending strain of 10  $\mu\text{m}$  at a frequency of 1 Hz and a force of 0.02 N. The storage modulus -  $E'$  and the dynamic damping factor -  $\tan \delta$  were collected as a function of temperature.

The Coefficient of Linear Thermal Expansion - CLTE was studied by Thermo-Mechanical Analysis - TMA in a Q400 thermo-mechanical analyser from TA Instruments (New Castle, DE, USA). The applied force was set to 0.02 N and the temperature program was scheduled from - 70 to 70 °C in air atmosphere (50 mL/min) at a constant heating rate of 2 °C/min. All thermo-mechanical tests were performed in triplicate.

#### **Microscopy.**

The fracture surfaces of the injection-moulded parts after the Charpy impact tests were analysed by Field Emission Scanning Electron Microscopy - FESEM (Oxford Instruments, Abingdon, UK) with an electron acceleration voltage of 2 kV. A gold-palladium coating was applied through sputtering (SC7620, from Quorum Technologies Ltd, East Sussex, UK). Additionally, to visualize the dispersion of nHA in the P(3HB-co-3HHx) matrix, the fracture surfaces were attacked with 6M hydrochloric acid - HCl (37 % purity, Panreac AppliChem, Barcelona, Spain) for 12 h to selectively remove nHA prior to observation [39].

### Statistical Analysis.

Statistical evaluation of the mechanical, thermal, and thermo-mechanical properties of P(3HB-co-3HHx)/nHA parts was carried out with the open source R software (<http://www.r-project.org>) with a Shapiro-Wilk test regarding a normal distribution for  $n < 1000$ . Tukey tests were performed to determine significant differences between the data on normally distributed data. In order to establish the non-parametric relationship between mechanical properties and nHA content in the parts, the Spearman's correlation test was followed. The number of tested samples for each test is included in **Table III.2.2.2.** and the level of significance was established as  $p < 0.05$  in all cases.

**Table III.2.2.2.** Number of tested samples (n) for each injection-moulded P(3HB-co-3HHx)/nanohydroxyapatite parts and the type of statistical test performed for each testing method with level of significance (p).

Testing method	n	Normality test	p	Significance test	p
Tensile	6	Shapiro-Wilk	0.05	Tukey	0.05
Flexural	6	Shapiro-Wilk	0.05	Tukey	0.05
Hardness	7	Shapiro-Wilk	0.05	Tukey	0.05
Impact strength	8	Shapiro-Wilk	0.05	Tukey	0.05
DSC	3	-	-	Kruskal-Wallis	0.05
TGA	3	-	-	Kruskal-Wallis	0.05
DMTA	3	-	-	Kruskal-Wallis	0.05
TMA	3	-	-	Kruskal-Wallis	0.05

## RESULTS AND DISCUSSION.

### Mechanical Characterization of the P(3HB-co-3HHx)/nHA parts.

The data collected for the mechanical properties from the tensile, flexural, hardness, and impact Charpy tests of the neat P(3HB-co-3HHx) and P(3HB-co-3HHx)/nHA composite parts produced with the different compositions is summarized in **Table III.2.2.3.** while **Figure III.2.2.1.** and **Figure III.2.2.2.** display the effect of nHA incorporation on the tensile and flexural properties. **Table III.2.2.4.** shows the correlation coefficient -  $r_s$  and the level of confidence - p for each mechanical property according to the Spearman's test.

### III. RESULTS & DISCUSSION

**Table III.2.2.3.** Mechanical properties of the injection-moulded parts of P(3HB-co-3HHx)/nHA.

Part	$\sigma_t$ (MPa)	$E_t$ (MPa)	$\varepsilon_b$ (%)	$\sigma_f$ (MPa)	$E_f$ (MPa)	Shore D hardness	Impact Strength (kJ/m <sup>2</sup> )
P(3HB-co-3HHx)	17.7 ± 1.1	1022.3 ± 59.2	19.4 ± 0.8	24.1 ± 1.9	735.3 ± 43.5	64.2 ± 0.8	5.1 ± 0.3
P(3HB-co-3HHx)/2.5nHA	16.1 ± 0.5*	1097.0 ± 52.3*	12.9 ± 0.3*	25.6 ± 1.0*	744.1 ± 26.3	64.0 ± 0.9	3.5 ± 0.2*
P(3HB-co-3HHx)/5nHA	15.8 ± 0.6	1113.1 ± 28.3	12.5 ± 0.8	26.4 ± 1.8	813.2 ± 24.1*	65.2 ± 0.8*	2.6 ± 0.2*
P(3HB-co-3HHx)/10nHA	15.5 ± 0.5	1398.2 ± 68.3*	10.4 ± 0.6*	26.7 ± 0.5	919.8 ± 38.6*	65.8 ± 1.1	2.2 ± 0.1*
P(3HB-co-3HHx)/20nHA	14.2 ± 0.2*	1681.4 ± 56.3*	6.5 ± 0.7*	26.9 ± 1.9	1182.5 ± 45.2	69.4 ± 0.5*	1.7 ± 0.2*

\* Indicates a significant difference compared with the previous sample ( $p < 0.05$ ).

**Table III.2.2.4.** Spearman's test for each mechanical property.

Mechanical properties	$r_s$	$p$
$\sigma_t$ (MPa)	- 0.917	0.028
$E_t$ (MPa)	+ 0.988	0.002
$\varepsilon_b$ (%)	- 0.903	0.035
$\sigma_f$ (MPa)	+ 0.782	0.118
$E_f$ (MPa)	+ 0.993	0.001
Shore D hardness	+ 0.977	0.004
Impact strength (kJ/m <sup>2</sup> )	- 0.839	0.032

The tensile properties of the injection-moulded P(3HB-co-3HHx) parts were relatively similar to those reported by Giubilini *et al.* [40], although the here-prepared materials were slightly less mechanically resistant and more ductile. These differences could be related to the 3HHx monomer content in the copolyester as well as to differences in processing. One can observe in both **Table III.2.2.3.** and **Figure III.2.2.1.** that the values of  $\sigma_t$  and  $\varepsilon_b$  decreased, while those of  $E_t$  increased with increasing nHA concentration in the nanocomposite parts. The Spearman's test confirmed the existence of a trend between the tensile properties of the nanocomposites and the nHA content, showing a negative  $r_s$  trend (inversely proportional correlation) for  $\sigma_t$  and  $\varepsilon_b$  and a positive trend (directly proportional correlation) for  $E_t$ , while in all cases  $p < 0.05$ . In particular, the addition of 20 wt.% of nHA produced a slight decrease of  $\sigma_t$  from 17.7 to 14.4 MPa, but an increase of nearly 64 % in  $E_t$  (from approximately 1 to 1.7 GPa) accompanied with a significant loss of ductility ( $\varepsilon_b$  was reduced from 19.4 to 6.5 %). The reduction in stress was probably caused by the poor interface adhesion between biopolymer and nanofiller. Higher interfacial adhesion can probably be promoted through the pre-treatment of nHA with silanes [41], but it could negatively affect the biocompatibility of the parts.

The increase in  $E_t$  was anticipated, since nHA forms highly rigid structures. Furthermore, as it will be discussed during the thermal characterization, the addition of nHA could promote higher degrees of crystallinity and, hence, higher stiffness. Although similar results have been reported earlier [42,43], the here-prepared parts

showed higher ductility due to the use of a more flexible PHA. The decrease observed in stiffness with increasing nHA content can be attributed to insufficient wetting and impregnation of the nanoparticles by the polymer matrix, mainly due to particle agglomeration during manufacture or processing of the materials [44]. However, melt-mixing methodologies using co-rotating twin-screw extruders, as adopted here, can generally yield well-dispersed nanocomposites [45]. Ductility loss was expected since the presence of nHA can prompt polymer crystallinity, hindering chain mobility due to adsorption of biopolymer chains on the surface of the nanoparticles [46,47].

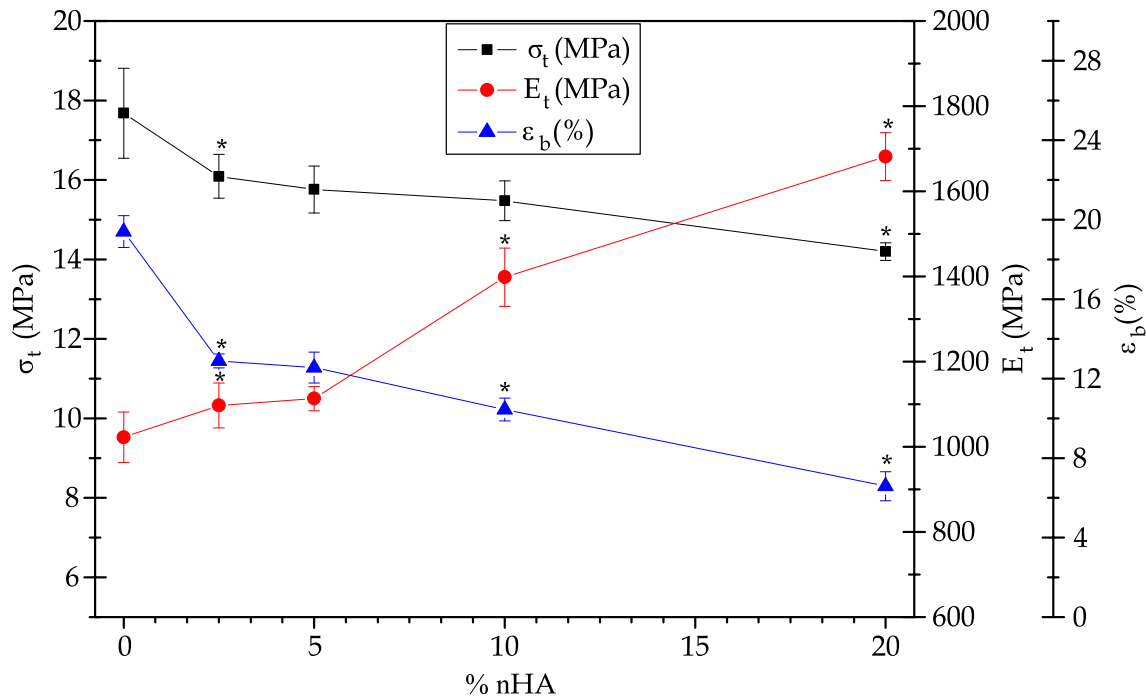


**Figure III.2.2.1.** Evolution of the main tensile properties of the injection-moulded parts of P(3HB-co-3HHx) with the content of nHA. \* Indicates a significant difference compared with the previous sample ( $p < 0.05$ ).

In **Figure III.2.2.2.**, it can be seen that the addition of nHA to P(3HB-co-3HHx) increased both  $\sigma_f$  and  $E_f$ , particularly the latter. The former increased up to a content of 5 wt.% of nHA and then became insensitive to higher nanoparticle contents, since the values showed no significant differences. Indeed, the Spearman's test showed a positive correlation ( $r_s > 0$ ) for both  $E_f$  and  $\sigma_f$ , however, for the latter, the statistical hypothesis should be rejected as  $p$  was higher than 0.05. Contrarily, the addition of 20 wt.% of nHA caused an increase of approximately 60 % of  $E_f$ , as similarly observed above for  $E_t$ . The resultant increase in mechanical strength can be related to the intrinsic high values of compressive strength and modulus of nHA, which are in the ranges of 500 – 1000 MPa and 80 – 110 GPa, respectively [48,49].

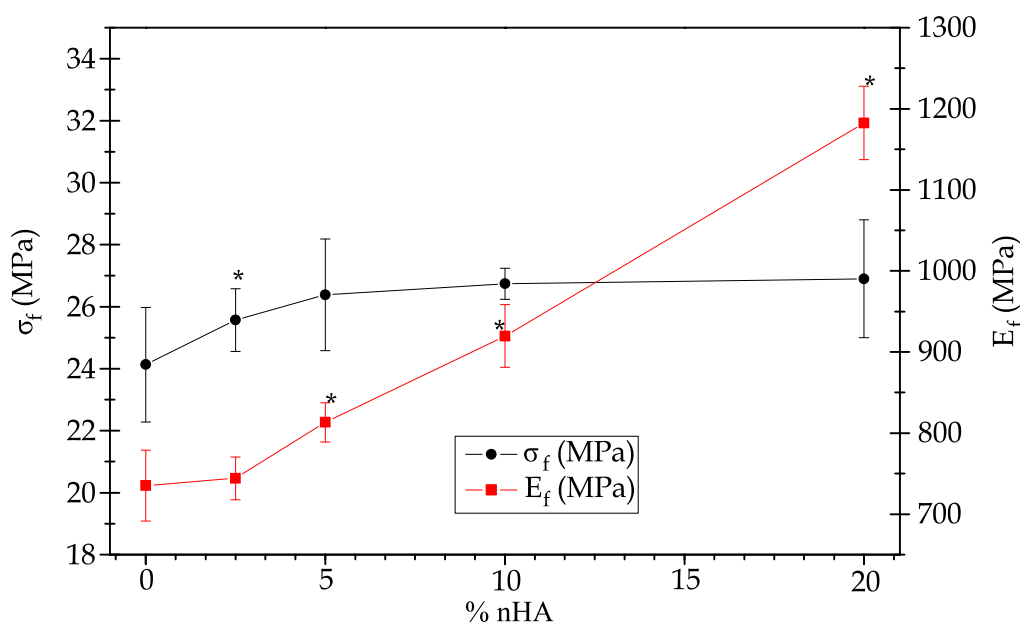


**Figure III.2.2.2.** Evolution of the main flexural properties in the injection-moulded parts of P(3HB-*co*-3HHx) with the content of nHA. \* Indicates a significant difference compared with the previous sample ( $p < 0.05$ ).

In comparison with the mechanical values of other degradable and non-degradable materials, the P(3HB-*co*-3HHx)/nHA parts produced in this study showed intermediate values to most biodegradable polymers and metal alloys. For instance, the  $E_t$  values of poly( $\epsilon$ -caprolactone) - PCL and PLA materials range between 400 - 600 MPa [50] and 2 - 3 GPa [51,52], respectively, while other biodegradable copolyesters such as poly(butylene adipate-*co*-terephthalate) - PBAT show significantly lower values [53]. However, PLA is a brittle polymer, which can limit its application in bone fixation devices, or any other biomedical device that would be subjected to local flexural stress or impacts. The values attained are relatively similar to those of poly(lactic-*co*-glycolic acid) - PLGA, that is, 1.4 - 2.8 GPa [54]. Indeed, PLGA is widely used in biomedical and pharmaceutical applications, but it shows longer degradation times, which can extend up to 12 months [55]. Regarding metal alloys, the  $E_t$  values of the most widely used stainless steels for implant fixing devices and screws, that is, SUS316L stainless steel and cobalt-chrome (Co - Cr) alloys, are around 180 GPa and 210 GPa, respectively [56]. Lower values have been reported for titanium - Ti and its light alloys, such as Ti-6Al-4V ELL, which are also widely used for making implant devices, having a value of around 110 GPa [57]. As shown above, in comparison to metal alloys, the elasticity of the P(3HB-*co*-3HHx)/nHA composites prepared in this study is nearer to that of the natural bone, which is in the 8 - 25 GPa range [5]. Thus, from a mechanical point of view, their use in bone scaffolds is promising.

As expected, hardness increased with the presence of nHA that, due to its ceramic nature, is highly rigid. The increase was significant at nHA contents higher than 2.5 wt.% and this effect was statistically corroborated by Spearman's test, showing a positive trend with a  $r_s$  value of  $\sim 0.98$ . In addition, molecular mobility could be reduced due to the presence of the nanoparticles [58]. In particular, the incorporation of 20 wt.% of nHA yielded an increase of 8 % in hardness. A similar increase in Shore D hardness was reported by Ferri *et al.* for PLA after the incorporation of nHA. In particular, it increased from 73.9, for neat PLA, up to 78.4, for the PLA composite containing 30 wt.% of nHA [39]. As also anticipated, the impact strength of the nanocomposites diminished significantly with increasing nHA content with significant differences between the samples, which was confirmed by the negative correlation obtained by the Spearman's test ( $r_s \approx -0.84$ ). For instance, the nanocomposite parts containing 20 wt.% of nHA revealed an impact strength approximately three times lower than that of the neat P(3HB-*co*-3HHx) part, that is, it reduced from 5.1 to 1.7 kJ/m<sup>2</sup>. Lower values of impact strength were reported for V-notched injection-moulded pieces of PLA, that is, 2.1 kJ/m<sup>2</sup> [51]. In addition, significantly higher values have been described for Ti-6Al-4V, with a Rockwell hardness C - HRC of 38 and approximately 112 kJ/m<sup>2</sup> impact strength [59]. In the case of natural bone, toughness varies widely with age and type. For instance, the impact strength of the femora ranges from 4 to 70 kJ/m<sup>2</sup> [60]. Therefore, the various mechanical tests revealed a clear tendency towards a decrease in ductility and an increase in stiffness of the injection-moulded parts with increasing nHA content, which are closer to those of the natural bone.

In summary, the here-developed P(3HB-*co*-3HHx)/nHA parts showed an improvement of the stiffness determined in terms of  $E_t$  and  $E_f$ , in which a positive trend was observed in both cases ( $r_s > 0$ ). The ductile properties,  $\epsilon_b$  and impact strength, showed negative trends ( $r_s < 0$ ), which was ascribed to a chain mobility reduction that also contributed to a hardness increase of the nanocomposite, showing a positive trend in the Spearman's test.

#### **Thermal Characterization of the P(3HB-*co*-3HHx)/nHA parts.**

**Figure III.2.2.3.** displays the DSC curves for the neat P(3HB-*co*-3HHx) part and the P(3HB-*co*-3HHx)/nHA composite parts with different nanoparticle contents. **Table III.2.2.5.** presents the thermal properties obtained from the second heating scan, after erasing the thermal history of the sample. At approximately 0 °C, one could observe a step change in the base lines, which corresponded to the  $T_g$  of P(3HB-*co*-3HHx). This

second-order thermal transition was located at  $-0.3\text{ }^{\circ}\text{C}$  for the neat biopolymer and it was significantly unaffected by the presence of nHA. The exothermic peaks located between  $40$  and  $70\text{ }^{\circ}\text{C}$  corresponded to  $T_{cc}$  of P(3HB-co-3HHx). In the case of the neat biopolymer part, this peak was located at  $49.8\text{ }^{\circ}\text{C}$ . It could be observed that the values of  $T_{cc}$  increased with increasing nHA content until  $10\text{ wt.}\%$ , and then slightly decreased at the highest content tested, that is,  $20\text{ wt.}\%$ . These results suggested that low nHA contents impaired the movement of P(3HB-co-3HHx) chains and, hence, hindered the crystallization process. A similar thermal behavior during the analysis of the second heating curves was recently observed by Senatov *et al.*, who associated the presence of nHA to a decrease in the molecular chain mobility of the biopolymer that impeded the crystallization process [61]. Finally, the crystalline P(3HB-co-3HHx) domains melted in the thermal range from  $100$  to  $150\text{ }^{\circ}\text{C}$  in two peaks. Furthermore, the occurrence of a broad melting region suggested the presence of heterogeneous crystallites with different degrees of perfection, commonly produced in PHAs with relatively high comonomer contents [62]. The thermogram of neat P(3HB-co-3HHx) revealed two melting temperatures ( $T_{m1}$  and  $T_{m2}$ ) at approximately  $113$  and  $140\text{ }^{\circ}\text{C}$ . Similar thermal properties were reported by Zhou *et al.* for P(3HB-co-3HHx) with  $11\text{ mol}\%$  content of 3HHx, who also observed a double-melting peak phenomenon in the DSC heating curves of this copolyester [63]. The presence of two melting peaks have been previously ascribed to the melting-recrystallization-melting process of P(3HB-co-3HHx) [64]. During this process, imperfect crystals melt at lower temperatures and the amorphous regions order into packed spherulites with thicker lamellar thicknesses that, thereafter, melt at higher temperatures. Alternatively, the melting peaks attained at low temperatures, that is,  $110 - 115\text{ }^{\circ}\text{C}$ , could also relate to the crystalline phase of the 3HHx-rich fractions. Lastly, one could observe that the melting profile of P(3HB-co-3HHx) was nearly unaffected by the nHA presence, indicating that the nanoparticles did not significantly influence the crystallization process.



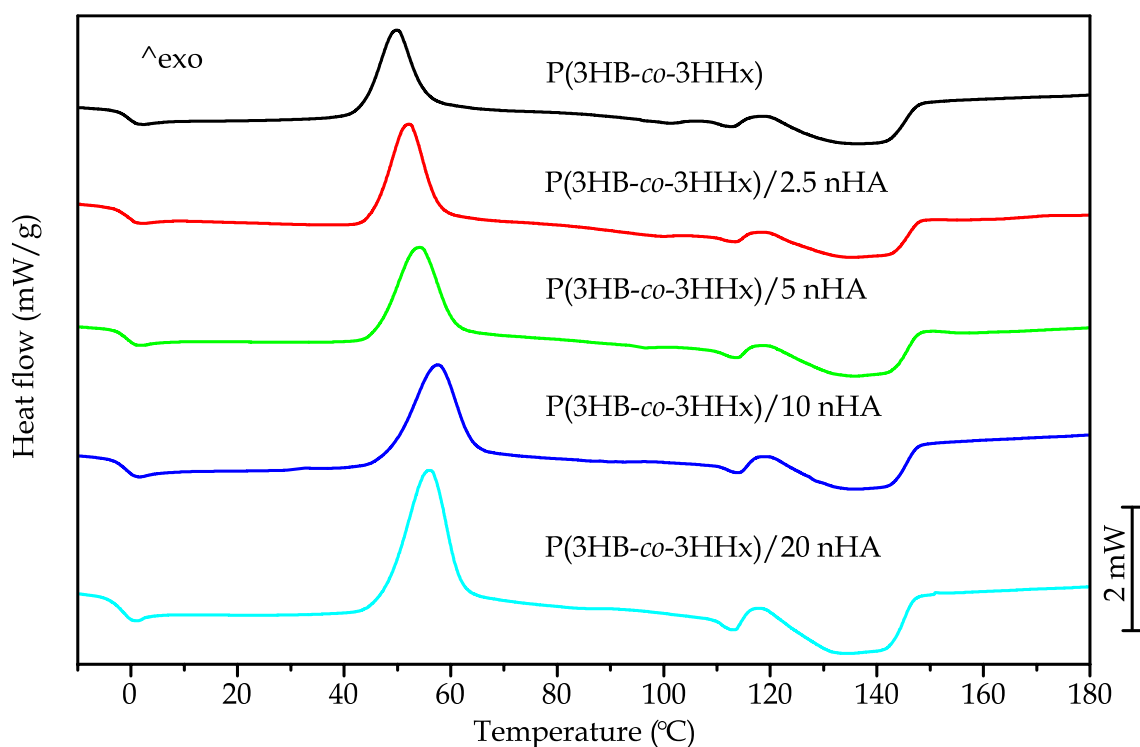


**Figure III.2.2.3.** DSC thermograms taken during second heating of the injection-moulded P(3HB-*co*-3HHx)/nHA parts.

**Table III.2.2.5.** Thermal properties of the injection-moulded P(3HB-*co*-3HHx)/nHA parts.

Part	$T_g$ (°C)	$T_{cc}$ (°C)	$T_{m1}$ (°C)	$T_{m2}$ (°C)	$\Delta H_{cc}$ (J/g)	$\Delta H_m$ (J/g)	$\chi_c$ (%)
P(3HB- <i>co</i> -3HHx)	$-0.3 \pm 0.1$	$49.8 \pm 0.5$	$112.9 \pm 0.5$	$139.7 \pm 0.3$	$20.7 \pm 0.5$	$31.2 \pm 0.4$	$21.4 \pm 1.8$
P(3HB- <i>co</i> -3HHx)/2.5nHA	$-0.2 \pm 0.1$	$52.1 \pm 0.4$	$113.6 \pm 0.3$	$140.9 \pm 0.4$	$29.8 \pm 0.4^*$	$35.0 \pm 0.5^*$	$24.3 \pm 2.4^*$
P(3HB- <i>co</i> -3HHx)/5nHA	$-0.4 \pm 0.2$	$54.1 \pm 0.2$	$113.8 \pm 0.4$	$139.4 \pm 0.2$	$31.8 \pm 0.6^*$	$40.1 \pm 0.3^*$	$28.9 \pm 2.2^*$
P(3HB- <i>co</i> -3HHx)/10nHA	$-0.4 \pm 0.2$	$57.4 \pm 0.3^*$	$114.3 \pm 0.2$	$139.0 \pm 0.3$	$29.0 \pm 0.5^*$	$32.5 \pm 0.4^*$	$24.7 \pm 1.5^*$
P(3HB- <i>co</i> -3HHx)/20nHA	$-0.3 \pm 0.1$	$55.9 \pm 0.4^*$	$113.4 \pm 0.5$	$139.1 \pm 0.4$	$25.9 \pm 0.4^*$	$29.0 \pm 0.1^*$	$24.8 \pm 1.4$

\* Indicates a significant difference compared with the previous sample ( $p < 0.05$ )

It can be seen that P(3HB-*co*-3HHx) showed a maximum  $\chi_c$  of 21.4 %. One can also observe that crystallinity varied significantly with nHA content. In particular, as nHA was gradually incorporated in higher percentages, the crystallinity increased steadily up to a maximum of nearly 29 % at 5 wt.% of nHA and then it slightly decreased to values close to 25 % for nHA contents of 10 and 20 wt.%. This result, in combination with the slightly higher  $T_{cc}$  and  $T_m$  values, suggests that the nanoparticles hindered the formation of crystals at low temperatures, but the crystals formed were slightly more perfect and more mass crystallized. This is in agreement with previous studies that concluded that the introduction of nHA into biopolyesters has an effect on the ordering of their molecular chains by acting as a nucleating agent [61,65].

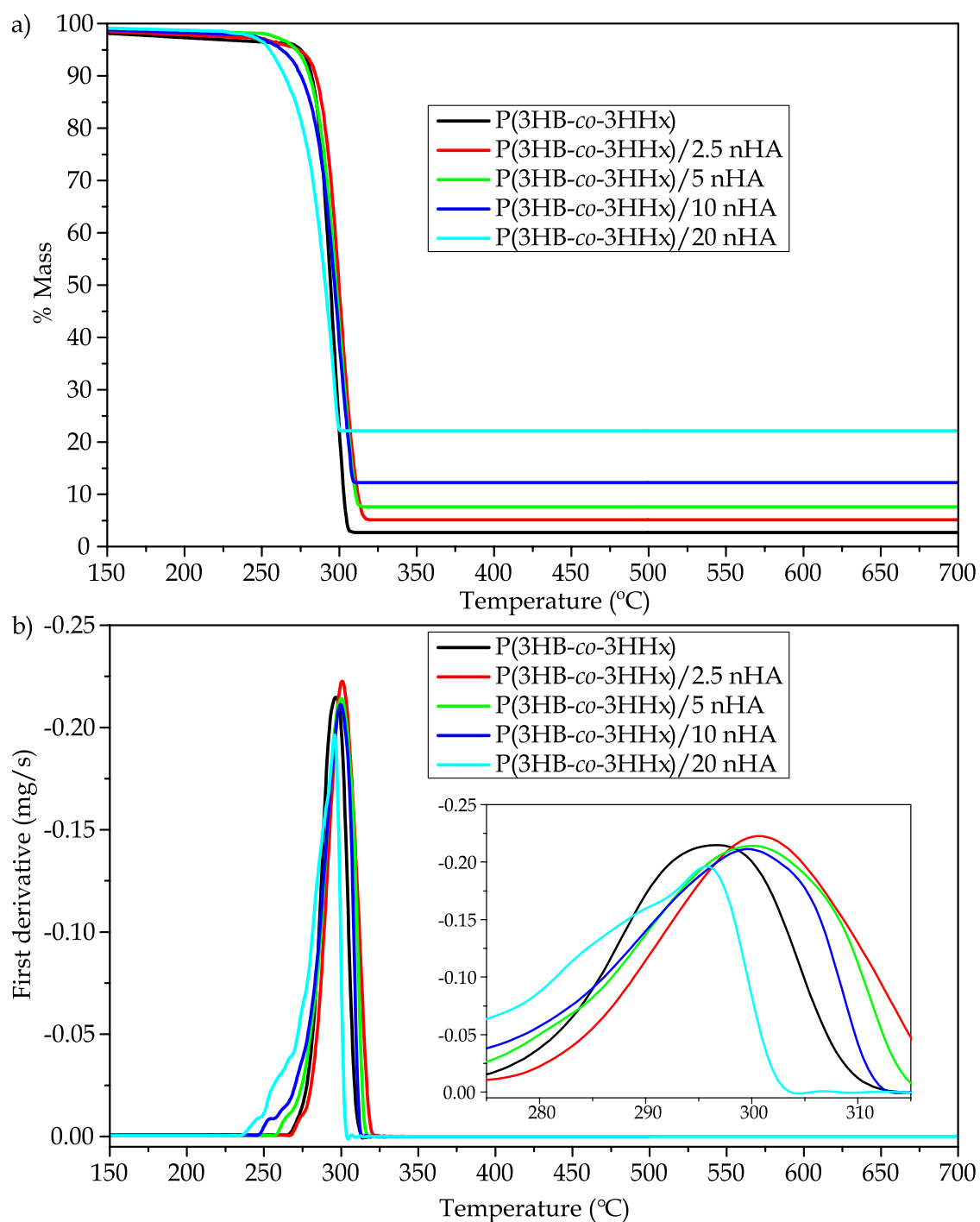


**Figure III.2.2.4.** Summary of the TGA test: a) mass loss curves *vs* temperature and b) first derivative thermogravimetric curves *vs* temperature.

**Figure III.2.2.4.** presents the thermogravimetric data for all the materials, while **Table III.2.2.6.** gathers the main thermal stability parameters obtained from the TGA curves. Thermal degradation of P(3HB-co-3HHx) was observed to occur through a one-step process, which is in agreement with the values reported by Li *et al.*, who showed that the thermal stability of the microbial copolyester was as high as 225 °C with almost no mass loss [20]. The  $T_{5\%}$  showed no significant differences with nHA contents of up to 5 wt.%, but a significant decrease was observed for higher loadings. The  $T_{\max}$  increased from 296.7 °C, for the neat P(3HB-co-3HHx) part, to 300.9 °C, for the part of P(3HB-co-3HHx) filled with 2.5 wt.% of nHA. This increase in thermal stability has been previously ascribed to the formation of strong hydrogen interactions and Van der Waals forces between the inorganic nanoparticles and the biopolymer chains during the melt-mixing process [66].

The values of  $T_{\max}$  remained nearly constant, showing no significant differences for nHA contents from 2.5 to 10 wt.%, but it significantly decreased to 295.6 °C in the part filled with 20 wt.% of nHA. The onset of degradation was also reduced for the most filled sample, showing a  $T_{5\%}$  value of 254.8 °C, which represents a reduction of approximately 18 °C in comparison to the unfilled P(3HB-co-3HHx) sample and its nanocomposites at low contents. These results further indicate that the nanoparticles formed aggregates at high contents, which created volumetric gradients of concentration [66]. In this regard, Bikiaris *et al.* suggested that when high amounts of nanosized filler aggregates are formed, the structure shifts from nanocomposite to microcomposite and, thus, the shielding effect of the nanosized particles is lessened [65]. In addition, Chen *et al.* reported that high loadings of nHA in P(3HH-co-3BV) lower the onset degradation temperature since they can catalyse thermal decomposition [67]. In any case, low nHA loadings (< 10 wt.%) slightly improved the thermal stability of P(3HB-co-3HHx) parts and their thermal stability is considered to be high enough for bone tissue engineering and biomedical applications, which can require thermal sterilization methods such as dry heat sterilization (160 °C for 2 h) and steam sterilization (121 °C for 20 – 60 min.) [68]. However, the relatively low  $T_m$  of P(3HB-co-3HHx) would limit the use of these techniques for sterilization and the resultant implantable biomedical devices should be sterilized at low temperatures using Ethylene Oxide – EO gas, gamma radiation or ozone. Finally, it can be observed that the residual mass at 700 °C increased gradually with the nHA content due to the high thermal stability of the mineral nanoparticles.

**Table III.2.2.6.** Main thermal degradation parameters of the injection-moulded P(3HB-co-3HHx)/nHA parts.

Part	T <sub>5%</sub> (°C)	T <sub>max</sub> (°C)	Residual Mass (%)
P(3HB-co-3HHx)	272.5 ± 2.3	296.7 ± 1.4	2.6 ± 0.3
P(3HB-co-3HHx)/2.5nHA	272.2 ± 1.7	300.9 ± 2.2	5.1 ± 0.5*
P(3HB-co-3HHx)/5nHA	272.4 ± 1.3	299.9 ± 1.7	7.6 ± 0.4*
P(3HB-co-3HHx)/10nHA	262.3 ± 1.8*	299.6 ± 1.8	12.2 ± 0.7*
P(3HB-co-3HHx)/20nHA	254.8 ± 1.3*	295.6 ± 1.6*	22.1 ± 0.8*

\* Indicates a significant difference compared with the previous sample ( $p < 0.05$ ).

### Thermo-mechanical Characterization of the P(3HB-co-3HHx)/nHA parts.

DMTA was carried out on the injection-moulded composite parts in order to understand the role played by nHA on the viscoelastic behavior of P(3HB-co-3HHx)/nHA. **Figure III.2.2.5.** illustrates the DMTA curves of the neat P(3HB-co-3HHx) part and the P(3HB-co-3HHx)/nHA composite parts with different nanoparticle contents. **Figure III.2.2.5a.** gathers the evolution of  $E'$  in the temperature sweep from  $-40$  to  $80$  °C at a frequency of 1 Hz. The  $T_g$  values and the corresponding values of  $E'$  at  $-40$ ,  $37$ , and  $70$  °C are presented in **Table III.2.2.7.**, since the first and last temperatures are representative of the stored elastic energy of the amorphous phase of P(3HB-co-3HHx) in its glassy and rubber states, respectively, whereas the middle one corresponds to the actual temperature of the human body. It can be observed that all the P(3HB-co-3HHx)-based parts presented a similar thermo-mechanical profile. In particular, the samples showed high  $E'$  values, that is, high stiffness, at temperatures below  $0$  °C and then  $E'$  sharply decreased. This thermo-mechanical change was produced because the temperature exceeded the alpha  $\alpha$ -relaxation of the biopolymer, which is related to its  $T_g$ . One can also observe that the rate of decrease of  $E'$  reduced somewhat when the temperature reached approximately  $40$  °C due to the occurrence of cold crystallization. The values of  $E'$  at  $-40$ ,  $37$ , and  $70$  °C of the neat P(3HB-co-3HHx) part were 1909.9, 519.2, and 210.5 MPa, respectively. The  $E'$  value attained at  $37$  °C was in accordance with the mechanical data, which indicated that only the P(3HB-co-3HHx) parts filled with the highest nHA contents, that is, 15 and 20 wt. %, showed significantly higher values. However, the results also indicated that the parts crystallized during the ageing process since the thermo-mechanical changes during and after cold crystallization were relatively low. As expected, the  $E'$  values progressively increased with increasing the nHA content, given the high stiffness of the nanoparticles. It is worth noting that the reinforcing effect was more noticeable at higher temperatures since the amorphous phase of P(3HB-co-3HHx) was in the rubber state. Indeed, at higher

temperatures, the thermo-mechanical response of all the P(3HB-co-3HHx) composite parts was significantly different, dependent upon the nHA content. For instance, at  $-40\text{ }^{\circ}\text{C}$  the  $E'$  value increased from 1935.2 MPa for the nanocomposite part containing 2.5 wt.% of nHA, to 2100.4 MPa for the part filled with 20 wt.% of nHA, whereas these values increased from 212.3 MPa to 333.1 MPa at  $70\text{ }^{\circ}\text{C}$ .

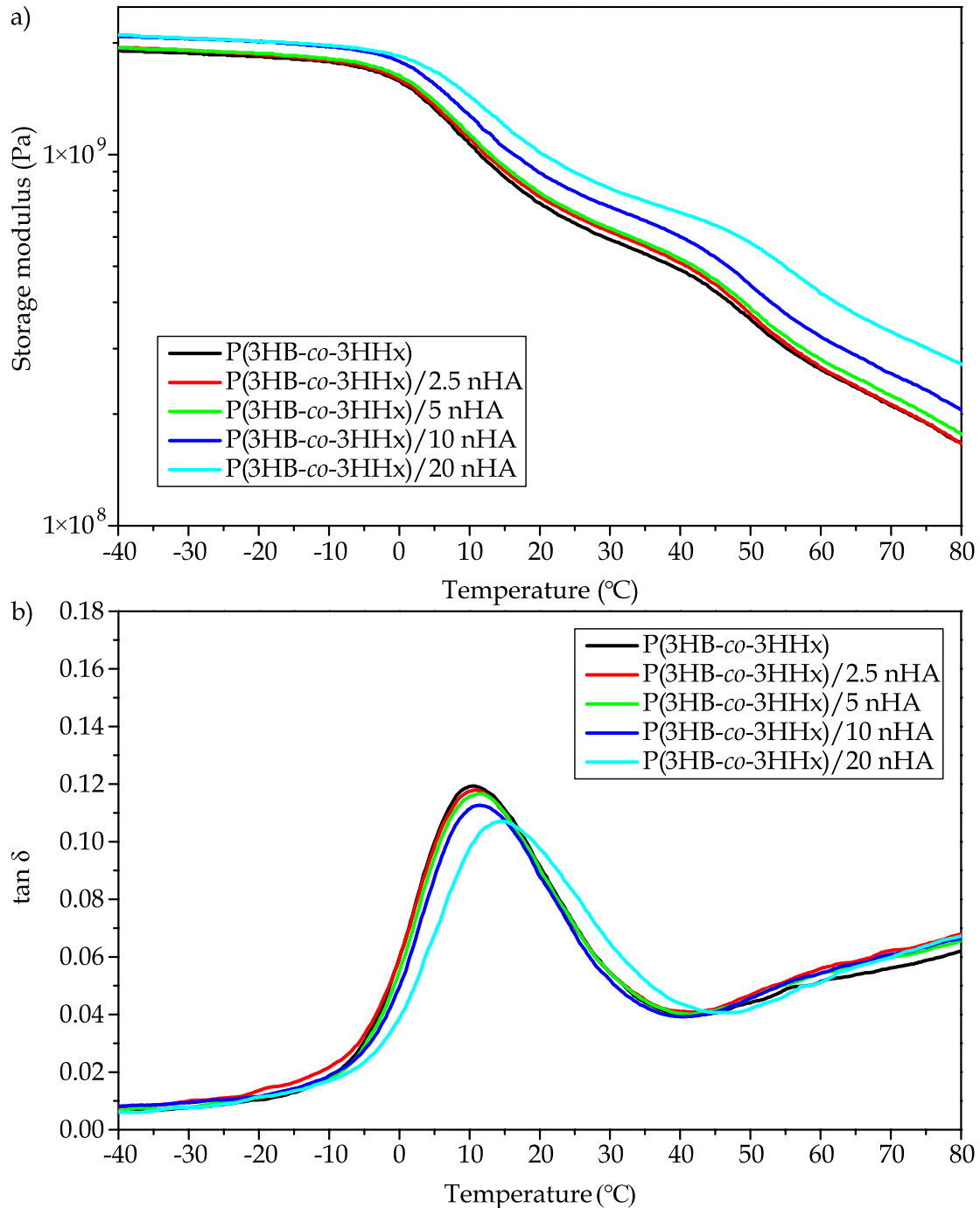


**Figure III.2.2.5.** Summary of the DMTA test: a) storage modulus *vs* temperature and b)  $\tan \delta$  *vs* temperature of the injection-moulded P(3HB-co-3HHx)/nHA parts.

### III. RESULTS & DISCUSSION

**Table III.2.2.7.** Thermo-mechanical properties of the injection-moulded P(3HB-co-3HHx)/nHA parts.

Part	DMTA				$T_g$ (°C)	TMA	
	tan $\delta$ peak (°C)	$E'$ at -40 °C (MPa)	$E'$ at 37 °C (MPa)	$E'$ at 70 °C (MPa)		CLTE ( $\mu/m^\circ C$ )	
						Below $T_g$	Above $T_g$
P(3HB-co-3HHx)	10.7 $\pm$ 0.4	1909.9 $\pm$ 50.2	519.2 $\pm$ 14.2	210.5 $\pm$ 2.5	-0.6 $\pm$ 0.2	64.3 $\pm$ 1.1	177.2 $\pm$ 4.6
P(3HB-co-3HHx)/2.5nHA	10.9 $\pm$ 0.2	1935.2 $\pm$ 41.7*	544.1 $\pm$ 26.3*	212.3 $\pm$ 3.1	-0.3 $\pm$ 0.2	61.3 $\pm$ 0.4*	176.1 $\pm$ 7.2*
P(3HB-co-3HHx)/5nHA	11.2 $\pm$ 0.3	1940.1 $\pm$ 82.5*	557.8 $\pm$ 17.1*	222.5 $\pm$ 4.6*	-0.1 $\pm$ 0.1	59.3 $\pm$ 0.5	175.0 $\pm$ 0.8
P(3HB-co-3HHx)/10nHA	11.4 $\pm$ 0.5	2090.3 $\pm$ 74.6*	639.0 $\pm$ 18.1*	256.8 $\pm$ 5.1*	-0.4 $\pm$ 0.2	58.2 $\pm$ 0.4	170.2 $\pm$ 3.8*
P(3HB-co-3HHx)/20nHA	14.5 $\pm$ 0.4*	2100.4 $\pm$ 65.1*	728.8 $\pm$ 26.6*	333.1 $\pm$ 3.4*	-0.3 $\pm$ 0.2	56.7 $\pm$ 0.7	159.1 $\pm$ 5.7*

\* Indicates a significant difference compared with the previous sample ( $p < 0.05$ ).

The tan  $\delta$  curves are shown in **Figure III.2.2.5b**. Since the position of the tan  $\delta$  peak gives an indication of the biopolymer's  $T_g$ , these values were also included in **Table III.2.2.7**. In the case of the neat P(3HB-co-3HHx) part, the tan  $\delta$  peak was located at 10.7 °C, which is similar to that reported by Valentini *et al.* [69]. It is worth mentioning that, in all cases, the tan  $\delta$  peaks were approximately 10 °C higher than the  $T_g$  values obtained by DSC. Since tan  $\delta$  represents the ratio of the viscous to the elastic response of a viscoelastic material, this indicates that part of the applied load was dissipated by energy dissipation mechanisms such as segmental motions, which are related to  $T_g$ , but part of the energy was also stored and released upon removal of the load at higher temperatures. One can observe that the incorporation of nHA shifted slightly the position of the tan  $\delta$  peaks and also reduced their intensity for the highest nHA loadings, that is, 10 and 20 wt. %. Decreasing tan  $\delta$  peaks intensity indicated that the nanocomposite parts showed a more elastic response and, hence, presented more potential to store the applied load rather than dissipating it [70]. This reduction is directly related to the higher  $E'$  values attained due to nanoparticle reinforcement and it confirmed that nHA imposed restrictions on the molecular motion of the P(3HB-co-3HHx) chains, resulting in a material with more elastic behavior [71]. It also correlated well with the DSC results shown above, indicating that P(3HB-co-3HHx) developed more crystallinity in the nanocomposite parts due to the nucleating effect of nHA and, thus, the less amorphous phase underwent glass transition.

The effect of temperature on the dimensional stability of the P(3HB-co-3HHx)/nHA parts was also determined by TMA. The CLTE, both below and above  $T_g$ , was obtained from the change in dimensions *vs* temperature and it is also included in **Table III.2.2.7**, along with the  $T_g$  values. In all cases, lower CLTE values were attained in the parts below  $T_g$ , due to the lower mobility of the P(3HB-co-3HHx) chains of the amorphous regions in the glassy state. As anticipated, both below and above  $T_g$ ,

the CLTE values decreased significantly with increasing nHA content due to the increasing replacement of the soft biopolymer matrix by a ceramic material with a considerably lower CLTE value, that is,  $13.6 \mu\text{m}/\text{m}^\circ\text{C}$  [72]. As a result, the CLTE value below  $T_g$  was reduced from  $64.3 \mu\text{m}/\text{m}^\circ\text{C}$  for the neat P(3HB-co-3HHx) part, to  $56.7 \mu\text{m}/\text{m}^\circ\text{C}$  for the nanocomposite part filled with 20 wt.% of nHA. Similarly, above  $T_g$ , it decreased from 177.2 to  $159.1 \mu\text{m}/\text{m}^\circ\text{C}$ , respectively. This thermo-mechanical response was slightly better than that of the PLA/nHA composites, in which the CLTE values below  $T_g$  decreased from 73 to  $71 \mu\text{m}/\text{m}^\circ\text{C}$  after the incorporation of 20 wt.% of nHA into PLA  $\mu\text{m}/\text{m}^\circ\text{C}$  [73]. These results point out that the nanocomposite parts prepared herein show excellent dimensional stability against temperature exposition. However, it is also worth mentioning that, as expected, the CLTE of Ti-based materials was significantly lower, having a mean value of  $8.7 \mu\text{m}/\text{m}^\circ\text{C}$  [72].

#### **Morphological Characterization of the P(3HB-co-3HHx)/nHA parts.**

**Figure III.2.2.6.** shows the samples before and after the various processing steps. Combining melt compounding and injection moulding represents a cost-competitive melt-processing methodology to produce a large number of parts using nanocomposites. According to this route, the P(3HB-co-3HHx) pellets and the nHA powder were pre-mixed and fed together to the co-rotating twin-screw extruder. In this way, pellets of nanocomposites containing different contents of dispersed nHA particles were obtained. They were subsequently injection moulded into dumbbell bars. All parts were defect-free and had a bright surface, the nHA content influencing their colour; neat P(3HB-co-3HHx) parts were yellow pale, typical of microbial PHA, while the presence of nanoparticles induced a whiter colour.

**Figure III.2.2.7.** shows the FESEM image, taken at  $10000\times$ , of the nHA powder. The nanoparticles show a flake-like morphology based on plates with sizes 60 - 120 nm and mean cross-sections of approximately 30 nm. This particular morphology of nHA has been reported to occur at pH values below 9, due to the solution environment changes by the  $\text{OH}^-$  ions during synthesis using polyethylene glycol - PEG as a template [74].



**Figure III.2.2.6.** Processing steps carried out to prepare the P(3HB-*co*-3HHx)/nHA parts; from left to right: as-received P(3HB-*co*-3HHx) pellets and nHA powder, compounded pellets of the nanocomposite, injection-moulded parts.

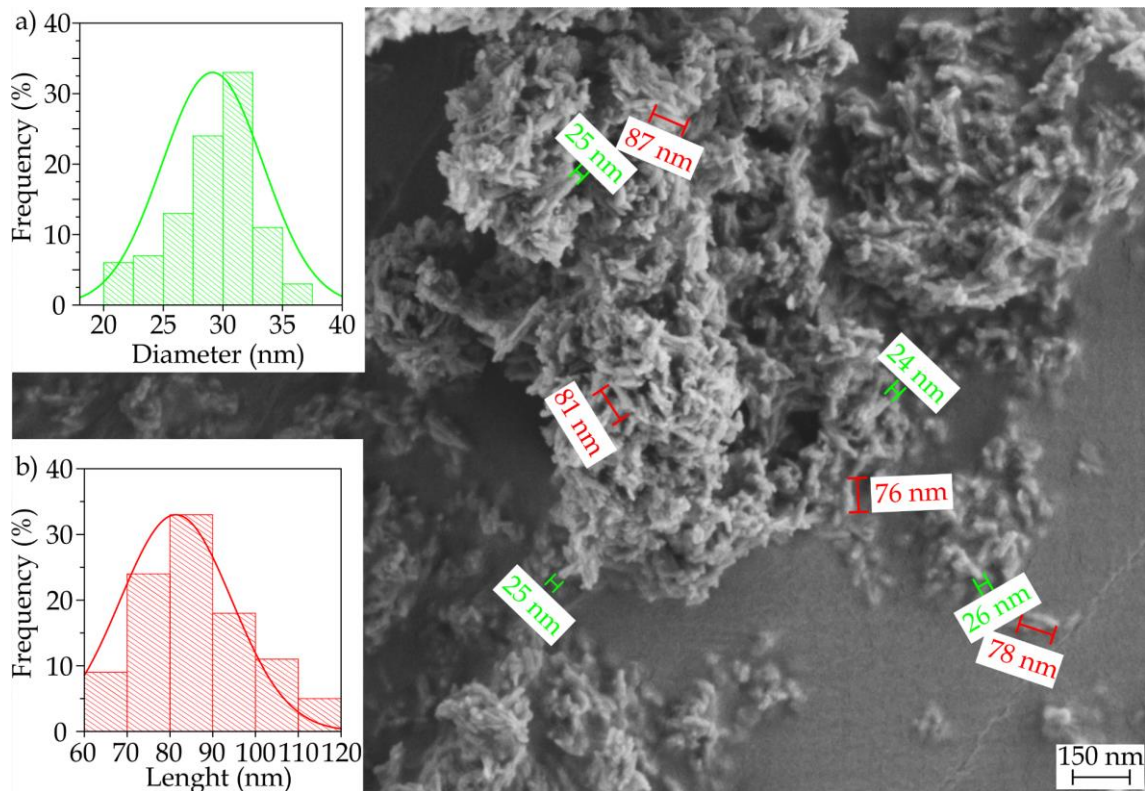


**Figure III.2.2.7.** FESEM images of the nanohydroxyapatite - nHA powder. Image was taken at 10000 × with scale marker 150 nm.

Micrographs obtained by FESEM of the fracture surfaces of the injection-moulded parts of P(3HB-*co*-3HHx) and the various P(3HB-*co*-3HHx)/nHA composites after the Charpy impact tests are gathered in **Figure III.2.2.8**. The fracture surface of the neat P(3HB-*co*-3HHx) part, shown in **Figure III.2.2.8a**, indicated that the material presented a relatively high toughness, since it yielded a rough surface with the presence of multiple microcracks and some holes. Some microparticles could be seen in the inset FESEM micrograph taken at higher magnification, which could be related to the presence of nucleating agents and/or fillers added by the manufacturer, such as Boron Nitride - BN. In this regard, Türkez, *et al.* have recently demonstrated that BN nanoparticles show slight cytotoxicity potential [75]. In particular, contents below 100



mg/L did not lead to lethal response on human primary alveolar epithelial cells – HPAEpiC, suggesting their safe and effective use in both pharmacological and medical applications.

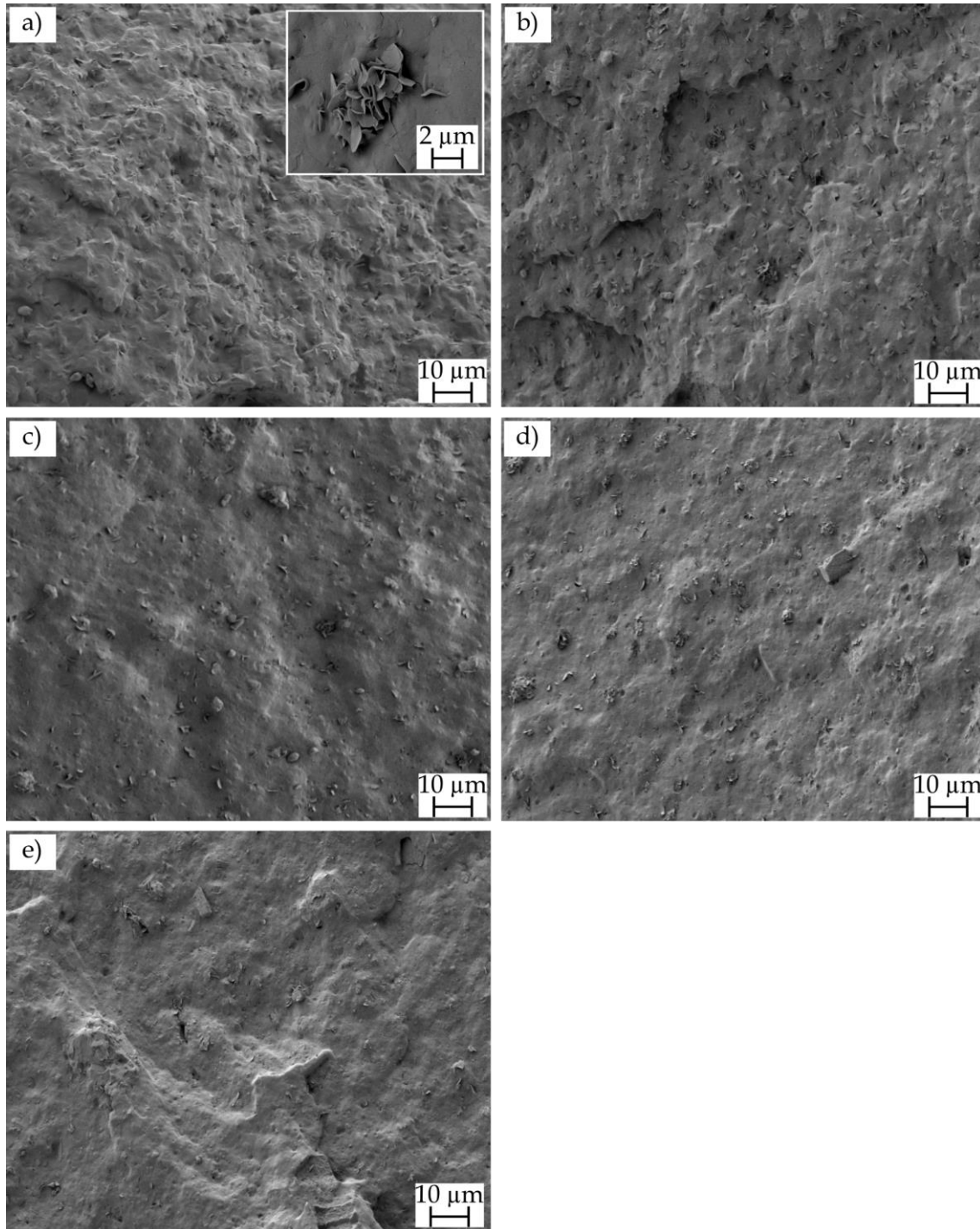


**Figure III.2.2.8.** FESEM images of the fracture surfaces of the injection-moulded P(3HB-co-3HHx)/nHA parts of: a) neat P(3HB-co-3HHx), b) P(3HB-co-3HHx)/2.5nHA, c) P(3HB-co-3HHx)/5nHA, d) P(3HB-co-3HHx)/10nHA and e) P(3HB-co-3HHx)/20nHA. Images were taken at  $500\times$  and with scale markers of  $10\ \mu\text{m}$ . Inset image showing the detail of the microparticles was taken at  $2500\times$  with scale marker of  $2\ \mu\text{m}$ .

**Figure III.2.2.8b-e.** gathers the fracture surfaces of the P(3HB-co-3HHx)/nHA composite parts. The morphological characteristics of the fracture surfaces for the nanocomposites filled with low nHA contents, that is, 2.5 and 5 wt.%, remained very similar to that of neat P(3HB-co-3HHx)/nHA. In all cases, the nanoparticles were relatively well dispersed and distributed within the biopolymer matrix. However, at higher contents, the nanoparticles tended to form some microaggregates and the resultant fracture surfaces were smoother, indicating that the nanocomposites were more brittle.

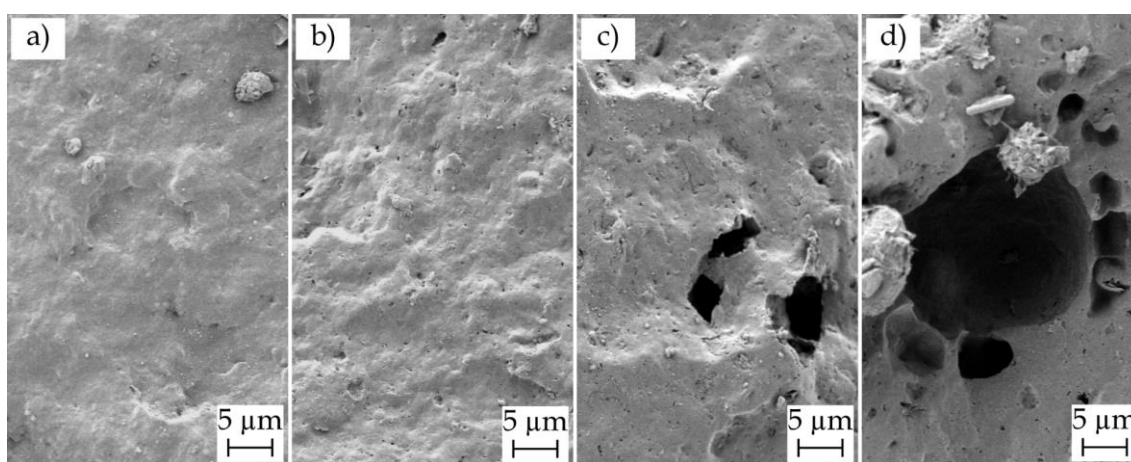


**Figure III.2.2.9.** FESEM images of the fracture surfaces of the injection-moulded P(3HB-co-3HHx)/nHA parts after selective attack with 6M HCl for 12 h: a) P(3HB-co-3HHx)/2.5nHA, b) P(3HB-co-3HHx)/5nHA, c) P(3HB-co-3HHx)/10nHA and d) P(3HB-co-3HHx)/20nHA. Images were taken at 1000 × with scale marker of 5 μm.

Due to the low nHA particle size and the presence of BN and/or additives in the P(3HB-co-3HHx) matrix, selective separation was carried out on the fracture surfaces of the nanocomposite parts, in order to better evaluate the dispersion of the nanoparticles. **Figure III.2.2.9.** presents the FESEM images of the fracture surfaces subjected to treatment with 6M HCl for 12 h. The voids and holes formed in the surfaces were related to removed/dissolved nHA and the overall void size and distribution gave an indication of the original particle dispersion. The micrographs revealed that some microholes were produced after the selective attack on the P(3HB-co-3HHx) parts filled with 10 and 20 wt.% of nHA, which should correspond to nHA aggregates, whereas the nanocomposites containing low nanoparticle loadings showed nano-sized holes well distributed along the biopolymer matrix, which suggested an efficient dispersion. Agglomeration was particularly noticeable for the nanocomposite part containing 20 wt. % of nHA, thus indicating that the presence of aggregates could induce particle debonding during fracture, as a result of the dissimilar mechanical strength and rigidity

of the ceramic nanoparticles and biopolymer matrix. Therefore, the present results correlate well with the mechanical and thermal properties described above, in which nHA loadings of up to 10 wt.% increased the mechanical and thermal performance of the P(3HB-co-3HHx) parts, whereas the highest nHA content impaired the overall properties due to nanoparticle aggregation.

## CONCLUSIONS.

One of the most exciting areas of new material development in the biomedical device community is resorbable polymers. As bone scaffolds, biodegradable and biocompatible polymers will maintain their strength until the liquid in contact begins the dissolution process, eventually leading to their complete elimination from the body, thus avoiding a second surgery for their removal. The herein-prepared injection-moulded composite parts of P(3HB-co-3HHx)/nHA showed a better matching of mechanical and thermo-mechanical performance than metal alloys to replace natural bone. While natural bone has a modulus ranging from about 8 - 25 GPa, the herein-prepared injection-moulded parts showed  $E_t$  values from approximately 1 up to 1.7 GPa and  $\epsilon_b$  values ranging from 6.5 to 19.4 %. The incorporation of up to 10 wt.% of nHA also improved slightly the thermal stability of the P(3HB-co-3HHx) parts and their thermal stability was considered to be high enough for bone tissue engineering, taking into account that nonthermal sterilization methods would be required. These balanced properties in terms of strength and ductility offer the biomedical industry a material that can accomplish different applications in bone reconstruction, for which high-stress materials are not needed, such as bone screws and small orthopedic plates or rods. Future works will explore the potential use of the P(3HB-co-3HHx)/nHA composites as drug delivery systems.

## ACKNOWLEDGMENTS.

Luis Quiles-Carrillo wants to thank GVA for his FPI grant (ACIF/2016/182) and the Spanish Ministry of Education, Culture, and Sports - MECD for his FPU grant (FPU15/03812). Sergio Torres-Giner acknowledges MICI for his Juan de la Cierva-Incorporación contract (IJCI-2016-29675). Juan Ivorra-Martinez wants to thank Universitat Politècnica de València for his FPI grant (PAID-2019- SP20190011). Microscopy services of the Universitat Politècnica de València - UPV are acknowledged for their help in collecting and analysing the FESEM images. Authors also thank Ercros S.A. for kindly supplying ErcrosBio® PH110. This research work was funded by the Spanish Ministry of Science and Innovation - MICI project numbers

RTI2018-097249-B-C21 and MAT2017-84909-C2-2-R and the POLISABIO program with grant number 2019-A02.

#### REFERENCES.

1. Ghiasi, M.S.; Chen, J.; Vaziri, A.; Rodriguez, E.K.; Nazarian, A. Bone fracture healing in mechanobiological modeling: a review of principles and methods. *Bone Reports* **2017**, *6*, 87–100 doi: 10.1016/j.bonr.2017.03.002.
2. Pankaj, P.; Xie, S. The risk of loosening of extramedullary fracture fixation devices. *Injury* **2019**, *50*, 66–72 doi: 10.1016/j.injury.2019.03.051.
3. Mugnai, R.; Tarallo, L.; Capra, F.; Catani, F. Biomechanical comparison between stainless steel, titanium and carbon-fiber reinforced polyetheretherketone volar locking plates for distal radius fractures. *Orthopaedics & Traumatology: Surgery & Research* **2018**, *3*, 33–99 doi: 10.1016/j.otsr.2018.05.002.
4. Shayesteh Moghaddam, N.; Jahadakbar, A.; Amerinatanzi, A.; Skoracki, R.; Miller, M.; Dean, D.; Elahinia, M. Fixation release and the bone bandaid: a new bone fixation device paradigm. *Bioengineering* **2017**, *4*, 5–26 doi: 10.3390/bioengineering4010005.
5. Heimbach, B.; Tonyali, B.; Zhang, D.; Wei, M. High performance resorbable composites for load-bearing bone fixation devices. *Journal of the Mechanical Behavior of Biomedical Materials* **2018**, *81*, 1–9 doi: 10.1016/j.jmbbm.2018.01.031.
6. Sun, B.; Tian, H.-Y.; Zhang, C.-X.; An, G. Preparation of biomimetic-bone materials and their application to the removal of heavy metals. *AIChE Journal* **2013**, *59*, 229–240 doi: 10.1002/aic.13802.
7. Gotman, I.; Swain, S.K.; Sharipova, A.; Gutmanas, E.Y. Bioresorbable Ca-phosphate-polymer/metal and Fe-Ag nanocomposites for macro-porous scaffolds with tunable degradation and drug release. *AIP Conference Proceedings* **2016**, *1783*, 20062–20072 doi: 10.1063/1.4966355.
8. Perale, G.; Hilborn, J. *Bioresorbable Polymers for Biomedical Applications: From Fundamentals to Translational Medicine*, 1 ed.; Elsevier: **2016**; Vol. 1.

9. Pertici, G. Introduction to bioresorbable polymers for biomedical applications. In *Bioresorbable Polymers for Biomedical Applications: From Fundamentals to Translational Medicine*, 1 ed.; Elsevier: **2017**; Vol. 1, pp. 3-29.
10. Saito, T.; Tomita, K.; Juni, K.; Ooba, K. In vivo and in vitro degradation of poly(3-hydroxybutyrate) in pat. *Biomaterials* **1991**, *12*, 309-312 doi: 10.1016/0142-9612(91)90039-D.
11. Williams, S.F.; Martin, D.P.; Horowitz, D.M.; Peoples, O.P. PHA applications: Addressing the price performance issue I. Tissue engineering. *International Journal of Biological Macromolecules* **1999**, *25*, 111-121 doi: 10.1016/s0141-8130(99)00022-7.
12. Singh, A.K.; Mallick, N. Biological system as reactor for the production of biodegradable thermoplastics, polyhydroxyalkanoates. In *Industrial Biotechnology: Sustainable Production and Bioresource Utilization*, 1 ed.; CRC Press: **2016**; Vol. 1, pp. 281-323.
13. Rodriguez-Contreras, A. Recent advances in the use of polyhydroxyalkanoates in biomedicine. *Bioengineering* **2019**, *6*, 82-96 doi: 10.3390/bioengineering6030082.
14. Shrivastav, A.; Kim, H.Y.; Kim, Y.R. Advances in the applications of polyhydroxyalkanoate nanoparticles for novel drug delivery system. *BioMed Research International* **2013**, *2013*, 1-12 doi: 10.1155/2013/581684.
15. Zinn, M.; Witholt, B.; Egli, T. Occurrence, synthesis and medical application of bacterial polyhydroxyalkanoate. *Advanced Drug Delivery Reviews* **2001**, *53*, 5-21 doi: 10.1016/S0169-409X(01)00218-6.
16. Shishatskaya, E.I.; Volova, T.G.; Gitelson, I.I. In vivo toxicological evaluation of polyhydroxyalkanoates. *Doklady Biological Sciences* **2002**, *383*, 109-111 doi: 10.1023/a:1015325504494.
17. Liu, M.-H.; Chen, Y., Jr.; Lee, C.-Y. Characterization of medium-chain-length polyhydroxyalkanoate biosynthesis by *Pseudomonas mosselii* TO7 using crude glycerol. *Bioscience, Biotechnology, and Biochemistry* **2018**, *82*, 532-539 doi: 10.1080/09168451.2017.1422386.

18. Yoshie, N.; Saito, M.; Inoue, Y. Effect of chemical compositional distribution on solid-state structures and properties of poly(3-hydroxybutyrate-co-3-hydroxyvalerate). *Polymer* **2004**, *45*, 1903–1911 doi: 10.1016/j.polymer.2004.01.025.
19. Ozdil, D.; Wimpenny, I.; Aydin, H.; Yang, Y. Biocompatibility of biodegradable medical polymers. In *Science and Principles of Biodegradable and Bioresorbable Medical Polymers*, 1 ed.; Elsevier: **2017**; Vol. 1, pp. 379-414.
20. Li, J.; Yin, F.; Li, D.; Ma, X.; Zhou, J. Mechanical, thermal, and barrier properties of PHBH/cellulose biocomposite films prepared by the solution casting method. *Bioresources* **2019**, *14*, 1219–1228 doi: 10.15376/biores.14.1.1219–1228.
21. Baidurah, S.; Murugan, P.; Sen, K.Y.; Furuyama, Y.; Nonome, M.; Sudesh, K.; Ishida, Y. Evaluation of soil burial biodegradation behavior of poly(3-hydroxybutyrate-co-3-hydroxyhexanoate) on the basis of change in copolymer composition monitored by thermally assisted hydrolysis and methylation-gas chromatography. *Journal of Analytical and Applied Pyrolysis* **2019**, *137*, 146–150 doi: 10.1016/j.jaap.2018.11.020.
22. Misra, S.K.; Valappil, S.P.; Roy, I.; Boccaccini, A.R. Polyhydroxyalkanoate (PHA)/inorganic phase composites for tissue engineering applications. *Biomacromolecules* **2006**, *7*, 2249–2258 doi: 10.1021/bm060317c.
23. Nagao, Y.; Takasu, A.; Boccaccini, A.R. Anode-selective electrophoretic deposition of a bioactive glass/sulfone-containing click polyester composite. *Macromolecules* **2012**, *45*, 3326–3334 doi: 10.1021/ma300396p.
24. Luckarift, H.R.; Sizemore, S.R.; Farrington, K.E.; Roy, J.; Lau, C.; Atanassov, P.B.; Johnson, G.R. Facile fabrication of scalable, hierarchically structured polymer/carbon architectures for bioelectrodes. *ACS Applied Material Interfaces* **2012**, *4*, 2082–2087 doi: 10.1021/am300048v.
25. Leite, Á.J.; Mano, J.F. Biomedical applications of natural-based polymers combined with bioactive glass nanoparticles. *Journal of Materials Chemistry B* **2017**, *5*, 4555–4568 doi: 10.1039/C7TB00404D.

26. Kawarazaki, I.; Takasu, A. Synthesis of unsaturated nonionic poly(ester-sulfones) via acyclic diene metathesis (ADMET) polymerization and anode-selective electrophoretic deposition. *Macromolecular Chemistry Physics* **2016**, *217*, 2595–2600 doi: 10.1002/macp.201600277.
27. Kehail, A.A.; Boominathan, V.; Fodor, K.; Chalivendra, V.; Ferreira, T.; Brigham, C.J. In vivo and in vitro degradation studies for poly(3-hydroxybutyrate-co-3-hydroxyhexanoate) biopolymer. *Journal of Polymer Environment* **2017**, *25*, 296–307 doi: 10.1007/s10924-016-0808-1.
28. Grøndahl, L.; Jack, K.; Goonasekera, C. Composite materials for bone repair. In *Biomedical composites*, 1 ed.; Elsevier: **2017**; Vol. 1, pp. 83-110.
29. Wypych, G. *Functional fillers: chemical composition, morphology, performance, applications*, 2 ed.; Elsevier: **2018**; Vol. 1.
30. Dorozhkin, S.V. Functionalized calcium orthophosphates (CaPO<sub>4</sub>) and their biomedical applications. *Journal of Materials Chemistry B* **2019**, *7*, 7471–7489 doi: 10.1039/C9TB01976F.
31. Dorozhkin, S.V. Biocomposites and hybrid biomaterials based on calcium orthophosphates. *Biomatter* **2011**, *1*, 3–56 doi: 10.4161/biom.1.1.16782.
32. Ma, B.; Han, J.; Zhang, S.; Liu, F.; Wang, S.; Duan, J.; Sang, Y.; Jiang, H.; Li, D.; Ge, S., *et al.* Hydroxyapatite nanobelt/poly(lactic acid) Janus membrane with osteoinduction/barrier dual functions for precise bone defect repair. *Acta Biomaterialia* **2018**, *71*, 108–117 doi: 10.1016/j.actbio.2018.02.033.
33. Iratwar, D.S.W.; Pisulkar, D.S.; Jõnec, D.A. Cranioplasty for prosthetic cranial reconstruction of skull defects using pre-fabricated polymethyl methacrylate grafts reinforced by hydroxyapatite particles intraoperatively in rural population of central India region: a pilot study. *International Journal of Medical and Biomedical Studies* **2019**, *3*, 155–158 doi: 10.32553/ijmbs.v3i11.738
34. Tsiapalis, D.; De Pieri, A.; Biggs, M.; Pandit, A.; Zeugolis, D.I. Biomimetic Bioactive biomaterials: the next generation of implantable devices. *ACS Biomaterials Science and Engineering* **2017**, *3*, 1172–1174 doi: 10.1021/acsbiomaterials.7b00372.

35. Galindo, T.G.P.; Chai, Y.; Tagaya, M. Hydroxyapatite nanoparticle coating on polymer for constructing effective biointeractive interfaces. *Journal of Nanomaterials* 2019, **2019**, 2019, 1–24 doi: 10.1155/2019/6495239.
36. Agüero, Á.; Garcia-Sanoguera, D.; Lascano, D.; Rojas-Lema, S.; Ivorra-Martinez, J.; Fenollar, O.; Torres-Giner, S. Evaluation of different compatibilization strategies to improve the performance of injection-molded green composite pieces made of polylactide reinforced with short flaxseed fibers. *Polymers* **2020**, *12*, 821–843 doi: 10.3390/polym12040821.
37. Rojas-Lema, S.; Quiles-Carrillo, L.; Garcia-Garcia, D.; Melendez-Rodriguez, B.; Balart, R.; Torres-Giner, S. Tailoring the properties of thermo-compressed polylactide films for food packaging applications by individual and combined additions of lactic acid oligomer and halloysite nanotubes. *Molecules* **2020**, *25*, 1976–1999 doi: 10.3390/molecules25081976.
38. Mahmood, H.; Pegoretti, A.; Brusa, R.S.; Ceccato, R.; Penasa, L.; Tarter, S.; Checchetto, R. Molecular transport through 3-hydroxybutyrate-co-3-hydroxyhexanoate biopolymer films with dispersed graphene oxide nanoparticles: gas barrier, structural and mechanical properties. *Polymer Testing* **2020**, *81*, 106181–106189 doi: 10.1016/j.polymertesting.2019.106181.
39. Ferri, J.; Jordá, J.; Montanes, N.; Fenollar, O.; Balart, R. Manufacturing and characterization of poly(lactic acid) composites with hydroxyapatite. *Journal of Thermoplastic Composite Materials* **2018**, *31*, 865–881 doi: 10.1016/j.polymertesting.2019.106181.
40. Giubilini, A.; Sciancalepore, C.; Messori, M.; Bondioli, F. New biocomposite obtained using poly(3-hydroxybutyrate-co-3-hydroxyhexanoate) (PHBH) and microfibrillated cellulose. *Journal of Applied Polymer Science* **2020**, *137*, 48953–48961 doi: 10.1002/app.48953.
41. Rehman, S.; Khan, K.; Mujahid, M.; Nosheen, S. Synthesis of nano-hydroxyapatite and its rapid mediated surface functionalization by silane coupling agent. *Material Science and Engineering: C* **2016**, *58*, 675–681 doi: 10.1016/j.msec.2015.09.014.



42. Medeiros, G.S.; Muñoz, P.A.; de Oliveira, C.F.; da Silva, L.C.; Malhotra, R.; Gonçalves, M.C.; Rosa, V.; Fachine, G.J. Polymer nanocomposites based on poly( $\epsilon$ -caprolactone), hydroxyapatite and graphene oxide. *Journal of Polymer Environment* **2020**, *28*, 331–342 doi: 10.1007/s10924-019-01613-w.
43. Pielichowska, K.; Król, K.; Majka, T.M. Polyoxymethylene-copolymer based composites with PEG-grafted hydroxyapatite with improved thermal stability. *Thermochimica Acta* **2016**, *633*, 98–107 doi: 10.1016/j.tca.2016.03.021.
44. Thorvaldsen, T.; Johnsen, B.B.; Olsen, T.; Hansen, F.K. Investigation of theoretical models for the elastic stiffness of nanoparticle-modified polymer composites. *Journal Nanomaterials* **2015**, *2015*, 1–17 doi: 10.1155/2015/281308.
45. Joseph, R.; McGregor, W.; Martyn, M.; Tanner, K.; Coates, P. Effect of hydroxyapatite morphology/surface area on the rheology and processability of hydroxyapatite filled polyethylene composites. *Biomaterials* **2002**, *23*, 4295–4302 doi: 10.1016/S0142-9612(02)00192-8.
46. Kalfus, J.; Jancar, J. Viscoelastic response of nanocomposite poly(vinyl acetate)–hydroxyapatite with varying particle shape–dynamic strain softening and modulus recovery. *Polymer Composites* **2007**, *28*, 743–747 doi: 10.1002/pc.20331.
47. Lin, E.K.; Kolb, R.; Satija, S.K.; Wu, W.-I. Reduced polymer mobility near the polymer/solid interface as measured by neutron reflectivity. *Macromolecules* **1999**, *32*, 3753–3757 doi: 10.1021/ma9814604.
48. Heise, U.; Osborn, J.; Duwe, F. Hydroxyapatite ceramic as a bone substitute. *International Orthopaedics* **1990**, *14*, 329–338 doi: 10.1007/BF00178768.
49. Oonishi, H. Orthopaedic applications of hydroxyapatite. *Biomaterials* **1991**, *12*, 171–178 doi: 10.1016/0142-9612(91)90196-H.
50. Yu, H.; Matthew, H.W.; Wooley, P.H.; Yang, S.Y. Effect of porosity and pore size on microstructures and mechanical properties of poly- $\epsilon$ -caprolactone–hydroxyapatite composites. *Journal of Biomedical Materials Research Part B Applied Biomaterials* **2008**, *86*, 541–547 doi: 10.1002/jbm.b.31054.

51. Quiles-Carrillo, L.; Montanes, N.; Pineiro, F.; Jorda-Vilaplana, A.; Torres-Giner, S. Ductility and toughness improvement of injection-moulded compostable pieces of polylactide by melt blending with poly( $\epsilon$ -caprolactone) and thermoplastic starch. *Materials* **2018**, *11*, 2138–2158 doi: 10.3390/ma11112138.
52. Lascano, D.; Moraga, G.; Ivorra-Martinez, J.; Rojas-Lema, S.; Torres-Giner, S.; Balart, R.; Boronat, T.; Quiles-Carrillo, L. Development of injection-molded polylactide pieces with high toughness by the addition of lactic acid oligomer and characterization of their shape memory behavior. *Polymers* **2019**, *11*, 2099–2118 doi: 10.3390/polym11122099.
53. Quiles-Carrillo, L.; Montanes, N.; Lagaron, J.; Balart, R.; Torres-Giner, S. In situ compatibilization of biopolymer ternary blends by reactive extrusion with low-functionality epoxy-based styrene-acrylic oligomer. *Journal of Polymer Environment* **2019**, *27*, 84–96 doi: 10.1007/s10924-018-1324-2.
54. Sheikh, F.A.; Ju, H.W.; Moon, B.M.; Lee, O.J.; Kim, J.H.; Park, H.J.; Kim, D.W.; Kim, D.K.; Jang, J.E.; Khang, G. Hybrid scaffolds based on PLGA and silk for bone tissue engineering. *Journal of Tissue Engineering and Regenerative Medicine* **2016**, *10*, 209–221 doi: 10.1002/term.1989.
55. Ji, Y.; ping Xu, G.; peng Zhang, Z.; jun Xia, J.; long Yan, J.; ha Pan, S. BMP-2/PLGA delayed-release microspheres composite graft, selection of bone particulate diameters, and prevention of aseptic inflammation for bone tissue engineering. *Annals of Biomedical Engineering* **2010**, *38*, 632–639 doi: 10.1007/s10439-009-9888-6.
56. Bender, S.; Chalivendra, V.; Rahbar, N.; El Wakil, S. Mechanical characterization and modeling of graded porous stainless steel specimens for possible bone implant applications. *International Journal of Engineering Science* **2012**, *53*, 67–73 doi: 10.1016/j.ijengsci.2012.01.004.
57. Niinomi, M.; Nakai, M. Titanium-based biomaterials for preventing stress shielding between implant devices and bone. *International Journal of Biomaterials* **2011**, *2011*, 1–10 doi: 10.1155/2011/836587.

58. Fouad, H.; Elleithy, R.; Alothman, O.Y. Thermo-mechanical, wear and fracture behavior of high-density polyethylene/hydroxyapatite nano composite for biomedical applications: effect of accelerated ageing. *Journal of Materials Science & Technology* **2013**, *29*, 573–581 doi: 10.1016/j.jmst.2013.03.020.
59. Popovich, A.; Sufiiarov, V.; Borisov, E.; Polozov, I.A. Microstructure and mechanical properties of Ti-6Al-4V manufactured by SLM. *Key Engineering Materials* **2015**, *651*, 677–682 doi: 10.4028/www.scientific.net/KEM.651-653.677.
60. Li, X.; Guo, C.; Liu, X.; Liu, L.; Bai, J.; Xue, F.; Lin, P.; Chu, C. Impact behaviors of poly-lactic acid based biocomposite reinforced with unidirectional high-strength magnesium alloy wires. *Progress in Natural Science: Materials International* **2014**, *24*, 472–478 doi: 10.1016/j.pnsc.2014.08.003.
61. Senatov, F.S.; Niaza, K.V.; Zadorozhnyy, M.Y.; Maksimkin, A.V.; Kaloshkin, S.D.; Estrin, Y.Z. Mechanical properties and shape memory effect of 3D-printed PLA-based porous scaffolds. *Journal of the Mechanical Behavior of Biomedical Materials* **2016**, *57*, 139–148 doi: 10.1016/j.jmbbm.2015.11.036.
62. Melendez-Rodriguez, B.; Castro-Mayorga, J.L.; Reis, M.A.M.; Sammon, C.; Cabedo, L.; Torres-Giner, S.; Lagaron, J.M. Preparation and characterization of electrospun food biopackaging films of poly(3-hydroxybutyrate-co-3-hydroxyvalerate) derived from fruit pulp biowaste. *Frontiers in Sustainable Food Systems*. **2018**, *2*, 1–16 doi: 10.3389/fsufs.2018.00038.
63. Zhou, J.; Ma, X.; Li, J.; Zhu, L. Preparation and characterization of a bionanocomposite from poly(3-hydroxybutyrate-co-3-hydroxyhexanoate) and cellulose nanocrystals. *Cellulose* **2019**, *26*, 979–990 doi: 10.1007/s10570-018-2136-1.
64. Yu, H.-Y.; Qin, Z.-Y.; Wang, L.-F.; Zhou, Z. Crystallization behavior and hydrophobic properties of biodegradable ethyl cellulose-g-poly(3-hydroxybutyrate-co-3-hydroxyvalerate): the influence of the side-chain length and grafting density. *Carbohydrate Polymers* **2012**, *87*, 2447–2454 doi: 10.1016/j.carbpol.2011.11.022.
65. Bikiaris, D. Can nanoparticles really enhance thermal stability of polymers? Part II: an overview on thermal decomposition of polycondensation polymers. *Thermochimica Acta* **2011**, *523*, 25–45 doi: 10.1016/j.tca.2011.06.012.

66. Pandele, A.M.; Constantinescu, A.; Radu, I.C.; Miculescu, F.; Ioan Voicu, S.; Ciocan, L.T. Synthesis and characterization of PLA-Micro-structured hydroxyapatite composite films. *Materials* **2020**, *13*, 274-287 doi: 10.3390/ma13020274.
67. Chen, D.Z.; Tang, C.Y.; Chan, K.C.; Tsui, C.P.; Yu, P.H.F.; Leung, M.C.P.; Uskokovic, P.S. Dynamic-mechanical properties and in vitro bioactivity of PHBV/HA nanocomposite. *Composites Science and Technology* **2007**, *67*, 1617-1626 doi: 10.1016/j.compscitech.2006.07.034.
68. Tipnis, N.P.; Burgess, D.J. Sterilization of implantable polymer-based medical devices: a review. *International Journal of Pharmaceutics* **2018**, *544*, 455-460 doi: 10.1016/j.ijpharm.2017.12.003.
69. Valentini, F.; Dorigato, A.; Rigotti, D.; Pegoretti, A. Polyhydroxyalkanoates/fibrillated nanocellulose composites for additive manufacturing. *Journal of Polymers and the Environment* **2019**, *27*, 1333-1341 doi: 10.1007/s10924-019-01429-8.
70. Torres-Giner, S.; Montanes, N.; Fenollar, O.; García-Sanoguera, D.; Balart, R. Development and optimization of renewable vinyl plastisol/wood flour composites exposed to ultraviolet radiation. *Materials & Design* **2016**, *108*, 648-658 doi: 10.1016/j.matdes.2016.07.037.
71. Quiles-Carrillo, L.; Boronat, T.; Montanes, N.; Balart, R.; Torres-Giner, S. Injection-moulded parts of fully bio-based polyamide 1010 strengthened with waste derived slate fibers pretreated with glycidyl- and amino-silane coupling agents. *Polymer Testing*. **2019**, *77*, 105875-105885 doi: 10.1016/j.polymertesting.2019.04.022.
72. Mohan, L.; Durgalakshmi, D.; Geetha, M.; Narayanan, T.S.; Asokamani, R. Electrophoretic deposition of nanocomposite (HAp+ TiO<sub>2</sub>) on titanium alloy for biomedical applications. *Ceramics International* **2012**, *38*, 3435-3443 doi: 10.1016/j.ceramint.2011.12.056.
73. Ferri, J.; Motoc, D.L.; Bou, S.F.; Balart, R. Thermal expansivity and degradation properties of PLA/HA and PLA/ $\beta$ TCP in vitro conditioned composites. *Journal of Thermal Analysis and Calorimetry* **2019**, *138*, 2691-2702 doi: 10.1007/s10973-019-08799-0.

74. Zuo, G.; Wei, X.; Sun, H.; Liu, S.; Zong, P.; Zeng, X.; Shen, Y. Morphology controlled synthesis of nano-hydroxyapatite using polyethylene glycol as a template. *Journal of Alloys and Compounds* **2017**, *692*, 693–697 doi: 10.1016/j.jallcom.2016.09.117.
75. Türkez, H.; Arslan, M.E.; Sönmez, E.; Açikyildiz, M.; Tatar, A.; Geyikoğlu, F. Synthesis, characterization and cytotoxicity of boron nitride nanoparticles: emphasis on toxicogenomics. *Cytotechnology* **2019**, *71*, 351–361 doi: 10.1007/s10616-019-00292-8



Sent to the journal.

### **III.2.3 P(3HB-co-3HHx)/nanohydroxyapatite (nHA) composites for the manufacturing of scaffolds by means of fused deposition modelling.**

Juan Ivorra-Martinez<sup>1</sup>, Ines Ferrer<sup>2</sup>, Roberto Aguado<sup>3</sup>, Marc Delgado-Aguilar<sup>3</sup>, Maria Luisa Garcia-Romeu<sup>2</sup> and Teodomiro Boronat<sup>1</sup>.

<sup>1</sup>Technological Institute of Materials - ITM, Universitat Politècnica de València - UPV, Plaza Ferrándiz y Carbonell 1, 03801 Alcoy (Spain).

<sup>2</sup>Depart. of Mechanical Engineering and Industrial Construction, University of Girona, c/M. Aurèlia Campmany, 61, Girona 17071 (Spain).

<sup>3</sup>LEPAMAP-PRODIS Research Group, University of Girona, c/M. Aurèlia Campmany, 61, Girona 17071 (Spain).





**Abstract.**

The development of nanocomposites prepared from P(3HB-co-3HHx) and nanohydroxyapatite -nHA for the development of 3D printed scaffolds by means of a two-stage extrusion process was carried out. Each thermal cycle promoted a thermal degradation identified by means of Differential Scanning Calorimetry - DSC, thermogravimetry - TGA and rheological measurements. The 3D printed structures exhibited increasing stiffness at increasing nHA content, while strength and strain at break was reduced. While the neat polymer exhibited a tensile strength of 18.2 MPa and a strain at break of 16.7 %, the composite with 10 wt.% of nHA had 16.0 MPa and 6.7 %. The raster angle also had an effect in the mechanical properties, the 0 ° exhibited the highest tensile strength but also the lower elongation at break, while the 45 °/- 45 ° deposition resulted in higher strain. Scaffolds were immersed in a Phosphate Buffer Saline - PBS to induce a hydrolytic degradation at 37 °C. As a result, a reduction on their weight up to 3 % in 8 weeks was observed, also a decreased compression strength from 12.2 MPa to 9.3 MPa in 8 weeks for the composite with 10 wt.% of nHA was observed. The obtained scaffolds could be employed as a medical device that help the bone regeneration process.

**Keywords:** nanohydroxyapatite - nHA; polyhydroxyalkanoates - PHAs; fused filament deposition modelling - FDM; Additive Manufacturing - AM; scaffold.

---



## INTRODUCTION.

Additive Manufacturing – AM has appeared as a novel manufacturing strategy based on the freedom of design, mass customization and the manufacture of complex structures, as well as rapid prototyping [1,2]. Out of the different AM techniques, encompassing stereolithography – SLA, Selective Laser Sintering – SLS, Contour Crafting – CC, Powder Bed Fusion – PBF or Fused Deposition Modelling – FDM, the latter has evolved over the last year to the point that it is currently applied in different sectors, such as construction, automotive, and biomedicine [3–5]. FDM, also known as 3D printing, has positively impacted the medical industry, particularly for the possibility of producing customized implants prostheses, scaffolds for tissue regeneration or even highly efficient drug delivery systems [6–8]. Unlike conventional processes, which may include casting, forging, or machining operations with high manufacturing costs for low-volume production series, AM is advantageous in terms of customization, as multiple operations are avoided and the production processes of customized prostheses, for instance, is clearly simplified even for complex geometries [9]. This is because of the layer-by-layer operation principle, which allows building up the final product following a Computer Aided Design – CAD software [10,11].

Among the different healthcare applications, in which FDM can be used, the manufacture of scaffolds for tissue engineering is an emerging trend. A clear example is the production of nHA-poly(lactic acid) scaffolds, which have been reported to benefit the reconstruction of large bone defects [12], as they enhance the adhesion and proliferation of cells to carry out the regeneration process of damaged tissue [13,14]. Indeed, one of the most important features in optimizing scaffold performance is to obtain successfully interconnected pores to promote the nutrient transport and integration with the surrounding tissue [15–17].

The development of medical devices can be satisfied by several materials, including metals (*i.e.* cobalt-chrome alloys or titanium), ceramic materials, and polymers and polymer-based composites [18], whose suitability is subjected to the final application. In the case of metallic materials, they have been historically used for medical implants due to their biocompatibility in the long term and high wear resistance, which allow their use in artificial joints, stents, or valves [19,20]. Ceramic materials, such as hydroxyapatite – HA and tricalcium phosphate – TCP are attracting interest in the medical sector due to their presence in bones, although its use is limited by its intrinsic fragility. Indeed, this limits its application as bulk material, and most of the works report

their use as prosthesis coating or filler [12,14,21,22]. Concretely, as HA represents around the 70 % by weight of the human bones and counts on osteoconductive capacity, it has been used in different applications in the field of tissue engineering, particularly for bone regeneration [23]. However, its powder-like structure and rigidity limit its application as bulk material, requiring the use of matrices to be embedded into, at least during the processing stage [22,24–26]. Among the matrices, thermoplastic materials deserve special attention, as they are mostly used in FDM. Polymers derived from fossil resources, such as polyethylene - PE, have been broadly used in applications such as implants. However, renewable polymers are also widely used in FDM, such as poly(lactic acid) - PLA, biopolyethylene - BioPE, polylactide-*co*-glycolide - PLGA or polyhydroxyalkanoates - PHAs [5,12,27–30]. Further, oil-based but biodegradable and compatible polymers are also attracting interest, particularly in combination with bio-based and biodegradable materials, such is the case of poly( $\epsilon$ -caprolactone) - PCL [31]. Out of the broad range of bio-sourced polymers, PHAs are gaining interest due to their compatibility, as some of their constituents can be naturally found in human blood [28], making them an excellent option for medical devices [30,32,33].

Apart from biocompatibility, which is a requirement for any medical device, the degradation rate of materials is also of interest, particularly for temporary implants and scaffolds that would require a second intervention for an after-use removal [34]. The degradation process of polymers within the human body is particularly critical, and some polymers may generate inflammation, such is the case of PLGA [35]. For instance, the oligomers released from PLA degradation have been reported to produce toxicity within the human body due to the accumulation of lactic acid, whereas the 3-hydroxybutyrate (3HB) from PHA degradation is a common metabolite in living species due to the breakage of long-chain fatty acids, meaning that PHA is biocompatible also in degradation conditions [36–38]. Indeed, the inflammatory response of PLA compared to poly(3-hydroxybutyrate-*co*-3-hydroxyhexanoate) - P(3HB-*co*-3HHx) has been previously reported to be higher in previous studies [39]. Among the different PHAs, poly(3-hydroxybutyrate) - P3HB is the most common, but its thermal stability is low and, thus, degradation is common during processing [40]. Copolymers such as P(3HB-*co*-3HHx) can achieve higher thermal stability, making its processing more suitable [41].

The use of composite materials opens a new paradigm, as the combination of two or more materials may result in interesting properties. For instance, the combination of polymers with ceramic fillers (*i.e.* HA) can improve biocompatibility and bone

regeneration capacity, while higher ductility is obtained [42]. Exemplarily, increasing HA contents on PLA resulted in higher biocompatibility and bioactivity of PLA, or cell proliferation enhancement in the case of PCL as matrix [43,44].

For all the above, the present work proposes the development of nanocomposites prepared from P(3HB-co-3HHx) and nHA for its application in AM, targeting the development of bioactive and biodegradable materials for 3D printing of medical devices. To this effect, standard tensile specimens were 3D printed to assess the mechanical properties and the effect from all the processing stages was also analysed by thermal and rheological studies. The main novelty focuses in the fabrication of P(3HB-co-3HHx)/nHA scaffolds that were submitted to a degradation in a Phosphate Buffer Saline - PBS for two months to measure the mechanical behaviour in a compression test.

## MATERIALS AND METHODS.

### Materials.

P(3HB-co-3HHx) commercial grade (Ercros® PH 110) was supplied by Ercros S.A. (Barcelona, Spain) in pellet form and was used as polymer matrix of the nanocomposites. The main characteristics of the polymer, according to the supplier, are reported in **Table III.2.3.1**. Commercially available nHA, purchased from Merck (Madrid, Spain) (Ref: 677418) was used as filler for the nanocomposites. According to the supplier, this nHA counted on a surface area higher than 9.4 m<sup>2</sup>/g determined by Brunauer-Emmet-Teller - BET analysis, the particle size was lower than 200 nm, the purity was reported to be equal or higher to 97 % and a molecular weight of 502.31 g/mol.

**Table III.2.3.1.** P(3HB-co-3HHx) characteristics according to the supplier.

Characteristic	Value	Units	Standard
Melt Flow Index - MFI	1	g/10min	ISO 1133-2 (160 °C and 2.16 kg)
Density	1.20	g/cm <sup>3</sup>	ISO 1183-1
Melting temperature	124	°C	ISO 11357
Glass transition temperature - T <sub>g</sub>	1	°C	ISO 11357
Tensile modulus	0.9	GPa	EN ISO 527
Strain at break	21	%	EN ISO 527
Vicat	62	°C	ISO 1133 (5 kg)

All reagents for characterization were acquired at Merck (Madrid, Spain) and were used without further purification.

**Nanocomposites preparation.**

The matrix and the filler were dried at 80 °C in an oven (Industrial Marsé, S.A., Barcelona, Spain) until constant weight to remove moisture. Subsequently, the materials were manually premixed in zippered bags at nHA contents of 0.0, 2.5, 5.0 and 10.0 wt.%. The resulting samples were labelled as P(3HB-co-3HHx)/nHA content. For instance, the sample containing 5.0 wt.% of nHA was codified as P(3HB-co-3HHx)/5nHA, while the neat matrix (0.0 wt.% nHA) was named as P3HB-co-3HHx. The premixture consisted of 800 g of material, which were passed through a twin-screw extruder from Dupra S.L. (Castalla, Spain). The extruder is equipped with 4 individual heating zones housing two 25 mm diameter screws with a length to diameter (L/D) ratio of 24. All extrusions were performed with a screw speed ranging from 20 to 25 rpm with a temperature profile of 140 - 145 - 150 - 155 °C. The pelletized nanocomposites were stored in hermetic plastic bags to prevent moisture uptake.

**Filament extrusion and 3D printing parameters.**

A single-screw extruder equipped with four heating zones, model Next 1.0 from 3devo (Utrecht, The Netherlands), was used to obtain the 3D printing filaments. The temperature profile from the inlet hopper to the nozzle was 150 - 155 - 160 - 150 °C, with an extrusion speed of 5 rpm. The extruder counts on a feedback cascade controller able to adjust the rotational speed of the spool to target the desired filament diameter. The diameter was set at 2.85 mm, obtaining average diameters of  $2.85 \pm 0.03$ ,  $2.85 \pm 0.05$ ,  $2.85 \pm 0.04$ , and  $2.84 \pm 0.10$ , for the nanocomposites containing 0.0, 2.5, 5.0, and 10.0 wt.% of nHA, respectively.

3D printing was carried out using an Ultimaker 3 (Utrecht, The Netherlands) equipped with a 0.8 mm nozzle. For the present work, two geometries were considered: tensile test specimens (**Figure III.2.3.1a.**), according to ISO 527 and scaffolds (**Figure III.2.3.1b.**). The printing parameters can be observed in **Table III.2.3.2.**

**Table III.2.3.2.** Printing parameters for the tensile test specimens and the scaffolds.

<b>Printing Process Parameter</b>	<b>Tensile test specimens</b>	<b>Scaffolds</b>
Printing temperature (°C)	170	170
Bed temperature (°C)	65	65
Printing speed (mm/s)	30	30
Layer height (mm)	0.2	0.2
Infill (%)	100	70
Raster angle (°)	0 °; 0 °/90 ° and 45 °/- 45 °	0 °/90 °
Printing orientation	Flat	Flat

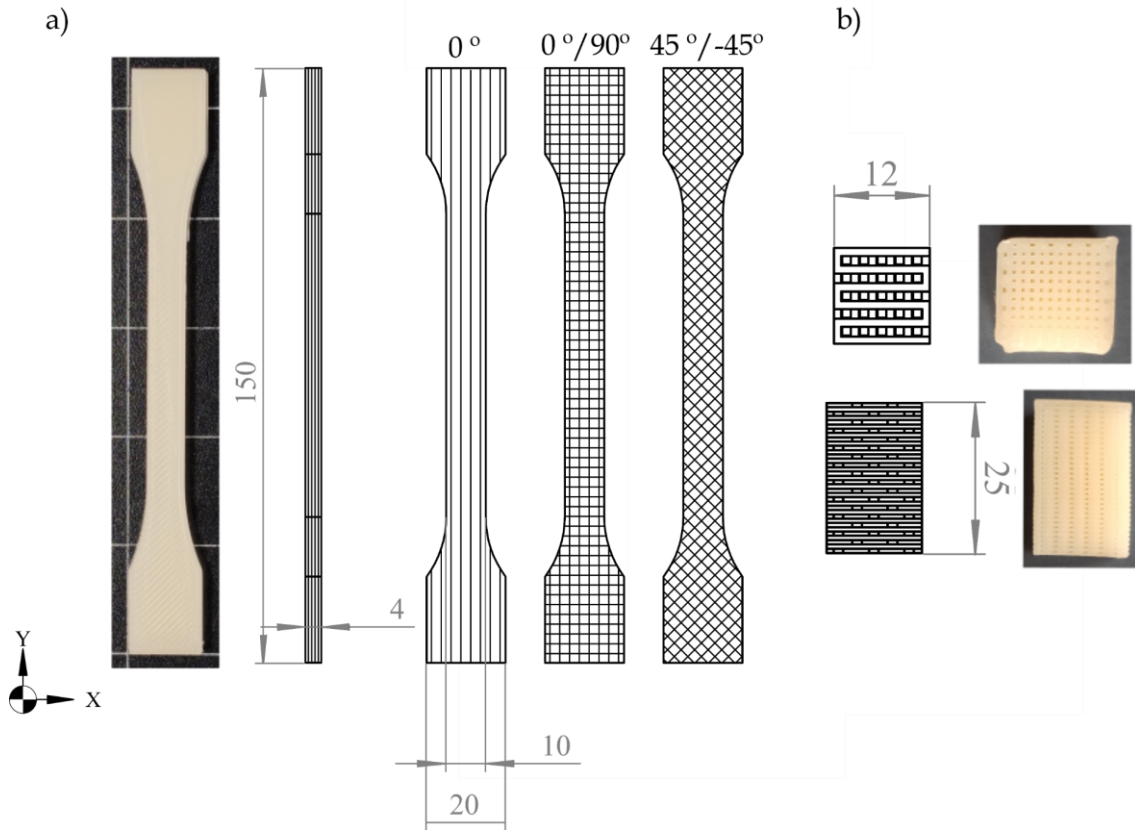


**Figure III.2.3.1.** Geometry and raster angle of the tensile test specimens a) and scaffolds b).

Three replicates were printed for each raster angle condition in the case of tensile test specimens, while fifteen scaffolds were printed. The infill of the scaffolds was set at 70 % to tailor the porosity of the resulting structures. While tensile tests were used to characterize the physical properties (mechanical, thermal and rheological), as it will be subsequently discussed, scaffolds were used to assess their degradation in a PBS by means of immersion. Compression tests were also carried out with the scaffolds.

#### **Physical and mechanical characterization of nanocomposites.**

Tensile test on tensile specimens and compression testing on scaffolds tests were carried out according to ISO 527 and ISO 604, respectively, in an ELIB 30 universal testing machine from S.A.E. Ibertest (Madrid, Spain), equipped with a 5 kN load cell and a crosshead speed of 5 mm/min. Three samples were tested for each mechanical characterization. The main parameters obtained were tensile strength -  $\sigma_t$ , elongation at break -  $\varepsilon_b$ , tensile modulus -  $E_t$ , compression strength at yield -  $\sigma_c$  and deformation at yield -  $\varepsilon_c$ .

Differential Scanning Calorimetry – DSC tests were performed over a small part of the extruded material – E, the filament – F, and the 3D-printed sample – 3D in a Mettler Toledo 821 from Mettler-Toledo Inc. (Schwerzenbach, Switzerland). First of all, a heating-cooling cycle was performed to remove the thermal history of the material by means of heating from 30 to 200 °C and cooling down to - 5 °C. The third heating scan went from 50 to 200 °C. Heating and cooling rates were set at 10 °C/min, using a nitrogen atmosphere with a flow rate of 66 mL/min. The DSC test provided the melting temperature –  $T_m$ , the cold crystallization temperature –  $T_{cc}$ , the melting enthalpy –  $\Delta H_m$ , and the cold crystallization enthalpy –  $\Delta H_{cc}$ .

$$\chi_c(\%) = \frac{\Delta H_m - \Delta H_{cc}}{\Delta H_m^0(1 - w)} \cdot 100 \quad \text{Equation III.2.3.1.}$$

Crystallinity was calculated from the enthalpies, the mass fraction of polymer ( $w$ ) and the normalized enthalpy for a fully crystalline sample –  $\Delta H_m^0$ , as reported in **Equation III.2.3.1**. The  $\Delta H_m^0$  values for P(3HB-co-3HHx) was considered as 146 J/g [45].

Thermogravimetric analysis – TGA was measured using samples with an average weight of 15 – 25 mg in a PT1000 from Linseis (Selb, Germany). The nanocomposites were placed in 70  $\mu$ L alumina crucibles and subjected to a heating from 30 to 700 °C. The heating rate was set at 20 °C/min and tests were performed in a nitrogen atmosphere. The main results considered were the onset degradation temperature at 5 wt.% loss –  $T_{5\%}$  and the maximum degradation rate –  $T_{max}$  obtained by the peak in the first derivative curve – DTG.

For the rheological measurements, discs of 25 mm diameter and 1 mm height after each processing stage (E, F, and 3D) were obtained for rheological measurements by means of compression moulding in a hot-plate press at 160 °C and 300 bar for 1 min. The rheological behavior was measured in an oscillatory rheometer AR G2 from TA Instruments (New Castle, USA). The rheometer configuration was plate-plate (25 mm of diameter) using a gap of 0.5 mm to allow the sample insertion. Frequency sweep experiments were carried out at a fixed strain of 0.1 %. The storage modulus –  $G'$ , loss modulus –  $G''$ , and the complex viscosity –  $\eta^*$  were determined from rheological measurements. The angular frequencies were swept from 100 to 0.01 Hz with five points per decade at 170 °C.



**Scaffolds characterization.**

Prior to immersion in PBS, scaffolds were numbered and weighted to obtain the initial mass –  $W_0$ . The scaffolds were then placed in individual bottles containing PBS and kept at 37 °C for 8 weeks. The PBS was replaced every week, taking out three scaffolds every two weeks for characterization purposes.

The total porosity of scaffolds was determined by gravimetry according to **Equation III.2.3.2.**, where  $\rho_{\text{scaffold}}$  is the density of the scaffold calculated from the apparent volume and the scaffold weight, and  $\rho_{\text{material}}$  is the density of each nanocomposite, [46]. Density was determined in a densitometer from Testing Machines Inc (Delaware, USA) with a resolution of 0.001 g/cm<sup>3</sup>.

$$\text{Total porosity} = 1 - \frac{\rho_{\text{scaffold}}}{\rho_{\text{material}}} \quad \text{Equation III.2.3.2.}$$

Prior to immersion scaffolds were weighted to obtain the initial weight ( $W_0$ ). Scaffolds were manually dried to remove the excess of PBS and weighted ( $W_w$ ) to obtain the amount of absorbed PBS ( $W_g$ ), according to **Equation III.2.3.3.** After this, samples were oven-dried to remove moisture and weighted ( $W_d$ ), allowing the determination of the weight loss ( $W_l$ ), according to **Equation III.2.3.4.** In each extraction, the pH of PBS was measured.

$$W_g(\%) = \frac{W_w - W_0}{W_0} \quad \text{Equation III.2.3.3.}$$

$$W_l(\%) = \frac{W_d - W_0}{W_0} \quad \text{Equation III.2.3.4.}$$

Surface morphology of the scaffolds (prior and after immersion in PBS) was assessed by means of Field Emission Scanning Electron Microscopy – FSEM in a Zeiss Ultra 55 FESEM microscope from Oxford Instruments (Abingdon, UK), operating at an accelerating voltage of 2 kV. Samples were coated with gold-palladium alloy in an EMITECH mod. SC7620 sputter coater from Quorum Technologies Ltd. (East Sussex, UK).

Finally, the chemical analysis of the scaffold surface was analysed by Attenuated Total Reflectance – Fourier-Transform Infrared Spectroscopy – ATR-FTIR. Bruker S.A. Vector 22 (Madrid, Spain) coupled with an ATR measuring accessory from Pike Technologies (Madison, WI, USA) were employed. Wavelengths between 4000 and 600 cm<sup>-1</sup> with a resolution of 4 cm<sup>-1</sup> were used for the scan and each spectrum was collected from an average of 10 measurements.

## RESULTS AND DISCUSSION.

**Mechanical properties of the P(3HB-co-3HHx)/nHA nanocomposites.**

The performance of the 3D-printed samples in tensile tests is displayed in **Figure III.2.3.2**. Materials printed with different raster angles are compared to those produced by injection moulding [47]. In any case, regardless of the manufacturing method, composites with the largest proportion of nHA (10 wt.%) consistently showed the lowest average values for the ultimate  $\sigma_t$  and the strain at break. Nonetheless, nHA also increased the stiffness of P(3HB-co-3HHx), as the  $E_t$  of the composites with 10 % of nHA was significantly higher than the rest of combinations for all the production processes. It can be inferred that the reinforcement effect produced by the nanoparticles limits the mobility of the polymer chains during tensile tests leading to a  $\varepsilon_b$  reduction [48].

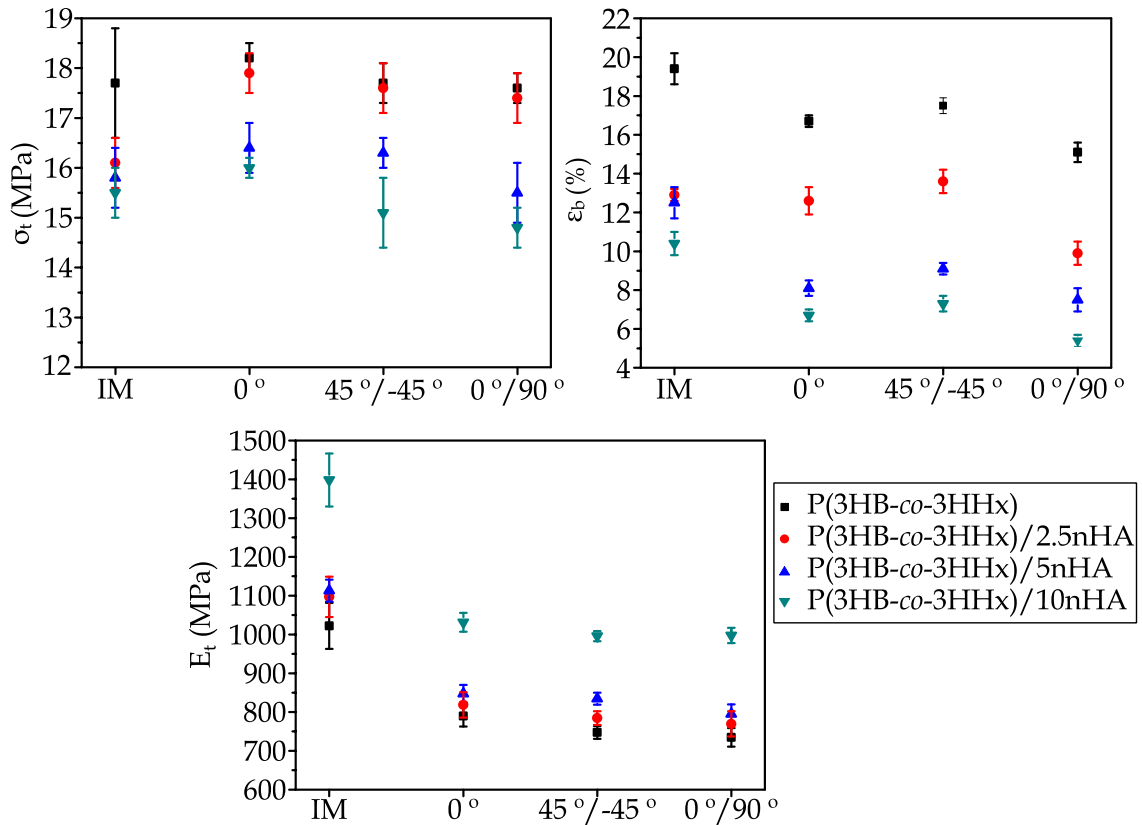


**Figure III.2.3.2.** Mechanical properties of the P(3HB-co-3HHx)/nHA tensile specimens at different raster angles and compared to injection moulding - IM.

Comparing samples with the same proportion of nHA, differences arise due to the high dependence of the AM on the raster angle employed. Those with the raster aligned with the direction of the force vector (0°) resulted in the best outputs in  $\sigma_t$  and stiffness ( $E_t$ ), since a favourable monoaxial orientation of P(3HB-co-3HHx) chains was

promoted [49]. In agreement, previous works using PLA for AM achieved the best  $\sigma_t$  values for low raster angles, between  $0^\circ$  and  $20^\circ$  [50]. Under these conditions, stress is transferred along the deposited lines, while higher angles imply transmission of mechanical stress at the interfaces of adjacent deposited lines [51]. Nonetheless, for the  $\varepsilon_b$ , the  $45^\circ/-45^\circ$  disposition provided the best results as also reported by Tian *et al.* [52]. In this case, the lines deposited have, unlike for  $0^\circ$  or  $0^\circ/90^\circ$  angles, certain ability to rotate, allowing for a slightly greater deformation before rupture.

Owing to the detrimental effects of pore formation during deposition, injection moulding outperformed 3D printing in most cases, both in terms of  $\sigma_t$  and in terms of  $E_t$ . Indeed, induced porosity is a well-known limitation of 3D printing [53]. In injection moulding, the packing pressure applied avoids pore generation [54]. As an exception to this trend, the samples printed with a raster angle of  $0^\circ$  consistently improved the tensile strength attained by injection moulding for all of P(3HB-*co*-3HHx)/(nHA) composites, regardless of the composition. However, the difference between P(3HB-*co*-3HHx) (without nHA) produced by injection moulding and that produced by 3D printing was non-significant, as evidenced by the completely overlapped intervals.

The polymeric matrix here in employed is highly sensitive to the shear rates applied. In the injection moulding process, the high shear stress promotes the degradation of P(3HB-*co*-3HHx) chains. Consequently, the reduction of the molecular weight leads to a diminishment of key mechanical properties, as found for PLA during injection moulding [55,56]. In contrast, lower shear rates were applied on samples produced by AM. This is also why, in the absence of nHA, P(3HB-*co*-3HHx) printed samples sustained greater  $\varepsilon_b$  rupture than those obtained by injection. All considered, the low shear induced degradation during 3D printing might compensate for its detrimental induction of porosity.

### **Thermal properties of the P(3HB-*co*-3HHx)/nHA nanocomposites.**

**Figure III.2.3.3.** shows the DSC thermograms collected for P(3HB-*co*-3HHx) and its composites produced after each thermal cycle, *i.e.* melt blending extrusion process (E), 3D printing filament fabrication (F), and 3D printed part (3D). In addition, the temperatures at which the thermal transitions occurred and their enthalpies are summarized in **Table III.2.3.3.** Given that P(3HB-*co*-3HHx) is a copolymer with two kinds of functional groups (carbonyl and ether) and with alkyl chains, three melting peaks are obtained found  $108^\circ\text{C}$  and  $162^\circ\text{C}$ , corresponding to the different kind of crystals formed. This behavior was not qualitatively modified by the introduction of

nHA. An exothermic peak assigned to cold crystallisation is observed around 50 °C. Moreover, the change of baseline at 0 – 5 °C is linked with the  $T_g$ .

The different thermal cycles at which the samples were submitted promoted a difference in the characteristic transition temperatures. The biggest differences emerged for the  $T_{cc}$ , which was reduced from 52.1 °C for P(3HB-co-3HHx) after the first extrusion process to 49.6 °C after 3D printing. Similar results were reported after a recycling process on dried and wet PLA [57]. This phenomenon was caused by the reduction of the molecular weight of the polymer chains that occurred due to the successive thermal cycles at which the sample was submitted. The presence of nHA reduced these differences, similarly to the effects found for the incorporation of cloisite into a polypropylene matrix [58].

Regarding the melting enthalpies, the differences between the thermal cycles were almost insignificant, whereas the cold crystallization enthalpy decreased notably. During each cycle, polymer chains are cleaved to a certain extent. This prompted the rearrangement of the polymer chains during the cooling cycle, and thus the degree of crystallinity increased. This behavior is typical when reprocessing polymers [59].

Generally, the addition of nHA did not affect the key thermal properties (namely, transition temperatures) but had a significant influence on the crystallinity degree. The introduction of the nanoparticles implied the establishment of new filler-matrix interactions, partially replacing previous polymer-polymer interactions [60]. This resulted in a loss of supramolecular order.

**Table III.2.3.3.** DSC characteristics of the P(3HB-co-3HHx)/nHA nanocomposites.

Code		$T_g$ (°C)	$T_{cc}$ (°C)	$T_{m1}$ (°C)	$T_{m2}$ (°C)	$T_{m3}$ (°C)	$\Delta H_{cc}$ (J/g)	$\Delta H_m$ (J/g)	$x_c$ (%)
P(3HB-co-3HHx)	E	0.8 ± 0.2	52.1 ± 0.1	108.5 ± 0.1	125.2 ± 0.1	161.3 ± 0.2	27.7 ± 0.2	49.6 ± 0.2	15.0 ± 0.2
	F	1.0 ± 0.1	50.1 ± 0.2	109.5 ± 0.3	126.7 ± 0.2	161.5 ± 0.2	27.1 ± 0.3	49.5 ± 0.3	15.3 ± 0.1
	3D	0.8 ± 0.1	49.6 ± 0.1	109.9 ± 0.2	126.5 ± 0.2	161.4 ± 0.1	24.0 ± 0.3	50.9 ± 0.1	18.5 ± 0.1
P(3HB-co-3HHx)/2.5nHA	E	1.1 ± 0.2	54.3 ± 0.2	110.6 ± 0.1	126.9 ± 0.1	161.6 ± 0.2	28.0 ± 0.1	45.0 ± 0.1	11.9 ± 0.1
	F	1.0 ± 0.1	54.3 ± 0.1	110.9 ± 0.3	126.9 ± 0.1	161.6 ± 0.1	26.7 ± 0.1	45.5 ± 0.1	13.2 ± 0.1
	3D	1.0 ± 0.1	54.1 ± 0.2	111.0 ± 0.3	127.1 ± 0.1	161.8 ± 0.1	23.5 ± 0.1	45.1 ± 0.1	15.2 ± 0.1
P(3HB-co-3HHx)/5nHA	E	1.0 ± 0.1	54.3 ± 0.2	111.2 ± 0.3	126.6 ± 0.1	161.9 ± 0.2	27.2 ± 0.1	37.3 ± 0.1	7.3 ± 0.1
	F	0.8 ± 0.1	55.5 ± 0.1	110.9 ± 0.2	126.8 ± 0.2	161.3 ± 0.2	25.1 ± 0.1	37.3 ± 0.1	8.8 ± 0.1
	3D	0.8 ± 0.1	55.6 ± 0.1	111.0 ± 0.1	128.6 ± 0.1	161.5 ± 0.1	24.4 ± 0.1	37.7 ± 0.1	9.6 ± 0.1
P(3HB-co-3HHx)/10nHA	E	0.7 ± 0.1	57.1 ± 0.2	112.1 ± 0.2	128.4 ± 0.2	161.8 ± 0.1	29.7 ± 0.1	36.2 ± 0.1	4.9 ± 0.1
	F	0.6 ± 0.2	58.1 ± 0.1	111.6 ± 0.2	128.7 ± 0.1	161.2 ± 0.2	26.7 ± 0.1	36.3 ± 0.1	7.3 ± 0.1
	3D	0.8 ± 0.1	57.9 ± 0.1	111.7 ± 0.1	127.7 ± 0.2	161.3 ± 0.1	25.0 ± 0.1	36.9 ± 0.1	9.0 ± 0.1

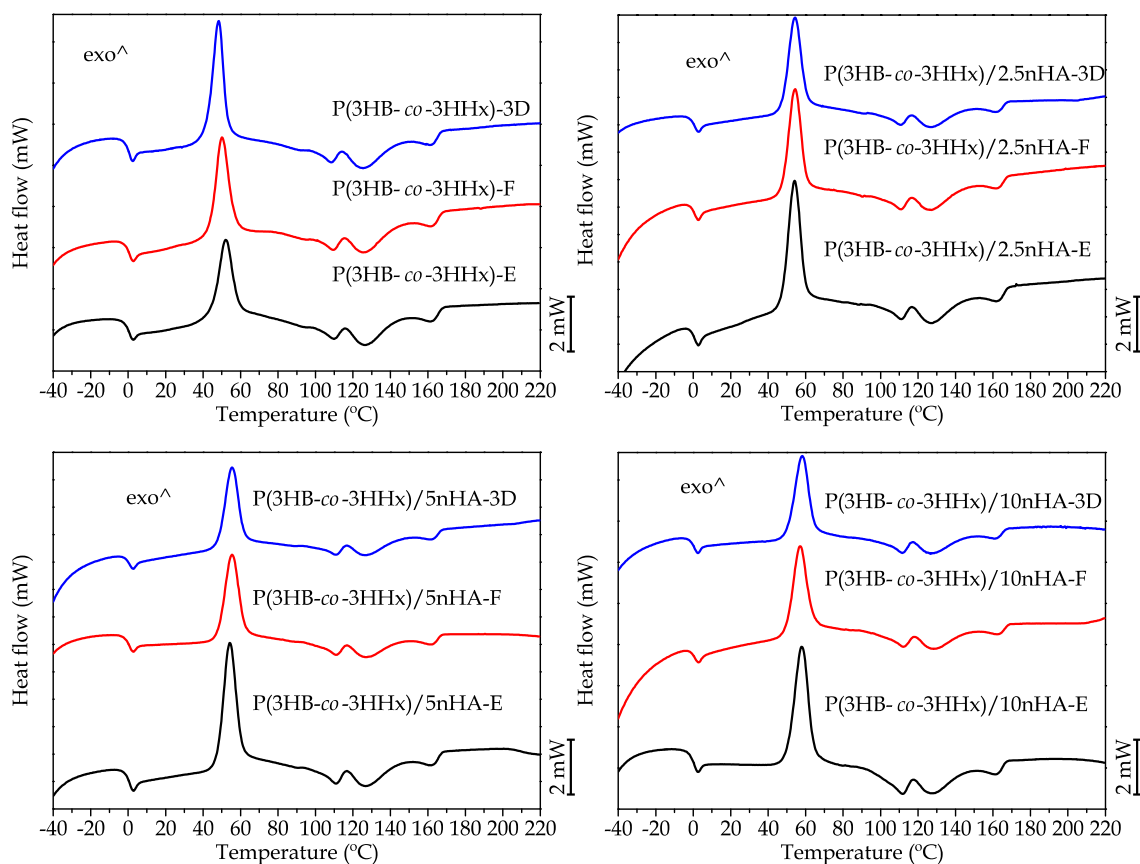


**Figure III.2.3.3.** DSC thermograms of the P(3HB-*co*-3HHx)/nHA nanocomposites.

**Table III.2.3.4.** collects the key temperature values from the TGA and DTG. For all the different samples analysed,  $T_{5\%}$  values were ranged between 261 °C and 271 °C. Small amounts of nHA (2.5 wt.%) increased the initial degradation temperature, but higher amounts of nanoparticles reduced the thermal stability of the sample. The cleavage of polymer chains due to the thermal cycles promoted a slight reduction in the thermal stability of the samples analysed [61]. Such reduction is not relevant enough to limit the manufacturing process [62].

Regarding  $T_{max}$ , a significant improvement was obtained for nHA additions up to 5 wt.%, with values around 292 °C. However, increasing the proportion of nHA to 10 % yielded a decrease, likely related to the loss of crystallinity that was mentioned above. Overall, the ceramic structure of these nanoparticles provides a high thermal stability, since nHA does not degrade below 700 °C. This improvement was caused by the formation of strong hydrogen bonds between the polymer (the acceptor) and the nanofiller (the donor) [63].

Finally, owing to the non-degradation of nHA between 50 and 700 °C, the residue obtained at the end of the test is proportional to its fraction in each material.

**Table III.2.3.4.** Thermal degradation properties of the P(3HB-*co*-3HHx)/nHA nanocomposites.

Code		T <sub>5%</sub> (°C)	T <sub>max</sub> (°C)	Residual weight (%)
P(3HB- <i>co</i> -3HHx)	E	267.5 ± 0.5	283.4 ± 0.3	2.1 ± 0.2
	F	270.3 ± 0.6	281.2 ± 0.4	3.2 ± 0.3
	3D	266.1 ± 0.7	280.3 ± 0.2	1.8 ± 0.3
P(3HB- <i>co</i> -3HHx)/2.5nHA	E	271.2 ± 0.4	288.2 ± 0.2	2.5 ± 0.4
	F	269.8 ± 0.5	286.7 ± 0.4	2.7 ± 0.3
	3D	269.9 ± 0.5	285.8 ± 0.5	3.4 ± 0.2
P(3HB- <i>co</i> -3HHx)/5nHA	E	268.7 ± 0.4	293.5 ± 0.3	7.1 ± 0.5
	F	267.9 ± 0.4	292.0 ± 0.2	6.8 ± 0.4
	3D	267.1 ± 0.3	291.1 ± 0.5	6.6 ± 0.3
P(3HB- <i>co</i> -3HHx)/10nHA	E	262.5 ± 0.5	288.7 ± 0.5	12.4 ± 0.4
	F	261.6 ± 0.4	286.8 ± 0.4	11.9 ± 0.3
	3D	261.1 ± 0.3	285.4 ± 0.4	11.9 ± 0.4

#### Rheological properties of the P(3HB-*co*-3HHx)/nHA nanocomposites.

The rheological properties of the different composites showed shear-thinning behavior, as presented in **Figure III.2.3.4**. First, a reduction in the complex viscosity was observed in each thermal cycle of the sample. For example, in P(3HB-*co*-3HHx) following melt bending extrusion (E), a complex viscosity of 3761 Pa s at 1 rad/s was obtained, whereas after the 3D printing process this parameter adopted a value of 3197 Pa s. This phenomenon, also found for PLA [64], confirms the hypothesis of thermal degradation that promotes the chain scission of the polymer chains. The difference on the complex viscosity through the different thermal cycles was notably reduced.

When the amount of hydroxyapatite increased, smaller differences between each cycle were recorded. A higher degree of particle dispersion typically results in higher values of complex viscosity, due to the greater number of particle-matrix interactions [65]. At the same time, during the melting state of the polymer, thermal degradation takes place. Both effects are overlapped during the processing of the materials. As a result, after each thermal cycle, complex viscosity decreased, but the differences that arose were smaller.

Additionally depending on the amount of nHA considered an increase of the complex viscosity was obtained due to the increase of the nanofiller. This is a typical behavior after the incorporation of particles in a polymer [66].

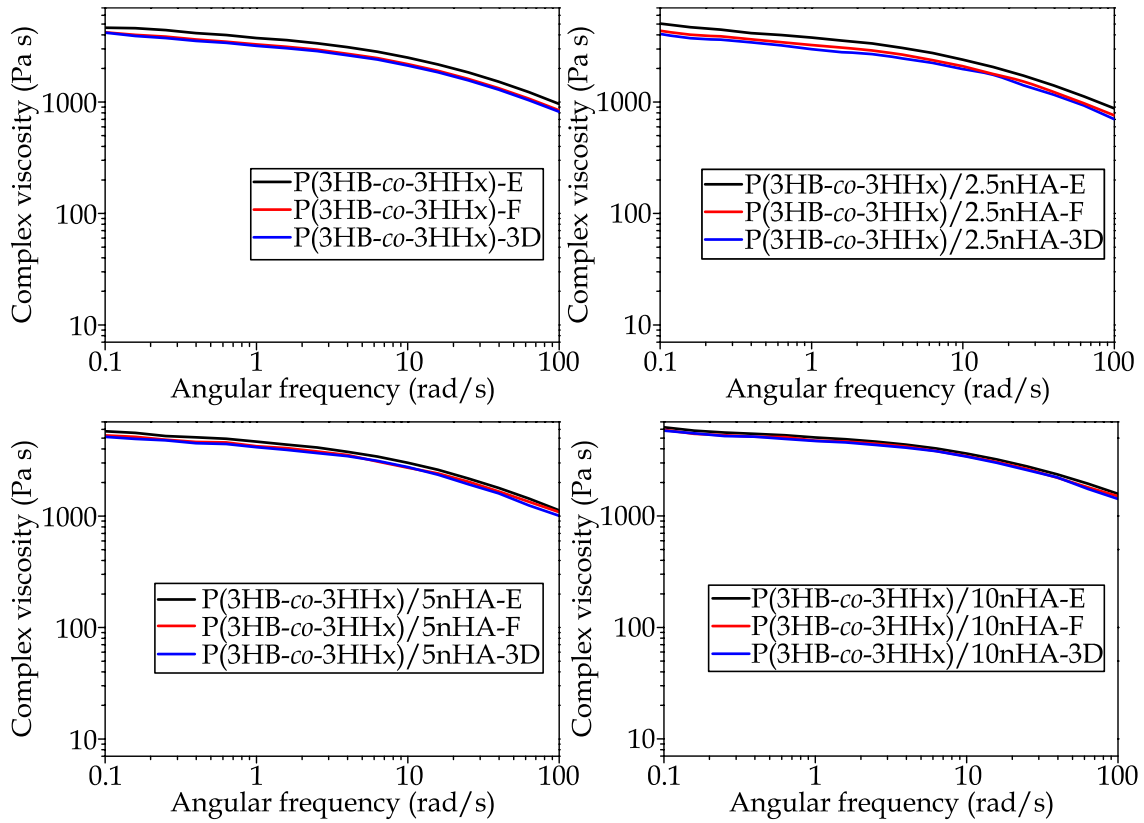


**Figure III.2.3.4.** Rheological behavior of the P(3HB-*co*-3HHx)/nHA nanocomposites.

#### Porosity of the PBS of the P(3HB-*co*-3HHx)/nHA nanocomposites.

**Table III.2.3.5.** shows the scaffold porosity and standard deviation obtained for each material composition. First to notice is the effect of introducing the hydroxyapatite increased the density of the composites due to the presence of the ceramic material [26]. The values obtained for the density ranged from the 1.215 g/cm<sup>3</sup> of the neat polymer up to 1.352 g/cm<sup>3</sup> for the composite with the highest ceramic content. Regarding the porosity obtained, with the manufacturing conditions (70 % infill) the calculated values were in all cases close to 0.2, with a difference of 4.1 % between all the compositions prepared.

**Table III.2.3.5.** Main porosity results for the AM scaffolds.

Code	Material density (g/cm <sup>3</sup> )	Scaffold Porosity
P(3HB- <i>co</i> -3HHx)	1.215 ± 0.008	0.222 ± 0.005
P(3HB- <i>co</i> -3HHx)/2.5nHA	1.254 ± 0.007	0.218 ± 0.006
P(3HB- <i>co</i> -3HHx)/5nHA	1.263 ± 0.007	0.214 ± 0.004
P(3HB- <i>co</i> -3HHx)/10nHA	1.352 ± 0.010	0.213 ± 0.006

## Saline degradation in PBS of the P(3HB-co-3HHx)/nHA nanocomposites.

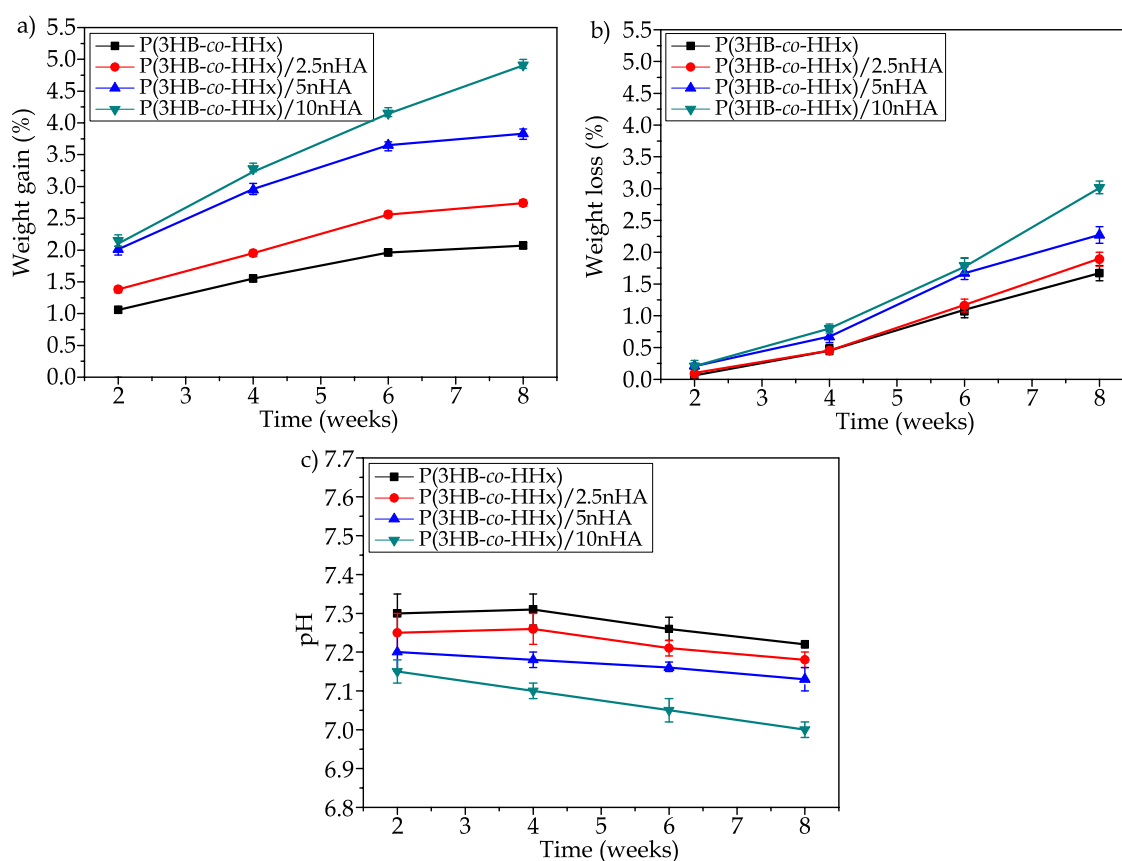


**Figure III.2.3.5.** Degradation behavior in PBS of the developed scaffolds over immersion weeks. Effect over : a) weight gain, b) weight loss and c) pH.

The immersion of the scaffolds in PBS during 8 weeks generated different effects, as indicated in **Figure III.2.3.5**. The first of them was the modification of the weight of the sample as a function of the time elapsed (**Figure III.2.3.5a**). The scaffold mass increased until reaching a mass gain of 4.9 % for the P(3HB-co-HHx)/10nHA composite or 2.1 % for P(3HB-co-HHx). Likely, the introduction of hydroxyapatite into a polymeric matrix increased the hydrophilicity of the material, promoting a higher moisture sorption during the assay [67]. After drying, the weight of the scaffolds was reduced up to 3.0 % for the composite with 10 wt.% nHA at the end of week 8. In this sense, some authors have reported that polymers such as PLA were not significantly degraded at 37 °C during 8 weeks of immersion [68]. Other works reported weight losses up to 6 % for polycaprolactone at room temperature [31]. The degradation of the scaffold starts with a cleavage of polymer chains, given that, at neutral or close-to-neutral pH, nucleophilic additions of water on carbonyl groups can be safely neglected (**Figure III.2.3.5b**). Then, the dissolution and the capillary water uptake of nHA particles boosted the degradation rate, as proposed by Sultana *et al.* [69]. Regarding once again



the pH, it is noteworthy that, even with the highest proportion of nHA, the diffusion rate of ions through the material was not high enough to prompt harsh pH variation. This is beneficial to the potential biocompatibility of the scaffold, as it helps avoid catalysing adverse reactions in contact with the human body.

**Figure III.2.3.6.** indicates the modification of the surface during these eight weeks and, especially in the cases of high nHA proportion (5 % and 10 %), mineralization by Ca-P deposition. It should be noted that this deposition of phosphorus-containing salts onto the surface of the scaffold increases the biocompatibility, since it eases osteoblast attachment and cell adhesion [70].

From the point of view of solid mechanics, scaffolds suffered a loss of mechanical properties that was proportional to the immersion time, as can be observed in **Figure III.2.3.7.** Hydrolytic degradation during immersion promoted a reduction in the molecular weight of the polymer [70]. As a result, the P(3HB-co-HHx)/10nHA composite, prior to immersion, showed a  $\sigma_f$  of 12.2 MPa with a  $\epsilon_c$  of 16.3 %, but attained values of 9.3 MPa and 8.3 %, respectively, after 8 weeks of immersion.

As in tensile tests on 3D printed specimens, the best strength and deformation values were obtained for the polymeric material without hydroxyapatite. The incorporation of an increasing amount of the osteoconductive additive promoted a reduction of mechanical properties such as the  $\sigma_f$  and  $\epsilon_c$ . Similar effects under compression tests have been reported for AM scaffolds from with PLA and nHA [71].

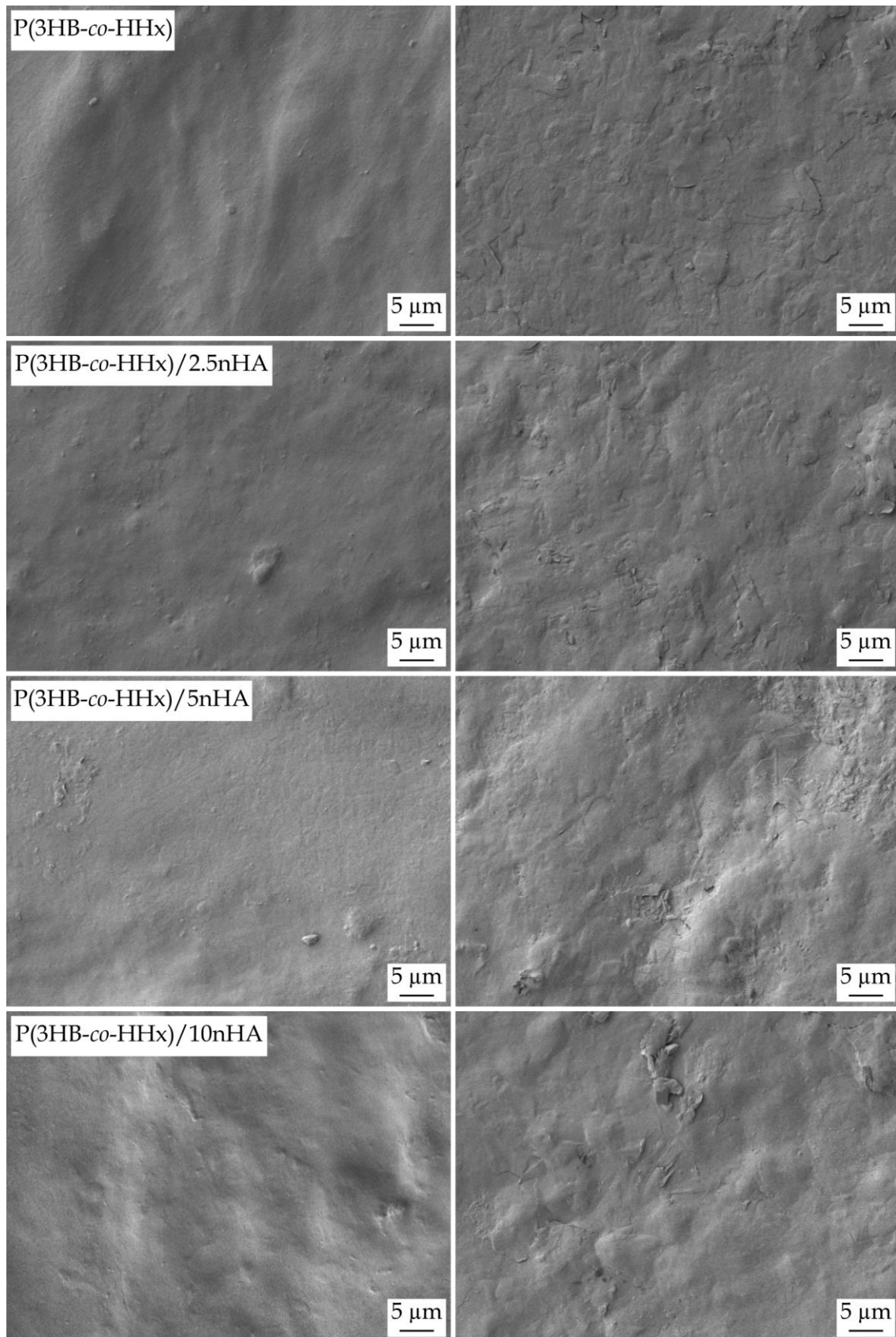


**Figure III.2.3.6.** FE-SEM images of the surface of scaffolds at week 0 (left) and week 8 (right) for the different compositions. Images taken at  $\times 1000$ .

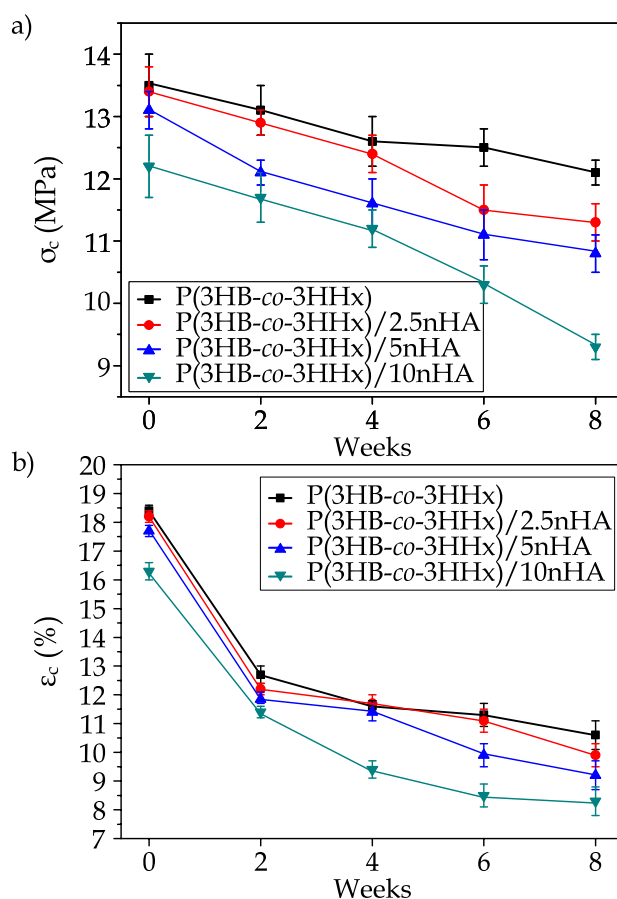


**Figure III.2.3.7.** Compression properties of the scaffolds at different immersion times: a) stress at yield point and b) deformation at yield point.

#### Chemical analysis of the PBS of the P(3HB-co-3HHx)/nHA nanocomposites.

The chemical analysis of the surface of the scaffolds before and after immersion in PBS is shown in **Figure III.2.3.8**. The scaffolds before immersion, showed characteristic peaks of P(3HB-co-3HHx) at  $1719\text{ cm}^{-1}$  belonging to the C=O stretching vibration of the crystalline region of the polymeric structure. Additionally, peaks also appeared at  $2928\text{ cm}^{-1}$  and  $2850\text{ cm}^{-1}$  corresponding to C-H vibration and asymmetric stretching of  $\text{CH}_2$  respectively [34,72]. For the composites with hydroxyapatite, a peak appeared in the range between  $1020 - 1080\text{ cm}^{-1}$ , which corresponds to the phosphate groups present in HA [73]. The presence of this peak was more noticeable when the amount of hydroxyapatite in each composite was increased.

After immersion, the spectrum of the scaffolds changed significantly because a coating layer was formed on the polymer surface, resulting in the peaks that could be observed at  $2928\text{ cm}^{-1}$  and  $2850\text{ cm}^{-1}$  disappearing altogether or acquiring a very low intensity and at  $1719\text{ cm}^{-1}$  the intensity was also reduced. The band associated to

hydroxyapatite ( $1020 - 1080 \text{ cm}^{-1}$ ) the peak appeared in all the composites considered because during the immersion in PBS, a hydroxyapatite layer was formed as observed in the morphology of the surface analysis [74].

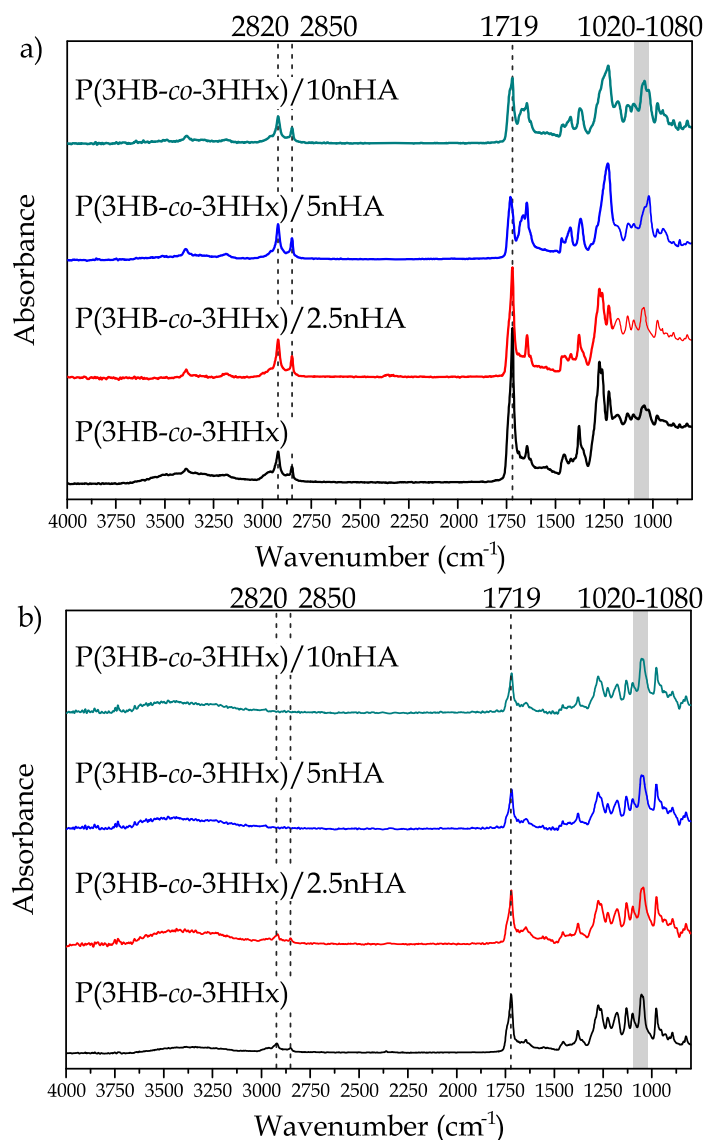


**Figure III.2.3.8.** Surface chemical composition measured by FTIR-ATR of the scaffolds: a) initial state b) after 8 weeks of immersion in PBS.

## CONCLUSIONS.

This work showed that P3HB-*co*-3HHx/nHA composites can be effectively used for the fabrication of scaffolds by fused deposition modelling. The manufacturing method involved different thermal treatments, namely a compounding process to obtain the composites and an extrusion process to obtain the filaments that were used in 3D printing. All these cycles resulted in slight thermal degradation, as seen from DSC studies with a higher  $\chi_c$  and a lower  $T_{cc}$ . The same test indicated that the incorporation

of ceramic nanoparticles decreased the crystallinity of the material. In TGA assays, cleavage of polymer chains reduced the temperature of  $T_{\max}$  up to 3 °C for the same composite. This effect was also observed in the rheology analysis, as each of the thermal cycles promoted a slight reduction of viscosity that was reduced by the incorporation of nHA.

Overall, increasing the amount of nHA in the composites decreased their tensile strength and their ductility. On the other hand, their stiffness increased with a tensile modulus near 750 MPa for the neat polymer up to values near 950 MPa for the 10 wt.% nHA. Regarding the pattern employed, the 0° raster angle gave rise to the highest strength, while the best ductility was obtained with the 45 °/- 45 ° pattern with a 17.5 % value in the elongation at break. The performance of scaffolds at compression test was also worsened by increasing amounts of nHA with 13.5 MPa for the neat polymer at week 0 while 12.2 MPa for the 10 wt.% nHA. Moreover, samples were subjected to an immersion process in phosphate buffer saline for 8 weeks, which resulted in certain degradation as observed from mass reduction up to 3.0 % and loss of mechanical properties up to 9.3 MPa for the 10 wt.% nHA at week 8. The immersion process led to only slight changes in the pH of the medium and to hydroxyapatite deposition on the scaffold surface that may favour its biocompatibility as observed in the FTIR analysis and the surface morphology. Regarding this key aspect, which we have so far only addressed *in vitro*, future research should contemplate *in vivo* studies.

#### **ACKNOWLEDGEMENTS.**

This research is a part of the grant PID2020-116496RB-C22 funded by MCIN/AEI/10.13039/501100011033. The authors also thank: Generalitat Valenciana-GVA for funding this research through the grant numbers AICO/2021/025 and CIGE/2021/094, Microscopy Services at UPV are acknowledged by their help in collecting and analysing images and the Sociedad de Ingeniería de Fabricación - SIF for the Mobility Grants for Young Researchers to carry out a research stage in Universitat de Girona - UdG. Juan Ivorra-Martinez wants to thank FPU19/01759 grant funded by MCIN/AEI/10.13039/501100011033 and, as appropriate, by ESF Investing in your future. Funding for open access charge: Universitat Politècnica de València. Marc Delgado-Aguilar is a Serra Húnter Fellow.

#### REFERENCES.

1. Ngo, T.D.; Kashani, A.; Imbalzano, G.; Nguyen, K.T.Q.; Hui, D. Additive manufacturing (3D printing): a review of materials, methods, applications and challenges. *Composites Part B: Engineering* **2018**, *143*, 172–196 doi: 10.1016/J.COMPOSITESB.2018.02.012.
2. Zhao, Y.; Chen, Y.; Zhou, Y. Novel mechanical models of tensile strength and elastic property of FDM AM PLA materials: experimental and theoretical analyses. *Materials & Design* **2019**, *181*, 108089–108099 doi: 10.1016/j.matdes.2019.108089.
3. Mohan, N.; Senthil, P.; Vinodh, S.; Jayanth, N. A Review on composite materials and process parameters optimisation for the fused deposition modelling process. *Virtual and Physical Prototyping* **2017**, *3*, 33–99 doi: 10.1080/17452759.2016.1274490.
4. Martín-Montal, J.; Pernas-Sánchez, J.; Varas, D. Experimental characterization framework for SLA additive manufacturing materials. *Polymers* **2021**, *13*, 1147–1163 doi: 10.3390/polym13071147.
5. Tarrés, Q.; Melbø, J.K.; Delgado-Aguilar, M.; Espinach, F.X.; Mutjé, P.; Chinga-Carrasco, G. Bio-polyethylene reinforced with thermo-mechanical pulp fibers: mechanical and micromechanical characterization and its application in 3D-printing by fused deposition modelling. *Composites Part B Engineering* **2018**, *153*, 70–77 doi: 10.1016/j.compositesb.2018.07.009.
6. Domínguez-Robles, J.; Utomo, E.; Cornelius, V.A.; Anjani, Q.K.; Korelidou, A.; Gonzalez, Z.; Donnelly, R.F.; Margariti, A.; Delgado-Aguilar, M.; Tarrés, Q.; *et al.* TPU-based antiplatelet cardiovascular prostheses prepared using fused deposition modelling. *Materials & Design* **2022**, *220*, 110837–11855 doi: 10.1016/J.MATDES.2022.110837.
7. Kumari Prasad, L.; Smyth, H. 3D printing technologies for drug delivery: a review 3D printing technologies for drug delivery: a review. *Drug Development and Industrial Pharmacy* **2016**, *42*, 1019–1031 doi: 10.3109/03639045.2015.1120743.

8. Sabaté Rovira, D.; Nielsen, H.M.; Taboryski, R.; Bunea, A.I. Additive manufacturing of polymeric scaffolds for biomimetic cell membrane engineering. *Materials & Design* **2021**, *201*, 109486–109497 doi: 10.1016/j.matdes.2021.109486.
9. Roopavath, U.K.; Kalaskar, D.M. Introduction to 3D printing in medicine. In *3D printing in medicine*, 1 ed.; Elsevier: **2017**; Vol. 1, pp. 1-20.
10. Yan, Q.; Dong, H.; Su, J.; Han, J.; Song, B.; Wei, Q.; Shi, Y. A review of 3D printing technology for medical applications. *Engineering* **2018**, *4*, 729–742 doi: 10.1016/J.ENG.2018.07.021.
11. Stansbury, J.W.; Idacavage, M.J. 3D printing with polymers: challenges among expanding options and opportunities. *Dental Materials* **2016**, *32*, 54–64 doi: 10.1016/J.DENTAL.2015.09.018.
12. Chen, X.; Gao, C.; Jiang, J.; Wu, Y.; Zhu, P.; Chen, G. 3D printed porous PLA/NHA composite scaffolds with enhanced osteogenesis and osteoconductivity in vivo for bone regeneration. *Biomedical materials* **2019**, *14*, 65003–65018 doi: 10.1088/1748-605X/ab388d.
13. Dwivedi, R.; Kumar, S.; Pandey, R.; Mahajan, A.; Nandana, D.; Katti, D.S.; Mehrotra, D. Polycaprolactone as biomaterial for bone scaffolds: review of literature. *Journal of Oral Biology and Craniofacial Research* **2020**, *10*, 381–388 doi: 10.1016/J.JOBCR.2019.10.003.
14. Dhandayuthapani, B.; Yoshida, Y.; Maekawa, T.; Sakthi Kumar, D. Polymeric scaffolds in tissue engineering application: a review. *International Journal of Polymer Science* **2011**, *2011*, 1–19 doi: 10.1155/2011/290602.
15. Billström, G.H.; Blom, A.W.; Larsson, S.; Beswick, A.D. Application of scaffolds for bone regeneration strategies: current trends and future directions. *Injury* **2013**, *44*, 28–33 doi: 10.1016/S0020-1383(13)70007-X.
16. Betz, M.W.; Yeatts, A.B.; Richbourg, W.J.; Caccamese, J.F.; Coletti, D.P.; Falco, E.E.; Fisher, J.P. Macroporous hydrogels upregulate osteogenic signal expression and promote bone regeneration. *Biomacromolecules* **2010**, *11*, 1160–1168 doi: 10.1021/BM100061Z.

17. Webster, T.J.; Ahn, E.S. Nanostructured biomaterials for tissue engineering bone. *Advances in Biochemical Engineering/Biotechnology* **2006**, *103*, 275–308 doi: 10.1007/10\_021.
18. Haleem, A.; Javaid, M. 3D printed medical parts with different materials using additive manufacturing. *Clinical Epidemiology Global Health* **2020**, *8*, 215–223 doi: 10.1016/J.CEGH.2019.08.002.
19. Strong, D.; Sirichakwal, I.; Manogharan, G.P.; Wakefield, T. Current state and potential of additive – hybrid manufacturing for metal parts. *Rapid Prototyping Journal* **2017**, *23*, 577–588 doi: 10.1108/RPJ-04-2016-0065.
20. Spierings, A.B.; Starr, T.L.; Wegener, K. Fatigue performance of additive manufactured metallic parts. *Rapid Prototyping Journal* **2013**, *19*, 88–94 doi: 10.1108/13552541311302932.
21. Song, J.; Gao, H.; Zhu, G.; Cao, X.; Shi, X.; Wang, Y. The preparation and characterization of polycaprolactone/graphene oxide biocomposite nanofiber scaffolds and their application for directing cell behaviors. *Carbon* **2015**, *95*, 1039–1050 doi: 10.1016/j.carbon.2015.09.011.
22. Nazeer, M.A.; Onder, O.C.; Sevgili, I.; Yilgor, E.; Kavakli, I.H.; Yilgor, I. 3D printed poly(lactic acid) scaffolds modified with chitosan and hydroxyapatite for bone repair applications. *Materials Today Communications* **2020**, *25*, 101515–101524 doi: 10.1016/J.MTCOMM.2020.101515.
23. Sabanna Kattimani, V.; Kondaka, sudheer; Prasad Lingamaneni, K. Hydroxyapatite–past, present, and future in bone regeneration. *Bone and Tissue Regeneration Insights* **2016**, *7*, 9–19 doi: 10.4137/BTRi.s36138.
24. Kim, C.G.; Han, K.S.; Lee, S.; Kim, M.C.; Kim, S.Y.; Nah, J. Fabrication of biocompatible polycaprolactone–hydroxyapatite composite filaments for the FDM 3D printing of bone scaffolds. *Applied sciences* **2021**, *11*, 6351–6360 doi: 10.3390/app11146351.
25. Fierz, F.C.; Beckmann, F.; Huser, M.; Irsen, S.H.; Leukers, B.; Witte, F.; Degistirici, Ö.; Andronache, A.; Thie, M.; Müller, B. The morphology of anisotropic 3D–printed hydroxyapatite scaffolds. *Biomaterials* **2008**, *29*, 3799–3806 doi: 10.1016/J.BIOMATERIALS.2008.06.012.



26. Esposito Corcione, C.; Gervaso, F.; Scalera, F.; Padmanabhan, S.K.; Madaghiele, M.; Montagna, F.; Sannino, A.; Licciulli, A.; Maffezzoli, A. Highly loaded hydroxyapatite microsphere/ PLA porous scaffolds obtained by fused deposition modelling. *Ceramics International* **2019**, *45*, 2803–2810 doi: 10.1016/j.ceramint.2018.07.297.
27. Yang, T.C. Effect of extrusion temperature on the physico-mechanical properties of unidirectional wood fiber-reinforced polylactic acid composite (WFRPC) components using fused deposition modeling. *Polymers* **2018**, *10*, 976–987 doi: 10.3390/polym10090976.
28. Ang, S.L.; Sivashankari, R.; Shaharuddin, B.; Chuah, J.A.; Tsuge, T.; Abe, H.; Sudesh, K. Potential applications of polyhydroxyalkanoates as a biomaterial for the aging population. *Polymer Degradation and Stability* **2020**, *181*, 109371–109389 doi: 10.1016/J.POLYMDEGRADSTAB.2020.109371.
29. Asghari, F.; Samiei, M.; Adibkia, K.; Akbarzadeh, A.; Davaran, S. Biodegradable and biocompatible polymers for tissue engineering application: a review. *Artificial Cells, Nanomedicine and Biotechnology* **2017**, *45*, 185–192 doi: 10.3109/21691401.2016.1146731.
30. Mehrpouya, M.; Vahabi, H.; Barletta, M.; Laheurte, P.; Langlois, V. Additive manufacturing of polyhydroxyalkanoates (PHAs) biopolymers: materials, printing techniques, and applications. *Materials Science and Engineering: C* **2021**, *127*, 112216–112229 doi: 10.1016/J.MSEC.2021.112216.
31. Ferrer, I.; Manresa, A.; Méndez, J.A.; Delgado-Aguilar, M.; Garcia-Romeu, M.L. Manufacturing PLA/PCL blends by ultrasonic molding technology. *Polymers* **2021**, *13*, 2412–2429 doi: 10.3390/polym13152412.
32. Wu, C.S. Characterization, functionality and application of siliceous sponge spicules additive-based manufacturing biopolymer composites. *Additive Manufacturing* **2018**, *22*, 13–20 doi: 10.1016/J.ADDMA.2018.04.034.
33. Bittolo Bon, S.; Jònec, I.; Morselli, D.; Degli Esposti, M.; Fabbri, P.; de Maria, C.; Foggi Viligiardi, T.; Morabito, A.; Giorgi, G.; Valentini, L. Printable smart 3D architectures of regenerated silk on poly(3-hydroxybutyrate-co-3-hydroxyvalerate). *Materials & Design* **2021**, *201*, 109492–109501 doi: 10.1016/j.matdes.2021.109492.

34. Rebia, R.A.; Rozet, S.; Tamada, Y.; Tanaka, T. Biodegradable P(3HB-co-3HHx)/PVA blend nanofibers: fabrication, characterization, in vitro degradation, and in vitro biocompatibility. *Polymer Degradation and Stability* **2018**, *154*, 124–136 doi: 10.1016/J.POLYMDEGRADSTAB.2018.05.018.
35. Washington, M.A.; Balmert, S.C.; Fedorchak, M. v.; Little, S.R.; Watkins, S.C.; Meyer, T.Y. Monomer sequence in PLGA microparticles: effects on acidic microclimates and in vivo inflammatory response. *Acta Biomaterialia* **2018**, *65*, 259–271 doi: 10.1016/J.ACTBIO.2017.10.043.
36. Lim, J.; You, M.; Li, J.; Li, Z. Emerging bone tissue engineering via polyhydroxyalkanoate (PHA)-based scaffolds. *Materials Science and Engineering: C* **2017**, *79*, 917–929 doi: 10.1016/j.msec.2017.05.132.
37. dos Santos, A.J.; Oliveira Dalla Valentina, L.V.; Hidalgo Schulz, A.A.; Tomaz Duarte, M.A. From obtaining to degradation of PHB: material properties. Part I. *Ingenieria y Ciencia* **2017**, *13*, 269–298 doi: 10.17230/ingciencia.13.26.10.
38. Ramot, Y.; Haim-Zada, M.; Domb, A.J.; Nyska, A. biocompatibility and safety of PLA and its copolymers. *Advanced Drug Delivery Reviews* **2016**, *107*, 153–162 doi: 10.1016/j.addr.2016.03.012.
39. Qu, X.-H.; Wu, Q.; Zhang, K.-Y.; Chen, G.Q. In vivo studies of poly(3-hydroxybutyrate-co-3-hydroxyhexanoate) based polymers: biodegradation and tissue reactions. *Biomaterials* **2006**, *27*, 3540–3548 doi: 10.1016/j.biomaterials.2006.02.015.
40. Arza, C.R.; Jannasch, P.; Johansson, P.; Magnusson, P.; Werker, A.; Maurer, F.H.J. Effect of additives on the melt rheology and thermal degradation of poly[(R)-3-hydroxybutyric acid]. *Journal of Applied Polymer Science* **2015**, *132*, 41836–41842 doi: 10.1002/app.41836.
41. Kovalcik, A.; Sangroniz, L.; Kalina, M.; Skopalova, K.; Humpolíček, P.; Omastova, M.; Mundigler, N.; Müller, A.J. Properties of scaffolds prepared by fused deposition modeling of poly(hydroxyalkanoates). *International Journal of Biological Macromolecules* **2020**, *161*, 364–376 doi: 10.1016/j.ijbiomac.2020.06.022.

- 
42. Festas, A.J.; Ramos, A.; Davim, J.P. Medical devices biomaterials—a review. *Proceedings of the Institution of Mechanical Engineers, Part L: Journal of Materials: Design and Applications* **2020**, *234*, 218–228 doi: 10.1177/1464420719882458.
43. Park, S.A.; Lee, S.H.; Kim, W.D. Fabrication of porous polycaprolactone/hydroxyapatite (PCL/HA) blend scaffolds using a 3D plotting system for bone tissue engineering. *Bioprocess Biosystems Engineering* **2011**, *34*, 505–513 doi: 10.1007/s00449-010-0499-2.
44. Prakash, C.; Singh, G.; Singh, S.; Linda, W.L.; Zheng, H.Y.; Ramakrishna, S.; Narayan, R. Mechanical reliability and in vitro bioactivity of 3D-printed porous polylactic acid–hydroxyapatite scaffold. *Journal of Materials Engineering and Performance* **2021**, *30*, 4946–4956 doi: 10.1007/s11665-021-05566-x.
45. Mahmood, H.; Pegoretti, A.; Brusa, R.S.; Ceccato, R.; Penasa, L.; Tarter, S.; Checchetto, R. Molecular transport through 3-hydroxybutyrate-co-3-hydroxyhexanoate biopolymer films with dispersed graphene oxide nanoparticles: gas barrier, structural and mechanical properties. *Polymer Testing* **2020**, *81*, 106181–106190 doi: 10.1016/j.polymertesting.2019.106181.
46. Loh, Q.L.; Choong, C. Three-dimensional scaffolds for tissue engineering applications: role of porosity and pore size. *Tissue Engineering Part B, Reviews* **2013**, *19*, 485–502 doi: 10.1089/ten.TEB.2012.0437.
47. Ivorra-Martinez, J.; Quiles-Carrillo, L.; Boronat, T.; Torres-Giner, S.; Covas, J.A. Assessment of the mechanical and thermal properties of injection-moulded poly(3-hydroxybutyrate-co-3-hydroxyhexanoate)/nanohydroxyapatite parts for use in bone tissue engineering. *Polymers* **2020**, *12*, 1389–1410 doi: 10.3390/polym12061389.
48. Bordes, P.; Pollet, E.; Bourbigot, S.; Avérous, L. Structure and properties of pha/clay nano-biocomposites prepared by melt intercalation. *Macromolecular Chemistry and Physics* **2008**, *209*, 1473–1484 doi: 10.1002/macp.200800022.
49. Chacón, J.M.; Caminero, M.A.; García-Plaza, E.; Núñez, P.J. Additive manufacturing of PLA structures using fused deposition modelling: effect of process parameters on mechanical properties and their optimal selection. *Materials & Design* **2017**, *124*, 143–157 doi: 10.1016/j.matdes.2017.03.065.

50. Kiendl, J.; Gao, C. Controlling toughness and strength of FDM 3D-printed PLA components through the raster layout. *Composites Part B Engineering* **2020**, *180*, 107562–107568 doi: 10.1016/j.compositesb.2019.107562.
51. Garzon-Hernandez, S.; Garcia-Gonzalez, D.; Jérusalem, A.; Arias, A. Design of FDM 3D printed polymers: an experimental-modelling methodology for the prediction of mechanical properties. *Materials & Design* **2020**, *188*, 108414–108424 doi: 10.1016/j.matdes.2019.108414.
52. Tian, J.; Zhang, R.; Wu, Y.; Xue, P. Additive manufacturing of wood flour/polyhydroxyalkanoates (PHA) fully bio-based composites based on micro-screw extrusion system. *Materials & Design* **2021**, *199*, 109418–109432 doi: 10.1016/j.matdes.2020.109418.
53. Cisneros-López, E.O.; Pal, A.K.; Rodriguez, A.U.; Wu, F.; Misra, M.; Mielewski, D.F.; Kiziltas, A.; Mohanty, A.K. Recycled poly(lactic acid)-based 3D printed sustainable biocomposites: a comparative study with injection molding. *Materials Today Sustainability* **2020**, *7*, 100027–100039 doi: 10.1016/j.mtsust.2019.100027.
54. Ecker, J. v; Haider, A.; Burzic, I.; Huber, A.; Eder, G.; Hild, S. Mechanical properties and water absorption behaviour of PLA and PLA/Wood composites prepared by 3D printing and injection moulding. *Rapid Prototyping Journal* **2019**, *25*, 672–678 doi: 10.1108/RPJ-06-2018-0149.
55. Komal, U.K.; Kasaudhan, B.K.; Singh, I. Comparative performance analysis of polylactic acid parts fabricated by 3D printing and injection molding. *Journal Materials Engineering Performance* **2021**, *30*, 6522–6528 doi: 10.1007/s11665-021-05889-9.
56. Xu, H.; Xie, L.; Hakkarainen, M. Beyond a model of polymer processing-triggered shear: reconciling shish-kebab formation and control of chain degradation in sheared poly(l-lactic acid). *ACS Sustainable Chemistry Engineering* **2015**, *3*, 1443–1452 doi: 10.1021/acssuschemeng.5b00320.
57. Garcia Gonçalves, L.M.; Rigolin, T.R.; Frenhe, B.M.; Prado Bettini, S.H. On the recycling of a biodegradable polymer: multiple extrusion of poly(lactic acid). *Materials Research* **2020**, *23*, 20200274–20200281 doi: 10.1590/1980-5373-MR-2020-0274.

- 
58. Touati, N.; Kaci, M.; Bruzaud, S.; Grohens, Y. The effects of reprocessing cycles on the structure and properties of isotactic polypropylene/cloisite 15A nanocomposites. *Polymers Degradation and Stability* **2011**, *96*, 1064–1073, doi: 10.1016/j.polymdegradstab.2011.03.015.
59. Agüero, A.; Morcillo, M.C.; Quiles-Carrillo, L.; Balart, R.; Boronat, T.; Lascano, D.; Torres-Giner, S.; Fenollar, O. Study of the influence of the reprocessing cycles on the final properties of polylactide pieces obtained by injection molding. *Polymers* **2019**, *11*, 1908–1929 doi: 10.3390/polym11121908.
60. Majerczak, K.; Wadkin-Snaith, D.; Magueijo, V.; Mulheran, P.; Liggat, J.; Johnston, K. Polyhydroxybutyrate: a review of experimental and simulation studies of the effect of fillers on crystallinity and mechanical properties. *Polymer International* **2022**, *71*, 1363–1424 doi: 10.1002/pi.6402.
61. Martín-Alfonso, J.E.; Franco, J.M. Influence of polymer reprocessing cycles on the microstructure and rheological behavior of polypropylene/mineral oil oleogels. *Polymer Testing* **2015**, *45*, 12–19 doi: 10.1016/j.polymertesting.2015.04.016.
62. Dhar, P.; Tarafder, D.; Kumar, A.; Katiyar, V. Effect of cellulose nanocrystal polymorphs on mechanical, barrier and thermal properties of poly(lactic acid) based bionanocomposites. *RSC Advances* **2015**, *5*, 60426–60440 doi: 10.1039/c5ra06840a.
63. Wang, S.; Chen, W.; Xiang, H.; Yang, J.; Zhou, Z.; Zhu, M. Modification and potential application of short-chain-length polyhydroxyalkanoate (scl-PHA). *Polymers* **2016**, *8*, 273–301 doi: 10.3390/polym8080273.
64. Arrigo, R.; Bartoli, M.; Malucelli, G. Poly(lactic acid)-biochar biocomposites: effect of processing and filler content on rheological, thermal, and mechanical properties. *Polymers* **2020**, *12*, 892–905 doi: 10.3390/POLYM12040892.
65. Mantia, F.P.L.; Morreale, M.; Scaffaro, R.; Tulone, S. Rheological and mechanical behavior of LDPE/calcium carbonate nanocomposites and microcomposites. *Journal Applied Polymer Science* **2013**, *127*, 2544–2552 doi: 10.1002/app.37875.

66. Petrucci, R.; Torre, L. Filled polymer composites. In *Modification of Polymer Properties*, 1 ed.; Elsevier: 2017; Vol. 1, pp. 23-46.
67. Jiang, W.; Shi, J.; Li, W.; Sun, K. Morphology, wettability, and mechanical properties of polycaprolactone/ hydroxyapatite composite scaffolds with interconnected pore structures fabricated by a mini-deposition system. *Polymer Engineering and Science* **2012**, *52*, 2396–2402 doi: 10.1002/pen.23193.
68. Fukushima, K.; Tabuani, D.; Dottori, M.; Armentano, I.; Kenny, J.M.; Camino, G. Effect of temperature and nanoparticle type on hydrolytic degradation of poly(lactic acid) nanocomposites. *Polymer Degradation and Stability* **2011**, *96*, 2120–2129 doi: 10.1016/j.polymdegradstab.2011.09.018.
69. Sultana, N.; Khan, T.H. In vitro degradation of PHBV scaffolds and NHA/PHBV composite scaffolds containing nanohydroxyapatite for bone tissue engineering. *Journal of Nanomaterials* **2012**, *2012*, 1–12 doi: 10.1155/2012/190950.
70. Jurak, M.; Wiącek, A.E.; Ładniak, A.; Przykaza, K.; Szafran, K. What affects the biocompatibility of polymers? *Advances in Colloid and Interface Science* **2021**, *294*, 102451–102476 doi: 10.1016/j.cis.2021.102451.
71. Wang, W.; Zhang, B.; Li, M.; Li, J.; Zhang, C.; Han, Y.; Wang, L.; Wang, K.; Zhou, C.; Liu, L.; *et al.* 3D printing of PLA/n-HA composite scaffolds with customized mechanical properties and biological functions for bone tissue engineering. *Composites Part B Engineering* **2021**, *224*, 109192–109204 doi: 10.1016/j.compositesb.2021.109192.
72. Pachekoski, W.M.; Dalmolin, C.; Agnelli, J.A.M. The influence of the industrial processing on the degradation of poly(hidroxybutyrate)-PHB. *Materials Research* **2013**, *16*, 237–332 doi: 10.1590/S1516-14392012005000180.
73. Laput, O.; Vasenina, I.; Salvadori, M.C.; Savkin, K.; Zuza, D.; Kurzina, I. Low-temperature plasma treatment of polylactic acid and PLA/HA composite material. *Journal of Material Science* **2019**, *54*, 11726–11738 doi: 10.1007/s10853-019-03693-4.

74. Gómez-Cerezo, M.N.; Lozano, D.; Arcos, D.; Vallet-Regi, M.; Vaquette, C. The effect of biomimetic mineralization of 3D-printed mesoporous bioglass scaffolds on physical properties and in vitro osteogenicity. *Materials Science and Engineering: C* **2020**, *109*, 110572–110583 doi: 10.1016/j.msec.2019.110572.





**Section III:**  
**Development of environmentally friendly  
formulations of polylactide for injection  
moulding and 3D printing.**

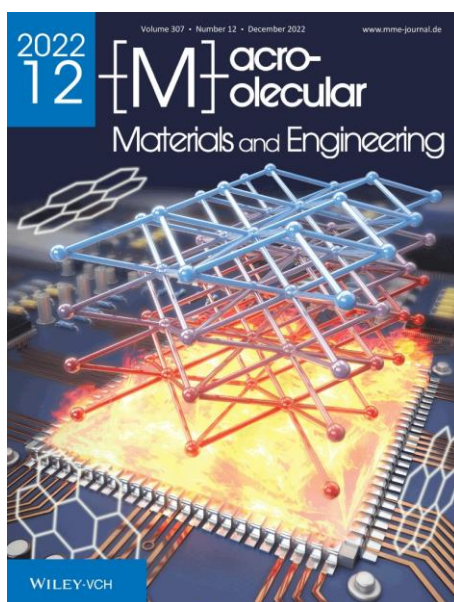


Adapted from the original manuscript.

### III.3.1 The potential of an itaconic acid diester as environmentally friendly plasticizer for injection-moulded polylactide parts.

Juan. Ivorra-Martinez<sup>1</sup>, Miguel Ángel Peydro<sup>1</sup>, Jaume Gomez-Caturla<sup>1</sup>, Teodomiro Boronat<sup>1</sup>, Rafael Balart<sup>1</sup>.

<sup>1</sup>Technological Institute of Materials – ITM, Universitat Politècnica de València – UPV, Plaza Ferrándiz y Carbonell 1, 03801 Alcoy (Spain).



**Macromolecular Materials and Engineering.**

**2022, 307(11): 2200360.**



## RESEARCH ARTICLE



# The Potential of an Itaconic Acid Diester as Environmentally Friendly Plasticizer for Injection-Molded Polylactide Parts

Juan Ivorra-Martinez,\* Miguel Angel Peydro, Jaume Gomez-Caturla, Teodomiro Boronat, and Rafa Balart

This work reports on the use of dibutyl itaconate (DBI) as an environmentally friendly plasticizer for polylactide (PLA) with different proportions of DBI in the 2.5–20 wt% (weight content) range. A co-rotating twin-screw extrusion process followed by injection molding is employed for the manufacturing of the samples. The results show that the plasticized PLA formulation with 10 wt% DBI offers the most balanced overall properties, with a noticeable increase in the elongation at break from 4.6% (neat PLA) up to 322%, with a tensile modulus of 1572 MPa, and a tensile strength of 23.8 MPa. In the case of 15 and 20 wt% DBI formulations, PLA reaches the saturation point with no more increase in the elongation at break and a clear decrease in the tensile modulus. DBI also decreases the glass transition temperature ( $T_g$ ) from 61.3 °C (neat PLA) down to 23.4 °C for plasticized PLA formulation containing 20 wt% DBI, thus showing the high plasticization efficiency of DBI.

(PHAs), being poly(3-hydroxybutyrate) (PHB) a very promising biobased and biodegradable polymer.<sup>[3]</sup> Despite these developments, poly(lactide) (PLA) is, by far, one of the most promising polyesters.<sup>[4]</sup> PLA is obtained from renewable resources from starch-rich compounds and offers biodegradation. In addition, it shows a reasonable price compared to PHAs and other biobased polyesters. For these reasons, PLA is currently being used in the food packaging industry.<sup>[5]</sup> Moreover, PLA is a widely used standard material in 3D printing and in the manufacturing of medical devices, since it is a biocompatible and resorbable polymer.<sup>[6–9]</sup> PLA is synthesized through biomass hydrolysis followed by fermentation, which produces lactic acid that is then converted into lactide, and subsequently,

into poly(lactide) by ring-opening polymerization (ROP).<sup>[10]</sup> Although its use provides the aforementioned advantages, there are some drawbacks mainly related to a high stiffness and a brittle behavior attributed to a  $T_g$  (glass transition temperature) above room temperature (close to 60 °C).<sup>[6–8]</sup>

To minimize this brittleness, several approaches have been explored. One technical solution is the use of plasticizers.<sup>[11,12]</sup> Another approach is blending PLA with other ductile polymers with or without compatibilizers.<sup>[13–15]</sup> Several researches have been carried out to obtain PLA with improved toughness by blending it with different biodegradable polymers such as poly( $\epsilon$ -caprolactone) (PCL), poly(butylene succinate) (PBS), poly(butylene adipate-co-terephthalate) (PBAT) or thermoplastic starch (TPS).<sup>[16–19]</sup> The main drawback when using blends is a remarked poor miscibility between PLA and the other polymer in the blend. This phenomenon leads to phase separation, which in turn, has a negative effect on the final mechanical properties. To overcome this situation, compatibilizers are often used to improve the load transfer between the polymer phase involved.<sup>[20–22]</sup> Ding et al. reported manufacturing of PLA blends with PBAT (70/30 respectively), with an interesting increase in the elongation at break from 6% (neat PLA) up to 30% for the uncompatibilized blend. The use of monomethoxy poly(ethylene glycol)-poly(lactide) di-block copolymers (MPEG-PLA) improved compatibility/miscibility between PLA and PBAT so the elongation increased up to 296%.<sup>[23]</sup> The use of plasticizers is reported as the simplest and most economical method to improve the ductility of PLA. In addition, plasticizers also contribute to better processability.<sup>[7,24]</sup> There are many plasticizer families with

## 1. Introduction

Plastics Europe's annual report showed a 50.7 million tons plastic total demand in 2019, from which 50% corresponded to several grades of polyethylene (PE) and polypropylene (PP). Among the most common uses for these polymers, the most popular one is the manufacture of packaging with a total share of 39.6%.<sup>[1]</sup> As a result, a large amount of polymer wastes is generated, leading to severe environmental issues that have led to an increased interest in the development of polymers from renewable sources and potential biodegradation (or disintegration in controlled compost soil).<sup>[2]</sup> In the last decade, important advances have been carried out on the development of polyesters obtained from bacterial fermentation or poly(hydroxyalkanoates)

J. Ivorra-Martinez, M. A. Peydro, J. Gomez-Caturla, T. Boronat, R. Balart  
 Institute of Materials Technology (ITM)  
 Universitat Politècnica de València (UPV)  
 Plaza Ferrándiz y Carbonell 1, Alcoy, Alicante 03801, Spain  
 E-mail: juaivmr@doctor.upves

The ORCID identification number(s) for the author(s) of this article can be found under <https://doi.org/10.1002/mame.202200360>

© 2022 The Authors. Macromolecular Materials and Engineering published by Wiley-VCH GmbH. This is an open access article under the terms of the Creative Commons Attribution-NonCommercial-NoDerivs License, which permits use and distribution in any medium, provided the original work is properly cited, the use is non-commercial and no modifications or adaptations are made.

DOI: 10.1002/mame.202200360



**Abstract.**

This work reports on the use of dibutyl itaconate - DBI as an environmentally friendly plasticizer for poly(lactic acid) - PLA with different proportions of DBI in the 2.5 - 20 wt.% range. A co-rotating twin-screw extrusion process followed by injection moulding was employed for the manufacture of the samples. The results showed that the plasticized PLA formulation with 10 wt.% DBI offered the most balanced overall properties, with a noticeable increase in the elongation at break from 4.6 % (neat PLA) up to 322 %, with a tensile modulus of 1572 MPa, and a tensile strength of 23.8 MPa. In the case of 15 and 20 wt.% DBI formulations, PLA reached the saturation point with no more increase in the elongation at break and a clear decrease in the tensile modulus. DBI also decreased the glass transition temperature -  $T_g$  from 61.3 °C (neat PLA) down to 23.4 °C for plasticized PLA formulation containing 20 wt.% DBI, thus showing the high plasticization efficiency of DBI.

**Keywords:** poly(lactic acid) - PLA; dibutyl itaconate - DBI; plasticizer; injection moulding - IM; biobased.

---





## INTRODUCTION.

Plastics Europe's annual report showed a 50.7 million tons plastic total demand in 2019, from which 50 % corresponded to several grades of poly(ethylene) - PE and poly(propylene) - PP. Among the most common uses for these polymers, the most popular one is the manufacture of packaging with a total share of 39.6 % [1]. As a result, a large amount of polymer waste is generated, leading to severe environmental issues that have led to an increased interest in the development of polymers from renewable sources and potential biodegradation (or disintegration in controlled compost soil)[2]. In the last decade, important advances have been carried out on the development of polyesters obtained from bacterial fermentation or poly(hydroxyalkanoates) - PHAs, being poly(3-hydroxybutyrate) - P3HB a very promising biobased and biodegradable polymer [3]. Despite these developments, polylactide - PLA is, by far, one of the most promising polyesters [4]. PLA is obtained from renewable resources from starch-rich compounds and offers biodegradation. In addition, it shows a reasonable price compared to PHAs and other biobased polyesters. For these reasons, PLA is currently being used in the food packaging industry [5]. Moreover, PLA is a widely used standard material in 3D printing and in the manufacturing of medical devices, since it is a biocompatible and resorbable polymer [6-9]. PLA is synthesized through biomass hydrolysis followed by fermentation, which produces lactic acid that is then converted into lactide, and subsequently, into polylactide by Ring-Opening Polymerization - ROP [10]. Although its use provides the aforementioned advantages, there are some drawbacks mainly related to a high stiffness and a brittle behaviour attributed to a glass transition temperature above room temperature (close to 60 °C) [6-8].

To minimize this brittleness, several approaches have been explored. One technical solution is the use of plasticizers [11,12]. Another approach is blending PLA with other ductile polymers with or without compatibilizers [13-15]. Several researches have been carried out to obtain PLA with improved toughness by blending it with different biodegradable polymers such as poly( $\epsilon$ -caprolactone) - PCL, poly(butylene succinate) - PBS, poly(butylene adipate-*co*-terephthalate) - PBAT or thermoplastic starch - TPS [16-19]. The main drawback when using blends is a remarked poor miscibility between PLA and the other polymer in the blend. This phenomenon leads to phase separation, which in turn, has a negative effect on the final mechanical properties. To overcome this situation, compatibilizers are often used to improve the load transfer between the polymer phase involved [20-22]. Ding *et al.* reported

manufacturing of PLA blends with PBAT (70/30 respectively), with an interesting increase in the elongation at break from 6 % (neat PLA) up to 30 % for the uncompatibilized blend. The use of monomethoxy poly(ethylene glycol)-polylactide diblock copolymers – MPEG-PLA improved compatibility/miscibility between PLA and PBAT so the elongation increased up to 296 % [23]. The use of plasticizers is reported as the simplest and most economical method to improve the ductility of PLA. In addition, plasticizers also contribute to better processability [7,24]. There are many plasticizer families with interesting plasticization properties. These plasticizers offer a wide range of molecular weights, nonetheless, the use of plasticizers with lower molecular weight results in a better plasticizing effect [5,10]. When plasticizers are added to PLA, the mobility of the polymer chains increases due to the reduction of the interactions between them [25]. The main problem that arises when plasticizers are used, is the possibility of plasticizer migration, being especially critical in those situations in which the plasticized polymer is in contact with food. This property highly depends on the compatibility of the plasticizer with the polymeric matrix. The use of high molecular weight plasticizers substantially reduces this migration phenomenon [7,26]. As a result of the modifications involved when a plasticizer is introduced into a polymer matrix, the most relevant one is the improvement of the ductile behavior as the elongation at break and the impact strength. Moreover, some physical properties like the tensile strength, tensile modulus, hardness and storage modulus are reduced due to the lower interaction between the polymer chains [7,27]. At the same time, the introduction of a plasticizer also promotes modifications on the thermal properties. Arrieta *et al.* reported that plasticization of PLA films with 15 wt.% limonene allowed to reduce the  $T_g$  of neat PLA by 30 °C; accordingly to this decrease in  $T_g$ , plasticized PLA with limonene (15 wt.%) resulted in a highly ductile polymer with an elongation at break of 150 % which was remarkably higher than that of neat PLA film (1.5 %) [28].  $T_g$  of PLA is close to 60 °C, which provides a rigid and fragile behaviour at room temperature, attributed to a low chain mobility state. The introduction of a plasticizer promotes a reduction in  $T_g$  close to room temperature, so that an enhancement of the polymer chain mobility is achieved, allowing to improve ductile properties of the mixture.

Nowadays, the most commonly used plasticizers in the polymer sector are petrochemically-derived. Among the different families, phthalates have been, with difference, the most used plasticizers in polymers, such as poly(vinyl chloride) – PVC. Phthalates have also given good plasticization properties to PLA [29]. Nevertheless, the increasing concern about environment has acted as the leading force for the development of environmentally friendly plasticizers. In fact, phthalates have been

increasingly substituted by other families such as sebacates, adipates, epoxidized vegetable oils - EVOs, citrates, among others, which are obtained from renewable resources [27,30,31]. Isosorbide diesters also offer interesting plasticization properties compared to traditional phthalates as Yang *et al.* have reported. They obtained very promising plasticization properties on PLA by using isosorbide dioctanoate - SDO (20 wt.%), compared to conventional dioctyl terephthalate - DOTP. The best outcome in this case was obtained with SDO plasticizer with an elongation at break of 281 % while the phthalate-based plasticizer only provided an elongation at break of 104 % [32].

As a result of an increasing environmental concern, plasticizers from natural resources are gaining special attention in PLA industry. In particular, the use of renewable raw materials and their biodegradability are of great interest [33]. Some of these environmentally friendly plasticizers with interesting plasticization properties on PLA, are Epoxidized Soybean Oil - ESO, Epoxidized Palm Oil - EPO, Oligomer of Lactic Acid - OLA, citrate oligoesters, malonate oligomers, triacetin, citrate esters, glycerol, adipates and poly(adipates), among others [26,33]. IA is a biological molecule obtained by fermentation of citric acid [34]. Itaconic acid could be used as a biobased building block for the polymer industry. Ma *et al.* reported interesting plasticization properties provided by itaconic acid-4-propylguaiaicol ester - IPE to poly(vinyl chloride) films [35]. Wu *et al.* reported the synthesis of Methyl Succinic Acid - MSA by direct hydrogenation of itaconic acid. Then, they copolymerized MSA with 1,4-butanediol to give a polymeric plasticizer, namely poly(butylene 2-methylsuccinate) - PBMS [36].

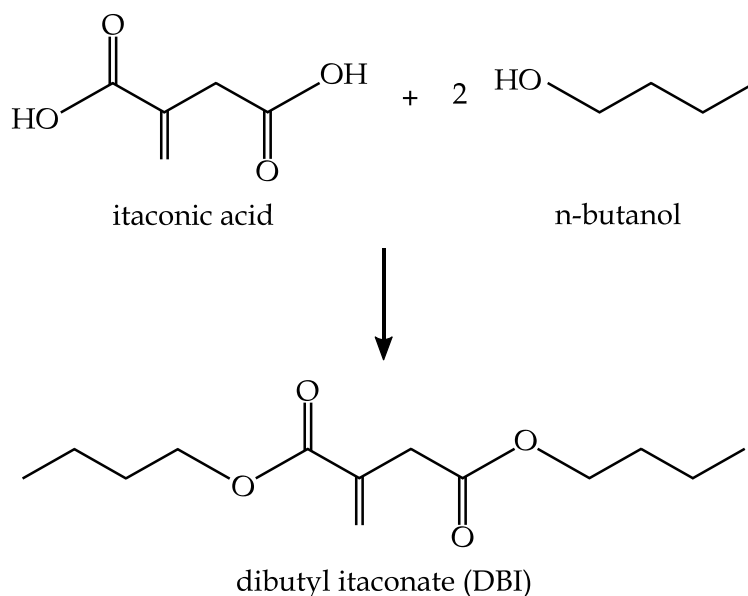


**Figure III.3.1.1.** Scheme of the reaction of itaconic acid - IA and n-butanol to give dibutyl itaconate - DBI.

The esterification of itaconic acid with n-butanol produces dibutyl itaconate – DBI (**Figure III.3.1.1.**), which proves to have great applicability as a plasticizer, lubricant, adhesive, crosslinker, and so on. Its dual functionality (ester and carbon-carbon double bond) offers a wide range of possibilities in the polymer industry as a biobased building block for polymers, copolymers, chemical modification of polymers macromolecules and hydrogels [37–39].

The novelty of this work relies on the evaluation, for the first time, of the potential of a diester of itaconic acid, namely DBI, as a plasticizer in PLA formulations with improved toughness and ductile properties. Plasticized PLA formulations with different DBI proportions in the 2.5 – 20 wt.% range were obtained by a co-rotating twin screw extrusion process followed by injection moulding to manufacture standard test samples. The processing conditions for the injection moulding stage were set according to a prior capillary rheology study which allowed to define optimum processing temperatures. In order to measure the final properties of the obtained materials, mechanical, thermal, thermo-mechanical and fracture morphology.

## MATERIALS AND METHODS.

### Materials and Solubility.

PLA grade PURAPOL L130 from Total Corbion PLA (Gorinchem, The Netherlands) with a minimum L-isomer content of 99 % and a melt flow index of 16 g/10 min (ISO 1133-A 210 °C/2.16 kg) was used in this study. Dibutyl itaconate – DBI was supplied by Sigma-Aldrich S.A. (Madrid, Spain), main properties are summarized in **Table III.3.1.1.**

**Table III.3.1.1.** Some thermal and physicochemical properties of DBI.

CAS number	2155-60-4
Molecular weight	242.31 g/mol
Ester content	96 %
Appearance	Transparent colourless liquid at 25 °C
Refraction index	n <sub>20</sub> /D 1.444
Boiling point	284 °C
Density	0.985 g/mL at 25 °C
Viscosity	5.6 mPa s
Acid index (itaconic acid)	Max 0.1 %
Water solubility	Very low
Surface tension	0.035 N/m at 25 °C

**Theoretical approach to solubility.**

The solubility parameter –  $\delta$  is crucial to achieve a correct dispersion of the additive in the polymeric matrix. The solubility parameters of both DBI and PLA were calculated following the Hoftyzer–Van Krevelen group contribution method. The  $\delta$  contained different contributions: dispersive forces –  $\delta_d$ , polar forces –  $\delta_p$ , and hydrogen bonding –  $\delta_h$  as seen in **Equation III.3.1.1**. Each of these parameters was obtained from the contribution of each of the molecular groups of the molecule given by D.W. van Krevelen *et al.* and K. te Nijenhuis *et al.* [40]. Additionally, the molar volume –  $V_m$  was obtained from the ratio between the molar mass –  $M_m$  and the density –  $\rho$ .

$$\delta = \sqrt{\delta_d^2 + \delta_p^2 + \delta_h^2} \text{ (MJ/m}^3\text{)}^{1/2} \quad \text{Equation III.3.1.1.}$$

Where:

$$\delta_d = \frac{\sum F_{di}}{V_m} \text{ (MJ/m}^3\text{)}^{1/2} \quad \text{Equation III.3.1.2.}$$

$$\delta_p = \frac{\sqrt{\sum F_{pi}^2}}{V_m} \text{ (MJ/m}^3\text{)}^{1/2} \quad \text{Equation III.3.1.3.}$$

$$\delta_h = \frac{\sqrt{\sum E_{hi}}}{V_m} \text{ (MJ/m}^3\text{)}^{1/2} \quad \text{Equation III.3.1.4.}$$

The group contribution method proposed by Hoftyzer and Van Krevelen provides the characteristic molar attraction constants for each chemical group for both the dispersive –  $F_{di}$  and the polar –  $F_{pi}$  contributions, allowing a rather accurate estimation of  $\delta_d$  and  $\delta_p$ , respectively, as indicated in **Equation III.3.1.2.** and **Equation III.3.1.3.** Nevertheless, the F-method cannot be applied to the calculation of  $\delta_h$ . As indicated by Hansen, the hydrogen bonding energy  $E_{hi}$  per structural group is almost constant and it is useful to estimate  $\delta_h$  as shown in **Equation III.3.1.4.** The group contribution method proposed by Hoftyzer and Van Krevelen provided the characteristic molar attraction constants for each chemical group for both the dispersive –  $F_{di}$  and the polar –  $F_{pi}$  contributions, allowing a rather accurate estimation of  $\delta_d$  and  $\delta_p$ , respectively, as indicated in **Equation III.3.1.2.** and **Equation III.3.1.3.** Nevertheless, the F-method cannot be applied to the calculation of  $\delta_h$ . As indicated by Hansen, the hydrogen bonding energy  $E_{hi}$  per structural group was almost constant and it was useful to estimate  $\delta_h$  as shown in **Equation III.3.1.4.** The three solubility coordinates can be plotted in a 3D-space with axes  $\delta_d$ ,  $\delta_p$ , and  $\delta_h$ , each one with the corresponding units of a solubility parameter, that is,  $(\text{MJ/m}^3)^{1/2}$ . The more similar the solubility parameter

coordinates of the plasticizer ( $\delta_d$  DBI,  $\delta_p$  DBI, and  $\delta_h$  DBI) to those of PLA ( $\delta_d$  PLA,  $\delta_p$  PLA, and  $\delta_h$  PLA), the better solubility/miscibility will be obtained. The geometrical 3D distance between the solubility parameters was a simple way to quantify how close is DBI to PLA in terms of their solubility parameter coordinates. As a 3D-space was considered, the solubility threshold (maximum distance to allow miscibility) of a particular polymer was defined as the maximum distance from the centre, which was represented as a spherical region in this 3D-space, with the centre located in the corresponding solubility parameter coordinates of the polymer. If the solubility parameter coordinates of a particular plasticizer fall inside this spherical region, the plasticizer may be miscible with the polymer. Otherwise, miscibility will be restricted. This threshold distance was characteristic of each polymer and was referred to as the radius of the solubility sphere,  $R_0$ , with units  $(\text{MJ}/\text{m}^3)^{1/2}$ . The region in which a plasticizer is miscible, is obtained by means of a thermodynamical difference that allowed to give miscible mixtures and took a value of  $R_0 = 10.7 (\text{MJ}/\text{m}^3)^{1/2}$  for PLA [11,41]. Thus, plasticizers inside PLA sphere will be miscible, while those outside will not. To quantify the distance between the base PLA and DBI, a parameter  $R_a$ , was defined as the geometrical distance between both solubility parameters as proposed by the Hansen solubility parameters – HSP theory (**Equation III.3.1.5**).

$$R_a = \sqrt{4(\delta_{d \text{ DBI}} - \delta_{d \text{ PLA}})^2 + (\delta_{p \text{ DBI}} - \delta_{p \text{ PLA}})^2 + (\delta_{h \text{ DBI}} - \delta_{h \text{ PLA}})^2} \quad \text{Equation III.3.1.5.}$$

The ratio between  $R_a$  and  $R_0$  allows determining the relative energy difference – RED according to **Equation III.3.1.6**. When values close to zero are obtained, a miscible mixture is achieved. Values higher than 1 stand for the plasticizer is outside the sphere defined by the PLA and the resulting blend is immiscible [11,42].

$$\text{RED} = \frac{R_a}{R_0} \quad \text{Equation III.3.1.6.}$$

### Processing of plasticized PLA formulations with DBI.

PLA was dried at 60 °C for 48 h in a dehumidifying dryer MDEO from Industrial Marsé, (Barcelona, Spain) to remove any residual moisture avoiding the hydrolysis. The necessary amount of each component was weighted and then pre-mixed in a zipper bag according to the compositions proposed in **Table III.3.1.2**. The pre-mixed materials were then fed into the main hopper of a co-rotating twin-screw extruder from Construcciones Mecánicas Dupra, S.L. (Alicante, Spain). This extruder had a screw diameter of 25 mm with a length-to-diameter ratio (L/D) of 24. The extrusion process was carried out with a residence time of 1 min in all cases. The temperature profile, from the hopper to the

die was set as follows: 185 – 180 – 175 – 170 °C. The different compositions were extruded and subsequently pelletized using an air-knife unit.

**Table III.3.1.2.** Summary of the plasticized PLA formulations with DBI according to the weight content – wt.%.

Code	PLA (wt.%)	DBI (wt.%)
PLA	100	0.0
2.5DBI-PLA	97.5	2.5
5DBI-PLA	95.0	5.0
10DBI-PLA	90.0	10.0
15DBI-PLA	85.0	15.0
20DBI-PLA	80.0	20.0

After the extrusion process, the pellets were stored in the dehumidifying dryer to avoid moisture absorption. Standard samples were obtained with the 270/70 injection moulding machine from Mateu & Solé (Barcelona, Spain) with 3 min as an average residence time. The introduction of the plasticizer induced a significant viscosity change of the base PLA polymer. To enhance processing of specimens of plasticized PLA formulations some adjustments in the temperature profile had to be done, since the viscosity was dramatically reduced by increasing DBI content.

**Table III.3.1.3.** Summary of the optimized temperature profiles for the injection moulding process of PLA and plasticized PLA formulations with DBI.

Code	Zone 1 (°C) (hopper)	Zone 2 (°C)	Zone 3 (°C)	Zone 4 (°C) (injection nozzle)
PLA	210	205	200	195
2.5DBI-PLA	205	200	195	190
5DBI-PLA	200	195	190	185
10DBI-PLA	195	190	185	180
15DBI-PLA	185	180	175	170
20DBI-PLA	175	170	165	160

These temperature profiles were obtained from a capillary rheology study that allowed optimizing temperatures to provide similar viscosity, which is a key factor in processing plasticized polymer formulations. Therefore, the lubrication effects provided by DBI allowed to decrease the temperature profile thus preventing DBI loss. Similar changes in processing temperatures have been proposed by Lascano *et al.* [43], in plasticized PLA formulations with Oligomers of Lactic Acid – OLA, since the decrease in viscosity produced by the plasticizers makes impossible processing by injection moulding without adjusting the temperature profile to obtain similar viscosities in all compositions. The temperature profiles considered for the processing of the injection moulded samples are summarized in **Table III.3.1.3.**

### Mechanical properties.

Tensile tests were carried out in a universal testing machine ELIB 50 from S.A.E. Ibertest (Madrid, Spain) on injection-moulded specimens (ISO 527-2:2012 type 1B shape). A 5-kN load cell was used, and the cross-head speed was set to 20 mm/min. Parameters like tensile strength -  $\sigma_t$ , elongation at break -  $\epsilon_b$ , and tensile modulus -  $E_t$  were recorded. Shore hardness was measured in a 676-D durometer from J. Bot Instruments (Barcelona, Spain), using the D-scale, on injection-moulded samples with 4 mm thickness, (ISO 868:2003). Impact behaviour was also studied on injection-moulded rectangular samples (ISO 179:2010 type 1 shape) by the Charpy impact test with a 6-J pendulum from Metrotec S.A. (San Sebastián, Spain). Samples were notched with a 0.25 mm radius "V" - notch type. All tests were performed at room temperature, and at least 5 specimens of each formulation were tested to obtain the corresponding parameters. The obtained results were averaged and the standard deviation was calculated.

### Morphology.

Fractured tensile test samples were subjected to a sputtering process with gold-palladium alloy in a SC7620 sputter coater from Quorum Technologies Ltd. (East Sussex, UK). Samples were placed in the vacuum chamber of a ZEISS ULTRA 55 Field Emission Scanning Electron Microscope - FESEM from Oxford Instruments (Abingdon, UK). The working distance was set to 4 mm and the acceleration voltage was 2 kV.

### Thermal properties.

Differential scanning calorimetry - DSC was used to assess the main properties of the plasticized PLA formulations with DBI. In particular, the melting temperature -  $T_m$ , the cold crystallization temperature -  $T_{cc}$ , melting enthalpy -  $\Delta H_m$ , cold crystallization enthalpy -  $\Delta H_{cc}$  and the degree of crystallinity -  $\chi_c$  were obtained from DSC runs. The degree of crystallinity was obtained with the **Equation III.3.1.7**, where  $w$  represents the weight fraction of PLA and  $\Delta H_m^0$  is the melt enthalpy of a theoretically fully crystalline PLA, which was considered as 93 J/g as reported in literature [44].

$$\chi_c(\%) = \frac{\Delta H_m - \Delta H_{cc}}{\Delta H_m^0 \cdot w} \cdot 100 \quad \text{Equation III.3.1.7.}$$

DSC runs were collected in a modulated heat flow DSC model Q2000 from TA Instruments (New Castle, DE, USA) with nitrogen atmosphere (66 mL/min) and a



sample weight between 5 and 7.5 mg. The dynamic DSC runs were performed into three stages. First a heating cycle was performed to erase the thermal history from 30 °C to 200 °C at 10 °C/min. Then, a controlled cooling step was carried out down to - 40 °C with a cooling rate of - 10 °C/min. Finally, a second heating cycle was performed up to 240 °C at 10 °C/min. The main parameters of thermogravimetric analysis - TGA, namely the onset degradation temperature -  $T_{5\%}$  (obtained at a mass loss of 5 %), the maximum degradation rate temperature -  $T_{max}$ , and the residual weight (%), were obtained in a thermogravimetric TG-DSC2 thermobalance from Mettler-Toledo (Columbus, OH, USA). Samples with an average weight of 6 mg were placed into alumina crucibles and subjected to a single dynamic heating program from 30 °C to 700 °C at a heating rate of 10 °C/min in air atmosphere. Additionally, a quantification of the DBI mass loss related to processing conditions, was obtained in isothermal TGA conditions at the maximum working temperatures in each temperature profile (see **Table III.3.1.2.**, zone 1). The heating rate to reach the desired isothermal temperature was 100 °C/min; once the target temperature was reached, the mass loss as a function of time was recorded for a total time of 40 min. All thermal tests were carried out in triplicate.

#### **Thermo-mechanical properties.**

Dynamic-Mechanical Thermal Analysis - DMTA was carried out in a Mettler-Toledo DMA1 (Columbus, OH, USA) in single cantilever mode. Samples with dimensions 20 × 6 × 3 mm<sup>3</sup> were used for DMTA characterization. The maximum dynamic deflection was set to 10 μm and the frequency for the sinusoidal deformation was set to 1 Hz. Regarding the heating cycle, tests started at - 100 °C and samples were heated up to 100 °C with a heating rate of 2 °C/min. Parameters like storage modulus -  $E'$  and dynamic damping factor -  $\tan \delta$  were recorded as a function of temperature.

To evaluate the dimensional stability, a Thermo-Mechanical Ansys - TMA was performed in a Q400 from TA Instruments (New Castle, DE, USA) was used. Rectangular samples sized 10 × 10 × 4 mm<sup>3</sup> were subjected to a heating cycle from - 20 °C to 100 °C at a heating rate of 2 °C/min and a constant load of 20 mN. The Coefficient of Linear Thermal Expansion - CLTE of the plasticized PLA formulations as the slope in the plot of the expansion *vs* temperature. All tests were carried out in triplicate.

**Rheological properties.**

The rheological properties of PLA and plasticized PLA formulations were obtained using a capillary rheometer ThermoHaake from Rheoflizer (Baden-Wurtemberg, Germany). This was equipped with a capillary of 1 mm diameter and a length-to-diameter ( $L/D$ ) = 10. The tests were performed according to ISO-11443. All materials were dried at 60 °C for 48 h in a dehumidifying dryer MDEO from Industrial Marsé, (Barcelona, Spain) to replicate the same residual moisture used in the processing by extrusion/injection moulding. All tests were carried out five times to obtain reliable results.

**RESULTS AND DISCUSSION.****Theoretical approach to solubility between PLA and DBI.**

**Table III.3.1.4.** shows the results obtained for each of the solubility components and the total solubility parameter. In all cases, similar values are shown for both components, which leads to the assumption that there may be solubility between both materials. Additionally, RED was found to be 0.62, which indicates that there may be solubility between PLA and DBI. For a plasticized PLA with derivatives of levulinic acid and valeric acid it was possible to observe a positive effect on the final properties showing that a plasticization process had taken place. For these plasticizers, the RED values obtained were comprised between 0.5 and 0.7 [45], thus being in a similar range to that obtained in this work.

**Table III.3.1.4.** Summary of the PLA and DBI solubility parameters according to the Hoftyzer–Van Krevelen group contribution method and RED.

	$\delta_d$ (MJ/m <sup>3</sup> ) <sup>1/2</sup>	$\delta_p$ (MJ/m <sup>3</sup> ) <sup>1/2</sup>	$\delta_h$ (MJ/m <sup>3</sup> ) <sup>1/2</sup>	$\delta$ (MJ/m <sup>3</sup> ) <sup>1/2</sup>	$R_a$	RED
PLA	15.3	8.4	11.0	20.7	–	–
DBI	15.1	2.8	7.6	17.1	6.6	0.62

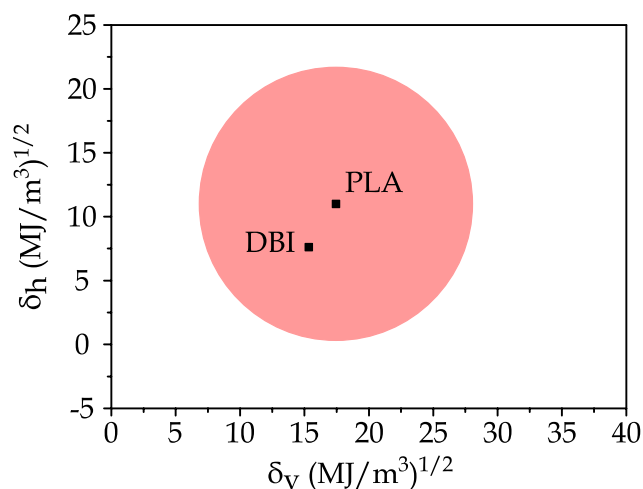


**Figure III.3.1.2.** Bagley's solubility diagram for PLA and DBI where the  $\delta_v = (\delta_d^2 + \delta_p^2)^{1/2}$ .

As observed in **Figure III.3.1.2.**, the Bagley's diagram also suggests that DBI has solubility with PLA. The red sphere indicates the solubility region of PLA, and the  $\delta$  coordinates of DBI fall into this region, thus indicating DBI is a good plasticizer for PLA, proved to its solubility with PLA. This theoretical approach has also been conducted with other linear polyesters such as P3HB to assess its solubility with different organic solvents [46]. Ramos *et al.* confirmed that the theoretical results were in agreement with the experimental results, thus suggesting the usefulness of the theoretical approach to select the appropriate solvent.

#### **Effect of DBI on the rheological properties of plasticized PLA formulations.**

In spite of the fact that some polymers show a shear-thickening (dilatant) behaviour, such as corn starch in water, almost all polymer melts show a shear-thinning behaviour, which is the typical non-Newtonian or pseudoplastic behaviour, characterized by a decrease in viscosity with rising the shear rate. Osswald *et al.* studied the rheology of different grades of PE, and PP and characterized their pseudoplastic behaviour [47]. Depending on the processing technique, the applied shear rate is different. For example, the shear rate used in an injection-moulding process is usually comprised between 100 and 10000  $s^{-1}$ , while lower shear rates between 10 and 1000  $s^{-1}$  are typically employed in extrusion processes [48]. Plasticizers usually provide a decrease in viscosity due to their lubricant effect on polymer chains. Therefore, it is useful to study the effects of DBI on the rheology of plasticized PLA formulations, as it allows to define the proper temperature profiles for optimizing the injection moulding process. Once a polymer reaches a low viscosity state due to high temperatures or plasticizer addition, a leakage from the cavity of the mold occurs and as a result, burrs

appear. To minimize this effect, the working temperatures were reduced, considering that the polymer flow must be enough to completely fill the mold.

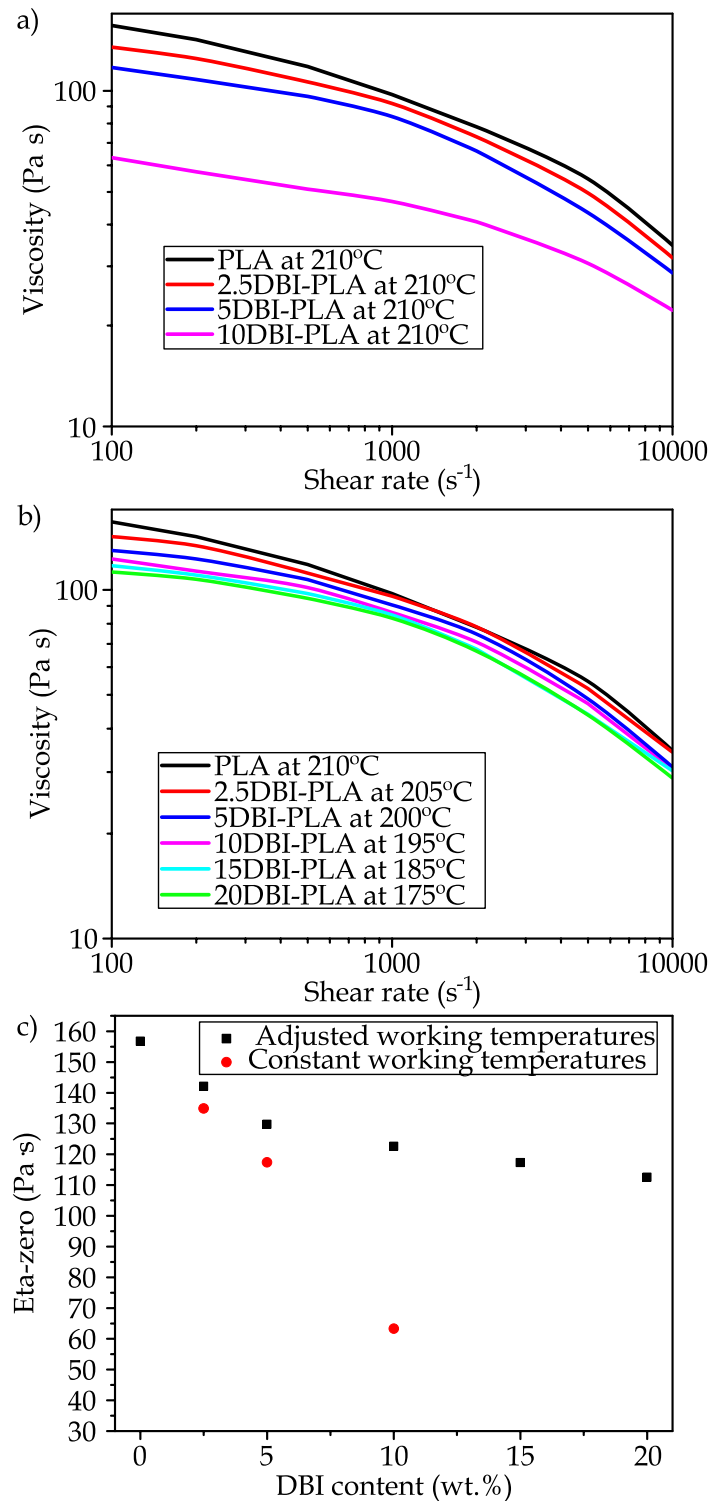


**Figure III.3.1.3.** Rheological behaviour of neat PLA and plasticized PLA formulations with different DBI content: a) viscosity  $vs$  shear rate at a constant temperature of 210 °C, b) viscosity  $vs$  shear rate after iteration process to give similar viscosity profile and c) Eta-zero  $vs$  DBI content.

In a first attempt to analyse the rheological behavior of PLA with DBI, a temperature of 210 °C and a shear rate range between 100 and 10000 s<sup>-1</sup> were selected, being this a usual working temperature for a PLA, and a usual shear rate for an injection moulding process. The results obtained by capillary rheometry are shown in **Figure III.3.1.3**. As seen in **Figure III.3.1.3a.**, not all materials could be tested under these conditions because the resulting viscosity at 210 °C was critically reduced and the equipment was not able to record the pressure generated to obtain the corresponding viscosity values. As Yoo *et al.* proposed, PLA viscosity can be modified with the working temperatures [49], so the behaviour of the formulations proposed can be controlled during the manufacturing by the programmed temperatures. **Figure III.3.1.3a.** shows plasticized PLA formulations with DBI at a constant temperature of 210 °C. Due to a reduction in the interaction of the polymer chains as a result of the plasticizer introduction, a remarkably lower viscosity was measured [50]. Sun *et al.* have reported similar decrease in viscosity of chitosan and zein protein mixtures by increasing the amount of different plasticizers [51]. Since viscosity plays a key role in injection moulding, to get similar rheological behaviour in all the plasticized PLA formulations, an iterative process was carried out to obtain the optimum temperatures for the injection moulding process. The resulting curves and temperatures are shown in **Figure III.3.1.3b**. The differences that emerge by the modification of the working temperatures can be also seen in **Figure III.3.1.3c.**, while a dramatic decrease of Eta-zero was observed at 210 °C, the iterative process carried out to optimize the working temperatures allowed to reduce the variations that arise with increasing plasticizer content.

#### **Effect of DBI on the mechanical properties of plasticized PLA formulations.**

The addition of DBI into the PLA polymeric matrix had a remarkable effect on the final mechanical properties of the considered PLA/DBI formulations as proven by **Table III.3.1.5.** and **Figure III.3.1.4**. First, the effect of the increase in plasticizer proportion over the stiffness of the material was studied. In this case, unplasticized PLA showed a tensile modulus of 4076 MPa and the addition of 2.5 wt.% DBI decreased the tensile modulus by 3.1 %, which suggests some plasticization. The effect of DBI on the stiffness was most noticeable at a DBI content of 10 wt.% leading to a remarkably lower tensile modulus of 1572 MPa, as it was expected. This tensile modulus is within the range of some commodities such as high-density poly(ethylene) – HDPE with tensile modulus ranging from 600 to 900 MPa and PP with tensile modulus comprised between 900 to 2000 MPa [52,53]. This decrease in stiffness provided by the DBI plasticizer can be explained by different theories such as the lubricity, the gel and the free volume theories

[54]. One of the most known phenomena about the introduction of plasticizers in polymers is the reduction in the attraction forces between the chains of the polymer (hydrogen bonding, van der Waals forces, and so on). As a result, the movement of the polymeric chains requires less energy [55]. In samples containing 15 and 20 wt.% DBI, a remarkable decrease in the  $E_t$  was observed, resulting in 58.5 MPa for the 20DBI-PLA. These results suggest that plasticized PLA formulations with more than 10 wt.% DBI have a tensile modulus value similar to thermoplastic poly(urethane) - TPU. For example, Bueno-Ferrer *et al.* developed different formulations of biobased TPU with tensile modulus ranging from 0.7 to 11.1 MPa [56]. Kumar *et al.* obtained similar results by plasticizing PLA with 30 wt.% of a polymeric plasticizer as PEG with a measured tensile modulus of 140 MPa [57]. Similar decrease in stiffness can also be achieved by blending PLA with poly( $\epsilon$ -caprolactone) - PCL. In this sense, Mittal *et al.* reported on PLA/PCL blends with a tensile modulus of 866 MPa by blending PLA with 50 wt.% PCL [58].

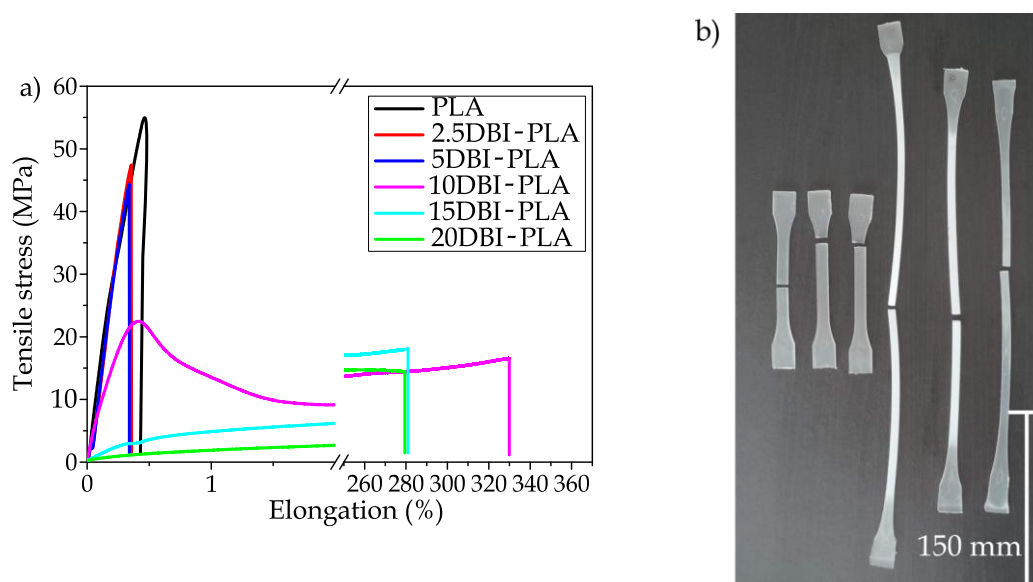


**Figure III.3.1.4.** a) Tensile stress *vs* elongation plots for neat PLA and plasticized PLA formulations with different DBI contents and b) appearance of PLA/DBI specimens after the tensile test (left neat PLA and right 20DBI-PLA) (scale bar = 100 mm).

The most surprising effect of DBI on mechanical properties is the drastic increase in elongation at break it provides. PLA is usually characterized by a brittle behavior [6]. As a result, a very low elongation at break (4.6 %) is obtained for unplasticized PLA. The addition of small amounts of plasticizer (up to 5 wt.% DBI) promoted a decrease in elongation at break, resulting in values between 3.1 % and 3.2 %. This effect has been observed when other plasticizers are used in small amounts in several polymers, and this phenomenon is known as anti-plasticization [59]. Nevertheless, plasticized PLA

with 10 wt.% DBI shows a considerable increase in the  $\varepsilon_b$  up to values of 322 %, which is clear evidence of the high plasticizing potential that DBI can provide to PLA. This exceptional plasticization effect exerted by DBI provides to PLA is observed in **Figure III.3.1.4a.** which gathers the characteristic stress–elongation curves of neat PLA and plasticized PLA formulations, together with the broken specimens after the tensile test (**Figure III.3.1.4b.**). For the 15 and 20 wt.%, the  $\varepsilon_b$  is not increased which is related to PLA reaching the saturation point due to plasticizer introduction as observed by Ferri *et al.* in plasticized PLA with 5 phr (parts by weight of plasticizer per 100 weight parts of base polymer) octyl epoxy stearate [60]. Xuan *et al.* reported plasticized PLA formulations with elongation at breaks comprised between 446 % and 643 % with 20 wt.% of different plasticizers derived from levulinic acid [61]. The results obtained with DBI are much better than the ones obtained with other biobased plasticizers such as those derived from chemically modified vegetable oils. Orue *et al.* reported an interesting increase in  $\varepsilon_b$  up to 25 % in PLA blends with 20 wt.% vegetable oil–derived plasticizers [62]. Thus, the obtained results suggest that esters from bioderived itaconic acid could represent a feasible technical solution for achieving effective PLA plasticization.

Regarding tensile strength, a clear decreasing trend as a function of the amount of plasticizer was obtained, which is also a typical plasticization effect. Tian *et al.* observed this behaviour in PLA films plasticized with triethyl citrate – TEC and glycerol triacetate – GTA, while Singh *et al.* reported this same tendency in poly(vinyl alcohol) – PVA films plasticized with sorbitol [63,64]. The effect of DBI on the internal structure of the base PLA polymer resulted in a reduction of the intermolecular forces between PLA polymer chains, resulting in a reduction of the maximum tensile strength [55]. Neat PLA is characterized by a  $\sigma_t$  of 55.0 MPa, while plasticized PLA with 10 wt.% DBI shows a  $\sigma_t$  of 23.8 MPa, which represents approximately half the value of neat PLA. It is important to bear in mind that the  $\sigma_t$  of most commodities is comprised in the 20 – 35 MPa range [65]. Therefore, plasticized PLA formulations containing 10 wt.% DBI provide balanced mechanical properties, similar to those of poly(olefins). As expected, a higher amount of plasticizer resulted in a decrease in  $\sigma_t$  down to 15.0 MPa (20 wt.% DBI).

**Table III.3.1.5.** Summary of mechanical properties of neat PLA and plasticized PLA formulations with different DBI contents.

Code	$E_t$ (MPa)	$\sigma_t$ (MPa)	$\epsilon_b$ (%)	Shore D hardness	Impact strength (kJ/m <sup>2</sup> )
PLA	4076 ± 34	55.0 ± 1.8	4.6 ± 0.5	81.0 ± 1.2	4.8 ± 0.2
2.5DBI-PLA	3949 ± 90	46.2 ± 1.7	3.2 ± 0.4	83.3 ± 1.0	4.8 ± 0.2
5DBI-PLA	3460 ± 50	44.4 ± 1.8	3.1 ± 0.4	81.5 ± 0.9	5.4 ± 0.2
10DBI-PLA	1572 ± 63	23.8 ± 0.4	322 ± 17	75.6 ± 1.1	7.7 ± 0.4
15DBI-PLA	162 ± 9	16.9 ± 0.8	263 ± 9	58.2 ± 1.8	nb
20DBI-PLA	58.5 ± 2	15.0 ± 0.1	262 ± 7	50.3 ± 0.6	nb

\*nb: no break was observed even on V-notched specimens.

The appearance of the tensile specimens after the tensile test is shown in **Figure III.3.1.4b**. It is clearly seen that for a DBI content of 10, 15, and 20 wt.%, the  $\epsilon_b$  is much higher than that of neat PLA or plasticized PLA formulations with low DBI content. This is indicative of a positive contribution of DBI towards the obtention of high ductile PLA materials. The whitening in the deformed region is promoted by the formation of voids during the tensile test as proposed by Chieng *et al.* [66], as well as a preferential PLA polymer chain alignment during axial deformation.

Additionally, **Table III.3.1.5.** shows the hardness results of the PLA-based materials as a function of the amount of DBI plasticizer content. As expected, since hardness is a resistant mechanical property, it follows the same tendency observed for the  $E_t$  and  $\sigma_t$ . The addition of small amounts of DBI does not vary Shore D hardness, maintaining values around 80 for 10 wt.% DBI plasticized PLA formulations show a remarkable difference in Shore D values in relation to neat PLA, decreasing the hardness from 81.1 down to 75.6. As the proportion of DBI is increased, Shore D hardness further decreases down to 50.3 for the sample containing 20 wt.% DBI. These results are in agreement with those reported by Bouti *et al.* on PLA plasticized with epoxidized sunflower oil [67].

As it has been stated, PLA is a rather brittle polymer with low toughness. Plasticization usually leads to improved toughness. It is important to bear in mind that toughness is related to the ability for energy absorption during deformation-break. Therefore, toughness is related to both tensile strength and elongation at break. Accordingly, toughness can be estimated by the area under the stress-strain curve. As observed in a qualitative way in **Figure III.3.1.4a.**, the area under the stress-strain curve increases with increasing DBI content, except from plasticized PLA formulations with 2.5 and 5.0 wt.% DBI, which show an evident lower area than neat PLA. **Table III.3.1.4.** also gathers the values of impact strength for neat PLA and its plasticized formulations



with DBI. As expected, DBI has a positive effect on impact strength over PLA for plasticized formulations with 10, 15, and 20 wt.%. In fact, the plasticized specimens with 15 and 20 wt.% DBI did not break due to a stiffness reduction. Despite the area under the stress-strain curves suggest lower toughness for low DBI content (5 wt.% or lower), these materials offer good behaviour in impact conditions. This phenomenon may be promoted by the higher  $\chi_c$  that DBI provides, as proposed by Lin *et al.* [68]. The low impact strength of neat PLA (4.8 kJ/m<sup>2</sup>) is improved as the DBI content increases, with values of 7.7 kJ/m<sup>2</sup> for plasticized PLA with 10 wt.% DBI. These results are in total accordance with those reported by Jiao *et al.* on PLA plasticized with 20 wt.% PEG [69]. In this case, DBI provided similar results with lower concentration.

#### **Effect of DBI on the morphology of plasticized PLA formulations.**

**Figure III.3.1.5.** shows the morphology of tensile test fractured samples of neat PLA and plasticized PLA/DBI blends. The introduction of DBI showed visual changes in the morphology of plasticized PLA formulations. The flat fracture surface of neat PLA (**Figure III.3.1.5a.**) is representative of a brittle behavior, implying low plastic deformation [66]. On the other hand, as the DBI content increases, a clear change in the surface morphology is detected, indicated by a rougher surface, ascribed to plastic deformation. This phenomenon occurred even on specimens with low DBI contents (5 wt.% or lower) although, as it has been mentioned above, they showed slightly lower ductile behaviour. A clear plasticization effect is noticed in **Figure III.3.1.5d.** for the 10DBI-PLA with a fracture surface with high roughness. Due to the improved  $\epsilon_b$  and, subsequently, ductility, ridges and tears emerged on the fracture surface [70]. This morphology was not observed in plasticized formulations with 15 and 20 wt.% DBI. In fact, their characteristic fracture morphologies show great roughness, but are smoother than the plasticized material with 10 wt.%. Similar findings were reported by Ahmad *et al.* in PLA formulations plasticized with 10 wt.% TEC. Moreover, they observed some phase separation at high TEC concentrations [71]. In this case, phase separation is not observed by FESEM, but the morphologies of plasticized formulations with 15 and 20 wt.% DBI suggest less plastic deformation that led to lower  $\epsilon_b$  values.

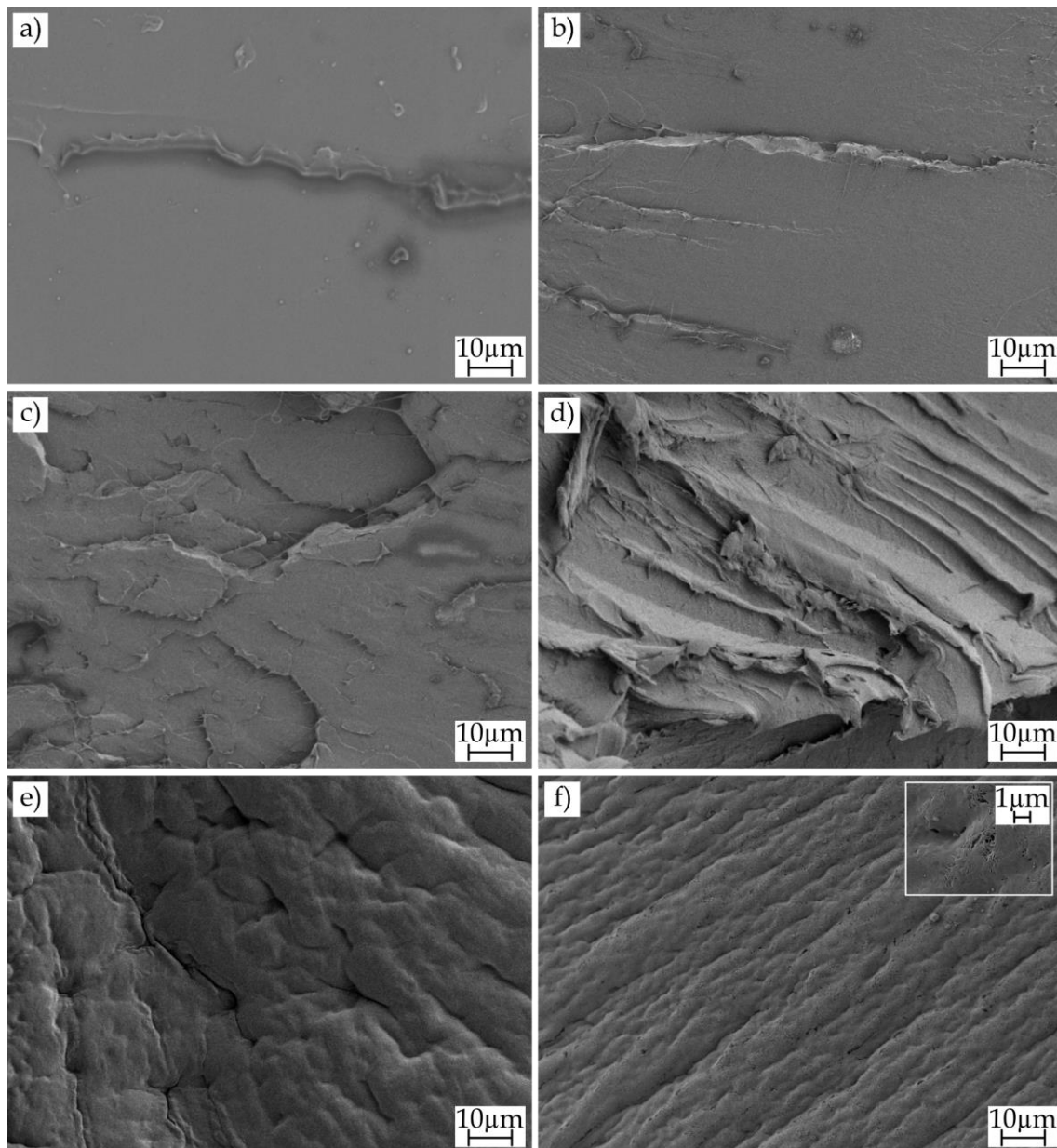


**Figure III.3.1.5.** FESEM images of the fractured surfaces from tensile tests taken at 500 × and inset at 5000 ×. a) PLA, b) 2.5DBI-PLA, c) 5DBI-PLA, d) 10DBI-PLA, e) 15DBI-PLA and f) 20DBI-PLA (scale bar = 10 μm in all images except the inset scale bar = 1 μm).

Despite the  $\epsilon_b$  results suggest a PLA structure saturation due to an excessive amount of plasticizer, no phase separation evidence was observed in all plasticized PLA formulations, which is representative of a miscible mixture. This demonstrates the theoretical solubility results previously analysed. The absence of phase separation is good for the system since phase separation phenomena derived from polymer structure saturation can exert a negative effect on mechanical properties as reported by Rojas *et al.* [72]. It is also worthy to note that the morphology of plasticized PLA formulations with high DBI content (*i.e.* 20 wt.%), show presence of voids at high magnification (**Figure**

III.3.1.5.). This phenomenon is usual when plasticizers are introduced, as reported by Celebi *et al.* and Iglesias *et al.* [73,74].

### Effect of DBI on thermal properties of plasticized PLA formulations

Plasticization of PLA with DBI resulted in a noticeable change in the thermal properties of the resulting materials. These changes were assessed by DSC (Figure III.3.1.6.) and the main results from the second heating step are gathered in Table III.3.1.6.

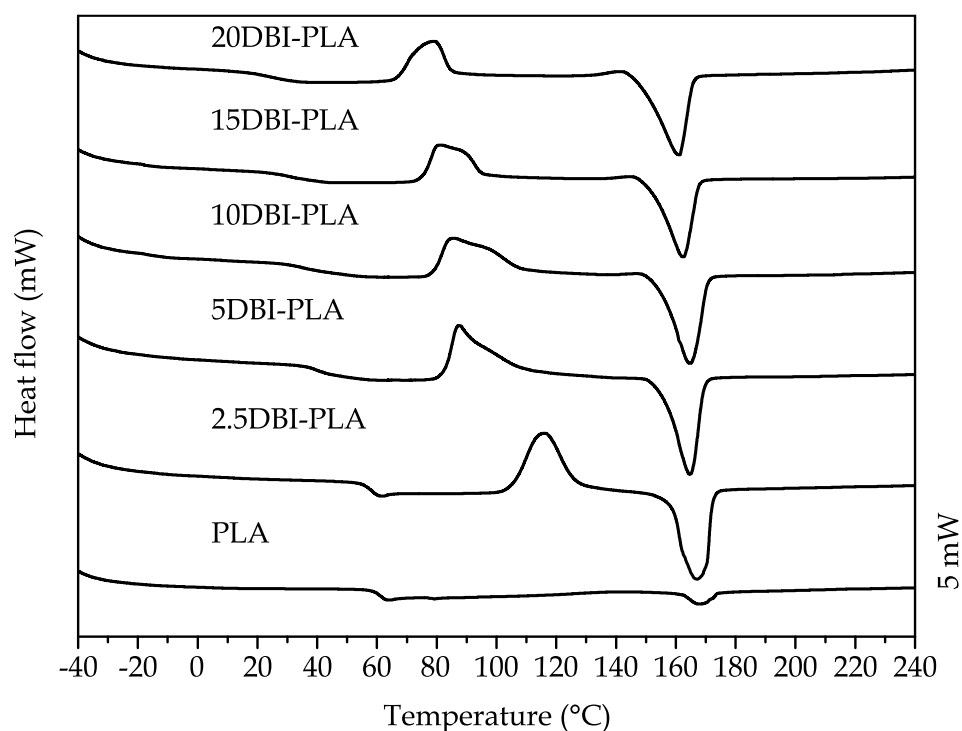


**Figure III.3.1.6.** DSC thermograms of the second heating step for neat PLA and plasticized PLA formulations with different DBI contents (scale bar = 5 mW).

One of the most relevant thermal parameters affected by the presence of a plasticizer in a polymer is the  $T_g$ . In fact, the efficiency of the plasticizer can be assessed by a decrease in  $T_g$  it can provide to the base polymer. Below the  $T_g$ , a polymer is in a glassy state characterized by highly restricted chain mobility. Above  $T_g$ , the polymer chains adopt a high mobility state, which provides increased ductility [27,75,76]. Unplasticized PLA has a  $T_g$  of 61.3 °C as observed by DSC [77]. The decrease in the  $T_g$  is significant in plasticized PLA formulations containing 5, 10, 15, and 20 wt.% DBI. The progressive increase in the amount of DBI into the PLA matrix leads to a noticeable decrease in  $T_g$  down to values of 23.4 °C for a DBI content of 20 wt.%. This suggests good plasticization efficiency, with a remarkable increase in chain mobility in the amorphous PLA domains [78]. As observed in mechanical characterization, plasticized PLA

formulations with 15 – 20 wt.% DBI show a low stiffness behaviour. This is in agreement with the low  $T_g$  values obtained by DSC. Similar changes in  $T_g$  were reported by Harte *et al.* with different citrate ester plasticizers with results suggesting that despite a decrease in  $T_g$  is related to an increase in chain mobility, there is not a direct relationship with mechanical properties [79]. Muller *et al.* work focused on the use of amorphous and semicrystalline PLA grades to obtain mono- and bilayer films with several plasticizers. They reported the influence of cinnamaldehyde in several bilayer PLA-based films and the effect of this plasticizer on mechanical performance [80]. As the DSC curve for neat PLA used in this study suggests, this is a semicrystalline PLA with a low degree of crystallinity grade as the small melting peak suggests, thus indicating low tendency to crystallize. Nevertheless, the only addition of 2.5 wt.% DBI leads to a remarkable change in the thermal behaviour with the appearance of a well-defined cold crystallization process with a peak located at 115.1 °C. This suggests that DBI clearly favours crystallization. As the DBI content increases, the crystallization peak is moved to lower temperatures, reaching a minimum of 77.7 °C for the plasticized PLA formulation containing 20 wt.% DBI. Choin *et al.* observed a similar effect when polyethylene glycol acrylate - PEGA was used as plasticizer in PLA by reactive extrusion - REX, resulting in a crystallization peak temperature of 85.2 °C for a PEGA content of 20 wt.% [81]. Ferri *et al.* reported the same phenomenon on plasticized PLA with Maleinized Linseed Oil - MLO plasticizer [82]. With regard to the melting peak temperature, neat PLA has a melt peak located at 168.7 °C. As the DBI content increases, a decrease down to 160.9 °C is observed. Hassouna *et al.* also observed this phenomenon with PEG plasticizer on PLA with a melt peak temperature decrease from 154 °C down to 150 °C for the plasticized PLA with 20 wt.% PEG and 10 wt.% maleic anhydride-grafted-PLA [83]. Regarding the normalized enthalpies, as the DBI content increased, the  $\Delta H_{cc}$  decreases while the melt enthalpy increases, thus indicating an increased crystallinity as shown in **Table III.3.1.6**.

**Table III.3.1.6.** Summary of thermal properties of neat PLA and plasticized PLA formulations with different DBI contents.

Code	$T_g$ (°C)	$T_{cc}$ (°C)	$T_m$ (°C)	$\Delta H_{cc}$ (J/g)	$\Delta H_m$ (J/g)	$\chi_c$ (%)
PLA	61.3 ± 2.3	-	168.7 ± 1.3	-	4.2 ± 0.2	4.5 ± 0.3
2.5DBI-PLA	58.2 ± 4.1	115.1 ± 1.4	166.8 ± 1.4	32.5 ± 1.3	37.8 ± 0.9	5.8 ± 1.2
5DBI-PLA	40.0 ± 1.3	87.3 ± 1.0	164.9 ± 1.7	22.2 ± 1.5	28.7 ± 0.8	7.2 ± 1.1
10DBI-PLA	35.2 ± 2.3	84.8 ± 1.5	164.5 ± 2.0	23.1 ± 0.9	34.0 ± 1.4	13.0 ± 1.9
15DBI-PLA	31.4 ± 2.2	80.8 ± 1.9	162.1 ± 2.1	20.9 ± 0.7	35.0 ± 1.3	17.8 ± 1.5
20DBI-PLA	23.4 ± 3.4	77.7 ± 1.7	160.9 ± 1.9	16.6 ± 0.8	34.8 ± 1.2	24.5 ± 1.9

The neat PLA used in this study has very low  $\chi_c$  of 4.5 %. Unlike other commercial PLA grades, which are more crystalline, as reported by Muller *et al.* that used a semicrystalline PLA with a  $\chi_c$  of 27 %. The degree of crystallinity is highly dependent on the polymer structure and the thermal cycle [80]. As shown by **Table III.3.1.6.**, the  $\chi_c$  shows an increasing trend as a function of the amount of DBI, reaching values up to 24.5 % for a plasticized PLA formulation containing 20 wt.% DBI. The crystallization of PLA was promoted by the introduction of different additives that enhance the formation of crystallization nuclei. Choi *et al.* managed to promote PLA crystallization by using up to 10 wt.% PEG on PLA. Higher amounts of PEG plasticizer resulted in a saturation of the plasticizer in the polymer structure and hence, the degree of crystallinity decreased [81]. Gumus *et al.* reported a clear increase in PLA crystallinity by the addition of nanoclay particles that act as heterogeneous nucleant [77].

TGA allows to evaluate thermal degradability through studying the mass loss with temperature. This mass loss is usually attributed to polymer chain scission at high temperatures and evaporation of low molecular weight compounds such as plasticizers. A comparison of the mass loss (wt.%) curves is shown in **Figure III.3.1.7.** while the main characteristic parameters are gathered in **Table III.3.1.7.** As seen in **Figure III.3.1.7.**, DBI is a volatile substance that evaporates at temperatures below than the PLA starts to decompose. Despite the boiling point of DBI is 284 °C,  $T_{5\%}$  is obtained at relatively low temperatures of 164.9 °C with a  $T_{max}$  located at 227.3 °C. These results agree with those reported by Richard *et al.* on octyl itaconate, with a characteristic mass loss onset temperature of 200 °C. In addition, they observed an increase in the mass loss onset as the length of the alkyl chain coupled to itaconic acid increased [84]. As a result of the high thermal sensitivity that DBI possesses, processing of PLA specimens with DBI is critical since the typical processing temperatures for PLA are between 180 – 200 °C. For this reason, as indicated previously, the temperature profile for both the extrusion and injection moulding was adjusted to avoid DBI loss. In spite of the fact that some DBI plasticizer was expected to be lost during processing, the overall effects on mechanical and thermal properties imply exceptional plasticization properties. Similar effects were reported by Arrieta *et al.* on plasticized PLA with limonene a high volatile compound. Despite the mass loss onset being very low (around 100 °C), limonene provided good plasticization properties to PLA films processed at 170 °C. These films offered an  $\epsilon_b$  of 165 % for a limonene content of 20 wt.% [28]. The same phenomenon was reported by Jimenez and co-workers in plasticized PLA formulations with poly(3-hydroxybutyrate) and several plasticizers like PEG, and ATBC. They reported processing of these PLA-based blends at 180 °C. This temperature can cause some plasticizer loss during

processing. They quantified this loss of about 0.5 wt.% after 1 min at 180 °C, and 1 wt.% after 6 min. Despite this slight plasticizer loss, the overall plasticizer efficiency was still very high as supported by the remarkable increase in  $\epsilon_b$  [85].

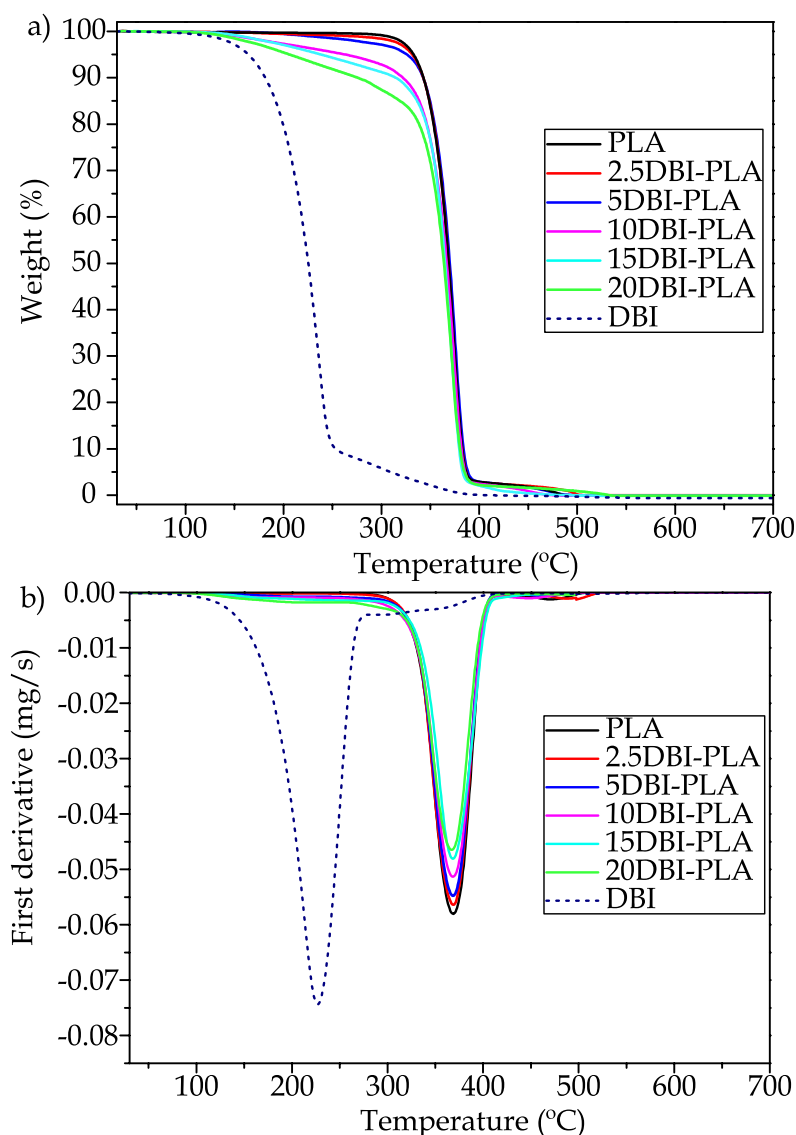


**Figure III.3.1.7.** TGA of neat PLA, DBI and plasticized PLA formulations with different DBI contents: a) weight loss curves *vs* temperature and b) first derivative - DTG curves *vs* temperature.

As seen in **Figure III.3.1.7.**, PLA thermal degradation (decomposition by chain scission) is characterized by a single mass loss process with a  $T_{5\%}$  of 333.4 °C and a  $T_{max}$  of 368.6 °C. Obviously, the TGA thermograms of plasticized PLA formulations with different DBI content show two overlapped mass loss steps, one corresponding to DBI evaporation, and a second one directly related to PLA decomposition. As the DBI content increases, the  $T_{5\%}$  of the plasticized PLA formulations decreases due to the high volatility of DBI. The maximum mass loss rate, mainly attributable to the PLA chain

scission, did not change in a remarkable way, showing values around 368 °C. A similar mass loss behaviour was reported by Sessini *et al.* for plasticized PLA formulations with a biobased polyether plasticizer derived from limonene [86]. With regard to the residual mass, it was comprised in a very narrow range of 0.3 - 0.7 % for all developed compositions. Battezzore *et al.* obtained a residue of 1 % at 800 °C on neat PLA [87].

**Table III.3.1.7.** Summary of thermal degradation properties of neat PLA, DBI and plasticized PLA formulations with different DBI contents.

Code	T <sub>5%</sub> (°C)	T <sub>max</sub> (°C)	Residual weight (%)
PLA	333.4 ± 1.3	368.6 ± 0.4	0.7 ± 0.2
2.5DBI-PLA	332.2 ± 1.1	368.1 ± 0.6	0.6 ± 0.2
5DBI-PLA	326.4 ± 1.3	368.3 ± 0.5	0.4 ± 0.2
10DBI-PLA	262.8 ± 1.3	368.5 ± 0.7	0.5 ± 0.2
15DBI-PLA	226.3 ± 1.2	368.8 ± 0.8	0.3 ± 0.2
20DBI-PLA	206.8 ± 1.4	364.7 ± 0.7	0.5 ± 0.2
DBI	164.9 ± 1.7	227.3 ± 1.4	0.3 ± 0.3

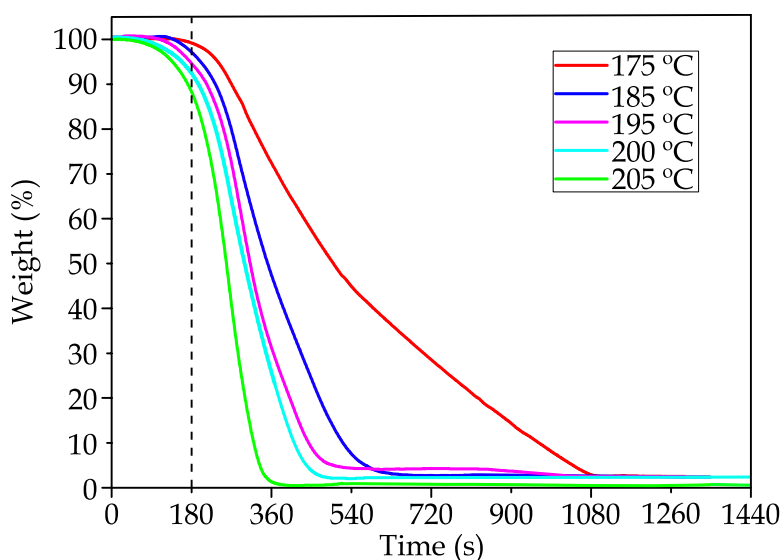


**Figure III.3.1.8.** TGA of DBI in terms of weight loss curves *vs* time for different isothermal temperatures.

Since the mass loss of the DBI due to its volatility is related to both exposure to high temperatures and time, the most aggressive thermal conditions used in the processing by injection moulding were reproduced in isothermal conditions, to give a quantitative estimation of the lost plasticizer during processing. To this end, isothermal TGA curves for DBI, at different temperatures were programmed and the mass loss was recorded as a function of the time (**Figure III.3.1.8**). Depending on the isothermal temperature scheduled, the plot evolution of the mass loss *vs* time is rather different.

As it was expected, the loss of the plasticizer as a result of its high volatility was reduced when the temperature of the isothermal profile was decreased, thus showing the importance of the rheological characterization, which allowed to reduce the processing temperatures, thus preventing the plasticizer from volatilizing. During the extrusion process, PLA/DBI formulations were exposed to a maximum temperature of 185 °C with a residence time of 1 min. Under these conditions, the mass loss related to DBI volatilization is almost negligible as indicated by **Figure III.3.1.8.** (blue line). With regard to the injection moulding process, the residence time is close to 3 min (dashed line in **Figure III.3.1.8.**). By considering the maximum temperatures of the corresponding temperature profile (see **Table III.3.1.3.**, zone 1), it is possible to quantify the maximum plasticizer loss. For plasticized PLA formulations with 2.5 wt.% DBI, the maximum temperature these formulations had to withstand was 205 °C. At this isothermal temperature and residence time (green line in **Figure III.3.1.8.**), the DBI loss is 11.5 %. Despite the nominal content was 2.5, the actual DBI content was 2.2 wt.% as suggested by the isothermal volatilization curves of DBI. As the isothermal temperature decreased, the corresponding percentage of DBI lost was remarkably reduced, thus leading to the following nominal (actual) DBI contents: 2.5DBI-PLA (2.2 wt.% DBI), 5DBI-PLA (4.6 wt.% DBI), 10DBI-PLA (9.4 wt.% DBI), 15DBI-PLA (14.5 wt.% DBI), and 20DBI-PLA (19.8 wt.% DBI). Despite this slight plasticizer loss, the mechanical and thermal characterization confirmed exceptional plasticization properties of DBI.

#### **Effect of DBI and temperature on dynamical-mechanical and dimensional properties of plasticized PLA formulations.**

A comparative plot of  $E'$  and  $\tan \delta$  is shown in **Figure III.3.1.9a.** and **Figure III.3.1.9b.**, respectively. The DMTA curve for neat PLA shows the typical  $\alpha$ -relaxation process, attributed to its  $T_g$ . This is distinguished by the decrease of  $E'$  by 3 orders of magnitude. Below its  $T_g$ , PLA behaves as a rigid and stiff polymer since only local rotational and vibrational motions are allowed (mainly related to secondary relaxation processes such as the  $\gamma$ - and  $\beta$ -relaxations). Once the glass transition temperature  $T_g$  is surpassed, long-range translational coordinated molecular motions of PLA chains can occur and this leads to a considerable softening [88,89]. In spite of the fact that several methods exist to estimate the glass transition temperature by using  $E'$ , the loss modulus -  $E''$  or the  $\tan \delta$ ; the use of  $\tan \delta$  to assess the  $T_g$  is the most widely employed methodology. Using the  $\tan \delta$  criterion, neat PLA is characterized by a  $T_g$  of 68.7 °C and, as also observed by DSC, this value is remarkably moved down to values of 39.7 °C for the plasticized PLA formulations containing 20 wt.% DBI.



**Table III.3.1.8.** Summary of the DMTA properties of neat PLA and plasticized PLA formulations with different DBI contents.

Code	T <sub>g</sub> (°C)	tan δ peak height	tan δ peak FWHM* (°C)	E' at - 20 °C (MPa)	E' at 25 °C (MPa)
PLA	68.7 ± 1.2	2.34	7.92	1855 ± 25	1748 ± 13
2.5DBI-PLA	62.0 ± 1.1	2.54	8.01	1820 ± 31	1722 ± 16
5DBI-PLA	56.7 ± 1.3	2.51	8.41	1832 ± 20	1714 ± 21
10DBI-PLA	45.3 ± 1.4	0.79	16.83	1686 ± 27	1353 ± 14
15DBI-PLA	44.5 ± 2.1	0.34	47.52	1510 ± 29	563 ± 10
20DBI-PLA	39.7 ± 2.2	0.20	85.15	1388 ± 15	437 ± 12

\*FWHM stands for the Full-Width at Half-Maximum taken from the tan δ peak.

Although the T<sub>g</sub> values obtained by DMTA (tan δ criterion) are higher than those observed by DSC, the obtained values follow the same decreasing tendency. Plasticizers have a remarkable effect on E' and tan δ (**Figure III.3.1.9b.**). The tan δ peak for neat PLA has a very narrow peak with a maximum value around 2.30, while plasticized formulations show a broader peak with noticeably lower tan δ values. For example, the tan δ peak maximum for the plasticized PLA formulation with 10 wt.% DBI is close to 0.8 and, as noticed in **Figure III.3.1.9b.**, the peak is broader than that of neat PLA (see **Table III.3.1.8.**). A similar phenomenon was reported by Maiza *et al.* on plasticized PLA formulations with ATBC and TEC with a remarkable decrease in the peak height related to tan δ [30]. Additionally, Shirai *et al.* showed that plasticization of PLA-thermoplastic starch blends with diethyl adipate - DEA, led to a T<sub>g</sub> (tan δ peak) above 36 °C, which was higher than the room temperature. Despite this, at room temperature the material exhibited highly ductile behavior as observed in the PLA/DBI system. They concluded that this was due to the fact that the tan δ peak was wide enough to allow PLA/TPS blend to behave as a ductile material at 25 °C [90]. It is worthy to note the decrease of T<sub>g</sub> (tan δ peak criterion) with increasing the DBI content in plasticized PLA formulations (**Table III.3.1.8.**). The tan δ peak height also decreases, but the peaks corresponding to highly plasticized PLA formulations show a broader peak, measured through the Full-Width at Half-Maximum - FWHM which changes from 7.92 °C up to 85.15 °C with 20 wt.% DBI. Maiza *et al.* also reported this peak widening with increasing the content of different biobased plasticizers in PLA formulations [30]. Even with T<sub>g</sub> values above room temperature (calculated from tan δ peak maximum), these formulations exhibit an extremely high ductile behavior since the glass transition relaxation occurs in a broader temperature range [89]. Similar findings have been reported by Quiles-Carrillo *et al.* in plasticized PLA formulations by reactive extrusion with Acrylated Epoxidized Soybean Oil - AESO [44]. As it has been observed by DSC, neat PLA shows a very low  $\chi_c$ , being mainly amorphous, thus, the cold crystallization

process is quite smooth. As the DBI content increases, the cold crystallization phenomenon is more evident, and this is confirmed by the increase of the  $E'$  in the temperature range comprised between 60 – 90 °C, depending on the DBI content as observed by DSC. Agüero *et al.* observed this cold crystallization phenomenon in PLA subjected to several reprocessing stages in a more noticeable manner since thermal degradation during processing reduces molecular weight, thus allowing short chains readily to increase the crystallinity [91].

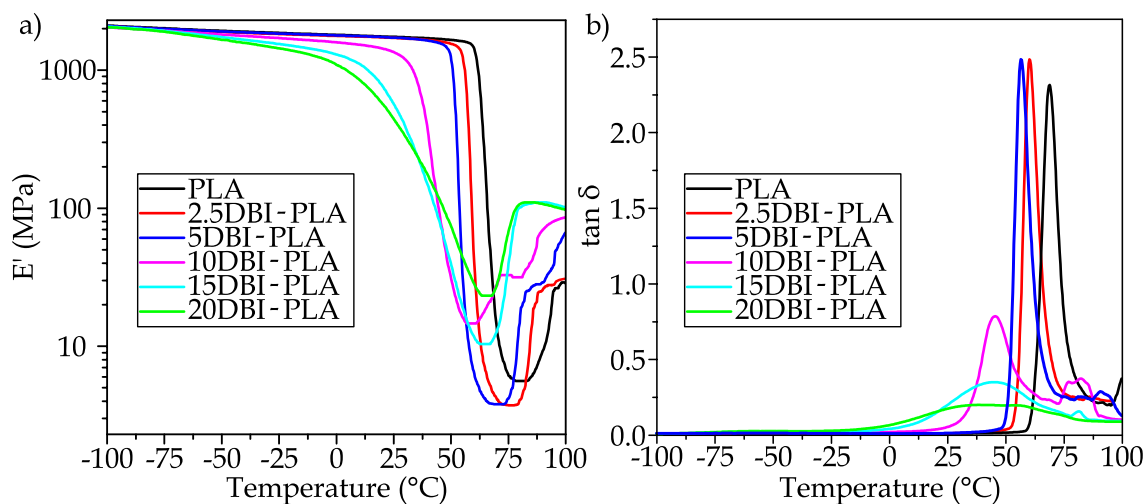


**Figure III.3.1.9.** DMTA curves of neat PLA and plasticized PLA formulations with different DBI contents: a)  $E'$  vs temperature and b)  $\tan \delta$  vs temperature.

Regarding dimensional stability, the CLTE was obtained from the slope of the dimensional change vs temperature curve obtained by TMA. **Figure III.3.1.10.** shows representative TMA curves of neat PLA and plasticized PLA formulations with increasing DBI content. These TMA curves show different regions. By taking neat PLA as the reference curve, three different regions are detected. At low temperatures (below 50 °C) a linear relationship is noticed. At high temperatures (above 90 °C) a linear relation between the dimensional change and temperature is also evident. The third region is that comprised between 50 – 90 °C, in which the glass transition occurs. Moreover, the shrinkage due to the cold crystallization is overlapped in this temperature range. Due to this overlapping, it is not easy to accurately assess the glass transition temperature from these TMA curves. Usually,  $T_g$  is calculated as the interception between the extrapolation of both linear regions below and above the  $T_g$ , but due to the overlapping of the glass transition process and the cold crystallization, an accurate  $T_g$  value cannot be obtained from these TMA plots. The dimensional stability was measured by calculating the CLTE below and above  $T_g$ . Neat PLA has a CLTE of 58.3  $\mu\text{m}/\text{m}^\circ\text{C}$  which is in agreement with the values reported by Balart *et al.* for neat PLA, around

78  $\mu\text{m}/\text{m}^\circ\text{C}$  [92]. As the DBI content increases, the free volume does so, and this results in increased CLTE up to values of 149.9  $\mu\text{m}/\text{m}^\circ\text{C}$  for the plasticized PLA formulation containing 20 wt.% DBI (Table III.3.1.9).

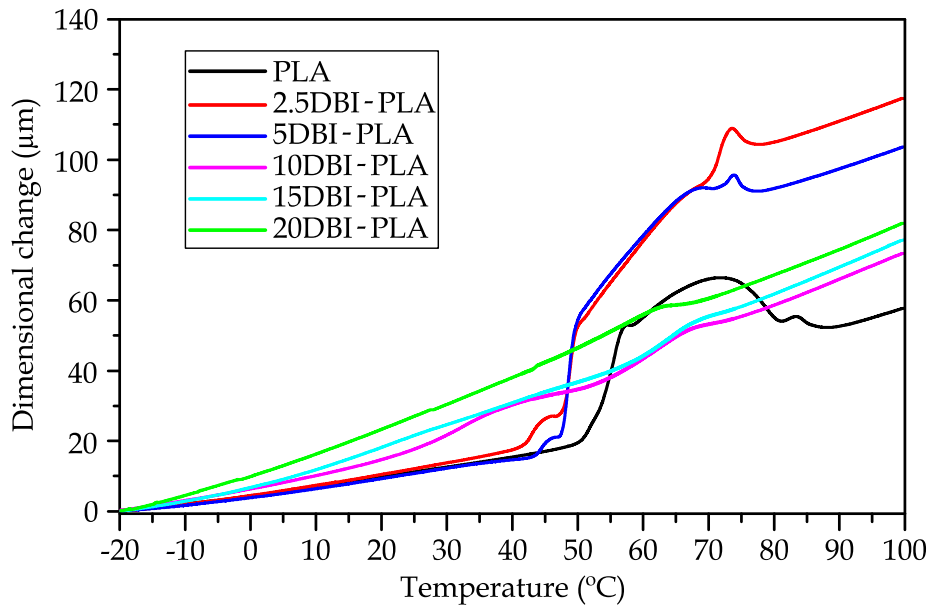


**Figure III.3.1.10.** Comparative plot of dimensional change *vs* temperature obtained by TMA corresponding to neat PLA and plasticized PLA formulations with different DBI contents.

**Table III.3.1.9.** Summary of the TMA results of neat PLA and plasticized PLA formulations with different DBI content.

Code	CLTE - 20 °C to 0 °C ( $\mu\text{m}/\text{m}^\circ\text{C}$ )	CLTE 90 °C to 100 °C ( $\mu\text{m}/\text{m}^\circ\text{C}$ )	Dimensional change ( $\mu\text{m}$ )
PLA	$58.3 \pm 1.3$	$155.7 \pm 2.2$	$57.3 \pm 1.2$
2.5DBI-PLA	$56.7 \pm 0.9$	$180.2 \pm 2.6$	$117.7 \pm 2.7$
5DBI-PLA	$52.3 \pm 1.2$	$168.0 \pm 2.4$	$108.8 \pm 2.6$
10DBI-PLA	$79.6 \pm 1.5$	$201.8 \pm 3.2$	$74.4 \pm 1.8$
15DBI-PLA	$87.3 \pm 2.1$	$209.1 \pm 3.8$	$77.9 \pm 1.4$
20DBI-PLA	$149.9 \pm 2.3$	$202.5 \pm 3.7$	$81.9 \pm 1.5$

The cold crystallization occurs in the 60 – 90 °C. During cold crystallization, PLA chains mobility is increased to give a more packed structure which in turn leads to a shrinkage process which is evidenced by a dimensional contraction. It is important to bear in mind that all samples were obtained by injection moulding with a fast-cooling process which inhibits crystallization. As seen in **Figure III.3.1.10.**, the plasticized PLA formulations with lower  $\chi_c$  are more sensitive to the cold crystallization at moderate temperatures and, subsequently, the observed shrinkage is more intense. Plasticized PLA with a higher amount of DBI did not show a noticeable shrinkage due to the greater ease of crystallization during processing as it has been confirmed by DSC. The ability of PLA to shrink is a common phenomenon; Nasrin *et al.* and Agüero *et al.* reported this

shrinkage during the TMA test on PLA [91,93]. Additionally, Espinach *et al.* observed this phenomenon in PLA composites with leached chemical fibers [94]. Despite  $T_g$  and the cold crystallization are overlapped, the cold crystallization (shrinkage) is observed in the temperature range of 75 to 90 °C. As observed by DSC, by increasing the DBI content the cold crystallization moves to lower temperatures of about 65 °C.

Once the cold crystallization process is finished, the dimensional change follows a linear tendency again and, therefore, it is possible to obtain the CLTE in this region. Below the  $T_g$ , only rotational and vibrational motions of long chains are allowed, while above the  $T_g$ , translational motions of long chains are possible, and these lead to a remarkably higher CLTE of 155.7  $\mu\text{m}/\text{m}^\circ\text{C}$ . In a similar way as below  $T_g$ , as the DBI increases the CLTE also does up to values around 200  $\mu\text{m}/\text{m}^\circ\text{C}$  for plasticized PLA formulations with 10, 15, and 20 wt.%. This trend was also reported by Espinach *et al.* on fiber-reinforced PLA composites [94].

During the injection moulding process, the polymer is progressively cooled inside the mold. This involves that the higher the CLTE value of the material, the more intensely the resulting injection-moulded part will shrink. A constant pressure must be applied in order to avoid the shrinkage of the injection-moulded parts while PLA is still in the melt state, thus avoiding the formation of sink marks [95–97].

### CONCLUSIONS.

DBI has shown high plasticizing efficiency over PLA formulations processed by extrusion and subsequent injection moulding. DBI addition led to a remarkable decrease in viscosity and hence, the temperature profile during injection moulding had to be adjusted to lower temperatures as suggested by capillary rheology characterization, which in turn, prevented the plasticizer from volatilizing. A remarkable increase in ductile properties was achieved with DBI leading to  $\epsilon_b$  of 322 % for 10DBI-PLA sample, which was considerably higher than the  $\epsilon_b$  of neat PLA (4.6 %). Higher DBI content on plasticized PLA formulations did not promote an increase in the elongation at break. In addition, the  $\sigma_t$  and the  $E_t$  were reduced. The  $\sigma_t$  changed from 55.0 MPa (neat PLA) down to values of 23.8 MPa for 10 wt.% DBI which is similar to most commodities. DSC showed two main effects related to DBI addition. On the one hand, a decrease in the  $T_g$  was observed with increasing DBI content from 61.3 °C (neat PLA) to values of 23.4 °C with a DBI content of 20 wt.%. On the other hand, the  $\chi_c$  increased with DBI content, and the cold crystallization process of PLA was moved to lower temperatures. Similar tendency was observed by DMTA. Despite the slight mass loss undergone by DBI during

the processing of plasticized PLA formulations with DBI due to its volatility, the plasticization efficiency is very good compared to other biobased plasticizers such as ATBC and TEC and broadens the potential of bio-derived itaconic acid and its esters as environmentally friendly plasticizers in PLA formulations.

#### **FUNDING.**

This research is a part of the grant PID2020-116496RB-C22 funded by MCIN/AEI/10.13039/501100011033, and the grant AICO/2021/025 funded by Generalitat Valenciana-GVA.

#### **ACKNOWLEDGEMENTS.**

Juan Ivorra-Martinez wants to thank FPU19/01759 grant funded by MCIN/AEI/10.13039/501100011033 and by ESF Investing in your future. Jaume Gomez-Caturla wants to thank Generalitat Valenciana-GVA, for his FPI grant (ACIF/2021/185) and grant FPU20/01732 funded by MCIN/AEI/10.13039/501100011033 and by ESF Investing in your future. Also, Microscopy Services at UPV are also acknowledged by their help in collecting and analysing images.

#### **REFERENCES.**

1. PlasticsEurope. Plastics-the facts 2020: An analysis of European plastics production, demand and waste data. Available online: (accessed on 08/08/2021).
2. Li, D.; Jiang, Y.; Lv, S.; Liu, X.; Gu, J.; Chen, Q.; Zhang, Y. Preparation of plasticized poly(lactic acid) and its influence on the properties of composite materials. *PLoS ONE* **2018**, *13*, 193520-193535 doi: 10.1371/journal.pone.0193520.
3. Argiz, L.; González-Cabaleiro, R.; Val del Río, Á.; González-López, J.; Mosquera-Corral, A. A novel strategy for triacylglycerides and polyhydroxyalkanoates production using waste lipids. *Science of The Total Environment* **2021**, *3*, 33-99 doi: 10.1016/j.scitotenv.2020.142944.
4. Djukić-Vuković, A.; Mladenović, D.; Ivanović, J.; Pejin, J.; Mojović, L. Towards sustainability of lactic acid and poly-lactic acid polymers production. *Renewable Sustainable Energy Reviews* **2019**, *108*, 238-252 doi: 10.1016/j.rser.2019.03.050.

5. Aliotta, L.; Vannozzi, A.; Panariello, L.; Gigante, V.; Coltelli, M.B.; Lazzeri, A. Sustainable micro and nano additives for controlling the migration of a biobased plasticizer from PLA-based flexible films. *Polymers* **2020**, *12*, 1366-1391 doi: 10.3390/POLYM12061366.
6. Wang, Y.; Qin, Y.; Zhang, Y.; Yuan, M.; Li, H.; Yuan, M. Effects of N-octyl lactate as plasticizer on the thermal and functional properties of extruded PLA-based films. *International Journal of Biological Macromolecules* **2014**, *67*, 58-63, doi: 10.1016/j.ijbiomac.2014.02.048.
7. Enumo, A., Jr.; Gross, I.P.; Saatkamp, R.H.; Pires, A.T.N.; Parize, A.L. Evaluation of mechanical, thermal and morphological properties of PLA films plasticized with maleic acid and its propyl ester derivatives. *Polymer Testing* **2020**, *88*, 106552-106561 doi: 10.1016/j.polymertesting.2020.106552.
8. Mihai, M.; Huneault, M.A.; Favis, B.D. Rheology and extrusion foaming of chain-branched poly(lactic acid). *Polymer Engineering & Science* **2010**, *50*, 629-642, doi: 10.1002/pen.21561.
9. Ivorra-Martinez, J.; Selles, M.A.; Sanchez-Caballero, S.; Boronat, T. Design and simulation of a resorbable bone fixation plate made by additive manufacturing for femoral mid-shaft fractures. *Journal of Applied Research in Technology & Engineering* **2021**, *2*, 11-16 doi: 10.4995/jarte.2021.14712.
10. Gálvez, J.; Correa Aguirre, J.P.; Hidalgo Salazar, M.A.; Mondragón, B.V.; Wagner, E.; Caicedo, C. Effect of extrusion screw speed and plasticizer proportions on the rheological, thermal, mechanical, morphological and superficial properties of PLA. *Polymers* **2020**, *12*, 2111-2132 doi: 10.3390/POLYM12092111.
11. Brüster, B.; Adjoua, Y.O.; Dieden, R.; Grysan, P.; Federico, C.E.; Berthé, V.; Addiego, F. Plasticization of polylactide with myrcene and limonene as bio-based plasticizers: conventional *vs.* reactive extrusion. *Polymers* **2019**, *11*, 1663-1684 doi: 10.3390/polym11081363.
12. Chieng, B.W.; Ibrahim, N.A.; Then, Y.Y.; Loo, Y.Y. Epoxidized jatropha oil as a sustainable plasticizer to poly(lactic acid). *Polymers* **2017**, *9*, 204-224 doi: 10.3390/polym9060204.

13. Sritham, E.; Phunsombat, P.; Chaishome, J. Tensile properties of PLA/PBAT blends and PLA fibre-reinforced PBAT composite. *MATEC Web of Conferences* **2018**, *192*, 1-4 doi: 10.1051/mateconf/201819203014.
14. Haneef, I.N.H.M.; Buys, Y.F.; Shaffiar, N.M.; Haris, N.A.; Hamid, A.M.A.; Shaharuddin, S.I.S. Mechanical, morphological, thermal properties and hydrolytic degradation behavior of polylactic acid/polypropylene carbonate blends prepared by solvent casting. *Polymer Engineering & Science* **2020**, *60*, 2876–2886 doi: 10.1002/pen.25519.
15. Fortelny, I.; Ujcic, A.; Fambri, L.; Slouf, M. Phase structure, compatibility, and toughness of PLA/PCL Blends: A Review. *Frontiers in Materials* **2019**, *6*, 1-13 doi: 10.3389/fmats.2019.00206.
16. Wachirahuttapong, S.; Thongpin, C.; Sombatsompop, N. Effect of PCL and compatibility contents on the morphology, crystallization and mechanical properties of PLA/PCL blends. *Energy Procedia* **2016**, *89*, 198-206 doi: 10.1016/j.egypro.2016.05.026.
17. Su, S.; Kopitzky, R.; Tolga, S.; Kabasci, S. Polylactide (PLA) and its blends with poly(butylene succinate) (PBS): a brief review. *Polymers* **2019**, *11*, 1193-1214 doi: 10.3390/polym11071193.
18. Arruda, L.C.; Magaton, M.; Bretas, R.E.S.; Ueki, M.M. Influence of chain extender on mechanical, thermal and morphological properties of blown films of PLA/PBAT blends. *Polymer Testing* **2015**, *43*, 27–37 doi: 10.1016/j.polymertesting.2015.02.005.
19. Przybytek, A.; Sienkiewicz, M.; Kucińska-Lipka, J.; Janik, H. Preparation and characterization of biodegradable and compostable PLA/TPS/ESO compositions. *Industrial Crops and Products* **2018**, *122*, 375–383 doi: 10.1016/j.indcrop.2018.06.016.
20. Koh, J.J.; Zhang, X.; He, C. Fully biodegradable poly(lactic acid)/starch blends: a review of toughening strategies. *International Journal of Biological Macromolecules* **2018**, *109*, 99–113 doi: 10.1016/j.ijbiomac.2017.12.048.

21. Su, S.; Duhme, M.; Kopitzky, R. Uncompatibilized pbat/pla blends: manufacturability, miscibility and properties. *Materials* **2020**, *13*, 1–17 doi: 10.3390/ma13214897.
22. Muthuraj, R.; Misra, M.; Mohanty, A.K. Biodegradable compatibilized polymer blends for packaging applications: a literature review. *Journal of Applied Polymer Science* **2018**, *135*, 45726–45761 doi: 10.1002/app.45726.
23. Ding, Y.; Feng, W.; Huang, D.; Lu, B.; Wang, P.; Wang, G.; Ji, J. Compatibilization of immiscible PLA-based biodegradable polymer blends using amphiphilic di-block copolymers. *European Polymer Journal* **2019**, *118*, 45–52 doi: 10.1016/j.eurpolymj.2019.05.036.
24. Jung, B.N.; Kang, D.H.; Shim, J.K.; Hwang, S.W. Physical and mechanical properties of plasticized butenediol vinyl alcohol copolymer/thermoplastic starch blend. *Journal of Vinyl & Additive Technology* **2019**, *25*, 109–116 doi: 10.1002/vnl.21621.
25. da Silva, J.A.; Dalmolin, C.; Pachekoski, W.M.; Becker, D. The combined effect of plasticizers and graphene on properties of poly(lactic acid). *Journal of Applied Polymer Science* **2018**, *135*, 46745–46758 doi: 10.1002/app.46745.
26. Burgos, N.; Martino, V.P.; Jiménez, A. Characterization and ageing study of poly(lactic acid) films plasticized with oligomeric lactic acid. *Polymer Degradation and Stability* **2013**, *98*, 651–658 doi: 10.1016/j.polymdegradstab.2012.11.009.
27. Darie-Niț, R.N.; Vasile, C.; Irimia, A.; Lipșa, R.; Râpă, M. Evaluation of some eco-friendly plasticizers for PLA films processing. *Journal of Applied Polymer Science* **2016**, *133*, 43223–43234 doi: 10.1002/app.43223.
28. Arrieta, M.P.; López, J.; Ferrándiz, S.; Peltzer, M.A. Characterization of PLA–limonene blends for food packaging applications. *Polymer Testing* **2013**, *32*, 760–768 doi: 10.1016/j.polymertesting.2013.03.016.
29. Jia, P.; Xia, H.; Tang, K.; Zhou, Y. Plasticizers derived from biomass resources: a short review. *Polymers* **2018**, *10*, 1303–1320 doi: 10.3390/polym10121303.



- 
30. Maiza, M.; Benaniba, M.T.; Quintard, G.; Massardier-Nageotte, V. Biobased additive plasticizing polylactic acid (PLA). *Polimeros* **2015**, *25*, 581-590, doi: 10.1590/0104-1428.1986.
  31. Gzyra-Jagięła, K.; Sulak, K.; Draczyński, Z.; Podzimek, S.; Gałęcki, S.; Jagodzińska, S.; Borkowski, D. Modification of poly(lactic acid) by the plasticization for application in the packaging industry. *Polymers* **2021**, *13*, 3651-3669 doi: 10.3390/polym13213651.
  32. Yang, Y.; Xiong, Z.; Zhang, L.; Tang, Z.; Zhang, R.; Zhu, J. Isosorbide dioctoate as a "green" plasticizer for poly(lactic acid). *Materials & Design* **2016**, *91*, 262-268, doi: 10.1016/j.matdes.2015.11.065.
  33. Tee, Y.B.; Talib, R.A.; Abdan, K.; Chin, N.L.; Jönec, R.K.; Yunos, K.F.M. Comparative study of chemical, mechanical, thermal, and barrier properties of poly(lactic acid) plasticized with epoxidized soybean oil and epoxidized palm oil. *BioResources* **2016**, *11*, 1518-1540 doi: 10.15376/BIORES.11.1.1518-1540.
  34. Huang, X.; Chen, M.; Lu, X.; Li, Y.; Li, X.; Li, J.J. Direct production of itaconic acid from liquefied corn starch by genetically engineered *Aspergillus terreus*. *Microbial Cell Factories* **2014**, *13*, 1-10 doi: 10.1186/s12934-014-0108-1.
  35. Ma, Y.; Kou, Z.; Jia, P.; Zhou, J. Effect of benzene ring and alkane chain contained bio-based plasticizers on the plasticizing performance of polyvinyl chloride films. *Chemical Papers* **2021**, *75*, 5515-5521 doi: 10.1007/s11696-021-01629-4.
  36. Wu, Y.; Xie, Q.; Gao, C.; Wang, T.; Wang, C. Synthesis and characterization of a novel aliphatic polyester based on itaconic acid. *Polymer Engineering & Science* **2014**, *54*, 2515-2521 doi: 10.1002/pen.23798.
  37. Gupta, V.K.; Sood, S.; Agarwal, S.; Saini, A.K.; Pathania, D. Antioxidant activity and controlled drug delivery potential of tragacanth gum-cl-poly(lactic acid-co-itaconic acid) hydrogel. *International Journal of Biological Macromolecules* **2018**, *107*, 2534-2543 doi: 10.1016/j.ijbiomac.2017.10.138.

38. Li, W.; Zhang, Z.Q.; Wu, L.J.; Liu, Q.; Cheng, X.D.; Xu, Z.Z. Investigating the relationship between structure of itaconylated starch and its sizing properties: viscosity stability, adhesion and film properties for wool warp sizing. *International Journal of Biological Macromolecules* **2021**, *181*, 291–300 doi: 10.1016/j.ijbiomac.2021.03.143.
39. Zia, K.M.; Noreen, A.; Zuber, M.; Tabasum, S.; Mujahid, M. Recent developments and future prospects on bio-based polyesters derived from renewable resources: a review. *International Journal of Biological Macromolecules* **2016**, *82*, 1028–1040 doi: 10.1016/j.ijbiomac.2015.10.040.
40. Van Krevelen, D.W. Properties of Polymers: Their Correlation with Chemical Structure; their Numerical Estimation and Prediction from Additive Group Contributions, 4 ed.; Elsevier: **2009**; Vol. 1.
41. Abbott, S. Chemical compatibility of poly(lactic acid): a practical framework using Hansen solubility parameters. In *Poly(Lactic Acid): synthesis, structures, properties, processing, and applications*, 1 ed.; Wiley Online Library: **2010**; Vol. 1, pp. 83–95.
42. Ruellan, A.; Guinault, A.; Sollogoub, C.; Ducruet, V.; Domenek, S. Solubility factors as screening tools of biodegradable toughening agents of polylactide. *Journal of Applied Polymer Science* **2015**, *132*, 42476–42487 doi: 10.1002/app.42476.
43. Lascano, D.; Moraga, G.; Ivorra-Martinez, J.; Rojas-Lema, S.; Torres-Giner, S.; Balart, R.; Boronat, T.; Quiles-Carrillo, L. Development of injection-moulded polylactide pieces with high toughness by the addition of lactic acid oligomer and characterization of their shape memory behavior. *Polymers* **2019**, *11*, 2099–2118 doi: 10.3390/polym11122099.
44. Quiles-Carrillo, L.; Montanes, N.; Lagaron, J.M.; Balart, R.; Torres-Giner, S. On the use of acrylated epoxidized soybean oil as a reactive compatibilizer in injection-moulded compostable pieces consisting of polylactide filled with orange peel flour. *Polymer International* **2018**, *67*, 1341–1351 doi: 10.1002/pi.5588.
45. Xuan, W.; Odelius, K.; Hakkarainen, M. Tunable polylactide plasticizer design: rigid stereoisomers. *European Polymer Journal* **2021**, *157*, 110649–110658 doi: 10.1016/j.eurpolymj.2021.110649.

- 
46. Ramos, A.F.; Muñoz, M.; Espinosa, A.; Cabeza, I.O.; Moreno-Sarmiento, N. Evaluation of poly(3-hydroxybutyrate) solubility in non-halogenated solvents to achieve an environmentally friendly recovery process from *Burkholderia cepacia* B27 cells. *Journal of Chemical Technology & Biotechnology* **2020**, *95*, 1657–1665 doi: 10.1002/jctb.6357.
47. Osswald, T.; Rudolph, N. *Polymer rheology*, 1 ed.; Hanser Publisher: **2015**; Vol. 1.
48. Khor, C.Y.; Ariff, Z.M.; Ani, F.C.; Mujeebu, M.A.; Abdullah, M.K.; Abdullah, M.Z.; Joseph, M.A. Three-dimensional numerical and experimental investigations on polymer rheology in meso-scale injection molding. *International Communications Heat Mass Transfer* **2010**, *37*, 131–139 doi: 10.1016/j.icheatmasstransfer.2009.08.011.
49. Yoo, H.M.; Jeong, S.-Y.; Choi, S.-W. Analysis of the rheological property and crystallization behavior of polylactic acid (Ingeo™ Biopolymer 4032D) at different process temperatures. *e-Polymers* **2021**, *21*, 702–709 doi: 10.1515/epoly-2021-0071.
50. Wang, B.; Chen, J.; Peng, H.; Gai, J.; Kang, J.; Cao, Y. Investigation on changes in the miscibility, morphology, rheology and mechanical behavior of melt processed cellulose acetate through adding polyethylene glycol as a plasticizer. *Journal Of Macromolecular Science Part B-Physics* **2016**, *55*, 894–907 doi: 10.1080/00222348.2016.1217185.
51. Sun, Y.; Liu, Z.; Zhang, L.; Wang, X.; Li, L. Effects of plasticizer type and concentration on rheological, physico-mechanical and structural properties of chitosan/zein film. *International Journal of Biological Macromolecules* **2020**, *143*, 334–340 doi: 10.1016/j.ijbiomac.2019.12.035.
52. Bird, E.T.; Bowden, A.E.; Seeley, M.K.; Fullwood, D.T. Materials selection of flexible open-cell foams in energy absorption applications. *Materials & Design* **2018**, *137*, 414–421 doi: 10.1016/j.matdes.2017.10.054.
53. Salih, S.E.; Hamood, A.F.; Abd Alsalam, A.H. Comparison of the characteristics of LDPE: PP and HDPE: PP polymer blends. *Modern Applied Science* **2013**, *7*, 33 doi: 10.5539/mas.v7n3p33.

54. Wypych, G. *Handbook of plasticizers*, 1 ed.; ChemTec Publishing: 2004; Vol. 1.
55. Bocqué, M.; Voirin, C.; Lapinte, V.; Caillol, S.; Robin, J.J. Petro-based and bio-based plasticizers: chemical structures to plasticizing properties. *Journal of Polymer Science, Part A: Polymer Chemistry* **2016**, *54*, 11–33 doi: 10.1002/pola.27917.
56. Bueno-Ferrer, C.; Hablot, E.; Garrigós, M.D.C.; Bocchini, S.; Averous, L.; Jiménez, A. Relationship between morphology, properties and degradation parameters of novative biobased thermoplastic polyurethanes obtained from dimer fatty acids. *Polymer Degradation and Stability* **2012**, *97*, 1964–1969, doi: 10.1016/j.polymdegradstab.2012.03.002.
57. Mohapatra, A.K.; Mohanty, S.; Nayak, S.K. Properties and characterization of biodegradable poly(lactic acid) (PLA)/poly(ethylene glycol) (PEG) and PLA/PEG/organoclay: a study of crystallization kinetics, rheology, and compostability. *Journal of Thermoplastic Composite Materials* **2016**, *29*, 443–463, doi: 10.1177/0892705713518812.
58. Mittal, V.; Akhtar, T.; Matsko, N. Mechanical, thermal, rheological and morphological properties of binary and ternary blends of PLA, TPS and PCL. *Macromolecular Materials and Engineering* **2015**, *300*, 423–435 doi: 10.1002/mame.201400332.
59. Mascia, L.; Kouparitsas, Y.; Nocita, D.; Bao, X. Antiplasticization of polymer materials: structural aspects and effects on mechanical and diffusion-controlled properties. *Polymers* **2020**, *12*, 769–805 doi: 10.3390/POLYM12040769.
60. Ferri, J.M.; Samper, M.D.; García-Sanoguera, D.; Reig, M.J.; Fenollar, O.; Balart, R. Plasticizing effect of biobased epoxidized fatty acid esters on mechanical and thermal properties of poly(lactic acid). *Journal Material Science* **2016**, *51*, 5356–5366 doi: 10.1007/s10853-016-9838-2.
61. Xuan, W.; Hakkarainen, M.; Odelius, K. Levulinic acid as a versatile building block for plasticizer design. *ACS Sustainable Chemistry & Engineering* **2019**, *7*, 12552–12562 doi: 10.1021/acssuschemeng.9b02439.

- 
62. Orue, A.; Eceiza, A.; Arbelaiz, A. Preparation and characterization of poly(lactic acid) plasticized with vegetable oils and reinforced with sisal fibers. *Industrial Crops and Products* **2018**, *112*, 170–180 doi: 10.1016/j.indcrop.2017.11.011.
63. Singh, A.A.; Sharma, S.; Srivastava, M.; Majumdar, A. Modulating the properties of polylactic acid for packaging applications using biobased plasticizers and naturally obtained fillers. *International Journal of Biological Macromolecules* **2020**, *153*, 1165–1175 doi: 10.1016/j.ijbiomac.2019.10.246.
64. Tian, H.; Liu, D.; Yao, Y.; Ma, S.; Zhang, X.; Xiang, A. Effect of sorbitol plasticizer on the structure and properties of melt processed polyvinyl alcohol films. *Journal of Food Science* **2017**, *82*, 2926–2932 doi: 10.1111/1750-3841.13950.
65. Unterweger, C.; Brüggemann, O.; Fürst, C. Synthetic fibers and thermoplastic short-fiber-reinforced polymers: properties and characterization. *Polymer Composites* **2014**, *35*, 227–236 doi: 10.1002/pc.22654.
66. Chieng, B.W.; Ibrahim, N.A.; Then, Y.Y.; Loo, Y.Y. Mechanical, thermal, and morphology properties of poly(lactic acid) plasticized with poly(ethylene glycol) and epoxidized palm oil hybrid plasticizer. *Polymer Engineering & Science* **2016**, *56*, 1169–1174 doi: 10.1002/pen.24350.
67. Bouti, M.; Irinislmane, R.; Belhaneche-Bensemra, N. Properties investigation of epoxidized sunflower oil as bioplasticizer for poly(lactic acid). *Journal of Polymers and the Environment* **2021**, 1–14 doi: 10.1007/s10924-021-02194-3.
68. Lin, L.; Deng, C.; Lin, G.-P.; Wang, Y.-Z. Super toughened and high heat-resistant poly(Lactic Acid) (PLA)-based blends by enhancing interfacial bonding and PLA phase crystallization. *Industrial & Engineering Chemistry Research* **2015**, *54*, 5643–5655 doi: 10.1021/acs.iecr.5b01177.
69. Li, F.-J.; Zhang, S.-D.; Liang, J.-Z.; Wang, J.-Z. Effect of polyethylene glycol on the crystallization and impact properties of polylactide-based blends. *Polymers for Advanced Technologies* **2015**, *26*, 465–475 doi: 10.1002/pat.3475.

70. Fenollar, O.; Garcia-Sanoguera, D.; Sanchez-Nacher, L.; Lopez, J.; Balart, R. Effect of the epoxidized linseed oil concentration as natural plasticizer in vinyl plastisols. *Journal Material Science* **2010**, *45*, 4406–4413, doi: 10.1007/s10853-010-4520-6.
71. Zuber, S.A.N.A.; Rusli, A.; Ismail, H. Effectiveness of triacetin and triethyl citrate as plasticizer in polyvinyl alcohol. *Proceedings of the 6th International Conference on Recent Advances in Materials, Minerals and Environment, RAMM 2018* **2019**; *17*, 560–567 doi: 10.1016/j.matpr.2019.06.335.
72. Rojas-Lema, S.; Ivorra-Martinez, J.; Gomez-Caturla, J.; Balart, R.; Garcia-Garcia, D. Manufacturing and compatibilization of binary blends of polyethylene and poly(butylene succinate) by injection molding. *Journal of Applied Research in Technology & Engineering* **2021**, *2*, 71-78 doi: 10.4995/jarte.2021.15727.
73. Celebi, H.; Gunes, E. Combined effect of a plasticizer and carvacrol and thymol on the mechanical, thermal, morphological properties of poly(lactic acid). *Journal of Applied Polymer Science* **2018**, *135*, 45895-45904 doi: 10.1002/app.45895.
74. Iglesias Montes, M.L.; Cyras, V.P.; Manfredi, L.B.; Pettarín, V.; Fasce, L.A. Fracture evaluation of plasticized polylactic acid / poly(3-hydroxybutyrate) blends for commodities replacement in packaging applications. *Polymer Testing* **2020**, *84*, 106375-106386 doi: 10.1016/j.polymertesting.2020.106375.
75. Altenhofen da Silva, M.; Adeodato Vieira, M.G.; Gomes Maçumoto, A.C.; Beppu, M.M. Polyvinylchloride (PVC) and natural rubber films plasticized with a natural polymeric plasticizer obtained through polyesterification of rice fatty acid. *Polymer Testing* **2011**, *30*, 478–484 doi: 10.1016/j.polymertesting.2011.03.008.
76. Van Der Sman, R.G.M. Predictions of glass transition temperature for hydrogen bonding biomaterials. *The Journal of Physical Chemistry B* **2013**, *117*, 16303–16313 doi: 10.1021/jp408184u.
77. Gumus, S.; Ozkoc, G.; Aytac, A. Plasticized and unplasticized PLA/organoclay nanocomposites: short- and long-term thermal properties, morphology, and nonisothermal crystallization behavior. *Journal of Applied Polymer Science* **2012**, *123*, 2837–2848 doi: 10.1002/app.34841.

- 
78. Mangeon, C.; Michely, L.; Rios de Anda, A.; Thevenieau, F.; Renard, E.; Langlois, V. Natural terpenes used as plasticizers for poly(3-hydroxybutyrate). *ACS Sustainable Chemistry & Engineering* **2018**, *6*, 16160–16168 doi: 10.1021/acssuschemeng.8b02896.
79. Harte, I.; Birkinshaw, C.; Jones, E.; Kennedy, J.; Debarra, E. The effect of citrate ester plasticizers on the thermal and mechanical properties of poly(DL-lactide). *Journal of Applied Polymer Science* **2013**, *127*, 1997–2003 doi: 10.1002/app.37600.
80. Muller, J.; González-Martínez, C.; Chiralt, A. Poly(lactic) acid (PLA) and starch bilayer films, containing cinnamaldehyde, obtained by compression moulding. *European Polymer Journal* **2017**, *95*, 56–70 doi: 10.1016/j.eurpolymj.2017.07.019.
81. Choi, K.M.; Choi, M.C.; Han, D.H.; Park, T.S.; Ha, C.S. Plasticization of poly(lactic acid) (PLA) through chemical grafting of poly(ethylene glycol) (PEG) via in situ reactive blending. *European Polymer Journal* **2013**, *49*, 2356–2364 doi: 10.1016/j.eurpolymj.2013.05.027.
82. Ferri, J.M.; Garcia-Garcia, D.; Montanes, N.; Fenollar, O.; Balart, R. The effect of maleinized linseed oil as biobased plasticizer in poly(lactic acid)-based formulations. *Polymer International* **2017**, *66*, 882–891 doi: 10.1002/pi.5329.
83. Hassouna, F.; Raquez, J.M.; Addiego, F.; Dubois, P.; Toniazzo, V.; Ruch, D. New approach on the development of plasticized polylactide (PLA): grafting of poly(ethylene glycol) (PEG) via reactive extrusion. *European Polymer Journal* **2011**, *47*, 2134–2144 doi: 10.1016/j.eurpolymj.2011.08.001.
84. Richard, J.V.; Delaite, C.; Riess, G.; Schuller, A.S. A comparative study of the thermal properties of homologous series of crystallisable n-alkyl maleate and itaconate monoesters. *Thermochimica Acta* **2016**, *623*, 136–143 doi: 10.1016/j.tca.2015.10.015.
85. Arrieta, M.P.; Samper, M.D.; Lopez, J.; Jimenez, A. Combined effect of poly(3-hydroxybutyrate) and plasticizers on polylactic acid properties for film intended for food packaging. *Journal of Polymers and the Environment* **2014**, *22*, 460–470 doi: 10.1007/s10924-014-0654-y.

86. Sessini, V.; Palenzuela, M.; Damián, J.; Mosquera, M.E.G. Bio-based polyether from limonene oxide catalytic ROP as green polymeric plasticizer for PLA. *Polymer* **2020**, *210*, 123003-123010 doi: 10.1016/j.polymer.2020.123003.
87. Battezzore, D.; Bocchini, S.; Alongi, J.; Frache, A. Rice husk as bio-source of silica: preparation and characterization of PLA-silica bio-composites. *RSC Advances* **2014**, *4*, 54703-54712 doi: 10.1039/c4ra05991c.
88. de Araújo, J.P.; Silva, R.C.; Lima, J.C.C.; Agrawal, P.; de Mélo, T.J.A. Mechanical and thermal behavior of PLA/PEgAA blends. *Macromolecular Symposia* **2016**, *367*, 82-89 doi: 10.1002/masy.201500140.
89. Cristea, M.; Ionita, D.; Iftime, M.M. Dynamic mechanical analysis investigations of PLA-based renewable materials: how are they useful? *Materials* **2020**, *13*, 5302-5323 doi: 10.3390/ma13225302.
90. Shirai, M.A.; Müller, C.M.O.; Grossmann, M.V.E.; Yamashita, F. Adipate and citrate esters as plasticizers for poly(lactic acid)/thermoplastic starch sheets. *Journal of Polymers and the Environment* **2015**, *23*, 54-61 doi: 10.1007/s10924-014-0680-9.
91. Agüero, A.; Morcillo, M.C.; Quiles-Carrillo, L.; Balart, R.; Boronat, T.; Lascano, D.; Torres-Giner, S.; Fenollar, O. Study of the influence of the reprocessing cycles on the final properties of polylactide pieces obtained by injection molding. *Polymers* **2019**, *11*, 1908-1929 doi: 10.3390/polym11121908.
92. Balart, J.F.; García-Sanoguera, D.; Balart, R.; Boronat, T.; Sánchez-Nacher, L. Manufacturing and properties of biobased thermoplastic composites from poly(lactic acid) and hazelnut shell wastes. *Polymer Composites* **2018**, *39*, 848-857 doi: 10.1002/pc.24007.
93. Nasrin, R.; Biswas, S.; Rashid, T.U.; Afrin, S.; Jahan, R.A.; Haque, P.; Rahman, M.M. Preparation of chitin-PLA laminated composite for implantable application. *Bioactive Materials* **2017**, *2*, 199-207 doi: 10.1016/j.bioactmat.2017.09.003.



94. Espinach, F.X.; Boufi, S.; Delgado-Aguilar, M.; Julián, F.; Mutjé, P.; Méndez, J.A. Composites from poly(lactic acid) and bleached chemical fibres: thermal properties. *Composites Part B: Engineering* **2018**, *134*, 169-176 doi: 10.1016/j.compositesb.2017.09.055.
95. Rosato, D.V.; Rosato, M.G. *Injection molding handbook*, 3 ed.; Springer Science & Business Media: **2012**; Vol. 1.
96. Panchal, R.R.; Kazmer, D.O. In-situ shrinkage sensor for injection molding. *Journal of Manufacturing Science & Engineering* **2010**, *132*, 64503-64509 doi: 10.1115/1.4002765.
97. Sun, X.; Tibbenham, P.; Zeng, D.; Su, X.; Huang, S.; Kang, H.T. Procedure development for predicting the sink mark of injection moulded thermoplastics by finite element method. *International Journal of Advanced Manufacturing* **2019**, *103*, 4095-4107 doi: 10.1007/s00170-019-03687-1.



Adapted from the original manuscript.

### III.3.2 Effect of infill parameters on mechanical properties in additive manufacturing.

Juan Ivorra-Martinez<sup>1</sup>, Luis Quiles-Carrillo<sup>1</sup>, Diego Lascano<sup>1</sup>, Santiago Ferrandiz<sup>1</sup>, Teodomiro Boronat<sup>1</sup>.

<sup>1</sup>Technological Institute of Materials - ITM, Universitat Politècnica de València - UPV, Plaza Ferrándiz y Carbonell 1, 03801 Alcoy (Spain).



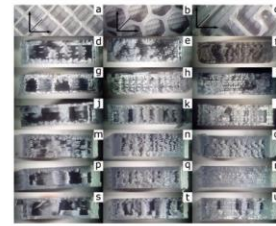
Dyna-Ingeniería e Industria.

2020, 95(4): 412.



# Effect of infill parameters on mechanical properties in additive manufacturing

## Efecto de los parámetros del relleno sobre las propiedades mecánicas en fabricación aditiva



Juan Ivorra-Martínez, Luis Quiles-Carrillo, Diego Lascano, Santiago Ferrandiz and Teodomiro Boronat  
Universitat Politècnica de València. Materials Technology Institute. Plaza Ferrándiz y Carbonell, s/n – 03801 Alcoy (Spain)

DOI: <http://dx.doi.org/10.6036/9674> | Recibido: 17/02/2020 • Inicio Evaluación: 04/12/2019 • Aceptado: 18/03/2020

### RESUMEN

- El propósito de este trabajo es estudiar y esbozar los efectos de los parámetros del relleno (porcentaje y patrón) de la fabricación por deposición fundida sobre las propiedades mecánicas de probetas de PLA. Se han analizado tres patrones de relleno (rectilíneo, panal de abeja y curva Hilbert), y tres porcentajes de relleno distintos (20, 60 y 90 por ciento). Las propiedades examinadas fueron resistencia a la tracción, módulo de tracción, alargamiento, tenacidad utilizando ensayo Charpy, morfología de las fracturas de los ensayos de tracción e impacto y análisis termomecánico. Además, se realizó un análisis térmico utilizando calorimetría diferencial de barrido al polímero virgen para determinar la temperatura de procesamiento. Los resultados mostraron la influencia de los parámetros de llenado en la impresión 3D sobre las propiedades mecánicas de la pieza obtenida. El patrón de llenado influye en gran medida en las propiedades mecánicas de las piezas con bajos porcentajes de relleno. El patrón de relleno de panal de abeja es el que tiene mejores resultados mecánicos de los tres analizados. La geometría del patrón de relleno también influye sobre el tiempo de procesado. Los cambios de dirección de las boquillas en patrones complejos alargan el tiempo de procesamiento. Los resultados obtenidos pueden influir significativamente en el diseño y la fabricación de piezas a medida mediante el modelado de la deposición de material fundido.
- Palabras clave:** Fabricación aditiva, modelado de deposición en fundido, porcentaje de relleno, patrón de relleno, PLA.

### ABSTRACT

The purpose of this paper is to study and outline the effects of infill parameters (percentage and pattern) using fused deposition manufacturing on mechanical properties of PLA printed samples. Three infill patterns were tested (rectilinear, honeycomb and Hilbert curve) while infill percentage was tested at three levels (20, 60 and 90 per cent). The properties examined were tensile strength, tensile modulus, elongation, Charpy impact test, morphology of the fractures of tensile and impact test and thermo mechanical analysis. Also, a thermal analysis was done using differential scanning calorimetry to the raw polymer in order to determine the processing temperature. Results showed the influence of the filling parameters in 3D printing on the mechanical properties of the obtained part. The filling pattern greatly influences the mechanical

properties of parts with low filling percentages. Honeycomb filling pattern is the one with better mechanical results. The complexity of the filling pattern influences on the processing time. Nozzle direction changes in complex patterns lengthening processing time. Results can significantly influence custom design and manufacturing of parts using material fused deposition modeling.

**Keywords:** Additive manufacturing, fused deposition modeling, infill percentage, infill pattern, PLA.

### 1. INTRODUCTION

Additive Manufacturing (AM), also known as 3D printing, has attracted attention for the manufacture of solids free form manufacturing (SFF) systems with increased competitiveness. The most common technique of AM is Fused Deposition Modelling (FDM), in which a thermoplastic material is heated to a semi-fused state and then extruded as an ultrafine filament, layer by layer, to construct a three-dimensional object following the trajectories defined in a computer-aided design data file.

Initially this technique provided designers with a tool to quickly generate an initial prototype of their ideas as 3D printing greatly simplifies prototype production regardless of mechanical properties, only appearance mattered [1, 2]. AM allows to reduce design and manufacturing processes from weeks to a few hours, allowing to innovate on the fly [3, 4]. In this way, efficiency can be increased, and production costs reduced in the manufacturing sector [5, 6].

But now any application can be tackled, the FDM process has been recognized as a reliable and an economical technique to be used in a large number of applications in various fields. Personalization of FDM manufactured parts has allowed the biomedical area to benefit from this processing technique, these include the manufacture of orthoprosthesis devices [7], dentistry [8], scaffolds [9], even parts as sensitive as cardiovascular stents [10]. Parts obtained by AM can also be used for practical applications, in which case they must withstand various amounts of mechanical and environmental stresses during its use. Therefore, it is important to know the required loading conditions and the physical properties of AM manufactured parts should be similar to those obtained by traditional processes such as injection [11, 12].

The quality and mechanical properties of a product manufactured by FDM depend on a large number of parameters whose combination is complex to understand [13, 14]. These parameters that influence the mechanical performance and quality of the parts obtained by FDM can be very diverse, such as the layer thick-



**Abstract.**

The purpose of this paper is to study and outline the effects of infill parameters (percentage and pattern) using Fused Deposition Modelling – FDM on mechanical properties of poly(lactic acid) – PLA printed samples. Three infill patterns were tested (rectilinear, honeycomb and Hilbert curve) while infill percentage was tested at three levels (20, 60 and 90 per cent). The properties examined were tensile strength, tensile modulus, elongation, Charpy impact test, morphology of the fractures of tensile and impact test and thermo–mechanical analysis. Also, a thermal analysis was done using Differential Scanning Calorimetry – DSC to the raw polymer in order to determine the processing temperature. Results showed the influence of the filling parameters in 3D printing on the mechanical properties of the obtained part. The filling pattern greatly influences the mechanical properties of parts with low filling percentages. Honeycomb filling pattern is the one with better mechanical results. The complexity of the filling pattern influences on the processing time. Nozzle direction changes in complex patterns lengthen processing time. Results can significantly influence custom design and manufacturing of parts using material fused deposition modelling.

**Keywords:** Additive Manufacturing – AM; Fused Deposition Modelling – FDM; infill percentage; infill pattern; poly(lactic acid) – PLA.

---





## INTRODUCTION.

Additive Manufacturing - AM, also known as 3D printing, has attracted attention for the manufacture of Solids Free Form - SFF systems with increased competitiveness. The most common technique of AM is Fused Deposition Modelling - FDM, in which a thermoplastic or an amorphous polymer is heated to a molten state or above its glass transition temperature and then extruded through a nozzle to be deposited layer by layer to construct a 3D object following the trajectories defined in a Computer Aided Design - CAD data file.

Initially this technique provided designers with a tool to quickly generate an initial prototype of their ideas as 3D printing greatly simplifies prototype production regardless of mechanical properties, only appearance mattered [1,2]. AM allows to reduce design and manufacturing processes from weeks to a few hours [3,4]. In this way, efficiency can be increased, and production costs reduced in the manufacturing sector [5,6].

But now any application can be tackled, the FDM process has been recognized as a reliable and an economical technique to be used in a large number of applications in various fields. Personalization of FDM manufactured parts has allowed the biomedical area to benefit from this processing technique, these include the manufacture of orthoprosthesis devices [7], dentistry [8], scaffolds [9], even parts as sensitive as cardiovascular stents [10]. Parts obtained by AM can also be used for practical applications, in which case they must withstand various amounts of mechanical and environmental stresses during its use. Therefore, it is important to know the required loading conditions and the physical properties of AM manufactured parts should be similar to those obtained by traditional processes such as injection [11,12].

The quality and mechanical properties of a product manufactured by FDM depend on a large number of parameters whose combination is complex to understand [13, 14]. These parameters that influence the mechanical performance and quality of the parts obtained by FDM can be very diverse, such as the layer thickness, raster angle, air gap, build orientation, feed rate and the filling pattern, among others [14, 15]. The effect on the mechanical properties of the slice thickness and the deposition velocity was analysed [16]. Other investigations confirm that the properties are highly influenced by the process parameters such as the study of the deposition velocity in terms of raster width on the mechanical performance of the parts [17]. Recent studies show that the modelling direction also plays a significant role in the mechanical properties as several

authors pointed [18, 19]. The infill density or air gap between the adjacent filaments also plays an important role in mechanical characteristics since the change would affect the bounding degree between two fibers which affects the tensile strength of the product [20]. The importance of filling density was also pointed out by other authors [21,22], since the parts with higher infill levels have more material and resist stress better. The infill rate shows high influence on the ultimate shear strength compared with other parameters. Its influence is nearly twice the one done by thickness and four times more than heat treatment [21]. Therefore it is necessary to determine the influence of the processing parameters on the mechanical behavior since it is crucial for functional parts [23] and a further investigation on the effect of other printing parameters, such as the type of infill and its density, as bibliography related to this topic is somewhat scarce. The studies of mechanical characteristics of parts obtained by FDM have been especially focused when ABS material has been used [11,24,25] while the PLA material used in this study has not been extensively analysed [9,24,26].

The present paper studies on the production process of FDM samples, in the study the effects of the manufacturing parameters are analysed (infill percentage and pattern) on the mechanical and thermo-mechanical properties of the produced specimens. Several researchers have worked on the effects either of the infill percentage and print orientation, this paper focuses on the infill density and the pattern on a wide range of properties such us mechanical properties, fracture morphology, dynamical-mechanical behavior and thermal properties.

#### **MATERIALS AND METHODS.**

##### **Materials.**

A PLA coil provided by BCN3D (Barcelona, Spain) has been used as raw material for this work, the material characteristics are shown in **Table III.3.2.1**. Prior to the manufacture the samples, the filaments were dried at 60 °C for 24 h in oven in order to remove moisture from the surrounding environment. Drying procedure was also applied before mechanical testing in order to prevent inconsistent results among the specimens.

**Table III.3.2.1.** Main commercial PLA employed to the manufacture of the samples.

Form of supply	Coil
Weight of coil	750 g
Diameter	2.85 mm
Maximum roundness deviation	0.03 mm
Density	1.24 g/cm <sup>3</sup>
Processing temperature range	190 - 220 °C

**Thermal characterization.**

Differential Scanning Calorimetry - DSC in a Mettler-Toledo DSC mod. 821 (Schwerzenbach, Switzerland) technique was employed to determine glass transition temperature -  $T_g$  and melting temperature -  $T_m$  values for the PLA in order to evaluate the extruder temperature range suggested by the provider (190 - 220 °C). The used samples had a weight in the 5 - 7 mg range. The thermal transitions were evaluated in a nitrogen atmosphere with a flow rate of 66 mL/min using a dynamic temperature program according the following sequence:

1<sup>st</sup> - Heating cycle from 30 °C to 200 °C at 10 °C/min

2<sup>nd</sup> - Cooling cycle from 200 °C to 0 °C at - 10 °C/min

3<sup>rd</sup> - Heating cycle from 0 °C to 350 °C at 10 °C/min

**Sample modelling.**

The PLA filaments were fed into a commercial FDM desktop printer model Sigmax supplied by BCN3D (Barcelona, Spain) which extrudes the material through a 0.4 mm nozzle onto a heated glass bed. The parameters applied during the FDM process are numerous and they may affect the properties and the print quality of the printed samples [27]. Thus, the printing parameters applied in the present work (**Table III.3.2.2.**) were kept constant for all the printed samples.

**Table III.3.2.2.** FDM parameters employed for the sample manufacture.

Nozzle temperature	210 °C
Bed temperature	40 °C
First layer height	0.3 mm
Layer height	0.1 mm
Shell thickness	1.2 mm
Printing speed	35 mm/s
Outline underspeed	20 mm/s

FreeCAD software [28], facilitated the development of the CAD data of the specimens. Then, Slic3r software [29] was used to slice the model in layers and generate a numerical control program based in G-code, Slic3r was chosen because it provides many customization options for infill patterns in comparison to other software. The specimens were simulated in Repetier-Host software [30] before printing.

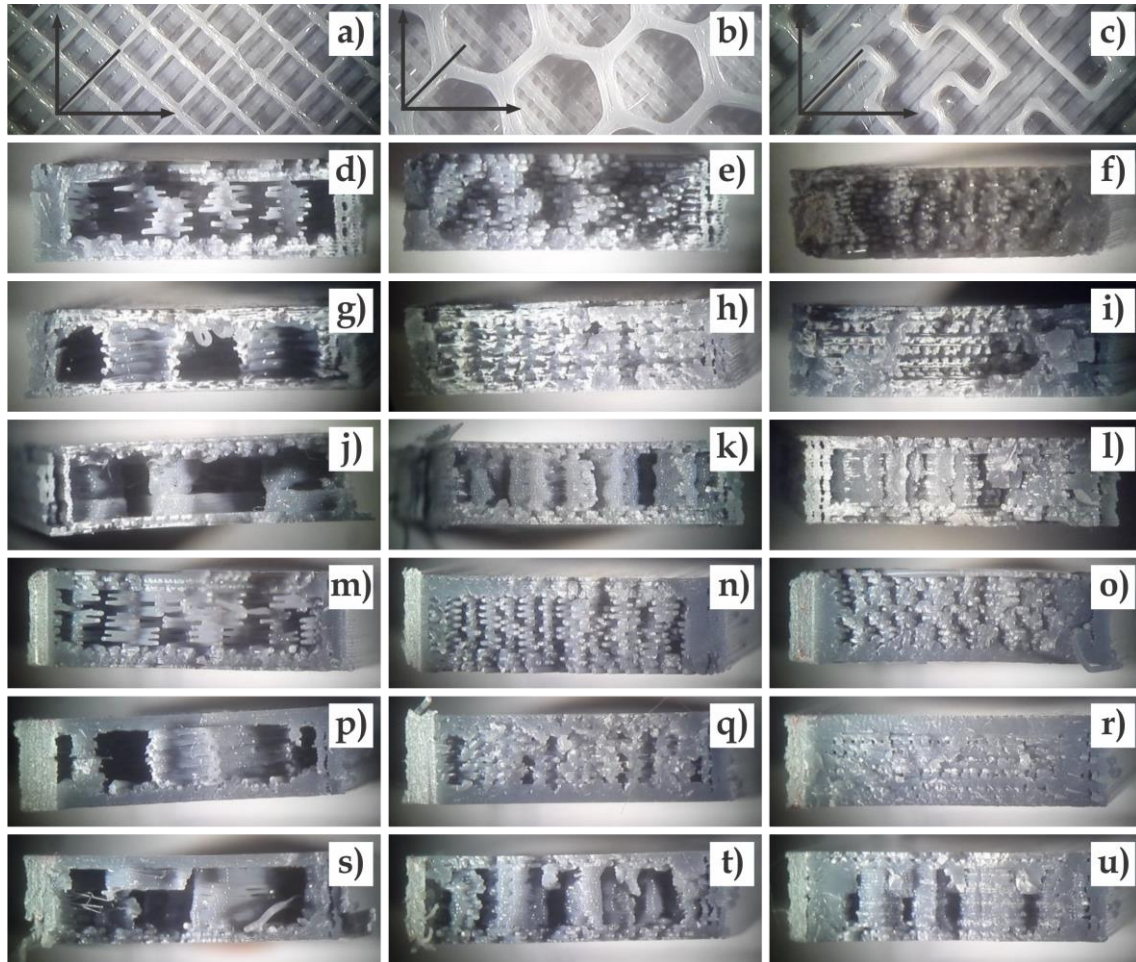


**Figure III.3.2.1.** Optical (8 ×) images. Images from a) to c) show a detail of the infill pattern: a) rectilinear 20 %, b) honeycomb and c) Hilbert 20 %. Images from d) to l) show a detail of fractured tensile test samples: d) rectilinear 20 %, e) rectilinear 60 %, f) rectilinear 90 %, g) honeycomb 20 %, h) honeycomb 60 %, i) honeycomb 90 %, j) Hilbert 20 %, k) Hilbert 60 % and l) Hilbert 90 %. Images from m) to u) show a detail of impact test samples: m) rectilinear 20 %, n) rectilinear 60 %, o) rectilinear 90 %, p) honeycomb 20 %, q) honeycomb 60 %, r) honeycomb 90 %, s) Hilbert 20 %, t) Hilbert 60 % and u) Hilbert 90 %.

The specimens were printed with three different filling patterns of the most common in 3D printing, rectilinear, honeycomb and Hilbert curve. The infill percentage also was varied in order to outline its effect on mechanical properties. The specimens were printed with infills percentages of 20, 60 and 90 %. However, rectilinear pattern

was used for the outer surface of all the printed samples. The test specimens to be printed are rectangular shaped with dimensions of  $78.5 \times 18 \times 5 \text{ mm}^3$ . **Figure III.3.2.1.** shows the three different infill patterns of the studied samples with 20 % infill percentage and at the bottom of all of them the straight pattern of the outer face can be seen. The specimens have a rectilinear pattern on the outer surface that does not allow observation of the inside of the piece. So, the printing process was stopped once a layer of infill had been laid in order to observe the morphology of the infill (**Figure III.3.2.1.**). It should be noted that the three patterns studied present a priority orientation at  $45^\circ$  from the main axes that would be located at the edges of the specimen.

### **Mechanical characterization.**

At the moment, the specific mechanical characterization of polymer parts manufactured by AM is not yet standardized [31–33], so test were done using standard characterization procedures. The tensile tests were performed using a universal test machine Ibertest ELIB 30 [34] which is equipped with a 5 kN load cell. In order to minimize the randomness of the results at least five different samples were tested, and the most relevant properties were averaged. A constant crosshead speed of 5 mm/min was applied in the tensile tests in order to obtain the tensile modulus, tensile strength and the elongation at break. The impact strength was obtained using a 1 J Charpy's pendulum supplied by Metrotec (San Sebastian, Spain) on 3D printed samples. Dynamic-Mechanical Thermal Analysis - DMTA tests were conducted using AR-G2 oscillatory rheometer Supplied by TA Instruments (New Castle, DE, USA) equipped with a special clamp system for solid samples which works in a combined shear-torsion mode. The samples used in the DMTA tests were scaled to 50 % compared to those used in the previous tests. They were subjected to a temperature sweep from  $30^\circ\text{C}$  to  $140^\circ\text{C}$  at  $2^\circ\text{C}/\text{min}$  under a maximum deformation of 0.1 %. Both the storage modulus -  $G'$  and the dynamic damping factor -  $\tan \delta$  were collected using a frequency of 1 Hz.

### **Optical microscopy.**

In order to obtain enlarged images of the test specimen after break in the tensile and Charpy tests, an Olympus SZX7 microscope supplied by Olympus Spain, S.A.U. (Barcelona, Spain) with a magnification range of  $0.8 \times$  to  $5.6 \times$  was used, which is multiplied by the  $10 \times$  eyepiece magnification. The microscope is equipped with a lighting equipment Olympus model KL 1500 LCD. An Olympus C-5060 wide zoom digital SLR camera was attached to the top of the magnifying glass to capture the images.

## RESULTS.

Prior to manufacture all the studied samples, the raw material was thermally characterized employing DSC technique in order to analyse both the suitability of the proposed material and the range of temperatures proposed by the supplier. **Figure III.3.2.2.** shows the DSC program for raw PLA for the third step of the proposed sequence, since the first two were to eliminate the thermal history of the sample. A step is observed in the baseline at about 60 – 70 °C which corresponds to the  $T_g$ . The value of the  $T_g$  is determined taking the inflexion point, obtaining a value of 63.3 °C. At 105.6 °C, the DSC curve presents an exothermic peak related to the reordering of the polymer chain produced by the cold crystallization process. There is another peak at 170.3 °C, but in this case, it is endothermic, it corresponds to the  $T_m$  of PLA. Then, from 328.8 °C there is an abrupt endothermic fall that indicates the degradation of PLA. Thus, the thermal analysis indicates that the extruder temperature range suggested by the provider (190 – 220 °C) is suitable to manufacture the planned samples since it is between the melting and the degradation and therefore it ensures that the PLA will be in molten state.

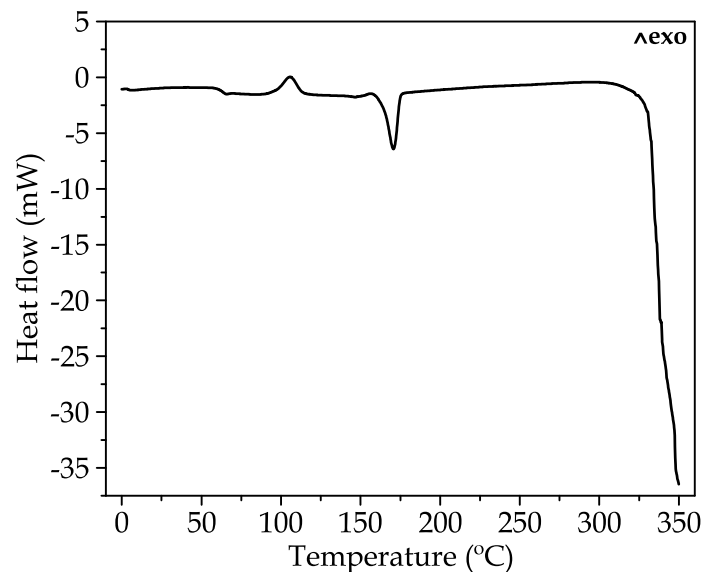


**Figure III.3.2.2.** DSC thermograms for raw PLA from 0 °C up to 350 °C.

The average weight of the 9 different types of specimens is shown in **Figure III.3.2.3.** It is observed that there are weight differences between the different patterns studied for the same infill percentage, these differences are more pronounced when the percentages are lower and decrease as the filling increases. The honeycomb pattern has the highest weight for all concentrations. For the concentrations of 20 % and 60 % honeycomb pattern is followed by the rectilinear pattern and the Hilbert pattern is in last position, however for the 90 % filling percentage the Hilbert pattern presents

values closer to the honeycomb pattern. The Hilbert pattern shows a linear increase in weight as the percentage of filling increases. This is not the case for the other two patterns. The increase between the 60 % and 90 % filling percentages is less sloped than when it increases between 20 % and 60 %. This is due to the geometry of the patterns.

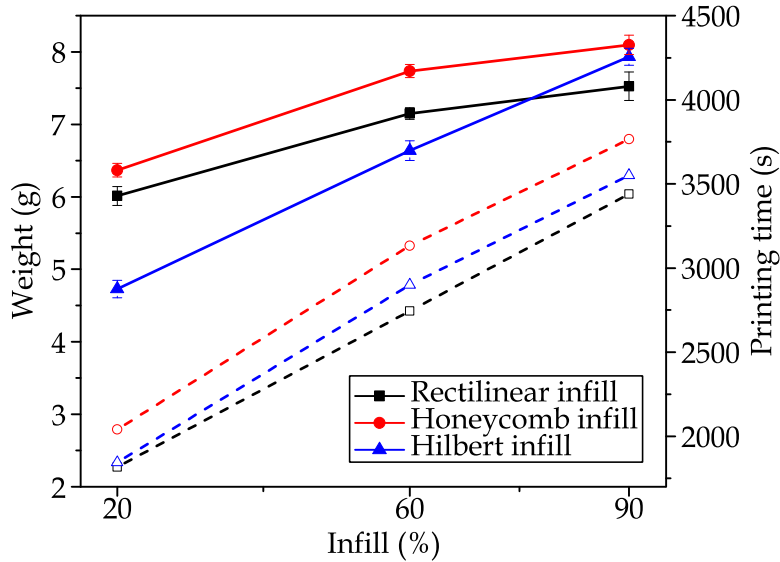


**Figure III.3.2.3.** Plot evolution of weight and printing time for different filling patterns as function of their infill percentage. Continuous line indicates the sample weight, while dashed line the printing time.

**Figure III.3.2.3.** also depicts the printing times for the studied samples, these processing times represented were obtained from Repetier-Host simulation software. The evolution of the processing time as function of the infill percentage for all the patterns is almost linear with a gradual increase of time as infill percentage rises. As infill percentage varies from 20 % to 60 % the processing time increases by 55 %, and if it varies to 90 % the time increases by 40 % more. The processing time is more dependent on the pattern used than on the amount of material used in printing. The pattern with the simplest geometry, the rectilinear one, is the one that has the lowest processing times for all the infill percentages, even though it is not the one with the least mass. This is due to the fact that the print head only moves in a straight line and does not make direction changes that lengthen the time. Therefore, the rectilinear pattern is the most recommended from a point of view of time efficiency. On the other hand, the honeycomb pattern is the one that spends the most time due to its hexagonal geometry.

The tensile modulus and strength values obtained in the tensile test are depicted in **Figure III.3.2.4.** As aforementioned, the investigated values were three different filling patterns and three different levels of infill percentage (20 %, 60 % and 90 %). Analysing the results, it can be seen that some trends have been developed when studied

parameters are varied. At every filling pattern, the tensile modulus always increased with the growth in the infill percentage which indicates that increasing the infill percentage raises the rigidity of the parts. There is a direct relationship between this resistant characteristic and the part weight since the curves present the same tendencies. The honeycomb pattern is the one with the highest values of tensile modulus, except for fillings of 90 % that are slightly surpassed by the rectilinear pattern. For infill percentages of 20 % there is a difference of 224.6 MPa between the highest value of tensile modulus (honeycomb) and the lowest value (Hilbert). In contrast, for fillings of 90 % the difference between the extreme values is reduced to 69.1 MPa. That is, the difference between the extreme values of tensile modulus decreases as the fill percentage increases. This indicates that the filling pattern is very important on the tensile modulus for low infill values, but its influence is diluted by increasing the percentage of infill. The variation of the infill percentage from 20 % to 90 % causes the value of the tensile modulus to increase by approximately 200 % for the Hilbert pattern, while for the rectilinear pattern it is 60 % and for the honeycomb in a 18 %.

**Figure III.3.2.4.** also shows the evolution of the tensile strength values of the tested specimens. For tensile strength an increasing tendency is observed with the increase of infill as it happened with the tensile modulus. It is observed that the infill pattern also influences the values of tensile strength. Honeycomb remains as the pattern with the best mechanical results for all filling levels and the rectilinear shows the lowest values. The tensile modulus for the honeycomb pattern for the different infill percentages studied increases very slightly. By increasing the percentage of filling from 60 % to 90 %, the increase in tensile modulus is practically negligible (7.3 MPa), which indicates that as the percentage of infill increases, the tensile modulus tends to stabilize. Therefore, if the parameter of interest is the tensile modulus, the honeycomb pattern should be chosen with low infill percentages in order to save material. The tensile strength shows a slight increasing trend for the three patterns studied, with the best values being the honeycomb pattern. This increase in tensile strength values with the increase in the percentage of infill is produced by the increase in material. The honeycomb pattern, thanks to its good cohesion and load distribution, shows a linear increase, while the Hilbert pattern does not show this effect.



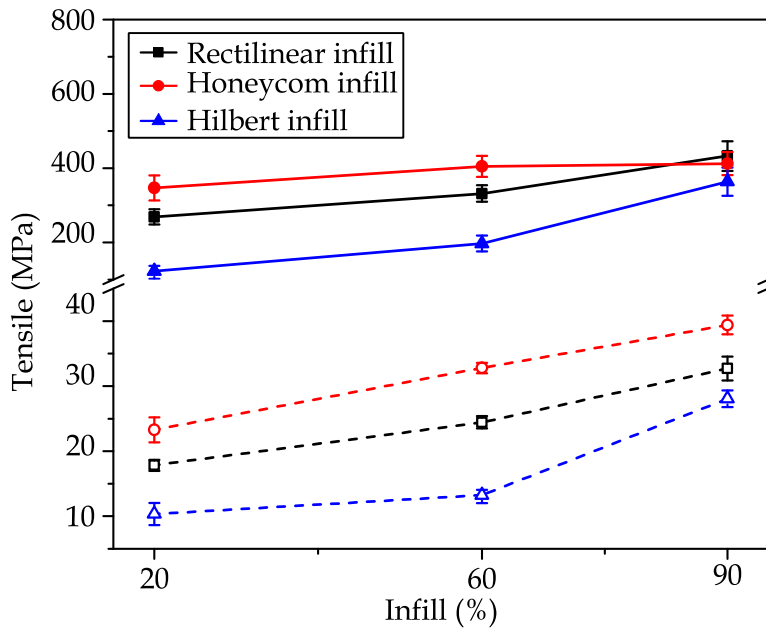


**Figure III.3.2.4.** Plot evolution of tensile modulus and tensile strength for different filling patterns as function of their infill percentage. Continuous lines indicate tensile modulus while dashed lines indicates tensile strength.

**Figure III.3.2.5.** shows the evolution of the elongation obtained in the tensile tests for the different filling patterns as function of the infill percentage. PLA presents low elongation at break values due to the brittleness nature of the material, in addition in the test pieces under study the elongation values are reduced as a consequence of the discontinuities produced by the FDM manufacturing process. These discontinuities are reduced as the infill percentage increases, regardless of the filling pattern used. Further, the Hilbert pattern presents the worst values of elongation with values that are one third of those that are obtained in pattern with the best result. The honeycomb pattern does not maintain a linear growth trend like the other two, for infill values above 60 % there is a more pronounced improvement in elongation. Therefore, it is verified that for the honeycomb pattern in values of infill to 90 %, elongations superior to the rectilinear pattern are obtained and altogether for high values of infill as a result of its internal structure.

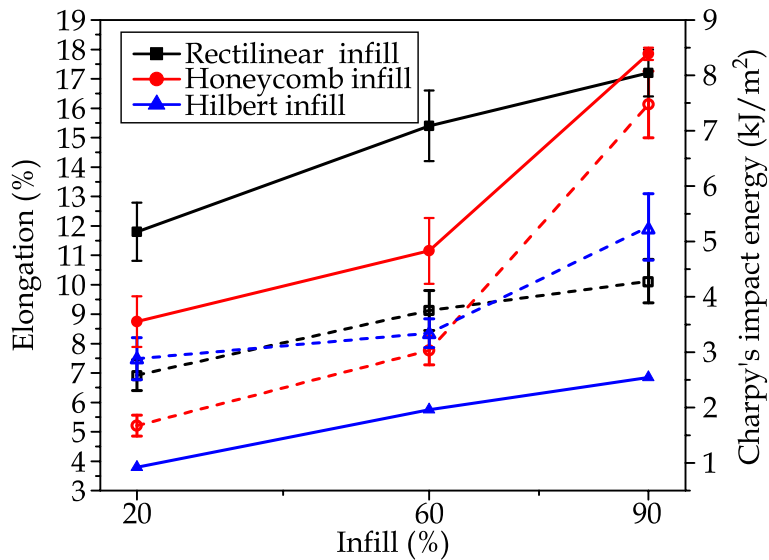


**Figure III.3.2.5.** Plot evolution of elongation and Charpy's impact energy absorbed for different filling patterns as function of the infill percentage. Continuous lines indicate the elongation values and dashed lines the Charpy's impact energy.

**Figure III.3.2.1.** also provides the fractured images from tensile tests. For the three patterns, it can be seen that as the infill percentage increases the size of the hollows produced by the patterns decreases. In spite of this, in all the specimens it is observed that the fracture is of a fragile character since the hollows act as stress concentrators.

The intrinsic brittleness of PLA combined with the internal hollows of the test specimens produced as application of the infill pattern during the manufacturing process leads to a low toughness. In this work, the toughness has been determined using the Charpy impact test, as summarized in **Figure III.3.2.5**. The low impact values obtained are a consequence of the notch that previously was made to the samples. For all the studied patterns, it is observed that ductility increases when the percentage of infill increases, this is due to the fact that the samples increase their mass and also the internal hollows are reduced. Furthermore, it is not observed any influence of the pattern on toughness since for the three infill values studied there is no predominant pattern nor worse. The behavior of the honeycomb pattern for the energy absorbed in the Charpy test confirms the performance shown for elongation. Since materials that have high elongation values also absorb more energy.

**Figure III.3.2.1.** also presents the fracture images of the samples after the impact tests. The standard machined notch used to carry out the tests can be seen at the right side of the test pieces. At the opposite end of the specimen there is no plastic deformation, which indicates the fragile type of the fracture. The three patterns with low

fill percentages have very large hollows that are reduced by increasing the fill percentage. The hollows act as stress concentrators, causing the material to absorb less energy on impact. For high infill percentages, the hollows are smaller, which causes better impact behavior as shown by the results.

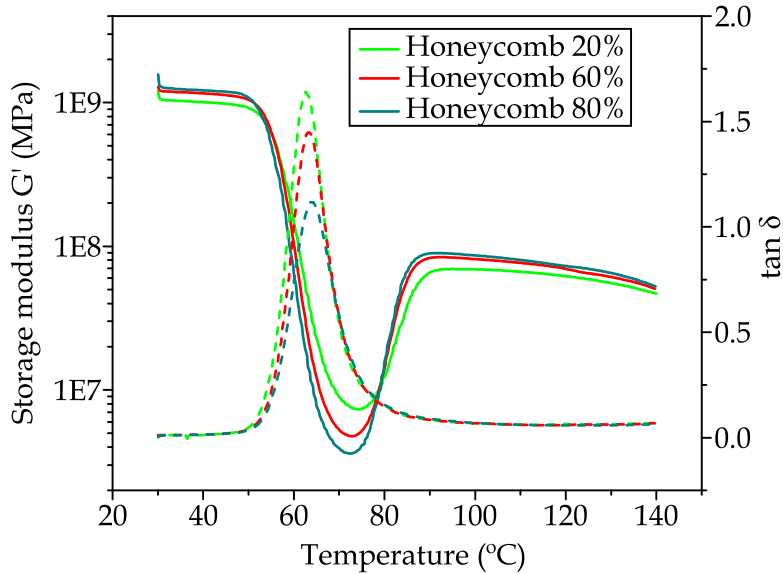


**Figure III.3.2.6.**  $G'$  and  $\tan \delta$  vs temperature for different infill amounts of honeycomb samples. Continuous lines indicate storage modulus while dashed line  $\tan \delta$ .

The Dynamic-Mechanical Thermal Analysis - DMTA (torsion mode) of the samples filled with honeycomb pattern is shown in **Figure III.3.2.6**. This analysis can be applied to the other two patterns, since they present the same behavior. **Figure III.3.2.6** shows the evolution of the  $G'$  for the samples with honeycomb pattern with the three different infill levels as a function of temperature. In the curves four different stages are observed, the first stage is below the  $T_g$  ranged 30 - 50 °C. As one can see, the initial storage modulus increases as the infill percentage increases with values of 1007 MPa, 1160 MPa and 12179 MPa at 40 °C for samples containing 20 %, 60 % and 90 % infill respectively indicating stiffer materials as pointed in previous analysis. In the range of 50 - 70 °C a softening of the material occurs; this phenomenon causes the  $G'$  modulus to be reduced by more than two orders of magnitude. The decrease is proportional to the amount of material in the sample. In this range,  $T_g$  of the material occurs, which confirms the temperature obtained with the DSC test. The  $G''$  values at 70 °C are 8.8 MPa, 5.2 MPa and 3.8 MPa for samples containing 20 %, 60 % and 90 % infill respectively. The third stage ranges between 70 °C and 90 °C, in it the PLA undergoes a cold crystallization process. The PLA analysed had previously suffered a cooling after the 3D printing process, but it was not able to full crystallize since this process requires

more time or temperature. When the temperature exceeds 70 °C, the necessary energy is provided to the material, so the PLA chains begin to move and pack resulting in an increase in crystallinity. By increasing the crystallinity, the material becomes stiffer as shown in the graph with a growth of  $G'$  in an order of magnitude. Once the crystallization process is finished, the storage module behaves similarly to the first stage, with maximum values for the samples with the highest infill percentage (90 %) with values of 86.3 MPa at a temperature of 100 °C, while the samples with infills of 20 % and 60 % reach values of 69.1 MPa and 81.5 MPa respectively.

In **Figure III.3.2.6.** the variation of the  $\tan \delta$  as a function of temperature is also depicted. If the maximum peak of  $\tan \delta$  is considered as a representative value of the  $T_g$ , values of 62.7 °C, 63.4 °C and 63.7 °C are obtained for the samples containing 20 %, 60 % and 90 % infill respectively. These values are very similar among them and with the value obtained in the DSC test (63.3 °C) since  $T_g$  is an intrinsic property of the material and practically does not depend on the cohesion or geometry of the 3D print. What stands out in **Figure III.3.2.6.** are the decreasing values of  $\tan \delta$  as the infill percentage increases. This trend is logical, as the material becomes stiffer the value of  $G'$  increases, which causes smaller losses. In fact, for the sample with 20 % honeycomb the maximum value of  $\tan \delta$  is 1.64 and this value is reduced to 1.12 for the 90 % honeycomb sample.

### CONCLUSIONS.

The effects of the infill pattern and percentage on the mechanical properties of PLA polymer specimens processed by FDM or material extrusion AM was studied. The manufacture of the specimens was controlled so that external factors such as humidity do not affect the results. Specimens were tested with three different infill patterns and with three different infill percentages. Tensile, impact and thermo-mechanical properties were examined in order to compare all levels with each other and the following results were obtained:

- The rectilinear pattern is the most recommended from a time efficiency point of view.
- Printing time is more dependent on the pattern used than on the amount of material used. As the complexity of the pattern increases, so does the processing time.
- The influence of the infill pattern on tensile values is significant for low infill percentage values but dilutes as the % infill increases. As the percentage load increases, the tensile characteristics among the three studied patterns become similar. So, for low

infill percentages it is advisable to use the honeycomb pattern and avoid the rectilinear pattern in order to achieve better mechanical characteristics.

- The intrinsic brittleness of the polymeric material used, PLA, combined with the discontinuities produced by the hollows of the patterns drag down the mechanical results since they act as stress concentrators and do not allow a correct transmission of internal forces.

#### ACKNOWLEDGMENTS.

This work was supported by the POLISABIO program grant number (2019-A02). Juan Ivorra-Martinez wants to thank UPV for the grant received through the PAID-01-19 program. Luis Quiles-Carrillo wants to thank MECD for his FPU grant (FPU15/03812). Diego Lascano wants to thank UPV for the grant received through the PAID-01-18 program.

#### REFERENCES.

1. Masood, SH. Intelligent rapid prototyping with fused deposition modelling. *Rapid Prototyping Journal* **1996**, 2, 24-33 doi: 10.1108/13552549610109054.
2. Gordelier TJ, Thies PR, Turner L. Optimising the FDM additive manufacturing process to achieve maximum tensile strength: a state-of-the-art review. *Rapid Prototyping Journal* **2019**, 25, 953-971 doi: 10.1108/rpj-07-2018-0183.
3. Attaran M. The rise of 3-D printing: The advantages of additive manufacturing over traditional manufacturing. *Business Horizons* **2017**, 3, 33-99doi: 10.1016/j.bushor.2017.05.011.
4. Berman B. 3D printing: the new industrial revolution. *Business Horizons* **2012**, 55, 155-162 doi: 10.1016/j.bushor.2011.11.003.
5. Despeisse, M.; Ford, S. The role of additive manufacturing in improving resource efficiency and sustainability. IFIP International Conference on Advances in Production Management Systems 2015, 460, 129-136 doi: 10.1007/978-3-319-22759-7\_15.
6. Gao W, Zhang Y, Ramanujan D. The status, challenges, and future of additive manufacturing in engineering. *Computer-Aided Design* **2015**, 69, 6965-89 doi: 10.1016/j.cad.2015.04.001.
7. Barrios-Muriel J, Romero-Sanchez F, Alonso-Sanchez FJ. Application of technologies of rapid prototyping in the fabrication of orthoprosthesis devices. *DYNA* **2016**, 91, 381-385 doi: 10.6036/7784.
8. Stansbury JW, Idacavage MJ. 3D printing with polymers: challenges among expanding options and opportunities. *Dental Materials* **2015**, 32, 54-64 doi: 10.1016/j.dental.2015.09.018.

9. Grémare A, Guduric V, Bareille R.. Characterization of printed PLA scaffolds for bone tissue engineering. *Journal of Biomedical Materials Research Part A* **2018**, *106*, 887–894 doi: 10.1002/jbm.a.36289.
10. Guerra AJ, Cano P, Rabionet M. 3D-printed PCL/PLA composite stents: towards a new solution to cardiovascular problems. *Materials* **2018**, *11*, 1679–1692 doi: 10.3390/ma11091679.
11. Dawoud M, Taha I, Ebeid SJ. Mechanical behaviour of ABS: An experimental study using FDM and injection moulding techniques. *Journal of Manufacturing Processes* **2016**, *21*, 39–45 doi: 10.1016/j.jmapro.2015.11.002.
12. Goh GD, Agarwala S, Goh GL. Additive manufacturing in unmanned aerial vehicles (UAVs): challenges and potential. *Aerospace Science and Technology* **2017**, *63*, 140–151 doi: 10.1016/j.ast.2016.12.019.
13. Mohamed OA, Masood SH, Bhowmik JL. Optimization of fused deposition modeling process parameters: a review of current research and future prospects. *Advances in Manufacturing* **2015**, *3*, 42–53 doi: 10.1007/s40436-014-0097-7.
14. Casavola C, Cazzato A, Moramarco V. Orthotropic mechanical properties of fused deposition modelling parts described by classical laminate theory. *Materials & Design* **2016**, *90*, 453–458 doi: 10.1016/j.matdes.2015.11.009.
15. Ulu E, Korkmaz E, Yay K. Enhancing the structural performance of additively manufactured objects through build orientation optimization. *Journal of Mechanical Design* **2015**, *137*, 111410–111419 doi: 10.1115/1.4030998.
16. Domingos M, Chiellini F, Gloria A. Effect of process parameters on the morphological and mechanical properties of 3D bioextruded poly( $\epsilon$ -caprolactone) scaffolds. *Rapid Prototyping Journal* **2012**, *18*, 56–67 doi: 10.1108/13552541211193502.
17. Araya-Calvo M, Lopez-Gomez I, Chamberlain-Simon N. Evaluation of compressive and flexural properties of continuous fiber fabrication additive manufacturing technology. *Additive Manufacturing* **2018**, *22*, 157–164 doi: 10.1016/j.addma.2018.05.007.
18. Boyard N, Christmann O, Rivette M. Support optimization for additive manufacturing: application to FDM. *Rapid Prototyping Journal* **2018**, *24*, 69–79 doi: 10.1108/RPJ-04-2016-0055.
19. Yosofi M, Kerbrat O, Mognol P. Framework to combine technical, economic and environmental points of view of additive manufacturing processes. *Procedia CIRP* **2018**, *69*, 118–123 doi: 10.1016/j.procir.2017.11.085.
20. Yang C, Tian X, Liu T. 3D printing for continuous fiber reinforced thermoplastic composites: mechanism and performance. *Rapid Prototyping Journal* **2017**, *23*, 209–215 doi: 10.1108/RPJ-08-2015-0098.
21. Torres J, Coteló J, Karl J. Mechanical property optimization of FDM PLA in shear with multiple objectives. *The Journal of The Minerals, Metals & Materials Society (TMS)* **2015**, *67*, 1183–1193 doi: 10.1007/s11837-015-1367-y.

22. Tymrak B, Kreiger M, Pearce JM. Mechanical properties of components fabricated with open-source 3-D printers under realistic environmental conditions. *Materials & Design* **2014**, *58*, 242–246 doi: 10.1016/j.matdes.2014.02.038.
23. Vaezi M, Chua CK. Effects of layer thickness and binder saturation level parameters on 3D printing process. *International Journal of Advanced Manufacturing Technology* **2011**, *53*, 275–284 doi: 10.1007/s00170-010-2821-1.
24. Rodríguez-Panes A, Claver J, Camacho A. The influence of manufacturing parameters on the mechanical behaviour of PLA and ABS pieces manufactured by FDM: a comparative analysis. *Materials* **2018**, *11*, 1333–1354 doi: 10.3390/ma11081333.
25. Wu W, Geng P, Li G. Influence of layer thickness and raster angle on the mechanical properties of 3D-printed PEEK and a comparative mechanical study between PEEK and ABS. *Materials* **2015**, *8*, 5834–5846 doi: 10.3390/ma8095271.
26. Valerga A, Batista M, Salguero J. Influence of PLA filament conditions on characteristics of FDM Parts. *Materials* **2018**, *11*, 1322–1335 doi: 10.3390/ma11081322.
27. Bellehumeur C, Li L, Sun Q. Modeling of bond formation between polymer filaments in the fused deposition modeling process. *Journal of Manufacturing Processes* **2004**, *6*, 170–178 doi: 10.1016/S1526-6125(04)70071-7.
28. FreeCAD software, release 0.18. Available from: <https://www.freecadweb.org/>.
29. Slic3r software release 1.3.0. Available from: <http://slic3r.org/>.
30. Repetier-Host software, release 2.1.6. Available from: <https://www.repetier.com/>.
31. Slotwinski JA. Mechanical Properties of Materials Made Via Additive Manufacturing. ASTM Standardization News 2013.
32. Forster A Materials testing standards for additive manufacturing of polymer materials: state of the art and standards applicability. 2015.
33. Monzon MD, Jò nec Z, Martinez A. Standardization in additive manufacturing: activities carried out by international organizations and projects. *International Journal of Advanced Manufacturing Technology* **2015**, *76*, 1111–1121 doi: 10.1007/s00170-014-6334-1.
34. Ibertest ELIB 30. Supplied by S.A.E. Ibertest (Madrid, Spain).





Adapted from the original manuscript.

### III.3.3 Design and simulation of a resorbable bone fixation plate made by Additive Manufacturing for femoral MID-shaft fractures.

Juan Ivorra-Martinez<sup>1</sup>, Samuel Sanchez-Caballero<sup>1</sup>, Miguel Ángel Selles<sup>1</sup>, Teodomiro Boronat<sup>1</sup>.





<sup>1</sup>Technological Institute of Materials - ITM, Universitat Politècnica de València - UPV, Plaza Ferrándiz y Carbonell 1, 03801 Alcoy (Spain).



JARTE.

2021, 2(1): 11.



**DESIGN AND SIMULATION OF A RESORBABLE BONE FIXATION PLATE  
MADE BY ADDITIVE MANUFACTURING FOR FEMORAL MID-SHAFT  
FRACTURES**J. Ivorra-Martinez <sup>a,\*</sup>, M.A. Selles <sup>a</sup>, S. Sanchez-Caballero <sup>b</sup>, T. Boronat <sup>a</sup><sup>a</sup>Materials Technology Institute, Universitat Politècnica de València, 03801 Alcoy, Spain.<sup>b</sup>Institute of Design for Manufacturing, Universitat Politècnica de València, 03801 Alcoy, Spain.**Abstract:**

Finite element method has been employed to establish the feasibility of a fixation plate made of PLA by additive manufacturing for femoral shaft fractures. For this purpose, Von Mises stress and the pressure contact between bones had been analysed. The proposed design has been compared with an actual titanium fixation plate as a point of reference.

**Keywords:** femur, mid-SHAFT, finite element method, resorbable, 3D printing.

**Cite as:** Ivorra-Martinez, J., Selles, M.A., Sanchez-Caballero, S., Boronat, T. (2021). Design and simulation of a resorbable bone fixation plate made by additive manufacturing for femoral MID-shaft fractures. *J Appl Res Eng Technol & Engineering*, 2(1), 11-16. <https://doi.org/10.4995/jarte.2021.14712>

**1. Introduction**

Femoral shaft fractures have an incidence of between 10 and 37 per 100,00 patients each year. Some of the main causes of this type of fracture are high-energy impacts as a result of car accidents or falls (K.J. Wu et al., 2019). The treatment usually requires a surgical intervention to introduce a fixation device to ensure stability during the healing process (C. Wu et al., 2020).

The addition of a fixation device acts as a bridge in the fracture, so the loads are transferred by the fixation plate (Heimbach et al., 2017). As a result, the bone surrounding the fixation plate is underloaded compared to its natural state, which leads to a stress shielding process (Arabnejad et al., 2017). Bones are a living tissue and consequently they will adapt to new loads through a process called remodelling (George et al., 2017), which leads to the reduction of its density (Ridzwan et al., 2006). As a result of the loss of density in the bone, the mechanical properties will deteriorate resulting in a future fracture (Heimbach et al., 2017; X. Wu et al., 2019).

The most common materials used for the manufacture of fixation plates are pure titanium or titanium alloys such as Ti-6Al-4V. These types of materials show a higher modulus of elasticity than human bone, resulting in a stress shielding process (Guastaldi et al., 2019; Junlei Li et al., 2020). Stainless steel is another material widely used for bone fixation but with less biocompatibility and corrosion resistance (Geetha et al., 2009). In recent years, the possibility of using biopolymers in biomedicine has been investigated with excellent results (Alizadeh-Osgouei et al., 2019). One of the most interesting biopolymers is PLA, some of the properties that make it a suitable material are excellent biocompatibility, easy to manufacture or hydrophobic in nature (Jiafeng Li et al., 2017; Narayanan et al., 2016). The ability to degrade

within the human body is an interesting property as it avoids a second surgical intervention to remove the fixation plate, the device degrades by body fluids and is reabsorbed by the body (Kanno et al., 2018).

The use of biopolymers such as PLA is closely related to additive manufacturing techniques (AM) such as fused deposition modelling (FDM). These techniques allow the manufacture of different geometries without using complex equipment (Parthasarathy et al., 2015), thus reducing costs (Singh et al., 2018). Another advantage of AM is the possibility of producing a custom fixation device for the patient (Murr et al., 2016; X. Wang et al., 2016), for which Computerized Tomography (CT) helps to create a solid 3D model of a bone that can be used as the basis for designing the fixation plate (Liu et al., 2019).

The main objective of this work is to evaluate the viability of the PLA resorbable bone fixation plate made by fusion deposition modelling. For this purpose, the PLA bone fixation plate is compared with titanium by using finite element analysis (FEA). This is done by analysing the pressure and displacement applied in the fracture area, as well as the resulting stress on the fixation plate.

**2. Materials and methods****2.1. Finite element modelling**

The two proposed models consist of a fracture of the femoral shaft with two types of fixation plates, a standard titanium and another 3D printed PLA (Figure 1). The dimensions of the titanium plates were 17.5 mm wide, 5 mm thick, 178 mm long and 10 holes of 4.5 mm according to the specifications proposed by the TIPSAN catalogue (TIPSAN, Bornova, Turkey). A thickness of

\*Corresponding author: J. Ivorra-Martinez, [juaivmar@doctor.upv.es](mailto:juaivmar@doctor.upv.es)



**Abstract.**

Finite Element Method - FEM has been employed to establish the feasibility of a fixation plate made of PLA by Additive Manufacturing - AM for femoral shaft fractures. For this purpose, Von Mises stress and the pressure contact between bones had been analyzed. The proposed design has been compared with an actual titanium fixation plate as a point of reference.

**Keywords:** femur; mid-SHAFT; Finite Element Method - FEM; resorbable; 3D printing.

---



## INTRODUCTION.

Femoral shaft fractures have an incidence of between 10 and 37 per 100000 patients each year. Some of the main causes of this type of fracture are high-energy impacts as a result of car accidents or falls [1]. The treatment usually requires a surgical intervention to introduce a fixation device to ensure stability during the healing process [2]. The addition of a fixation device acts as a bridge in the fracture, so the loads are transferred by the fixation plate [3]. As a result, the bone surrounding the fixation plate is underloaded compared to its natural state, which leads to a stress shielding process [4]. Bones are a living tissue and consequently they will adapt to new loads through a process called remodelling [5], which leads to the reduction of its density [6]. As a result of the loss of density in the bone, the mechanical properties will deteriorate resulting in a future fracture [3,7].

The most common materials used for the manufacture of fixation plates are pure titanium or titanium alloys such as Ti-6Al-4V. These types of materials show a higher modulus of elasticity than human bone, resulting in a stress shielding process [8,9]. Stainless steel is another material widely used for bone fixation but with less biocompatibility and corrosion resistance [10]. In recent years, the possibility of using biopolymers in biomedicine has been investigated with excellent results [11]. One of the most interesting biopolymers is PLA, some of the properties that make it a suitable material are excellent biocompatibility, easy to manufacture or hydrophobic in nature [12,13]. The ability to degrade within the human body is an interesting property as it avoids a second surgical intervention to remove the fixation plate, the device degrades by body fluids and is reabsorbed by the body [14]. The use of biopolymers such as PLA is closely related to Additive Manufacturing - AM techniques such as Fused Deposition Modelling - FDM. These techniques allow the manufacture of different geometries without using complex equipment [15], thus reducing costs [16]. Another advantage of AM is the possibility of producing a custom fixation device for the patient [17,18], for which Computerized Tomography - CT helps to create a solid 3D model of a bone that can be used as the basis for designing the fixation plate [19].

The main objective of this work is to evaluate the viability of the PLA resorbable bone fixation plate made by Fused Deposition Modelling - FDM. For this purpose, the PLA bone fixation plate is compared with titanium by using Finite Element Analysis - FEA. This is done by analysing the pressure and displacement applied in the fracture area, as well as the resulting stress on the fixation plate.

## METHODS.

**Finite element modelling.**

The two proposed models consist of a fracture of the femoral shaft with two types of fixation plates, a standard titanium and another 3D printed PLA (**Figure III.3.3.1.**). The dimensions of the titanium plates were 17.5 mm wide, 5 mm thick, 178 mm long with 10 holes of 4.5 mm according to the specifications proposed by the TIPSAN catalogue (TIPSAN, Bornova, Turkey). A thickness of 5 mm is also considered for the modelling of the PLA plate. Simplified screws (**Figure III.3.3.3.**) of the same material as the plate are used for placement in the bone. For the idealization of the femur, a cylinder is considered as cancellous bone and a tube as cortical bone (**Figure III.3.3.2.**). The dimensions considered in the model were for an average man of 50 years old (**Table III.3.3.1.**). The solid parts had different linear isotropic properties and are represented in **Table III.3.3.2.**

In order to ensure the correct stability of the fracture during the recuperation, the mechanical properties along the time were tested. To this propose, the properties of degraded PLA after 30 days inside human body had been considered. Spiridon *et al.* proposed that PLA immersed in Simulated Body Fluid - SBF for one month, will lose about 22.8 % of its tensile modulus -  $E_t$  and 32.9 % of its tensile strength -  $\sigma_t$  [20].

The geometry was meshed using Siemens NX 12.0, (Siemens, Munich, Germany) with 3D elements CTETRA(10) with 10 nodes for each element. The number of elements in each part was 160320 for cortical bone, 102201 for cancellous bone, 21547 for each screw, 437149 for PLA and 152687 for titanium.

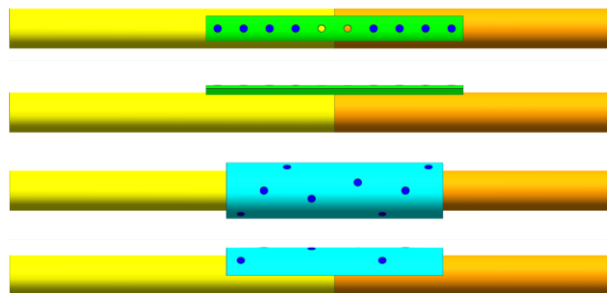


**Figure III.3.3.1.** 3D model of femur shaft fracture with fixation plate, titanium (green), PLA (blue).



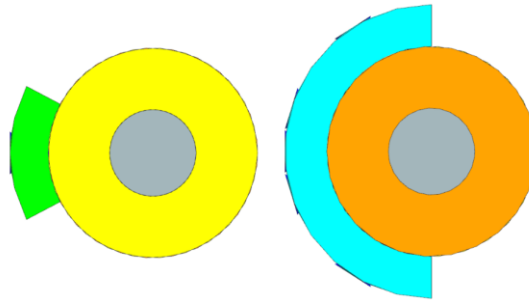


Figure III.3.3.2. Femur section with fixation plate, titanium (green), PLA (blue).

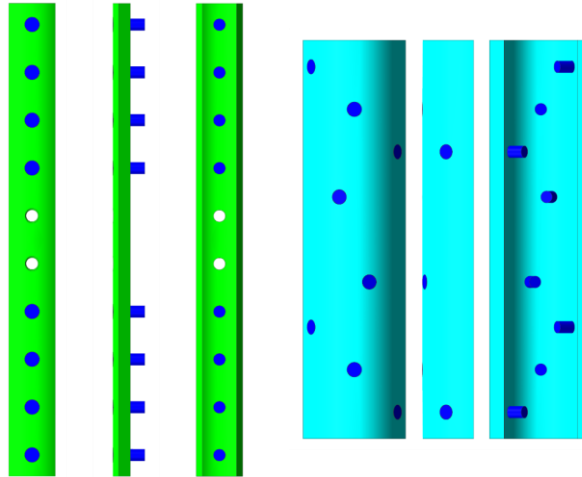


Figure III.3.3.3. Fixation plates with screws, titanium (green), PLA (blue).

Table III.3.3.1. Dimensions for femur model employed in the FEM model.

Dimension	Value	Reference
Length	450 mm	[21]
Total bone section	650 mm <sup>2</sup>	[21]
Cortical bone section	500 mm <sup>2</sup>	[21]
Head femur offset	42.2 mm	[22]

Table III.3.3.2. Isotropic properties of materials.

Material	$E_t$ (MPa)	$\sigma_t$ (MPa)	Poisson's ratio	Reference
Cortical bone	16350	-	0.26	[23]
Cancellous bone	137	-	0.30	[23]
Titanium	110000	920	0.34	[25,26]
PLA	3368	56.6	0.30	[26]
PLA - 30 days	2702	37.9	0.30	[20]

#### Contact surfaces.

The contacts between the different bodies ensure the correct transfer of load between them. In order to reduce the computational cost, frictionless contacts were established between the bone plate and the plate screw. Only the contact in the fractured area was modelled with a friction coefficient of 0.46 as proposed by Wang *et al.* [27], so that the displacement on the contact surfaces can be established. Finally, the screws were attached to the cortical bone because the focus of the study was on the fixation plate.

#### Boundary and loading conditions.

For the simulation, a fixed support was applied at the base (0 degree of freedom) and a 1400 N compression force was applied at the top. The load represents a single-leg standing position as Wang *et al.* and McClellan *et al.* proposed [28,29]. This load should be applied on the femur head (**Figure III.3.3.4.**), since the model was simplified and the femur head was not modelled, the force was applied on one node (where femoral head should be) and connected with bone by a rigid region RBE2.

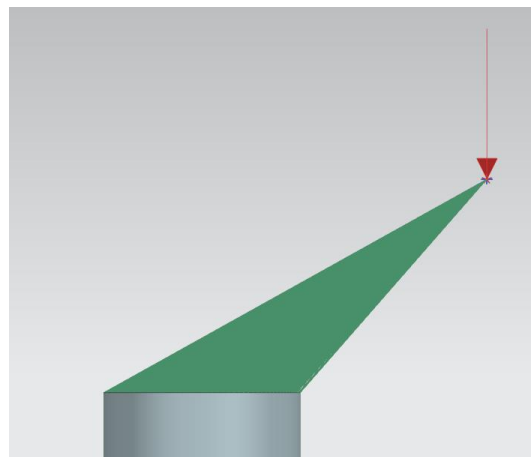


**Figure III.3.3.4.** Load application on the rigid region.

### RESULTS AND DISCUSSION.

#### Fracture surface contact results.

Ensuring the fracture healing process is the most important parameter of this study. For this purpose, the mobility and the pressure applied on the fracture surface are the main factors. While the longitudinal strain applied to fractures was shown to promote the healing process [28], mobility at the fracture site disturbs callus formation [29]. For this purpose, a friction contact between the bone fragments was established and the resulting pressure and displacement after the force was applied was analysed.

The femur undergoes at flexural tensile state by the loads applied, in this case the compressive area corresponds to right part and the traction area corresponds to the left. The fixation plate was placed on the left (traction) to avoid bone separation. Titanium fixation plate acts as a point of reference, this kind of plates are widely applied in traumatology surgeries [9,32]. The pressure distribution in titanium model (**Figure III.3.3.5.** up-right) shows a maximum pressure of 34.0 MPa and progressively decreases until 0 MPa.

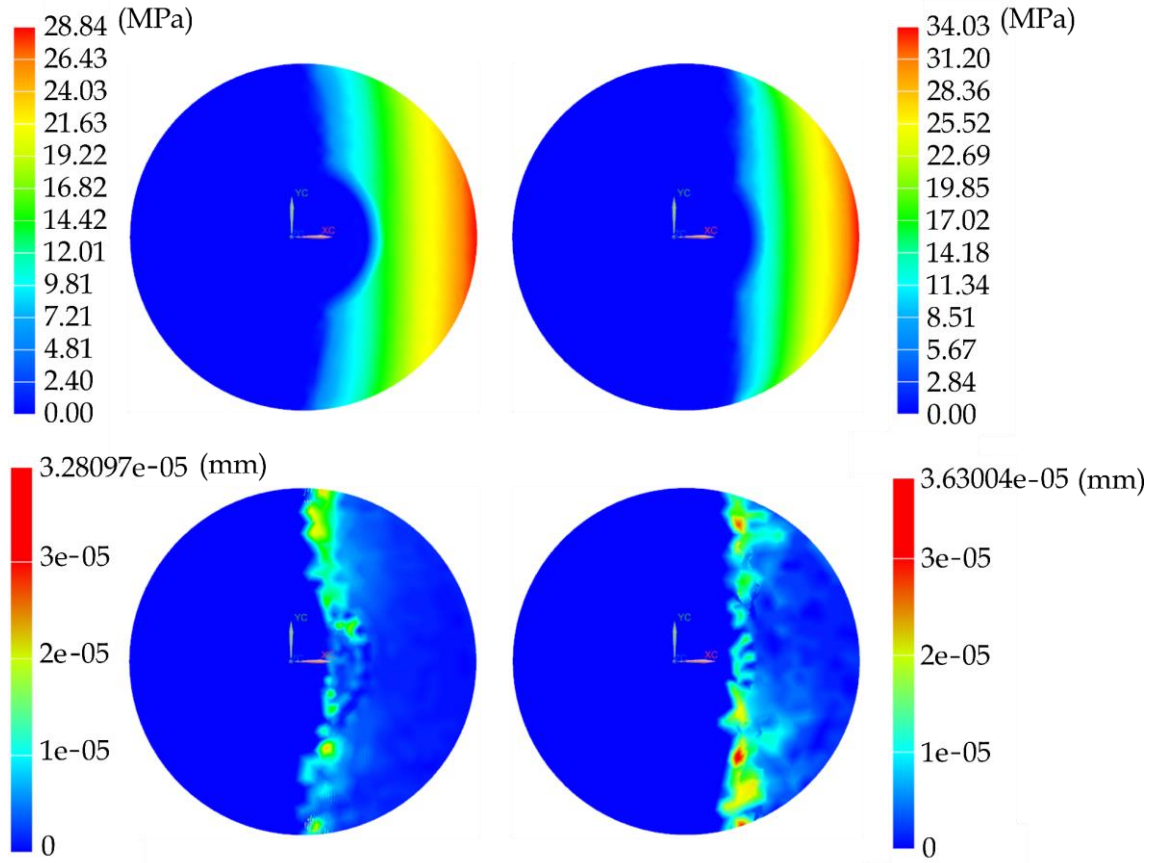


**Figure III.3.3.5.** Pressure in MPa (up) and displacement in mm (down), 3D printed PLA (left) and Titanium (right).

The results when using PLA are quite similar, but in this case the maximum pressure is 28.8 MPa. An interesting result is in the cancellous bone, in this case the pressure is close to 0 MPa due to the difference between the elastic modulus of both types of bones (the cortical bone is approximately 120 times stiffer than cancellous bone). In order to achieve these results, the 3D printed PLA section was modelled with a higher section.

The force applied to the top generates a shear stress on the contact surfaces that promotes de displacement. Since the contact was modelled as frictional, the area where

more pressure is applied, displacement is avoided. The area where pressure tends to 0, the frictional forces cannot prevent the displacement and therefore a small displacement appears. However, in both cases the displacements are quite close to 0 mm (about  $10^{-5}$  mm). Kim *et al.* [33] predicted the healing process for different fixation plates. In all cases the bone formation started from the site where more pressure was applied during the loading.

#### **Von Mises stress.**

Another important parameter to avoid the failure of the medical device is the distribution of stress. The results of the FEM (**Figure III.3.3.6.**) indicated that in both cases the maximum tensile strengths were located around the holes due to the contact between the screw and the fixation plate. In those cases, the screws acted as a transmission element between the bone and the fixation plate. For the titanium fixation plate, the maximum Von Mises stress was 739.6 MPa (under tensile strength) in the top hole while most of the elements were below 47 MPa. In the case of the screw, the maximum stress appears near where the contact changes from screw/bone for screw/fixation plate. In addition, another area of maximum stress was induced by the screw head stress concentrator. Different results were obtained for PLA, where the maximum Von Mises stress was 51.9 MPa. For this, the design of the fixation plate introduced some modifications with respect to the standard of titanium, although the number of screws is the same, they were distributed throughout the area. The modification allowed a better stability in the fractured area and a reduction of the Von Mises stress. Tang *et al.* [23] obtained a Von Mises stress 130.2 MPa with 250 N load. In a linear material model as the one employed in these cases, if the same load was applied, the resulting stress would be about 730 MPa. This means that the result reported by Tang *et al.* would be similar than the one obtained in this work.

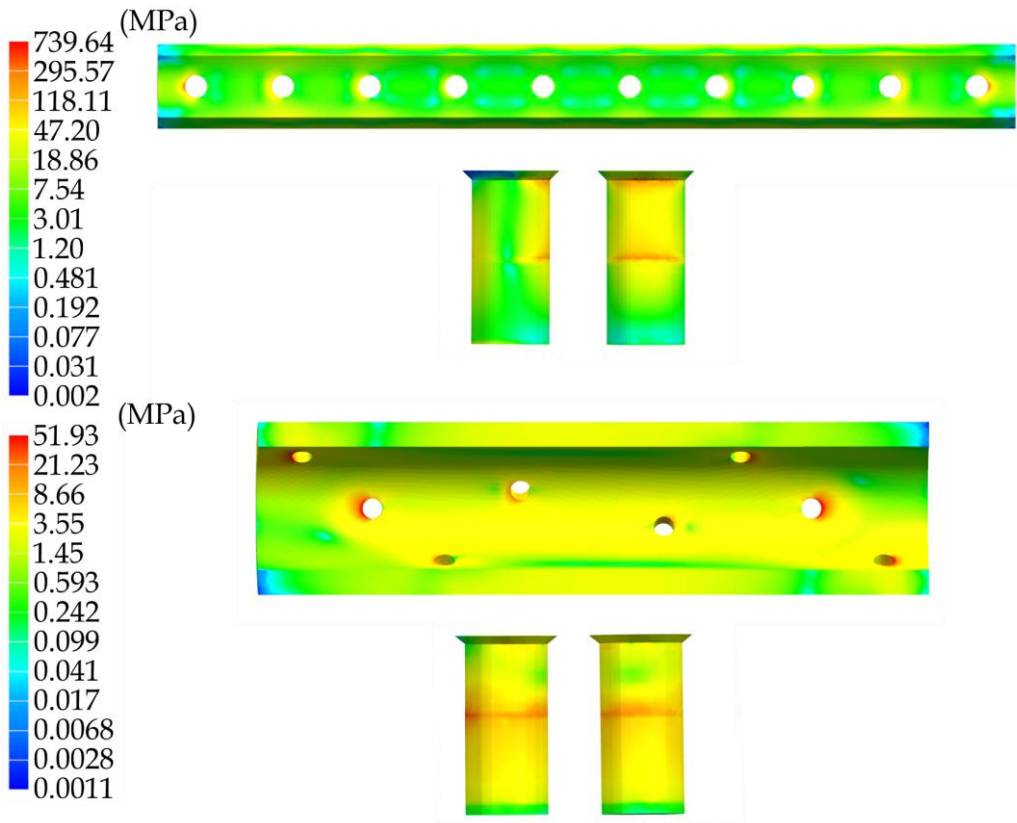


**Figure III.3.3.6.** Von Mises stress (MPa) distribution for titanium (up) and 3D printed PLA (down).

**Effect of the degradation on PLA.**

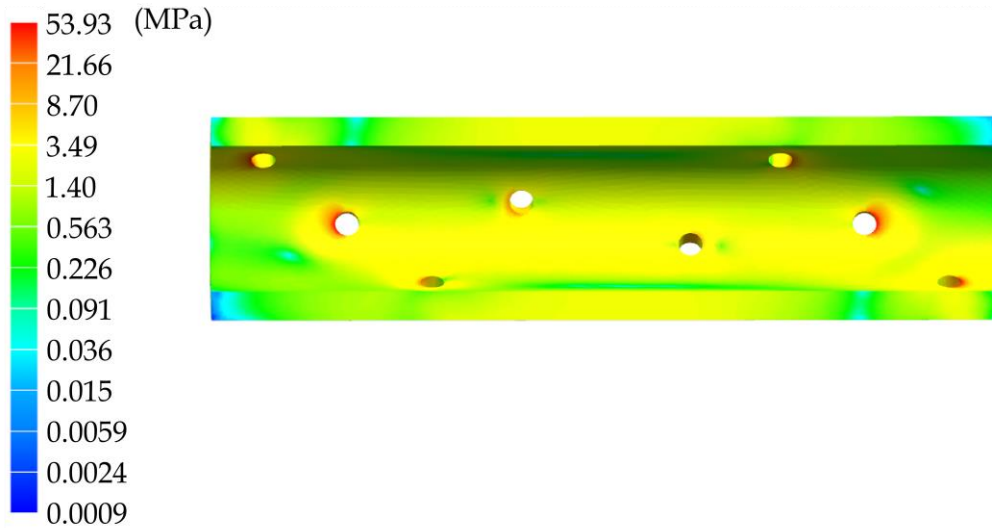


**Figure III.3.3.7.** Von Mises stress distribution for 30 days degradation PLA.

The previous model has been re-simulated with the PLA properties after 30 days in SBF by the assumption is that the only difference between in the degraded one is the effect on the mechanical properties proposed in **Table III.3.3.2.**

The proposed results in **Figure III.3.3.7.** showed an increase in Von Mises stress due to the decrease on  $E_t$ . In this situation the maximum Von Mises stress was 53.9 MPa, a 3.9 % increase in stress compared to the new PLA fixation plate. Under these conditions, the device would break due to the tensile strength after 30 day in SBF is about 37.9 MPa.

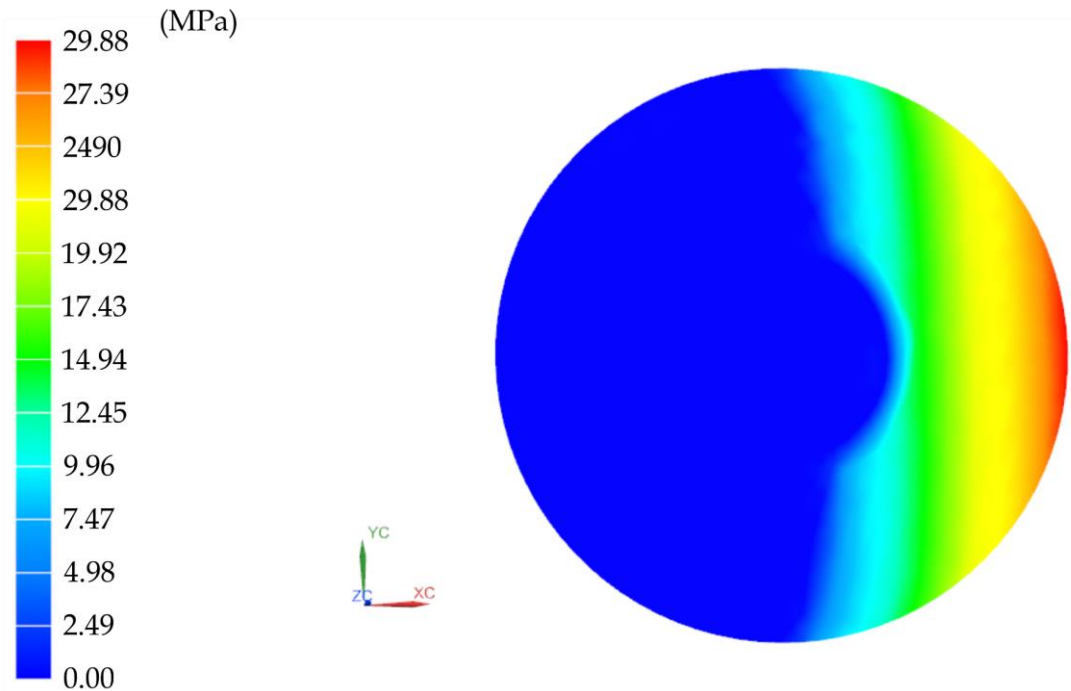


**Figure III.3.3.8.** Pressure contact distribution for 30 days degradation PLA.

A problem without no-linear effects, the increase of stress would be equivalent to the reduction of  $E_t$ . In this case, the contact pressure between the ends of the bone produced a no-linear effect. As can be seen in **Figure III.3.3.8.**, the pressure contact increased from 28.84 MPa with a nondegraded devices to 29.88 MPa after 30-day implantation.

### CONCLUSIONS.

In this work, the main objective was to study the feasibility of the 3D printed PLA femoral fixation plate. In comparison with a titanium fixation plate, similar results were obtained in the contact of the fracture surface, making possible the bone regeneration process. PLA properties over the time take an important role on the correct functionality of the fixation plate. Even the stress results on a new fixation plate were positive, after 30 day of degradation the fixation plate would brake under the proposed load. To this effect, the utilization of additives could help to control the loss of properties inside the human body. One important aspect is that the patient activity would not be recovered

just after the intervention and during the recuperation process the activity of the patient must be reduced. This means that the patient should not be on a single standing leg over this period. Nevertheless, the results, suggest that other bones with less load could be treated with this kind of fixation plate.

#### ACKNOWLEDGEMENTS.

Juan Ivorra-Martinez wants to thank FPU19/01759 grant funded by MCIN/AEI/10.13039/501100011033 and by ESF Investing in your future.

#### REFERENCES

1. Wu, K.-J.; Li, S.-H.; Yeh, K.-T.; Chen, H.; Lee, R.-P.; Yu, T.-C.; Peng, C.-H.; Liu, K.-L.; Yao, T.-K.; Wang, J.-H. The risk factors of nonunion after intramedullary nailing fixation of femur shaft fracture in middle age patients. *Medicine* **2019**, *98*, 16559–16565 doi: 10.1097/MD.00000000000016559.
2. Wu, C.; Zheng, K.; Fang, J.; Steven, G.P.; Li, Q. Time-dependent topology optimization of bone plates considering bone remodeling. *Computer Methods in Applied Mechanics and Engineering* **2020**, *359*, 112702–112720 doi: 10.1016/j.cma.2019.112702.
3. Heimbach, B.; Grassie, K.; Shaw, M.T.; Olson, J.R.; Wei, M. Effect of hydroxyapatite concentration on high-modulus composite for biodegradable bone-fixation devices. *Journal of Biomedical Materials Research Part B: Applied Biomaterials* **2017**, *3*, 33–99 doi: 10.1002/jbm.b.33713.
4. Arabnejad, S.; Johnston, B.; Tanzer, M.; Pasini, D. Fully porous 3D printed titanium femoral stem to reduce stress-shielding following total hip arthroplasty. *Journal of Orthopaedic Research* **2017**, *35*, 1774–1783 doi: 10.1002/jor.23445.
5. George, D.; Allena, R.; Remond, Y. Mechanobiological stimuli for bone remodeling: mechanical energy, cell nutriments and mobility. *Computer Methods in Biomechanics and Biomedical Engineering* **2017**, *20*, 91–92 doi: 10.1080/10255842.2017.1382876.
6. Ridzwan, M.; Shuib, S.; Hassan, A.; Shokri, A.; Ibrahim, M. Optimization in implant topology to reduce stress shielding problem. *Journal of Applied Sciences* **2006**, *6*, 2768–2773 doi: 10.3923/jas.2006.2768.2773.

7. Wu, X.; Wang, Z.; Li, H.; Li, Y.; Wang, H.; Tian, W. Biomechanical evaluation of osteoporotic fracture: metal fixation versus absorbable fixation in Sawbones models. *Injury* **2019**, *50*, 1272–1276 doi: 10.1016/j.injury.2019.05.023.
8. Guastaldi, F.; Martini, A.; Rocha, E.; Hochuli-Vieira, E.; Guastaldi, A. Ti-15Mo alloy decreases the stress concentration in mandibular angle fracture internal fixation hardware. *Journal of Maxillofacial and Oral Surgery* **2019**, *19*, 1–7 doi: 10.1007/s12663-019-01251-8.
9. Li, J.; Qin, L.; Yang, K.; Ma, Z.; Wang, Y.; Cheng, L.; Zhao, D. Materials evolution of bone plates for internal fixation of bone fractures: a review. *Journal of Materials Science & Technology* **2020**, *36*, 190–208 doi: 10.1016/j.jmst.2019.07.024.
10. Geetha, M.; Singh, A.K.; Asokamani, R.; Gogia, A.K. Ti based biomaterials, the ultimate choice for orthopaedic implants—a review. *Progress in materials science* **2009**, *54*, 397–425 doi: 10.1016/j.pmatsci.2008.06.004.
11. Alizadeh-Osgouei, M.; Li, Y.; Wen, C. A comprehensive review of biodegradable synthetic polymer–ceramic composites and their manufacture for biomedical applications. *Bioactive materials* **2019**, *4*, 22–36 doi: 10.1016/j.bioactmat.2018.11.003.
12. Li, J.; Li, Z.; Ye, L.; Zhao, X.; Coates, P.; Caton-Rose, F. Structure and biocompatibility improvement mechanism of highly oriented poly(lactic acid) produced by solid die drawing. *European Polymer Journal* **2017**, *97*, 68–76 doi: 10.1016/j.eurpolymj.2017.09.038.
13. Narayanan, G.; Vernekar, V.N.; Kuyinu, E.L.; Laurencin, C.T. Poly(lactic acid) – based biomaterials for orthopaedic regenerative engineering. *Advanced drug delivery reviews* **2016**, *107*, 247–276 doi: 10.1016/j.addr.2016.04.015.
14. Kanno, T.; Sukegawa, S.; Furuki, Y.; Nariai, Y.; Sekine, J. Overview of innovative advances in bioresorbable plate systems for oral and maxillofacial surgery. *Japanese Dental Science Review* **2018**, *54*, 127–138 doi: 10.1016/j.jdsr.2018.03.003.
15. Parthasarathy, J. *Additive manufacturing of medical devices. Innovations, advances, and applications*, 1 ed.; CRC Press: **2015**, Vol. 1.



16. Singh, D.; Singh, R.; Boparai, K.S. Development and surface improvement of FDM pattern based investment casting of biomedical implants: a state of art review. *Journal of Manufacturing Processes* **2018**, *31*, 80–95 doi: 10.1016/j.jmapro.2017.10.026.
17. Murr, L.E. Frontiers of 3D printing/ additive manufacturing: from human organs to aircraft fabrication. *Journal of Materials Science & Technology* **2016**, *32*, 987–995 doi: 10.1016/j.jmst.2016.08.011.
18. Wang, X.; Xu, S.; Zhou, S.; Xu, W.; Leary, M.; Choong, P.; Qian, M.; Brandt, M.; Xie, Y.M. Topological design and additive manufacturing of porous metals for bone scaffolds and orthopaedic implants: a review. *Biomaterials* **2016**, *83*, 127–141 doi: 10.1016/j.biomaterials.2016.01.012.
19. Liu, B.; Zhang, S.; Zhang, J.; Xu, Z.; Chen, Y.; Liu, S.; Qi, W.; Yang, L. A personalized preoperative modeling system for internal fixation plates in long bone fracture surgery – a straightforward way from CT images to plate model. *The International Journal of Medical Robotics and Computer Assisted Surgery* **2019**, *15*, 2029–2052 doi: 10.1002/rcs.2029.
20. Spiridon, I.; Tanase, C.E. Design, characterization and preliminary biological evaluation of new lignin–PLA biocomposites. *International journal of biological macromolecules* **2018**, *114*, 855–863 doi: 10.1016/j.ijbiomac.2018.03.140.
21. Klein, K. F., Hu, J., Reed, M. P., Hoff, C. N., & Rupp, J. D. (2015). Development and validation of statistical models of femur geometry for use with parametric finite element models. *Annals of biomedical engineering*, *43*, 2503–2514 doi: 10.1007/s10439–015–1307–6.
22. Sariali, E., Mouttet, A., Pasquier, G., & Durante, E. (2009). Three–dimensional hip anatomy in osteoarthritis: analysis of the femoral offset. *The Journal of arthroplasty*, *24*, 990–997 doi: 10.1016/j.arth.2008.04.031.
23. Li, J.; Yin, P.; Zhang, L.; Chen, H.; Tang, P. Medial anatomical buttress plate in treating displaced femoral neck fracture a finite element analysis. *Injury* **2019**, *50*, 1895–1900 doi: 10.1016/j.injury.2019.08.024.

24. Nurettin, D.; Burak, B. Feasibility of carbon-fiber-reinforced polymer fixation plates for treatment of atrophic mandibular fracture: a finite element method. *Journal of Cranio-Maxillofacial Surgery* **2018**, *46*, 2182-2189 doi: 10.1016/j.jcms.2018.09.030.
25. Zhao, X.; Niinomi, M.; Nakai, M.; Hieda, J.; Ishimoto, T.; Nakano, T. Optimization of Cr content of metastable  $\beta$ -type Ti-Cr alloys with changeable Young's modulus for spinal fixation applications. *Acta biomaterialia* **2012**, *8*, 2392-2400 doi: 10.1016/j.actbio.2012.02.010.
26. Tymrak, B.; Kreiger, M.; Pearce, J.M. Mechanical properties of components fabricated with open-source 3D printers under realistic environmental conditions. *Materials & Design* **2014**, *58*, 242-246 doi: 10.1016/j.matdes.2014.02.038.
27. Wang, J.; Ma, J.-X.; Lu, B.; Bai, H.-H.; Wang, Y.; Ma, X.-L. Comparative finite element analysis of three implants fixing stable and unstable subtrochanteric femoral fractures: proximal femoral nail antirotation (PFNA), proximal femoral locking plate (PFLP), and reverse less invasive stabilization system (LISS). *Orthopaedics & Traumatology: Surgery & Research* **2020**, *106*, 95-101 doi: 10.1016/j.otsr.2019.04.027.
28. McClellan, R.T. The variable angle hip fracture nail relative to the Gamma 3: a finite element analysis illustrating the same stiffness and fatigue characteristics. *Advances in orthopedics* **2013**, *2013*, 1-11 doi: 10.1155/2013/143801.
29. Wang, A.-y.; Peng, J.; Sun, M.-x.; Sui, X.; Wang, X.; Tian, Y.; Lu, S.-b. Biomechanical comparison of different structural bone grafting in femoral heads' defects of weight-bearing region. *Journal of Medical Biomechanics* **2006**, *4*, 71-75 doi: 10.1016/j.arthro.2015.06.051.
30. Elkins, J.; Marsh, J.L.; Lujan, T.; Peindl, R.; Kellam, J.; Anderson, D.D.; Lack, W. Motion predicts clinical callus formation: construct-specific finite element analysis of supracondylar femoral fractures. *The Journal of bone and joint surgery. American volume* **2016**, *98*, 276-284 doi: 10.2106/JBJS.O.00684.
31. Jahagirdar, R.; Scammell, B.E. Principles of fracture healing and disorders of bone union. *Surgery (Oxford)* **2009**, *27*, 63-69 doi: 10.1016/J.MPSUR.2008.12.011.

32. Hayes, J.; Richards, R. The use of titanium and stainless steel in fracture fixation. *Expert review of medical devices* **2010**, *7*, 843–853 doi: 10.1586/erd.10.53.
33. Kim, H.-J.; Chang, S.-H.; Jònec, H.-J. The simulation of tissue differentiation at a fracture gap using a mechano–regulation theory dealing with deviatoric strains in the presence of a composite bone plate. *Composites Part B: Engineering* **2012**, *43*, 978–987 doi: 10.1016/j.compositesb.2011.09.011.



## **IV. CONCLUSIONS.**



## IV.1. Partial conclusions.

After analysing the obtained results in the different works and taking into account the specific objectives proposed at the start of the thesis, the partial conclusions of each one of the developed blocks are about to be defined.

### IV.1.1. With regard to the development of environmentally friendly formulations and composites with polyhydroxyalkanoates.

The incorporation of PCL for the obtention of binary blends with P(3HB-*co*-3HHx) allowed to increase the ductility and the toughness of the blends as it was established by the mechanical characterization of the different samples. A maximum improvement of 56 % in impact strength was achieved, as well as an increase in elongation at break from 13.9 % observed in the neat polymer up to 461 % for the blends. All that even demonstrating a lack of compatibility of the different phases, demonstrated by the invariability of the main thermal parameters analysed by DSC.

The viability of obtaining WPC from the blend of P(3HB-*co*-3HHx) with ASF was demonstrated. The incorporation of the waste leads to an increase in the brittleness of the material due to a lack of affinity of the polymer with the lignocellulosic filler which worsens their adhesion and therefore the load transfer. To improve the interaction between the phases, a lactic acid-derived oligomer was introduced, which enhances the load transfer between the polymer and the filler. Additionally, a plasticizing phenomenon was also induced, which increased the ductile properties of the polymer matrix. As a result of the combination of both effects, composites with high content in lignocellulosic filler are obtained with superior elongation capacity in comparison with the neat polymer.

The use of natural origin plasticizers have especial interest due to their low toxicity and therefore a major possibility of being introduced in the food sector. P3HB is a material known for its marked brittleness due to the ageing phenomenon that it undergoes at room temperature. The use of geranile-derived materials has proven the plasticizing capacity of a P3HB matrix, allowing the improvement ductile properties such as elongation at break and impact strength. This improvement in ductile properties is ascribed to a reduction in the  $T_g$  observed in DSC and DMTA altogether with a reduction in the stiffness of the material, as it as observed in the tensile and DMTA tests. From a thermal point of view, the incorporation of the plasticizers reduces the thermal stability of the materials due to the high volatility of the terpenoids. Nonetheless, the

working temperatures used during extrusion and injection are compatible with the geranile-derived materials selected. The incorporation of those plasticizers also reduces the necessary amount of time to achieve complete disintegration of the samples in composting conditions.

### **IV.1.2. With regard to the manufacturing of polyhydroxyalkanoates by 3D printing and injection moulding for medical applications.**

The use of polyhydroxyalkanoates was analysed through the use of P(3HB-co-3HHx) and a 3D printer equipped with a screw in order to make it possible to directly print with pellets. The carried-out study establishes that the most relevant element over the mechanical properties is the printing pattern direction, providing higher resistance when it is aligned with the stress direction. Another important factor is the printing temperature, up until 180 °C allowed to obtain an improvement in the mechanical properties due to a higher adhesion in the deposited lines. However, if this temperature is surpassed, a loss in properties is produced as a result of a thermal degradation of the material. Due to the marked effect that the  $\chi_c$  exerts over the final properties of P(3HB-co-3HHx), the use of a cooling fan and temperature of the hot bed are key to the final properties of the material. A slow cooling leads to an increase in the  $\chi_c$  that promotes the formation of internal cracks that finally weaken the material.

The introduction of nHA has a clear effect that increases both stiffness and brittleness of the P(3HB-co-3HHx) matrix in samples obtained by injection. It is for this reason that the interest of this material lies on the osteoconductive behavior that the incorporation of nanoparticles provides it with, which helps the bone regeneration process of the patient. This effect can be observed at room temperature with the results of the tensile tests and in dynamic thermal conditions in the DMTA results. The incorporation of nHA allows to slightly improve the thermal stability of the material and it also provides it with a nucleating effect that allows to increase the  $\chi_c$  of the sample. The dispersion of the additive is a key factor during processing since the incorporation of nHA is related to the formation of agglomerates within the polymeric structure that provide a negative effect over the final properties of the nanocomposites. It is for this reason that especial attention must be put in the processing in order to achieve a correct dispersion.



Moreover, these same formulations were considered for its use in AM. In a first stage, the effect of the different thermal cycles to which this material is submitted during processing was analysed, from a first extrusion cycle for the mixing of the polymer with the additives, thereafter a process for obtaining the filament and finally the printing process. It was observed that each cycle leads to a slight loss in the properties of the material due to a reduction in the molecular weight of the polymer chains. Tensile test samples were made with the filaments of P(3HB-co-3HHx) with nHA, which were characterized. The samples with a raster angle aligned with the stress direction and less amounts of osteoconductive additive achieved similar or even better results than the injected samples. Additionally, the processing of scaffolds was carried out, which were subjected to a degradation process in a PBS for 8 weeks in order to determine the degradation of the polymer. After the 8 weeks a reduction in the compression mechanical properties of the scaffolds and the superficial deposition of hydroxyapatite present in the saline solution were observed, which are signs of an improvement in the biocompatibility of the material.

#### **IV.1.3. With regard to the development of environmentally friendly formulations of polylactide for injection moulding and 3D printing.**

The use of an itaconic acid derivative as it is DBI has proved to be a perfect candidate for the plasticizing of PLA. By means of the incorporation of this additive it is possible to get a polymer with high ductile properties, with an elongation at break of 322 % and a reduction on its stiffness that directly leads to the material not being able to be tested under impact conditions. This reduction in the stiffness of PLA is also detected in the tensile tests in which the tensile modulus reaches very low values similar to those of low density polyethylene but using totally natural raw materials. The plasticizing effect is associated with thermal changes in the material, as it is a clear diminishing in the  $T_g$  of the material, as it was observed through DSC and DMTA. This thermal transition was close to room temperature and therefore it provided PLA with a ductile behavior. The introduction of the aforementioned plasticizer is ascribed to a loss in thermal stability that can be sorted out by reducing the working temperature. This fact is possible due to an increase in the fluidity of the material.

The use of different infill patterns in AM has a relevant impact over the final properties of the sample and the printing time. On the one hand, it is advisable to use a linear pattern in order to reduce the printing times, reducing their complexity and therefore the required time to print it. On the other hand, in order to achieve the best

mechanical properties, it interesting to use the infill pattern with a honeycomb structure.

The design and validation of a PLA fixation plate obtained through AM for bone fixation in case of femur breakage is proposed as an alternative to substitute the current titanium plates. Due to the difference in the mechanical behavior of both materials, a resizing of the plate is required in order to reach a suitable resistance. The advantage that the use of PLA has the capacity to be progressively reabsorbed in the human body. This implies that a second surgery is not needed to remove the prosthesis.

### **IV.2 General conclusions.**

As final conclusions for the present thesis, it is highlighted through the different developed works that new polymer formulations have been proposed which can be employed in different industrial sectors as it could be the packaging sector for the plasticized aliphatic polyesters with improved ductile properties or the developed binary blend. Another sector that could be the objective of this thesis is the furniture sector, in which the developed WPC poses great potential, substituting products typically made of wood.

Finally, the medical sector could also make use of the materials herein developed through the use of hydroxyapatite in order to facilitate bone regeneration. Additionally, the study of printing parameters such as temperatures or filling patterns in AM can have a great implication in the final properties of those materials. In medicine, AM is gaining especial importance, an example of this is the interest for the development of new medical devices produced through 3D printing.

## **VI. REFERENCES.**



1. Vasile, C.; Pamfil, D.; Stoleru, E.; Baican, M. New developments in medical applications of hybrid hydrogels containing natural polymers. *Molecules* **2020**, *25*, 1539–1607 doi: 10.3390/molecules25071539.
2. Kalirajan, C.; Dukle, A.; Nathanael, A.J.; Oh, T.-H.; Manivasagam, G. A critical review on polymeric biomaterials for biomedical applications. *Polymers* **2021**, *13*, 3015–3042 doi: 10.3390/polym13173015.
3. Rebelo, R.; Fernandes, M.; Fangueiro, R. Biopolymers in medical implants: a brief review. *Procedia engineering* **2017**, *3*, 33–99 doi: 10.1016/j.proeng.2017.07.034.
4. Das, T.K.; Prusty, S. Review on conducting polymers and their applications. *Polymer-plastics technology and engineering* **2012**, *51*, 1487–1500 doi: 10.1080/03602559.2012.710697.
5. Guo, Q.; Zhang, X. A review of mechanochromic polymers and composites: from material design strategy to advanced electronics application. *Composites Part B: Engineering* **2021**, *227*, 109434–109452 doi: 10.1016/j.compositesb.2021.109434.
6. Lu, Y.; Shah, K.W.; Xu, J. Synthesis, morphologies and building applications of nanostructured polymers. *Polymers* **2017**, *9*, 506–535 doi: 10.3390/polym9100506.
7. Pendhari, S.S.; Kant, T.; Desai, Y.M. Application of polymer composites in civil construction: a general review. *Composite structures* **2008**, *84*, 114–124 doi: 10.1016/j.compstruct.2007.06.007.
8. Keller, T. Overview of fibre-reinforced polymers in bridge construction. *Structural engineering international* **2002**, *12*, 66–70 doi: 10.2749/101686602777965595.
9. Arefin, A.M.; Khatri, N.R.; Kulkarni, N.; Egan, P.F. Polymer 3D printing review: Materials, process, and design strategies for medical applications. *Polymers* **2021**, *13*, 1499–1523 doi: 10.3390/polym13091499.
10. Stansbury, J.W.; Idacavage, M.J. 3D printing with polymers: challenges among expanding options and opportunities. *Dental materials* **2016**, *32*, 54–64 doi: 10.1016/j.dental.2015.09.018.
11. Zhou, L.Y.; Fu, J.; He, Y. A review of 3D printing technologies for soft polymer materials. *Advanced Functional Materials* **2020**, *30*, 2000187–2000225 doi: 10.1002/adfm.202000187.
12. Patil, A.; Patel, A.; Purohit, R. An overview of polymeric materials for automotive applications. *Materials Today: Proceedings* **2017**, *4*, 3807–3815 doi: 10.1016/j.matpr.2017.02.278.
13. Wiese, M.; Thiede, S.; Herrmann, C. Rapid manufacturing of automotive polymer series parts: a systematic review of processes, materials and challenges. *Additive manufacturing* **2020**, *36*, 101582–101595 doi: 10.1016/j.addma.2020.101582.
14. Shah, V.; Bhaliya, J.; Patel, G.M.; Deshmukh, K. Advances in polymeric nanocomposites for automotive applications: a review. *Polymers for Advanced Technologies* **2022**, *33*, 3023–3048 doi: 10.1002/pat.5771.

15. Liu, Y.; Du, H.; Liu, L.; Leng, J. Shape memory polymers and their composites in aerospace applications: a review. *Smart materials and structures* **2014**, *23*, 23001–23024 doi: 10.1088/0964-1726/23/2/023001.
16. Bashir, M.; Rajendran, P. A review on electroactive polymers development for aerospace applications. *Journal of Intelligent Material Systems and Structures* **2018**, *29*, 3681–3695 doi: 10.1177/1045389X18798951.
17. Alsabri, A.; Al-Ghamdi, S.G. Carbon footprint and embodied energy of PVC, PE, and PP piping: perspective on environmental performance. *Energy Reports* **2020**, *6*, 364–370 doi: 10.1016/j.egy.2020.11.173.
18. Walker, S.; Rothman, R. Life cycle assessment of bio-based and fossil-based plastic: a review. *Journal of Cleaner Production* **2020**, *261*, 121158–121173 doi: 10.1016/j.jclepro.2020.121158.
19. Benavides, P.T.; Lee, U.; Zarè-Mehrjerdi, O. Life cycle greenhouse gas emissions and energy use of polylactic acid, bio-derived polyethylene, and fossil-derived polyethylene. *Journal of Cleaner Production* **2020**, *277*, 124010–124021 doi: 10.1016/j.jclepro.2020.124010.
20. Hong, M.; Chen, E.Y.X. Chemically recyclable polymers: a circular economy approach to sustainability. *Green Chemistry* **2017**, *19*, 3692–3706 doi: 10.1039/c7gc01496a.
21. Ramesh, P.; Vinodh, S. State of art review on life cycle assessment of polymers. *International Journal of Sustainable Engineering* **2020**, *13*, 411–422 doi: 10.1080/19397038.2020.1802623.
22. Huang, S.J. Polymer Waste Management–Biodegradation, Incineration, and Recycling. *Journal of Macromolecular Science, Part A* **1995**, *32*, 593–597 doi: 10.1080/10601329508010272.
23. Xayachak, T.; Haque, N.; Parthasarathy, R.; King, S.; Emami, N.; Lau, D.; Pramanik, B.K. Pyrolysis for plastic waste management: an engineering perspective. *Journal of Environmental Chemical Engineering* **2022**, *10*, 108865–108882 doi: 10.1016/j.jece.2022.108865.
24. Flizikowski, J.; Kruszelnicka, W.; Macko, M. The development of efficient contaminated polymer materials shredding in recycling processes. *Polymers* **2021**, *13*, 1–44 doi: 10.3390/polym13050713.
25. Fernandes, M.; Salvador, A.; Alves, M.M.; Vicente, A.A. Factors affecting polyhydroxyalkanoates biodegradation in soil. *Polymer Degradation and Stability* **2020**, *182*, 109408–109422 doi: 10.1016/j.polymdegradstab.2020.109408.
26. Yakabe, Y.; Nohara, K.; Hara, T.; Fujino, Y. Factors affecting the biodegradability of biodegradable polyester in soil. *Chemosphere* **1992**, *25*, 1879–1888 doi: 10.1016/0045-6535(92)90027-O.
27. Pischedda, A.; Tosin, M.; Degli-Innocenti, F. Biodegradation of plastics in soil: the effect of temperature. *Polymer Degradation and Stability* **2019**, *170*, 109017–109024 doi: 10.1016/j.polymdegradstab.2019.109017.

28. Lotto, N.T.; Calil, M.R.; Guedes, C.G.F.; Rosa, D.S. The effect of temperature on the biodegradation test. *Selected Papers Presented at Symposia B and F at the Brazilian* **2004**, *24*, 659–662 doi: 10.1016/j.msec.2004.08.009.
29. Grima, S.; Bellon-Maurel, V.; Feuilloley, P.; Silvestre, F. Aerobic biodegradation of polymers in solid-state conditions: a review of environmental and physicochemical parameter settings in laboratory simulations. *Journal of Polymers and the Environment* **2000**, *8*, 183–195 doi: 10.1023/A:1015297727244.
30. Kijchavengkul, T.; Auras, R.; Rubino, M.; Selke, S.; Ngouajio, M.; Fernandez, R.T. Biodegradation and hydrolysis rate of aliphatic aromatic polyester. *Polymer Degradation and Stability* **2010**, *95*, 2641–2647 doi: 10.1016/j.polymdegradstab.2010.07.018.
31. Göpferich, A.; Tessmar, J. Polyanhydride degradation and erosion. *Advanced Drug Delivery Reviews* **2002**, *54*, 911–931 doi: 10.1016/S0169-409X(02)00051-0.
32. Zahn, D. On the role of water in amide hydrolysis. *European Journal of Organic Chemistry* **2004**, *2004*, 4020–4023 doi: 10.1002/ejoc.200400316.
33. Mandal, P.; Jönec, R. Polycaprolactone: a biodegradable polymer with its application in the field of self-assembly study. *Journal of Macromolecular Science, Part A: Pure and Applied Chemistry* **2020**, *58*, 111–129 doi: 10.1080/10601325.2020.1831392.
34. Webb, A.R.; Yang, J.; Ameer, G.A. Biodegradable polyester elastomers in tissue engineering. *Expert Opinion on Biological Therapy* **2004**, *4*, 801–812 doi: 10.1517/14712598.4.6.801.
35. Kawai, F.; Hu, X. Biochemistry of microbial polyvinyl alcohol degradation. *Applied Microbiology and Biotechnology* **2009**, *84*, 227–237 doi: 10.1007/s00253-009-2113-6.
36. Gupta, A.P.; Kumar, V. New emerging trends in synthetic biodegradable polymers – polylactide: a critique. *European Polymer Journal* **2007**, *43*, 4053–4074 doi: 10.1016/j.eurpolymj.2007.06.045.
37. Mtibe, A.; Motloug, M.P.; Bandyopadhyay, J.; Ray, S.S. Synthetic biopolymers and their composites: advantages and limitations – an overview. *Macromolecular Rapid Communications* **2021**, *42*, 2100130–2100158 doi: 10.1002/marc.202100130.
38. Garcia-Garcia, D.; Carbonell-Verdu, A.; Jordá-Vilaplana, A.; Balart, R.; Garcia-Sanoguera, D. Development and characterization of green composites from bio-based polyethylene and peanut shell. *Journal of Applied Polymer Science* **2016**, *133*, 43940–43952 doi: 10.1002/app.43940.
39. Samal, S.K.; Fernandes, E.G.; Corti, A.; Chiellini, E. Bio-based polyethylene-lignin composites containing a pro-oxidant/pro-degradant additive: preparation and characterization. *Journal of Polymers and the Environment* **2014**, *22*, 58–68 doi: 10.1007/s10924-013-0620-0.

40. Siracusa, V.; Blanco, I. Bio-polyethylene (bio-PE), bio-polypropylene (bio-PP) and bio-poly(ethylene terephthalate) (bio-PET): recent developments in bio-based polymers analogous to petroleum-derived ones for packaging and engineering applications. *Polymers* **2020**, *12*, 1641–1658 doi: 10.3390/APP10155029.
41. Winnacker, M.; Rieger, B. Biobased polyamides: recent advances in basic and applied research. *Macromolecular rapid communications* **2016**, *37*, 1391–1413 doi: 10.1002/marc.201600181.
42. Ahmadi, R.; Ullah, A. Synthesis and characterization of unsaturated biobased-polyamides from plant oil. *ACS Sustainable Chemistry and Engineering* **2020**, *8*, 8049–8058 doi: 10.1021/acssuschemeng.0c02692.
43. Hauenstein, O.; Agarwal, S.; Greiner, A. Bio-based polycarbonate as synthetic toolbox. *Nature Communications* **2016**, *7*, 11862–11869 doi: 10.1038/ncomms11862.
44. Garrison, M.D.; Storch, P.J.; Eck, W.S.; Adams, V.H.; Fedick, P.W.; Harvey, B.G. BPA-free high-performance sustainable polycarbonates derived from non-estrogenic bio-based phenols. *Green Chemistry* **2021**, *23*, 8016–8029 doi: 10.1039/d1gc01500a.
45. Chen, L.; Pelton, R.E.O.; Smith, T.M. Comparative life cycle assessment of fossil and bio-based polyethylene terephthalate (PET) bottles. *Journal of Cleaner Production* **2016**, *137*, 667–676 doi: 10.1016/j.jclepro.2016.07.094.
46. Liptow, C.; Tillman, A.M. A comparative life cycle assessment study of polyethylene based on sugarcane and crude oil. *Journal of Industrial Ecology* **2012**, *16*, 420–435 doi: 10.1111/j.1530-9290.2011.00405.x.
47. Morschbacker, A. Bio-ethanol based ethylene. *Polymer Reviews* **2009**, *49*, 79–84 doi: 10.1080/15583720902834791.
48. Chen, G.Q.; Patel, M.K. Plastics derived from biological sources: present and future: a technical and environmental review. *Chemical Reviews* **2012**, *112*, 2082–2099 doi: 10.1021/cr200162d.
49. Miller, K.K.; Zhang, P.; Nishizawa-Brennen, Y.; Frost, J.W. Synthesis of biobased terephthalic acid from cycloaddition of isoprene with acrylic acid. *ACS Sustainable Chemistry and Engineering* **2014**, *2*, 2053–2056 doi: 10.1021/sc5003038.
50. Tachibana, Y.; Kimura, S.; Kasuya, K.I. Synthesis and verification of biobased terephthalic acid from furfural. *Scientific Reports* **2015**, *5*, 8249–8254 doi: 10.1038/srep08249.
51. Ma, Y.; Liu, H.; Wu, J.; Yuan, L.; Wang, Y.; Du, X.; Wang, R.; Marwa, P.W.; Petlulu, P.; Chen, X., et al. The adverse health effects of bisphenol A and related toxicity mechanisms. *Environmental Research* **2019**, *176*, 108575–108592 doi: 10.1016/j.envres.2019.108575.
52. Yum, S.; Kim, H.; Seo, Y. Synthesis and characterization of isosorbide based polycarbonates. *Polymer* **2019**, *179*, 121685–121691 doi: 10.1016/j.polymer.2019.121685.



- 
53. Yang, H.S.; Cho, S.; Lee, M.; Eom, Y.; Chae, H.G.; Park, S.A.; Jang, M.; Oh, D.X.; Hwang, S.Y.; Park, J. Preparation of sustainable fibers from isosorbide: merits over bisphenol-a based polysulfone. *Materials and Design* **2021**, *198*, 109284–109293 doi: 10.1016/j.matdes.2020.109284.
54. Louw, J.; Farzad, S.; Görgens, J.F. Polyethylene furanoate: techno-economic analysis of biobased production. *Biofuels, Bioproducts and Biorefining* **2022**, *17*, 1–18 doi: 10.1002/bbb.2430.
55. Rosenboom, J.G.; Hohl, D.K.; Fleckenstein, P.; Storti, G.; Morbidelli, M. Bottle-grade polyethylene furanoate from ring-opening polymerisation of cyclic oligomers. *Nature Communications* **2018**, *9*, 2701–2708 doi: 10.1038/s41467-018-05147-y.
56. Kunamaneni, S. Bioplastics innovation: commercialization strategies for polyethylene furanoate (PEF) and polyhydroxy alkanates (PHA). *Biofuels, Bioproducts and Biorefining* **2022**, *17*, 1–16 doi: 10.1002/bbb.2438.
57. Kaikade, D.S.; Sabnis, A.S. Polyurethane foams from vegetable oil-based polyols: a review. *Polymer Bulletin* **2022**, *11*, 1–23 doi: 10.1007/s00289-022-04155-9.
58. Biswas, A.; Cheng, H.N.; Kim, S.; Appell, M.; Boddu, V.; Alves, C.R.; Furtado, R.F. Preparation of sorbitol-based polyurethanes and their semi-interpenetrating polymer networks. *Journal of Applied Polymer Science* **2019**, *136*, 47602–47610 doi: 10.1002/app.47602.
59. Khandaray, J.C.; Gite, V.V. Fully biobased polyester polyols derived from renewable resources toward preparation of polyurethane and their application for coatings. *Journal of Applied Polymer Science* **2019**, *136*, 47558–47567 doi: 10.1002/app.47558.
60. He, J.; Song, L.; Wang, Z. The conversion of castor oil to a series of functional polyamides inspired by natural silks. *Industrial Crops and Products* **2022**, *181*, 114852–114860 doi: 10.1016/j.indcrop.2022.114852.
61. Martino, L.; Basilissi, L.; Farina, H.; Ortenzi, M.A.; Zini, E.; Di Silvestro, G.; Scandola, M. Bio-based polyamide 11: synthesis, rheology and solid-state properties of star structures. *European Polymer Journal* **2014**, *59*, 69–77 doi: 10.1016/j.eurpolymj.2014.07.012.
62. Chakraborty, I.; Chatterjee, K. Polymers and composites derived from castor oil as sustainable materials and degradable biomaterials: current status and emerging trends. *Biomacromolecules* **2020**, *21*, 4639–4662 doi: 10.1021/acs.biomac.0c01291.
63. Ma, W.; Chen, K.; Li, Y.; Hao, N.; Wang, X.; Ouyang, P. Advances in cadaverine bacterial production and its applications. *Engineering* **2017**, *3*, 308–317 doi: 10.1016/J.ENG.2017.03.012.
64. Froidevaux, V.; Negrell, C.; Caillol, S.; Pascault, J.P.; Boutevin, B. Biobased amines: from synthesis to polymers; present and future. *Chemical Reviews* **2016**, *116*, 14181–14224 doi: 10.1021/acs.chemrev.6b00486.

65. Hocker, S.; Rhudy, A.K.; Ginsburg, G.; Kranbuehl, D.E. Polyamide hydrolysis accelerated by small weak organic acids. *Polymer* **2014**, *55*, 5057–5064 doi: 10.1016/j.polymer.2014.08.010.
66. Deshoules, Q.; Le Gall, M.; Dreanno, C.; Arhant, M.; Priour, D.; Le Gac, P.Y. Modelling pure polyamide 6 hydrolysis: influence of water content in the amorphous phase. *Polymer Degradation and Stability* **2021**, *183*, 109435–109443 doi: 10.1016/j.polymdegradstab.2020.109435.
67. Basu, A.; Domb, A.J. Recent advances in polyanhydride based biomaterials. *Advanced Materials* **2018**, *30*, 1706815–1706825 doi: 10.1002/adma.201706815.
68. Shah, A.A.; Kato, S.; Shintani, N.; Kamini, N.R.; Nakajima–Kambe, T. Microbial degradation of aliphatic and aliphatic–aromatic co-polyesters. *Applied Microbiology and Biotechnology* **2014**, *98*, 3437–3447 doi: 10.1007/s00253-014-5558-1.
69. Peng, S.; Wu, L.; Li, B.G.; Dubois, P. Hydrolytic and compost degradation of biobased PBSF and PBAF copolyesters with 40–60 mol% BF unit. *Polymer Degradation and Stability* **2017**, *146*, 223–228 doi: 10.1016/j.polymdegradstab.2017.07.016.
70. Erbetta, C.D.C.; Viegas, C.C.B.; Freitas, R.F.S.; Sousa, R.G. Synthesis and thermal and chemical characterization of the poly(D,L-lactide-co-glycolide) copolymer. *Polimeros* **2011**, *21*, 376–382 doi: 10.1590/S0104-14282011005000063.
71. In Jeong, S.; Kim, B.S.; Lee, Y.M.; Ihn, K.J.; Kim, S.H.; Kim, Y.H. Morphology of elastic poly(L-lactide-co-ε-caprolactone) copolymers and in vitro and in vivo degradation behavior of their scaffolds. *Biomacromolecules* **2004**, *5*, 1303–1309 doi: 10.1021/bm049921i.
72. Fortelny, I.; Ujcic, A.; Fambri, L.; Slouf, M. Phase structure, compatibility, and toughness of PLA/PCL blends: a review. *Frontiers in Materials* **2019**, *6*, 1–13 doi: 10.3389/fmats.2019.00206.
73. Vacaras, S.; Baciut, M.; Lucaciu, O.; Dinu, C.; Baciut, G.; Crisan, L.; Hedesiu, M.; Crisan, B.; Onisor, F.; Armencea, G., et al. Understanding the basis of medical use of poly-lactide-based resorbable polymers and composites—a review of the clinical and metabolic impact. *Drug Metabolism Reviews* **2019**, *51*, 570–588 doi: 10.1080/03602532.2019.1642911.
74. Luo, Q.; Liu, X.; Li, Z.; Huang, C.; Zhang, W.; Meng, J.; Chang, Z.; Hua, Z. Degradation model of bioabsorbable cardiovascular stents. *PLoS ONE* **2014**, *9*, 110278–110287 doi: 10.1371/journal.pone.0110278.
75. Darie-Niță, R.N.; Râpă, M.; Frackowiak, S. Special features of polyester-based materials for medical applications. *Polymers* **2022**, *14*, 951–1000 doi: 10.3390/polym14050951.
76. Torres, E.; Dominguez-Candela, I.; Castello-Palacios, S.; Vallés-Lluch, A.; Fombuena, V. Development and characterization of polyester and acrylate-based composites with hydroxyapatite and halloysite nanotubes for medical applications. *Polymers* **2020**, *12*, 1703–1716 doi: 10.3390/POLYM12081703.

- 
77. Bergström, J.S.; Hayman, D. An overview of mechanical properties and material modeling of polylactide (PLA) for medical applications. *Annals of Biomedical Engineering* **2016**, *44*, 330–340 doi: 10.1007/s10439-015-1455-8.
78. Alam, F.; Verma, P.; Mohammad, W.; Teo, J.; Varadarajan, K.M.; Kumar, S. Architected poly(lactic acid)/poly( $\epsilon$ -caprolactone)/halloysite nanotube composite scaffolds enabled by 3D printing for biomedical applications. *Journal of Materials Science* **2021**, *56*, 14070–14083 doi: 10.1007/s10853-021-06145-0.
79. Yeo, T.; Ko, Y.G.; Kim, E.J.; Kwon, O.K.; Chung, H.Y.; Kwon, O.H. Promoting bone regeneration by 3D-printed poly(glycolic acid)/hydroxyapatite composite scaffolds. *Journal of Industrial and Engineering Chemistry* **2021**, *94*, 343–351 doi: 10.1016/j.jiec.2020.11.004.
80. El-Naggar, M.E.; Othman, S.I.; Allam, A.A.; Morsy, O.M. Synthesis, drying process and medical application of polysaccharide-based aerogels. *International Journal of Biological Macromolecules* **2020**, *145*, 1115–1128 doi: 10.1016/j.ijbiomac.2019.10.037.
81. Elmowafy, E.; Abdal-Hay, A.; Skouras, A.; Tiboni, M.; Casettari, L.; Guarino, V. Polyhydroxyalkanoate (PHA): applications in drug delivery and tissue engineering. *Expert Review of Medical Devices* **2019**, *16*, 467–482 doi: 10.1080/17434440.2019.1615439.
82. Ali, I.; Jamil, N. Polyhydroxyalkanoates: current applications in the medical field. *Frontiers in Biology* **2016**, *11*, 19–27 doi: 10.1007/s11515-016-1389-z.
83. De Frates, K.; Markiewicz, T.; Gallo, P.; Rack, A.; Weyhmiller, A.; Jarmusik, B.; Hu, X. Protein polymer-based nanoparticles: fabrication and medical applications. *International Journal of Molecular Sciences* **2018**, *19*, 1717–1737 doi: 10.3390/ijms19061717.
84. Wang, J.; Tavakoli, J.; Tang, Y. Bacterial cellulose production, properties and applications with different culture methods – a review. *Carbohydrate Polymers* **2019**, *219*, 63–76 doi: 10.1016/j.carbpol.2019.05.008.
85. Moon, R.J.; Martini, A.; Nairn, J.; Simonsen, J.; Youngblood, J. Cellulose nanomaterials review: structure, properties and nanocomposites. *Chemical Society Reviews* **2011**, *40*, 3941–3994 doi: 10.1039/c0cs00108b.
86. Nechyporchuk, O.; Belgacem, M.N.; Bras, J. Production of cellulose nanofibrils: a review of recent advances. *Industrial Crops and Products* **2016**, *93*, 2–25 doi: 10.1016/j.indcrop.2016.02.016.
87. Singh, D.K.; Ray, A.R. Biomedical applications of chitin, chitosan, and their derivatives. *Journal of Macromolecular Science – Reviews in Macromolecular Chemistry and Physics* **2000**, *40*, 69–83 doi: 10.1081/MC-100100579.
88. Gopinath, V.; Saravanan, S.; Al-Maleki, A.R.; Ramesh, M.; Vadivelu, J. A review of natural polysaccharides for drug delivery applications: special focus on cellulose, starch and glycogen. *Biomedicine and Pharmacotherapy* **2018**, *107*, 96–108 doi: 10.1016/j.biopha.2018.07.136.

89. Singhvi, M.S.; Zinjarde, S.S.; Gokhale, D.V. Polylactic acid: synthesis and biomedical applications. *Journal of Applied Microbiology* **2019**, *127*, 1612–1626 doi: 10.1111/jam.14290.
90. Suriyamongkol, P.; Weselake, R.; Narine, S.; Moloney, M.; Shah, S. Biotechnological approaches for the production of polyhydroxyalkanoates in microorganisms and plants – a review. *Biotechnology Advances* **2007**, *25*, 148–175 doi: 10.1016/j.biotechadv.2006.11.007.
91. Grigore, M.E.; Grigorescu, R.M.; Iancu, L.; Ion, R.M.; Zaharia, C.; Andrei, E.R. Methods of synthesis, properties and biomedical applications of polyhydroxyalkanoates: a review. *Journal of Biomaterials Science, Polymer Edition* **2019**, *30*, 695–712 doi: 10.1080/09205063.2019.1605866.
92. McAdam, B.; Fournet, M.B.; McDonald, P.; Mojicevic, M. Production of polyhydroxybutyrate (PHB) and factors impacting its chemical and mechanical characteristics. *Polymers* **2020**, *12*, 1–20 doi: 10.3390/polym12122908.
93. Avella, M.; Martuscelli, E.; Raimo, M. Review properties of blends and composites based on poly(3-hydroxy)butyrate (PHB) and poly(3-hydroxybutyrate-hydroxyvalerate) (PHBV) copolymers. *Journal of Materials Science* **2000**, *35*, 523–545 doi: 10.1023/A:1004740522751.
94. Chen, Y.; Hung, S.T.; Chou, E.; Wu, H.S. Review of polyhydroxyalkanoates materials and other biopolymers for medical applications. *Mini-Reviews in Organic Chemistry* **2018**, *15*, 105–121 doi: 10.2174/1570193X146661707211503036.
95. Butt, F.I.; Muhammad, N.; Hamid, A.; Moniruzzaman, M.; Sharif, F. Recent progress in the utilization of biosynthesized polyhydroxyalkanoates for biomedical applications – Review. *International Journal of Biological Macromolecules* **2018**, *120*, 1294–1305 doi: 10.1016/j.ijbiomac.2018.09.002.
96. Bugnicourt, E.; Cinelli, P.; Lazzeri, A.; Alvarez, V. Polyhydroxyalkanoate (PHA): review of synthesis, characteristics, processing and potential applications in packaging. *Express Polymer Letters* **2014**, *8*, 791–808 doi: 10.3144/expresspolymlett.2014.82.
97. Srubar, W.V.; Wright, Z.C.; Tsui, A.; Michel, A.T.; Billington, S.L.; Frank, C.W. Characterizing the effects of ambient aging on the mechanical and physical properties of two commercially available bacterial thermoplastics. *Polymer Degradation and Stability* **2012**, *97*, 1922–1929 doi: 10.1016/j.polymdegradstab.2012.04.011.
98. Wang, S.; Chen, W.; Xiang, H.; Yang, J.; Zhou, Z.; Zhu, M. Modification and potential application of short-chain-length polyhydroxyalkanoate (scl-PHA). *Polymers* **2016**, *8*, 273–301 doi: 10.3390/polym8080273.
99. Tan, D.; Nano, Y.; Tong, Y.; Chen, G.Q. Grand challenges for Industrializing polyhydroxyalkanoates (PHAs). *Trends in Biotechnology* **2021**, *39*, 953–963 doi: 10.1016/j.tibtech.2020.11.010.
100. Kaur, L.; Khajuria, R.; Parihar, L.; Dimpal Singh, G. Polyhydroxyalkanoates: biosynthesis to commercial production– a review. *Journal of Microbiology, Biotechnology and Food Sciences* **2017**, *6*, 1098–1106 doi: 10.15414/jmbfs.2017.6.4.1098–1106.

101. Qi, Y.; Chilkoti, A. Growing polymers from peptides and proteins: a biomedical perspective. *Polymer Chemistry* **2014**, *5*, 266–276 doi: 10.1039/c3py01089a.
102. Xi, X.; Pizzi, A.; Gerardin, C.; Liao, J.; Amirou, S.; Abdalla, S. Glutaraldehyde-wheat gluten protein adhesives for wood bonding. *Journal of Adhesion* **2021**, *97*, 88–100 doi: 10.1080/00218464.2019.1630821.
103. Guo, M.; Wang, G. Whey protein polymerisation and its applications in environmentally safe adhesives. *International Journal of Dairy Technology* **2016**, *69*, 481–488 doi: 10.1111/1471-0307.12303.
104. Guo, M.; Wang, G. Milk protein polymer and its application in environmentally safe adhesives. *Polymers* **2016**, *8*, 324–336 doi: 10.3390/polym8090324.
105. Wei, Y.; Yao, J.; Shao, Z.; Chen, X. Water-resistant zein-based adhesives. *ACS Sustainable Chemistry and Engineering* **2020**, *8*, 7668–7679 doi: 10.1021/acssuschemeng.0c01179.
106. Avinc, O.; Khoddami, A. Overview of poly(lactic acid)(PLA) fibre. *Fibre Chemistry* **2009**, *41*, 391–401 doi: 10.1007/s10692-010-9213-z.
107. Capuana, E.; Lopresti, F.; Ceraulo, M.; La Carrubba, V. Poly-L-lactic acid (PLLA)-based biomaterials for regenerative medicine: a review on processing and applications. *Polymers* **2022**, *14*, 1153–1182 doi: 10.3390/polym14061153.
108. Farah, S.; Anderson, D.G.; Langer, R. Physical and mechanical properties of PLA, and their functions in widespread applications – a comprehensive review. *Advanced Drug Delivery Reviews* **2016**, *107*, 367–392 doi: 10.1016/j.addr.2016.06.012.
109. Petersson, L.; Kvien, I.; Oksman, K. Structure and thermal properties of poly(lactic acid)/cellulose whiskers nanocomposite materials. *Composites Science and Technology* **2007**, *67*, 2535–2544 doi: 10.1016/j.compscitech.2006.12.012.
110. Drieskens, M.; Peeters, R.; Mullens, J.; Franco, D.; Iemstra, P.J.; Hristova-Bogaerds, D.G. Structure versus properties relationship of poly(lactic acid). I. effect of crystallinity on barrier properties. *Journal of Polymer Science, Part B: Polymer Physics* **2009**, *47*, 2247–2258 doi: 10.1002/polb.21822.
111. Morisato, A.; He, Z.; Pinnau, I. Gas permeation properties of poly(alkyl acetylenes). *Proceedings of the 1999 218th ACS National Meeting* **1999**, *2*, MACR-12.
112. Trifol, J.; Plackett, D.; Sillard, C.; Szabo, P.; Bras, J.; Daugaard, A.E. Hybrid poly(lactic acid)/nanocellulose/nanoclay composites with synergistically enhanced barrier properties and improved thermo-mechanical resistance. *Polymer International* **2016**, *65*, 988–995 doi: 10.1002/pi.5154.
113. Koppolu, R.; Lahti, J.; Abitbol, T.; Swerin, A.; Kuusipalo, J.; Toivakka, M. Continuous processing of nanocellulose and polylactic acid into multilayer barrier coatings. *ACS Applied Materials and Interfaces* **2019**, *11*, 11920–11927 doi: 10.1021/acsam.9b00922.
114. Park, K.I.; Xanthos, M. A study on the degradation of polylactic acid in the presence of phosphonium ionic liquids. *Polymer Degradation and Stability* **2009**, *94*, 834–844 doi: 10.1016/j.polymdegradstab.2009.01.030.

115. Codari, F.; Lazzari, S.; Soos, M.; Storti, G.; Morbidelli, M.; Moscatelli, D. Kinetics of the hydrolytic degradation of poly(lactic acid). *Polymer Degradation and Stability* **2012**, *97*, 2460–2466 doi: 10.1016/j.polymdegradstab.2012.06.026.
116. Qi, X.; Ren, Y.; Wang, X. New advances in the biodegradation of poly(lactic acid). *International Biodeterioration & Biodegradation* **2017**, *117*, 215–223 doi: 10.1016/j.ibiod.2017.01.010.
117. Najafi, N.; Heuzey, M.C.; Carreau, P.J.; Wood-Adams, P.M. Control of thermal degradation of polylactide (PLA)–clay nanocomposites using chain extenders. *Polymer Degradation and Stability* **2012**, *97*, 554–565 doi: 10.1016/j.polymdegradstab.2012.01.016.
118. Ahmed, J.; Varshney, S.K. Polylactides–chemistry, properties and green packaging technology: a review. *International Journal of Food Properties* **2011**, *14*, 37–58 doi: 10.1080/10942910903125284.
119. Notta-Cuvier, D.; Odent, J.; Delille, R.; Murariu, M.; Lauro, F.; Raquez, J.M.; Bennani, B.; Dubois, P. Tailoring polylactide (PLA) properties for automotive applications: effect of addition of designed additives on main mechanical properties. *Polymer Testing* **2014**, *36*, 1–9 doi: 10.1016/j.polymertesting.2014.03.007.
120. Morales, A.P.; Güemes, A.; Fernandez-Lopez, A.; Valero, V.C.; de La Rosa Llano, S. Bamboo–polylactic acid (PLA) composite material for structural applications. *Materials* **2017**, *10*, 1286–1308 doi: 10.3390/ma10111286.
121. Arockiam, A.J.; Subramanian, K.; Padmanabhan, R.G.; Selvaraj, R.; Bagal, D.K.; Rajesh, S. A review on PLA with different fillers used as a filament in 3D printing. *2nd International Conference on Functional Materials, Manufacturing and Performances, ICFMMP 2021* **2021**, *50*, 2057–2064 doi: 10.1016/j.matpr.2021.09.413.
122. Mehrpouya, M.; Vahabi, H.; Janbaz, S.; Darafsheh, A.; Mazur, T.R.; Ramakrishna, S. 4D printing of shape memory polylactic acid (PLA). *Polymer* **2021**, *230*, 124080–124097 doi: 10.1016/j.polymer.2021.124080.
123. Lou, C.W.; Yao, C.H.; Chen, Y.S.; Hsieh, T.C.; Lin, J.H.; Hsing, W.H. Manufacturing and properties of PLA absorbable surgical suture. *Textile Research Journal* **2008**, *78*, 958–965 doi: 10.1177/0040517507087856.
124. Felfel, R.M.; Ahmed, I.; Parsons, A.J.; Haque, P.; Walker, G.S.; Rudd, C.D. Investigation of crystallinity, molecular weight change, and mechanical properties of PLA/PBG bioresorbable composites as bone fracture fixation plates. *Journal of Biomaterials Applications* **2012**, *26*, 765–789 doi: 10.1177/0885328210384532.
125. Esmailzadeh, J.; Hesarakhi, S.; Ebrahimzadeh, M.H.; Asghari, G.H.; Kachooei, A.R. Creep behavior of biodegradable triple–component nanocomposites based on PLA/PCL/bioactive glass for ACL interference screws. *Archives of Bone and Joint Surgery* **2019**, *7*, 531–537.
126. Grémare, A.; Guduric, V.; Bareille, R.; Heroguez, V.; Latour, S.; L'Heureux, N.; Fricain, J.C.; Catros, S.; Le Nihouannen, D. Characterization of printed PLA scaffolds for bone tissue engineering. *Journal of Biomedical Materials Research – Part A* **2018**, *106*, 887–894 doi: 10.1002/jbm.a.36289.

127. Tyler, B.; Gullotti, D.; Mangraviti, A.; Utsuki, T.; Brem, H. Polylactic acid (PLA) controlled delivery carriers for biomedical applications. *Advanced drug delivery reviews* **2016**, *107*, 163–175 doi: 10.1016/j.addr.2016.06.018.
128. Suriyamongkol, P.; Weselake, R.; Narine, S.; Moloney, M.; Shah, S. Biotechnological approaches for the production of polyhydroxyalkanoates in microorganisms and plants – a review. *Biotechnology advances* **2007**, *25*, 148–175 doi: 10.1016/j.biotechadv.2006.11.007.
129. Keshavarz, T.; Roy, I. Polyhydroxyalkanoates: bioplastics with a green agenda. *Current opinion in microbiology* **2010**, *13*, 321–326 doi: 10.1016/j.mib.2010.02.006.
130. Anjum, A.; Zuber, M.; Zia, K.M.; Noreen, A.; Anjum, M.N.; Tabasum, S. Microbial production of polyhydroxyalkanoates (PHAs) and its copolymers: a review of recent advancements. *International journal of biological macromolecules* **2016**, *89*, 161–174 doi: 10.1016/j.ijbiomac.2016.04.069.
131. Reddy, C.; Ghai, R.; Kalia, V.C. Polyhydroxyalkanoates: an overview. *Bioresource technology* **2003**, *87*, 137–146 doi: 10.1016/S0960-8524(02)00212-2.
132. Koller, M.; Gasser, I.; Schmid, F.; Berg, G. Linking ecology with economy: Insights into polyhydroxyalkanoate-producing microorganisms. *Engineering in Life Sciences* **2011**, *11*, 222–237 doi: 10.1002/elsc.201000190.
133. Philip, S.; Jönec, T.; Roy, I. Polyhydroxyalkanoates: biodegradable polymers with a range of applications. *Journal of Chemical Technology and Biotechnology* **2007**, *82*, 233–247 doi: 10.1002/jctb.1667.
134. Możejko-Ciesielska, J.; Kiewisz, R. Bacterial polyhydroxyalkanoates: still fabulous? *Microbiological Research* **2016**, *192*, 271–282 doi: 10.1016/j.micres.2016.07.010.
135. Choonut, A.; Prasertsan, P.; Klomklao, S.; Sangkharak, K. Study on mcl-PHA production by novel thermotolerant Gram-positive isolate. *Journal of Polymers and the Environment* **2020**, *28*, 2410–2421 doi: 10.1007/s10924-020-01779-8.
136. Davis, R.; Kataria, R.; Cerrone, F.; Woods, T.; Kenny, S.; O'Donovan, A.; Guzik, M.; Shaikh, H.; Duane, G.; Gupta, V.K., et al. Conversion of grass biomass into fermentable sugars and its utilization for medium chain length polyhydroxyalkanoate (mcl-PHA) production by *Pseudomonas* strains. *Bioresource Technology* **2013**, *150*, 202–209 doi: 10.1016/j.biortech.2013.10.001.
137. Eraslan, K.; Aversa, C.; Nofar, M.; Barletta, M.; Gisario, A.; Salehiyan, R.; Goksu, Y.A. Poly(3-hydroxybutyrate-co-3-hydroxyhexanoate) (PHBH): synthesis, properties, and applications – a review. *European Polymer Journal* **2022**, *167*, 111044–111059 doi: 10.1016/j.eurpolymj.2022.111044.
138. Meereboer, K.W.; Misra, M.; Mohanty, A.K. Review of recent advances in the biodegradability of polyhydroxyalkanoate (PHA) bioplastics and their composites. *Green Chemistry* **2020**, *22*, 5519–5558 doi: 10.1039/d0gc01647k.

139. Gopi, S.; Kontopoulou, M.; Ramsay, B.A.; Ramsay, J.A. Manipulating the structure of medium-chain-length polyhydroxyalkanoate (mcl-PHA) to enhance thermal properties and crystallization kinetics. *International Journal of Biological Macromolecules* **2018**, *119*, 1248–1255 doi: 10.1016/j.ijbiomac.2018.08.016.
140. Galego, N.; Rozsa, C. Thermal decomposition of some poly( $\beta$ -hydroxyalkanoates). *Polymer International* **1999**, *48*, 1202–1204 doi: 10.1002/(SICI)1097-0126(199912)48:12<1202::AID-PI223>3.0.CO;2-D.
141. Kai, D.; Loh, X.J. Polyhydroxyalkanoates: chemical modifications toward biomedical applications. *ACS Sustainable Chemistry and Engineering* **2014**, *2*, 106–119 doi: 10.1021/sc400340p.
142. Carrasco, F.; Dionisi, D.; Martinelli, A.; Majone, M. Thermal stability of polyhydroxyalkanoates. *Journal of Applied Polymer Science* **2006**, *100*, 2111–2121 doi: 10.1002/app.23586.
143. Keskin, G.; Klzll, G.; Bechelany, M.; Pochat-Bohatier, C.; Öner, M. Potential of polyhydroxyalkanoate (PHA) polymers family as substitutes of petroleum based polymers for packaging applications and solutions brought by their composites to form barrier materials. *Pure and Applied Chemistry* **2017**, *89*, 1841–1848 doi: 10.1515/pac-2017-0401.
144. Prudnikova, S.V.; Boyandin, A.N.; Kalacheva, G.S.; Sinskey, A.J. Degradable polyhydroxyalkanoates as herbicide carriers. *Journal of Polymers and the Environment* **2013**, *21*, 675–682 doi: 10.1007/s10924-012-0561-z.
145. R Sodian, J.S.S., D P Martin, A Egozy, U Stock, J E Mayer Jr, J P Vacanti. Technical report: fabrication of a trileaflet heart valve scaffold from a polyhydroxyalkanoate biopolyester for use in tissue engineering. *Tissue Engineering* **2000**, *6*, 183–188 doi: 10.1089/107632700320793.
146. Prakash, P.; Lee, W.H.; Ching, Y.; Wong, H.S.J.; Parumasivam, T. Advances in polyhydroxyalkanoate nanocarriers for effective drug delivery: an overview and challenges. *Nanomaterials* **2022**, *12*, 175–195 doi: 10.3390/nano12010175.
147. Pramanik, N.; Mitra, T.; Khamrai, M.; Bhattacharyya, A.; Mukhopadhyay, P.; Gnanamani, A.; Basu, R.K.; Kundu, P.P. Characterization and evaluation of curcumin loaded guar gum/polyhydroxyalkanoates blend films for wound healing applications. *RSC Advances* **2015**, *5*, 63489–63501 doi: 10.1039/c5ra10114j.
148. Pulingam, T.; Appaturi, J.N.; Parumasivam, T.; Ahmad, A.; Sudesh, K. Biomedical applications of polyhydroxyalkanoate in tissue engineering. *Polymers* **2022**, *14*, 2141–2165 doi: 10.3390/polym14112141.
149. Tashjian, R.Z.; Kolz, C.W.; Suter, T.; Henninger, H.B. Biomechanics of polyhydroxyalkanoate mesh-augmented single-row rotator cuff repairs. *American journal of orthopedics* **2016**, *45*, 527–533.
150. Puthumana, M.; Santhana Gopala Krishnan, P.; Nayak, S.K. Chemical modifications of PLA through copolymerization. *International Journal of Polymer Analysis and Characterization* **2020**, *25*, 634–648 doi: 10.1080/1023666X.2020.1830650.



151. Lee, I.; Panthani, T.R.; Bates, F.S. Sustainable poly(lactide-*b*-butadiene) multiblock copolymers with enhanced mechanical properties. *Macromolecules* **2013**, *46*, 7387–7398 doi: 10.1021/ma401508b.
152. Singh, M.; Kumar, P.; Ray, S.; Kalia, V.C. Challenges and opportunities for customizing polyhydroxyalkanoates. *Indian Journal of Microbiology* **2015**, *55*, 235–249 doi: 10.1007/s12088-015-0528-6.
153. Da Silva, M.A.; Vieira, M.G.A.; Maçumoto, A.C.G.; Beppu, M.M. Polyvinylchloride (PVC) and natural rubber films plasticized with a natural polymeric plasticizer obtained through polyesterification of rice fatty acid. *Polymer Testing* **2011**, *30*, 478–484 doi: 10.1016/j.polymertesting.2011.03.008.
154. Bocqué, M.; Voirin, C.; Lapinte, V.; Caillol, S.; Robin, J.J. Petro-based and bio-based plasticizers: chemical structures to plasticizing properties. *Journal of Polymer Science, Part A: Polymer Chemistry* **2016**, *54*, 11–33 doi: 10.1002/pola.27917.
155. Wypych, G. *Handbook of plasticizers*, 1 ed.; ChemTec Publishing: 2004; Vol. 1.
156. Arrieta, M.P.; Samper, M.D.; López, J.; Jiménez, A. Combined effect of poly(3-hydroxybutyrate) and plasticizers on polylactic acid properties for film Intended for food packaging. *Journal of Polymers and the Environment* **2014**, *22*, 460–470 doi: 10.1007/s10924-014-0654-y.
157. Mekonnen, T.; Mussone, P.; Khalil, H.; Bressler, D. Progress in bio-based plastics and plasticizing modifications. *Journal of Materials Chemistry A* **2013**, *1*, 13379–13398 doi: 10.1039/c3ta12555f.
158. Koning, C.; Van Duin, M.; Pagnouille, C.; Jerome, R. Strategies for compatibilization of polymer blends. *Progress in Polymer Science (Oxford)* **1998**, *23*, 707–757 doi: 10.1016/S0079-6700(97)00054-3.
159. Imre, B.; Pukánszky, B. Compatibilization in bio-based and biodegradable polymer blends. *European Polymer Journal* **2013**, *49*, 1215–1233 doi: 10.1016/j.eurpolymj.2013.01.019.
160. Aji, A.; Utracki, L.A. Interphase and compatibilization of polymer blends. *Polymer Engineering and Science* **1996**, *36*, 1574–1585 doi: 10.1002/pen.10554.
161. Ebadi-Dehaghani, H.; Barikani, M.; Khonakdar, H.A.; Jafari, S.H.; Wagenknecht, U.; Heinrich, G. On O<sub>2</sub> gas permeability of PP/PLA/clay nanocomposites: a molecular dynamic simulation approach. *Polymer Testing* **2015**, *45*, 139–151 doi: 10.1016/j.polymertesting.2015.05.010.
162. Takayama, T.; Todo, M.; Tsuji, H. Effect of annealing on the mechanical properties of PLA/PCL and PLA/PCL/LTI polymer blends. *Journal of the Mechanical Behavior of Biomedical Materials* **2011**, *4*, 255–260 doi: 10.1016/j.jmbbm.2010.10.003.
163. Luyt, A.S.; Gasmi, S. Influence of blending and blend morphology on the thermal properties and crystallization behaviour of PLA and PCL in PLA/PCL blends. *Journal of Materials Science* **2016**, *51*, 4670–4681 doi: 10.1007/s10853-016-9784-z.

164. Arrieta, M.P.; Samper, M.D.; Aldas, M.; López, J. On the use of PLA-PHB blends for sustainable food packaging applications. *Materials* **2017**, *10*, 1008–1034 doi: 10.3390/ma10091008.
165. Luchian-Lupu, A.M.; Zaharescu, T.; Lungulescu, E.M.; Râpă, M.; Iovu, H. Availability of PLA/SIS blends for packaging and medical applications. *Radiation Physics and Chemistry* **2020**, *172*, 108696–108704 doi: 10.1016/j.radphyschem.2020.108696.
166. Lupu, A.M.; Zaharescu, T.; Râpă, M.; Mariş, M.; Iovu, H. Availability of PLA/SIS blends for packaging and medical applications. Part II: contribution of stabilizer agents. *Radiation Physics and Chemistry* **2022**, *201*, 110446–110455 doi: 10.1016/j.radphyschem.2022.110446.
167. Chen, C.C.; Chueh, J.Y.; Tseng, H.; Huang, H.M.; Lee, S.Y. Preparation and characterization of biodegradable PLA polymeric blends. *Biomaterials* **2003**, *24*, 1167–1173 doi: 10.1016/S0142-9612(02)00466-0.
168. D'Anna, A.; Arrigo, R.; Frache, A. PLA/PHB blends: biocompatibilizer effects. *Polymers* **2019**, *11*, 1416–1428 doi: 10.3390/polym11091416.
169. Kervran, M.; Vagner, C.; Cochez, M.; Ponçot, M.; Saeb, M.R.; Vahabi, H. Thermal degradation of polylactic acid (PLA)/polyhydroxybutyrate (PHB) blends: a systematic review. *Polymer Degradation and Stability* **2022**, *201*, 4408–4414 doi: 10.1016/j.polymdegradstab.2022.109995.
170. Feng, F.; Ye, L. Structure and property of polylactide/polyamide blends. *Journal of Macromolecular Science, Part B: Physics* **2010**, *49*, 1117–1127 doi: 10.1080/00222341003609179.
171. García-Masabet, V.; Pérez, O.S.; Cailloux, J.; Abt, T.; Sánchez-Soto, M.; Carrasco, F.; Maspoch, M.L. PLA/PA bio-blends: Induced morphology by extrusion. *Polymers* **2020**, *12*, 10–32 doi: 10.3390/polym12010010.
172. Wang, X.; Peng, S.; Chen, H.; Yu, X.; Zhao, X. Mechanical properties, rheological behaviors, and phase morphologies of high-toughness PLA/PBAT blends by in-situ reactive compatibilization. *Composites Part B: Engineering* **2019**, *173*, 107028–107038 doi: 10.1016/j.compositesb.2019.107028.
173. Ding, Y.; Lu, B.; Wang, P.; Wang, G.; Ji, J. PLA-PBAT-PLA tri-block copolymers: effective compatibilizers for promotion of the mechanical and rheological properties of PLA/PBAT blends. *Polymer Degradation and Stability* **2018**, *147*, 41–48 doi: 10.1016/j.polymdegradstab.2017.11.012.
174. Akrami, M.; Ghasemi, I.; Azizi, H.; Karrabi, M.; Seyedabadi, M. A new approach in compatibilization of the poly(lactic acid)/thermoplastic starch (PLA/TPS) blends. *Carbohydrate Polymers* **2016**, *144*, 254–262 doi: 10.1016/j.carbpol.2016.02.035.
175. Ferri, J.M.; Garcia-Garcia, D.; Sánchez-Nacher, L.; Fenollar, O.; Balart, R. The effect of maleinized linseed oil (MLO) on mechanical performance of poly(lactic acid)-thermoplastic starch (PLA-TPS) blends. *Carbohydrate Polymers* **2016**, *147*, 60–68 doi: 10.1016/j.carbpol.2016.03.082.

- 
176. Homklin, R.; Hongsriphan, N. Mechanical and thermal properties of PLA/PBS cocontinuous blends adding nucleating agent. *10th Eco-Energy and Materials Science and Engineering Symposium, EMSES 2012* **2013**, *34*, 871–879 doi: 10.1016/j.egypro.2013.06.824.
177. Suwanamornlert, P.; Kerddonfag, N.; Sane, A.; Chinsirikul, W.; Zhou, W.; Chonhenchob, V. Poly(lactic acid)/poly(butylene-succinate-co-adipate) (PLA/PBSA) blend films containing thymol as alternative to synthetic preservatives for active packaging of bread. *Food Packaging and Shelf Life* **2020**, *25*, 100515–100527 doi: 10.1016/j.fpsl.2020.100515.
178. Lehtinen, P.; Väisänen, T.; Salmi, M. The Effect of Local heating by laser irradiation for aluminum, deep drawing steel and copper sheets in incremental sheet forming. *Physics Procedia* **2015**, *78*, 312–319 doi: 10.1016/j.phpro.2015.11.045.
179. Calle, M.A.G.; Salmi, M.; Mazzariol, L.M.; Alves, M.; Kujala, P. Additive manufacturing of miniature marine structures for crashworthiness verification: scaling technique and experimental tests. *Marine Structures* **2020**, *72*, 102764–102782 doi: 10.1016/j.marstruc.2020.102764.
180. Delic, M.; Evers, D.R. The effect of additive manufacturing adoption on supply chain flexibility and performance: an empirical analysis from the automotive industry. *International Journal of Production Economics* **2020**, *228*, 107689–107704 doi: 10.1016/j.ijpe.2020.107689.
181. Gibson, I.; Srinath, A. Simplifying medical additive manufacturing: making the surgeon the designer. *Procedia Technology* **2015**, *20*, 237–242 doi: 10.1016/j.protcy.2015.07.038.
182. Kestila, A.; Nordling, K.; Miikkulainen, V.; Kaipio, M.; Tikka, T.; Salmi, M.; Auer, A.; Leskela, M.; Ritala, M. Towards space-grade 3D-printed, ALD-coated small satellite propulsion components for fluidics. *Additive Manufacturing* **2018**, *22*, 31–37 doi: 10.1016/j.addma.2018.04.023.
183. Kretzschmar, N.; Chekurov, S.; Salmi, M.; Tuomi, J. Evaluating the readiness level of additively manufactured digital spare parts: an industrial perspective. *Applied Sciences–Basel* **2018**, *8*, 1837–1853 doi: 10.3390/app8101837.
184. Conner, B.P.; Manogharan, G.P.; Martof, A.N.; Rodomsky, L.M.; Rodomsky, C.M.; Jordan, D.C.; Limperos, J.W. Making sense of 3-D printing: creating a map of additive manufacturing products and services. *Additive Manufacturing* **2014**, *1*, 64–76 doi: 10.1016/j.addma.2014.08.005.
185. Baumers, M.; Dickens, P.; Tuck, C.; Hague, R. The cost of additive manufacturing: machine productivity, economies of scale and technology-push. *Technological Forecasting and Social Change* **2016**, *102*, 193–201 doi: 10.1016/j.techfore.2015.02.015.
186. Ghomi, E.R.; Khosravi, F.; Neisiany, R.E.; Singh, S.; Ramakrishna, S. Future of additive manufacturing in healthcare. *Current Opinion in Biomedical Engineering* **2021**, *17*, 100255–100263 doi: 10.1016/j.cobme.2020.100255.

187. Singh, S.; Ramakrishna, S. Biomedical applications of additive manufacturing: present and future. *Current Opinion in Biomedical Engineering* **2017**, *2*, 105–115 doi: 10.1016/j.cobme.2017.05.006.
188. van Noort, R. The future of dental devices is digital. *Dental Materials* **2012**, *28*, 3–12 doi: 10.1016/j.dental.2011.10.014.
189. Pettersson, A.B.V.; Salmi, M.; Vallittu, P.; Serlo, W.; Tuomi, J.; Makitie, A.A. Main clinical use of additive manufacturing (three-dimensional printing) in Finland restricted to the head and neck area in 2016–2017. *Scandinavian Journal of Surgery* **2020**, *109*, 166–173 doi: 10.1177/1457496919840958.
190. Zadpoor, A.A.; Malda, J. Additive manufacturing of biomaterials, tissues, and organs. *Annals of Biomedical Engineering* **2017**, *45*, 1–11 doi: 10.1007/s10439-016-1719-y.
191. Ballard, D.H.; Mills, P.; Duszak, R.; Weisman, J.A.; Rybicki, F.J.; Woodard, P.K. Medical 3D Printing cost-savings in orthopedic and maxillofacial surgery: cost analysis of operating room time saved with 3D printed anatomic models and surgical guides. *Academic Radiology* **2020**, *27*, 1103–1113 doi: 10.1016/j.acra.2019.08.011.
192. Tack, P.; Victor, J.; Gemmel, P.; Annemans, L. 3D-printing techniques in a medical setting: a systematic literature review. *Biomedical Engineering Online* **2016**, *15*, 115–136 doi: 10.1186/s12938-016-0236-4.
193. Yang, T.; Lin, S.; Xie, Q.; Ouyang, W.; Tan, T.; Li, J.; Chen, Z.; Yang, J.; Wu, H.; Pan, J. Impact of 3D printing technology on the comprehension of surgical liver anatomy. *Surgical Endoscopy* **2019**, *33*, 411–417 doi: 10.1007/s00464-018-6308-8.
194. Salmi, M.; Paloheimo, K.S.; Tuomi, J.; Ingman, T.; Makitie, A. A digital process for additive manufacturing of occlusal splints: a clinical pilot study. *Journal of the Royal Society Interface* **2013**, *10*, 20130203–20130209 doi: 10.1098/rsif.2013.0203.
195. Javaid, M.; Haleem, A. Current status and challenges of additive manufacturing in orthopaedics: an overview. *Journal of clinical orthopaedics and trauma* **2019**, *10*, 380–386 doi: 10.1016/j.jcot.2018.05.008.
196. Lin, L.W.; Fang, Y.F.; Liao, Y.X.; Chen, G.; Gao, C.X.; Zhu, P.Z. 3D printing and digital processing techniques in dentistry: a review of literature. *Advanced Engineering Materials* **2019**, *21*, 1801013–1801041 doi: 10.1002/adem.201801013.
197. Peltola, M.J.; Vallittu, P.K.; Vuorinen, V.; Aho, A.A.; Puntala, A.; Aitasalo, K.M. Novel composite implant in craniofacial bone reconstruction. *European Archives of Oto-Rhino-Laryngology* **2012**, *269*, 623–628 doi: 10.1007/s00405-011-1607-x.
198. Murr, L.E.; Gaytan, S.; Medina, F.; Lopez, H.; Martinez, E.; Machado, B.; Hernandez, D.; Martinez, L.; Lopez, M.; Wicker, R. Next-generation biomedical implants using additive manufacturing of complex, cellular and functional mesh arrays. *Philosophical Transactions of the Royal Society A: Mathematical, Physical and Engineering Sciences* **2010**, *368*, 1999–2032 doi: 10.1098/rsta.2010.0010.

- 
199. Ramakrishnaiah, R.; Mohammad, A.; Divakar, D.D.; Kotha, S.B.; Celur, S.L.; Hashem, M.I.; Vallittu, P.K.; Rehman, I.U. Preliminary fabrication and characterization of electron beam melted Ti-6Al-4V customized dental implant. *Saudi journal of biological sciences* **2017**, *24*, 787–796 doi: 10.1016/j.sjbs.2016.05.001.
200. Aquino, R.P.; Barile, S.; Grasso, A.; Saviano, M. Envisioning smart and sustainable healthcare: 3D printing technologies for personalized medication. *Futures* **2018**, *103*, 35–50 doi: 10.1016/j.futures.2018.03.002.
201. Emelogu, A.; Marufuzzaman, M.; Thompson, S.M.; Shamsaei, N.; Bian, L. Additive manufacturing of biomedical implants: a feasibility assessment via supply-chain cost analysis. *Additive Manufacturing* **2016**, *11*, 97–113 doi: 10.1016/j.addma.2016.04.006.
202. standards, I. Additive manufacturing - general principles - fundamentals and vocabulary. 2021; Vol. 52900.
203. Tuomi, J.; Paloheimo, K.; Björkstrand, R.; Salmi, M.; Paloheimo, M.; Mäkitie, A.A. Medical applications of rapid prototyping – from applications to classification. In *Innovative Developments in Design and Manufacturing*, CRC Press: **2009**; Vol. 1, pp. 719–722.
204. Ventola, C.L. Medical applications for 3D printing: current and projected uses. *Pharmacy and Therapeutics* **2014**, *39*, 704–712.
205. Salmi, M. Possibilities of preoperative medical models made by 3D printing or additive manufacturing. *Journal of Medical Engineering* **2016**, *2016*, 1–6 doi: 10.1155/2016/6191526.
206. Marro, A.; Bandukwala, T.; Mak, W. Three-dimensional printing and medical imaging: a review of the methods and applications. *Current problems in diagnostic radiology* **2016**, *45*, 2–9 doi: 10.1067/j.cpradiol.2015.07.009.
207. Bücking, T.M.; Hill, E.R.; Robertson, J.L.; Maneas, E.; Plumb, A.A.; Nikitichev, D.I. From medical imaging data to 3D printed anatomical models. *PloS one* **2017**, *12*, 178540–178550 doi: 10.1371/journal.pone.0178540.
208. Wang, X.; Xu, S.; Zhou, S.; Xu, W.; Leary, M.; Choong, P.; Qian, M.; Brandt, M.; Xie, Y.M. Topological design and additive manufacturing of porous metals for bone scaffolds and orthopaedic implants: a review. *Biomaterials* **2016**, *83*, 127–141 doi: 10.1016/j.biomaterials.2016.01.012.
209. Salmi, M.; Tuomi, J.; Paloheimo, K.; Paloheimo, M.; Björkstrand, R.; Mäkitie, A.A.; Mesimäki, K.; Kontio, R. Digital design and rapid manufacturing in orbital wall reconstruction. In *Innovative Developments in Design and Manufacturing*, CRC Press: **2009**; Vol. 1, pp. 357–360.
210. Prasad, L.K.; Smyth, H. 3D printing technologies for drug delivery: a review. *Drug development and industrial pharmacy* **2016**, *42*, 1019–1031 doi: 10.3109/03639045.2015.1120743.
211. Akmal, J.S.; Salmi, M.; Mäkitie, A.; Björkstrand, R.; Partanen, J. Implementation of industrial additive manufacturing: intelligent implants and drug delivery systems. *Journal of functional biomaterials* **2018**, *9*, 41–55 doi: 10.3390/jfb9030041.

212. Hieu, L.; Bohez, E.; Vander Sloten, J.; Phien, H.; Vatcharaporn, E.; Binh, P.; An, P.; Oris, P. Design for medical rapid prototyping of cranioplasty implants. *Rapid Prototyping Journal* **2003**, *9*, 175–186 doi: 10.1108/13552540310477481.
213. Hieu, L.; Bohez, E.; Vander Sloten, J.; Phien, H.; Esichaikul, V.; Binh, P.; An, P.; To, N.; Oris, P. Design and manufacturing of personalized implants and standardized templates for cranioplasty applications. *2002 IEEE International Conference on Industrial Technology, 2002 IEEE ICIT'02.* **2002**, *2*, 1025-1030 doi: 10.1109/ICIT.2002.1189312.
214. Liu, K.; Zhang, Q.; Li, X.; Zhao, C.; Quan, X.; Zhao, R.; Chen, Z.; Li, Y. Preliminary application of a multi-level 3D printing drill guide template for pedicle screw placement in severe and rigid scoliosis. *European Spine Journal* **2017**, *26*, 1684–1689 doi: 10.1007/s00586-016-4926-1.
215. Paterson, A.M.; Donnison, E.; Bibb, R.J.; Ian Campbell, R. Computer-aided design to support fabrication of wrist splints using 3D printing: a feasibility study. *Hand Therapy* **2014**, *19*, 102–113 doi: 10.1177/1758998314544802.
216. Ten Kate, J.; Smit, G.; Breedveld, P. 3D-printed upper limb prostheses: a review. *Disability and Rehabilitation: Assistive Technology* **2017**, *12*, 300–314 doi: 10.1080/17483107.2016.1253117.
217. Herbert, N.; Simpson, D.; Spence, W.D.; Ion, W. A preliminary investigation into the development of 3-D printing of prosthetic sockets. *Journal of Rehabilitation Research & Development* **2005**, *42*, 141–146 doi: 10.1682/jrrd.2004.08.0134.
218. Rosický, J.; Grygar, A.; Chapcak, P.; Bouma, T.; Rosicky, J. Application of 3D Scanning in Prosthetic and Orthotic Clinical Practice. In *Proceedings of Proceedings of the 7th international conference on 3D body scanning technologies* **2016**, *7*, 88-97 doi: 10.15221/16.088.
219. Bártolo, P.; Chua, C.; Almeida, H.; Chou, S.; Lim, A. Biomanufacturing for tissue engineering: present and future trends. *Virtual and Physical Prototyping* **2009**, *4*, 203–216 doi: 10.1080/17452750903476288.
220. Bidanda, B.; Bártolo, P.J. *Virtual prototyping & bio manufacturing in medical applications*, 2 ed.; Springer: **2007**; Vol. 1.
221. Danna, N.R.; Leucht, P. Designing resorbable scaffolds for bone defects. *Bulletin of the NYU Hospital for Joint Diseases* **2019**, *77*, 39–44.
222. Zadpoor, A.A. Design for additive bio-manufacturing: from patient-specific medical devices to rationally designed meta-biomaterials. *International Journal of Molecular Sciences* **2017**, *18*, 1607–1625 doi: 10.3390/ijms18081607.
223. Culmone, C.; Smit, G.; Breedveld, P. Additive manufacturing of medical instruments: a state-of-the-art review. *Additive manufacturing* **2019**, *27*, 461–473 doi: 10.1016/j.addma.2019.03.015.
224. Tappa, K.; Jammalamadaka, U. Novel biomaterials used in medical 3D printing techniques. *Journal of functional biomaterials* **2018**, *9*, 17–33 doi: 10.3390/jfb9010017.

- 
225. Wang, K.; Ho, C.-C.; Zhang, C.; Wang, B. A review on the 3D printing of functional structures for medical phantoms and regenerated tissue and organ applications. *Engineering* **2017**, *3*, 653–662 doi: 10.1016/J.ENG.2017.05.013.
226. Bonfield, C.M.; Kumar, A.R.; Gerszten, P.C. The history of military cranioplasty. *Neurosurgical focus* **2014**, *36*, 18–22 doi: 10.3171/2014.1.FOCUS13504.
227. Morselli, C.; Zaed, I.; Tropeano, M.; Cataletti, G.; Iaccarino, C.; Rossini, Z.; Servadei, F. Comparison between the different types of heterologous materials used in cranioplasty: a systematic review of the literature. *Journal of neurosurgical sciences* **2019**, *63*, 723–736 doi: 10.23736/S0390-5616.19.04779-9.
228. Khader, B.A.; Towler, M.R. Materials and techniques used in cranioplasty fixation: a review. *Materials Science & Engineering C–Materials for Biological Applications* **2016**, *66*, 315–322 doi: 10.1016/j.msec.2016.04.101.
229. Ghasemi-Mobarakeh, L.; Kolahreez, D.; Ramakrishna, S.; Williams, D. Key terminology in biomaterials and biocompatibility. *Current Opinion in Biomedical Engineering* **2019**, *10*, 45–50 doi: 10.1016/j.cobme.2019.02.004.
230. Kalaskar, D.M. *3D printing in medicine*, 2 ed.; Woodhead Publishing: **2017**; Vol. 1.
231. Souza, F.Á.; Furtado, T.S.M.; Dayube, U.R.C.; Melo, W.M.; Nishioka, R.S.; Poli, P.P.; Maiorana, C.; de Carvalho, P.S.P. Comparative in vivo study of alloy titanium implants with two different surfaces: biomechanical and SEM analysis. *Clinical oral investigations* **2019**, *23*, 1–15 doi: 10.1007/s00784-019-02872-6.
232. Pina, S.; Ferreira, J.M. Bioresorbable plates and screws for clinical applications: a review. *Journal of Healthcare Engineering* **2012**, *3*, 243–260 doi: 10.1260/2040-2295.3.2.243.
233. Ghiasi, B.; Sefidbakht, Y.; Jònec, M. Hydroxyapatite for Biomedicine and Drug Delivery. In *Nanomaterials for Advanced Biological Applications*, Springer: **2019**; Vol. 104, pp. 85–120.
234. Perale, G.; Hilborn, J. *Bioresorbable polymers for biomedical applications: from fundamentals to translational medicine*, 1 ed.; Woodhead Publishing: **2016**; Vol. 1.
235. Stal, L.J. Biopolymer. In *encyclopedia of astrobiology*, Springer Berlin Heidelberg: 2011; Vol. 1, pp.225–344 .
236. Ruso, J.M.; Messina, P.V. Biopolymers in regenerative medicine: overview, current advances and future trends. In *Biopolymers for Medical Applications*, 1 ed.; CRC Press: **2017**; Vol. 1, pp. 9–45.
237. Zhen, Z.; Xi, T.; Zheng, Y. Surface modification by natural biopolymer coatings on magnesium alloys for biomedical applications. In *Surface Modification of Magnesium and its Alloys for Biomedical Applications*, Woodhead Publishing: **2015**; Vol. 2, pp. 301–333.
238. Pertici, G. Introduction to bioresorbable polymers for biomedical applications. In *Bioresorbable polymers for biomedical applications*, Woodhead Publishing: **2017**; Vol. 1, pp. 3–29.

239. Sukegawa, S.; Kanno, T.; Yamamoto, N.; Nakano, K.; Takabatake, K.; Kawai, H.; Nagatsuka, H.; Furuki, Y. Biomechanical loading comparison between titanium and unsintered hydroxyapatite/poly-L-lactide plate system for fixation of mandibular subcondylar fractures. *Materials* **2019**, *12*, 1557–1569 doi: 10.3390/ma12091557.
240. Rodriguez-Contreras, A. Recent advances in the use of polyhydroxyalkanoates in biomedicine. *Bioengineering* **2019**, *6*, 82–96 doi: 10.3390/bioengineering6030082.
241. Brunel, D.G.; Pachekoski, W.M.; Dalmolin, C.; Agnelli, J.A.M. Natural additives for poly(hydroxybutyrate-co-hydroxyvalerate)-PHBV: effect on mechanical properties and biodegradation. *Materials Research* **2014**, *17*, 1145–1156 doi: 10.1590/1516-1439.235613.
242. El-Hadi, A.M. Miscibility of crystalline/amorphous/crystalline biopolymer blends from PLLA/PDLLA/PHB with additives. *Polymer-Plastics Technology and Materials* **2019**, *58*, 31–39 doi: 10.1080/03602559.2018.1455863.
243. Fizir, M.; Dramou, P.; Dahiru, N.S.; Ruya, W.; Huang, T.; He, H. Halloysite nanotubes in analytical sciences and in drug delivery: a review. *Microchimica Acta* **2018**, *185*, 389–422 doi: 10.1007/s00604-018-2908-1.
244. Wypych, G. *Functional fillers: chemical composition, morphology, performance, applications*, 1 ed.; ChemTec Publishing: **2018**; Vol. 1.
245. Dorozhkin, S.V. Functionalized calcium orthophosphates (CaPO<sub>4</sub>) and their biomedical applications. *Journal of Materials Chemistry B* **2019**, *7*, 7471–7489 doi: 10.1039/C9TB01976F.
246. Ma, B.; Han, J.; Zhang, S.; Liu, F.; Wang, S.; Duan, J.; Sang, Y.; Jiang, H.; Li, D.; Ge, S. Hydroxyapatite nanobelt/poly(lactic acid) Janus membrane with osteoinduction/barrier dual functions for precise bone defect repair. *Acta biomaterialia* **2018**, *71*, 108–117 doi: 10.1016/j.actbio.2018.02.033.
247. Narayanan, T.S.; Park, I.-S.; Lee, M.-H. *Surface modification of magnesium and Its alloys for biomedical applications: modification and coating techniques*, 1 ed.; Woodhead Publishing: **2015**; Vol. 2.
248. Iratwar, S.W.; Pisulkar, S.; Patil, A. Cranioplasty for prosthetic cranial reconstruction of skull defects using pre-fabricated polymethyl methacrylate grafts reinforced by hydroxyapatite particles intraoperatively in rural population of central india region: a pilot study. *International Journal of Medical and Biomedical Studies* **2019**, *3*, 155–158 doi: 10.32553/ijmbs.v3i11.738.
249. Galindo, T.G.P.; Chai, Y.; Tagaya, M. Hydroxyapatite nanoparticle coating on polymer for constructing effective biointeractive interfaces. *Journal of Nanomaterials* **2019**, *2019*, 1–23 doi: 10.1155/2019/6495239.
250. Ramesh, N.; Moratti, S.C.; Dias, G.J. Hydroxyapatite-polymer biocomposites for bone regeneration: a review of current trends. *Journal of Biomedical Materials Research Part B: Applied Biomaterials* **2018**, *106*, 2046–2057 doi: 10.1002/jbm.b.33950.



## **VII. APPENDIX.**



## VII.1. Table index.

Table I.2.3.1. Effectiveness of some plasticizers in terms of mechanical and thermal properties of PLA. Adapted from [157].....	61
Table I.2.3.2. Effectiveness of some plasticizers in terms of mechanical and thermal properties of P(3HH- <i>co</i> -3BV). Adapted from [157]. .....	61
Table I.3.4.1. Calcium orthophosphate formulations [245].....	74
Table I.3.4.2. Hydroxyapatite with biopolymers. Reproduced from [250]......	76
Table III.1.1.1. Code and composition in weight % - (wt.%) of binary blends of P(3HB- <i>co</i> -3HHx)/PCL. ....	101
Table III.1.1.2. Thermal properties of P(3HB- <i>co</i> -3HHx)/PCL binary blends during the first heating cycle 15 day after processing to complete secondary crystallization. ....	105
Table III.1.1.3. Thermal properties of P(3HB- <i>co</i> -3HHx)/PCL binary blends obtained during the second heating cycle after a heating-cooling process to remove thermal history. ....	108
Table III.1.1.4. CLTE of P(3HB- <i>co</i> -3HHx)/PCL blends with different PCL wt.%, below and above $T_g$ , obtained by TMA.....	111
Table III.1.1.5. Summary of the mechanical properties from tensile, flexural and hardness tests, of P(3HB- <i>co</i> -3HHx)/PCL.....	115
Table III.1.2.1. Summary of sample compositions according to the weight content - wt.% of P(3HB- <i>co</i> -3HHx) and ASF and the addition of OLA as parts Per Hundred Resin - phr of P(3HB- <i>co</i> -3HHx)-ASF composite.....	137
Table III.1.2.2. Summary of the mechanical properties of the P(3HB- <i>co</i> -3HHx)-ASF/OLA composites with different compositions. ....	141
Table III.1.2.3. Main thermal parameters of the P(3HB- <i>co</i> -3HHx)-ASF/OLA composites with different compositions, obtained by DSC. ....	149
Table III.1.2.4. Summary of the main thermal degradation parameters of P(3HB- <i>co</i> -3HHx)-ASF/OLA composites with different compositions. ....	151
Table III.1.2.5. Main DMTA parameters of P(3HB- <i>co</i> -3HHx)-ASF/OLA composites with different compositions. ....	153
Table III.1.2.6. Summary of the main TMA properties of neat P(3HB- <i>co</i> -3HHx) and P(3HB- <i>co</i> -3HHx)-ASF/OLA with different compositions. ....	156
Table III.1.2.7. Values of the diffusion coefficient and the corrected diffusion coefficient for P(3HB- <i>co</i> -3HHx) and the P(3HB- <i>co</i> -3HHx)-ASF composites processed with OLA. ....	159
Table III.1.3.1. Physical properties and chemical structure of geranyl esters uses as plasticizers for P3HB. ....	177
Table III.1.3.2. Composition and labelling of different formulations of P3HB plasticized with different geranyl esters in terms of weigh percentage - wt.% and per hundred resin - phr. ....	180
Table III.1.3.3. Solubility parameters of P3HB and the different geraniol esters employed as plasticizers. ....	183
Table III.1.3.4. Main mechanical properties of the P3HB and plasticized P3HB formulations with different geranyl esters. ....	185
Table III.1.3.5. Main thermal properties of neat P3HB and plasticized P3HB formulations with different geranyl esters. ....	187

Table III.1.3.6. Main thermal properties of P3HB and plasticized P3HB formulations with different geranyl esters, obtained by DMTA. ....	189
Table III.2.1.1. Printing parameters used for G-code generation of P(3HB-co-3HHx) 3D-printed materials.....	214
Table III.2.1.2. Printing conditions used for 3D-printing P(3HB-co-3HHx)-based materials.....	215
Table III.2.1.3. Summary of the mechanical properties of the samples printed with transversal (T) raster angle and with the layer fan working. ....	217
Table III.2.1.4. Summary of the mechanical properties of the samples printed with longitudinal (L) raster angle and with the layer fan working. ....	217
Table III.2.1.5. Summary of the mechanical properties of the samples printed with transversal (T) raster angle and without the layer fan. ....	221
Table III.2.1.6. Summary of the mechanical properties of the samples printed with longitudinal (L) raster and without the layer fan. ....	221
Table III.2.1.7. Summary of the DSC test of the samples under different AM conditions. ....	228
Table III.2.2.1. Code and composition of the samples prepared according to the % weight content - wt.% of P(3HB-co-3HHx) and nHA. ....	252
Table III.2.2.2. Number of tested samples (n) for each injection-moulded P(3HB-co-3HHx)/nanohydroxyapatite parts and the type of statistical test performed for each testing method with level of significance (p).....	255
Table III.2.2.3. Mechanical properties of the injection-moulded parts of P(3HB-co-3HHx)/nHA.....	256
Table III.2.2.4. Spearman's test for each mechanical property. ....	256
Table III.2.2.5. Thermal properties of the injection-moulded P(3HB-co-3HHx)/nHA parts.....	261
Table III.2.2.6. Main thermal degradation parameters of the injection-moulded P(3HB-co-3HHx)/nHA parts. ....	264
Table III.2.2.7. Thermo-mechanical properties of the injection-moulded P(3HB-co-3HHx)/nHA parts.....	266
Table III.2.3.1. P(3HB-co-3HHx) characteristics according to the supplier.....	289
Table III.2.3.2. Printing parameters for the tensile test specimens and the scaffolds. ....	290
Table III.2.3.3. DSC characteristics of the P(3HB-co-3HHx)/nHA nanocomposites. ....	296
Table III.2.3.4. Thermal degradation properties of the P(3HB-co-3HHx)/nHA nanocomposites. ....	298
Table III.2.3.5. Main porosity results for the AM scaffolds.....	299
Table III.3.1.1. Some thermal and physicochemical properties of DBI.....	328
Table III.3.1.2. Summary of the plasticized PLA formulations with DBI according to the weight content - wt.%.....	331
Table III.3.1.3. Summary of the optimized temperature profiles for the injection moulding process of PLA and plasticized PLA formulations with DBI. ....	331
Table III.3.1.4. Summary of the PLA and DBI solubility parameters according to the Hoflyzer-Van Krevelen group contribution method and RED. ....	334
Table III.3.1.5. Summary of mechanical properties of neat PLA and plasticized PLA	

---

formulations with different DBI contents. ....	340
Table III.3.1.6. Summary of thermal properties of neat PLA and plasticized PLA formulations with different DBI contents. ....	344
Table III.3.1.7. Summary of thermal degradation properties of neat PLA, DBI and plasticized PLA formulations with different DBI contents.....	347
Table III.3.1.8. Summary of the DMTA properties of neat PLA and plasticized PLA formulations with different DBI contents. ....	349
Table III.3.1.9. Summary of the TMA results of neat PLA and plasticized PLA formulations with different DBI content. ....	351
Table III.3.2.1. Main commercial PLA employed to the manufacture of the samples. ...	375
Table III.3.2.2. FDM parameters employed for the sample manufacture. ....	375
Table III.3.3.1. Dimensions for femur model employed in the FEM model. ....	397
Table III.3.3.2. Isotropic properties of materials. ....	397

## VII.2. Figure index.

Figure I.1.2.1. Classification of thermoplastic polymers according to their origin (petrochemical or renewable resources) and their potential biodegradation at the end of the life cycle.....	33
Figure I.1.3.1. Scheme of biobased poly(ethylene) synthesis from sugarcane. ....	35
Figure I.1.3.2. Chemical structure of a) petroleum-based poly(sulfone), b) isosorbide-based poly(sulfone), c) petroleum-based poly(carbonate), and d) isosorbide-based poly(carbonate).....	36
Figure I.1.3.3. Chemical structure of a) petroleum-based poly(ethylene terephthalate) and b) biobased poly(ethylene furanoate) from 2,5-furandicarboxylic acid. ....	37
Figure I.1.3.4. Schematic representation of the molecular structure of castor oil, basic triglyceride for obtaining sebacic acid for the synthesis of bio poly(amides) and base polyol for the synthesis of bio poly(urethanes). ....	38
Figure I.1.3.5. Schematic representation of the chemical structure of different types of polyamides with different renewable content.....	39
Figure I.1.3.6. Schematic representation of the monomer unit of various petroleum-derived poly(esters) with the additional feature of biodegradability. ....	40
Figure I.1.3.7. Schematic representation of the chemical structure of cellulose with $\beta$ -(1 $\rightarrow$ 4) glycosidic linkages. ....	41
Figure I.1.3.8. Representation of the chemical structure of: a) cellulose and b) chitin. ....	42
Figure I.1.3.9. Schematic representation of the constituent chains of starch: linear amylose and branched amylopectin molecules, b) comparison of the structure of polysaccharides based on glycosidic bonds: starch, glycogen and cellulose. ....	43
Figure I.1.3.10. Schematic representation of the general basic unit of PHA and the different possibilities depending on the repeating unit "m" and the radical or side group "R" (up) and schematic representation of the monomer unit of the most commercially used PHA (down). ....	45
Figure I.2.1.1. a) Schematic representation of PLA synthesis routes from biomass fermentation. ....	47
Figure I.2.1.2. Chemical structure of lactic acid isomers.....	48
Figure I.2.1.3. Schematic plot of the hydrolytic degradation or cleavage of polylactide. 49	
Figure I.2.2.1. Electron microscopy image of <i>C. necator</i> DSM 545 cells with P3HB inclusions. Image reproduced from [132]. ....	50
Figure I.2.2.2. Classification of PHA depending on the carbon atoms in the monomer unit. ....	51
Figure I.2.2.3. Schematic representation of the mechanism of thermal degradation of poly(3-hydroxybutyrate) by cis-elimination. ....	53
Figure I.2.3.2. Schematic representation of the chemical structure of different P3HB-based copolymers with improved toughness. ....	56
Figure I.2.3.4. Schematic representation of the different classical plasticization theories. Adapted from [154]. ....	58
Figure I.2.3.5. Schematic representation of the chemical structure of some common plasticizers for PLA and PHA.....	60
Figure I.3.1.1. Properties of the different AM processes. ....	63

Figure I.3.2.1. Main benefits of AM in medical field.....	65
Figure I.3.2.2. a) implants, b) medical models, c) tools, instruments and parts for medical devices and d) scaffolds for biomanufacturing.....	66
Figure I.3.2.3. Workflow employed for the obtention of medical models.....	67
Figure I.3.2.4. Workflow employed for biomanufacturing.....	69
Figure I.3.3.1. Additive manufacturing processes applied in medical applications.....	70
Figure II.1. Summary diagram of the work carried out.....	81
Figure III.1.1.1. Chemical structure of 3-hydroxyalkanoic acids used to synthesize P(3HB-co-3HHx).....	99
Figure III.1.1.2. Comparative plot of the differential scanning calorimetry, DSC thermograms of P(3HB-co-3HHx)/PCL blends: a) first heating cycle after processing and aging for 15 days, b) second heating after cooling in a controlled rate.....	106
Figure III.1.1.4. DMTA of P(3HB-co-3HHx)/PCL blends: a) $E'$ vs temperature, and b) $\tan \delta$ vs temperature.....	113
Figure III.1.1.5. Plot evolution of the impact absorbed energy of neat P(3HB-co-3HHx) and P(3HB-co-3HHx)/PCL blends with increasing PCL wt.%.....	116
Figure III.1.1.6. FESEM images at $1000 \times$ of the impact fracture surface morphologies of P(3HB-co-3HHx)/PCL binary blends with different PCL wt.%: a) 10, b) 20, c) 30 and d) 40....	117
Figure III.1.1.7. FESEM images at $1000 \times$ of the impact fracture surface morphologies of P(3HB-co-3HHx)/PCL binary blends, subjected to PCL selective extraction, with different PCL wt.%: a) 10, b) 20, c) 30 and d) 40.....	118
Figure III.1.2.1. Visual aspect of almond shell flour particles obtained by FESEM at $100 \times$ and a histogram of their size distribution.....	136
Figure III.1.2.2. FESEM images at $1000 \times$ (left side) and $2500 \times$ (right side) corresponding to P(3HB-co-3HHx)-ASF composite with 30 wt.% ASF with different OLA content, a) & b) 0 phr OLA, b) & c) 10 phr OLA and e) & f) 20 phr OLA.....	144
Figure III.1.2.3. Comparative plot of the second heating curves obtained by dynamic DSC of the different P(3HB-co-3HHx)-ASF/OLA composites with different compositions.....	147
Figure III.1.2.4. Comparative plot P(3HB-co-3HHx)-ASF/OLA composites with different compositions: a) TGA curves vs temperature and b) DTG vs temperature.....	150
Figure III.1.2.5. Comparative plot of DMTA curves of P(3HB-co-3HHx)-ASF/OLA composites with different compositions: a) Storage modulus vs temperature and b) $\tan \delta$ vs temperature.....	155
Figure III.1.2.6. Water uptake of P(3HB-co-3HHx)-ASF/OLA composites with different compositions. Evolution of the water uptake for a period of 9 weeks.....	158
Figure III.1.3.1. Chemical structure of poly(3-hydroxybutyrate) and different geranyl-based plasticizers.....	178
Figure III.1.3.2. DSC analysis of neat P3HB and plasticized P3HB formulations with different geranyl esters: a) first heating scan, b) cooling and c) second heating scan.....	188
Figure III.1.3.3. DMTA curves of neat P3HB and plasticized P3HB formulations with different geranyl esters in terms of: a) $E'$ vs temperature and b) $\tan \delta$ vs temperature.....	190
Figure III.1.3.4. FESEM images of impact fractured samples ( $250 \times$ and insets at $2500 \times$ ) of neat P3HB and plasticized P3HB formulations with different geranyl esters: a) P3HB, b) P3HB/GEA, c) P3HB/GEP, d) P3HB/GEB and e) P3HB/GEI.....	191

Figure III.1.3.5. Visual aspect of neat P3HB and plasticized P3HB formulations with different geranyl esters at different incubation times during the disintegration test in controlled compost soil.....	193
Figure III.1.3.6. Weight loss evolution over time at the disintegration test in controlled compost soil of neat P3HB and plasticized P3HB formulations with different geranyl esters...194	
Figure III.2.1.1. Summary of the ANOVA analysis for PHPH 3D-printed samples by using the layer fan during the cooling process. This shows the Pareto diagram standardized effect (left row) and the main effects diagram (right row) for tensile strength, elongation at break and tensile modulus.....	218
Figure III.2.1.2. Summary of the ANOVA analysis for PHPH 3D-printed samples by switching off the layer fan during the cooling process. This shows the Pareto diagram standardized effect (left row) and the main effects diagram (right row) for tensile strength, elongation at break and tensile modulus. ....	222
Figure III.2.1.3. Summary of the ANOVA analysis for 3D-printed P(3HB-co-3HHx) specimens with and without the layer fan, Pareto diagram standardized effect (left row) and the main effects diagram (right row) for tensile strength, elongation at break and tensile modulus. ....	225
Figure III.2.1.4. Fracture morphology of 3D-printed P(3HB-co-3HHx) tensile specimens obtained by Field Emission Scanning Electron Microscopy FESEM: a) Image taken at 100 × magnifications of a specimen 3D-printed with transversal raster (T) and b) Image taken at 200 × magnifications of a specimen 3D-printed with longitudinal raster (L).....	227
Figure III.2.1.5. Comparison of the normalized FTIR spectra in the 1770 - 1690 cm <sup>-1</sup> range, for 3D-printed specimens with different heated bead temperatures, a constant hotend of 175 °C, and the layer fan switched on. Deconvoluted peaks are indicated in dashed lines. ....	230
Figure III.2.1.6. Comparison of the normalized FTIR spectra in the 1770 - 1690 cm <sup>-1</sup> range, for different samples 3D-printed at 175 °C hotend and 60 °C heated bed with and without layer fan. Deconvoluted peaks are indicated in dashed lines. ....	231
Figure III.2.1.7. Examples of the P(3HB-co-3HHx) 3D-printed parts: a) dog bone samples with both infills; b) pencil pot and c) benchy and a calibration cube.....	232
Figure III.2.2.1. Evolution of the main tensile properties of the injection-moulded parts of P(3HB-co-3HHx) with the content of nHA. * Indicates a significant difference compared with the previous sample (p < 0.05). ....	257
Figure III.2.2.2. Evolution of the main flexural properties in the injection-moulded parts of P(3HB-co-3HHx) with the content of nHA. * Indicates a significant difference compared with the previous sample (p < 0.05).....	258
Figure III.2.2.3. DSC thermograms taken during second heating of the injection-moulded P(3HB-co-3HHx)/nHA parts. ....	261
Figure III.2.2.4. Summary of the TGA test: a) mass loss curves <i>vs</i> temperature and b) first derivate thermogravimetric curves <i>vs</i> temperature.....	262
Figure III.2.2.5. Summary of the DMTA test: a) storage modulus <i>vs</i> temperature and b) tan δ <i>vs</i> temperature of the injection-moulded P(3HB-co-3HHx)/nHA parts. ....	265
Figure III.2.2.6. Processing steps carried out to prepare the P(3HB-co-3HHx)/nHA parts; from left to right: as-received P(3HB-co-3HHx) pellets and nHA powder, compounded pellets of the nanocomposite, injection-moulded parts. ....	268
Figure III.2.2.7. FESEM images of the nanohydroxyapatite - nHA powder. Image was taken at 10000 × with scale marker 150 nm. ....	268
Figure III.2.2.8. FESEM images of the fracture surfaces of the injection-moulded P(3HB-	



<i>co</i> -3HHx)/nHA parts of: a) neat P(3HB- <i>co</i> -3HHx), b) P(3HB- <i>co</i> -3HHx)/2.5nHA, c) P(3HB- <i>co</i> -3HHx)/5nHA, d) P(3HB- <i>co</i> -3HHx)/10nHA and e) P(3HB- <i>co</i> -3HHx)/20nHA. Images were taken at 500 × and with scale markers of 10 μm. Inset image showing the detail of the microparticles was taken at 2500 × with scale marker of 2 μm. ....	269
Figure III.2.2.9. FESEM images of the fracture surfaces of the injection-moulded P(3HB- <i>co</i> -3HHx)/nHA parts after selective attack with 6M HCl for 12 h: a) P(3HB- <i>co</i> -3HHx)/2.5nHA, b) P(3HB- <i>co</i> -3HHx)/5nHA, c) P(3HB- <i>co</i> -3HHx)/10nHA and d) P(3HB- <i>co</i> -3HHx)/20nHA. Images were taken at 1000 × with scale marker of 5 μm. ....	270
Figure III.2.3.1. Geometry and raster angle of the tensile test specimens a) and scaffolds b). ....	291
Figure III.2.3.2. Mechanical properties of the P(3HB- <i>co</i> -3HHx)/nHA tensile specimens at different raster angles and compared to injection moulding - IM. ....	294
Figure III.2.3.3. DSC thermograms of the P(3HB- <i>co</i> -3HHx)/nHA nanocomposites. ....	297
Figure III.2.3.4. Rheological behavior of the P(3HB- <i>co</i> -3HHx)/nHA nanocomposites. ....	299
Figure III.2.3.5. Degradation behavior in PBS of the developed scaffolds over immersion weeks. Effect over : a) weight gain, b) weight loss and c) pH. ....	300
Figure III.2.3.6. FE-SEM images of the surface of scaffolds at week 0 (left) and week 8 (right) for the different compositions. Images taken at × 1000. ....	302
Figure III.2.3.7. Compression properties of the scaffolds at different immersion times: a) stress at yield point and b) deformation at yield point. ....	303
Figure III.2.3.8. Surface chemical composition measured by FTIR-ATR of the scaffolds: a) initial state b) after 8 weeks of immersion in PBS. ....	304
Figure III.3.1.1. Scheme of the reaction of itaconic acid - IA and n-butanol to give dibutyl itaconate - DBI. ....	327
Figure III.3.1.2. Bagley's solubility diagram for PLA and DBI where the $\delta_v = (\delta_d^2 + \delta_p^2)^{1/2}$ . ....	335
Figure III.3.1.3. Rheological behaviour of neat PLA and plasticized PLA formulations with different DBI content: a) viscosity <i>vs</i> shear rate at a constant temperature of 210 °C, b) viscosity <i>vs</i> shear rate after iteration process to give similar viscosity profile and c) Eta-zero <i>vs</i> DBI content. ....	336
Figure III.3.1.4. a) Tensile stress <i>vs</i> elongation plots for neat PLA and plasticized PLA formulations with different DBI contents and b) appearance of PLA/DBI specimens after the tensile test (left neat PLA and right 20DBI-PLA) (scale bar = 100 mm). ....	338
Figure III.3.1.5. FESEM images of the fractured surfaces from tensile tests taken at 500 × and inset at 5000 ×. a) PLA, b) 2.5DBI-PLA, c) 5DBI-PLA, d) 10DBI-PLA, e) 15DBI-PLA and f) 20DBI-PLA (scale bar = 10 μm in all images except the inset scale bar = 1 μm). ....	342
Figure III.3.1.6. DSC thermograms of the second heating step for neat PLA and plasticized PLA formulations with different DBI contents (scale bar = 5 mW). ....	343
Figure III.3.1.7. TGA of neat PLA, DBI and plasticized PLA formulations with different DBI contents: a) weight loss curves <i>vs</i> temperature and b) first derivative - DTG curves <i>vs</i> temperature. ....	346
Figure III.3.1.8. TGA of DBI in terms of weight loss curves <i>vs</i> time for different isothermal temperatures. ....	347
Figure III.3.1.9. DMTA curves of neat PLA and plasticized PLA formulations with different DBI contents: a) $E'$ <i>vs</i> temperature and b) $\tan \delta$ <i>vs</i> temperature. ....	350

Figure III.3.1.10. Comparative plot of dimensional change *vs* temperature obtained by TMA corresponding to neat PLA and plasticized PLA formulations with different DBI contents. ....351

Figure III.3.2.1. Optical (8 ×) images. Images from a) to c) show a detail of the infill pattern a) rectilinear 20 %, b) honeycomb and c) Hilbert 20 %. Images from d) to l) show a detail of fractured tensile test samples: rectilinear 20 %, e) rectilinear 60 %, f) rectilinear 90 %, g) honeycomb 20 %, h) honeycomb 60 %, i) honeycomb 90 %, j) Hilbert 20 %, k) Hilbert 60 % and l) Hilbert 90 %. Images from m) to u) show a detail of impact test samples: m) rectilinear 20 %, n) rectilinear 60 %, o) rectilinear 90 %, p) honeycomb 20 %, q) honeycomb 60 %, r) honeycomb 90 %, s) Hilbert 20 %, t) Hilbert 60 % and u) Hilbert 90 %.....376

Figure III.3.2.2. DSC thermograms for raw PLA from 0 °C up to 350 °C.....378

Figure III.3.2.3. Plot evolution of weight and printing time for different filling patterns as function of their infill percentage. Continuous line indicates the sample weight, while dashed line the printing time. ....379

Figure III.3.2.4. Plot evolution of tensile modulus and tensile strength for different filling patterns as function of their infill percentage. Continuous lines indicate tensile modulus while dashed lines indicate tensile strength. ....381

Figure III.3.2.5. Plot evolution of elongation and Charpy’s impact energy absorbed for different filling patterns as function of the infill percentage. Continuous lines indicate the elongation values and dashed lines the Charpy’s impact energy. ....382

Figure III.3.2.6.  $G'$  and  $\tan \delta$  *vs* temperature for different infill amounts of honeycomb samples. Continuous lines indicate storage modulus while dashed line  $\tan \delta$ . ....383

Figure III.3.3.1. 3D model of femur shaft fracture with fixation plate, titanium (green), PLA (blue).....396

Figure III.3.3.2. Femur section with fixation plate, titanium (green), PLA (blue).....397

Figure III.3.3.3. Fixation plates with screws, titanium (green), PLA (blue). ....397

Figure III.3.3.4. Load application on the rigid region. ....398

Figure III.3.3.5. Pressure in MPa (up) and displacement in mm (down), 3D printed PLA (left) and Titanium (right). ....399

Figure III.3.3.6. Von Mises stress (MPa) distribution for titanium (up) and 3D printed PLA (down).....401

Figure III.3.3.7. Von Mises stress distribution for 30 days degradation PLA.....401

Figure III.3.3.8. Pressure contact distribution for 30 days degradation PLA. ....402